MAGNETOHYDRODYNAMIC WAVES IN THE SOLAR ATMOSPHERE: HEATING AND SEISMOLOGY

EDITED BY: Tom Van Doorsselaere, Valery M. Nakariakov, Bo Li and
Patrick Antolin

PUBLISHED IN: Frontiers in Astronomy and Space Sciences and
Frontiers in Physics

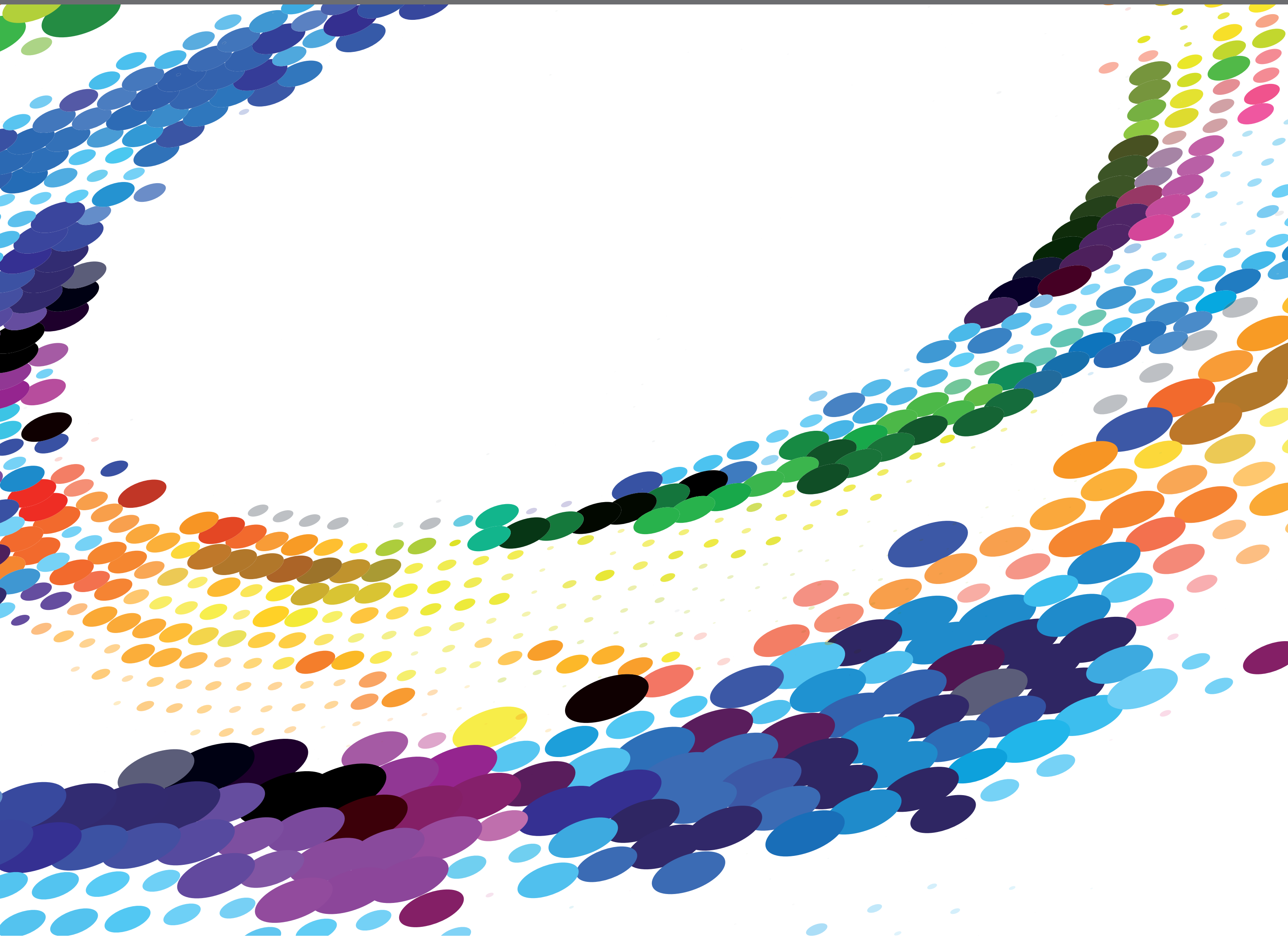

frontiers Research Topics

ISSN 1664-8714
ISBN 978-2-88963-525-2
DOI 10.3389/978-2-88963-525-2

About Frontiers

Frontiers is more than just an open-access publisher of scholarly articles: it is a pioneering approach to the world of academia, radically improving the way scholarly research is managed. The grand vision of Frontiers is a world where all people have an equal opportunity to seek, share and generate knowledge. Frontiers provides immediate and permanent online open access to all its publications, but this alone is not enough to realize our grand goals.

Frontiers Journal Series

The Frontiers Journal Series is a multi-tier and interdisciplinary set of open-access, online journals, promising a paradigm shift from the current review, selection and dissemination processes in academic publishing. All Frontiers journals are driven by researchers for researchers; therefore, they constitute a service to the scholarly community. At the same time, the Frontiers Journal Series operates on a revolutionary invention, the tiered publishing system, initially addressing specific communities of scholars, and gradually climbing up to broader public understanding, thus serving the interests of the lay society, too.

Dedication to Quality

Each Frontiers article is a landmark of the highest quality, thanks to genuinely collaborative interactions between authors and review editors, who include some of the world's best academicians. Research must be certified by peers before entering a stream of knowledge that may eventually reach the public - and shape society; therefore, Frontiers only applies the most rigorous and unbiased reviews.
Frontiers revolutionizes research publishing by freely delivering the most outstanding research, evaluated with no bias from both the academic and social point of view. By applying the most advanced information technologies, Frontiers is catapulting scholarly publishing into a new generation.

What are Frontiers Research Topics?

Frontiers Research Topics are very popular trademarks of the Frontiers Journals Series: they are collections of at least ten articles, all centered on a particular subject. With their unique mix of varied contributions from Original Research to Review Articles, Frontiers Research Topics unify the most influential researchers, the latest key findings and historical advances in a hot research area! Find out more on how to host your own Frontiers Research Topic or contribute to one as an author by contacting the Frontiers Editorial Office: researchtopics@frontiersin.org

MAGNETOHYDRODYNAMIC WAVES IN THE SOLAR ATMOSPHERE: HEATING AND SEISMOLOGY

Topic Editors:
Tom Van Doorsselaere, KU Leuven, Belgium
Valery M. Nakariakov, University of Warwick, United Kingdom
Bo Li, Shandong University, China
Patrick Antolin, Northumbria University, United Kingdom

Citation: Van Doorsselaere, T., Nakariakov, V. M., Li, B., Antolin, P., eds. (2020). Magnetohydrodynamic Waves in the Solar Atmosphere: Heating and Seismology. Lausanne: Frontiers Media SA. doi: 10.3389/978-2-88963-525-2

Table of Contents

frontiers
in Astronomy and Space Sciences

EDITORIAL
published: 23 January 2020
doi: 10.3389/fspas.2019.00079

Editorial: Magnetohydrodynamic Waves in the Solar Atmosphere: Heating and Seismology

Tom Van Doorsselaere[1]*, *Valery M. Nakariakov*[2,3], *Bo Li*[4] *and Patrick Antolin*[5,6]

[1] Department of Mathematics, Centre for mathematical Plasma Astrophysics, KU Leuven, Leuven, Belgium, [2] Department of Physics, Centre for Fusion, Space and Astrophysics, University of Warwick, Coventry, United Kingdom, [3] St. Petersburg Branch, Special Astrophysical Observatory, Russian Academy of Sciences, St. Petersburg, Russia, [4] School of Space Science and Physics, Shandong University, Weihai, China, [5] Department of Mathematics, Physics and Electrical Engineering, Northumbria University, Newcastle upon Tyne, United Kingdom, [6] School of Mathematics and Statistics, University of St. Andrews, St. Andrews, United Kingdom

Keywords: solar physics, MHD waves, solar corona, solar coronal seismology, coronal heating

OPEN ACCESS

Edited and reviewed by:
*Scott William McIntosh,
National Center for Atmospheric Research (UCAR), United States*

Correspondence:
*Tom Van Doorsselaere
tom.vandoorsselaere@kuleuven.be*

Specialty section:
This article was submitted to Stellar and Solar Physics, a section of the journal Frontiers in Astronomy and Space Sciences

Received: *29 November 2019*
Accepted: *24 December 2019*
Published: *23 January 2020*

Citation:
Van Doorsselaere T, Nakariakov VM, Li B and Antolin P (2020) Editorial: Magnetohydrodynamic Waves in the Solar Atmosphere: Heating and Seismology. Front. Astron. Space Sci. 6:79. doi: 10.3389/fspas.2019.00079

Editorial on the Research Topic

Magnetohydrodynamic Waves in the Solar Atmosphere: Heating and Seismology

Historically, following the seminal paper on what is now called "Alfvén" waves (Alfvén, 1942), the theoretical understanding of Magnetohydrodynamic (MHD) waves in uniform media of infinite extent rapidly reached substantial sophistication as summarized in the classics by Cowling (1957) and Braginskii (1965). In particular, the role that MHD waves may play in heating the solar atmosphere was pointed out by Cowling as early as in the 1950s (see Cowling, 1962, and references therein). That the structuring in the physical parameters of the solar atmosphere may strongly affect MHD waves was then recognized (e.g., Uchida, 1968; Rosenberg, 1970; Zaitsev and Stepanov, 1975). Even though they paved the way for the now-called "coronal seismology," most modeling studies (e.g., Uchida, 1970; Edwin and Roberts, 1983; Poedts et al., 1990) focused on utilizing the waves for coronal heating (e.g., Ionson, 1978; Hollweg et al., 1982). This modeling was an endeavoring effort, however, because no observational feedback was available, given the lack of instrumental development at the time. Indeed, some scientists even believed that there were no waves in the solar corona. Despite the lack of observational support, many pioneering papers appeared in this subject area.

Substantial indirect evidence suggesting that MHD waves played a key role in explaining the strong emission and broad non-thermal line widths in the upper chromosphere, transition region and corona already existed from observations with Skylab (Feldman et al., 1988), HRTS (Dere and Mason, 1993), and SUMER (Chae et al., 1998). However, there are two key times in transforming the field of coronal wave studies from its early stages to its current level.

The first key discovery was the direct imaging of coronal waves in the SOHO and TRACE era (late 1990s and early 2000s). This came in three important papers that showed the direct evidence of (1) slow waves in footpoints of coronal loops (Berghmans and Clette, 1999) and (2) transverse kink waves in flaring active regions (Aschwanden et al., 1999; Schrijver et al., 1999). The big impact of these papers is in the fact they provided ample feedback on the earlier models for coronal waves. As a result, these discoveries have triggered an avalanche of observational papers on these types of waves, accompanied with detailed analytical and numerical models. Because direct imaging observations of waves suggested insufficient energy for coronal heating (a topic still under debate, see e.g., Terradas et al., 2018), research focus expanded toward their seismological potential (Nakariakov and Ofman, 2001). With coronal seismology, the aim is to use observed wave properties to obtain physical properties of the coronal structure with which the wave is associated, by the comparison with models.

The second key discovery was the realization that MHD waves are truly omnipresent in the solar atmosphere. This was shown explicitly for the first time with the CoMP instrument (Tomczyk et al., 2007), which only narrowly preceded the Hinode observations (De Pontieu et al., 2007). More recently, a comprehensive analysis of EUV movies of the corona demonstrated the omni-presence of decayless kink oscillations of coronal loops, interpreted as natural standing oscillations continuously sustained by some still debated mechanism (Anfinogentov et al., 2015). These papers have transformed the field, because the observed wave events went from rare observations to space-filling in the corona. Furthermore, the current instrumentation allows to spatially, temporally and spectrally resolve individual aspects of waves. As a result, many researchers are once again considering heating aspects of MHD waves in the solar corona, eschewing somewhat the seismology aspect. Still, it has not been conclusively shown if and how these waves contribute to coronal heating (Arregui, 2015; Hinode Review Team et al., 2019, chapter 6.1).

It must be noted that wave based coronal heating theories are aplenty, and that many of those are theoretically able to produce and maintain a corona (for a review see e.g., Priest, 2014). However, the real challenge lies in identifying key observable predictions from these theories that would allow to discriminate them against observations. This challenge implies, on one hand, conducting advanced numerical simulations of the various wave physical processes—a task that requires enormous amount of computing power due to both, the local and global aspects of wave propagation and dissipation in the heterogeneous solar atmosphere. On the other hand, the challenge requires the synthesis of observable quantities (imaging and spectropolarimetry) from the numerical results, targeting specific instruments and observation conditions—a task known as forward modeling, only possible through the continuous development of atomic databases such as CHIANTI (Dere et al., 1997), and forward modeling codes such as FoMo (Van Doorsselaere et al., 2016).

The historical perspective shows clear trends in the field of MHD waves in the solar atmosphere, in parallel with the development of instrumentation, data analysis techniques, computing power and numerical modeling codes: first there was a strong focus on wave heating, later a strong emphasis on seismology, and now both heating and seismological aspects and their combination are on the cutting edge of the ongoing research efforts.

The main motivation in organizing this special issue in Frontiers of Astronomy & Space Sciences is the 20th anniversary of the discovery of waves in the solar corona. Celebrating the first aforementioned key discovery, our aim for this issue was to give an overview of the current efforts in the field, through the display of currently ongoing Research Topics. This issue shows that there is a healthy balance between observational and modeling papers in the field of MHD waves in the solar atmosphere, following the larger trend in solar physics. Moreover, the two main directions in the field are reflected very well in this content collection: using the observed MHD waves for coronal seismology and coronal heating. This shows perhaps that a new balance has been found within the community between these two important research directions.

In the current special issue, we see also an accent on the basic understanding of wave phenomena in MHD and beyond. This shows two aspects: (1) Wave behavior in MHD is not completely understood yet at a theoretical level, and (2) a significant effort is now being done to understand what is happening beyond MHD (e.g., two fluids). This opens up potential for even more applications in the solar atmosphere, and indicates that there is a lot of room to expand, perhaps by focusing on the smaller scales that are not accessible by MHD waves.

AUTHOR CONTRIBUTIONS

TV wrote the initial draft. PA and BL added several paragraphs. VN gave comments.

FUNDING

TV was supported by the European Research Council (ERC) under the European Union's Horizon 2020 research and innovation programme (grant agreement No. 724326) and the C1 grant TRACEspace of Internal Funds KU Leuven. PA acknowledges funding from his STFC Ernest Rutherford Fellowship (No. ST/R004285/1). VN acknowledges funding from STFC consolidated grant ST/P000320/1, and the Russian Foundation for Basic Research Grant No. 18-29-21016. BL was supported by the National Natural Science Foundation of China (41674172 and 11761141002).

REFERENCES

Alfvén, H. (1942). Existence of electromagnetic-hydrodynamic waves. *Nature* 150, 405–406. doi: 10.1038/150405d0

Anfinogentov, S. A., Nakariakov, V. M., and Nisticò, G. (2015). Decayless low-amplitude kink oscillations: a common phenomenon in the solar corona? *Astron. Astrophys.* 583:A136. doi: 10.1051/0004-6361/2015 26195

Arregui, I. (2015). Wave heating of the solar atmosphere. *ArXiv e-prints*.

Aschwanden, M. J., Fletcher, L., Schrijver, C. J., and Alexander, D. (1999). Coronal loop oscillations observed with the transition region and coronal explorer. *Astrophys. J.* 520, 880–894. doi: 10.1086/3 07502

Berghmans, D., and Clette, F. (1999). Active region euv transient brightenings – first results by eit of soho jop80. *Solar Phys.* 186, 207–229. doi: 10.1023/A:1005189508371

Braginskii, S. I. (1965). Transport processes in a plasma. *Rev. Plasma Phys.* 1:205. doi: 10.1007/978-3-319-62006-0_3

Chae, J., Schühle, U., and Lemaire, P. (1998). SUMER measurements of nonthermal motions: constraints on coronal heating mechanisms. *Astrophys. J.* 505, 957–973. doi: 10.1086/306179

Cowling, T. G. (1957). *Magnetohydrodynamics*. New York, NY: Interscience Publishers.

Cowling, T. G. (1962). Magnetohydrodynamics. *Rep. Prog. Phys.* 25, 244–286.

De Pontieu, B., McIntosh, S. W., Carlsson, M., Hansteen, V. H., Tarbell, T. D., Schrijver, C. J., et al. (2007). Chromospheric Alfvénic waves strong enough to power the solar wind. *Science* 318, 1574–1577. doi: 10.1126/science.1151747

Dere, K. P., Landi, E., Mason, H. E., Monsignori Fossi, B. C., and Young, P. R. (1997). CHIANTI - an atomic database for emission lines. *Astron. Astrophys. Suppl. Ser.* 125, 149–173. doi: 10.1051/aas:1997368

Dere, K. P., and Mason, H. E. (1993). Nonthermal velocities in the solar transition zone observed with the high-resolution telescope and spectrograph. *Solar Phys.* 144, 217–241. doi: 10.1007/BF00627590

Edwin, P. M., and Roberts, B. (1983). Wave propagation in a magnetic cylinder. *Solar Phys.* 88, 179–191.

Feldman, U., Doschek, G. A., and Seely, J. F. (1988). Solar spectroscopy in the far-ultraviolet-X-ray wavelength regions - Status and prospects. *J. Opt. Soc. Am. B Opt. Phys.* 5, 2237–2251. doi: 10.1364/JOSAB.5.002237

Hinode Review Team, Al-Janabi, K., Antolin, P., Baker, D., Bellot Rubio, L. R., Bradley, L., et al. (2019). Achievements of Hinode in the first eleven years. *Publ. Astron. Soc. Jpn.* 71:R1. doi: 10.1093/pasj/psz084

Hollweg, J. V., Jackson, S., and Galloway, D. (1982). Alfven waves in the solar atmospheres - Part three - Nonlinear waves on open flux tubes. *Solar Phys.* 75, 35–61. doi: 10.1007/BF00153458

Ionson, J. A. (1978). Resonant absorption of Alfvénic surface waves and the heating of solar coronal loops. *Astrophys. J.* 226, 650–673. doi: 10.1086/156648

Nakariakov, V. M., and Ofman, L. (2001). Determination of the coronal magnetic field by coronal loop oscillations. *Astron. Astrophys.* 372, L53–L56. doi: 10.1051/0004-6361:20010607

Poedts, S., Goossens, M., and Kerner, W. (1990). Temporal evolution of resonant absorption in solar coronal loops. *Comput. Phys. Commun.* 59, 95–103. doi: 10.1016/0010-4655(90)90159-X

Priest, E. (2014). *Magnetohydrodynamics of the Sun* Cambridge, UK: Cambridge University Press.

Rosenberg, H. (1970). Evidence for MHD pulsations in the solar corona. *Astron. Astrophys.* 9:159.

Schrijver, C. J., Title, A. M., Berger, T. E., Fletcher, L., Hurlburt, N. E., Nightingale, R. W., et al. (1999). A new view of the solar outer atmosphere by the Transition Region and Coronal Explorer. *Solar Phys.* 187, 261–302.

Terradas, J., Magyar, N., and Van Doorsselaere, T. (2018). Effect of magnetic twist on nonlinear transverse kink oscillations of line-tied magnetic flux tubes. *Astrophys. J.* 853:35. doi: 10.3847/1538-4357/aa9d0f

Tomczyk, S., McIntosh, S. W., Keil, S. L., Judge, P. G., Schad, T., Seeley, D. H., et al. (2007). Alfven waves in the solar corona. *Science* 317, 1192–1196. doi: 10.1126/science.1143304

Uchida, Y. (1968). Propagation of hydromagnetic disturbances in the solar corona and Moreton's wave phenomenon. *Solar Phys.* 4, 30–44. doi: 10.1007/BF00146996

Uchida, Y. (1970). Diagnosis of coronal magnetic structure by flare-associated hydromagnetic disturbances. *Publ. Astron. Soc. Jpn.* 22:341.

Van Doorsselaere, T., Antolin, P., Yuan, D., Reznikova, V., and Magyar, N. (2016). Forward modelling of optically thin coronal plasma with the fomo tool. *Front. Astron. Space Sci.* 3:4. doi: 10.3389/fspas.2016.00004

Zaitsev, V. V., and Stepanov, A. V. (1975). On the rigin of pulsations of type IV solar radio emission. *Issled. Geomagn. Aeron. Fiz. Solntsa Vyp*, 3–10.

Conflict of Interest: The authors declare that the research was conducted in the absence of any commercial or financial relationships that could be construed as a potential conflict of interest.

frontiers in Astronomy and Space Sciences

ORIGINAL RESEARCH
published: 04 March 2019
doi: 10.3389/fspas.2019.00010

Resonant Damping of Propagating Kink Waves in Non-stationary, Longitudinally Stratified, and Expanding Solar Waveguides

Michael S. Ruderman[1,2]*, *Daria Shukhobodskaya*[1] *and Alexandr A. Shukhobodskiy*[1,3]

[1] Solar Physics and Space Plasma Research Centre (SP2RC), University of Sheffield, Sheffield, United Kingdom, [2] Laboratory of Interplanetary Medium, Space Research Institute (IKI) Russian Academy of Sciences, Moscow, Russia, [3] Department of Photonics, ITMO University, Saint-Petersburg, Russia

OPEN ACCESS

Edited by:
Patrick Antolin,
University of St Andrews,
United Kingdom

Reviewed by:
Keiji Hayashi,
National Astronomical Observatories (CAS), China
Marcel L. Goossens,
KU Leuven, Belgium

Correspondence:
Michael S. Ruderman
m.s.ruderman@sheffield.ac.uk

Specialty section:
This article was submitted to Stellar and Solar Physics, a section of the journal Frontiers in Astronomy and Space Sciences

Received: *17 December 2018*
Accepted: *08 February 2019*
Published: *04 March 2019*

Citation:
Ruderman MS, Shukhobodskaya D and Shukhobodskiy AA (2019) Resonant Damping of Propagating Kink Waves in Non-stationary, Longitudinally Stratified, and Expanding Solar Waveguides. Front. Astron. Space Sci. 6:10. doi: 10.3389/fspas.2019.00010

Propagating kink waves have been observed in many magnetic waveguides in the solar atmosphere, like coronal magnetic loops, spicules, and fine structures of prominences. There are also observational evidences that these waves are damped. At present resonant absorption is considered as the most likely candidate for explaining this damping. First the attenuation of propagating kink waves due to resonant absorption was studied using the simplest model with a straight magnetic tube and the density only varying in the radial direction. Later a more advanced model with the density also varying along the tube was used. It was shown that the variation of the wave amplitude along the tube is determined by the combined effect of resonant damping and the longitudinal density variation. In our article we extend the analysis of resonant damping of propagating kink waves to take into account the magnetic loop expansion. We also consider non-stationary magnetic tubes to model, for example, cooling coronal loops. In particular, we found that cooling enhances the wave amplitude and the loop expansion makes this effect more pronounced.

Keywords: solar atmosphere, plasma, waves, magnetic field, resonant absorption

1. INTRODUCTION

Propagating kink waves have been observed in many magnetic waveguides in the solar atmosphere, like coronal magnetic loops (Tomczyk et al., 2007; Tomczyk and McIntosh, 2009), spicules (De Pontieu et al., 2007; He J. et al., 2009; He J.-S. et al., 2009), fine structures of prominences (Okamoto et al., 2007), and in filament threads (Lin et al., 2007, 2009). It was also observed that these waves damp. At present resonant absorption is considered as the most likely candidate for explaining this damping. The theoretical modeling of the spatial damping of traveling kink waves due to resonant absorption has been carried out by Terradas et al. (2010) and Verth et al. (2010) analytically, and by Pascoe et al. (2010, 2011) numerically. In all these article the simplest model of a straight magnetic tube with the density only varying in the radial direction was used.

Later mode sophisticate models were used. Soler et al. (2011a) took into account the effect of partial ionization in the single-fluid approximation. As a result, kink waves were damped by both resonant absorption and ion-neutral collisions. Soler et al. (2011b) studied the resonant absorption of propagating kink waves in the presence of flow. Soler et al. (2011c) investigated the propagation and resonant absorption of kink waves in a magnetic tube with the density varying both along and across the tube. They showed that the variation of the wave amplitude along the tube is determined by the combined effect of resonant damping and the longitudinal density variation. Ruderman et al. (2010) studied the effect of non-linearity on the resonant damping of propagating kink waves and showed that non-linearity can strongly enhance the damping efficiency.

All papers cited above used the theory of resonant damping that can be called classical. In this theory the wave amplitude decays exponentially with the distance from the place where it is driven. This result is based on the assumption that a propagating kink wave is an eigenmode of the linearized dissipative magnetohydrodynamics (MHD). In the case of standing kink oscillations (Ruderman and Roberts, 2002) showed that after the initial perturbation the kink oscillation of a perturbed magnetic tube is very well-described by an eigenmode of the linear dissipative MHD after a transitional time of order of the oscillation period everywhere but in a vicinity of the resonant surface. However, in the vicinity of the resonant surface phase mixing continues until it creates perturbations with so small spatial scale that viscosity and/or resistivity stops it. Only after that the perturbation is described by an eigenmode of the linear dissipative MHD everywhere. It was shown numerically that, for typical parameters of coronal magnetic loops, the time when the phase mixing stops is at least by an order of magnitude larger than the typical damping time of kink oscillations (Arregui, 2015).

Hence, we conclude that the main assumption of the classical theory of resonant damping is not satisfied. This problem was addressed numerically by Pascoe et al. (2012, 2013), and analytically by Hood et al. (2013). It was shown that at the initial stage the amplitude variation with the distance from the driver is described by the Gaussian profile. And only later the amplitude decays exponentially. As a result, the damping length of a kink wave is somewhat longer than that predicted by the classical theory of resonant damping. Hence, to correctly describe the spatial damping of propagating kink waves we need to use the advanced theory developed by Hood et al. (2013). The importance of Gaussian damping strongly depends on the thickness of the transitional layer where the density drops from large value inside the tube to low value in the surrounding plasma. It also depends on the ratio of densities inside and outside the tube. The distance where the transition from the Gaussian to exponential damping occurs reduces fast when the thickness of the layer decreases, and also when the ratio of densities increases.

Ruderman and Terradas (2013) carried out an analytical analysis of resonant damping of standing kink waves similar to that made by Hood et al. (2013) for propagating kink waves. They, in particular, concluded that the classical theory of resonant damping underestimates the damping time. But, for typical values of coronal magnetic loop parameters, the error never exceeds 20%. Although a similar estimate was not obtained for propagating kink waves, on the basis of the analogy between the spatial damping of propagating waves and temporal damping of standing waves, we believe that, although the classical theory of resonant damping underestimates the damping length, the error is quite moderate. On the other hand, the advanced theory of resonant damping is much more complex than the classical theory. Hence, in this article we will use the classical theory of resonant damping.

Sometime it is observed that waveguides in the solar atmosphere are non-stationary. For example, Aschwanden and Terradas (2008) and Aschwanden and Schrijver (2011) reported observations of kink oscillations of cooling coronal loops. Inspired by these observations Ruderman (2011b) and Shukhobodskiy et al. (2018) studied the resonant damping of kink oscillations of cooling coronal magnetic loops. Morton et al. (2010) and Ballester et al. (2018) investigated the propagation of magnetosonic waves in a cooling plasma. In our paper we extend their analysis to propagating kink waves in non-stationary magnetic flux tubes. In particular, we study the kink wave propagation in cooling coronal loops.

Our article is organized as follows. In the next section we formulate the problem and present the governing equations. In section 3 we derive the equation governing the evolution of kink waves propagating along non-stationary magnetic tubes. In section 4 we derive the expression determining resonant damping of kink waves. In section 5 we derive the equation for the wave amplitude. In section 6 we consider kink wave propagation in static and non-expanding magnetic tubes. In section 7 we study kink wave propagation in non-stationary and expanding magnetic tubes. Finally, in section 8 we summarize the results obtained in the paper.

2. PROBLEM FORMULATION AND GOVERNING EQUATIONS

We study propagating kink waves along a straight magnetic tube with the circular cross-section of variable radius (see **Figure 1**). The characteristic radius of the tube cross-section is R_*. Since the tube expands the magnetic field is spatially dependent, but the scale of its spatial variation is $L_* \gg R_*$. This assumption implies that we consider a thin magnetic tube. Below we use cylindrical coordinates r, φ, z with the z-axis coinciding with the tube axis. We consider an axisymmetric equilibrium meaning that all equilibrium quantities are independent of φ. The magnetic field is not twisted meaning that its azimuthal component is zero. Its radial and axial components are expressed in terms of the magnetic flux function ψ as

$$B_r = -\frac{1}{r}\frac{\partial \psi}{\partial z}, \quad B_z = \frac{1}{r}\frac{\partial \psi}{\partial r}. \tag{2.1}$$

Ruderman et al. (2017) (Paper I in what follows) showed that in the thin tube approximation

$$\psi = \frac{1}{2} r^2 h(z). \tag{2.2}$$

This expression is valid both in the tube and in its immediate surrounding.

It follows from Equations (2.1) to (2.2) that

$$B_r = -\frac{1}{2} r h'(z), \quad B_z = h(z). \tag{2.3}$$

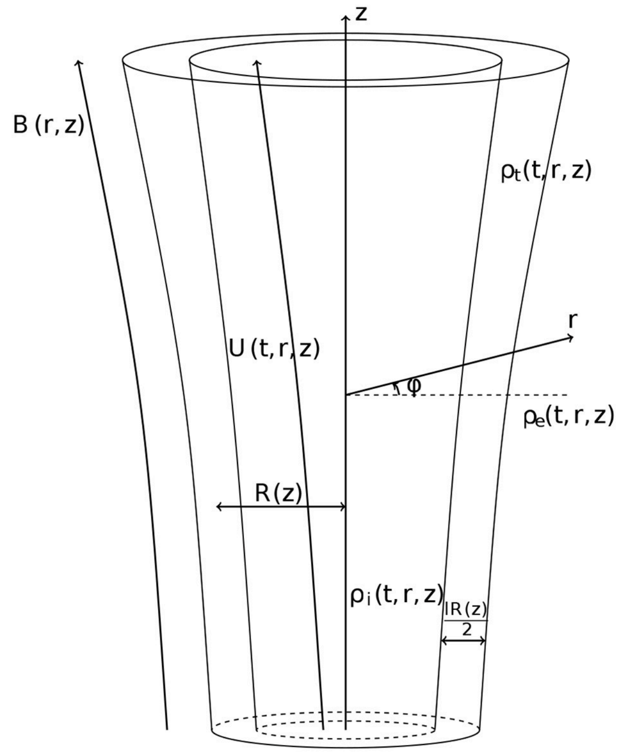

FIGURE 1 | Sketch of the equilibrium.

Since $h'(z) \sim h(z)/L_*$, it follows that

$$\frac{B_r}{B_z} = \mathcal{O}(\varepsilon), \quad B = h(z)\big[1 + \mathcal{O}(\varepsilon^2)\big], \tag{2.4}$$

where $\varepsilon = R_*/L_*$ and $B = (B_r^2 + B_z^2)^{1/2}$ is the magnetic field magnitude.

The plasma density varies both along and across the tube. The tube consists of a core region and a boundary layer where the density monotonically decreases from its value ρ_i inside the tube to its value ρ_e in the surrounding plasma. Here and below the indices "i" and "e" indicate that a quantity is calculated in the core region and in the surrounding plasma, respectively. The characteristic thickness of the boundary layer is lR_*, where $l \ll 1$. This implies that we use the thin boundary approximation. The transitional layer boundaries are defined by equations

$$r = R(z)(1 - l/2), \quad r = R(z)(1 + l/2). \tag{2.5}$$

Now it follows from the magnetic flux conservation that the magnetic field tube magnitude and the tube radius are related by the approximate equation

$$BR^2 = \text{const}. \tag{2.6}$$

It follows from Equations (2.2) to (2.6) that the transitional layer boundaries are magnetic field lines and their equations can be written in an alternative form as

$$\psi = \psi_i \equiv \frac{1}{2}BR^2\left(1 - \frac{l}{2}\right)^2, \quad \psi = \psi_e \equiv \frac{1}{2}BR^2\left(1 + \frac{l}{2}\right)^2. \tag{2.7}$$

In the core region and in the surrounding plasma the characteristic scale of density variation is L_* both in the longitudinal and radial direction. In the transitional layer the characteristic scale of density variation in the longitudinal direction is also L_*, but it is lR_* in the radial direction. The density also can depend on time. The temporal variation of density can cause the plasma flow along the magnetic field lines. Again, the velocity only weakly varies in the radial direction in the core region and outside of the tube, but it varies on the scale lR_* in the transitional layer. The density ρ and velocity $\boldsymbol{U} = (U_r, 0, U_z)$ are related by the mass conservation equation

$$\frac{\partial \rho}{\partial t} + \frac{1}{r}\frac{\partial(\rho r U_r)}{\partial r} + \frac{\partial(\rho U_z)}{\partial z} = 0. \tag{2.8}$$

Since the velocity is parallel to the magnetic field it follows from Equation (2.4) that

$$\frac{U_r}{U_z} = \mathcal{O}(\varepsilon), \quad U = U_z\big[1 + \mathcal{O}(\varepsilon^2)\big], \tag{2.9}$$

where $U = (U_r^2 + U_z^2)^{1/2}$ is the velocity magnitude. We integrate Equation (2.8) over the area of the tube core cross-section, that is over a circle of radius $R(z)(1 - l/2)$. As a result we obtain

$$R^2(1 - l/2)^2\left(\frac{\partial \rho}{\partial t} + \frac{\partial(\rho U_z)}{\partial z}\right) + 2(\rho r U_r)\big|_{r=R(1-l/2)} = 0. \tag{2.10}$$

It follows from Equations (2.3), (2.4), to (2.6) that $hR^2 = \text{const}$. Using this equation and Equations (2.3), (2.4), and (2.9) yields

$$\left.\frac{U_r}{U}\right|_{r=R(1-l/2)} = \left.\frac{B_r}{B}\right|_{r=R(1-l/2)} = -\frac{h'R(1 - l/2)}{2h} = R'(1 - l/2). \tag{2.11}$$

Substituting this result in Equation (2.10) we obtain in the leading order approximation with respect to ε and l

$$\frac{\partial \rho_i}{\partial t} + \frac{1}{R^2}\frac{\partial(\rho_i R^2 U_i)}{\partial z} = 0. \tag{2.12}$$

Next we integrate (Equation 2.8) over the ring region $R(1+l/2) \le r \le \varsigma R$, where $\varsigma - 1 \gg l$ and ς is of the order of unity. This yields

$$R^2\big(\varsigma^2 - 1 - l - l^2/4\big)\left(\frac{\partial \rho}{\partial t} + \frac{\partial(\rho U_z)}{\partial z}\right) + 2(\rho r U_r)\Big|_{r=R(1+l/2)}^{\varsigma R} = 0. \tag{2.13}$$

Similar to Equation (2.9) we obtain

$$\left.\frac{U_r}{U}\right|_{r=\varsigma R} = \varsigma R'. \tag{2.14}$$

Using Equation (2.11) with $-l$ substituted for l and (2.14) we obtain from Equation (2.13)

$$R^2\left(\varsigma^2 - 1 - l - l^2/4\right)\left(\frac{\partial\rho}{\partial t} + \frac{\partial(\rho U_z)}{\partial z}\right) + 2RR'\left((\rho U)\Big|_{\varsigma R} - (\rho U)\Big|_{r=R(1+l/2)}\right) = 0.$$

In the leading order approximation with respect to ε and l we neglect l in comparison with unity, and take $U_z \approx U$ and

$$(\rho U)\Big|_{\varsigma R} \approx (\rho U)\Big|_{r=R(1+l/2)}$$

in Equation (2.13). Then, dividing the obtained equation by $R^2(\varsigma^2 - 1)$ yields

$$\frac{\partial\rho_e}{\partial t} + \frac{1}{R^2}\frac{\partial(\rho_e R^2 U_e)}{\partial z} = 0. \tag{2.15}$$

It was shown in Paper I that long linear kink waves, which are waves with the wavelength much larger than R_*, in an expanding and non-stationary magnetic tube is described by the equation

$$\rho_i\left(\frac{\partial}{\partial t} + \frac{U_i}{R^2}\frac{\partial}{\partial z}R^2\right)\left(\frac{\partial\eta}{\partial t} + U_i\frac{\partial\eta}{\partial z}\right) + \rho_e\left(\frac{\partial}{\partial t} + \frac{U_e}{R^2}\frac{\partial}{\partial z}R^2\right)\left(\frac{\partial\eta}{\partial t} + U_e\frac{\partial\eta}{\partial z}\right) - \frac{2B^2}{\mu_0}\frac{\partial^2\eta}{\partial z^2} = \mathcal{L}, \tag{2.16}$$

where

$$\mathcal{L} = \frac{\delta P}{R^2} + \frac{B^2}{\mu_0}\frac{\partial^2(l\eta + \delta\eta)}{\partial z^2} - \rho_e\left(\frac{\partial}{\partial t} + \frac{U_e}{R^2}\frac{\partial}{\partial z}R^2\right)\left(\frac{\partial}{\partial t} + U_e\frac{\partial}{\partial z}\right)(l\eta + \delta\eta). \tag{2.17}$$

In this equations μ_0 is the magnetic permeability of free space, P is the perturbation of magnetic pressure,

$$\eta = \frac{\xi_{\perp i}}{R}, \tag{2.18}$$

and $\xi_\perp$ is the plasma displacement in the φ = const plane and perpendicular to the magnetic field lines. In the case of non-expanding tube $\xi_\perp = \xi_r$, where ξ_r is the radial component of the plasma displacement. In a slowly expanding tube $\xi_\perp = \xi_r[1 + \mathcal{O}(\varepsilon)]$. In the thin tube approximation $\xi_{\perp i}$ is independent of r. This property is same as that first obtained in the case of non-expanding magnetic tubes (e.g., Ruderman and Erdélyi, 2009). The quantities $\delta\eta$ and δP are the jumps across the transitional layer defined by

$$\delta\eta = \frac{1}{R}\left(\xi_\perp\big|_{\psi=\psi_e} - \xi_\perp\big|_{\psi=\psi_i}\right), \quad \delta P = P\big|_{\psi=\psi_e} - P\big|_{\psi=\psi_i}. \tag{2.19}$$

Equation (2.17) with the right-hand side defined by Equation (2.19) is used below to study the propagation of kink waves.

In the thin tube approximation the radial and azimuthal components of both the plasma displacement and magnetic field perturbation are independent of r inside the tube and proportional to r^{-2} outside the tube. The wave energy density is equal to the sum of the kinetic and magnetic energy density. The kinetic energy density is proportional to the sum of the squares of the radial and azimuthal components of the plasma displacement, and the magnetic energy density is proportional to the sum of the squares of the radial and azimuthal components of the magnetic field perturbation. Hence, the wave energy density is independent of r inside the tube and proportional to r^{-4} outside the tube. The energy behavior in the boundary layer strongly depends on the dissipative coefficients and can be either monotonic or oscillatory. At distances from the place where the wave is driven that are much smaller than the damping distance the wave energy density in the transitional layer is quite small, of the order of $l/R_* \ll 1$. However, at distances comparable with the damping distance almost all energy is concentrated in the transition layer due to resonant absorption.

3. DERIVATION OF THE EVOLUTIONARY EQUATION

In this section we consider propagation of kink waves along an expanding and non-stationary magnetic tube. Using Equations (2.12) and (2.15) we transform Equation (2.11) to

$$(\rho_i + \rho_e)\frac{\partial^2\eta}{\partial t^2} + 2(\rho_i U_i + \rho_e U_e)\frac{\partial^2\eta}{\partial t\partial z} + \left(\rho_i U_i^2 + \rho_e U_e^2 - \frac{2B_0^2}{\mu_0}\right)\frac{\partial^2\eta}{\partial z^2} + \left\{\frac{\partial}{\partial t}(\rho_i U_i + \rho_e U_e) + \frac{1}{R^4}\frac{\partial}{\partial z}\left[R^4(\rho_i U_i^2 + \rho_e U_e^2)\right]\right\}\frac{\partial\eta}{\partial z} - \left[\frac{\partial}{\partial t}(\rho_i + \rho_e) + \frac{\partial}{\partial z}(\rho_i U_i + \rho_e U_e)\right]\frac{\partial\eta}{\partial t} = 0. \tag{3.1}$$

Now we consider waves with the length much longer than R_*, but much shorter than L_*. We denote the ratio of the characteristic wavelength to L_* as $\epsilon \ll 1$. The condition the wavelength is much larger than R_* implies that $\epsilon \gg \varepsilon = R_*/L_*$. We also assume that the wave period is much shorter than the characteristic scale of the temporal density variation. To study the wave propagation we look for the solution to Equation (3.1) in the form

$$\eta = S\exp(i\epsilon^{-1}\theta), \tag{3.2}$$

where θ is real and S is complex (Bender and Orszag, 1978). The presence of transitional layer results in the resonant damping of waves. We will see below that the damping length is of the order l^{-1} times the wavelength. On the other hand, the effect of inhomogeneity manifests itself on a distance from the place where the wave is driven that is of the order of ϵ^{-1} times the wavelength. We would like to derive the equation for the wave amplitude that takes both effects into account in the same order approximation. In accordance with this we put $l = \epsilon$. When $l \gg \epsilon$ the effect of resonant absorption strongly dominates the effect of the axial density variation that can be neglected. In the opposite case where $l \ll \epsilon$ the effect of the axial density variation strongly dominates the effect of resonant absorption. We will see below that $\mathcal{L}$ is of the order of ϵ^{-1} when $l = \epsilon$. This estimate inspires us to introduce $\widetilde{\mathcal{L}} = \epsilon\mathcal{L}$. The characteristic time of wave damping due to resonant absorption is ϵ^{-1} times the wave period. If the characteristic time of density variation is much larger than that time then its effect can be neglected. On the other hand, if the characteristic time of density variation is much smaller then the damping time then the effect of density variation will strongly dominate the wave damping. We aim to study the competition of the two effects. In accordance with this we assume that the ratio of the wave period to the characteristic time of density variation is of the order of ϵ. Substituting $\eta = S\exp(i\epsilon^{-1}\theta)$ in Equation (3.1) and collecting terms proportional to ϵ^{-2} in the obtained equation yields

$$(\rho_i+\rho_e)\omega^2-2(\rho_iU_i+\rho_eU_e)k\omega+\left(\rho_iU_i^2+\rho_eU_e^2-\frac{2B_0^2}{\mu_0}\right)k^2=0, \tag{3.3}$$

where

$$\omega = -\frac{\partial\theta}{\partial t}, \quad k = \frac{\partial\theta}{\partial z}. \tag{3.4}$$

This approximation is usually called the approximation of geometrical optics.

Next, we collect terms proportional to ϵ^{-1}. This results in

$$\begin{aligned}
&(\rho_i+\rho_e)\left(S\frac{\partial\omega}{\partial t}+2\omega\frac{\partial S}{\partial t}\right)+2(\rho_iU_i+\rho_eU_e)\left(S\frac{\partial\omega}{\partial z}+\omega\frac{\partial S}{\partial z}-k\frac{\partial S}{\partial t}\right)\\
&-\left(\rho_iU_i^2+\rho_eU_e^2-\frac{2B_0^2}{\mu_0}\right)\left(S\frac{\partial k}{\partial z}+2k\frac{\partial S}{\partial z}\right)\\
&-\left\{\frac{\partial}{\partial t}(\rho_iU_i+\rho_eU_e)+\frac{1}{R^4}\frac{\partial}{\partial z}\left[R^4(\rho_iU_i^2+\rho_eU_e^2)\right]\right\}kS\\
&-\left[\frac{\partial}{\partial t}(\rho_i+\rho_e)+\frac{\partial}{\partial z}(\rho_iU_i+\rho_eU_e)\right]\omega S = ie^{-il^{-1}\theta}\widetilde{\mathcal{L}}.
\end{aligned} \tag{3.5}$$

Multiplying this equation by SR^4 and using Equation (2.6) we obtain

$$\begin{aligned}
&R^4(\rho_i+\rho_e)\frac{\partial(\omega S^2)}{\partial t}-R^4(\rho_iU_i+\rho_eU_e)\left[\frac{\partial(kS^2)}{\partial t}-\frac{\partial(\omega S^2)}{\partial z}\right]\\
&-\frac{\partial}{\partial z}\left[\left(\rho_iU_i^2+\rho_eU_e^2-\frac{2B_0^2}{\mu_0}\right)kR^4S^2\right]\\
&-kR^4S^2\frac{\partial}{\partial t}(\rho_iU_i+\rho_eU_e)\\
&-\left[\frac{\partial}{\partial t}(\rho_i+\rho_e)+\frac{\partial}{\partial z}(\rho_iU_i+\rho_eU_e)\right]\omega R^4S^2 = ie^{-il^{-1}\theta}SR^4\widetilde{\mathcal{L}}.
\end{aligned} \tag{3.6}$$

We further transform this equation to

$$\begin{aligned}
&\frac{\partial}{\partial t}\left\{R^4S^2\left[(\rho_i+\rho_e)\omega-(\rho_iU_i+\rho_eU_e)k\right]\right\}\\
&+R^4(\rho_iU_i+\rho_eU_e)\frac{\partial(\omega S^2)}{\partial z}-\frac{\partial}{\partial z}\left[\left(\rho_iU_i^2+\rho_eU_e^2-\frac{2B_0^2}{\mu_0}\right)kR^4S^2\right]\\
&-\left[2\frac{\partial}{\partial t}(\rho_i+\rho_e)+\frac{\partial}{\partial z}(\rho_iU_i+\rho_eU_e)\right]\omega R^4S^2\\
&= ie^{-il^{-1}\theta}SR^4\widetilde{\mathcal{L}}.
\end{aligned} \tag{3.7}$$

We now transform the terms on the left-hand side of this equation that are not full derivatives. Using Equations (2.12) and (2.15) we obtain

$$\begin{aligned}
&R^4(\rho_iU_i+\rho_eU_e)\frac{\partial(\omega S^2)}{\partial z}\\
&\quad-\left[2\frac{\partial}{\partial t}(\rho_i+\rho_e)+\frac{\partial}{\partial z}(\rho_iU_i+\rho_eU_e)\right]\omega R^4S^2\\
&\quad= R^4(\rho_iU_i+\rho_eU_e)\frac{\partial(\omega S^2)}{\partial z}\\
&\quad+\left[2(\rho_iU_i+\rho_eU_e)\frac{\partial R^2}{\partial z}+R^2\frac{\partial}{\partial z}(\rho_iU_i+\rho_eU_e)\right]\omega R^2S^2\\
&\quad= R^4(\rho_iU_i+\rho_eU_e)\frac{\partial(\omega S^2)}{\partial z}+\omega S^2\frac{\partial}{\partial z}\left[R^4(\rho_iU_i+\rho_eU_e)\right]\\
&\quad= \frac{\partial}{\partial z}\left[(\rho_iU_i+\rho_eU_e)\omega R^4S^2\right].
\end{aligned} \tag{3.8}$$

Using this result we reduce Equation (3.7) to

$$\begin{aligned}
&\frac{\partial}{\partial t}\left\{R^4S^2\left[(\rho_i+\rho_e)\omega-(\rho_iU_i+\rho_eU_e)k\right]\right\}\\
&\quad+\frac{\partial}{\partial z}\left\{R^4S^2\left[(\rho_iU_i+\rho_eU_e)\omega-\left(\rho_iU_i^2+\rho_eU_e^2-\frac{2B_0^2}{\mu_0}\right)k\right]\right\}\\
&= ie^{-il^{-1}\theta}SR^4\widetilde{\mathcal{L}}.
\end{aligned} \tag{3.9}$$

Finally, introducing

$$V=\frac{\omega}{k}, \quad \mathcal{E}=R^4S^2\left[(\rho_i+\rho_e)\omega-(\rho_iU_i+\rho_eU_e)k\right], \tag{3.10}$$

and using Equation (3.3) we rewrite Equation (3.9) as

$$\frac{\partial\mathcal{E}}{\partial t}+\frac{\partial(V\mathcal{E})}{\partial z}=ie^{-il^{-1}\theta}SR^4\widetilde{\mathcal{L}}. \tag{3.11}$$

Here $\mathcal{E}$ is proportional to the wave energy density per unit length along the magnetic tube.

Below we assume that the temporal variation of the density is very slow. To be specific, we consider as an example kink waves in cooling coronal loops. One observation of kink oscillation of a cooling coronal loop was reported by Aschwanden and Schrijver (2011). In this event the period of fundamental mode was 395 s, and the loop length was 163 Mm. Hence, the phase speed of the kink wave was 893 km/s. The cooling time was 2050 s. Taking this time as the characteristic time in Equation (2.12), and the loop length as the characteristic length, we obtain the estimate $U_i \sim 80$ km/s. Aschwanden and Schrijver (2011) did not give any information about the temperature of the plasma surrounding the loop. Cooling mainly occurs due to radiation with the intensity proportional to the plasma density squared. The plasma in the loop is much denser than that surrounding the loop. Hence, even if the external plasma cools, its cooling time is much larger than that of the plasma in the loop, and we can expect that $U_e \ll U_i$. Consequently, we conclude that in the event reported by Aschwanden and Schrijver (2011) the speed of the flow induced by cooling is much smaller than the phase speed.

On the basis of this example we introduce the definition that the temporal density variation is very slow if the flow speed induced by this variation is much smaller than the phase speed. The assumption that the temporal density variation is very slow enables us to neglect the terms containing U_i and U_e in Equation (3.3). In addition, we only consider waves propagating in the positive z-direction. Then Equation (3.3) reduces to

$$\omega = C_k k, \quad C_k^2 = \frac{2B^2}{\mu_0(\rho_i + \rho_e)}. \tag{3.12}$$

We also can neglect the terms proportional to U_i and U_e in the expression for $\mathcal{E}$ and write it in the approximate form as

$$\mathcal{E} = (\rho_i + \rho_e)\omega R^4 S^2. \tag{3.13}$$

4. DERIVATION OF EXPRESSION FOR $\widetilde{\mathcal{L}}$

The assumption that the temporal variation of density is very slow enables us to use the linear equations of static MHD to describe the plasma motion in the transitional layer. However, we take the dependence of the density on time. To remove the singularity at the resonant surface we take the viscosity into account. Below we use the system of equations derived by Shukhobodskiy and Ruderman (2018). In this system ψ is used as an independent variable instead of r. Since Shukhobodskiy and Ruderman (2018) considered a static problem with the density independent on time they took the perturbation of all variables proportional to $e^{-i\omega t}$. However, it is easy to restore the time dependence. It suffices to substitute $\partial/\partial t$ for $-i\omega$. As a result, we obtain

$$P = -\frac{1}{\mu_0}\left(rB^2\frac{\partial w}{\partial\psi} + iB^2\frac{\xi_\varphi}{r} - B_r\frac{\partial w}{\partial z} + B_z\frac{w}{r}\right), \tag{4.1}$$

$$\begin{aligned}\frac{\partial^2 w}{\partial t^2} &= \frac{rB^2 B_z}{\mu_0\rho}\frac{\partial}{\partial z}\left(\frac{B_z}{r^2B^2}\frac{\partial(rw)}{\partial z}\right) + \frac{B^2}{\rho}\left[B_r\frac{\partial}{\partial z}\left(\frac{P}{B^2}\right)\right. \\ &\quad \left. - rB^2\frac{\partial}{\partial\psi}\left(\frac{P}{B^2}\right)\right] + \nu\frac{\partial}{\partial t}\left(r^2B_z^2\frac{\partial^2 w}{\partial\psi^2} - \frac{w}{r^2}\right),\end{aligned} \tag{4.2}$$

$$\begin{aligned}\frac{\partial^2\xi_\varphi}{\partial t^2} &= -\frac{iP}{\rho r} + \frac{B_z}{\mu_0\rho r}\frac{\partial}{\partial z}\left[r^2B_z\frac{\partial}{\partial z}\left(\frac{\xi_\varphi}{r}\right)\right] \\ &\quad + \nu\frac{\partial}{\partial t}\left(r^2B_z^2\frac{\partial^2\xi_\varphi}{\partial\psi^2} - \frac{\xi_\varphi}{r^2}\right).\end{aligned} \tag{4.3}$$

In these equations ξ_φ is the φ-component of the plasma displacement, $w = B\xi_\perp$, and ν is the kinematic viscosity. We note that r is the function of ψ and z. These equations are valid both in the transitional layer as well as in the core region and external plasma where we can neglect the terms proportional to ν. The characteristic scale of variation of perturbations with respect to z is $l\varepsilon^{-1}R_* \gg R_*$. The characteristic time of variation of perturbations is $l\varepsilon^{-1}R_*/V_*$, where V_* is the characteristic value of the phase speed. We can take $V_*^2 = B_*^2/(\mu_0\rho_*)$, where B_* and ρ_* are the characteristic values of the magnetic field and density, respectively. Using these estimates we obtain that $P \sim l^{-2}\varepsilon^2 V_*^2 R_*^{-1}\xi_\varphi$. Then the ratio of the left-hand side of Equation (4.1) to the second term in the brackets in this equation is of the order of $l^{-2}\varepsilon^2 \ll 1$, which implies that the left-hand side of Equation (4.1) can be neglected. The ratio of the third term in the brackets on the right-hand side of Equation (4.1) to the fourth term is $l^{-1}\varepsilon^2 \ll 1$, so the third term also can be neglected. As a result, Equation (4.1) reduces to

$$r^2B\frac{\partial w}{\partial\psi} + iB\xi_\varphi + w = 0. \tag{4.4}$$

Finally, since in the core region the dependence of both B and $\xi_\perp$ on ψ can be neglected, in this region we also can drop the first term in Equation (4.4).

In the WKB method all dependent variables must have the same functional form. In accordance with this, recalling that $\eta = S\exp(i\epsilon^{-1}\theta)$ and $l = \epsilon$, we put

$$w = \hat{w}e^{il^{-1}\theta}, \quad \xi_\varphi = \hat{\xi}_\varphi e^{il^{-1}\theta}, \quad P = \hat{P}e^{il^{-1}\theta}. \tag{4.5}$$

Using the relations $w = B\xi_\perp$, $\eta = \xi_{\perp i}/R$ and $\eta = S\exp(i\epsilon^{-1}\theta)$, and taking into account that the dependence of $\xi_\perp$ on ψ in the core region can be neglected we obtain the expression valid in the core region,

$$\hat{w}_i = BRS. \tag{4.6}$$

Substituting Equations (4.5) and (4.6) in Equation (4.1) with the small terms neglected, and in Equation (4.3) with $\nu = 0$, and collecting the leading terms with respect to l we obtain the following equations valid in the core region,

$$i\hat{\xi}_\varphi + RS = 0, \tag{4.7}$$

$$\hat{P} = -il^{-2}r\rho\left(\omega^2 - \frac{B^2k^2}{\mu_0\rho}\right)\hat{\xi}_\varphi. \tag{4.8}$$

Eliminating $\hat{\xi}_\varphi$ from these equations yields

$$\hat{P} = l^{-2}r\rho RS\left(\omega^2 - \frac{B^2k^2}{\mu_0\rho}\right). \tag{4.9}$$

Now we proceed to calculating $\widetilde{\mathcal{L}}$. First we further simplify Equations (4.2)–(4.4). We note that we can take $r(\psi, z) \approx R(z)$ in the transitional layer. Using Equations (2.3) and (2.4) we also take $B_z \approx B$. We can disregard the dependence of B on ψ. Finally, the characteristic scale of both the density and perturbations of all quantities in the transitional layer is $\psi_e - \psi_i = lBR^2$. Using these estimates we can easily show that the second term in the square brackets in Equation (4.2) strongly dominates the first term, and the second terms in brackets in terms proportional to ν are much smaller than the first terms. Finally, the ratio of the third and first terms in Equation (4.4) is of the order of l. Hence, the third term can be dropped. Then, using Equation (2.6) we reduce the system of Equations (4.2)–(4.4) to

$$r^2 \frac{\partial w}{\partial \psi} + i\xi_\varphi = 0, \tag{4.10}$$

$$\frac{\partial^2 w}{\partial t^2} = \frac{B^2}{\mu_0 \rho R} \frac{\partial^2 (wR)}{\partial z^2} - \frac{RB^2}{\rho} \frac{\partial P}{\partial \psi} + \nu R^2 B^2 \frac{\partial^3 w}{\partial t \partial \psi^2}, \tag{4.11}$$

$$\frac{\partial^2 \xi_\varphi}{\partial t^2} = -\frac{iP}{\rho R} + \frac{RB^2}{\mu_0 \rho} \frac{\partial^2}{\partial z^2} \left(\frac{\xi_\varphi}{R} \right) + \nu R^2 B^2 \frac{\partial^3 \xi_\varphi}{\partial t \partial \psi^2}. \tag{4.12}$$

4.1. Solution Outside of the Dissipative Layer

To obtain the solution in the transitional layer we use the method of matched asymptotic expansions (e.g., Bender and Orszag, 1978). In accordance with this method we split the transitional layer in the dissipative layer and two layers sandwiching this layer where we can neglect viscosity. We look for the solution to the linear dissipative MHD in the dissipative layer and to the linear ideal MHD outside of this layer. Then we match the two solutions in the two overlap layer where the both solutions are valid. The solution in the dissipative layer is called internal, and the solution outside of the dissipative layer external.

We start from looking for the solution to the linear ideal MHD outside of the dissipative layer embracing the resonance surface defined by the equation $\psi = \psi_A$, where ψ_A is determined by the condition $V_A(\psi_A) = C_k$. Since the variation of P in the transitional layer is of the order of lP_i, we can substitute $P_i(\psi = \psi_i)$ for P in Equation (4.12). Now, we substitute Equations (4.5) and (4.6) in Equations (4.10)–(4.12). Since we need to calculate $\widetilde{\mathcal{L}}$ in the leading order approximation with respect to l, we only keep leading terms. As a result, we obtain

$$R^2 \frac{\partial \hat{w}}{\partial \psi} + i\hat{\xi}_\varphi = 0, \tag{4.13}$$

$$k^2 \left(C_k^2 - V_A^2 \right) \hat{w} = \frac{l^2 RB^2}{\rho} \frac{\partial \hat{P}}{\partial \psi}, \tag{4.14}$$

$$\left(C_k^2 - V_A^2 \right) \hat{\xi}_\varphi = \frac{i\rho_i}{\rho_A} RS \left(C_k^2 - V_{Ai}^2 \right), \tag{4.15}$$

where $V_A = B(\mu_0 \rho)^{-1/2}$ is the Alfvén speed and $\rho_A = \rho(\psi = \psi_A)$. When deriving Equations (4.14) and (4.15) we used the relation $\omega = C_k k$. It follows from Equation (4.15) that

$$\hat{\xi}_\varphi = \frac{i\rho_i RS(C_k^2 - V_{Ai}^2)}{\rho_A (C_k^2 - V_A^2)}. \tag{4.16}$$

We see that there is a singularity of $\hat{\xi}_\varphi$ at $\psi = \psi_A(t, z)$. Substituting Equation (4.16) in Equation (4.13) and integrating the obtained equation yields

$$\hat{w} = \begin{cases} \hat{w}(\psi = \psi_i) + \displaystyle\int_{\psi_i}^{\psi} \frac{S(C_k^2 - V_{Ai}^2)}{R(C_k^2 - V_A^2)} d\psi_1, & \psi < \psi_A, \\ \hat{w}(\psi = \psi_e) - \displaystyle\int_{\psi}^{\psi_e} \frac{S(C_k^2 - V_{Ai}^2)}{R(C_k^2 - V_A^2)} d\psi_1, & \psi > \psi_A. \end{cases} \tag{4.17}$$

While $\hat{\xi}_\varphi$ has a singularity of the form $(\psi - \psi_A)^{-1}$, $\hat{w}$ only has a logarithmic singularity. Finally, substituting this result in Equation (4.14) and integrating the obtained equation results in

$$\hat{\Phi} = \begin{cases} \hat{\Phi}(\psi = \psi_i) + \dfrac{k^2(C_k^2 - V_{Ai}^2)}{l^2 RB^2} \\ \quad \int_{\psi_i}^{\psi} \left(\hat{w}(\psi = \psi_i) + \int_{\psi_i}^{\psi_1} \frac{S(C_k^2 - V_{Ai}^2)}{R(C_k^2 - V_A^2)} d\psi_2 \right) d\psi_1, & \psi < \psi_A, \\ \hat{\Phi}(\psi = \psi_e) - \dfrac{k^2(C_k^2 - V_{Ai}^2)}{l^2 RB^2} \\ \quad \int_{\psi}^{\psi_e} \left(\hat{w}(\psi = \psi_e) - \int_{\psi_1}^{\psi_e} \frac{S(C_k^2 - V_{Ai}^2)}{R(C_k^2 - V_A^2)} d\psi_2 \right) d\psi_1, & \psi > \psi_A, \end{cases} \tag{4.18}$$

where $\hat{\Phi}$ is defined by the equation

$$\frac{\partial \hat{\Phi}}{\partial \psi} = \frac{1}{\rho} \frac{\partial \hat{P}}{\partial \psi}. \tag{4.19}$$

It is easy to see that $\hat{P}$ is continuous at $\psi = \psi_A$.

4.2. Solution Inside the Dissipative Layer

We now look for the solution in the dissipative layer embracing the resonant surface. Ruderman et al. (1995) was the first to show that solution character in the dissipative layer depends on the value of viscosity (see also Ruderman and Roberts, 2002; Goossens et al., 2011). The spatial dependence of variable perturbations in the dissipative layer is monotonic when the viscosity is not very small, while it is oscillatory for very small values of viscosity. Ruderman et al. (1995) studied a planar problem where the transition from monotonic to oscillatory behavior is determined by the relative values of two small parameters, the ratio of the thickness of transitional layer to the wavelength, and the inverse Reynolds number. He also studied the temporal damping of kink waves. However, the results that he obtained is easily translated to the spatial damping and cylindrical geometry. In this case, the variable spatial dependence is determined by the relative values of three small parameters, l, $\varepsilon = R_*/L_*$, and the inverse Reynolds number Re^{-1}, where $\mathrm{Re} = R_* V_*/\nu$. The parameter determining the character of the spatial variation of variable perturbations in the dissipative layer is $l(\varepsilon \mathrm{Re})^{1/3}$. When $l(\varepsilon \mathrm{Re})^{1/3} \ll 1$ the spatial dependence of variable perturbations in the dissipative layer is monotonic, while it is oscillatory when $l(\varepsilon \mathrm{Re})^{1/3} \gtrsim 1$. We mainly aim to apply the results of this study to the solar atmosphere, where the typical value is $l \gtrsim 0.1$, $\varepsilon \gtrsim 0.01$, while $\mathrm{Re} \gg 10^6$, so that $l(\varepsilon \mathrm{Re})^{1/3} > 1$, which implies that the behavior of perturbations in the dissipative layer is oscillatory. However, in this case the equations describing the motion in the dissipative layer are very complex and, at present, it is not clear how to solve them. On the other hand, we only need to calculate the jumps of w and P across the dissipative layer. Ruderman et al. (1995) found that these jumps are independent of the value of viscosity. The only condition that must be satisfied is that Re is sufficiently large, so that the thickness of the dissipative layer is much smaller than the thickness of the transitional layer. This result was later confirmed in subsequent studies (see, e.g., the review by Goossens et al., 2011). The solution of equations describing the plasma motion in the dissipative layer in the case when $l(\varepsilon\mathrm{Re})^{1/3} \ll 1$ is relatively simple. The result that the jumps of w and P across the dissipative layer are independent of $l(\varepsilon\mathrm{Re})^{1/3}$ was obtained for a static magnetic tube with a constant cross-section radius. However, it looks like a viable conjecture to assume that this result remains correct even for a non-stationary and expanding tube. We note that the following derivation is similar to that in the case of a non-expanding tube. The only difference that in the case of a non-expanding tube we use the variable r, while in our derivation we use the variable ψ instead.

Hence, we assume that $l(\varepsilon\mathrm{Re})^{1/3} \ll 1$. Since the thickness of the dissipative layer is much smaller than the thickness of the transitional layer we can approximate any equilibrium quantity in the dissipative layer by its first non-zero term of Taylor expansion with respect to $\psi - \psi_A$. In particular, we can substitute $\rho_A = \rho(\psi = \psi_A)$ for ρ and take

$$C_k^2 - V_A^2 = -\Delta(\psi - \psi_A), \quad \Delta = \left.\frac{\partial V_A^2}{\partial \psi}\right|_{\psi=\psi_A}. \tag{4.20}$$

Since we assume that the density monotonically decreases in the radial direction in the transitional layer, it follows that $\Delta > 0$. Now, substituting Equation (4.5) in Equation (4.12), collecting terms of the order of l^{-2}, using Equations (4.9) and (4.20), and substituting $P(\psi = \psi_i)$ for P we obtain

$$\Delta(\psi - \psi_A)\hat{\xi}_\varphi + il\nu k^{-1} C_k R^2 B^2 \frac{\partial^2 \hat{\xi}_\varphi}{\partial \psi^2} = -\frac{i\rho_i}{\rho_A} RS\left(C_k^2 - V_{Ai}^2\right). \tag{4.21}$$

When deriving this equation we took into account that $\omega = C_k k$.

The thickness of the dissipative layer is defined by the condition that the two terms on the left-hand side of Equation (4.21) are of the same order. Using Equations (2.2) and (2.4) we easily obtain that this thickness is

$$\delta_A = \left(\frac{l\nu C_k}{kRB\Delta}\right)^{1/3} \sim lR_*(\varepsilon\mathrm{Re})^{-1/3}. \tag{4.22}$$

Then the condition that the thickness of the dissipative layer is much smaller than the thickness of the transitional layer reduces to $\varepsilon\mathrm{Re} \gg 1$. For typical conditions in the solar atmosphere this inequality is definitely satisfied. Together with the condition that the spatial behavior of variable perturbations in the dissipative layer is non-oscillatory this gives

$$1 \ll \varepsilon\mathrm{Re} \ll l^{-3}. \tag{4.23}$$

The solution in the dissipative layer has to match the solution outside of this layer in the overlap layer defined by $\delta_A \ll |r - r_A| \ll lR_*$. Using Equation (4.16) we obtain that the solution in the overlap layer has the form

$$\hat{\xi}_\varphi = -\frac{i\rho_i RS(C_k^2 - V_{Ai}^2)}{\rho_A \Delta(\psi - \psi_A)} + \mathcal{O}\big((\psi - \psi_A)^{-2}\big). \tag{4.24}$$

Hence, the solution to Equation (4.21) must have this form for $|\psi - \psi_A| \gg R_* B_* \delta_A$. The solution to Equation (4.21) satisfying this condition is obtained in **Appendix A**. It is given by Equation (A6). Using Equation (A1) we rewrite it as

$$\hat{\xi}_\varphi = -\frac{\rho_i S(C_k^2 - V_{Ai}^2)}{\rho_A B \Delta \delta_A} F(\Psi), \tag{4.25}$$

where

$$\Psi = \frac{\psi - \psi_A}{RB\delta_A}, \quad F(\Psi) = \int_0^\infty \exp\left(i\sigma\Psi - \tfrac{1}{3}\sigma^3\right) d\sigma. \tag{4.26}$$

Using Equations (4.25) and (4.26) we obtain from Equation (4.13)

$$\hat{w} = \frac{\rho_i S(C_k^2 - V_{Ai}^2)}{\rho_A R \Delta} G(\Psi), \tag{4.27}$$

where

$$G(\Psi) = \int_0^\infty \frac{e^{i\sigma\Psi} - 1}{\sigma} e^{-\sigma^3/3} d\sigma. \tag{4.28}$$

The functions $F(\Psi)$ and $G(\Psi)$ were introduced by Goossens et al. (1995).

Finally, substituting Equation (4.5) in Equation (4.11), collecting terms of the order of l^{-2}, and using the relation $\omega = C_k k$, and Equations (4.20) and (4.22), and (4.26)–(4.28) we obtain

$$\frac{\partial \hat{\Phi}}{\partial \Psi} = \frac{\rho_i k^2 S \delta_A^2 (C_k^2 - V_{Ai}^2)}{l^2 \rho_A} \left(\frac{dF}{d\Psi} - \Psi G(\Psi)\right). \tag{4.29}$$

4.3. Matching Solutions

The matching procedure is the following. First we find the asymptotic expansion of the internal solution valid for $\Psi \gg 1$. Next we find the expansion of the external solution valid for $|\psi - \psi_A| \ll BR^2$. Then we substitute $\psi - \psi_A = RB\delta_A\Psi$ in this expansion. The matching condition is that the leading terms of the two expansions must coincide.

We found that it is more convenient to compare not the expansions but the jumps across the dissipative layer. The jump of w across the dissipative layer is given by $w(\Psi) - w(-\Psi)$ with $\Psi \gg 1$. We obtain

$$\begin{aligned} G(\Psi) - G(-\Psi) &= 2i\int_0^\infty \frac{\sin(\sigma\Psi)}{\sigma} e^{-\sigma^3/3} d\sigma \\ &= 2i\int_0^\infty \frac{\sin\sigma}{\sigma}\left[1 + \left(e^{-\sigma^3/3\Psi^3} - 1\right)\right] d\sigma \\ &= \pi i + 2i\int_0^\infty \frac{\sin\sigma}{\sigma}\left(e^{-\sigma^3/3\Psi^3} - 1\right) d\sigma. \end{aligned} \tag{4.30}$$

It is obvious that the second term in this expression tends to zero as $\Psi \to \infty$. Using this result we obtain from Equation (4.27) that the jump of $\hat{w}$ across the dissipative layer is

$$\hat{w}(\Psi) - \hat{w}(-\Psi) = \frac{\pi i \rho_i S(C_k^2 - V_{Ai}^2)}{\rho_A R \Delta}[1 + o(1)]. \tag{4.31}$$

Using Equation (4.17) we obtain another asymptotic expression for the jump of $\hat{w}$ across the dissipative layer,

$$\hat{w}(\psi - \psi_A) - \hat{w}(\psi_A - \psi) = \delta\hat{w} - \mathcal{P}\int_{\psi_i}^{\psi_e} \frac{S(C_k^2 - V_{Ai}^2)}{R(C_k^2 - V_A^2)} d\psi + o(1), \tag{4.32}$$

where $\delta\hat{w} = \hat{w}(\psi = \psi_e) - \hat{w}(\psi = \psi_i)$ and $\mathcal{P}$ indicates the principal Cauchy part of an integral. This asymptotic expression is valid for $|\psi - \psi_A| \ll 1$. The leading terms of the two asymptotic expressions, one given by Equation (4.31) and the other by Equation (4.32), must coincide. It follows from this condition that

$$\delta\hat{w} = \frac{\pi i \rho_i S(C_k^2 - V_{Ai}^2)}{\rho_A R \Delta} + \mathcal{P}\int_{\psi_i}^{\psi_e} \frac{S(C_k^2 - V_{Ai}^2)}{R(C_k^2 - V_A^2)} d\psi. \tag{4.33}$$

Now we calculate $\delta\hat{\Phi} = \hat{\Phi}(\psi = \psi_e) - \hat{\Phi}(\psi = \psi_i)$. Using Equation (4.29) we obtain that the jump of P across the dissipative layer is given by

$$\begin{aligned}\hat{\Phi}(\Psi) - \hat{\Phi}(-\Psi) \\ = \frac{\rho_i k^2 S \delta_A^2 (C_k^2 - V_{Ai}^2)}{l^2 \rho_A} \int_{-\Psi}^{\Psi} \left(\frac{dF}{d\Psi_1} - \Psi_1 G(\Psi_1)\right) d\Psi_1.\end{aligned} \tag{4.34}$$

The integral on the right-hand side of this equation is evaluated in **Appendix B**. Using Equation (B8) we obtain

$$\hat{\Phi}(\Psi) - \hat{\Phi}(-\Psi) = -\frac{\pi i \rho_i k^2 S \delta_A (C_k^2 - V_{Ai}^2)\Psi^2}{2 l^2 \rho_A}[1 + o(1)]. \tag{4.35}$$

This result and the matching condition imply that the expansion with respect to $\psi - \psi_A$ of the jump of P across the dissipative layer calculated using the external solution must start from the term proportional to $(\psi - \psi_A)^2$. In particular, it follows from this condition that the term in this expansion proportional to unity must be zero. Using Equation (4.18) we write this condition as

$$\begin{aligned}\delta\hat{\Phi} = \frac{k^2(C_k^2 - V_{Ai}^2)}{l^2 R B^2}\Bigg[\int_{\psi_A}^{\psi_e}\left(\hat{w}(\psi = \psi_e) - \int_{\psi}^{\psi_e} \frac{S(C_k^2 - V_{Ai}^2)}{R(C_k^2 - V_A^2)} d\psi_1\right) d\psi \\ + \int_{\psi_i}^{\psi_A}\left(\hat{w}(\psi = \psi_i) + \int_{\psi_i}^{\psi} \frac{S(C_k^2 - V_{Ai}^2)}{R(C_k^2 - V_A^2)} d\psi_1\right) d\psi\Bigg].\end{aligned} \tag{4.36}$$

where $\delta\hat{\Phi} = \hat{\Phi}(\psi = \psi_e) - \hat{\Phi}(\psi = \psi_i)$. Since $\delta\hat{w}/\hat{w} = \mathcal{O}(l)$ and we only need to calculate $\delta\hat{\Phi}$ in the leading order approximation with respect to l, we can substitute $\hat{w}(\psi = \psi_e) \approx \hat{w}(\psi = \psi_i) = RBS$. Then, noticing that the only quantity that depends on ψ in Equation (4.36) is V_A, each single integral is of the order of l, and each double integral is of the order of l^2, we reduce this equation in the leading order approximation with respect to l to

$$\delta\hat{\Phi} = \frac{k^2 S(C_k^2 - V_{Ai}^2)(\psi_e - \psi_i)}{l^2 B}. \tag{4.37}$$

We note that we would obtain exactly the same expression for $\delta\hat{\Phi}$ if we assume from the very beginning that we can neglect the jump of the pressure perturbation across the dissipative layer. This assumption was first made *ad hog* by Hollweg and Yang (1988). Later it was rigorously proved in 1D plasma equilibrium by Goossens et al. (1995).

Since the jump of Φ across the dissipative layer is zero, it follows that the expression for Φ obtained using the ideal MHD equations is a continuous function in the whole transitional layer. Then, using Equation (4.37) we obtain from Equation (4.18) the expression valid in the whole transitional layer in the leading order approximation with respect to l,

$$\hat{\Phi} = \hat{\Phi}(\psi = \psi_i) + \frac{k^2 S(C_k^2 - V_{Ai}^2)(\psi - \psi_i)}{l^2 B}. \tag{4.38}$$

When deriving this expression we neglected the second terms in the brackets in Equation (4.18) because their ratios to the first terms are of the order of l. Using Equation (4.19) we obtain

$$\delta\hat{P} \equiv \hat{P}(\psi = \psi_e) - \hat{P}(\psi = \psi_i) = \frac{k^2 S(C_k^2 - V_{Ai}^2)}{l^2 B}\int_{\psi_i}^{\psi_e} \rho(\psi)\, d\psi. \tag{4.39}$$

Now we proceed to calculating $\widetilde{\mathcal{L}}$. We substitute $\eta = S e^{i\epsilon^{-1}\theta}$, $\delta\eta = (\delta\hat{w}/RB)e^{i\epsilon^{-1}\theta}$, and $\delta P = \delta\hat{P}\, e^{i\epsilon^{-1}\theta}$ in Equation (2.17). Then, using Equation (3.12) and the condition of very slow temporal density variation implying that $U_e \ll C_k$ we obtain

$$\widetilde{\mathcal{L}} = e^{i\epsilon^{-1}\theta}\left[l\frac{\delta\hat{P}}{R^2} - \frac{1}{2}(\rho_i - \rho_e)\omega^2\left(S + l^{-1}\frac{\delta\hat{w}}{RB}\right)\right]. \tag{4.40}$$

Finally, using Equations (4.33) and (4.37) we arrive at

$$\widetilde{\mathcal{L}} = 2e^{i\epsilon^{-1}\theta}\omega C_k S(\rho_i + \rho_e)(\Upsilon - i\gamma), \tag{4.41}$$

where

$$\gamma = \frac{\pi k C_k^2(\rho_i - \rho_e)^2}{8 l \rho_A B R^2 \Delta(\rho_i + \rho_e)}, \tag{4.42}$$

$$\Upsilon = \frac{k(\rho_i - \rho_e)}{4(\rho_i + \rho_e)}\left(-1 + \frac{C_k^2}{l\rho_i B R^2}\mathcal{P}\int_{\psi_i}^{\psi_e} \frac{\rho - \rho_i}{C_k^2 - V_A^2} d\psi\right). \tag{4.43}$$

5. DERIVATION OF GOVERNING EQUATION FOR THE WAVE AMPLITUDE

The wave evolution is described by Equation (3.11) with $\mathcal{E}$ and $\widetilde{\mathcal{L}}$ given by Equations (3.13) and (4.41), respectively. We write $S = Ae^{i\chi}$. Then, substituting Equations (3.13) and (4.41) in Equation (3.11), multiplying the obtained equation by $e^{-2i\chi}$, and separating the real and imaginary parts yields

$$\frac{\partial Q}{\partial t} + \frac{\partial(C_k Q)}{\partial z} = -2\gamma C_k Q, \tag{5.1}$$

$$\frac{\partial\chi}{\partial t} + C_k\frac{\partial\chi}{\partial z} = C_k\Upsilon, \tag{5.2}$$

where $Q = (\rho_i + \rho_e)\omega R^4 A^2$. Equation (5.1) determines the temporal and spatial dependence of the wave amplitude, while Equation (5.2) describes a small phase shift. We are mainly interested in the variation of the wave amplitude in space and time, so we do not use Equation (5.2) below.

6. WAVE PROPAGATION ALONG A STATIC AND NON-EXPANDING WAVEGUIDE

In this section we reproduce the results previously obtained for static and non-expanding waveguides. Hence, we assume that the tube radius is constant and equal to R.

6.1. Waveguide Homogeneous in the Axial Direction

Here we consider the same problem as that studied by Terradas et al. (2010), which is the resonant damping of kink waves propagating along a magnetic tube homogeneous in the axial direction. We now assume that the density only varies in the radial direction. We assume that a harmonic wave is driven at $z = 0$ and propagates in the region $z > 0$. In that case A is independent of time and it follows from Equation (5.1) that $A = A_0 e^{-\gamma z}$, where A_0 is the amplitude at $z = 0$. Using the relation $\psi = \frac{1}{2}Br^2$ we obtain from Equation (4.20)

$$\Delta = -\frac{B}{\mu_0 \rho_A^2 R}\frac{d\rho}{dr}\bigg|_A. \tag{6.1}$$

In this case both k and ω are constant. Hence, $\theta = kz - \omega t$, which implies that the wavenumber is $k_* = l^{-1}k$. Now, using Equation (6.1) and the relation $C_k = V_A(r_A)$ yields

$$\frac{\gamma}{k_*} = \frac{\pi(\rho_i - \rho_e)^2}{8R(\rho_i + \rho_e)|d\rho/dr|_A}. \tag{6.2}$$

This expression coincides with that obtained by Terradas et al. (2010) (see their Equation (10) with $m = 1$).

6.2. Waveguide With the Density Varying in the Axial Direction

Now we study the resonant damping of kink waves propagating along a magnetic tube with the density varying along the tube. This problem was first addressed by Soler et al. (2011c). We aim to reproduce their results. We assume that $\rho_i(z)/\rho_e(z) = \zeta =$ const and $\rho(r,z)/\rho_e(z) = f(r)$. Previously these assumptions were made by Dymova and Ruderman (2006) when studying resonant damping of standing kink waves, and by Soler et al. (2011c) when studying resonant damping of propagating kink waves. We again assume that the kink wave with the amplitude A_0 and the constant frequency ω is driven at $z = 0$. Since now C_k is a function of z, the same is true for the wavenumber: $k(z) = \omega/C_k(z)$. Note that in non-scaled variables the wavenumber is $k_*(z) = l^{-1}k(z)$.

Since Q is again independent of t it immediately follows from Equation (5.1) that

$$A = A_0\sqrt{\frac{C_k}{C_f}}\exp\left(-\int_0^z \gamma(z_1)\,dz_1\right). \tag{6.3}$$

When deriving this equation we used the relation $\rho_i C_k^2 = \rho_f C_f^2$. Equation (6.1) remains valid. Then, using the relation $\rho(r,z) = f(r)\rho_e(z)$ we obtain from Equation (4.42)

$$\gamma = \frac{\omega(\zeta - 1)}{2\pi\mathcal{G}(\zeta + 1)C_k(z)}, \tag{6.4}$$

where

$$\mathcal{G} = \frac{4lR|f'(r_A)|}{\pi^2(\zeta - 1)}. \tag{6.5}$$

$\mathcal{G} = 4/\pi^2$ for the linear density profile, and $2/\pi$ for the sinusoidal density profile. After substituting Equation (6.4) in Equation (6.3) we obtain the equation coinciding with Equation (38) in Soler et al. (2011c).

7. WAVE PROPAGATION ALONG AN EXPANDING AND NON-STATIONARY WAVEGUIDE

As an example of application of the general theory we consider a generalization of the same problem that was studied by Soler et al. (2011c), and take the loop expansion and cooling into account. We first describe the general method for studying the wave propagation, and then apply it to a particular loop with given cross-section radius and density variation along the tube, and the temporal density variation.

7.1. General Theory

We assume that a kink wave is driven at one of the loop footpoints and impose the boundary condition

$$\omega = \omega_0, \quad A = A_0 \quad \text{at} \quad z = 0. \tag{7.1}$$

Driving starts at $t = 0$. Before that the loop is at rest, so we also have the initial condition

$$A = 0 \quad \text{at} \quad t = 0. \tag{7.2}$$

The equations describing the wave propagation are solved for $t > 0$ and $z > 0$.

We start from calculating $\theta(t,z)$. It follows from dispersion Equation (3.12), $\omega = C_k k$, and Equation (3.4) that $\theta(t,z)$ satisfies the equation

$$\frac{\partial\theta}{\partial t} + C_k(t,z)\frac{\partial\theta}{\partial z} = 0. \tag{7.3}$$

Since $\theta(t,z)$ is defined with the accuracy up to an additive constant we can take $\theta(0,0) = 0$. Then it follows from Equation (7.1) that

$$\theta = -\omega_0 t \quad \text{at} \quad z = 0. \tag{7.4}$$

Since the loop is at rest at $t = 0$ we can take

$$\theta = 0 \quad \text{at} \quad t = 0. \tag{7.5}$$

The equation of characteristics of Equation (7.3) is

$$\frac{dz}{dt} = C_k(t, z). \tag{7.6}$$

It follows from Equation (7.3) that $\theta = \text{const}$ along a characteristic. We consider the characteristic that starts at the coordinate origin. Let its equation be $z = z_b(t)$, where $z_b(0) = 0$. This characteristic separates the perturbed and unperturbed regions in the (t, z)-plane, so we will call it the boundary characteristic. Let us consider a point with coordinates (t_1, z_1) satisfying the condition $z_1 > z_b(t_1)$. This implies that this point is above the boundary characteristic. Since the characteristic containing the point (t_1, z_1) cannot intersect the boundary characteristic, it follows that it starts at the z-axis. Then, using Equation (7.5) we obtain $\theta(t_1, z_1) = 0$.

Now we consider a point (t_1, z_1) that is below the boundary characteristic meaning that $z_1 < z_b(t_1)$. Let the characteristic containing this point starts at $t = \tau(t_1, z_1)$ on the t-axis. Then $\theta(t_1, z_1) = -\omega_0\tau(t_1, z_1)$. As a result, we determine $\theta(t, z)$ in the whole region $t > 0, z > 0$. Differentiating $\theta(t, z)$ with respect to t we calculate ω. Then $k = \omega/C_k$.

Next we proceed to solving Equation (5.1). The equation of characteristics of this equation is also Equation (7.6). The variation of Q along the characteristic is defined by

$$\frac{dQ}{dt} = -\left(2\gamma C_k + \frac{\partial C_k}{\partial z}\right) Q. \tag{7.7}$$

After substituting in this equation a solution to Equation (7.6) found when calculating $\theta(t, z)$, Equation (7.7) becomes the equation determining the variation of Q along a characteristic. The solution to this equation must satisfy the initial condition

$$Q = (\rho_i + \rho_e)\omega_0 R^4 A_0^2 \quad \text{at} \quad t = \tau(t_1, z_1). \tag{7.8}$$

In this equation the equilibrium quantities are calculated at $t = \tau$ and $z = 0$.

We now consider a point (t_1, z_1) with $z_1 > z_b(t_1)$, which implies that it is above the boundary characteristic. In that case the characteristic that contains this point starts at the z-axis where $A = 0$. Then it follows that $A(t_1, z_1) = 0$, that is the tube is at rest for $z > z_b(t)$. Hence, the equation $z = z_b(t)$ describes the propagation of the wave front along the magnetic tube. Below we apply the general theory to particular cases.

7.2. Wave Propagation in Cooling and Expanding Coronal Loop

We now consider the kink wave propagation in a coronal loop of half-circle shape immersed in an isothermal atmosphere. We assume that the loop is in a vertical plane. Cooling of coronal plasma mainly occurs due to radiation. The radiation intensity is proportional to the plasma density squared. Since the plasma density inside the loop is substantially higher than that of the surrounding plasma, the plasma inside the loop cools much faster than that outside the loop. This observation inspires us to make a viable assumption that cooling only occurs inside the loop, while its temperature outside the loop does not change. Then the density inside and outside the loop is given by

$$\rho_i = \rho_f \exp\left(-\frac{L}{\pi H(t)} \sin\frac{\pi z}{L}\right), \quad \rho_e = \frac{\rho_f}{\zeta} \exp\left(-\frac{L}{\pi H_0} \sin\frac{\pi z}{L}\right), \tag{7.9}$$

where L is the length of the loop. Following to Aschwanden and Terradas (2008) and Ruderman (2011a,b) we assume that the plasma density inside the loop decreases exponentially, so that

$$H(t) = H_0 e^{-t/t_c}. \tag{7.10}$$

Here we do not discuss the mechanisms of coronal loop cooling, although the main cause of cooling of moderately hot coronal loops with the temperature of the order of or less than 1.5 MK is the radiative cooling. Magyar et al. (2015) studied transverse oscillations of radiatively cooling coronal loops numerically. They did not present the dependence of temperature on time. However, in general their results related to the time dependence of the oscillation amplitude are in good agreement with that obtained by Ruderman (2011a,b) who assumed the exponential temperature decay. Hence, it seems that the exponential dependence of temperature on time is a reasonable approximation. The pressure inside the loop is assumed to be in equilibrium with the outside medium during the cooling. Since the plasma beta in the corona is very low this condition does not impose any serious restriction on the plasma parameters.

We adopt a model of expanding coronal loop first introduced by Ruderman et al. (2008), and later also used by Shukhobodskiy and Ruderman (2018) and Shukhobodskiy et al. (2018). In this model the cross-section radius of the magnetic tube is given by

$$R(z) = R_f \lambda \sqrt{\frac{\cosh(L/2l_c) - 1}{\cosh(L/2l_c) - \lambda^2 + (\lambda^2 - 1)\cosh(z/l_c - L/2l_c)}}. \tag{7.11}$$

Here l_c is a free parameter with the dimension of length, and λ is the expansion factor equal to the ratio of the cross-section radius at the loop apex and footpoints, that is $\lambda = R(L/2)/R_f$. In our numerical study we took $L/l_c = 6$ and $l = 0.2$. Here it is worth making a comment. In section 2 we imposed the condition that $L_* \gg R_*$, where L_* is the characteristic scale of the tube radius variation along the tube, and R_* is the characteristic tube radius. In the model that we adopted here $L_* = l_c = L/6$. Since typically $L \sim 50R_*$, it follows that $L_*/R_* \sim 8$. Hence, the condition $L_* \gg R_*$ is satisfied. The condition that the speed of the flow caused by cooling is much smaller than the phase speed is

$$\mathcal{N} = L(t_c C_f)^{-1} \ll 1. \tag{7.12}$$

In our analysis we neglect the effect of the tube curvature and consider it as straight. To our knowledge the effect of tube curvature on the propagation and damping of kink waves has not been studied. However, it was studied in the case of standing waves. Van Doorsselaere et al. (2004) analytically and Terradas et al. (2006) numerically showed that the coronal loop curvature has very minor effect on the frequency and damping of kink

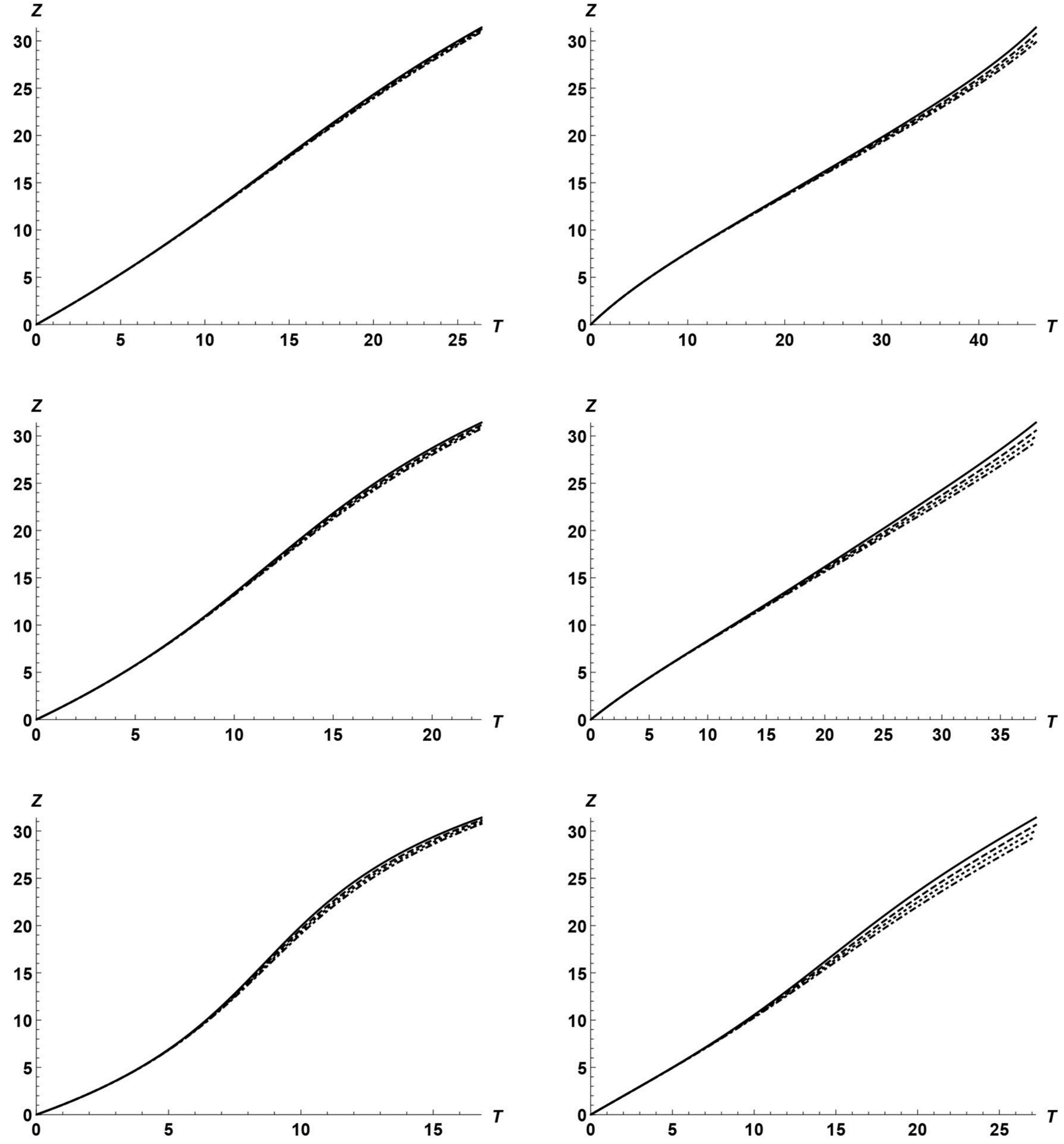

FIGURE 2 | Dependence of the wave front position on time. The calculations continued until the wave front reaches the other end of the magnetic tube. The left panels correspond to λ = 1 and the right to λ = 1.5. The upper, middle, and lower panels correspond to $\kappa = 0.5$, $\kappa = 1$, and $\kappa = 2$, respectively. The solid, dashed, dotted, and dash-dotted curves correspond to $\mathcal{N} = 1/3$, $\mathcal{N} = 0.2$, $\mathcal{N} = 0.1$, and $\mathcal{N} = 0$, respectively.

oscillations. It looks like a viable assumption that the same is true for propagating waves when the curvature radius is much larger than the tube radius.

The main aim of our study is to investigate the effect of cooling on the kink wave propagation. Since cooling decreases ρ_i it increases C_k. Hence, the stronger the cooling is the faster the wave perturbation launched at one footpoint at $t = 0$ reaches the other footpoint. We studied the wave propagation for $\mathcal{N} = 0$ (no cooling), $\mathcal{N} = 0.1$ (slow cooling), $\mathcal{N} = 0.2$ (moderate cooling), and $\mathcal{N} = 1/3$ (strong cooling). In the case of strong cooling the wave front arrives at the second footpoint at $t = t_{\text{end}}$. In all other cases the wave front arrives at the second footpoint at $t > t_{\text{end}}$. We calculated the spatial dependence of the wave frequency, wavenumber, and the amplitude at $t = t_{\text{end}}$. At $z = 0$ the wave frequency is $l^{-1}\omega_0$ and the wavenumber is $l^{-1}\omega_0/C_f$. In our calculation we took the wavelength at $z = 0$ equation to one fifth of L, that is $L = 10\pi l C_f/\omega_0 = 2\pi C_f/\omega_0$.

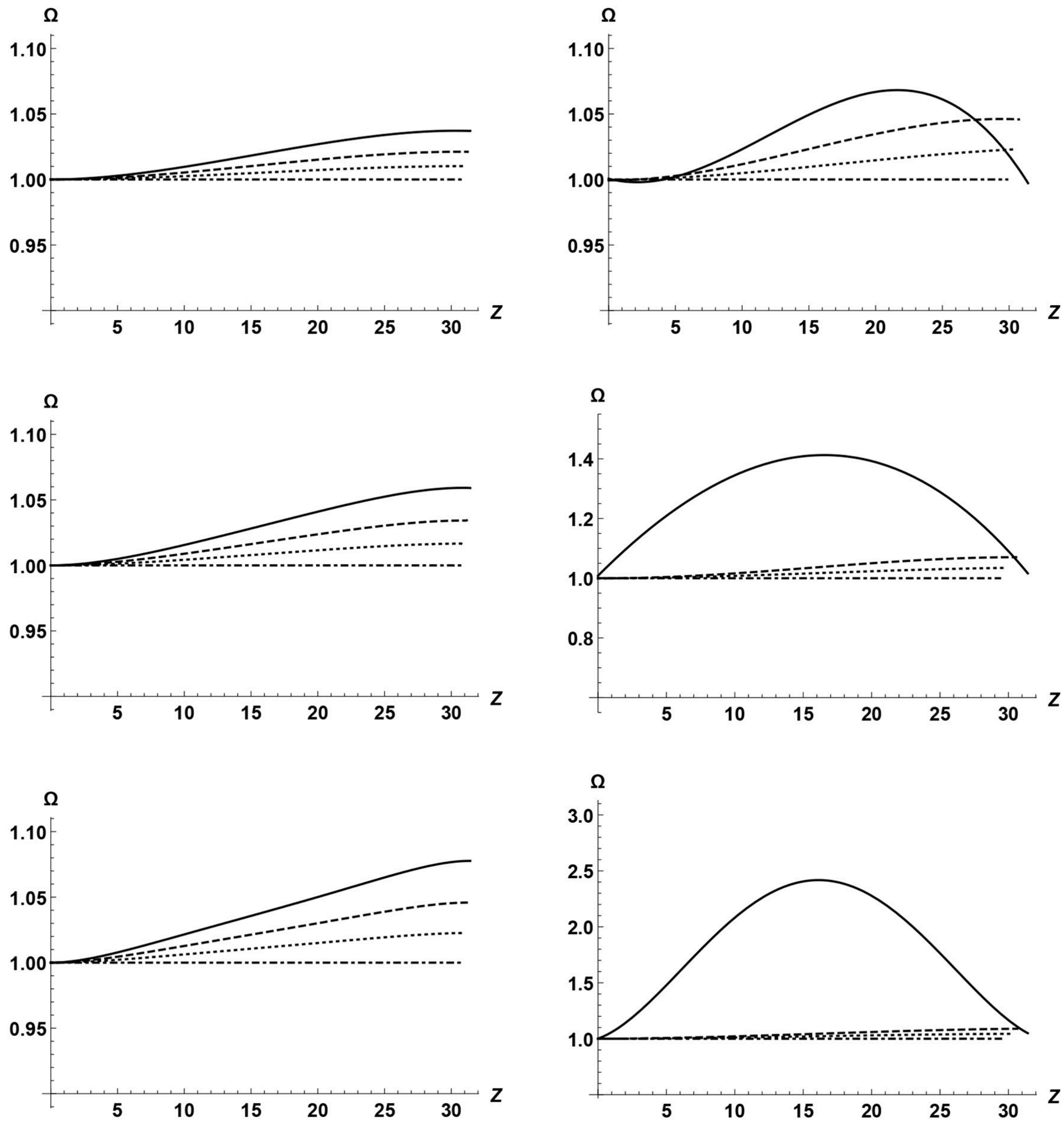

FIGURE 3 | Dependence of the frequency on the distance along the loop for $T = T_{\text{end}}$. The left panels correspond to $\lambda = 1$ and the right to $\lambda = 1.5$. The upper, middle, and lower panels correspond to $\kappa = 0.5$, $\kappa = 1$, and $\kappa = 2$, respectively. The solid, dashed, dotted, and dash-dotted curves correspond to $\mathcal{N} = 1/3$, $\mathcal{N} = 0.2$, $\mathcal{N} = 0.1$, and $\mathcal{N} = 0$, respectively.

We introduce the dimensionless variables and parameters,

$$T = \frac{t\omega_0}{l},\ Z = \frac{z\omega_0}{lC_f},\ \Omega = \frac{l\omega}{\omega_0},\ K = \frac{lkC_f}{\omega_0},\ T_{\text{end}} = \frac{t_{\text{end}}\omega_0}{l},$$

$$\kappa = \frac{L}{\pi H_0},\ \alpha = \frac{\mathcal{N}}{10\pi} = \frac{L}{10\pi t_c C_f}. \tag{7.13}$$

Using the relation $BR^2 = \text{const}$ we obtain

$$C_k^2 = \frac{C_f^2 R_f^4(\zeta + 1)}{R^4[\zeta \exp(-\kappa e^{\alpha T}\sin(0.1Z)) + \exp(-\kappa \sin(0.1Z))]}. \tag{7.14}$$

Then the characteristic Equation (7.6) reduces to

$$\frac{dZ}{dT} = \frac{R_f^2\sqrt{\zeta + 1}}{R^2\sqrt{\zeta \exp(-\kappa e^{\alpha T}\sin(0.1Z)) + \exp(-\kappa \sin(0.1Z))}}. \tag{7.15}$$

The quantity T_{end} is defined by the equation $Z_b(T_{\text{end}}) = \omega_0 L(lC_f)^{-1}$, where $Z_b(T)$ is the solution to Equation (7.15) with $\alpha = 1/30\pi$ satisfying the initial condition $Z_b(0) = 0$. Using Equation (7.15) we calculated the dependence of the wave front position on time for various values of κ and λ. This dependence is shown in **Figure 2**. We see that the stronger the cooling is the faster the wave front moves. This results is not surprising because

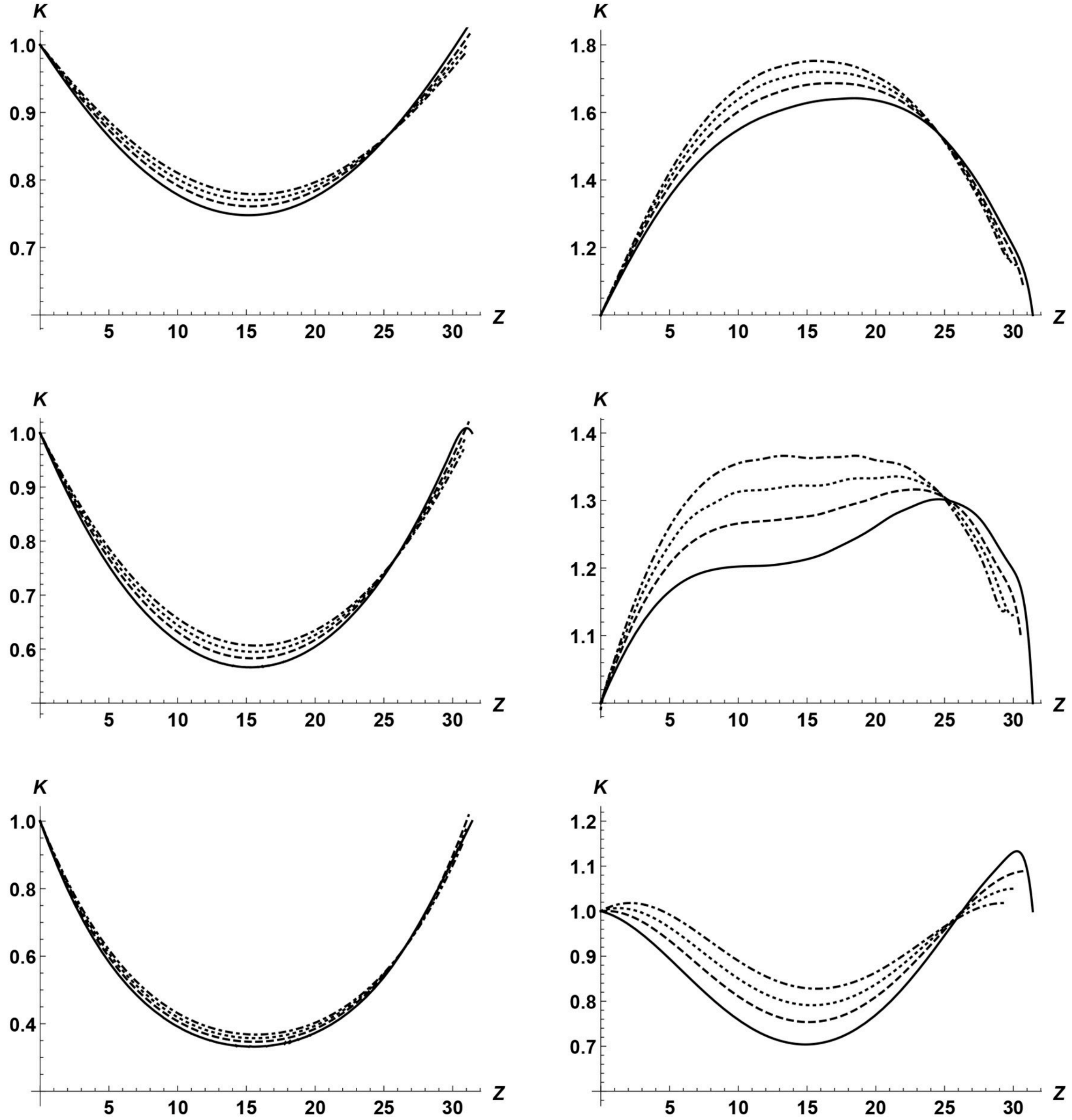

FIGURE 4 | Dependence of the wave number on the distance along the loop for $t = t_{\text{end}}$. The left panels correspond to $\lambda = 1$ and the right to $\lambda = 1.5$. The upper, middle, and lower panels correspond to $\kappa = 0.5$, $\kappa = 1$, and $\kappa = 2$, respectively. The solid, dashed, dotted, and dash-dotted curves correspond to $\mathcal{N} = 1/3$, $\mathcal{N} = 0.2$, $\mathcal{N} = 0.1$, and $\mathcal{N} = 0$, respectively.

the cooling causes the enhancement of the phase speed C_k. We can also see that the effect of cooling is rather weak, although the tube expansion makes it more pronounced.

We also calculated the dimensionless frequency Ω and wavenumber K for various values of λ, Ω, and κ. The results are presented in **Figures 3**, **4**. First of all, we note the frequency is constant when there is no cooling as it must be. When there is cooling, in a non-expanding loop the frequency increases with the distance from the footpoint where the wave is driven. The stronger the cooling is the more pronounced this effect is. However, this effect is quite weak. The dependence of frequency on the cooling rate is much stronger in an expanding loop. We see that it is especially strong when the tube expands and the loop height substantially exceeds the atmospheric scale height. The situation with the wavenumber is quite similar. Again cooling almost does affect it in non-expanding loops, while in expanding loops the effect of cooling is quite noticeable.

Finally, **Figure 5** displays the variation of the amplitude along the loop. It is worth noticing that, in most cases, the amplitude first increases and then starts to decay. The amplitude increase is related with the stratification, while the decay is cased by the resonant damping. We can see that cooling always results

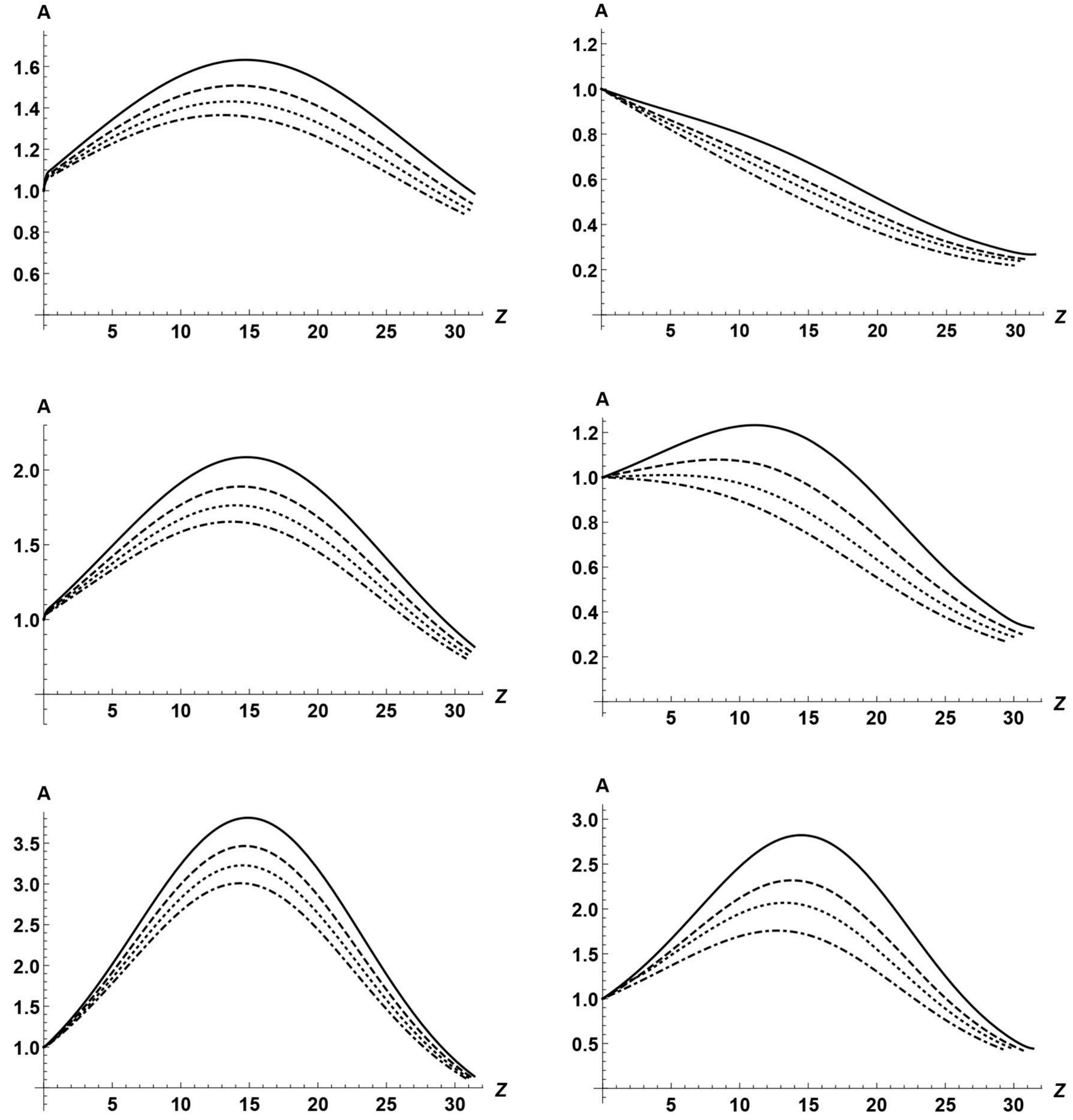

FIGURE 5 | Dependence of the amplitude on the distance along the loop for $t = t_{\text{end}}$. The left panels correspond to $\lambda = 1$ and the right to $\lambda = 1.5$. The upper, middle, and lower panels correspond to $\kappa = 0.5$, $\kappa = 1$, and $\kappa = 2$, respectively. The solid, dashed, dotted, and dash-dotted curves correspond to $\mathcal{N} = 1/3$, $\mathcal{N} = 0.2$, $\mathcal{N} = 0.1$, and $\mathcal{N} = 0$, respectively.

in the amplification of waves. This result is similar to that found by Ruderman (2011a,b); Ruderman et al. (2017), and Shukhobodskiy et al. (2018) in the case of standing kink waves.

8. SUMMARY AND CONCLUSIONS

In this article we studied the kink wave propagation along an expanding magnetic tube with the density varying along the tube and in time. The tube consists of the core region where the density is almost independent of the radial coordinate, and the boundary layer where the density decreasing fast from its value inside the core region to its value in the surrounding plasma. This value is assumed to be thin meaning that its thickness is much smaller than the tube radius. We used the cold plasma approximation. We also used the thin tube approximation meaning that the wave length is much larger than the tube radius, and the short wave approximation meaning that the wavelength is much smaller than the characteristic scale of the density and tube radius variation along the tube. Using the WKB method we derived the equation describing the dependence of the wave amplitude on time and on the distance along the tube.

First we studied the kink wave propagation in a magnetic tube homogeneous in the axial direction. In this case the only effect affecting the wave propagation is the wave damping due to resonant absorption. We reproduced the results previously obtained by Terradas et al. (2010).

We then proceeded to studying the kink wave propagation in a magnetic tube with the density varying in the axial direction. In this case the wave propagation are affected both by resonance absorption and the axial inhomogeneity. We reproduced the analysis by Soler et al. (2011c).

Finally, we studied the kink wave propagation in an expanding and non-stationary magnetic tube. We obtained the general expressions determining the spatial and temporal dependence of wave frequency, wavenumber, and amplitude. We then applied the general theory to a particular case of kink wave propagating along a cooling coronal loop. We assumed that the loop has a half-circle shape and immersed in an isothermal atmosphere, the temperature of plasma inside the loop decays exponentially, while the temperature of the surrounding plasma does not change. We adopted the dependence of the loop cross-section on the distance along the loop previously used by Ruderman et al. (2008, 2017) and Shukhobodskiy et al. (2018). The equations governing the wave propagation were solved numerically. We assumed that the wave was started to be driven at one of the footpoints at the same time when the plasma inside the loop started to cool. Our main aim was to study the dependence of the wave properties on the intensity of cooling. First we studied the dependence of the distance that the wavefront travels on time. We found that the stronger the cooling is the larger the distance that the wave front travel at a given time. This is an expected result because cooling enhances the phase speed thus accelerating the wavefront. We also calculated the dependence of the wave frequency and wave number on the distance along the tube. When doing so we chose the moment of time when the wavefront arrives at the second footpoint in the case of strongest cooling. The general conclusion is that cooling results in the increase of the wave frequency. In contrast, it is difficult to make any definite conclusion about the effect of cooling on the wavenumber. Finally, we investigated the dependence of the wave amplitude on the distance along the tube. In most cases the amplitude first growths due to the equilibrium quantity variation along the tube, and then its starts to decay due to resonant damping. We found that cooling enhances the wave amplitude. This result is similar to one previously obtained for standing kink waves (Ruderman, 2011a,b; Shukhobodskiy et al., 2018).

AUTHOR CONTRIBUTIONS

All authors listed have made a substantial, direct and intellectual contribution to the work, and approved it for publication.

ACKNOWLEDGMENTS

The authors acknowledge the support by Science and Technology Facilities Council UK (STFC), grant ST/M000826/.

REFERENCES

Arregui, I. (2015). Wave heating of the solar atmosphere. *Philos. Trans. R. Soc.* 373:20140261. doi: 10.1098/rsta.2014.0261

Aschwanden, M. J., and Schrijver, C. J. (2011). Coronal loop oscillations observed with atmospheric imaging assembly – kink mode with cross-sectional and density oscillations. *Astrophys. J.* 736:102. doi: 10.1088/0004-637X/736/2/102

Aschwanden, M. J., and Terradas, J. (2008). The effect of radiative cooling on coronal loop oscillations. *Astrophys. J. Lett.* 686, L127–L130. doi: 10.1086/592963

Ballester, J. L., Carbonell, M., Soler, R., and Terradas, J. (2018). The temporal behaviour of MHD waves in a partially ionized prominence-like plasma: effect of heating and cooling. *Astron. Astrophys.* 609:A6. doi: 10.1051/0004-6361/201731567

Bender, C. M., and Orszag, S. A. (1978). *Advanced Mathematical Methods for Scientists and Engineers*. New York, NY: McGraw-Hill.

De Pontieu, B., McIntosh, S. W., Carlsson, M., Hansteen, V. H., Tarbell, T. D., Schrijver, C. J., et al. (2007). Chromospheric Alfvénic waves strong enough to power the solar wind. *Science* 318, 1574–1577. doi: 10.1126/science.1151747

Dymova, M. V., and Ruderman, M. S. (2006). Resonantly damped oscillations of longitudinally stratified coronal loops. *Astron. Astrophys*. 457, 1059–1070. doi: 10.1051/0004-6361:20065051

Goossens, M., Erdélyi, R., and Ruderman, M. S. (2011). Resonant MHD waves in the solar atmosphere. *Space Sci. Rev*. 158, 289–338. doi: 10.1007/s11214-010-9702-7

Goossens, M., Ruderman, M. S., and Hollweg, J. V. (1995). Dissipative MHD solutions for resonant Alfvén waves in 1-dimensional magnetic flux tubes. *Solar Phys*. 157, 75–102. doi: 10.1007/BF00680610

He, J., Marsch, E., Tu, C., and Tian, H. (2009). Excitation of kink waves due to small-scale magnetic reconnection in the chromosphere? *Astrophys. J.* 705, L217–L222. doi: 10.1088/0004-637X/705/2/L217

He, J.-S., Tu, C.-Y., Marsch, E., Guo, L.-J., Yao, S., and Tian, H. (2009). Upward propagating high-frequency Alfvén waves as identified from dynamic wave-like spicules observed by SOT on Hinode. *Astron. Astrophys.* 497, 425–535. doi: 10.1051/0004-6361/200810777

Hollweg, J. V., and Yang, G. (1988). Resonance absorption of compressible magnetohydrodynamic waves at thin "surfaces". *J. Geophys. Res.* 93, 5423–5436. doi: 10.1029/JA093iA06p05423

Hood, A. W., Ruderman, M. S., Pascoe, D. J., De Moortel, I., Terradas, J., and Wright, A. N. (2013). Damping of kink waves by mode coupling I. Analytical treatment. *Astron. Astrophys.* 551:A39. doi: 10.1051/0004-6361/201220617

Lin, Y., Engvold, O., Rouppe van der Voort, L. H. M., and van Noort, M. (2007). Evidence of traveling waves in filament threads. *Sol. Phys.* 246, 65–72. doi: 10.1007/s11207-007-0402-8

Lin, Y., Soler, R., Engvold, O., Ballester, J. L., Langangen, Ø., Oliver, R., et al. (2009). Swaying threads of a solar filament. *Astrophys. J.* 704, 870–876. doi: 10.1088/0004-637X/704/1/870

Magyar, N., Van Doorsselaere, T., and Marcu, A. (2015). Numerical simulations of transverse oscillations in radiatively cooling coronal loops. *Astron. Astrophys.* 582:A117. doi: 10.1051/0004-6361/201526287

Morton, R. J., Hood, A. W., and Erdélyi, R. (2010). Propagating magneto-hydrodynamic waves in a cooling homogenous coronal plasma. *Astron. Astrophys.* 512:A23. doi: 10.1051/0004-6361/200913365

Okamoto, T. J., Tsuneta, S., Berger, T. E., Ichimoto, K., Katsukawa, Y., Lites, B. W., et al. (2007). Coronal transverse magnetohydrodynamic waves in a solar prominence. *Science* 318, 1577–1580. doi: 10.1126/science.1145447

Pascoe, D. J., Hood A. W., De Moortel, I., and Wright, A. N. (2012). Spatial damping of propagating kink waves due to mode coupling. *Astron. Astrophys.* 539:A37. doi: 10.1051/0004-6361/201117979

Pascoe, D. J., Hood A. W., De Moortel, I., and Wright, A. N. (2013). Damping of kink waves by mode coupling II. Parametric study and seismology. *Astron. Astrophys.* 551:A40. doi: 10.1051/0004-6361/201220620

Pascoe, D. J., Wright, A. N., and De Moortel, I. (2010). Coupled Alfvén and kink oscillations in coronal loops. *Astrophys. J.* 711, 990–996. doi: 10.1088/0004-637X/711/2/990

Pascoe, D. J., Wright, A. N., and De Moortel, I. (2011). Propagating coupled Alfvén and kink oscillations in an arbitrary inhomogeneous corona. *Astrophys. J.* 731:73. doi: 10.1088/0004-637X/731/1/73

Ruderman, M. S. (2011a). Transverse oscillations of coronal loops with slowly changing density. *Solar Phys.* 271, 41–54. doi: 10.1007/s11207-011-9772-z

Ruderman, M. S. (2011b). Resonant damping of kink oscillations of cooling coronal magnetic loops. *Astron. Astrophys*. 534:A78. doi: 10.1051/0004-6361/201117416

Ruderman, M. S., and Erdélyi, R. (2009). Transverse oscillations of coronal loops. *Space Sci. Rev.* 149, 199–228. doi: 10.1007/s11214-009-9535-4

Ruderman, M. S., Goossens, M., and Andries, J. (2010). Nonlinear propagating kink waves in thin magnetic tubes. *Phys. Plasmas* 17:082108. doi: 10.1063/1.3464464

Ruderman, M. S., and Roberts, B. (2002). The damping of coronal loop oscillations. *Astrophys.J.* 577, 475–486. doi: 10.1086/342130

Ruderman, M. S., Shukhobodskiy, A. A., and Erdélyi, R. (2017). Kink oscillations of cooling coronal loops with variable cross-section. *Astron. Astrophys*. 602:A50. doi: 10.1051/0004-6361/201630162

Ruderman, M. S., and Terradas, J. (2013). Damping of coronal loop kink oscillations due to mode conversion. *Astron. Astrophys*. 555:A27. doi: 10.1051/0004-6361/201220195

Ruderman, M. S., Tirry, W., and Goossens, M. (1995). Non-stationary resonant Alfvén surface waves in one-dimensional magnetic plasmas. *J. Plasma Phys*. 54, 129–148. doi: 10.1017/S0022377800018407

Ruderman, M. S., Verth, G., and Erdélyi, R. (2008). Transverse oscillations of longitudinally stratified coronal loops with variable cross section. *Astrophys. J.* 686, 694–700. doi: 10.1086/591444

Shukhobodskiy, A. A., and Ruderman, M. S. (2018). Resonant damping of kink oscillations of thin expanding magnetic tubes. *Astron. Astrophys.* 615:A156. doi: 10.1051/0004-6361/201732396

Shukhobodskiy, A. A., Ruderman, M. S., and Erdélyi, R. (2018). Resonant damping of kink oscillations of thin cooling and expanding coronal magnetic loops. *Astron. Astrophys.* 619:A173. doi: 10.1051/0004-6361/201833714

Soler, R., Oliver, R., and Ballester, J. L. (2011a). Spatial damping of propagating kink waves in prominence threads. *Astrophys. J.* 726:102. doi: 10.1088/0004-637X/726/2/102

Soler, R., Terradas, J., and Goossens, M. (2011b). Spatial damping of propagating kink waves due to resonant absorption: effect of background flow. *Astrophys. J.* 734:80. doi: 10.1088/0004-637X/734/2/80

Soler, R., Terradas, J., Verth, G., and Goossens, M. (2011c). Resonantly damped propagating kink waves in longitudinally stratified solar waveguides. *Astrophys. J.* 736:10. doi: 10.1088/0004-637X/736/1/10

Terradas, J., Goossens, M., and Verth, G. (2010). Selective spatial damping of propagating kink waves due to resonant absorption. *Astron. Astrophys.* 524:A23. doi: 10.1051/0004-6361/201014845

Terradas, J., Oliver, R., and Ballester, J. L. (2006). Damping of kink oscillations in curved coronal loops. *Astrophys. J.* 650, L91–L94. doi: 10.1086/508569

Tomczyk, S., and McIntosh, S. W. (2009). Time-distance seismology of the solar corona with CoMP. *Astrophys. J.* 697, 1384–1391. doi: 10.1088/0004-637X/697/2/1384

Tomczyk, S., McIntosh, S. W., Keil, S. L., Judge, P. G., Schad, T., Seeley, D., et al. (2007). Alfvén waves in the solar corona. *Science* 317, 1192–1196. doi: 10.1126/science.1143304

Van Doorsselaere, T., Debosscher, A., Andries, J., and Poedts, S. (2004). The effect of curvature on quasi-modes in coronal loops. *Astron. Astrophys.* 424, 1065–1074. doi: 10.1051/0004-6361:20041239

Verth, G., Terradas, J., and Goossens, M. (2010). Observational evidence of resonantly damped propagating kink waves in the solar corona. *Astrophys. J.* 718, L102–L105. doi: 10.1088/2041-8205/718/2/L102

Conflict of Interest Statement: The authors declare that the research was conducted in the absence of any commercial or financial relationships that could be construed as a potential conflict of interest.

APPENDIX

A. Solution to Equation (4.21)

In this section we obtain the solution to Equation (4.21) satisfying the asymptotic condition Equation (4.24). To simplify calculations we introduce the notation

$$\Psi = \frac{\psi - \psi_A}{RB\delta_A}, \quad h = \frac{\rho_i S(C_k^2 - V_{Ai}^2)}{\rho_A B \Delta \delta_A}. \tag{A1}$$

Using this notation we rewrite Equation (4.21) as

$$\Psi \hat{\xi}_\varphi + i \frac{\partial^2 \hat{\xi}_\varphi}{\partial \Psi^2} = -ih. \tag{A2}$$

To solve this equation we use the Fourier transform with respect to Ψ defined by

$$\mathcal{F}[\hat{\xi}_\varphi] = \int_{-\infty}^{\infty} \hat{\xi}_\varphi e^{-i\sigma\Psi} \, d\Psi, \quad \hat{\xi}_\varphi = \frac{1}{2\pi} \int_{-\infty}^{\infty} \mathcal{F}[\hat{\xi}_\varphi] e^{i\sigma\Psi} \, d\sigma. \tag{A3}$$

Applying this transform to Equation (A2) we obtain

$$\frac{\partial}{\partial \sigma} \mathcal{F}[\hat{\xi}_\varphi] + \sigma^2 \mathcal{F}[\hat{\xi}_\varphi] = -2\pi h \delta(\sigma), \tag{A4}$$

where $\delta(\sigma)$ is the delta-function. The solution to this equation decaying as $|\sigma| \to \infty$ is given by

$$\mathcal{F}[\hat{\xi}_\varphi] = -2\pi h H(\sigma) e^{-\sigma^3/3}, \tag{A5}$$

where $H(\sigma)$ is the Heaviside step function. Calculating the inverse Fourier transform we obtain

$$\hat{\xi}_\varphi = -h \int_0^\infty \exp\left(i\sigma\Psi - \tfrac{1}{3}\sigma^3\right) d\sigma. \tag{A6}$$

Using the integration by parts we obtain the asymptotic expression valid for $|\Psi| \gg 1$,

$$\hat{\xi}_\varphi = -\frac{ih}{\Psi} + \mathcal{O}\left(\Psi^{-2}\right). \tag{A7}$$

Using Equation (A1) it is straightforward to verify that Equation (A7) coincides with Equation (4.24).

B. Evaluation of Integral in Equation (4.34)

In this section we evaluate the integral on the right-hand side of Equation (4.34) for $|\Psi \gg 1$. We immediately obtain

$$\int_{-\Psi}^{\Psi} \left(\Psi_1 G(\Psi_1) - \frac{dF}{d\Psi_1} \right) d\Psi_1 = -F(\Psi) + F(-\Psi) + \int_{-\Psi}^{\Psi} \Psi_1 G(\Psi_1) \, d\Psi_1. \tag{B1}$$

It is obvious that

$$F(\Psi) - F(-\Psi) = 2i \int_0^\infty \sin(\sigma\Psi) \, e^{-\sigma^3/3} d\sigma = \mathcal{O}(1). \tag{B2}$$

Changing the order of integration we obtain

$$\int_{-\Psi}^{\Psi} \Psi_1 G(\Psi_1) \, d\Psi_1 = 2i \int_0^\infty [\sin(\sigma\Psi) - (\sigma\Psi)\cos(\sigma\Psi)] \frac{e^{-\sigma^3/3}}{\sigma^3} d\sigma. \tag{B3}$$

Then, using the integration by parts yields

$$\int_{-\Psi}^{\Psi} \Psi_1 G(\Psi_1) \, d\Psi_1 = i\Psi^2 \int_0^\infty \frac{\sin(\sigma\Psi)}{\sigma} e^{-\sigma^3/3} d\sigma + I(\Psi), \tag{B4}$$

where

$$I(\Psi) = i \int_0^\infty \left[(\sigma\Psi)\cos(\sigma\Psi) - \sin(\sigma\Psi) \right] e^{-\sigma^3/3} d\sigma. \tag{B5}$$

Again using the integration by parts we obtain

$$I(\Psi) = i \int_0^\infty \left(\sigma^3 - 2\right) \sin(\sigma\Psi) e^{-\sigma^3/3} d\sigma = \mathcal{O}(1). \tag{B6}$$

With the aid of the variable substitution we obtain

$$\int_0^\infty \frac{\sin(\sigma\Psi)}{\sigma} e^{-\sigma^3/3} d\sigma = \int_0^\infty \frac{\sin\sigma}{\sigma} e^{-\sigma^3/3\Psi^2} d\sigma = \frac{\pi}{2}[1 + o(1)]. \tag{B7}$$

Using Equations (B1), (B2), (B4), (B6), and (B7) we finally arrive at

$$\int_{-\Psi}^{\Psi} \left(\Psi_1 G(\Psi_1) - \frac{dF}{d\Psi_1} \right) d\Psi_1 = \frac{\pi i}{2} \Psi^2 [1 + o(1)]. \tag{B8}$$

frontiers
in Astronomy and Space Sciences

ORIGINAL RESEARCH
published: 04 March 2019
doi: 10.3389/fspas.2019.00011

A Fresh Look at Waves in Ion-Electron Plasmas

Rony Keppens[1,2]* *and Hans Goedbloed*[3]

[1] Centre for mathematical Plasma Astrophysics, KU Leuven, Leuven, Belgium, [2] School of Physics and Astronomy, Yunnan University, Kunming, China, [3] DIFFER, TU/e Science Park, Eindhoven, Netherlands

Exploiting the general dispersion relation describing all waves in an ideal ion-electron fluid, we revisit established treatments on wave families in a cold ion-electron plasma. These contain the magnetohydrodynamic Alfvén and fast waves at low frequencies, long wavelengths, but are enriched by short wavelength resonance behaviors, electrostatic and electromagnetic mode types, and cut-off frequencies distinguishing propagating from evanescent waves. Our theoretical treatment exploits purely polynomial expressions, which for the cold ion-electron case only depend on 2 parameters: the ratio of masses over charges μ and the ratio E of the electron gyro frequency to the combined ion-electron plasma frequency. We provide a complete description of all waves, which stresses the intricate variation of all five branches of eigenfrequencies $\omega(k, \vartheta)$ depending on wavenumber k and angle ϑ between wavevector and magnetic field B. Corresponding 5-mode phase and group diagrams provide insight on wave transformations and energy transport. Special cases, like the high frequency modes in magneto-ionic theory following from Appleton-Hartree dispersion relations, are naturally recovered and critically discussed. Faraday rotation for electromagnetic waves is extended to all propagation angles ϑ. The discussion covers all cold ion-electron plasma waves, up into the relativistic regime.

Keywords: waves, cold plasmas, 2-fluid theory, magnetohydrodynamic, electromagnetic wave theory

OPEN ACCESS

Edited by:
Bo Li,
Shandong University, China

Reviewed by:
Jinsong Zhao,
Purple Mountain Observatory (CAS), China
Paul Cally,
Monash University, Australia

****Correspondence:***
Rony Keppens
rony.keppens@kuleuven.be

Specialty section:
This article was submitted to Stellar and Solar Physics, a section of the journal Frontiers in Astronomy and Space Sciences

Received: *11 January 2019*
Accepted: *12 February 2019*
Published: *04 March 2019*

Citation:
Keppens R and Goedbloed H (2019) A Fresh Look at Waves in Ion-Electron Plasmas. Front. Astron. Space Sci. 6:11. doi: 10.3389/fspas.2019.00011

1. INTRODUCTION

The theory of wave propagation in ion-electron plasmas is covered in many textbooks (Stix, 1992; Boyd and Sanderson, 2003; Bittencourt, 2004; Chen, 2016; Thorne and Blandford, 2017), and can be considered established. The starting point for many treatments is based on a 2-fluid approach, where one solves for plane wave solutions $\exp\left[i(\mathbf{k}\cdot\mathbf{x}-\omega t)\right]$ in an otherwise homogeneous medium, usually magnetized with uniform magnetic field $\mathbf{B}$. In the rest frame of a homogeneous ion-electron mixture, assumed to be charge-neutral such that number densities obey $n_e = Zn_i$ when ions have charge number Z, the equilibrium electric field and current vanish, while each species has its own pressure p_e, p_i. The dispersion relation between wave frequency ω and wavenumber $k =| \mathbf{k} |$ is then usually obtained from linearizing the Maxwell equations, traditionally introducing dielectric, susceptibility and conductivity tensors, to quantify displacement vector, polarization vector and current vector relations to the electric field, respectively. In general, this leaves a large variety of wave modes that are particularly aware of the orientation angle ϑ between wavevector $\mathbf{k}$ and the magnetic field $\mathbf{B}$, while the wave properties can differ greatly according to frequency and wavelength. Indeed, when we have electron and ion masses given by m_e and m_i, the plasma is characterized by its ratio of masses over charges $\mu = Zm_e/m_i$, and this background ion-electron mixture introduces its own set of typical frequencies and wavelengths. The former include the electron and ion plasma frequencies $\omega_{pe} = \sqrt{e^2 n_e/\epsilon_0 m_e}$ and $\omega_{pi} = \sqrt{\mu}\omega_{pe}$ and the electron and ion cyclotron frequencies $\Omega_e = eB/m_e$ (where electron charge is $-e$) and $\Omega_i = \mu\Omega_e$. Lenghscales relate to typical speeds in the system, such as the light speed $c = 1/\sqrt{\mu_0\epsilon_0}$ and the electron and ion sound speeds. One such lengthscale is the skin depth $\delta = c/\omega_p$, where it turns out convenient to combine the plasma frequencies into $\omega_p^2 = \omega_{pe}^2 + \omega_{pi}^2$. The governing dispersion relation equally follows (e.g., Goedbloed and Poedts, 2004) from a standard linearization of the governing equations of motion for each species, combined with Maxwell equations. We will in what follows rewrite and analyse this general form of the dispersion relation, but specify deliberately to the cold ion-electron case, where the species pressures (and sound speeds) vanish $p_e = 0 = p_i$. We can normalize all frequencies to the plasma frequency $\bar{\omega} = \omega/\omega_p$, and for such cold ion-electron plasma, only two dimensionless parameters remain in the description, namely

$$E = \Omega_e/\omega_p\,, \quad I = \Omega_i/\omega_p\,. \tag{1}$$

That only two parameters cover the full complexity of wave modes in a cold ion-electron plasma is well-known, and is at the basis of the classical Clemmow-Mullaly-Allis plots that feature in most textbooks (Stix, 1992; Bittencourt, 2004; Thorne and Blandford, 2017), which classify wave modes and associated wave normal surfaces (plots of ω/k vs. ϑ, which are figures of revolution about **B**). In what follows, we will discuss all wave modes and suggest a new classification scheme based on the polynomial form of the governing dispersion relation. That the ideal two-fluid description leads to a 12th order polynomial in the wave frequency ω is well-known (Denisse and Delcroix, 1961), although one frequently exploits lower order polynomials to cover e.g., only the high frequency electromagnetic waves (following e.g., the Appleton-Hartree description), or conversely focuses on the three low frequency branches that relate to the magnetohydrodynamic (MHD) slow, Alfvén and fast mode pairs (Stringer, 1963; Ishida et al., 2005; Damiano et al., 2009; Bellan, 2012; Zhao, 2015). An eight order polynomial approximation, valid above the lower hybrid frequency, was exploited in Zhao (2017) to cover whistler waves and the three high frequency electromagnetic mode pairs. We will instead start from the full 12th order equation, only making the cold plasma assumption, such that the slow MHD modes become marginal solutions $\omega^2 = 0$. We make contact with the mentioned textbook treatments, showing how the usual dielectric tensor treatments are indeed mathematically fully equivalent. The advantage of the polynomial method over the dielectric tensor method is the direct relationship of the solutions of the dispersion equation to the primitive two-fluid variables, which would also be exploited in corresponding numerical time stepping codes. This advantage was also pointed out by Bellan (2012), who gave a similar analysis for the low frequency domain. The present paper exploits the polynomial method to full effect to provide the crucial phase and groups diagrams for all values of the parameters, together with their animations.

2. DISPERSION RELATION FOR COLD ION-ELECTRON PLASMAS

Following Goedbloed and Poedts (2004), the general dispersion relation for an ideal ion-electron fluid can be written as a twelfth-order polynomial in $\bar{\omega}$, where one distinguishes six pairs of forward and backward propagating modes, since the expression is actually sixth order in $\bar{\omega}^2$. This already eliminated a pair $\bar{\omega}^2 = 0$ of marginal entropy-like modes, and the special case of a cold ion-electron fluid can factor out another $\bar{\omega}^2 = 0$ solution, corresponding to the slow magnetohydrodynamic (backward and forward) waves. It is a matter of algebra to show that the remaining 10th order polynomial can be rewritten to

$$\bar{k}^4 \bar{A}(\bar{\omega}^2, \lambda^2) - \bar{k}^2 \bar{\omega}^2 \bar{B}(\bar{\omega}^2, \lambda^2) + \bar{\omega}^4 \bar{C}(\bar{\omega}^2) = 0\,, \tag{2}$$

where $\bar{k} = \delta k$, $\lambda^2 = \cos^2\vartheta$, containing three 3rd order polynomials in $\bar{\omega}^2$ given by

$$\begin{aligned}
\bar{A} &= \bar{\omega}^6 - (1 + E^2 + I^2)\bar{\omega}^4 \\
&\quad + \left[(1 + EI)EI + \lambda^2(E^2 + I^2 - EI)\right]\bar{\omega}^2 - \lambda^2(EI)^2\,, && (3)\\
\bar{B} &= 2\bar{\omega}^6 - (4 + 2E^2 + 2I^2)\bar{\omega}^4 + \left[2(1 + EI)^2\right. \\
&\quad \left.+ (1 + \lambda^2)(E^2 + I^2 - EI)\right]\bar{\omega}^2 - EI(1 + EI)(1 + \lambda^2)\,, && (4)\\
\bar{C} &= (\bar{\omega}^2 - 1)\left[\bar{\omega}^4 - (2 + E^2 + I^2)\bar{\omega}^2 + (1 + EI)^2\right]. && (5)
\end{aligned}$$

Unlike most textbook treatments, which take Equation (2) at fixed frequency and solve for both roots in $\bar{k}^2$, we will consider a given wavenumber $\bar{k}$, and use the dispersion relation to quantify all five roots in $\bar{\omega}^2$. In what follows, we will also systematically drop the overbars on $\bar{k}$ and $\bar{\omega}$, as we will always work with dimensionless frequencies and wavenumbers.

2.1. Cut-Off Frequencies

Cut-off frequencies relate to large wavelength (small wavenumber k) limiting behavior, and Equation (2) reveals instantly that special frequencies then follow from the zeros of the $\bar{C}$ polynomial. These are computed simply as

$$\begin{aligned}
\omega_c^2 &= 1\,, && (6)\\
\omega_{u,l}^2 &= 1 + \frac{E^2 + I^2}{2} \pm |\, E - I \,| \sqrt{\frac{(E + I)^2}{4} + 1}\,. && (7)
\end{aligned}$$

Hence, the $\omega_c^2 = 1$ cutoff happens exactly at the combined plasma frequency (this reads as $\omega^2 = \omega_p^2$ when restoring dimensions). The latter pair $\omega_{u,l}^2$ distinguishes the upper (+) from the lower (−) cut-off frequency. For $E = 0$, the three cut-offs coincide at the plasma frequency (noting that $I = \mu E$).

In general, the three cut-off frequencies are independent of the angle ϑ, but their relative ordering is influenced by the values of both parameters E, I or equivalently, E and μ. Since μ is normally considered fixed in a specific plasma (e.g., it assumes the value $\mu \approx 1/1{,}836$ in a fully ionized hydrogen plasma), the magnetic field strength in essence determines the other parameter E, going from unmagnetized $E = 0$ cases, to strongly magnetized regimes

$E \to \infty$. A special case is obtained for an electron-positron or pair plasma where $\mu = 1$, when $\omega_{u,l}^2$ coincide to $\omega_l^2 = \omega_u^2 = 1 + E^2$ (Keppens and Goedbloed, in press). For an arbitrary μ, it is clear that $\omega_u^2 \geq 1$ (and the equality holds for the unmagnetized case $E = 0$), but the lower cut-off may be below, equal to, or above unity. The equality of ω_c^2 with ω_l^2 corresponds to the specific field strength where $E = 1/\mu - 1$. A plot of the three cut-off frequencies for a $\mu = 1/1{,}836$ hydrogen plasma vs. E is shown in **Figure 1**. The vertical dashed lines indicate special values for E, e.g., where $E = 1/\mu - 1$, where the ordering of the three cut-offs changes. The right panel in **Figure 1** shows a zoom on the behavior near this value. The above exact expressions for the cut-off frequencies, valid for all values of E, can also be used to get approximate expressions in limits of small or large E regimes. Obviously, the small E limit makes all cut-offs approach their unmagnetized regime: all 3 become the plasma frequency. The opposite, large E limit is easily evaluated to give as upper and lower cut-off (both way above the third cut-off at plasma frequency):

$$\lim_{E\to\infty} \omega_u^2 = E^2 \,, \tag{8}$$

$$\lim_{E\to\infty} \omega_l^2 = E^2\mu^2 \,. \tag{9}$$

2.2. Resonances

Resonances occur at large wavenumbers (short wavelengths), and Equation (2) shows that then the zeros of $\bar{A}$ come into play. The three resonances obtained from $\bar{A} = 0$ can be computed using standard root-finding for polynomial expressions (or, could be explicitly obtained through Cardano's formulae for the roots of a third order polynomial). For a given set of parameters (E, I) or (E, μ), the 3 resonances still depend on the orientation angle ϑ. The exact variation of the three resonances at any (ϑ, E, μ) requires to compute the three roots from

$$\omega^6 - \left[1 + E^2(1+\mu^2)\right]\omega^4 + E^2\left[\mu + \mu^2E^2 + \lambda^2(1-\mu+\mu^2)\right]\omega^2 - \lambda^2E^4\mu^2 = 0 \,. \tag{10}$$

For each of the three resonances, we typically find monotonic behavior $\omega(\vartheta)$ between the extremal angles of parallel to perpendicular orientation. **Figure 1** also shows the range in values obtained for the three resonances, for the same fixed value of $\mu = 1/1{,}836$, as function of the remaining E parameter. Three different colors indicate the three resonance ranges. The top (purple) one is seen to stay above unity, and stays between the upper cut-off and E^2 for large E. This purple resonance range always shows increasing frequencies when going from parallel (solid) to perpendicular (dashed) behavior. The middle (blue) range is bounded from above by E^2, and stays below unity until we reach the $E = \sqrt{\mu^2 - \mu + 1}/\mu$ value, which lies in between the dotted lines shown at $E = 1/\mu - 1$ and $E = 1/\mu$ (right panel). Ultimately, its range becomes bounded by the μ^2E^2 curve. This blue resonance will relate to the fast magnetosonic wave branch. The lowest resonance range (red) always stays below the μ^2E^2 line and below unity. In fact, this resonance range extends all the way to zero at exactly perpendicular orientation, and will be shown to relate to the Alfvén branch.

We can get approximate expressions for the three resonances by setting $\mu = 0$ (which is unphysical, but is at the basis of the often used Appleton-Hartree dispersion relation, see section 5.3). We then obtain one solution at zero frequency (which will relate to the red or Alfvén branch), and the purple and blue resonances become

$$\omega^2 \approx \tfrac{1}{2}\left[1 + E^2 \pm \sqrt{(1+E^2)^2 - 4E^2\lambda^2}\right]. \tag{11}$$

Note that setting $\mu = 0$ eliminates the (normalized) ion cyclotron frequency I from the description.

The plots for the general $\mu \neq 0$ case in **Figure 1** reveal how the red resonance range actually always decreases in frequency, with angle going from parallel to perpendicular, while the purple one is always increasing in frequency, going from parallel to perpendicular orientations. The blue resonance range on the other hand first decreases in frequency, up to the value $E = \sqrt{\mu^2 - \mu + 1}/\mu$. From then on, the blue range increases in frequency from parallel to perpendicular. The dashed (perpendicular) and solid (parallel) limits are easily obtained analytically, since

$$\bar{A}(\lambda = 0) = \omega^2\left[\omega^4 - (1 + E^2 + I^2)\omega^2 + (1 + EI)EI\right] \,, \tag{12}$$

$$\bar{A}(\lambda = 1) = (\omega^2 - 1)\left[\omega^4 - (E^2 + I^2)\omega^2 + (EI)^2\right] \,. \tag{13}$$

The solutions to the perpendicular ($\lambda = 0$) case are thus threefold: one at zero frequency, related to non-propagation of Alfvén waves perpendicular to the magnetic field, the other two solutions from $\omega^4 - (1 + E^2 + I^2)\omega^2 + (1 + EI)EI = 0$ are known as the upper and lower hybrid resonance, given by our purple and blue dashed lines in **Figure 1**, respectively. These upper and lower hybrid resonances are thus generally given by

$$\omega_\pm^2 = \frac{1}{2}\left[1 + E^2 + I^2 \pm \sqrt{(1 + E^2 + I^2)^2 - 4(1 + EI)EI}\right] . \tag{14}$$

Their limits for low magnetization ($E \ll 1$) become 1 and 0, as the electrostatic mode remains and the fast mode becomes marginal (see further). In the limit of high magnetization ($E \gg 1$), we find that $\omega_+^2 \approx E^2$ while $\omega_-^2 \approx \mu^2E^2 = I^2$.

It can be noted that for the pair plasma case where $\mu = 1$, the above discussion of resonances and cut-offs simplifies significantly: e.g., the blue resonance range collapses on the curve E^2. Also, for a pair plasma, the purple resonance range extends (at exactly perpendicular propagation) to the upper cut-off value ω_u^2 (Keppens and Goedbloed, in press).

2.3. Low and High Frequency Limits

The dispersion relation Equation (2) also shows clearly the limits at both high and low frequencies, where the plane wave phase speed $v_{ph} = \omega/k$ attains a finite value. At high frequencies, we find that we obtain a double-valued solution at light speed behavior, as we can instantly write this limit as

$$(1 - v_{ph}^2)^2 = 0 \,. \tag{15}$$

Hence, we expect two solutions that will behave as electromagnetic waves at high frequencies. These high frequency solutions, together with a finite phase speed, require large

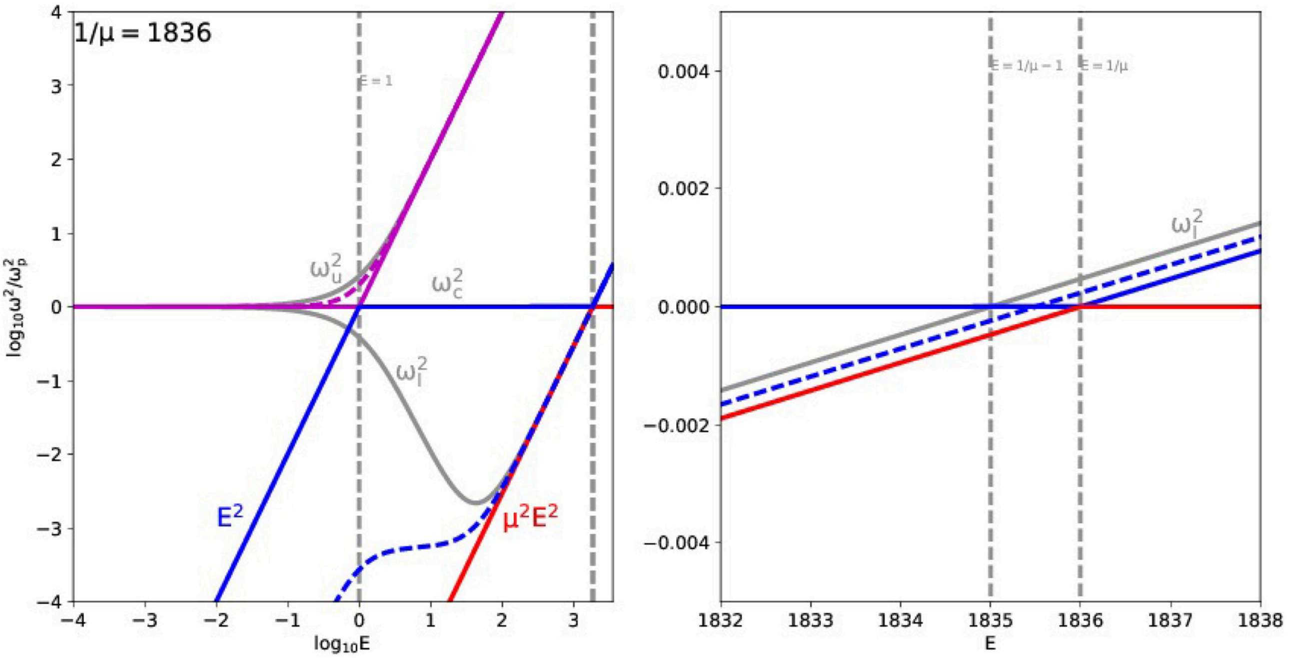

FIGURE 1 | Cut-off frequencies and resonance frequencies ordering for given μ, as function of E. The right panel is a zoom on the behavior near $E = 1/\mu$. Note the horizontal logarithmic scale for E-values in the left (weakly magnetized plasma), vs. a linear scale in the right panel (strongly magnetized). The upper and lower cut-offs $\omega^2_{U,l}$ are plotted as gray solid lines (the $\omega_C^2 = 1$ is the middle horizontal line). The vertical dashed gray lines indicate the special values $E = 1$, $E = 1/\mu - 1$ and $E = 1/\mu$. For each E value, the three colored (purple, blue and red) curve pairs indicate resonance ranges, where parallel propagation corresponds to the solid line, and perpendicular to the dashed line. The red range reaches its perpendicular limit at zero frequency, hence no dashed red line appears.

wavenumbers. Hence, together with the three resonances that occur at large wavenumbers, these two will serve to organize the 5 solution branches.

At low frequencies, we similarly retrieve the following solutions

$$v^2_{ph,F} = \frac{EI}{1+EI}\,, \tag{16}$$

$$v^2_{ph,A} = \lambda^2 \frac{EI}{1+EI}\,. \tag{17}$$

These are actually fast (F) and Alfvén (A) waves, at least at large wavelengths (required to make the phase speed finite at low frequencies). Hence, they will augment the 3 cut-offs to organize the 5 solution branches. The combination $EI/(1+EI)$ can be recognized as the relativistically correct expression for the Alfvén speed v_A. This speed is more commonly written in terms of the magnetization parameter $\sigma = B^2/(\mu_0 c^2 \rho h)$ where $\rho = n_e m_e + n_i m_i$ and the specific enthalpy $h = 1$ for a cold plasma, and we get (temporarily restoring dimensions):

$$\frac{v_A^2}{c^2} = \frac{EI}{1+EI} = \frac{\sigma}{1+\sigma} = \frac{B^2}{\rho h \mu_0 c^2 + B^2}\,. \tag{18}$$

3. DISPERSION DIAGRAMS

We will now analyse dispersion diagrams, which are obtained as solutions $\omega^2(k, \vartheta)$ to the general dispersion relation. We first fix a parameter set (E, μ). Then, at fixed wavenumber and orientation, Equation (2) is a polynomial of degree 5 in ω^2, and due to the symmetry of the underlying determinant (Goedbloed and Poedts, 2004), there will always be five real solutions. We will first address the special orientations of parallel and perpendicular propagation. We plot in **Figure 2** two dispersion diagrams, one for parallel (left) and one for perpendicular (right) orientation, for the choice where $\mu = 1/1{,}836$ and $E = 1.5$.

3.1. Parallel Propagation

A first observation we can directly make from Equation (2) is that parallel propagation ($\lambda = 1$) can always factor out the solution $\omega^2 = 1$, since $\bar{A}(\omega^2 = 1, \lambda = 1) = 0 = \bar{B}(\omega^2 = 1, \lambda = 1)$. This solution is also retained at all angles when $E = 0$, where it actually represents the electrostatic mode, which is a non-propagating plasma oscillation. We will find that $E \neq 0$ cases will turn this mode into a propagating solution, for all angles away from parallel.

The other 4 pairs in Equation (2) for $\lambda = 1$ are intricately mixed, but it is possible to write the remaining 8th order expression as

$$\begin{aligned}&\left[\omega^4 + \omega^3|E-I| - \omega^2(1+EI+k^2) - \omega|E-I|k^2 + k^2EI\right]\\ &\times\left[\omega^4 - \omega^3|E-I| - \omega^2(1+EI+k^2) + \omega|E-I|k^2 + k^2EI\right] = 0\,.\end{aligned} \tag{19}$$

Note that $|E - I| = (1-\mu)E$ as $\mu \le 1$, and in the case of a pair plasma ($\mu = 1$), this leads to a full factorization

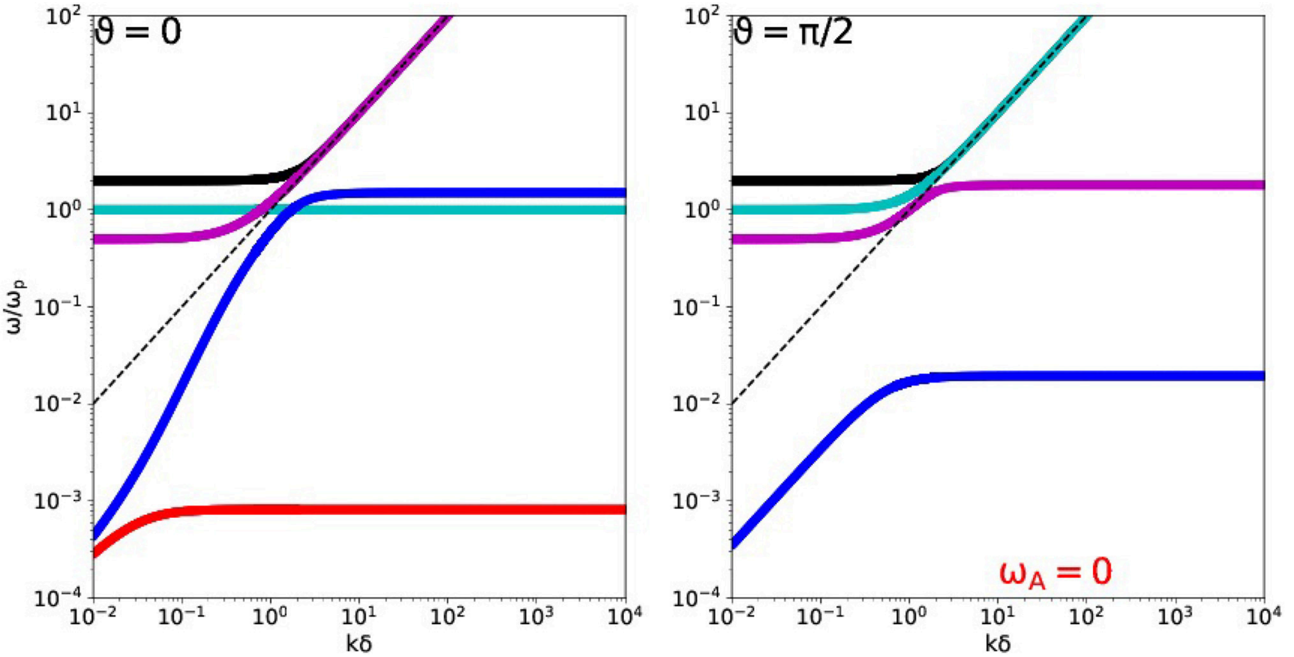

FIGURE 2 | Dispersion diagram for a hydrogen ion-electron plasma at $E = 1.5$. Shown are the 5 branches at parallel **(Left)** and perpendicular **(Right)** propagation. The dashed black line corresponds to light speed behavior.

of all solution branches (Keppens and Goedbloed, in press). However, for $\mu \neq 1$, Equation (19) does not seem to offer real advantage, since the original formulation was already a 4th order polynomial in ω^2, and its four solution pairs ω_1^2, ω_2^2, ω_3^2 and ω_4^2 retain their meaning as forward and backward propagating mode pairs. Instead, both factors in Equation (19) mix forward and backward pairs: if ω_i is solution to its first factor, $-\omega_i$ will be a solution to its second factor. Still, many textbook treatments in fact rely on the factorization in Equation (19). This, as we will discuss further on, implies a description in left and right circularly polarized waves, and indeed left and right circular polarizations switch roles when going forward or backward in time, or under mirror symmetry (see also Keppens and Demaerel, 2016). It is important to note that the forward-backward means of categorizing the solutions is fully consistent with combined PT symmetry, i.e., flipping the time direction and mirroring space.

We rather use the original Equation (2) to compute at which k-values any of the other 4 branches intersects with the $\omega^2 = 1$ solution. This will prove useful when we vary the orientation angle ϑ away from parallel, as we will show further on: these k-values are special as they correspond to those locations where we will first witness avoided crossings of branches. This turns out to be at values

$$k^2 = \frac{EI \pm |E - I|}{EI - 1 \pm |E - I|} \,. \tag{20}$$

Of course, only positive values need to be considered for k^2. A careful analysis of Equation (20) shows that only one sign combination is positive as long as $E < 1$, and hence in such cases only one other branch will intersect the $\omega^2 = 1$ range (e.g., see **Figure 2** for $E = 0.5$, left panel: in this case, the cyan and purple branch cross). However, both sign combinations are positive for $1 < E < 1/\mu - 1$, implying that two branches intersect the $\omega^2 = 1$ branch (e.g., see **Figure 2** for $E = 1.5$, left panel: here we find a crossing between the cyan and both purple and blue branches). Further one positive value (i.e., one intersection) follows in the narrow range $1/\mu - 1 < E < 1/\mu$, and both sign combinations are positive when $1/\mu < E$, leading again to two crossings of the $\omega^2 = 1$ branch. When $E > 1/\mu$, the branches crossing $\omega^2 = 1$ are actually the fast (blue) and Alfvén (red) branch, instead of the purple and blue branch found in **Figure 2** (for $E = 1.5$, left panel). In the limit $E \to \infty$, both sign combinations in Equation (20) lead to $k^2 = 1$, since then the fast and Alfvén branch essentially coincide, as seen from Equations (16–17). Note that the pair plasma case is again naturally contained as a special case where $E = I$. Knowing explicitly the special k-values where branches cross at parallel orientation is also especially useful when wanting to quantify the full phase and group speed variations for all branches, as done in section 4: the phase and group diagrams display intricate wave exchange occuring at these wavenumbers.

3.2. Perpendicular Propagation

At perpendicular propagation ($\lambda = 0$), one marginal frequency pair $\omega^2 = 0$ is contained in Equation (2), and this mode relates to the long wavelength Alfvén waves, which do not propagate perpendicular to the magnetic field. Another solution at perpendicular propagation is found to be $\omega^2 - 1 - k^2 = 0$.

Indeed, for $\lambda = 0$, we can factor Equation (2) into

$$\begin{aligned}&\omega^2(\omega^2 - 1 - k^2)\\ &\left\{\omega^6 - \omega^4(2 + E^2 + I^2 + k^2) + \omega^2\left[(1 + EI)^2 + k^2(1 + E^2 + I^2)\right]\right.\\ &\left.-k^2EI(1 + EI)\right\} = 0\,. \qquad (21)\end{aligned}$$

In the special case of a pair plasma ($E = I$), a complete factorization can be obtained, as the final term then becomes $(\omega^2 - 1 - E^2)(\omega^4 - \omega^2(1 + E^2 + k^2) + k^2E^2)$. The latter term also factorizes in the unphysical limit where $\mu = 0$, making $I = 0$ (see further on in section 5.3), which makes the 6th order term write as $\omega^2(\omega^4 - \omega^2(2 + E^2 + k^2) + 1 + k^2(1 + E^2))$. The branch $\omega^2 - 1 - k^2 = 0$ is in plasma physics referred to as the 'ordinary' or O mode. The three solutions mixed up in the 6th order term are collectively named 'extraordinary' or E (or X, depending on the textbook at hand). In line with this terminology, and acknowledging the fact that one of these three solutions will be a high frequency electromagnetic wave, we will use the label ω_X (and the black color) for its highest frequency solution, and call ω_O (in cyan color) the mode that relates to the $\omega^2 = 1 + k^2$ branch.

Figure 2, right panel, shows the 5 solution branches for perpendicular propagation, for a hydrogen plasma case where $E = 1.5$. The marginal (red) Alfvén-related branch is mentioned in the figure for completeness. The ordinary mode $\omega^2 - 1 - k^2 = 0$ branch (cyan) starts horizontally at unit normalized frequency and goes up like $\propto k^2$. Direct comparison with its parallel counterpart (right panel) shows how the (purple and cyan) branches have changed connectivity between their long wavelength vs. short wavelength behavior. This is due to avoided crossings, that show up in oblique orientations, which we discuss next.

3.3. Oblique Orientations

At any orientation different from parallel or perpendicular, we must resort to numerical evaluation of the 5 roots in Equation (2), which is rather straightforward. **Figure 3** shows this for two representative angles for the case with $(E, \mu) = (1.5, 1/1{,}836)$. Its left panel took a very small angle $\vartheta = 0.001$, while the right panel has $\vartheta = \pi/3$. Comparison with **Figure 2** shows that oblique propagation demonstrates avoided crossings of branches, occurring near the special k values computed from Equation (20). The inset in the left panel shows this avoided crossing quite clearly. Note how the blue, purple and cyan branch are all affected. Indeed, when we animate the dispersion curves for this case $E = 1.5$ with angle, only the parallel case is special in its connectivity showing true branch crossings, and all other angles have the 5 branches neatly ordered in frequency: the red lies below the blue, found in turn below the purple, which is below the cyan, and the black branch always lies at the top.

This behavior is generic, and the avoided crossings occur according to the predictions on the basis of Equation (20), as is illustrated in **Figure 4** for a case where $E = 0.5$ and only one branch intersects the $\omega^2 = 1$ branch at parallel orientation. The left panel of **Figure 4** shows the avoided crossing between the cyan and purple branch, again at $\vartheta = 0.001$ (note the inset).

Since for E-values beyond $E = 1/\mu - 1$, the cut-off ordering changes as discussed before with $\omega_l^2 > \omega_c^2$, avoided crossings affect the blue branch only up to $E = 1/\mu$. Beyond $E > 1/\mu$, both the blue and red branch will demonstrate avoided crossings.

The color scheme of the branches in **Figures 2–4** is chosen in accord with the red, blue and purple resonance ranges we discussed in section 2.2 and quantified in **Figure 1**. We introduce a convenient labeling $(A/F/M/O/X)$ for the 5 wave modes through ω_A (red), ω_F (blue), ω_M (purple), ω_O (cyan) and ω_X (black). Indeed, for all but parallel orientations, the red (Alfvén at small wavenumber), blue (Fast at small wavenumber) and purple branch connect to the corresponding resonance value at that angle. The parallel case is different, since then avoided crossings become true crossings, and only then the cyan branch becomes the non-propagating solution $\omega^2 = 1$, its purple branch crosses it to go to electromagnetic behavior, while the blue and red branch connect to the other two resonance frequencies. This is of particular interest, since textbook classifications of wave modes in a cold plasma rely on specific wave properties at parallel or perpendicular orientations. Our analysis suggests that it is more natural to organize the waves according to the 5 branches retained in Equation (2), and handle the special cases when branches can cross separately. In the special case of a pair plasma, a further avoided crossing with the then special (non-propagating) branch $\omega^2 = 1 + E^2$ at perpendicular orientations can occur, and needs to be accounted for (Keppens and Goedbloed, in press).

4. 5-MODE PHASE AND GROUP DIAGRAMS

4.1. Phase Diagrams

We can show the full complexity of the 5 wave mode pairs in a cold plasma in an alternative way. Up till now, we stressed the $i = 1, 2, \ldots 5$ solutions $\omega_i^2(k, \vartheta)$ for fixed ϑ, and plotted them in dispersion diagram views vs. k. We can also stress the full and intricate variation with angle ϑ, by fixing a wavenumber k. It is then insightful to plot the dimensionless phasespeed ω_i/kc for all 5 modes, and all angles. This is best done in polar plots where we show $(\omega_i/kc)\hat{\mathbf{n}}$, where $\hat{\mathbf{n}} = \mathbf{k}/k$. These are surfaces of revolution about the magnetic field direction, so that we can plot their 2D cross-section and take the magnetic field to be horizontal (i.e., $\mathbf{B} = B\hat{\mathbf{e}}_x$), making $\hat{\mathbf{n}} = (\cos\vartheta, \sin\vartheta)$. These phase diagrams then vary with wavenumber k, but the ordering of the branches discussed previously means that at all but parallel orientations, they remain always nested surfaces. The special k values where branches cross at parallel orientations, represent mode transformations occuring when the surfaces locally touch oneanother.

We plot some representative 5-mode phase diagrams in **Figure 5** for the hydrogen case at $E = 1.5$, shown previously in dispersion diagrams in **Figures 2**, **3**. At large wavelengths (small k), we can recognize that the red and blue branch correspond to the long wavelength, low frequency Alfvén and fast magnetohydrodynamic (MHD) modes, respectively. At small wavelengths (large k), the cyan and black branches

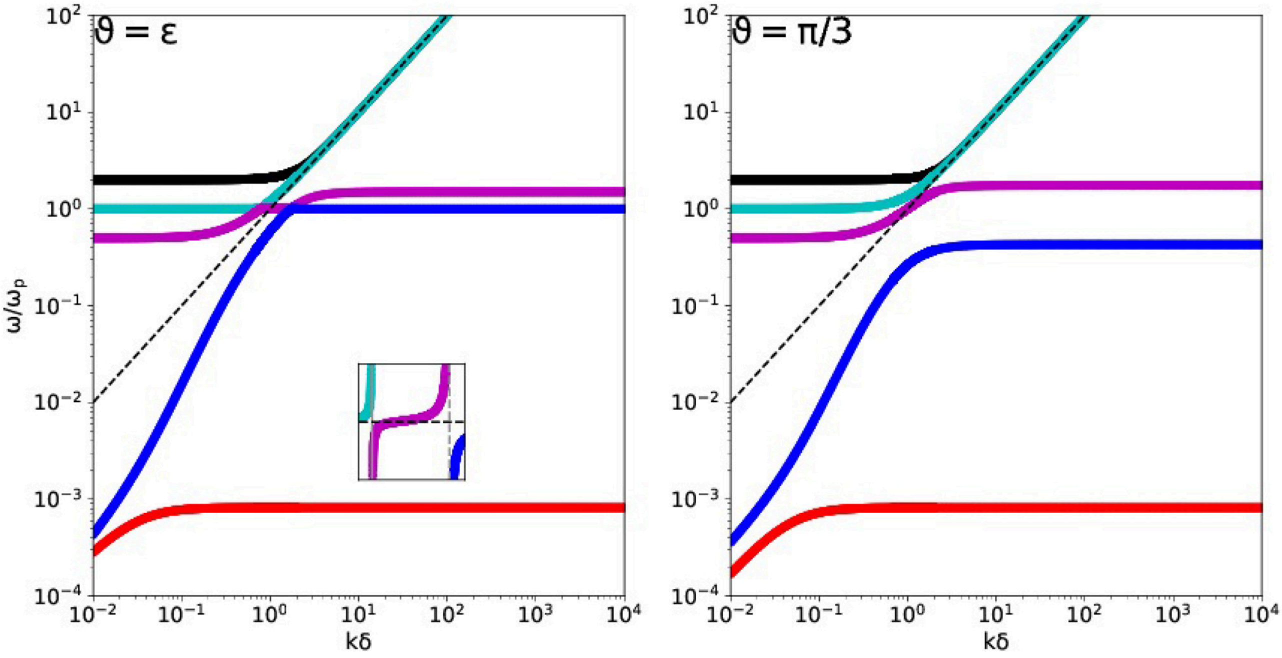

FIGURE 3 | Dispersion diagram for a hydrogen ion-electron plasma at $E = 1.5$. Shown are the 5 branches at near-parallel $\vartheta = 0.001$ (left) and oblique $\vartheta = \pi/3$ propagation. The former shows avoided crossings (see inset). The dashed black line corresponds to light speed behavior.

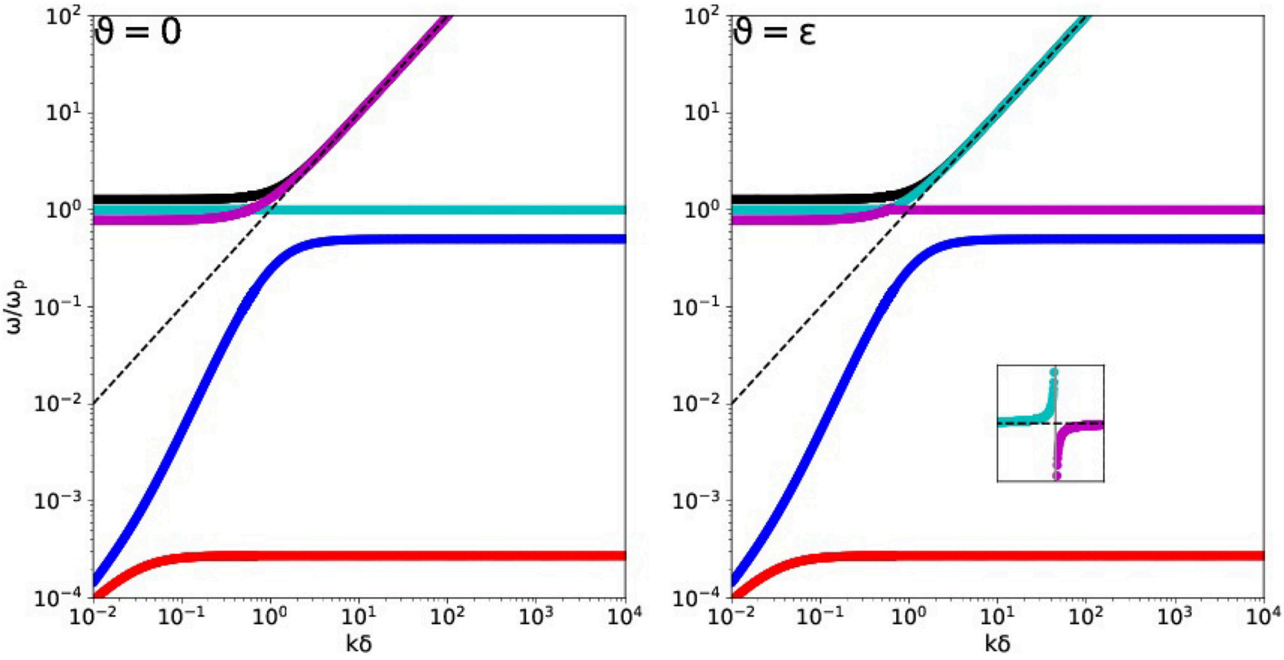

FIGURE 4 | Dispersion diagram for a hydrogen ion-electron plasma at $E = 0.5$. Shown are the 5 branches at parallel **(Left)** and near-parallel $\vartheta = 0.001$ **(Right)** propagation. The latter shows avoided crossings (see inset). The dashed black line corresponds to light speed behavior.

correspond to phase speeds nearing the light speed, and they are the familiar electromagnetic waves. Note that all branches that (partly) lie above the dashed vertical line in **Figures 2–4** have phase speeds above the light speed c, which does not pose any physical problem as we are quantifying phase speeds here. It is even possible to identify when branches go from superluminal to subluminal phase speeds, happening at specific $k-\vartheta$ combinations for particularly the purple branch. Animated views (available from the first author's homepage[1]) of these 5-mode phase diagrams reveal their variations with wavenumber most clearly, as well as the mode transformations happening at parallel orientation, when these nested surfaces of revolution locally touch at specific k values (from Equation 20).

4.2. Group Diagrams

While the 5-mode phase diagrams provide insight in the wave transformations, the way energy is transported is quantified from the group speed. Here, the real power of the polynomial representation comes in, since starting from the dispersion relation (2) written as

$$\omega^{10} + c_4\omega^8 + c_3\omega^6 + c_2\omega^4 + c_1\omega^2 + c_0 = 0\,, \qquad (22)$$

we can easily compute the corresponding group speed $\partial\omega/\partial\mathbf{k}$ by implicit derivation. The dependency of the coefficients $c_i(E, I;\, k^2, \lambda^2)$ implies that we only need to use $\partial k^2/\partial\mathbf{k} = 2\mathbf{k}$ and $\partial\lambda^2/\partial\mathbf{k} = 2\lambda/k[\hat{\mathbf{b}} - \lambda\hat{\mathbf{n}}]$ where $\hat{\mathbf{b}} = \mathbf{B}/B$ and $\hat{\mathbf{n}} = \mathbf{k}/k$. The resulting expression can be manipulated into

$$\frac{\partial\omega}{\partial\mathbf{k}} = -\lambda k\frac{P_4}{P_9}\hat{\mathbf{b}} + \left(\frac{\lambda^2 kP_4 - kP_8}{P_9}\right)\hat{\mathbf{n}}\,. \qquad (23)$$

In this expression, we find the following polynomials

$$\begin{aligned} P_4 &= \omega^4(EI - E^2 - I^2) + \omega^2\left[(1+EI)EI + k^2(E^2+I^2-EI)\right] \\ &\quad - k^2E^2I^2\,, & (24) \\ P_8 &= -2\omega^8 + \omega^6\alpha_6 - \omega^4\alpha_4 + \omega^2\alpha_2 - 2\lambda^2E^2I^2k^2\,, & (25) \\ P_9 &= 5\omega^9 + 4c_4\omega^7 + 3c_3\omega^5 + 2c_2\omega^3 + c_1\omega\,. & (26) \end{aligned}$$

In the P_8 polynomial, the $\alpha_{6,4,2}$ coefficients are

$$\begin{aligned} \alpha_6 &= 4 + 2E^2 + 2I^2 + 2k^2\,, & (27) \\ \alpha_4 &= 2(1+EI)^2 + (1+\lambda^2)(E^2+I^2-EI) \\ &\quad + 2k^2(1+E^2+I^2)\,, & (28) \\ \alpha_2 &= (1+EI)(1+\lambda^2)EI + 2k^2\left[(1+EI)EI\right. \\ &\quad \left. + \lambda^2(E^2+I^2-EI)\right]\,. & (29) \end{aligned}$$

These (admittedly lengthy) expressions can, however, easily be evaluated for each of the 5 branches, and this for all directions and wavenumbers. Indeed, the only thing we need to do is to compute the 5 solutions as zeros of the polynomial in Equation (22) (which is how all previous results shown were obtained), and then evaluate the RHS of expression (23) accordingly. Zeros of the P_9 polynomial may need special treatment, but those actually correspond to the double roots of the original polynomial. Since we found that the branches almost never intersect (except at the special crossings discussed previously), this situation hardly occurs. At perpendicular orientations, the Alfvén related branch is marginal $\omega_A = 0$, but this case can also be handled separately (it has zero group speed).

The resulting 5-mode group speed diagrams are intricate, and some are shown in **Figure 6** for the same hydrogen plasma with $E = 1.5$. The variation with wavenumber provides fascinating views on the anisotropy inherent in all 5 wave modes. At the special wavenumbers where modes transform, also these diagrams show drastic deformations, which are only appreciated in animated views (available from the first author's homepage[1]). In **Figure 6**, the top left panel corresponds to long wavelength behavior, where the typical Friedrichs diagram containing Alfvén (red) and fast (blue) waves is recovered, while the other three waves have all smaller groupspeeds. This is opposite to the behavior at short wavelengths, where the two electromagnetic modes (purple ω_O or O and black ω_X or X) have group speeds that approach the light circle. As group speeds, all speeds obtained with formula (23) lie within the light circle, but their relative ordering and morphology is rather complicated. This is shown at selected wavenumbers in the four panels of **Figure 6**.

5. RELATION TO TEXTBOOK TREATMENTS

5.1. Refractive Index Views

Textbook treatments (e.g., Stix, 1992; Bittencourt, 2004; Thorne and Blandford, 2017) rather emphasize that the dispersion relation Equation (2) gives direct information on the refractive index $n^2 = k^2/\omega^2$. When we consider a given frequency ω, next to the choice of (E, μ) and an orientation ϑ, the solutions to Equation (2) follow directly from

$$n^2 = \frac{\bar{B} \pm \left(\bar{B}^2 - 4\bar{A}\bar{C}\right)^{\frac{1}{2}}}{2\bar{A}}\,. \qquad (30)$$

At most two real solutions can exist at given frequency, and this is then used to classify the wave modes in various types. Frequency ranges where only one real solution is found, or no real solution at all, must be accounted for. Of course, two complex solutions can always be found, but then the waveform $\exp\left[i(\mathbf{k}\cdot\mathbf{x} - \omega t)\right]$ adopted with real ω and complex k has an evanescent, instead of propagating behavior. Using the solution (30) in Equation (2), after adding a factor $\bar{A}n^2$ on each side of the equality sign, allows one to write the solutions also as (Bittencourt, 2004)

$$n^2 = 1 - \frac{2(\bar{A} - \bar{B} + \bar{C})}{2\bar{A} - \bar{B} \pm \left(\bar{B}^2 - 4\bar{A}\bar{C}\right)^{\frac{1}{2}}}\,. \qquad (31)$$

The discriminant appearing in Equations (30-31) can be reworked to

$$\begin{aligned} \bar{B}^2 - 4\bar{A}\bar{C} &= \left[\omega^2(E^2+I^2-EI) - EI(1+EI)\right]^2\sin^4\vartheta \\ &\quad + 4(\omega^2-1)^2(E-I)^2\omega^2\cos^2\vartheta\,. \qquad (32) \end{aligned}$$

This expression is general, and can be used to rewrite Equation (31) for the special cases of parallel or perpendicular orientations to the formulae in Equations (19–21).

---

[1] http://perswww.kuleuven.be/Rony_Keppens

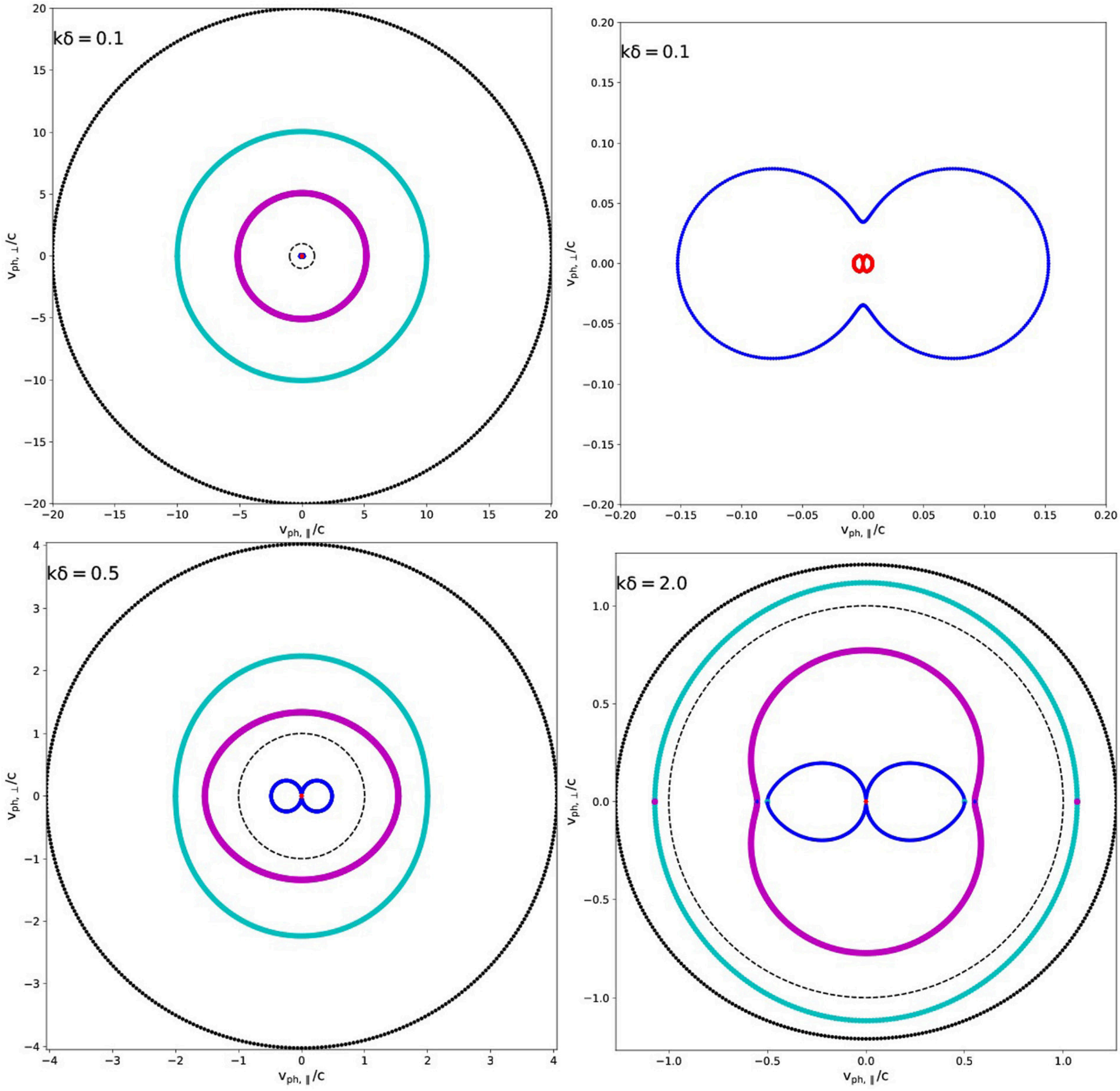

FIGURE 5 | Selected 5-mode phase diagrams at three different values of $k = 0.1$ (top row), 0.5 (bottom left), 2.0 (bottom right). The dashed black circle always indicates the light circle, hence notice the varying scale. This is for a hydrogen plasma with $E = 1.5$, as in **Figures 2**, **3**, and we exploit the same color scheme: electromagnetic modes are black (ω_X) and cyan (ω_O), followed by purple (ω_M or Middle), blue (ω_F or Fast) and red (ω_A or Alfvén) wave. Note that in the $k = 2$ (bottom right) plot, at parallel orientation (horizontal central line), mode exchanges occurred between the cyan, purple and blue branches. We always show all 5 branches, such that the red Alfvén branch requires further zooming in to see its details: this is done in the top right panel for the $k = 0.1$ case.

For completeness, we note that textbook treatments typically exploit the following quantities

$$R = \frac{\omega^2 - \omega(E-I) - (1+EI)}{(\omega - E)(\omega + I)}, \tag{33}$$

$$L = \frac{\omega^2 + \omega(E-I) - (1+EI)}{(\omega + E)(\omega - I)}, \tag{34}$$

$$P = \frac{\omega^2 - 1}{\omega^2}. \tag{35}$$

These appear in the combinations $S = (R+L)/2$ and $D = (R-L)/2$, which obey the equality $S^2 - D^2 = RL$, and together with P, they build up the cold plasma dielectric tensor, which relates the displacement vector $\mathbf{D}$ (giving $\nabla \times \mathbf{B} = \mu_0 \partial \mathbf{D}/\partial t$, including displacement currents) to the electric field $\mathbf{E}$ through $\mathbf{D} = \epsilon_0 \overline{\overline{\boldsymbol{\epsilon}}} \cdot \mathbf{E}$, with

$$\overline{\overline{\boldsymbol{\epsilon}}} = \begin{pmatrix} S & -iD & 0 \\ iD & S & 0 \\ 0 & 0 & P \end{pmatrix}. \tag{36}$$

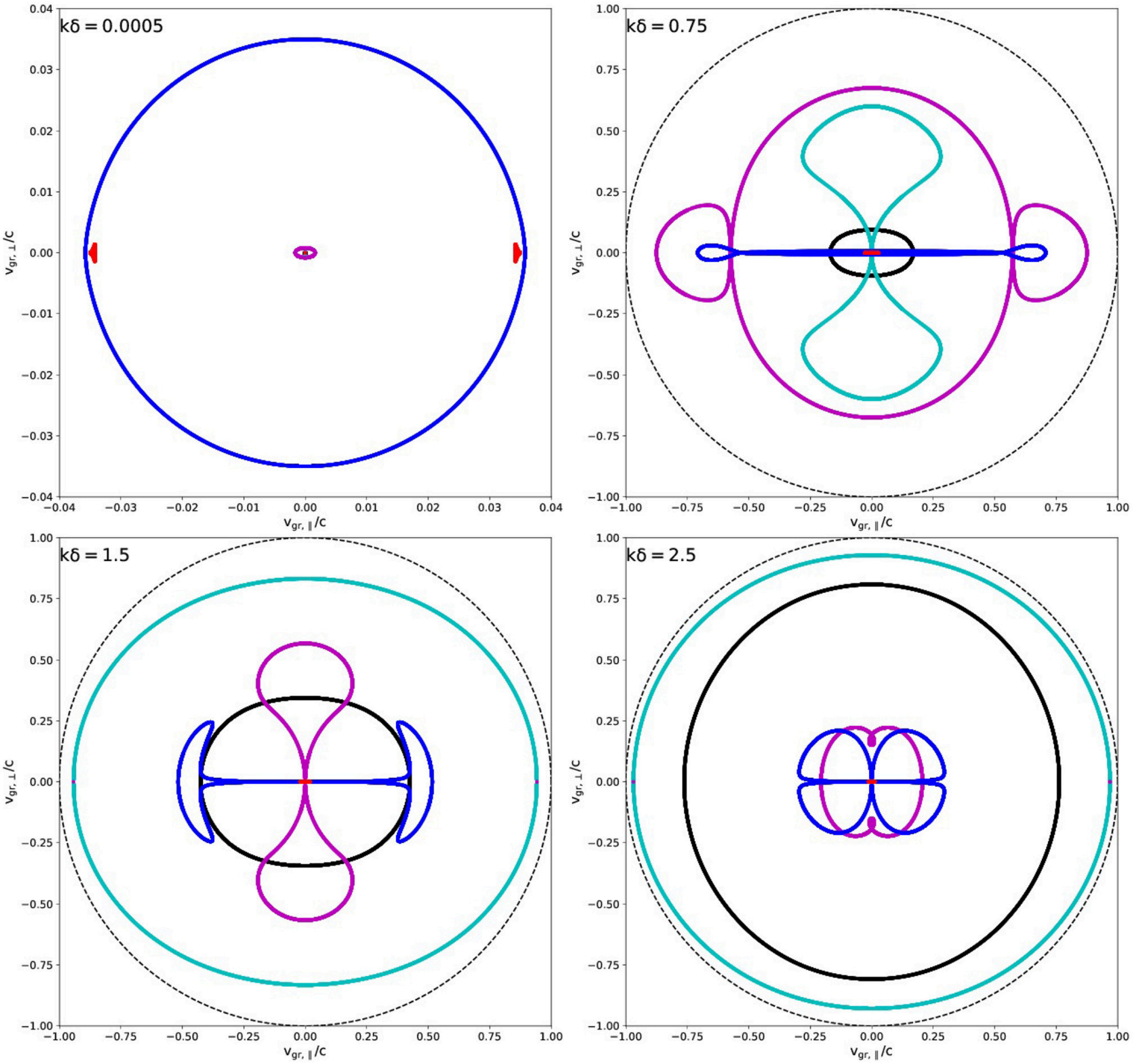

FIGURE 6 | Selected 5-mode group diagrams at four different values of $k = 0.0005, 0.75, 1.5, 2.5$. The dashed black circle (with unit radius) always indicates the light circle, notice the varying scale used in the top left plot. This is for a hydrogen plasma with $E = 1.5$, as in **Figures 2**, **3**, **5** phase, using the same color scheme: electromagnetic modes are black (ω_X) and cyan (ω_O), followed by purple (ω_M or Middle), blue (ω_F or Fast) and red (ω_A or Alfvén) wave.

We wrote the tensor components here with the 3rd dimension parallel to **B**, and the **k**-**B** plane as the 1-3 plane. The dispersion relation, and all discussions of polarization in terms of the wave electric field orientation w.r.t. **B** and **k**, then follow from

$$\mathbf{k} \times (\mathbf{k} \times \mathbf{E}) + (\omega^2/c^2)\overline{\overline{\boldsymbol{\epsilon}}} \cdot \mathbf{E} = \mathbf{0}\,. \tag{37}$$

The governing dispersion relation is still given by Equation (30), where the only difference appears as follows: $\bar{A} \rightarrow A$, where $\bar{A} = \omega^2(\omega^2 - E^2)(\omega^2 - I^2)A$, and similarly for $\bar{B}$ and $\bar{C}$. In the A, B and C formulations, one can write $C = PRL$, $A = S\sin^2\vartheta + P\cos^2\vartheta$, and $B = RL\sin^2\vartheta + PS(1+\cos^2\vartheta)$. It is then customary to rewrite the governing dispersion relation as

$$\tan^2\vartheta = \frac{-P(n^2 - R)(n^2 - L)}{(Sn^2 - RL)(n^2 - P)}\,. \tag{38}$$

From this latter expression, one can see that $n^2 \rightarrow \infty$ implies $\tan^2\vartheta = -P/S$, and this latter formula gives $\bar{A} = 0$, which we used to discuss cold plasma resonances. Cut-offs on the other hand are found from $P = 0$, $R = 0$ or $L = 0$, and these make

$\bar{C} = \omega^2(\omega^2 - E^2)(\omega^2 - I^2)PRL$ vanish. Since further

$$D = \frac{(I - E)\omega}{(\omega^2 - E^2)(\omega^2 - I^2)}\,, \tag{39}$$

the pair plasma case leaves $D = 0$ (rendering the dielectric tensor diagonal), while $S = L = R$.

One may recognize the dispersion relation for parallel propagation given by Equation (19) as $n^2 = L$ and $n^2 = R$, with $P = 0$ giving the $\omega^2 = 1$ factor. The $n^2 = R$ and $n^2 = L$ correspond to right-hand and left-hand circularly polarized waves, respectively. We note again that this mixes forward and backward mode pairs from the original formulation. Similarly, the "ordinary" $\omega^2 - 1 - k^2 = 0$ branch from perpendicular propagation in Equation (21) can be written as $n^2 = P$. The remaining "extraordinary" term, can then be recognized from Equation (38) as $n^2 = RL/S$.

We can plot all dispersion diagrams in terms of the refractive index, and this is done in **Figure 7**, for exactly the same parameters as taken in **Figure 3**. Note again the avoided crossings at near-parallel orientations (left panel). The horizontal dashed lines are indicating fixed frequencies where $\log_{10}\omega = -4, -0.1, 0.1$, respectively. These return in **Figure 8** below.

5.2. CMA Related Wave Normal Surfaces

The standard way to discuss cold ion-electron plasma waves, uses the refractive index viewpoint and the solutions obtained as in Equation (30). When both solutions are real, these 2 solutions at fixed frequency lead to a first classification as being "fast" or "slow," depending on their corresponding phase speed. Two more labels relate to the limiting behaviors at parallel and perpendicular orientations. At parallel orientations, we obtained Equation (19) which (artificially) separates 4 of the 5 mode pairs into $n^2 = R$ or right-hand circularly polarized waves, vs. $n^2 = L$ for left-hand polarized waves. A corresponding R or L label is then used to classify the mode. At perpendicular orientation, we noted that Equation (21) contains the "ordinary" (O) mode $\omega^2 - 1 - k^2 = 0$, next to the 3 "extraordinary" (E) ones mixed up in $n^2 = RL/S$. Collectively, the labels fast/slow, L/R, and O/E then serve to identify specific wave mode behavior. We note however that both classifications miss out one of the 5 branches, since the $\omega^2 = 1$ solution is left out from the L/R scheme, and the marginal $\omega_A^2 = 0$ pair is left out from the O/E scheme. To make matters worse, the 5 branches show avoided crossings as soon as one deviates from exactly parallel orientations (and in the case of a pair plasma, this is also true at exactly perpendicular orientations, see Keppens and Goedbloed, in press), and this seems unaccounted for in textbook treatments. That the branches that are left out from the L/R vs. O/E labeling do not correspond at all (one being cyan or ω_O, the other being red or ω_A for the $E = 1.5$ case used in our figures), is yet another aspect to be considered.

A way to categorize the diversity of wave modes in a cold plasma is using the classical Clemmow-Mullaly-Allis or CMA diagram (Stix, 1992). When plotting $1/\omega^2$ vs. EI/ω^2 (or variations thereoff, like E^2/ω^2 or E/ω), the lines corresponding to $P = 0$, $R = 0$ or $R = \infty$ and $L = 0$ or $L = \infty$, $S = 0$ and $RL = PS$ divide this phase-space into sixteen distinct regions. These regions correspond to differences in wave propagation characteristics, best visualized through the wave normal surfaces, which plot phase velocity $(1/n)[\vartheta]$ for all angles ϑ. The 16 regions correspond to topologically distinct morphologies of the wave normal surface plots, and they can contain zero, one or two solutions depending on the chosen frequency. In **Figure 8**, we show this CMA-related view of the wave normal surfaces for the $E = 1.5$ hydrogen plasma considered earlier, and this at three fixed frequencies such that $\log_{10}(\omega) = -4, -0.1, 0.1$, from left to right. These frequencies are also indicated in the refractive index plots shown in **Figure 7**, and we adopted the coloring scheme we introduced for labeling the 5 wave modes ω_A (red), ω_F (blue), ω_M (purple), ω_O (cyan) and ω_X (black). Note e.g., how the blue ω_F branch is in the textbook way a "fast" mode for the left panel, while it becomes a "slow" mode in the middle panel, although in all cases it corresponds to the blue branch that behaves as fast MHD waves at long wavelengths. We did not add the traditional L/R or O/E labels to the surfaces, as they confuse wave modes due to avoided crossings. Indeed, at $\vartheta = 0$ **Figure 2** (left panel) shows that at $\log_{10}(\omega) = 0.1$ one intersects the purple and blue branch which are L and R, respectively, while at any finite angle (see **Figure 2**, right panel or **Figure 3**) the cyan ω_O and purple ω_M branch matter. The $\vartheta = \pi/2$ panel from **Figure 2** has ω_O as cyan being "ordinary" or O, while ω_F, ω_X and ω_M are all "extraordinary" or E, but has no label for the Alfvén mode, while it appears as the "slow" mode in the leftmost panel of **Figure 8**. We rather opt to use the 5-mode identification which appears naturally, and handle the complications of avoided crossings separately.

5.3. Magneto-Ionic Theory and the Appleton-Hartree Relation

A well-known special case of the general cold ion-electron plasma dispersion relation is the Appleton-Hartree equation. It ignores ion motion, and assumes that one is interested in high frequency waves only. In particular, it is valid for frequencies above the electron plasma frequency ω_{pe} (the dimensional quantity where $\omega_{pe}^2 = e^2 n_e/\epsilon_0 m_e$), which should be above the ion plasma and ion gyrofrequency. The Appleton-Hartree relation describes high frequency electromagnetic waves that travel at arbitrary angle ϑ, and is used in magneto-ionic theory (Bittencourt, 2004; Thorne and Blandford, 2017).

The Appleton-Hartree relation turns out to be a rather curious limit of the general dispersion relation, where one sets the charge to mass ratio to the unphysical value $\mu = 0$ (or equivalently, where one sets $I = 0$). This limit of Equation (2) allows one to factor out a $\omega^2 = 0$ pair, and one is left with the 8th order polynomial (4th order in ω^2) given by

$$\begin{aligned}\omega^8 - \omega^6(3 + E^2 + 2k^2) + \omega^4\left[3 + E^2 + 2k^2(2 + E^2) + k^4\right]\\ - \omega^2\left[1 + k^2(2 + (1 + \lambda^2)E^2) + k^4(1 + E^2)\right] + k^4\lambda^2E^2 = 0\,.\end{aligned} \tag{40}$$

Textbook discussions (Bittencourt, 2004; Chen, 2016; Thorne and Blandford, 2017) rather write this relation in the form given

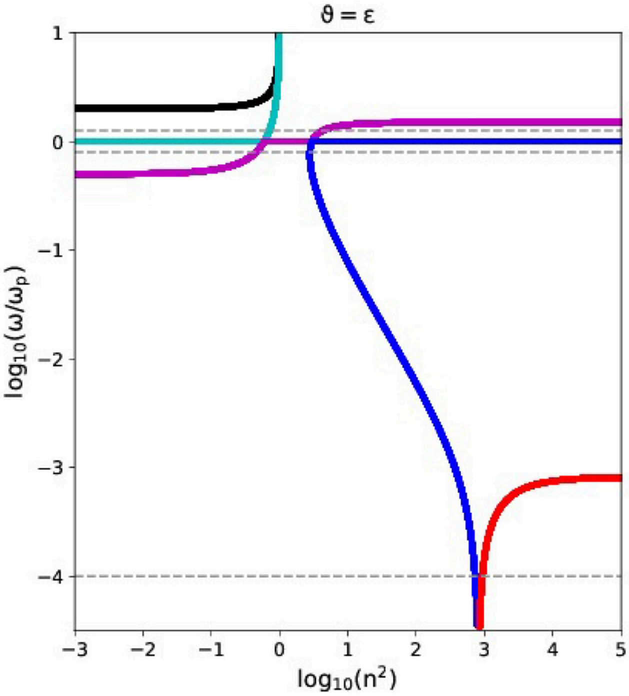

FIGURE 7 | Dispersion diagram for a hydrogen ion-electron plasma at $E = 1.5$, this time displayed in refractive index view. The parameters and panels correspond to the $E = 1.5$ hydrogen plasma at near-parallel $\vartheta = 0.001$ (left) and oblique $\vartheta = \pi/3$ propagation from **Figure 3**. The horizontal dashed lines correspond to the fixed frequencies for which **Figure 8** shows wave normal surfaces.

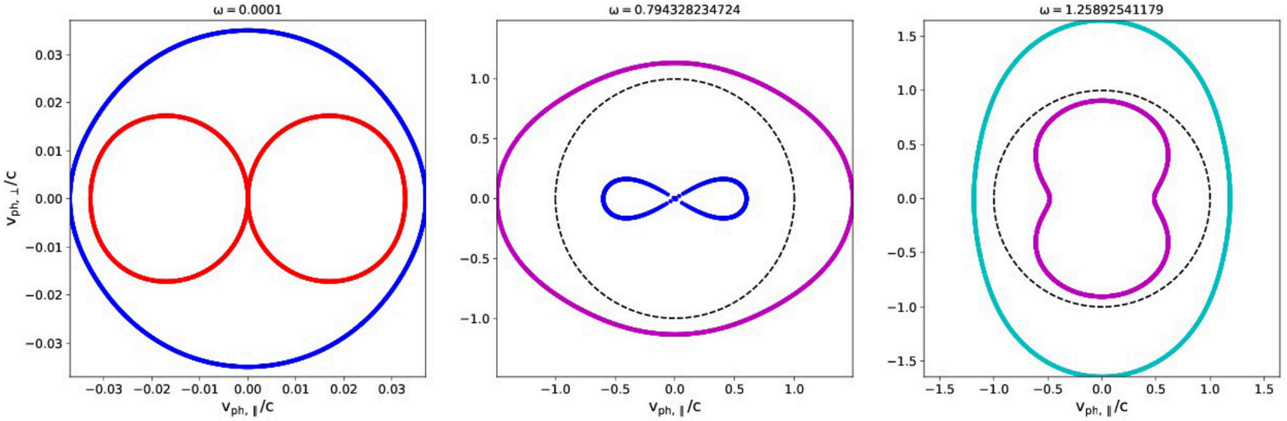

FIGURE 8 | Wave normal surfaces at fixed frequencies for the hydrogen ion-electron plasma at $E = 1.5$.

by Equation (31), where if we exploit expression (32), we can write Equation (40) also as

$$n^2 = 1 - \frac{1/\omega^2}{1 - \frac{(E^2/\omega^2)\sin^2\vartheta}{2(1-1/\omega^2)} \pm \left(\frac{(E^2/\omega^2)\sin^4\vartheta}{4(1-1/\omega^2)^2} + (E^2/\omega^2)\cos^2\vartheta\right)^{1/2}}. \tag{41}$$

It is clear that the polynomial form (40) is preferable, to discuss how its four solution pairs relate to the original 5 from the full dispersion relation (2). Note that the assumption of $\mu = 0$ means that the dimensionless frequency used in these expression is actually $\bar{\omega} = \omega/\omega_{pe}$ (where previously it meant ω/ω_p).

Figure 9 shows the dispersion relation comparison between the 5 modes of the true ion-electron dispersion relation at $E = 1.5$, and the 4-mode approximation made by Appleton-Hartree. The bottom panel actually quantifies the differences in frequencies, which are hardly distinguishable in the top panel. The approximate dispersion relation (40) also has the $\omega^2 = 1$ solution for exactly parallel orientation, and we find indeed at this near-parallel angle a similar avoided crossing behavior for the 4

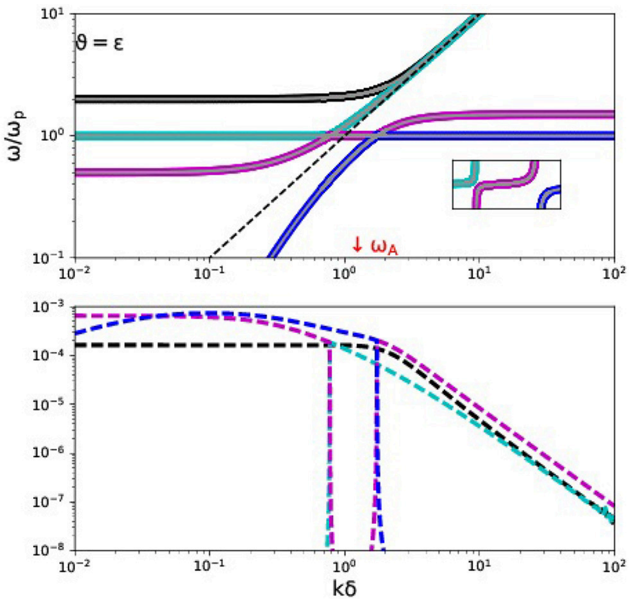

FIGURE 9 | Comparing the Appleton-Hartree approximation to the actual hydrogen ion-electron plasma dispersion diagram for $E = 1.5$, at a near-parallel orientation ($\vartheta = 0.001$). The top panel shows the branches (ω_A is off the scale shown) as in **Figure 3** (left panel) in the same color scheme, while the gray lines that are overplotted correspond to the 4 modes of the Appleton-Hartree approximation. The inset shows their agreement near the avoided crossings. The bottom panel quantifies their difference: this is largest at small wavenumbers.

retained modes. The Appleton-Hartree approximation contains the $I = 0$ limit of the crossings from Equation (20), so it has $k^2 = E/(E \pm 1)$ as special wavenumbers. Note that the Appleton-Hartree relation always discards the Alfvén related branch ω_A. The limit $\mu = 0$ obviously implies that all subtleties related to field strengths above $E = 1/\mu - 1$, which enrich the actual dispersion relation with cut-off frequencies that change their relative ordering (see section 2.1 and **Figure 1**) are completely left out of this approximation. Since we noted that beyond $E = 1/\mu$ both the ω_F and ω_A branch will demonstrate avoided crossings, this aspect can not be discussed on the basis of Appleton-Hartree. Finally, the assumption $\mu = 0$ is obviously completely inappropriate for a pair plasma, where $E = I$ and $\mu = 1$.

5.4. Faraday Rotation

A final well-known effect that is described by the (cold) ion-electron plasma dispersion relation is Faraday rotation (FR). The effect is usually described for purely parallel propagation, where as noted earlier, the dispersion relation in the form of Equation (19) is recognized as the product $(n^2 - L)(n^2 - R) = 0$. At fixed frequency ω, and paying special attention to the high-frequency electromagnetic branches (which are those for frequencies $\omega > \omega_u$ above the upper cutoff frequency from Equation 7), the solution from $n^2 - L$ is left circularly polarized (LCP), while $n^2 = R$ is right circularly polarized (RCP). The corresponding breaking n_L and n_R indices differ through their difference in wavenumber, as $n_L - n_R = c\Delta k/\omega$. A linearly polarized wave (which can always be decomposed in a LCR and RCP wave) that travels along a magnetic field ends up with its plane of polarization rotated over a finite angle. We can quantify this in a variety of ways, e.g., by using the expressions (33, 34), we find that without any approximation, we can write

$$n_L^2 - n_R^2 = \frac{2(E - I)\omega}{(\omega^2 - E^2)(\omega^2 - I^2)} \,. \qquad (42)$$

This expression demonstrates that for purely parallel propagation, the Faraday effect vanishes for an electron-positron plasma (see also Stewart and Laing, 1992), and that we can approximate the difference in breaking index using the Appleton-Hartree-type recipe ($\mu = 0$, high frequencies) to the textbook expression

$$n_L - n_R \approx \frac{E}{\omega^3} \quad \left[\equiv \frac{\Omega_e \omega_{pe}^2}{\omega^3} \right] , \qquad (43)$$

where the expression between brackets temporarily restores the dimensions. We can then use this latter expression to get the usual quantification for the change in angle χ for a linearly polarized wave, written with the so-called rotation measure RM as

$$\chi = \mathrm{RM}\, \lambda^2 = \frac{e^3 \lambda^2}{8\pi^2 m_e^2 \epsilon_0 c^3} \int B_\parallel n_e \, dl \,, \qquad (44)$$

where the integral is along the line of sight (LOS) and $B_\parallel$ is the component of **B** along it.

We note however that the proxy from Equation (43) is better written as $(E - I)/\omega^3$ to allow for the vanishing FR effect when $\mu = 1$ and propagation is along the magnetic field ($\vartheta = 0$). Moreover, we meanwhile recognize that this difference in phase speed between the high-frequency wave pair can actually be quantified readily for all angles ϑ. The FR effect for a specific $E = 1.5$ hydrogen plasma case is then shown in **Figure 10**, where the left panel shows the actual $\vartheta = 0$ variation in $n_L - n_R$ as function of frequency in red, the proxy from Equation (43) in blue, and the exact expression (42) in dashed red-blue. The right panel quantifies $\Delta n(\vartheta, \omega)$, where the parallel (red line) result is the same as in the left panel. It is clear from this plot that the variation is a smooth function of ϑ, and that one can meaningfully extend the FR quantification, as a corresponding phase speed difference at fixed frequency, for all angles (and for all local magnetic field and number density values incorporated in E). In that sense, the widely adopted RM quantification from Equation (44) is a (usually good) approximation only, since the integral quantifying the line of sight variation of the parallel magnetic field may just as well take the local $\Delta n(\vartheta, \omega; E)$ value into account when a field region with varying orientation in **B** is traversed by a wave with fixed LOS-oriented wavevector **k**.

This realization is important to revisit the claim that electron-positron plasmas do not show any Faraday rotation (Stewart and Laing, 1992): this statement is true for purely parallel propagation, but a quantification for all angles similar to what is shown in **Figure 10**, right panel, shows that finite to large $\Delta n(\vartheta, \omega; E)$ exist for cold electron-positron plasmas, especially near $\vartheta = \pi/2$ and at frequencies just above ω_u.

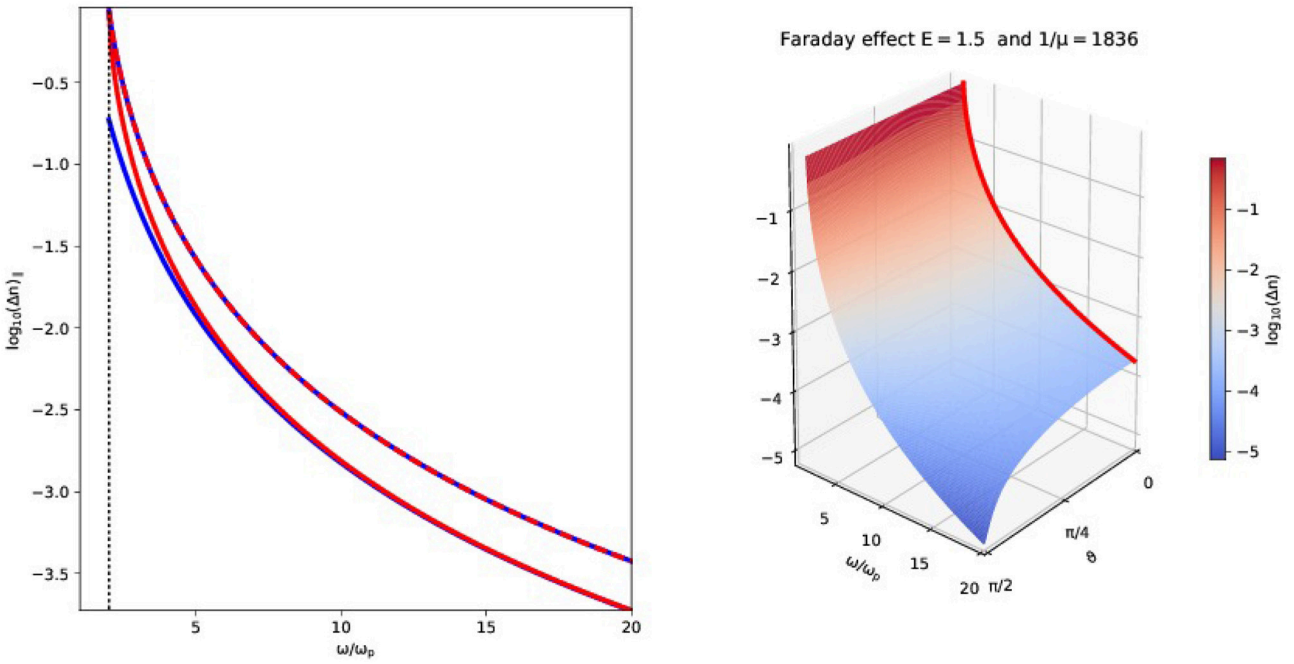

FIGURE 10 | Faraday rotation for an $E = 1.5$ proton-electron plasma. The left panel quantifies with the blue solid line the textbook expression $n_L - n_R \approx E/\omega^3$ as function of frequency (above the upper cut-off frequency, indicated as a vertical dotted line). The actual, exact value of $n_L - n_R$ is given by the red solid line. The dashed red-blue line shows the exact correspondence for the $n_L^2 - n_R^2$ variation. The right panel repeats the red solid line at parallel propagation, but shows how the difference in breaking index between the two electromagnetic waves varies smoothly with angle ϑ.

6. CONCLUSIONS

We have revisited the cold ion-electron plasma wave theory, and summarize our main findings as follows:

- The traditional means of using the plasma dielectric tensor for obtaining dispersion relations is equivalent to our polynomial-based treatment. This polynomial description emphasizes the 5 real solution pairs $\pm\omega_X$, $\pm\omega_O$, $\pm\omega_M$, $\pm\omega_F$, and $\pm\omega_A$ of forward-backward propagating waves, at fixed (real) wavenumber k. The only plasma parameters that matter are the dimensionless ratios μ and E.
- The traditional labeling of waves as fast/slow, L/R, O/E type, which rather fixes a real frequency ω and solves for (real or complex) k has some distinct disadvantages, since avoided crossings of the 5 branches actually alters the connectivity between small and large wavenumber solution branches, from those found at parallel (and sometimes also perpendicular, as in pair plasmas) behavior. The fast/slow terminology confuses the established ordering of MHD waves at low frequency, large wavenumber in slow-Alfvén-fast, which is the cornerstone of all MHD spectroscopy (Goedbloed and Poedts, 2004; Goedbloed et al., 2010, 2019). Our cold assumption has removed the slow MHD waves from the description, which will return in warm plasmas.
- We can use the polynomial representation to predict the wavenumbers for avoided crossings by Equation (20), and at fixed μ, the prevailing E value dictates which and how many branches cross. Our description is valid for all combinations of (E, μ), and covers especially also the high magnetization regime where $E > 1/\mu$. It covers all cold plasma waves, up to full relativistic magnetization.
- The polynomial dispersion relation form gives us a direct means to quantify and visualize the full 5-mode phase and group diagrams, for all wavenumbers k, which contain all relevant information on wave anisotropy and energy flow. These are very different from the wave normal surfaces at fixed frequencies, which are exploited in the CMA classification. In particular, they show intricate changeovers when the wavenumber crosses the special values from Equation (20).
- The Appleton-Hartree dispersion relation is a curious, unphysical limit setting $\mu = 0$, which gives satisfactory agreement on the high-frequency waves (and also contains some of the avoided crossings). It fails completely for pair plasmas, and misses all intricacy associated with $E > 1/\mu - 1$ regimes.
- Faraday rotation can be meaningfully extended to propagation angles different from $\vartheta = 0$, and the corresponding exact value of the refractive index difference $\Delta n(\vartheta, \omega; E)$ depending on angle, frequency and E can easily be quantified and used for rotation measure computations.

Further work should discuss the full variation of the wave polarizations, based on the 6 × 6 matrix formulation exploited in Goedbloed and Poedts (2004) and Goedbloed et al. (2019), which led to the polynomial dispersion relation. Also, the effects of a warm plasma can be easily incorporated, since then a 6th order polynomial in ω^2

enters, bringing in the slow MHD modes. This is left for future work.

DATA AVAILABILITY

The datasets generated for this study are available on request to the corresponding author.

AUTHOR CONTRIBUTIONS

RK performed the analysis of the dispersion relation and produced the figures for this article. It is based on the general dispersion relation derived by HG, and simplified here to cold plasmas. Both authors iterated the paper and jointly improved the presentation.

FUNDING

This research was supported by the KU Leuven (GOA/2015-014).

ACKNOWLEDGMENTS

RK thanks Yunnan University and Chun Xia for kind hospitality during his sabbatical stay.

REFERENCES

Bellan, P. M. (2012). Improved basis set for low frequency plasma waves. *J. Geophys. Res.* 117:A12219. doi: 10.1029/2012JA017856

Bittencourt, J. A. (2004). *Fundamentals of Plasma Physics. 3rd Edn.* New York, NY: Springer-Verlag.

Boyd, T. J. M., and Sanderson, J. J. (2003). *The Physics of Plasmas.*

Chen, F. F. (2016). *Introduction to Plasma Physics and Controlled Fusion. 3rd Edn.* Springer.

Damiano, P. A., Wright, A. N., and McKenzie, J. F. (2009). Properties of Hall magnetohydrodynamic waves modified by electron inertia and finite Larmor radius effects. *Phys. Plasmas* 16:062901. doi: 10.1063/1.3142479

Denisse, J. F., and Delcroix, J. L. (1961). *Théorie des Ondes Dans Les Plasmas.*

Goedbloed, J. P., Keppens, R., and Poedts, S. (eds.). (2010). *Advanced Magnetohydrodynamics.* Cambridge, UK: Cambridge University Press.

Goedbloed, J. P., Keppens, R., and Poedts, S. (eds.). (2019). *Magnetohydrodynamics of Laboratory and Astrophysical Plasmas.* Cambridge, UK: Cambridge University Press.

Goedbloed, J. P. and Poedts, S. (2004). *Principles of Magnetohydrodynamics.* Cambridge University Press.

Ishida, A., Cheng, C. Z., and Peng, Y.-K. M. (2005). Properties of low and medium frequency modes in two-fluid plasma. *Phys. Plasmas* 12:052113. doi: 10.1063/1.1905604

Keppens, R., and Demaerel, T. (2016). Stability of ideal MHD configurations. I. Realizing the generality of the G operator. *Phys. Plasmas* 23:122117. doi: 10.1063/1.4971811

Keppens, R., and Goedbloed, H. (in press). Wave modes in a cold pair plasma: the complete phase and group diagram point-of-view. *J. Plasma Phys.*

Stewart, G. A. and Laing, E. W. (1992). Wave propagation in equal-mass plasmas. *J. Plasma Phys.* 47, 295–319. doi: 10.1017/S0022377800024247

Stix, T. H. (1992). *Waves in Plasmas.* New York, NY: American Institute of Physics.

Stringer, T. E. (1963). Low-frequency waves in an unbounded plasma. *J. Nuclear Ener.* 5, 89–107. doi: 10.1088/0368-3281/5/2/304

Thorne, K. S., and Blandford, R. D. (2017). *Modern Classical Physics: Optics, Fluids, Plasmas, Elasticity, Relativity, and Statistical Physics.* Princeton, NJ: Princeton University Press.

Zhao, J. (2015). Dispersion relations and polarizations of low-frequency waves in two-fluid plasmas. *Phys. Plasmas* 22:042115. doi: 10.1063/1.4919257

Zhao, J. (2017). Properties of whistler waves in warm electron plasmas. *Astrophys. J.* 850:13. doi: 10.3847/1538-4357/aa906f

Conflict of Interest Statement: The authors declare that the research was conducted in the absence of any commercial or financial relationships that could be construed as a potential conflict of interest.

frontiers
in Astronomy and Space Sciences

ORIGINAL RESEARCH
published: 11 April 2019
doi: 10.3389/fspas.2019.00020

Mixed Properties of MHD Waves in Non-uniform Plasmas

Marcel L. Goossens[1]*, **Inigo Arregui**[2,3] **and Tom Van Doorsselaere**[1]

[1] Department of Mathematics, Centre for Mathematical Plasma Astrophysics, KU Leuven, Leuven, Belgium, [2] Instituto de Astrofísica de Canarias, Santa Cruz de Tenerife, Spain, [3] Departamento de Astrofísica, Universidad de La Laguna, San Cristóbal de La Laguna, Spain

This paper investigates the mixed properties of MHD waves in a non-uniform plasma. It starts with a short revision of MHD waves in a uniform plasma of infinite extent. In that case the MHD waves do not have mixed properties. They can be separated in Alfvén waves and magneto-sonic waves. The Alfvén waves propagate parallel vorticity and are incompressible. In addition they have no parallel displacement component. The magneto-sonic waves are compressible and in general do have a parallel component of displacement but do not propagate parallel vorticity. This clear separation has been the reason why there has been a strong inclination in the literature to use this classification in the study of MHD waves in non-uniform plasmas. The main part of this paper is concerned with MHD waves in a non-uniform plasma. It is shown that the MHD waves in that situation in general propagate both vorticity and compression and hence have mixed properties. Finally, the close connection between resonant absorption and MHD waves with mixed properties is discussed.

Keywords: magnetohydrodynamics (MHD), Sun: atmosphere, Sun: magnetic fields, Sun: corona, Sun: oscillations, waves

Edited by:
Xueshang Feng,
State Key Laboratory of Space Weather, National Space Science Center (CAS), China

Reviewed by:
S. P. Rajaguru,
Indian Institute of Astrophysics, India
Xi Luo,
Chinese Academy of Sciences, China

***Correspondence:**
Marcel L. Goossens
marcel.goossens@kuleuven.be

Specialty section:
This article was submitted to Stellar and Solar Physics, a section of the journal Frontiers in Astronomy and Space Sciences

Received: *16 January 2019*
Accepted: *19 March 2019*
Published: *11 April 2019*

Citation:
Goossens ML, Arregui I and Van Doorsselaere T (2019) Mixed Properties of MHD Waves in Non-uniform Plasmas. Front. Astron. Space Sci. 6:20. doi: 10.3389/fspas.2019.00020

1. INTRODUCTION

Most textbooks on Magnetohydrodynamics (MHD) and plasma physics contain at least an elementary discussion of MHD waves in a uniform plasma of infinite extent (see e.g., Thompson, 1964; Mestel and Weiss, 1974; Goedbloed, 1983; Goossens, 2003; Goedbloed and Poedts, 2004; Walker, 2004). It is shown that the MHD waves are either Alfvén waves or slow/fast magneto-sonic waves. The Alfvén waves are incompressible and propagate parallel vorticity. They do not have a parallel component of displacement and are driven by magnetic tension only. The magneto-sonic waves are compressible and have a parallel component of displacement. They do not propagate parallel vorticity and are driven by pressure and magnetic tension. In non-uniform plasmas the situation can be very different. The clear division between Alfvén waves and magneto-sonic waves is no longer present. The MHD waves have mixed properties in non-uniform plasmas. Mixed properties mean that the general rule is that MHD waves propagate both parallel vorticity as in classic Alfvén waves and compression as in classic magneto-sonic waves. This behavior causes exciting wave physics. For instance, the phenomenon of MHD waves with mixed properties can lead to damping, with relevance in explaining the attenuation observed in coronal and prominence oscillations and discussed by Goossens et al. (2002a, 2011), Terradas et al. (2006), Arregui et al. (2008), Pascoe et al. (2010, 2011), among many others. The use of the information on wave damping has also been found useful to perform solar coronal seismology (see e.g., Goossens et al., 2002a, 2008; Arregui et al., 2007; Goossens, 2008). The mixed properties arise because in an inhomogeneous plasma the Eulerian perturbation of total pressure couples with the dynamics of the motion (Hasegawa and Uberoi, 1982). Mathematically this is translated into the fact that the differential equations for the radial component of the Lagrangian displacement ξ_r and the Eulerian perturbation of total pressure P' are coupled to algebraic equations for compression $\nabla \cdot \vec{\xi}$, the parallel and perpendicular projections of the Lagrangian displacement $\xi_\|, \xi_\perp$, and vorticity $\nabla \times \vec{\xi}$ [1]. The coupling of the equations is due to the coupling functions C_A and C_S which were introduced by Sakurai et al. (1991b) in their study of resonant absorption. The relevance of the coupling functions goes beyond resonant absorption. The spatial behavior of the coupling functions and of the local Alfvén frequency ω_A and local cusp frequency ω_C determine the spatial behavior of the various components of velocity and vorticity and of compression. The simultaneous presence of compression and vorticity is hard to avoid.

Goossens et al. (2009) investigated the forces that drive these waves and found that the magnetic tension force always dominates the pressure force for the kink mode. In addition, they showed that compression is small in the particular case of thin tubes. Hence, these waves do not have the typical properties of fast magneto-sonic waves and behave more as Alfvén waves. Goossens et al. (2011) reconsidered these waves in their section on quasi-modes and decided to call them surface Alfvén waves. In the present paper, we continue the theoretical investigation of the nature of the waves. In section 2, we describe pure Alfvén and pure magneto-acoustic waves in a uniform plasma of infinite extent, by analysing their eigenfrequencies, eigenfunctions, vorticity and compression. In section 3, the analysis is generalized to MHD waves in non-uniform plasmas, which propagate both compression and parallel vorticity at the same time. This leads to new expressions for the components of vorticity that are derived for axi-symmetric/non-axi-symmetric motions in a non-uniform 1-dimensional cylindrical plasma. In section 4, we show that resonant Alfvén /slow waves are characterized by strong shear in the perpendicular/parallel component of displacement with large values of the parallel/perpendicular component of vorticity. This strong shear causes violent KH-instabilities (Terradas et al., 2008; Antolin et al., 2018) that accelerate the damping of the MHD waves and facilitate heating of plasma (Antolin et al., 2015; Arregui, 2015; Terradas and Arregui, 2018).

2. LINEAR MHD WAVES OF A UNIFORM PLASMA OF INFINITE EXTENT

The properties of MHD waves in a uniform plasma of infinite extent are often used to characterize MHD waves in general. For a uniform plasma of infinite extent the MHD waves can be subdivided into two classes with distinct properties. The first class contains the magneto-sonic waves. They are compressive but do not propagate parallel vorticity. The second class contains the Alfvén waves. Alfvén waves propagate parallel vorticity and are incompressible. The equilibrium quantities are constant. The constant magnetic field

$$\vec{B}_0 = B_0 \vec{1}_z, \tag{1}$$

is used to define the direction of the z- axis of a Cartesian system of coordinates. The equilibrium density and pressure are constant

$$p_0 = \text{constant}, \ \rho_0 = \text{constant}. \tag{2}$$

In what follows $\vec{\xi}$ is the Lagrangian displacement. In the present subsection the background is static and uniform. As a consequence solutions can be obtained in the form of plane harmonic waves and $\vec{\xi}$ is written

$$\vec{\xi}(\vec{r};t) = \hat{\vec{\xi}} \exp(i(\vec{k}.\vec{r} - \omega t)) = \hat{\vec{\xi}} \exp(i(k_x x + k_y y + k_z z - \omega t)). \tag{3}$$

Here $\hat{\vec{\xi}}$ is the constant amplitude of $\vec{\xi}$, $\vec{k} = k_x \vec{1}_x + k_y \vec{1}_y + k_z \vec{1}_z$ is the wave vector, and ω is the frequency of the wave. In what follows the hat on $\vec{\xi}$ will be dropped. Since the constant magnetic field defines a preferred direction a clever choice of dependent wave variables is X, Y, Z defined as

$$\begin{aligned} k_z \xi_z = X &= \text{displacement parallel to } \vec{B}_0, \\ \nabla \cdot \vec{\xi} = i\, \vec{k} \cdot \vec{\xi} = i\, Y &= \text{compression}, \\ (\nabla \times \vec{\xi})_z = i\, (\vec{k} \times \vec{\xi})_z = i\, Z &= \text{component of vorticity} \\ &\quad \text{parallel to } \vec{B}_0. \end{aligned} \tag{4}$$

X, Y, Z are dimensionless quantities and allow us to obtain an elegant version of the governing equations. In terms of these variables the equations for linear ideal MHD waves can be written as

$$\begin{aligned} \omega^2 X - k_z^2 v_S^2 Y &= 0, \\ k^2 v_A^2 X + (\omega^2 - k^2(v_A^2 + v_S^2)) Y &= 0, \\ (\omega^2 - \omega_A^2) Z &= 0. \end{aligned} \tag{5}$$

v_A, v_S are the Alfvén velocity and the velocity of sound. They are defined by

$$v_A^2 = \frac{B_0^2}{\mu\ \rho_0}, \ \ v_S^2 = \frac{\gamma p_0}{\rho_0}. \tag{6}$$

ω_A is the local Alfvén frequency. It is defined as

$$\omega_A^2 = \frac{(\vec{k} \cdot \vec{B})^2}{\mu \rho} = k_z^2\ v_A^2 = k_\|^2\ v_A^2. \tag{7}$$

In a uniform plasma v_A, v_S, ω_A are constant. In a non-uniform plasma these quantities depend on position.

The system (5) consists of two uncoupled subsets of equations. The first subset is the third equation for the variable Z. The

---

[1] The standard definition of vorticity in fluid dynamics is $\nabla \times \vec{v}$. Here the analysis uses the Lagrangian displacement $\vec{\xi}$ and $\nabla \times \vec{\xi}$ is referred to as vorticity. Since $\vec{v} = -i\omega\vec{\xi}$ it follows that $\nabla \times \vec{v} = -i\omega \nabla \times \vec{\xi}$. $\nabla \cdot \vec{v}$ is a measure for the rate of variation of the volume of a material fluid element. In the present paper $\nabla \cdot \vec{\xi}$ is referred to as compression.

second subset contains the wave variables ξ_z and Y. The first type of MHD waves are characterized by

$$Y = 0,\ Z \neq 0,\ \xi_z = 0,\quad \omega^2 = \omega_A^2. \tag{8}$$

They are the classic Alfvén waves. The eigenfrequencies associated with the Alfvén waves (8) are infinitely degenerate as they only depend on the parallel component of the wave vector $\vec{k}$. Alfvén waves do not cause compression and have no component of the displacement parallel to the magnetic field. They are the only waves that propagate parallel vorticity in a uniform plasma of infinite extent. The only restoring force is the magnetic tension force. Note also that Alfvén waves in a uniform plasma of infinite extent exist for any wave vector $\vec{k} = (k_x, k_y, k_z)$.

The displacement $\vec{\xi}$ for Alfvén waves is

$$\vec{\xi}_A = (-\frac{k_y}{k_x}\vec{1}_x + \vec{1}_y)\xi_y \ = \ (\vec{1}_x - \frac{k_x}{k_y}\vec{1}_y)\xi_x. \tag{9}$$

For $k_y = 0$ we obtain the popular result $\vec{\xi}_A = \xi_y \vec{1}_y$. These y-independent Alfvén waves are a special case. In the cylindrical case $k_y = 0$ and $k_y \neq 0$ correspond to respectively axisymmetric waves with $m = 0$ and to non-axisymmetric waves with $m \neq 0$ with m the azimuthal wave number. For a wave vector with both horizontal components of the wave vector different from zero both horizontal components of the displacement vector are non-zero. Let us now keep $k_y \neq 0,\ k_z \neq 0$ and mimic a situation with non-uniformity in the x- direction and a resonant condition where $\lim k_x \rightarrow +\infty$ so that $\mid k_y \mid \ll \mid k_x \mid, \mid k_z \mid \ll \mid k_x \mid$. Find then

$$\frac{\mid \xi_y \mid}{\mid \xi_x \mid} = \frac{\mid k_x \mid}{\mid k_y \mid} \gg 1,\quad \vec{\xi}_A \approx \xi_y\ \vec{1}_y. \tag{10}$$

The motion in the Alfvén wave is predominantly in the y- direction and rapidly varying in the x- direction. The displacement (10) is not y- independent because of the factor $\exp(ik_y y)$ with $k_y \neq 0$. The $\approx$ sign means that the two components (ξ_x, ξ_y) are non-zero but ξ_y is far larger in absolute value than ξ_x. The two components are needed to satisfy the incompressibility condition.

For a general wave vector $\vec{k} = (k_x, k_y, k_z)^t$ the three components of vorticity $\nabla \times \vec{\xi}$ are non-zero. In addition to the parallel component $(\nabla \times \vec{\xi})_z$ also the components in planes normal to $\vec{B}_0$ are non-zero:

$$\begin{aligned}&(\nabla \times \vec{\xi})_z = i(k_x\xi_y - k_y\xi_x),\ \ (\nabla \times \vec{\xi})_x = -ik_z\xi_y,\\ &(\nabla \times \vec{\xi})_y = ik_z\xi_x,\ \ \xi_x = -\frac{k_y}{k_x}\xi_y.\end{aligned} \tag{11}$$

For our later discussion on resonant Alfvén waves it is instructive to look at the components of vorticity $\nabla \times \vec{\xi}$ under conditions that mimic resonant behavior, i.e., when $\mid k_y \mid \ll \mid k_x \mid, \mid k_z \mid \ll \mid k_x \mid$ and find that

$$\frac{\mid (\nabla \times \vec{\xi})_z \mid}{\mid (\nabla \times \vec{\xi})_x \mid} \approx \frac{\mid k_x \mid}{\mid k_z \mid} \gg 1,\quad \frac{\mid (\nabla \times \vec{\xi})_z \mid}{\mid (\nabla \times \vec{\xi})_y \mid} \approx \frac{\mid k_x \mid}{\mid k_z \mid}\frac{\mid k_x \mid}{\mid k_y \mid} \gg 1.$$

Hence

$$\mid (\nabla \times \vec{\xi})_y \mid \ll \mid (\nabla \times \vec{\xi})_x \mid \ll \mid (\nabla \times \vec{\xi})_z \mid,$$

so that

$$\nabla \times \vec{\xi} \approx (\nabla \times \vec{\xi})_z\ \vec{1}_z \approx ik_x\ \xi_y\ \vec{1}_z. \tag{12}$$

Here also the $\approx$ sign means that the three components $(\nabla \times \vec{\xi})$ are non-zero but the parallel component is far larger in absolute value than the two horizontal components.

The second class of MHD waves corresponds to

$$Y \neq 0,\ Z = 0,\ \xi_z = \xi_\parallel \neq 0. \tag{13}$$

They are the magneto-sonic waves. They cause compression but do not propagate parallel vorticity. However, they cause horizontal vorticity. Their displacement has a component parallel to the magnetic field that is driven by the magnetic pressure force. The dispersion relation is

$$(\omega^2)^2 - k^2(v_S^2 + v_A^2)\omega^2 + k_z^2 k^2 v_S^2 v_A^2 = 0. \tag{14}$$

The well-known solutions for the eigenfrequencies are

$$\omega^2 = \omega_{sl,f}^2 = \frac{k^2(v_S^2 + v_A^2)}{2}\left\{1 \pm \left(1 - \frac{4\omega_C^2}{k^2(v_S^2 + v_A^2)}\right)^{1/2}\right\}. \tag{15}$$

$k^2 = k_x^2 + k_y^2 + k_z^2$, ω_C, and v_C are the cusp frequency, and the cusp velocity.

$$\omega_C^2 = \frac{v_S^2}{v_S^2 + v_A^2}\omega_A^2 = k_\parallel^2 v_C^2 = k_z^2 v_C^2,\ \ v_C^2 = \frac{v_S^2 v_A^2}{v_S^2 + v_A^2}. \tag{16}$$

In Equation (15) "sl" corresponds to the minus sign, and "f" to the plus sign. The corresponding waves are the slow and fast magneto-sonic waves. The frequencies of the magneto-sonic waves depend on the three components (k_x, k_y, k_z) of the wave vector $\vec{k}$. They depend in the same way on k_x and k_y because of isotropy in the planes normal to $\vec{B}_0$. It is instructive to consider the variation of $\omega_{sl,f}^2$ as function of k_x for fixed values of (k_y, k_z). The cut-off frequencies ω_I, ω_{II} are defined as

$$\omega_I^2 = \omega_{sl}^2(k_x = 0, k_y, k_z),\ \ \omega_{II}^2 = \omega_f^2(k_x = 0, k_y, k_z). \tag{17}$$

Also

$$\lim\nolimits_{k_x \rightarrow \infty} \omega_{sl}^2 = \omega_C^2,\ \ \lim\nolimits_{k_x \rightarrow \infty} \omega_f^2 = \infty \tag{18}$$

The cut-off frequencies $\omega_I,\ \omega_{II}$ and the characteristic frequencies $\omega_A,\ \omega_C$ obey the sequence of inequalities

$$\omega_C^2 \leq \omega_{sl}^2 \leq \omega_I^2 \leq \omega_A^2 \leq \omega_{II}^2 \leq \omega_f^2 < +\infty. \tag{19}$$

Hence the spectrum of linear motions of a uniform plasma of infinite extent can be divided in a slow subspectrum $]\omega_C,\ \omega_I]$, a degenerate Alfvén point spectrum ω_A and a fast subspectrum

$[\omega_{II}, \quad +\infty[$. The first equality in (18) means that ω_C is an accumulation point of the slow subspectrum.

The magneto-sonic waves are driven by tension and pressure forces and cause variations in density and pressure and horizontal vorticity.

The solutions for the eigenfunctions are

$$\vec{\xi}_{sl,f} = (\vec{1}_x + \frac{k_y}{k_x}\,\vec{1}_y + \frac{\omega_{sl,f}^2 - k^2 v_A^2}{\omega_{sl,f}^2}\;\frac{k_z}{k_x}\vec{1}_z)\;\xi_x, \tag{20}$$

or equivalently,

$$\vec{\xi}_{sl,f} = (\frac{\omega_{sl,f}^2}{\omega_{sl,f}^2 - k^2 v_A^2}\;\frac{k_x}{k_z}\vec{1}_x + \frac{\omega_{sl,f}^2}{\omega_{sl,f}^2 - k^2 v_A^2}\;\frac{k_y}{k_z}\vec{1}_y + \vec{1}_z)\xi_z. \tag{21}$$

The popular view is that the horizontal motion (ξ_x, ξ_y) is the dominant motion for fast waves while the parallel motion ξ_z is the dominant motion for slow waves. In order to point out that this is not the general rule, ξ_x is used as the measuring unit in (20) and ξ_z in (21). It is straightforward to show that in general the parallel component in (20) is not small compared to the horizontal components, and similarly that the horizontal components in (21) are not *per se* much smaller than the parallel component. However, for strong magnetic fields, i.e., $v_A \gg v_S$ it can be shown that

$$\vec{\xi}_f \approx (\vec{1}_x + \frac{k_y}{k_x}\,\vec{1}_y)\;\xi_x; \quad \vec{\xi}_{sl} \approx \xi_z\vec{1}_z. \tag{22}$$

The popular view corresponds to the limiting case of a strong field.

The parallel component of vorticity $(\nabla \times \vec{\xi})_z = iZ$ is of course zero. However, the horizontal components are non-zero

$$\nabla \times \vec{\xi} = -i\;k_z\;\frac{k^2\;v_A^2}{\omega_{sl,f}^2}\;\xi_x\;(\frac{k_y}{k_x}\vec{1}_x - \vec{1}_y). \tag{23}$$

For $k_y = 0$ the expressions (20) for the displacement $\vec{\xi}$ and (23) for vorticity $\nabla \times \vec{\xi}$ can be simplified to

$$\vec{\xi}_{sl,f} = (\vec{1}_x + \frac{\omega_{sl,f}^2 - k^2 v_A^2}{\omega_{sl,f}^2}\;\frac{k_z}{k_x}\vec{1}_z)\;\xi_x, \quad \nabla \times \vec{\xi} = i\;k_z\;\frac{k^2\;v_A^2}{\omega_{sl,f}^2}\;\xi_x\;\vec{1}_y. \tag{24}$$

Keep $k_y \neq 0,\; k_z \neq 0$ and finite and mimic a situation with non-uniformity in the x- direction and a turning point where $k_x = 0$ and find

$$\vec{\xi}_{sl,f} = (\frac{\omega_{I,II}^2}{\omega_{I,II}^2 - k^2 v_A^2}\;\frac{k_y}{k_z}\vec{1}_y + \vec{1}_z)\xi_z. \tag{25}$$

In summary for a uniform plasma of infinite extent the division is clear. The equation for vorticity is uncoupled from the equations for compression and parallel displacement. The waves have either parallel vorticity and no compression and no parallel displacement, these are the Alfvén waves, or they have compression and parallel displacement and no parallel vorticity, they are magneto-sonic waves. There are no waves with compression and parallel vorticity at the same time. There is no mixing of properties.

For a pressureless plasma with

$$v_S^2 = 0, \tag{26}$$

the solutions for the magnetosonic waves are

$$\begin{aligned} \omega_C^2 &= 0,\;\; \omega_{sl}^2 = 0,\;\; \omega_f^2 = k^2 v_A^2, \\ \xi_z &= 0,\;\; \vec{\xi}_f = (\vec{1}_x + \frac{k_y}{k_x}\,\vec{1}_y)\;\xi_x, \quad \nabla \times \vec{\xi} = -i\;k_z \\ &\qquad \xi_x\;(\frac{k_y}{k_x}\vec{1}_x - \vec{1}_y). \end{aligned} \tag{27}$$

In this situation there are no slow waves and the fast magneto-sonic waves have no parallel motions. The parallel motions are driven by the gradient of plasma pressure and here plasma pressure vanishes by assumption. The absence of slow waves and of parallel motions is a general result for a pressureless plasma. In what follows, no particular attention will be devoted to pressureless plasmas. The equations for MHD waves for a pressureless plasma are easily obtained by putting $v_S^2 = 0$ in the general equations.

3. MIXED PROPERTIES IN NON-UNIFORM PLASMAS

The aim of the present section is to show that MHD waves in a non-uniform plasma have mixed properties. In general they propagate compression and parallel vorticity at the same time. The phenomenon of mixed properties follows from the fact that the equations that describe the linear motions are coupled, unlike for the case of a uniform plasma of infinite extent. In particular the focus is on MHD waves on 1-D cylindrical plasma columns. The equilibrium model is a straight cylindrical plasma column of radius R in static equilibrium. In what follows we use cylindrical coordinates r, φ, z. The magnetic field has both an axial and an azimuthal component

$$\vec{B_0} = B_{z,0}\vec{1}_z + B_{\varphi,0}\vec{1}_\varphi. \tag{28}$$

The equilibrium density $\rho_0(r)$, equilibrium pressure $p_0(r)$, and the components of the equilibrium magnetic field $B_{z,0}(r), B_{\varphi,0}(r)$ are functions of r or constant. The equilibrium quantities satisfy the equation of static equilibrium

$$\frac{d}{dr}(p_0 + \frac{B_0^2}{2\mu}) = -\frac{B_{\varphi,0}^2}{\mu r}, \;\; B_0^2 = B_{\varphi,0}^2 + B_{z,0}^2. \tag{29}$$

In a nonuniform plasma v_S^2, v_A^2, ω_A^2, and ω_C^2 are functions of position. In what follows f' and δf denote respectively the Eulerian and Lagrangian variation of a quantity f. In linear theory they are related as

$$\delta f = f' + \frac{df_0}{dr}\xi_r, \tag{30}$$

with f_0 the equilibrium value of f. In the following equations $P' = p' + \vec{B}_0 \cdot \vec{B}'/\mu$ is the Eulerian perturbation of total pressure; p' is the Eulerian perturbation of plasma pressure. $\vec{\xi}$ is the Lagrangian displacement.

We use the mixed field line / magnetic surface triad $(\vec{b}, \vec{n}, \vec{\pi})$ defined by Goedbloed et al. (2010) in their Equations (17.23). In the present case of a straight cylindrical flux tube with the equilibrium magnetic field $\vec{B}_0$ defined in the Equation (28)

$$\vec{n} = \vec{1}_r,\ \vec{b} = \vec{1}_B = \vec{1}_\parallel,\ \vec{\pi} = \vec{1}_\perp,$$

with $\vec{1}_\parallel, \vec{1}_\perp$ the unit vectors in the magnetic surfaces respectively parallel and perpendicular to the magnetic field lines.

ξ_r is the radial component of Lagrangian displacement and $\xi_\parallel, \xi_\perp$ are the projections of the Lagrangian displacement in the magnetic surfaces parallel and perpendicular to the magnetic field lines:

$$\xi_\perp = (\xi_\varphi B_{z,0} - \xi_z B_{\varphi,0})/B,\ \ \xi_\parallel = \vec{\xi} \cdot \vec{B}_0/B_0. \tag{31}$$

Since the equilibrium quantities are independent of φ and z the wave variables can be put proportional to the exponential factor $\exp[i(m\varphi + k_z z)]$ with m, k_z the azimuthal and axial wave numbers, m is an integer. For example, for the Lagrangian displacement we write

$$\vec{\xi}(\vec{r};\, t) = \hat{\vec{\xi}}(r) \exp(i(m\varphi + k_z z - \omega t)). \tag{32}$$

$\hat{\vec{\xi}}(r)$ is the radially varying amplitude of $\vec{\xi}$. In what follows the hat on $\vec{\xi}$ and on the other wave variables will be omitted. It is convenient to introduce the wave vector $\vec{k} = (0, m/r, k_z)$.

The linear MHD waves can be described by two ordinary differential equations for ξ_r and P' (see e.g., Appert et al., 1974; Sakurai et al., 1991b; Goossens et al., 1992, 1995)

$$\begin{aligned} D\frac{d(r\,\xi_r)}{dr} &= C_1 r\,\xi_r - C_2 r\,P', \\ D\frac{dP'}{dr} &= C_3 \xi_r - C_1 P'. \end{aligned} \tag{33}$$

The coefficient functions D, C_1, C_2, C_3 are given by

$$\begin{aligned} D &= \rho_0(v_S^2 + v_A^2)(\omega^2 - \omega_A^2)(\omega^2 - \omega_C^2), \\ C_1 &= \frac{2}{\mu r} B_{\varphi,0}^2\, \omega^4 - (v_S^2 + V_A^2)(\omega^2 - \omega_C^2)\frac{2 m f_B}{\mu r^2} B_{\varphi,0}, \\ C_2 &= \omega^4\ - (v_S^2 + v_A^2)(\omega^2 - \omega_C^2)\left(\frac{m^2}{r^2} + k_z^2\right) \\ &= (\omega^2 - \omega_I^2)(\omega^2 - \omega_{II}^2), \\ C_3 &= D\left[\rho_0\,(\omega^2 - \omega_A^2) + \frac{2B_{\varphi,0}}{\mu}\frac{d}{dr}\left(\frac{B_{\varphi,0}}{r}\right)\right] \\ &+ \frac{4\omega^4 B_{\varphi,0}^4}{\mu^2 r^2} - 4\rho_0\,(v_S^2 + v_A^2)(\omega^2 - \omega_C^2)\omega_A^2 \frac{B_{\varphi,0}^2}{\mu r^2}. \end{aligned} \tag{34}$$

v_A and v_S are the Alfvén speed and the speed of sound as before and are defined in Equation (6). In a non-uniform plasma they are functions of position. The quantities f_B and g_B are defined as

$$f_B = \vec{k}\cdot\vec{B}_0 = k_z B_{z,0} + \frac{m\ B_{\varphi,0}}{r},\ \ g_B = (\vec{k}\times\vec{B}_0)\vec{1}_r = \frac{m\ B_{z,0}}{r} - k_z B_{\varphi,0}. \tag{35}$$

The frequencies ω_A and ω_C are the local Alfvén frequency and the local cusp frequency as before. They are defined for the planar case in Equation (7). Here in the cylindrical case their squares are defined as

$$\omega_A^2 = \frac{f_B^2}{\mu\rho_0} = \frac{\left(k_z B_{z,0} + \dfrac{m}{r}B_{\varphi,0}\right)^2}{\mu\rho_0},\ \ \omega_C^2 = \frac{v_S^2}{v_S^2 + v_A^2}\omega_A^2. \tag{36}$$

Note that ω_A and ω_C are functions of position. For a given set of wave numbers (m, k_z) ω_A and ω_C map out two ranges of frequencies known as the Alfvén continuum and the cusp continuum. The frequencies $\omega_I,\ \omega_{II}$ are defined as

$$\omega_{I,II}^2 = \frac{1}{2}\left(\frac{m^2}{r^2} + k_z^2\right)(v_S^2 + v_A^2)\left\{1 \pm \left[1 - \frac{4\omega_C^2}{\left(\dfrac{m^2}{r^2} + k_z^2\right)(v_S^2 + v_A^2)}\right]^{1/2}\right\}. \tag{37}$$

They are the cylindrical analogues of the Cartesian cut-off frequencies defined in (17). Here they are not cut-off frequencies but rather frequencies that restrict the Sturmian or anti-Sturmian behavior of the spectrum as explained by Goedbloed (1975, 1983).

To emphasize that parallel motions are solely driven by the gradient plasma pressure force, the parallel component of the equation of motion is written as

$$\rho_0\ \omega^2\ \xi_\parallel = \frac{i f_B}{B_0}\ \delta p. \tag{38}$$

δp is the Lagrangian variation of plasma pressure.

For the discussion of the mixed properties it is necessary to look at the wave variables $\xi_\perp,\ \ \xi_\parallel, \nabla\cdot\vec{\xi}$ and $(\nabla\times\vec{\xi})$. They are given by expressions in ξ_r and P' and their derivatives. Algebraic expressions for $\xi_\perp,\ \ \xi_\parallel, \nabla\cdot\vec{\xi}$ can be found in e.g., Sakurai et al. (1991b)

$$\begin{aligned} \rho_0(\omega^2 - \omega_A^2)\xi_\perp &= \frac{i}{B_0}\ C_A, \\ \rho_0(\omega^2 - \omega_C^2)\xi_\parallel &= \frac{i f_B}{B_0}\ \frac{v_S^2}{v_S^2 + v_A^2}\ C_S, \\ \nabla\cdot\vec{\xi} &= \frac{-\omega^2}{\rho_0\ (v_S^2 + v_A^2)(\omega^2 - \omega_C^2)}\ C_S. \end{aligned} \tag{39}$$

The coupling functions are defined as (see e.g., Sakurai et al., 1991b)

$$C_A = g_B\ P' - \frac{2 f_B B_{\varphi,0} B_{z,0}}{\mu r}\ \xi_r,\ \ \ C_S = P' - \frac{2B_{\varphi,0}^2}{\mu r}\ \xi_r. \tag{40}$$

They are linear combinations of P' and ξ_r. The coefficients of ξ_r in C_A and C_S vanish when the equilibrium magnetic field is straight $B_{\varphi,0} = 0$. C_A depends on the azimuthal wave number m and the longitudinal wave number k_z. C_S on the other hand is independent of the wave numbers (m, k_z). The coupling functions play an essential role for the mixing properties of MHD waves and for resonant absorption. They are called coupling functions for the good reason that they couple the differential equations (33) for ξ_r and P' to the expressions for all of the remaining wave variables $\xi_\perp,\ \xi_\parallel, \nabla \cdot \vec{\xi},\ (\nabla \times \vec{\xi})$. First they couple the differential equations for ξ_r and P' to the algebraic equations (39) for $\xi_\perp,\ \xi_\parallel, \nabla \cdot \vec{\xi}$. When $C_A \neq 0$ the first equation of (39) implies that $\xi_\perp \neq 0$. Similarly when $C_S \neq 0$ the second and third equation of (39) imply that $\nabla \cdot \vec{\xi} \neq 0$. When in addition to $C_S \neq 0$ also $v_S \neq 0$ it follows that $\xi_\parallel \neq 0$.

Let us now consider $(\nabla \times \vec{\xi})$. In section 2 it was pointed out that a division of linear waves can be based on compression, parallel displacement and parallel vorticity. A characterization based on the components (ξ_x, ξ_y, ξ_z) is in general not possible. When we move from Cartesian geometry to cylindrical geometry the horizontal components (ξ_x, ξ_y) are replaced by the components $(\xi_r, \xi_\perp)$ in the planes normal to $\vec{B}_0$ and ξ_z is replaced by the component $\xi_\parallel$ parallel to the equilibrium magnetic field. For a uniform plasma of infinite extent, the MHD waves could be divided into incompressible waves that propagate parallel vorticity, i.e., the Alfvén waves and waves that propagate compression and have a parallel displacement component i.e., the magneto-sonic waves. In what follows it will be shown that for a non-uniform plasma MHD waves propagate both compression and parallel vorticity and have non-zero radial, perpendicular and parallel components of displacement and vorticity. To the best of our knowledge expressions for the components of $(\nabla \times \vec{\xi})$ are not available in the literature. They are

$$\begin{aligned}
(\nabla \times \xi)_r &= i\,\frac{g_B}{B_0}\,\xi_\parallel - i\,\frac{f_B}{B_0}\,\xi_\perp,\\
(\nabla \times \vec{\xi})_\parallel &= \frac{d\xi_\perp}{dr} + P_\perp \xi_\perp + P_\parallel \xi_\parallel - i\frac{g_B}{B_0}\xi_r,\\
(\nabla \times \vec{\xi})_\perp &= -\frac{d\xi_\parallel}{dr} + Q_\perp \xi_\perp + Q_\parallel \xi_\parallel + i\frac{f_B}{B_0}\xi_r. \qquad (41)
\end{aligned}$$

Expressions for $P_\perp, P_\parallel, Q_\perp, Q_\parallel$ are

$$\begin{aligned}
P_\perp &= \frac{B_{z,0}}{B_0}\frac{1}{r}\frac{d}{dr}\left(\frac{rB_{z,0}}{B_0}\right) + \frac{B_{\varphi,0}}{B_0}\frac{d}{dr}\left(\frac{B_{\varphi,0}}{B_0}\right),\\
P_\parallel &= \frac{B_{z,0}}{B_0}\frac{1}{r}\frac{d}{dr}\left(\frac{rB_{\varphi,0}}{B_0}\right) - \frac{B_{\varphi,0}}{B_0}\frac{d}{dr}\left(\frac{B_{z,0}}{B_0}\right),\\
Q_\perp &= \frac{B_{z,0}}{B_0}\frac{d}{dr}\left(\frac{B_{\varphi,0}}{B_0}\right) - \frac{B_{\varphi,0}}{B_0}\frac{1}{r}\frac{d}{dr}\left(\frac{rB_{z,0}}{B_0}\right),\\
Q_\parallel &= -\frac{B_{z,0}}{B_0}\frac{d}{dr}\left(\frac{B_{z,0}}{B_0}\right) + \frac{B_{\varphi,0}}{B_0}\frac{1}{r}\frac{d}{dr}\left(\frac{rB_{\varphi,0}}{B_0}\right).
\end{aligned}$$

The Equations (41) show that the components of $(\nabla \times \vec{\xi})$ can be expressed in terms of $(\xi_r, \xi_\perp, \xi_\parallel)$. Since $\xi_\perp, \xi_\parallel$ are expressed in terms of ξ_r and P' it follows that also the components of $(\nabla \times \vec{\xi})$ can be expressed in terms of ξ_r and P'. When $(\xi_r, \xi_\perp, \xi_\parallel)$ are non-zero, the components of vorticity are in general also non-zero. All of the wave variables are coupled. The MHD waves have mixed properties, they propagate both compression and parallel vorticity and have non-zero radial, perpendicular and parallel components of displacement and vorticity. In general all wave variables are non-zero. A situation in which a subset of the wave variables is not coupled to the other wave variables is an exception. Such a situation will appear for axi-symmetric motions in the presence of a straight field. The clear division into Alfvén waves and magneto-sonic waves that exists for a uniform plasma of infinite extent does not any longer hold.

Hence in general for linear MHD waves on a non-uniform plasma

$$\begin{aligned}
\xi_r &\neq 0, \quad P' \neq 0,\\
\xi_\perp &\neq 0, \quad \xi_\parallel \neq 0,\\
\nabla \cdot \vec{\xi} &\neq 0, \quad (\nabla \times \vec{\xi}) \neq 0. \qquad (42)
\end{aligned}$$

Let us consider the special case of axi-symmetric motions with $m = 0$. The expressions for $f_B,\ g_B,\ C_A,\ C_S$ can be simplified to

$$\begin{aligned}
f_B &= k_z B_{z,0}, \quad g_B = -k_z\ B_{\varphi,0},\\
C_A &= -k_z B_{\varphi,0}\{P' + 2\,\frac{B_{z,0}^2\ \xi_r}{\mu r}\}, \quad C_S = P' - 2\frac{B_{\varphi,0}^2}{\mu r}\xi_r. \qquad (43)
\end{aligned}$$

For a twisted magnetic field with both a longitudinal component $B_{z,0}$ and a non-zero azimuthal component $B_{\varphi,0}$, the coupling functions C_A and C_S are non-zero. This implies that the preceding analysis on mixed properties also applies to axi-symmetric motions. The axi-symmetric motions propagate vorticity and compression. The situation is different when the magnetic field is straight.

Since C_A and C_S are functions of position the coupling of the equations depends on position and so does the strength of the mixing of the wave properties. For example a wave can start off as a predominantly fast wave, change into a wave that has both fast and Alfvén properties and turn into a predominantly Alfvénic wave. MHD waves have mixed properties and have different appearances in different parts of the plasma because of the inhomogeneity of the plasma. This phenomenon was discussed by Goossens et al. (2002b), Goossens (2008), and Goossens et al. (2011, 2012, 2014). Waves with mixed properties are also referred to as coupled MHD waves (Pascoe et al., 2010, 2011). This is a rather strange name as it seems to suggest that there are two or more waves involved.

Let us now focus on MHD waves in the presence of a straight field. For a straight field $(B_{\varphi,0} = 0)$ the magnetic surfaces are cylinders: $r =$ constant, and the φ- and z- directions are the directions in the magnetic surfaces respectively perpendicular and parallel to the magnetic field lines. The r- direction is normal to the magnetic surfaces. Hence ξ_r is associated with motions normal or across magnetic surfaces; $\xi_\parallel = \xi_z$ are motions along the magnetic field lines and $\xi_\perp = \xi_\varphi$ are motions in the magnetic surfaces perpendicular to the magnetic field lines. For a straight field the expressions for $f_B,\ g_B,\ C_A,\ C_S$ are simplified to

$$\begin{aligned} f_B &= k_z B_{z,0}, \quad g_B = \frac{m}{r} B_{z,0}, \\ C_A &= g_B\, P' = \frac{m}{r} B_{z,0}\, P', \quad C_S = P'. \end{aligned} \tag{44}$$

The coupling functions $C_A,\ C_S$ only contain P'. The coefficients of ξ_r in C_A and C_S vanish when $B_{\varphi,0} = 0$. Hence the coupling of the waves variables is solely due to P' as will become clear in what follows. As far as the wave numbers (m, k_z) are concerned, C_A no longer depends on k_z, only on m.

The differential equations (33) for ξ_r and P' and the algebraic equations for $\xi_\perp,\ \xi_\parallel, \nabla \cdot \vec{\xi}$ (39) are now

$$\begin{aligned} D\frac{d(r\xi_r)}{dr} &= -C_2 r P', \\ \frac{dP'}{dr} &= \rho_0\,(\omega^2 - \omega_A^2)\xi_r, \\ \rho_0\,(\omega^2 - \omega_A^2)\xi_\varphi &= \frac{im}{r} P', \\ \rho_0(\omega^2 - \omega_C^2)\xi_z &= ik_z \frac{v_S^2}{v_S^2 + v_A^2} P', \quad \rho_0\,\omega^2 \xi_z = ik_z \delta p, \\ \nabla \cdot \vec{\xi} &= \frac{-\omega^2 P'}{\rho_0\,(v_S^2 + v_A^2)(\omega^2 - \omega_C^2)}. \end{aligned} \tag{45}$$

Use now (41) and note that for a straight field

$$P_\perp = \frac{1}{r}, \quad P_\parallel = 0, \quad Q_\perp = 0, \quad Q_\parallel = 0,$$

to obtain

$$\begin{aligned} (\nabla \times \xi)_r &= i(\frac{m}{r}\xi_z - k_z \xi_\varphi), \\ (\nabla \times \xi)_\varphi &= -\frac{d\xi_z}{dr} + ik_z \xi_r, \\ (\nabla \times \xi)_z &= \frac{d\xi_\varphi}{dr} + \frac{\xi_\varphi}{r} - i\frac{m}{r}\xi_r. \end{aligned} \tag{46}$$

Equations (45) and (46) govern the MHD waves on a non-uniform straight cylindrical plasma column with a straight magnetic field. There is a natural subdivision between, respectively, axi-symmetric motions with $m = 0$ and non-axisymmetric motions with $m \neq 0$. The reason being that the equation for ξ_φ for $m = 0$ is decoupled from the remaining equations. Let us first focus on axi-symmetric motions with $m = 0$.

$$C_A = 0, \quad C_S = P'. \tag{47}$$

The equation for $\xi_\perp = \xi_\varphi$ is decoupled from the remaining equations

$$\rho_0\,(\omega^2 - \omega_A^2)\,\xi_\varphi = 0. \tag{48}$$

Equation (48) can be satisfied in two ways. First of all by choosing

$$\omega^2 = \omega_A^2, \quad \xi_\varphi \neq 0. \tag{49}$$

The second choice is

$$\omega^2 \neq \omega_A^2, \quad \xi_\varphi = 0. \tag{50}$$

The solutions given in (49) and (50) correspond respectively to the axi-symmetric Alfvén waves and the sausage magneto-sonic waves. The axi-symmetric MHD waves are decoupled in sausage magneto-sonic waves and axi-symmetric Alfvén waves. The solutions for the axi-symmetric magneto-sonic waves are

$$\begin{aligned} & P' \neq 0, \\ & \xi_r \neq 0,\ \xi_z \neq 0,\ \xi_\varphi = 0, \\ & \nabla \cdot \vec{\xi} = \frac{-\omega^2 P'}{\rho_0(v_S^2 + v_A^2)(\omega^2 - \omega_C^2)} \neq 0, \\ & (\nabla \times \vec{\xi})_r = 0,\ (\nabla \times \vec{\xi})_z = 0. \\ & (\nabla \times \vec{\xi})_\varphi = -ik_z \frac{d}{dr}\left\{ \frac{v_S^2}{v_A^2 + v_S^2} \frac{1}{\rho_0(\omega^2 - \omega_C^2)} \right\} P' \\ & \quad + ik_z \frac{\omega^2}{\rho_0(\omega^2 - \omega_A^2)(\omega^2 - \omega_C^2)} \frac{v_A^2}{v_A^2 + v_S^2} \frac{dP'}{dr}. \end{aligned} \tag{51}$$

The solutions for the axi-symmetric Alfvén waves are

$$\begin{aligned} & P' = 0, \\ & \xi_r = 0, \quad \xi_z = 0, \quad \xi_\varphi \neq 0, \\ & \nabla \cdot \vec{\xi} = 0, \\ & (\nabla \times \vec{\xi})_r = -ik_z \xi_\varphi, \quad (\nabla \times \vec{\xi})_\varphi = 0, \quad (\nabla \times \vec{\xi})_z = \frac{1}{r}\frac{d}{dr}(r\xi_\varphi). \end{aligned} \tag{52}$$

For an axi-symmetric non-uniform 1-dimensional cylindrical plasma this is the only case where pure Alfvén waves show up in the analysis. Each magnetic surface oscillates with its own local Alfvén frequency. In a twisted magnetic field, $C_A \neq 0$ for $m = 0$ so that the equations are coupled and the corresponding MHD waves have mixed magneto-acoustic and Alfvén properties. Also $C_S \neq 0$ for any azimuthal wave number m. The absence of pure Alfvén waves in a non-uniform 1-D cylindrical plasma for azimuthal wave numbers $m \neq 0$ is in stark contrast to the situation for a magnetic flux tube with piece wise constant density and magnetic field. Spruit (1982) showed that solutions with $\nabla \cdot \vec{v} = 0$ exist for any m. H. Spruit correctly identified these solutions as Alfvén waves. Flow patterns for Alfvén waves with $m = 0$ and $m = 1$ are shown on Figure 1 in Spruit (1982). In addition to the Alfvén waves there are compressive waves. The fact that pure non-axisymmetric Alfvén waves do not exist in a non-uniform straight plasma cylinder is an illustration of how the non-uniformity produces waves with mixed properties.

Let us now turn back to the non-axisymmetric MHD waves with $m \neq 0$. Actually the analysis also holds for axi-symmetric MHD waves with $\xi_\varphi = 0$. Excluded from the analysis are the axi-symmetric Alfvén waves defined in (52). The Equation (46) can be rewritten as

$$\begin{aligned}
(\nabla \times \xi)_r &= k_z \frac{m}{r} \frac{v_A^2}{v_S^2 + v_A^2} \frac{\omega^2}{\rho_0(\omega^2 - \omega_A^2)(\omega^2 - \omega_C^2)} P', \\
(\nabla \times \xi)_\varphi &= -ik_z \frac{d}{dr} \left\{ \frac{v_S^2}{v_A^2 + v_S^2} \frac{1}{\rho_0(\omega^2 - \omega_C^2)} \right\} P' \\
&\quad + ik_z \frac{\omega^2}{\rho_0(\omega^2 - \omega_A^2)(\omega^2 - \omega_C^2)} \frac{v_A^2}{v_A^2 + v_S^2} \frac{dP'}{dr}, \\
(\nabla \times \xi)_z &= -i \frac{m}{r} \frac{1}{\left\{\rho_0(\omega^2 - \omega_A^2)\right\}^2} \frac{d}{dr} \left\{\rho_0(\omega^2 - \omega_A^2)\right\} P'
\end{aligned} \tag{53}$$

Note that the expressions for the components of vorticity for axi-symmetric magneto-sonic waves can be obtained from (53) by putting $m = 0$.

Here all wave variables are coupled and all wave variables are non-zero. In case of a straight field, it is the non-zero Eulerian perturbation of total pressure $P' \neq 0$ that produces MHD waves with mixed properties reminiscent of Alfvén waves and magneto-sonic waves. See also the comments by Hasegawa and Uberoi (1982) in their Chapter 3 on MHD waves in an inhomogeneous medium.

Special interest goes to the components of $\nabla \times \xi$. It is obvious that $(\nabla \times \xi)_r \neq 0$ irrespective if the equilibrium is uniform or not. The same is true for $(\nabla \times \xi)_\varphi$. The second term is always non-zero. The first term is non-zero for a non-uniform equilibrium and for a piece-wise constant density model the derivative results in a delta-function contribution. The parallel component $(\nabla \times \xi)_z$ is non-zero for a non-uniform equilibrium with

$$\frac{d}{dr} \left\{\rho_0(\omega^2 - \omega_A^2)\right\} \tag{54}$$

different from zero. In a fully non-uniform equilibrium this condition is satisfied everywhere. In a piece-wise constant density model the derivative results in a delta-function contribution.

Let us try to understand the cause of the vorticity. The equilibrium model is a 1-D straight cylinder with the equilibrium quantities functions of the radial distance r to the axis. There is no baroclinic source of vorticity since the iso-surfaces of density and pressure coincide. Equations (41) combined with the expressions for $P_\perp, P_\parallel, Q_\perp, Q_\parallel$ in principle contain all the information. They are rather complicated and do not allow a straightforward interpretation. Physical insight can be gained by considering the case of a straight field. For a straight field the equation of motion in the horizontal planes follows from the 2nd and 3rd equations of Equation (45).

$$-\rho_0\, \omega^2\, \vec{\xi}_h = -\nabla_h P' - \rho_0\, \omega_A^2\, \vec{\xi}_h. \tag{55}$$

$\vec{\xi}_h$ is the displacement in horizontal planes and ∇_h is the gradient operator in horizonal planes

$$\vec{\xi}_h = (\xi_r, \xi_\varphi, 0), \quad \nabla_h = (\frac{d}{dr},\ i\frac{m}{r},\ 0).$$

The left hand side of Equation (55) is mass density times acceleration. The first term in the right hand side of Equation (55) is the horizontal gradient total pressure force; the second term is mass density times the magnetic tension force

$$\vec{T} = -\omega_A^2\, \vec{\xi}_h, \quad -\frac{1}{\rho_0}\nabla_h P' = -(\omega^2 - \omega_A^2)\vec{\xi}_h.$$

Hence

$$-\frac{1}{\rho_0}\nabla_h P' = \frac{\omega^2 - \omega_A^2}{\omega_A^2}\ \vec{T}. \tag{56}$$

The importance of tension force compared to the horizontal pressure force depends on the frequency of the wave. When $\omega^2 \approx \omega_A^2$ the magnetic tension force dominates; when $\omega^2 >> \omega_A^2$ then the the horizontal pressure force dominates; when $\omega^2 << \omega_A^2$ the horizontal pressure force and the magnetic tension force are of equal strength. For other values of ω^2 the actual ratio has to be computed.

From Equation (55)

$$\omega^2\ (\nabla \times \vec{\xi}_h) = \nabla \times (\frac{1}{\rho_0}\nabla_h P') - \nabla \times \vec{T}. \tag{57}$$

This shows that vorticity generated by the horizontal motions is due to the horizontal component of the gradient pressure force and the magnetic tension force. Equation (55) can be solved for ξ_h as

$$\vec{\xi}_h = \Phi\ \nabla_h P', \quad \Phi = \frac{1}{\rho_0(\omega^2 - \omega_A^2)}. \tag{58}$$

We can use Equation (56) to estimate for the relative contribution of the magnetic tension force and the horizontal gradient pressure force to the vorticity. Since $(\omega^2 - \omega_A^2)/\omega_A^2$ is non-constant in a non-uniform plasma we anticipate that the magnetic tension force is the dominant contributor to vorticity for $\omega^2 \approx \omega_A^2$; while the horizontal pressure force is the dominant contributor for $\omega^2 >> \omega_A^2$. Since

$$\nabla \times \nabla_h P' = k_z \frac{m}{r} P' \vec{1}_r + ik_z \frac{dP'}{dr} \vec{1}_\varphi,$$

the result for vorticity is

$$\nabla \times \vec{\xi}_h = \frac{d\Phi}{dr}\ \frac{im}{r}\ P'\vec{1}_z + k_z\ \Phi\ \left\{ \frac{m}{r} P'\ \vec{1}_r + i\frac{dP'}{dr}\ \vec{1}_\varphi \right\}\ . \tag{59}$$

Equation (59) follows from Equation (53) when we remove from this equation the contribution due to the parallel motions.

In the same manner, we can consider the equation of motion parallel to the magnetic field lines. From the 4th equation of Equation (45) it follows that ξ_z is given by

$$\xi_z = ik_z\ \Psi\ P', \quad \Psi = \frac{1}{\rho_0(\omega^2 - \omega_C^2)}\ \frac{v_S^2}{v_S^2 + v_A^2}. \tag{60}$$

The result for vorticity associated with the parallel motion is then

$$\nabla \times (\xi_z \vec{1}_z) = ik_z \left\{ -\frac{d\Psi}{dr} P' \vec{1}_\varphi + \Psi\left(-\frac{dP'}{dr}\vec{1}_\varphi + \frac{i\,m}{r} P' \vec{1}_r\right) \right\}. \tag{61}$$

This shows that vorticity generated by the parallel motions is due to the gradient pressure and vanishes in a pressureless plasma when $v_S^2 = 0$. The sum of $\nabla \times \vec{\xi}_h$ given by Equation (59) and $\nabla \times (\xi_z \vec{1}_z)$ given by Equation (61) is equal to the result given in Equation (53).

Equations (58) and (59) show that the horizontal motions and vorticity associated with horizontal motions are controlled by the function

$$\Phi = \frac{1}{\rho_0(\omega^2 - \omega_A^2)}.$$

Conversely Equations (60) and (61) show that the parallel motions and vorticity associated with parallel motions are controlled by the function

$$\Psi = \frac{1}{\rho_0(\omega^2 - \omega_C^2)}\ \frac{v_S^2}{v_S^2 + v_A^2}.$$

For non-axisymmetric MHD waves on a non-uniform plasma column with a straight magnetic field all wave variables are non-zero and coupled. The coupling factor is P'. This means that any given variable can be expressed in terms of another wave variable. Let us see what we can do with for example compression and parallel vorticity. Together with the parallel displacement ξ_z these are the two quantities that were used in section 2 to distinguish between Alfvén waves and magneto-sonic waves. The expressions for compression $\nabla \cdot \vec{\xi}$ and for parallel vorticity $(\nabla \times \vec{\xi})_z$ for non-axisymmetric motions in a straight field can be rewritten in compact form as

$$\nabla \cdot \vec{\xi} = N_C\ P', \quad (\nabla \times \vec{\xi})_z = i\ m\ N_V\ P', \tag{62}$$

with

$$\begin{aligned} N_C &= \frac{-\omega^2}{\rho_0\ (v_S^2 + v_A^2)(\omega^2 - \omega_C^2)}, \\ N_V &= \frac{-1}{r\left\{\rho_0(\omega^2 - \omega_A^2)\right\}^2} \frac{d}{dr}\left\{\rho_0(\omega^2 - \omega_A^2)\right\}. \end{aligned} \tag{63}$$

The ratio of parallel vorticity to compression is

$$\frac{\mid (\nabla \times \vec{\xi})_z \mid}{\mid \nabla \cdot \vec{\xi} \mid} = \mid m \mid\ \frac{\mid N_V \mid}{\mid N_C \mid}. \tag{64}$$

In addition to the parallel component of vorticity also the components in horizontal planes, i.e., $(\nabla \times \vec{\xi})_\varphi, (\nabla \times \vec{\xi})_r$ are as a rule non-zero in a non-uniform plasma. MHD waves turn out to be very efficient *in situ* generators of vorticity in non-uniform plasmas. This equation shows that a non-axisymmetric compressional motion immediately generates vorticity and vice versa a vortical motion generates compression. It is impossible to have one property without the other one. MHD waves that propagate compression but no vorticity or vice versa do not exist. The waves have always mixed properties.

The cylindrical model with a straight magnetic field has a Cartesian analogue. The Cartesian version has a vertical magnetic field along the z- axis and the direction of inhomogeneity along the x- axis. The cylindrical case with a straight field and axi-symmetric waves with $m = 0$ then corresponds to $k_y = 0$. For $k_y = 0$ the Cartesian equations for the wave variables are decoupled in equations for the magneto-sonic waves and equations for Alfvén waves. However, for $k_y \neq 0$ the equations are coupled and the MHD waves have mixed properties. Examples of this behavior can be found in Tirry and Berghmans (1997), Tirry et al. (1997), De Groof and Goossens (2000, 2002), and De Groof et al. (2002).

4. RESONANT ABSORPTION OF MHD WAVES

Let us turn to the discussion of resonant absorption and resonant MHD waves. We have already pointed out that the coupling functions C_A and C_S depend on position. This implies that the strength of the mixing of the wave properties depends on position. MHD waves have mixed properties and have different appearances in different parts of the plasma because of the inhomogeneity of the plasma. The phenomenon that the properties of MHD waves change as the wave propagates through a non-uniform environment is most clearly at work in resonant absorption. For example, in case of resonant Alfvén waves the MHD wave arrives at a position where it can behave as an almost pure Alfvén wave. Similarly, in case of resonant cusp waves the MHD arrives at a position where it can behave as a slow wave for perpendicular propagation. Resonant absorption and resonant waves have been discussed previously (see e.g., Goossens et al., 2011). We shall review aspects related to the displacement components $\xi_r,\ \xi_\perp,\ \xi_\parallel$, and P'. We shall focus on the behavior of compression $\nabla \cdot \vec{\xi}$ and vorticity $\nabla \times \vec{\xi}$ for resonant waves. The coupling functions C_A and C_S play an important role here also. Look back at the expression for the coefficient function D (34). The local Alfvén frequency $\omega_A(r)$ and the local cusp frequency $\omega_C(r)$ vary with position r and they map out two intervals of frequencies

$$\begin{aligned} \mathrm{AC} &= [\min \omega_A(r),\ \ \max \omega_A(r)\ ], \\ \mathrm{SC} &= [\min \omega_C(r),\ \ \max \omega_C(r)\ ] \end{aligned}$$

They are known as the Alfvén continuum (AC) and the slow or cusp continuum (SC) (Appert et al., 1974; Chen and Hasegawa, 1974; Goedbloed, 1983). For a frequency ω either in the Alfvén continuum or the slow continuum the coefficient function $D = 0$ at the position r_A where the frequency is equal to the local Alfvén frequency $\omega = \omega_A(r_A)$ or at the position r_C where the frequency is equal to the local cusp frequency $\omega = \omega_C(r_C)$. The system of differential equations (33) have regular singular points at the positions $r = r_A$ and $r = r_C$.

Let us first consider the Alfvén continuum. For a frequency in the Alfvén continuum the dispersion relation for Alfvén waves is locally satisfied. Each magnetic surface oscillates at its own Alfvén continuum frequency. Let us determine the structure of the MHD wave with a frequency in the Alfvén continuum. The MHD waves live on $[0, +\infty[$ in the r- direction. Solutions over the full spatial interval can be found in Poedts et al. (1989, 1990), Sakurai et al. (1991a), Goossens and Poedts (1992), Tirry and Goossens (1996), Ruderman and Roberts (2002), Van Doorsselaere et al. (2004), and Soler et al. (2013). Away from the resonant surface the MHD wave can be predominantly magnetosonic. During its propagation through the non-uniform plasma the MHD wave might change in a wave that has both magnetosonic and Alfvén properties. Close to and at the resonant surface the MHD wave is almost completely an Alfvén wave. Here we focus on the spatial behavior close to the singular point $r = r_A$ where $\omega = \omega_A(r_A)$. We follow Sakurai et al. (1991b), Goossens et al. (1992, 1995), and Tirry and Goossens (1996). They used Frobenius-Fuchs solutions around the singular point $r = r_A$ where $\omega = \omega_A(r_A)$ and introduced a new radial variable $s = r - r_A$. This analysis is valid in the interval $[-s_A, s_A]$ where the linear Taylor polynomial is an accurate approximation of $\omega^2 - \omega_A^2(r)$:

$$\omega^2 - \omega_A^2 \approx \Delta_A \, s, \quad \Delta_A = \frac{d}{dr}(\omega^2 - \omega_A^2)_{r_A} \tag{65}$$

The outcome of the application of the Frobenius-Fuchs method is the fundamental conservation law for resonant Alfvén waves

$$C_A(s) \equiv g_B P' - \frac{2 f_B B_{\varphi,0} \, B_{z,0}}{\mu r_A} \, \xi_r = \text{constant}, \tag{66}$$

and the solutions for ξ_r and P'

$$\begin{aligned} \xi_r(s) &= \frac{g_B}{\rho_0 \, B_0^2 \, \Delta_A} C_A \ln(|\ s\ |) + \begin{cases} \xi_- & s < 0 \\ \xi_+ & s > 0, \end{cases} \\ P'(s) &= \frac{2 f_B B_{\varphi,0} B_{z,0}}{\mu r_A \; \rho_0 \; B_0^2 \Delta_A} C_A \ln(|\ s\ |) + \begin{cases} P'_- & s < 0 \\ P'_+ & s > 0. \end{cases} \end{aligned} \tag{67}$$

All equilibrium quantities are evaluated at $s = 0$ $(r = r_A)$. The solutions for ξ_r and P' are characterized by a logarithmic singularity and a jump. The jump in a quantity Q is defined as

$$[Q] = \lim_{s \to 0^+} Q(s) - \lim_{s \to 0^-} Q(s).$$

Recall the equation for $\xi_\perp$

$$\rho_0(\omega^2 - \omega_A^2)\xi_\perp = \frac{i}{B_0} \, C_A.$$

Hence close to $s = 0$

$$s \, \xi_\perp \approx i \, \frac{C_A}{\rho_0 \; B_0 \; \Delta_A}. \tag{68}$$

This means that $\xi_\perp$ has a $1/s$- singularity and a $\delta(s)$- contribution. These singularities dominate those present in ξ_r and P'. The equation for the parallel component $\xi_\parallel$ is

$$\rho_0(\omega^2 - \omega_C^2)\xi_\parallel = \frac{i f_B}{B_0} \, \frac{v_S^2}{v_S^2 + v_A^2} \; C_S.$$

The coefficient of $\xi_\parallel$ in the left hand side of this equation is finite and non-zero for frequencies in the Alfvén continuum. The function C_S is a linear combination of ξ_r and P' and can contain a logarithmic term $\ln(|\ s\ |)$ and a jump. This implies that $\xi_\parallel$ contains at most a logarithmic term $\ln(|\ s\ |)$ and a jump and is dominated by $\xi_\perp$. Hence close to $s = 0$ we are in a situation that closely resembles that described in Equation (10) when we make the transformation

$$x \to r, \ \ y \to \perp, \ \ z \to \parallel \tag{69}$$

and note that

$$|\ \xi_\parallel\ | \le |\ \xi_r\ | \ \ll \ |\ \xi_\perp, \quad \vec{\xi}_A \approx \xi_\perp \vec{1}_\perp. \tag{70}$$

The motion (70) in the Alfvén wave is predominantly in the $\perp$-direction and rapidly varying in the r- direction. The $\approx$ sign means that the three components $(\xi_\parallel, \xi_r, \xi_\perp)$ are non-zero but $\xi_\perp$ is far larger in absolute value than the two other components.

Consider now Equations (41) for the components of $\nabla \times \vec{\xi}$ and identify the first term in the right hand side of the equation for $(\nabla \times \vec{\xi})_\parallel$ as the dominant term overall. Hence

$$\begin{aligned} (\nabla \times \vec{\xi})_\parallel \ &\approx \ \frac{d\xi_\perp}{dr} \ = \ \frac{d}{dr}\left\{ \frac{1}{\rho_0(\omega^2 - \omega_A^2)} \frac{i \, C_A}{B_0} \right\} \\ &\approx \ -\frac{i \, C_A}{B_0} \frac{1}{\left\{\rho_0(\omega^2 - \omega_A^2)\right\}^2} \frac{d}{dr} \left\{\rho_0(\omega^2 - \omega_A^2)\right\} \\ &\approx \ -i \frac{C_A}{\rho_0 \; B_0 \; \Delta_A} \; \frac{1}{s^2}. \end{aligned} \tag{71}$$

$(\nabla \times \vec{\xi})_\parallel$ has a $1/s^2$- singularity. The remaining components $(\nabla \times \vec{\xi})_r$ and $(\nabla \times \vec{\xi})_\perp$ are non-zero and both have a $1/s$- singularity when $f_B \neq 0$ and $Q_\perp \neq 0$. Hence use the transformation (69) to help us to identify the inequalities (12) but now as

$$|\ (\nabla \times \vec{\xi})_\perp\ | \le \ |\ (\nabla \times \vec{\xi})_r)\ | \ \ \ll \ \ |\ (\nabla \times \vec{\xi})_\parallel\ |, \tag{72}$$

so that

$$\nabla \times \vec{\xi} \ \approx \ (\nabla \times \vec{\xi})_\parallel \vec{1}_\parallel. \tag{73}$$

Here also the $\approx$ sign means that the three components $(\nabla \times \vec{\xi})$ are non-zero but the parallel component is far larger in absolute value than the two horizontal components.

In summary

$$\lim_{s\to 0}\frac{\mid \xi_\perp \mid}{\mid \xi_r \mid} = +\infty,\ \lim_{s\to 0}\frac{\mid \xi_\perp \mid}{\mid \xi_\parallel \mid} = +\infty,\ \lim_{s\to 0}\frac{\mid (\nabla\times\vec{\xi})_\parallel \mid}{\mid (\nabla\times\vec{\xi})_{r,\perp} \mid} = +\infty. \tag{74}$$

Hence the dominant dynamics is in the perpendicular motions. The jumps in ξ_r and P' (67) are due to dissipative effects. At and in the vicinity of the resonant position $s = 0$ the resonant MHD wave has very strong Alfvén wave properties. Its properties match the properties derived on the basis of very simple principles for Alfvén waves that mimic a resonant situation in section 2. The resonant Alfvén wave is linked to the outside world by the coupling function C_A.

A comment on the case of axi-symmetric motions with $m = 0$. The expressions for $f_B,\ g_B,\ C_A,\ C_S$ for axi-symmetric motions are given in (43). In particular it was pointed out that for a twisted magnetic field with both a longitudinal component $B_{z,0}$ and a non-zero azimuthal component $B_{\varphi,0}$ the coupling functions C_A and C_S are non-zero. Hence the preceding analysis on resonant properties also applies to axi-symmetric motions. Resonant absorption of axi-symmetric motions in the Alfvén continuum was investigated by Giagkiozis et al. (2016) for an a non-straight magnetic field and in the slow continuum by Yu et al. (2017a,b) for a straight magnetic field. In addition, the preceding analysis for the behavior of the various variables can be repeated for a pressureless plasma. The additional simplification is that $\xi_\parallel = 0$. The behavior of the resonant waves at and in the vicinity of the resonant position is to a large extent insensitive to plasma pressure.

The mathematical results in (68) for $\xi_\perp$ and (71) for $(\nabla\times\vec{\xi})_\parallel$ mean that there are strong counterstreaming flows in the perpendicular direction at and close to $s = 0$. Of course in reality infinite values for $\xi_\perp$ do not occur. We shall see that these infinite values are replaced by finite and very large values. This is the basis for the Kelvin-Helmholtz instability in Alfvén waves first investigated by Terradas et al. (2008) and subsequently studied by several groups (see e.g., Antolin et al., 2014, 2015, 2018).

Let us now turn to the slow continuum. The analysis for a frequency in the slow continuum parallels that for Alfvén waves (see e.g., Sakurai et al., 1991b; Goossens and Ruderman, 1995). The MHD waves live on $[0,\infty[$. Here we focus on the spatial behavior close to the singular point $r = r_C$ where $\omega = \omega_C(r_C)$. The variable s is now defined as $s = r - r_C$ with r_C the position where $\omega^2 = \omega_C^2(r_C)$. This analysis is valid in the interval $[-s_C, s_C]$ where the linear Taylor polynomial is an accurate approximation of $\omega^2 - \omega_C^2(r)$:

$$\omega^2 - \omega_C^2 \approx \Delta_C\, s,\quad \Delta_C = \frac{d}{dr}(\omega^2 - \omega_C^2)_{r_C}. \tag{75}$$

The outcome is the fundamental conservation law for resonant slow waves

$$C_S(s) \equiv P' - \frac{2B_{\varphi,0}^2\,\xi_r}{\mu r} = \text{constant}, \tag{76}$$

and the solutions for ξ_r and P'

$$\begin{aligned} \xi_r(s) &= \frac{\omega_C^4}{(B_0^2/\mu)\,\omega_A^2\,\Delta_C} C_S\ \ln(\mid s \mid) + \begin{cases} \xi_- & s < 0 \\ \xi_+ & s > 0, \end{cases} \\ P'(s) &= \frac{2\,\omega_C^4\,B_{\varphi,0}^2}{r_C\,B_0^2\,\omega_A^2\,\Delta_C} C_S \ln(\mid s \mid) + \begin{cases} P'_- & s < 0 \\ P'_+ & s > 0. \end{cases} \end{aligned} \tag{77}$$

Recall the equation for $\xi_\parallel$

$$\rho_0(\omega^2 - \omega_C^2)\xi_\parallel = \frac{i f_B}{B_0}\,\frac{v_S^2}{v_S^2 + v_A^2}\,C_S.$$

Hence close to $s = 0$

$$s\,\xi_\parallel = \frac{i f_B}{B_0\,\rho_0\,\Delta_C}\,\frac{v_S^2}{v_S^2 + v_A^2}\,C_S. \tag{78}$$

This means that $\xi_\parallel$ has a $1/s$- singularity and a $\delta(s)$- contribution. These singularities dominate those present in ξ_r and P'.

The equation for the perpendicular component $\xi_\perp$ is

$$\rho_0(\omega^2 - \omega_A^2)\xi_\perp = \frac{i}{B_0}\,C_A.$$

The coefficient of $\xi_\perp$ in the left hand side of this equation is finite and non-zero for frequencies in the cusp continuum. The function C_A is a linear combination of ξ_r and P' and can contain a logarithmic term $\ln(\mid s \mid)$ and a jump. This implies that $\xi_\perp$ contains at most a logarithmic term $\ln(\mid s \mid)$ and a jump and is dominated by $\xi_\parallel$. Hence close to $s = 0$ we are in a situation

$$\mid \xi_\perp \mid \le \mid \xi_r \mid \ \ll\ \mid \xi_\parallel \mid,\quad \vec{\xi}_S \approx \xi_\parallel \vec{1}_\parallel. \tag{79}$$

The motion (79) in the slow wave is predominantly in the $\parallel$-direction and rapidly varying in the r- direction. The $\approx$ sign means that the three components $(\xi_\parallel, \xi_r, \xi_\perp)$ are non-zero but $\xi_\parallel$ is far larger in absolute value than the two other components.

Recall from (39) the equation for $\nabla\cdot\vec{\xi}$ as

$$\nabla\cdot\vec{\xi} = \frac{-\omega^2}{\rho_0\,(v_S^2 + v_A^2)(\omega^2 - \omega_C^2)}\,C_S$$

and find that in the vicinity of $s = 0$ $\nabla\cdot\vec{\xi}$ behaves as

$$s\,(\nabla\cdot\vec{\xi}) = -\frac{\omega_C^2}{\rho_0\,\Delta_C\,(v_S^2 + v_A^2)}\,C_S. \tag{80}$$

$\nabla\cdot\vec{\xi}$ has a $1/s$- singularity and a $\delta(s)$- contribution in the same way as $\xi_\parallel$. Consider now Equations (41) for the components of $\nabla\times\vec{\xi}$ and identify the first term in the right hand side of the equation for $(\nabla\times\vec{\xi})_\perp$ as the dominant term overall. Hence

$$\begin{aligned} (\nabla\times\vec{\xi})_\perp &\approx -\frac{d\xi_\parallel}{dr} \ =\ -\frac{d}{dr}\left\{\frac{1}{\rho_0(\omega^2 - \omega_C^2)}\,\frac{i f_B}{B_0}\,\frac{v_S^2}{v_S^2 + v_A^2}\,C_S\right\} \\ &\approx \frac{i f_B}{B_0}\,\frac{v_S^2}{v_S^2 + v_A^2}\,C_S\,\frac{1}{\left\{\rho_0(\omega^2 - \omega_C^2)\right\}^2}\,\frac{d}{dr}\left\{\rho_0(\omega^2 - \omega_C^2)\right\} \end{aligned}$$

$$\approx i \frac{f_B}{\rho_0 \, B_0 \, \Delta_C} \, \frac{v_S^2}{v_S^2 + v_A^2} \, C_S \, \frac{1}{s^2}. \tag{81}$$

$(\nabla \times \vec{\xi})_\perp$ has a $1/s^2$-singularity. The remaining components $(\nabla \times \vec{\xi})_r$ and $(\nabla \times \vec{\xi})_\parallel$ are non-zero and both have a $1/s$-singularity when $g_B \neq 0$ and $P_\parallel \neq 0$.

$$\mid (\nabla \times \vec{\xi})_\parallel \mid \, \leq \, \mid (\nabla \times \vec{\xi})_r) \mid \quad \ll \quad \mid (\nabla \times \vec{\xi})_\perp \mid, \tag{82}$$

so that

$$\nabla \times \vec{\xi} \, \approx \, (\nabla \times \vec{\xi})_\perp \vec{1}_\perp. \tag{83}$$

Here also the $\approx$ sign means that the three components $(\nabla \times \vec{\xi})$ are non-zero but the perpendicular component is far larger in absolute value than the radial and parallel components.

In summary

$$\lim_{s \to 0} \frac{\mid \xi_\parallel \mid}{\mid \xi_r \mid} = +\infty, \; \lim_{s \to 0} \frac{\mid \xi_\parallel \mid}{\mid \xi_\perp \mid} = +\infty, \; \lim_{s \to 0} \frac{\mid (\nabla \times \vec{\xi})_\perp \mid}{\mid (\nabla \times \vec{\xi})_{r,\parallel} \mid} = +\infty. \tag{84}$$

The dominant dynamics is in the component in the magnetic surfaces and parallel to the magnetic field lines. In the vicinity of the resonant magnetic surface the wave is almost exactly a slow wave in a homogeneous plasma with its wave vector almost perpendicular to the magnetic field.

The mathematical results in (78) for $\xi_\parallel$ and (81) for $\nabla \times \vec{\xi}_\perp$ mean that there are strong counterstreaming flows in the parallel direction at and close to $s = 0$. Of course in reality infinite values for $\xi_\perp$ do not occur. We shall see that these infinite values are replaced by finite and very large values. Our prediction is that this is the basis for the Kelvin-Helmholtz instability in slow resonant waves. This possible Kelvin-Helmholtz instability has not yet been studied.

5. CONCLUSIONS

Pure Alfvén waves and pure magneto-acoustic waves exist in a uniform plasma of infinite extent. In a non-uniform plasma the MHD waves combine the properties of the classic Alfvén waves and of magneto-sonic waves in a uniform plasma of infinite extent. The mixing of the properties is controlled by the coupling functions C_A and C_S. The general rule is that MHD waves in a non-uniform plasma propagate both compression and parallel vorticity and that the parallel, perpendicular, and radial components of displacement and vorticity are non-zero. Vortex motions driven by MHD waves are as far as we can anticipate not different from vortex motions generated by other sources. Our analysis shows that MHD waves in non-uniform plasmas are very efficient *in situ* generators of vorticity. In a non-uniform plasma MHD waves can fill the whole space with vorticity. Vortex motions are expected to be very prominent where resonant conditions are satisfied. The signatures of vortex motions in the process of resonant Alfvén damping are very strong sheared azimuthal motions. Observational aspects of these strong sheared azimuthal motions and possible turbulent behavior have been investigated by Okamoto et al. (2015) and compared to results of numerical simulations by Antolin et al. (2015). Of course in a pressureless plasma the parallel component of the displacement is zero. The exception to the general rule of mixed properties are axi-symmetric waves in the presence of a straight magnetic field. The coupling functions depend on position. Hence as an MHD waves propagates through a non-uniform plasma its properties change. Resonant absorption is a clear example of this phenomenon. In case of resonant Alfvén waves the MHD wave arrives at a position where it behaves as an almost pure Alfvén wave. Similarly, in case of resonant cusp waves the MHD arrives at a position where it behaves as a slow wave for perpendicular propagation. Resonant absorption for MHD waves with frequencies in the Alfvén / slow continuum is controlled by the coupling functions C_A and C_S. Analysis of the motions associated with the resonant Alfvén /slow waves shows that the resonant waves are characterized by strong shear in the perpendicular/parallel component of displacement with large values of the parallel/perpendicular component of vorticity. This strong shear causes violent KH-instabilities that accelerate the damping of the MHD waves and facilitate heating of plasma.

AUTHOR CONTRIBUTIONS

All authors listed have made a substantial, direct and intellectual contribution to the work, and approved it for publication. The three authors contributed in equal parts to this paper.

FUNDING

IA was supported by the Spanish Ministry of Economy and Competitiveness (MINECO) through projects AYA2014-55456-P (Bayesian Analysis of the Solar Corona) and AYA2014-60476-P (Solar Magnetometry in the Era of Large Solar Telescopes) and FEDER funds. TV was supported by the GOA-2015-014 (KU Leuven) and the European Research Council (ERC) under the European Union's Horizon 2020 research and innovation programme (grant agreement No. 724326).

ACKNOWLEDGMENTS

It is a great pleasure for MG to acknowledge the wise advice by J. P. (Hans) Goedbloed to use projections on the directions $\vec{1}_r, \vec{1}_\parallel, \vec{1}_\perp$ and not to try to define a coordinate system based on these directions.

REFERENCES

Antolin, P., Okamoto, T. J., De Pontieu, B., Uitenbroek, H., Van Doorsselaere, T., and Yokoyama, T. (2015). Resonant absorption of transverse oscillations and associated heating in a solar prominence. II. Numerical aspects. *Astrophys. J.* 809:72. doi: 10.1088/0004-637X/809/1/72

Antolin, P., Schmit, D., Pereira, T. M. D., De Pontieu, B., and De Moortel, I. (2018). Transverse wave induced Kelvin-Helmholtz rolls in spicules. *Astrophys. J.* 856:44. doi: 10.3847/1538-4357/aab34f

Antolin, P., Yokoyama, T., and Van Doorsselaere, T. (2014). Fine strand-like structure in the solar corona from magnetohydrodynamic transverse oscillations. *Astrophys. J. Lett.* 787:L22. doi: 10.1088/2041-8205/787/2/L22

Appert, K., Gruber, R., and Vaclavic, J. (1974). Continuous spectra of a cylindrical magnetohydrodynamic equilibrium. *Phys. Fluids* 17:1471. doi: 10.1063/1.1694918

Arregui, I. (2015). Wave heating of the solar atmosphere. *R. Soc. Lond. Philos. Trans. Ser. A* 373:20140261. doi: 10.1098/rsta.2014.0261

Arregui, I., Andries, J., Van Doorsselaere, T., Goossens, M., and Poedts, S. (2007). MHD coronal seismology using the period and damping of resonantly damped quasi-mode kink oscillations. *Astron. Astrophys.* 463, 333–338. doi: 10.1051/0004-6361:20065863

Arregui, I., Terradas, J., Oliver, R., and Ballester, J. (2008). Damping of fast magnetohydrodynamic oscillations in quiescent filament threads. *Astrophys. J.* 682, L141–L144. doi: 10.1086/591081

Chen, L., and Hasegawa, A. (1974). Plasma heating by spatial resonance of Alfven wave. *Phys. Fluids* 17, 1399–1403. doi: 10.1063/1.1694904

De Groof, A., and Goossens, M. (2000). Randomly driven fast waves in coronal loops. II. With coupling to Alfvén waves. *Astron. Astrophys.* 356, 724–734.

De Groof, A., and Goossens, M. (2002). Fast and Alfvén waves driven by azimuthal footpoint motions. II. Random driver. *Astron. Astrophys.* 386:691. doi: 10.1051/0004-6361:20020204

De Groof, A., Paes, K., and Goossens, M. (2002). Fast and Alfvén waves driven by azimuthal footpoint motions. I. Periodic driver. *Astron. Astrophys.* 386:681. doi: 10.1051/0004-6361:20020203

Giagkiozis, I., Goossens, M., Verth, G., Fedun, V., and Van Doorsselaere, T. (2016). Resonant absorption of axisymmetric modes in twisted magnetic flux tubes. *Astrophys. J.* 823:71. doi: 10.3847/0004-637X/823/2/71

Goedbloed, J. P. (1975). Spectrum of ideal magnetohydrodynamics of axisymmetric toroidal systems. *Phys. Fluids* 18, 1258–1268. doi: 10.1063/1.861012

Goedbloed, J. P. (1983). *Lecture Notes on Ideal Magnetohydrodynamics*. Rijnhuizen: FOM-Institut voor Plasmafysica, 83–145.

Goedbloed, J. P., Keppens, R., and Poedts, S. (2010). *Advanced Magnetohydrodynamics*. Cambridge, UK: Cambridge University Press.

Goedbloed, J. P. H., and Poedts, S. (2004). *Principles of Magnetohydrodynamics*. Cambridge, UK: Cambridge University Press.

Goossens, M. (2003). *An Introduction to Plasma Astrophysics and Magnetohydrodynamics*. Vol. 294 of Astrophysics and Space Science Library. Dordrecht: Kluwer Academic Publishers.

Goossens, M. (2008). "Seismology of kink oscillations in coronal loops: two decades of resonant damping," in *IAU Symposium, Vol. 247*, eds R. Erdélyi and C. A. Mendoza-Briceño (Cambridge, UK), 228–242.

Goossens, M., Andries, J., and Aschwanden, M. J. (2002a). Coronal loop oscillations. An interpretation in terms of resonant absorption of quasi-mode kink oscillations. *Astron. Astrophys.* 394:L39. doi: 10.1051/0004-6361:20021378

Goossens, M., Andries, J., Soler, R., Van Doorsselaere, T., Arregui, I., and Terradas, J. (2012). Surface alfvén waves in solar flux tubes. *Astrophys. J.* 753:111. doi: 10.1088/0004-637X/753/2/111

Goossens, M., Arregui, I., Ballester, J. L., and Wang, T. J. (2008). Analytic approximate seismology of transversely oscillating coronal loops. *Astron. Astrophys.* 484, 851–857. doi: 10.1051/0004-6361:200809728

Goossens, M., de Groof, A., and Andries, J. (2002b). "Waves and oscillations in magnetic fields," in *SOLMAG 2002, Proceedings of the Magnetic Coupling of the Solar Atmosphere Euroconference, Vol. 505 of ESA Special Publication*, ed H. Sawaya-Lacoste (Noordwijk), 137–144.

Goossens, M., Erdélyi, R., and Ruderman, M. S. (2011). Resonant MHD Waves in the Solar Atmosphere. *Space Sci. Rev.* 158, 289–338. doi: 10.1007/s11214-010-9702-7

Goossens, M., Hollweg, J. V., and Sakurai, T. (1992). Resonant behaviour of MHD waves on magnetic flux tubes. III - Effect of equilibrium flow. *Solar Phys.* 138, 233–255. doi: 10.1007/BF00151914

Goossens, M., and Poedts, S. (1992). Linear resistive magnetohydrodynamic computations of resonant absorption of acoustic oscillations in sunspots. *Astrophys. J.* 384, 348–360. doi: 10.1086/170878

Goossens, M., and Ruderman, M. S. (1995). Conservation laws and connection formulae for resonant MHD waves. *Phys. Scripta Vol. T* 60, 171–184. doi: 10.1088/0031-8949/1995/T60/021

Goossens, M., Ruderman, M. S., and Hollweg, J. V. (1995). Dissipative MHD solutions for resonant Alfven waves in 1-dimensional magnetic flux tubes. *Solar Phys.* 157:75. doi: 10.1007/BF00680610

Goossens, M., Soler, R., Terradas, J., Van Doorsselaere, T., and Verth, G. (2014). The transverse and rotational motions of magnetohydrodynamic kink waves in the solar atmosphere. *Astrophys. J.* 788:9. doi: 10.1088/0004-637X/788/1/9

Goossens, M., Terradas, J., Andries, J., Arregui, I., and Ballester, J. L. (2009). On the nature of kink MHD waves in magnetic flux tubes. *Astron. Astrophys.* 503, 213–223. doi: 10.1051/0004-6361/200912399

Hasegawa, A., and Uberoi, C. (1982). *The Alfvén Wave*. Advances in Fusion Science and Engineering DOE Critical Review Series. Office of Energy Research; US Department of Energy.

Mestel, L., and Weiss, N. O., (eds.). (1974). *Magnetohydrodynamics*. Swiss Society Astronomy and Astrophysics Fourth Advanced Course, Geneva Observatory.

Okamoto, T. J., Antolin, P., De Pontieu, B., Uitenbroek, H., Van Doorsselaere, T., and Yokoyama, T. (2015). Resonant absorption of transverse oscillations and associated heating in a solar prominence. I. Observational aspects. *Astrophys. J.* 809:71. doi: 10.1088/0004-637X/809/1/71

Pascoe, D. J., Wright, A. N., and De Moortel, I. (2010). Coupled Alfvén and kink oscillations in coronal loops. *Astrophys. J.* 711, 990–996. doi: 10.1088/0004-637X/711/2/990

Pascoe, D. J., Wright, A. N., and De Moortel, I. (2011). Propagating coupled Alfvén and kink oscillations in an arbitrary inhomogeneous corona. *Astrophys. J.* 731:73. doi: 10.1088/0004-637X/731/1/73

Poedts, S., Goossens, M., and Kerner, W. (1989). Numerical simulation of coronal heating by resonant absorption of Alfven waves. *Solar Phys.* 123, 83–115. doi: 10.1007/BF00150014

Poedts, S., Goossens, M., and Kerner, W. (1990). On the efficiency of coronal loop heating by resonant absorption. *Astrophys. J.* 360, 279–287. doi: 10.1086/169118

Ruderman, M. S., and Roberts, B. (2002). The damping of coronal loop oscillations. *Astrophys. J.* 577, 475–486. doi: 10.1086/342130

Sakurai, T., Goossens, M., and Hollweg, J. V. (1991a). Resonant behaviour of magnetohydrodynamic waves on magnetic flux tubes II. Absorption of sound waves by sunspots. *Solar Phys.* 133, 247–262. doi: 10.1007/BF00149889

Sakurai, T., Goossens, M., and Hollweg, J. V. (1991b). Resonant behaviour of MHD waves on magnetic flux tubes. I - Connection formulae at the resonant surfaces. *Solar Phys.* 133, 227–245. doi: 10.1007/BF00149888

Soler, R., Goossens, M., Terradas, J., and Oliver, R. (2013). The behavior of transverse waves in nonuniform solar flux tubes. I. Comparison of ideal and resistive results. *Astrophys. J.* 777:158. doi: 10.1088/0004-637X/777/2/158

Spruit, H. C. (1982). Propagation speeds and acoustic damping of waves in magnetic flux tubes. *Solar Phys.* 75, 3–17. doi: 10.1007/BF00153456

Terradas, J., Andries, J., Goossens, M., Arregui, I., Oliver, R., and Ballester, J. L. (2008). Nonlinear instability of kink oscillations due to shear motions. *Astrophys. J. Lett.* 687, L115–L118. doi: 10.1086/593203

Terradas, J., and Arregui, I. (2018). Temporal and spatial scales for coronal heating by Alfvén wave dissipation in transverse loop oscillations. *Res. Notes Am. Astron. Soc.* 2:196. doi: 10.3847/2515-5172/aaeb26

Terradas, J., Oliver, R., and Ballester, J. L. (2006). Damped coronal loop oscillations: time-dependent results. *Astrophys. J.* 642, 533–540. doi: 10.1086/500730

Thompson, W. B. (1964). "Chapter V: Magnetohydrodynamics II," in *An Introduction to Plasma Physics, 2nd Edn.* (Oxford: Pergamon Press Ltd.), 65–96.

Tirry, W. J., and Berghmans, D. (1997). Wave heating of coronal loops driven by azimuthally polarised footpoint motions. II. The time-dependent behaviour in ideal MHD. *Astron. Astrophys.* 325:329.

Tirry, W. J., Berghmans, D., and Goossens, M. (1997). Temporal evolution of resonant absorption in coronal loops. Excitation by footpoint motions normal to the magnetic surfaces. *Astron. Astrophys.* 322, 329–339.

Tirry, W. J., and Goossens, M. (1996). Quasi-modes as dissipative magnetohydrodynamic eigenmodes: results for one-dimensional equilibrium states. *Astrophys. J.* 471:501. doi: 10.1086/177986

Van Doorsselaere, T., Andries, J., Poedts, S., and Goossens, M. (2004). Damping of coronal loop oscillations: calculation of resonantly damped kink oscillations of one-dimensional nonuniform loops. *Astrophys. J.* 606, 1223–1232. doi: 10.1086/383191

Walker, A. (ed.). (2004). *Magnetohydrodynamic Waves in Geospace*. Magnetohydrodynamic Waves in Geospace. Series: Series in Plasma Physics. Bristol, PA: Taylor and Francis.

Yu, D. J., Van Doorsselaere, T., and Goossens, M. (2017a). Resonant absorption of surface sausage and surface kink modes under photospheric conditions. *Astrophys. J.* 850:44. doi: 10.3847/1538-4357/aa9223

Yu, D. J., Van Doorsselaere, T., and Goossens, M. (2017b). Resonant absorption of the slow sausage wave in the slow continuum. *Astron. Astrophys.* 602:A108. doi: 10.1051/0004-6361/201630355

Conflict of Interest Statement: The authors declare that the research was conducted in the absence of any commercial or financial relationships that could be construed as a potential conflict of interest.

frontiers
in Astronomy and Space Sciences

ORIGINAL RESEARCH
published: 12 April 2019
doi: 10.3389/fspas.2019.00022

Coronal Loop Seismology Using Standing Kink Oscillations With a Lookup Table

David J. Pascoe[1]*, **Alan W. Hood**[2] **and Tom Van Doorsselaere**[1]

[1] Department of Mathematics, Centre for Mathematical Plasma Astrophysics, KU Leuven, Leuven, Belgium, [2] School of Mathematics and Statistics, University of St Andrews, St Andrews, United Kingdom

The transverse structure of coronal loops plays a key role in the physics but the small transverse scales can be difficult to observe directly. For wider loops the density profile may be estimated by forward modeling of the transverse intensity profile. The transverse density profile may also be estimated seismologically using kink oscillations in coronal loops. The strong damping of kink oscillations is attributed to resonant absorption and the damping profile contains information about the transverse structure of the loop. However, the analytical descriptions for damping by resonant absorption presently only describe the behavior for thin inhomogeneous layers. Previous numerical studies have demonstrated that this thin boundary approximation produces poor estimates of the damping behavior in loops with wider inhomogeneous layers. Both the seismological and forward modeling approaches suggest loops have a range of layer widths and so there is a need for a description of the damping behavior that accurately describes such loops. We perform a parametric study of the damping of standing kink oscillations by resonant absorption for a wide range of inhomogeneous layer widths and density contrast ratios, with a focus on the values most relevant to observational cases. We describe the damping profile produced by our numerical simulations without prior assumption of its shape and compile our results into a lookup table which may be used to produce accurate seismological estimates for kink oscillation observations.

Keywords: magnetohydrodynamics (MHD), Sun: corona, Sun: magnetic fields, Sun: oscillations, waves and instabilities

Edited by:
Valery M. Nakariakov,
University of Warwick,
United Kingdom

Reviewed by:
Jiajia Liu,
University of Sheffield,
United Kingdom
Sergey Anfinogentov,
Institute of Solar-Terrestrial Physics
(RAS), Russia

***Correspondence:**
David J. Pascoe
david.pascoe@kuleuven.be

Specialty section:
This article was submitted to
Stellar and Solar Physics,
a section of the journal
Frontiers in Astronomy and Space
Sciences

Received: *18 January 2019*
Accepted: *20 March 2019*
Published: *12 April 2019*

Citation:
Pascoe DJ, Hood AW and
Van Doorsselaere T (2019) Coronal
Loop Seismology Using Standing Kink
Oscillations With a Lookup Table.
Front. Astron. Space Sci. 6:22.
doi: 10.3389/fspas.2019.00022

1. INTRODUCTION

Coronal loops are modeled as density structures in the solar atmosphere which act as waveguides for several types of magnetohydrodynamic (MHD) modes. One of the most readily detectable are standing kink oscillations, which causes periodic transverse perturbations of the loop axis. These oscillations were first detected using the Transition Region And Coronal Explorer (TRACE; Aschwanden et al., 1999, 2002; Nakariakov et al., 1999). The number of observations has greatly increased since the launch of the Atmospheric Imaging Assembly (AIA; Lemen et al., 2012) onboard the Solar Dynamics Observatory (SDO). Catalogs of observations have been produced by Zimovets and Nakariakov (2015) and Goddard et al. (2016). Kink oscillations attract a lot of attention due to their potential for seismological studies of the coronal plasma (e.g., reviews by De Moortel and Nakariakov, 2012; Stepanov et al., 2012; Pascoe, 2014; De Moortel et al., 2016), in particular to estimate the strength of the coronal magnetic field (e.g., Nakariakov et al., 1999; Nakariakov and Ofman, 2001; Van Doorsselaere et al., 2007; White and Verwichte, 2012; Pascoe et al., 2016; Sarkar et al., 2016).

Kink oscillations are observed to be strongly damped, only having a detectable amplitude for a few cycles, which is attributed to resonant absorption (e.g., Chen and Hasegawa, 1974). Coronal loops are modeled as having a higher density than the surrounding plasma, and for resonant absorption to take place only requires that the transition between the higher and lower density plasma is smooth. Inside this inhomogeneous layer, wave energy is transferred from kink to Alfvén modes where the local Alfvén speed matches the kink speed C_k. The timescale of this process is comparable to the period of oscillation (e.g., Hollweg and Yang, 1988; Goossens et al., 1992, 2002; Ruderman and Roberts, 2002).

Resonant absorption is a robust mechanism which occurs even in loops which are not cylindrically symmetric (Terradas et al., 2008b; Pascoe et al., 2011). Furthermore, numerical studies demonstrate that the Kelvin-Helmholtz instability (e.g., Terradas et al., 2008a; Antolin et al., 2015; Okamoto et al., 2015; Magyar and Van Doorsselaere, 2016; Hillier et al., 2019) is most efficient in loops with thin inhomogeneous layers. This instability leads to a mixing of plasma and effective widening of the inhomogeneous layer (e.g., Goddard et al., 2018; Karampelas and Van Doorsselaere, 2018) in addition to increased heating due to phase mixing (e.g., Heyvaerts and Priest, 1983; Karampelas et al., 2017; Pagano et al., 2018; Guo et al., 2019) which can account for observations of broad differential emission measures in coronal loops (Van Doorsselaere et al., 2018).

The transverse density profile can be described by two dimensionless parameters; the density contrast ratio being the ratio of the density at the center of the loop to the density far from it $\zeta = \rho_0/\rho_e$, and the width of the inhomogeneous layer normalized to the minor loop radius $\epsilon = l/R$. The damping rate due to resonant absorption depends on both of these parameters. For this reason the problem is underdetermined when trying to infer ζ and ϵ from the (exponential) damping time alone and some additional information is required (e.g., Goossens et al., 2008; Arregui and Asensio Ramos, 2014; Arregui and Goossens, 2019). Pascoe et al. (2013) produced a more accurate description of the damping profile due to resonant absorption, which includes the initial Gaussian damping regime of kink oscillations in addition to the later exponential damping regime. This damping profile is characterized by two damping times and so allows both ζ and ϵ to be estimated. This method was first applied by Pascoe et al. (2016) and later extended by Pascoe et al. (2017a,c) to include additional effects such as a time-dependent period of oscillation, the presence of additional parallel harmonics, and the use of Bayesian analysis (e.g., Arregui et al., 2013; Arregui, 2018) to improve the estimation of uncertainties. This seismological method requires both the Gaussian and exponential damping regimes to be accurately detected in the data and so depends on the oscillation data having a sufficiently high quality.

Another method for estimating ϵ is by forward modeling the appearance of the density profile for direct comparison with the transverse EUV intensity profile of the loop (Goddard et al., 2017; Pascoe et al., 2017b). It is possible to apply both of these methods simultaneously to observational data. This was recently demonstrated by Pascoe et al. (2018) for a loop for which the oscillation data alone was too noisy to allow strong constraint of ζ and ϵ. However, the spatial information from the intensity profile produced a strong constraint on ϵ, such that the oscillation data was only required to infer ζ when both methods were applied simultaneously. On the other hand, the value of $\epsilon \approx 0.9$ for this observation is significantly outside the validity of the thin boundary (TB) approximation. To correct for this effect, Pascoe et al. (2018) performed a narrow parametric study using the TB estimate as a starting point. The result of this study was a change in the estimated value of ζ from the TB value of 2.3 to a value of 2.8 based on numerical simulations for $\epsilon = 0.9$. This case demonstrates the need for a seismological method that can account for the behavior of kink oscillations in loops with wide inhomogeneous layers without the need for separate studies and corrections applied afterwards. The use of a self-consistent seismological method is particularly important for future development of techniques for data analysis where multiple observational signatures are forward modeled and a systematic error arising from the TB approximation would have a deleterious influence on other observables. For example, the EUV intensity is $I \propto \rho^2$ and so a change in inferred density contrast from 2.3 to 2.8 in the example above corresponds to an intensity change by a factor of approximately 1.5.

In this paper we study the behavior of kink oscillations of coronal loops for various transverse density profiles. Our aim is to provide a simple method of estimating the damping profile for a chosen profile which may be used for seismological investigations. The damping profiles for resonant absorption used in previous studies and this one are described in section 2. The results of our parametric study and the generation of a lookup table (LUT) are presented in section 3. In section 4 we present examples of the application of our method to synthetic test cases and observational data. Conclusions are presented in section 5.

2. DAMPING PROFILE FOR KINK OSCILLATIONS

Initial applications of resonant absorption to explain the strong damping of kink oscillations (Goossens et al., 1992, 2002; Ruderman and Roberts, 2002) considered only the asymptotic state of the system. The damping profile was an exponential of the form

$$\mathcal{D}(t) = \exp\left(-\frac{t}{\tau_d}\right), \tag{1}$$

$$\tau_d = \frac{4P}{\pi^2 \kappa \epsilon}, \tag{2}$$

where τ_d is the exponential damping time, P is the period of oscillation, $\kappa = (\rho_0 - \rho_e)/(\rho_0 + \rho_e)$ and the factor $4/\pi^2$ corresponds to a linear transition between ρ_0 and ρ_e. In this paper we consider a linear profile for the density in the inhomogeneous layer since it is the simplest smooth profile, can describe the widest range of possible structures, and is the only profile for which the analytical solution for all times is presently known (see discussion section 6.2 of Pascoe et al., 2018).

Numerical simulations by Pascoe et al. (2012) demonstrated that the damping profile of strongly damped propagating kink oscillations is more accurately described by a Gaussian damping profile rather than an exponential one. The existence of these two regimes was reconciled by the analytical description derived by Hood et al. (2013) which described the damping profile for all times and demonstrates that Gaussian and exponential profile can be obtained in the limits of small and large time, respectively. The derivation by Hood et al. (2013) was performed for propagating kink waves with the damping rate expressed in terms of damping length scales but we may consider the case of standing kink waves with a damping time using the long wavelength limit $\lambda = C_{\mathrm{k}}P$, giving

$$\mathcal{D}\left(t\right) = \exp\left(-\frac{t^2}{2\tau_{\mathrm{g}}^2}\right), \tag{3}$$

$$\tau_{\mathrm{g}} = \frac{2P}{\pi\kappa\epsilon^{1/2}}. \tag{4}$$

We note that the relationship between damping length scales (propagating waves) and timescales (standing waves) has been demonstrated explicitly for the exponential regime (e.g., comparing the derivations of Goossens et al., 2002; Terradas et al., 2010) but presently not the Gaussian regime. Nonetheless we demonstrate the applicability of this relationship (proposed by Pascoe et al., 2010) by comparison with our numerical simulations. The applicability of this relationship has also previously been demonstrated in numerical simulations by Ruderman and Terradas (2013) and Magyar and Van Doorsselaere (2016).

Pascoe et al. (2013) proposed a general damping profile (GDP) that combined both of these damping regimes into a single approximation. This is described in terms of a switch from the Gaussian damping profile that applies at the start of the oscillation to the exponential profile which applies later.

$$\mathcal{D}\left(t\right) = \begin{cases} \exp\left(-\frac{t^2}{2\tau_{\mathrm{g}}^2}\right) & t \leq t_{\mathrm{s}} \\ A_{\mathrm{s}}\exp\left(-\frac{t-t_{\mathrm{s}}}{\tau_{\mathrm{d}}}\right) & t > t_{\mathrm{s}} \end{cases}, \tag{5}$$

$$t_{\mathrm{s}} = \frac{P}{\kappa}, \tag{6}$$

where the switch from the Gaussian to exponential damping regime occurs at t_{s} and $A_{\mathrm{s}} = \mathcal{D}\left(t = t_{\mathrm{s}}\right)$.

The above damping profiles are also based on the thin tube approximation. In this limit the period of the fundamental standing kink mode is

$$P_{\mathrm{k}} = 2L/C_{\mathrm{k}} \tag{7}$$

where L is the loop length, and the kink speed for a low-β plasma (uniform magnetic field) is

$$C_{\mathrm{k}} = C_{\mathrm{A0}}\sqrt{\frac{2\zeta}{\zeta+1}}, \tag{8}$$

where C_{A0} is the internal Alfvén speed. The thin tube thin boundary (TTTB) approximation for the period of oscillation of kink modes therefore depends on ζ but not ϵ (Goossens et al., 2008). However, the parametric studies by Van Doorsselaere et al. (2004) and Soler et al. (2014) find that P_{k} does depend on ϵ outside of the applicability of the TB approximation.

To illustrate the different damping profiles, **Figure 1** shows the results of our numerical simulations (described in section 3) for three values of ϵ with $\zeta = 2$. For this value of density contrast the GDP suggests a switch from the Gaussian to exponential damping regime at $t = 3P$. For kink oscillations in low density contrast loops such as these, the Gaussian damping profile (blue curves) provides a much better description than the exponential damping profile (red curves), and the general damping profile (green curves) further improves the description for later times. As expected, all three analytical profiles become poorer as ϵ increases and the TB approximation becomes less appropriate.

In this paper we wish to characterize the damping behavior of kink oscillations as accurately as possible, and without prior assumption of the form of the damping profile. The plus symbols in **Figure 1** represent the amplitudes A_i which we use to characterize the oscillation. These amplitudes are defined at every half cycle of the oscillation. The LUT damping profile (dashed lines) is constructed from these amplitudes by spline interpolation. The dashed lines indicate that this method allows us to accurately describe the damping of the kink oscillation, albeit at a cost of requiring more information. The exponential and Gaussian damping profiles can each be characterized by a single parameter, i.e., the damping time τ_{d} or τ_{g}. The GDP combines both the Gaussian and exponential damping regimes and so is characterized by both these damping times (with the switch time given in terms of these two parameters in Equation 6). For the six cycles indicated in **Figure 1** our interpolation method uses 13 parameters, or more generally $2n+1$ parameters for n cycles. On the other hand, this number is still sufficiently small that the results of hundreds of numerical simulations can be compiled into a lookup table of minimal size.

For each of the three simulations in **Figure 1**, and the additional simulations presented in section 3, the amplitudes A_i used to describe the LUT damping profile were found by a least-squares fit to the data using MPFIT (Markwardt, 2009). Simulation data covered at least six cycles of the oscillation, with a greater number for simulations with smaller values of ζ or ϵ for which the damping is weaker and so there are a greater number of cycles at an observable amplitude. This is also intended to ensure that the exponential damping regime is present in the data, which occurs later for smaller ζ. This allows the damping profile to be extrapolated beyond the number of simulated cycles using an exponential profile with the last measured damping time. We require that the LUT damping profile function is able

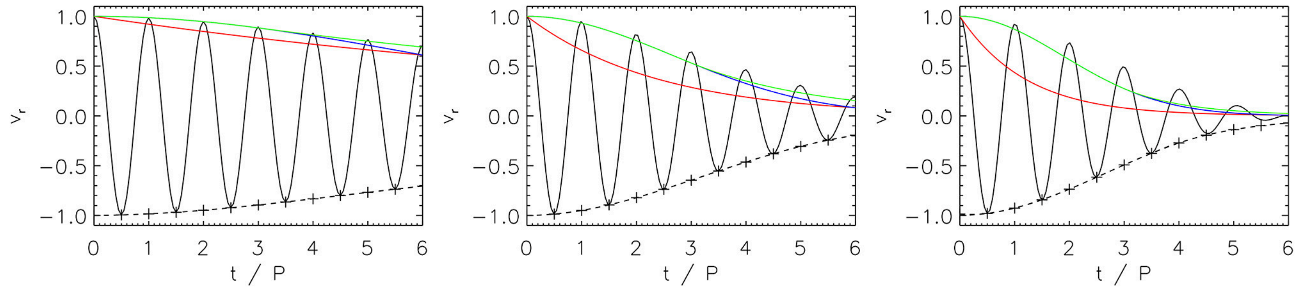

FIGURE 1 | Comparison of kink oscillations calculated by numerical simulations (solid lines) with the analytical damping profiles (colored lines). The red, blue, and green lines correspond to the exponential, Gaussian, and general damping profiles, respectively. The plus symbols represent the amplitudes used to characterize the oscillation in our lookup table (LUT). The LUT damping profiles (dashed lines) are constructed from these amplitudes by spline interpolation. The **left**, **middle**, and **right** panels show the results for $\epsilon = 0.1$, 0.5, and 1.0, with $\zeta = 2$ for all cases.

to return results for arbitrary values of time in order for it to appropriately handle requests from the user or from a fitting routine transparently i.e., without needing to take the details of individual simulations into account.

3. PARAMETRIC STUDY

In this section we study the behavior of kink oscillations in coronal loops for various combinations of ζ and ϵ. Soler et al. (2014) and Van Doorsselaere et al. (2004) performed similar numerical studies investigating the damping time for the exponential regime. These studies demonstrated that the thin boundary approximation produces poor estimates of the damping behavior in loops with wider inhomogeneous layers.

As in Soler et al. (2014), we consider $L/R = 100$ which is typical for observations of standing kink oscillations. Weak dependence of the damping on the longitudinal wavenumber k_z has been demonstrated by Van Doorsselaere et al. (2004). Numerical simulations were performed using a Lax-Wendroff code to solve the linear MHD equations in cylindrical coordinates (r, θ, z) for $m = 1$ symmetry corresponding to kink oscillations (and the Alfvén waves generated by resonant absorption). The magnetic field is constant and aligned with the z-direction. This code was previously used in Pascoe et al. (2012, 2013, 2015) and Hood et al. (2013) to study the spatial damping of propagating kink waves and here is applied to the case of the temporal damping of standing kink waves by appropriate choice of boundary and initial conditions. The boundary conditions are line-tied to simulate the loop footpoints being fixed in the photosphere, while the boundary in the r-direction is placed sufficiently far away to not affect the results. The fundamental longitudinal harmonic of the standing kink mode is excited by a perturbation to the radial and azimuthal velocities of the form

$$\mathbf{v}\,(r,\theta,z) = (v_r, v_\theta, v_z) = (\xi_r \cos\theta, \xi_\theta \sin\theta, 0)\sin(\pi z/L), \quad (9)$$

$$\xi_r\,(r) = \begin{cases} 1 & r \le R \\ R^2/r^2 & r > R \end{cases}, \quad (10)$$

$$\xi_\theta\,(r) = \begin{cases} -1 & r \le R \\ R^2/r^2 & r > R \end{cases}. \quad (11)$$

In the following simulations, the numerical domain covers $r = [0, 10R]$ and $z = [0, 100R]$, with a resolution of $1,000 \times 1,000$ grid points. Each of our 300+ simulations took approximately 1 h to run using 80 × 2.8 GHz processor cores. We study the standing mode by considering the variation in the amplitude of the transverse velocity measured at the loop apex $z = L/2$.

Figure 2 shows the simulations performed in our parametric study which were used to generate the first version of our lookup table. The solid, dashed, and dotted lines correspond to the damping rates shown in the right panel. These damping profiles are based on the TB approximation for the Gaussian damping profile and so will not accurately describe the behavior for large ϵ but serve as an indication of the range of parameters we are interested in considering with respect to observational studies. The curves demonstrate that we are not equally interested in all regions of the ζ-ϵ parameter space. Large amplitude standing kink oscillations are typically observed for fewer than 6 cycles (e.g., Goddard and Nakariakov, 2016) and so we are mainly interested in parameters which produce this level of damping. The dotted, solid, and dashed lines correspond to $\tau_g/P = 1$, 2, and 5, respectively, and indicate the parameters we expect to be relevant to observations. For large values of both ζ and ϵ, kink oscillations would be very strongly damped and hence unlikely to be reliably detected. The shorter time series available would also generally limit the seismological information that could be obtained. Unlike ϵ which has the defined upper limit of 2, there is no upper limit for ζ. However, the damping rate is asymptotic in this limit and so we can consider a reasonable upper limit, which is taken to be 7 in this study but may be extended in the future (e.g., high contrast filament threads considered by Arregui et al., 2008). For small values of both ζ and ϵ the oscillations would be weakly damped. Such oscillations are not typically observed, although we are still interested in the behavior for small values of ϵ with regard to checking convergence of our results to the analytical profiles based on the TB approximation.

The distribution of the simulations we have performed reflects these areas of interest. When compiling the results of these simulations into a lookup table, it is therefore not convenient to use a 2D array to describe the ζ-ϵ plane. Instead, the results are considered as a list of scattered positions in the parameter

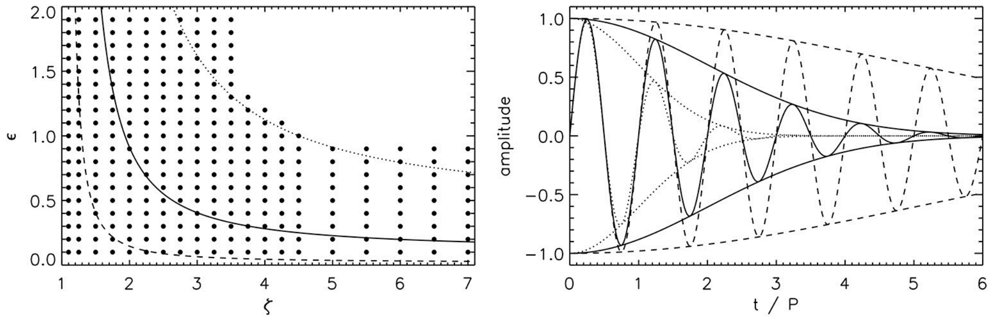

FIGURE 2 | The black circles denote the 300 numerical simulations that comprise version 1.0 of our LUT. The solid, dashed, and dotted lines correspond to the damping rates shown in the right panel. These damping profiles are based on the TB approximation for the Gaussian damping profile but serve as an indication of the range of parameters we are interested in considering with respect to observational studies.

space using the IDL routine GRIDDATA which can be used to interpolate our simulation results to return the damping profile for an arbitrary value of ζ and ϵ. Additional simulations were performed for testing purposes, including generating synthetic observational data used in section 4. These additional simulations are not included version 1.0 LUT but may be in future applications of the LUT to actual observational data. The use of a LUT and interpolation methods for scattered data allows the method to be improved over time by incorporating additional results as they are obtained. Other examples of a LUT strategy for solar applications include the CHIANTI emission database (Del Zanna et al., 2015) used as part of EUV forward modeling codes such as FoMo (Van Doorsselaere et al., 2016), and the CAISAR code for inversions of solar Ca II spectra (Beck et al., 2015).

The LUT and the corresponding IDL code are available at https://github.com/djpascoe/kinkLUT. The routine requires as input the values of ϵ, ζ, and the normalized times $t_n = t/P$ at which the damping profile is desired. The value of each amplitude A_i is determined by 2D interpolation of the simulation results using the IDL routine GRIDDATA. (In this paper we use the linear method, chosen as the simplest method with fewest assumptions, for which requested grid points are linearly interpolated from triangles formed by Delaunay triangulation. These triangles were constructed with the TRIANGULATE routine and are included in the LUT save file). The damping profile is then returned by spline interpolation of these amplitudes A_i for the user-requested times t_n. This procedure can be used within a forward modeling function used for comparing a model with data. For example, a simple model for an oscillation with a single harmonic and no background trend, as considered in this paper, is

$$y(t) = A_0 \sin\left(\frac{2\pi t}{P} + \phi\right) \mathcal{D}_{LUT}(t_n, \epsilon, \zeta), \tag{12}$$

where A_0 is the initial amplitude of a sinusoidal oscillation with period P and phase shift ϕ, and the damping profile $\mathcal{D}_{LUT}$ is based on our lookup table. We demonstrate the results of such a method in section 4.

3.1. Dependence of Period of Oscillation and Damping Rate on Transverse Density Profile

Here we compare the results of our parametric study with the analytical profiles discussed in section 2 and previous numerical studies.

Figure 3 shows the dependence of the kink mode behavior on ζ. For an exponential or Gaussian damping profile it is convenient to characterize the damping with the damping time (or length scale for propagating waves). However, in this study we make no assumption about the shape of the damping profile and so we consider the damping which has occurred after a certain time, or a certain number of oscillation cycles since the period of oscillation also depends on ζ. The colored lines correspond to the theoretical damping rates based on the TB approximation and an exponential (red), Gaussian (blue), or general (green) damping profile.

The top panels of **Figure 3** demonstrate the case of a thin inhomogeneous layer ($\epsilon = 0.1$) where the TB approximation is appropriate. The top left panel reproduces the known dependence of the shape of the damping profile on ζ. For lower density contrasts the Gaussian profile better describes the damping. The GDP which combines both profiles, with a switch from Gaussian to exponential that depends on ζ, provides a significantly better approximation for all values of ζ. The switch time occurs at $5P$ for $\zeta = 1.5$ and so the general and Gaussian damping profiles are identical for $\zeta \leq 1.5$.

The bottom panels of **Figure 3** demonstrate the case of a finite inhomogeneous layer ($\epsilon = 0.5$) where the TB approximation is less appropriate. The estimated period of oscillation is still reasonable but the damping is being significantly overestimated. The amplitude is taken at the earlier time of $2.5P$ since the damping is stronger for the larger value of ϵ. At this earlier time, the Gaussian damping profile is always a better approximation than the exponential profile for the range of $\zeta \leq 7$ considered. The switch time occurs at $2.5P$ for $\zeta \approx 2.3$, and so it is expected that the Gaussian estimate is better than the exponential estimate for density contrasts lower than this value. However, it also remains a better overall estimate for contrasts not too much above this value due to the exponential estimate being

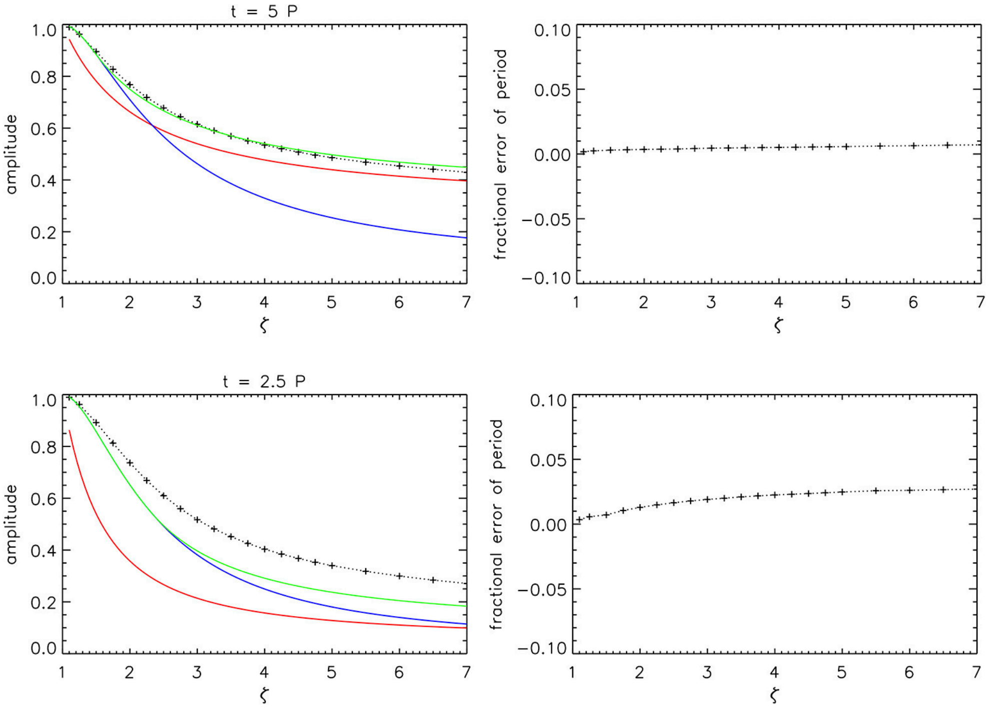

FIGURE 3 | Dependence of the damping of the kink oscillation on the density contrast ratio ζ. The **top** panels show results for $\epsilon = 0.1$ and the **bottom** panels for $\epsilon = 0.5$. The left panels show the kink oscillation amplitude (plus symbols) taken at a fixed time ($t = 5P$ or $2.5P$) The colored lines show the estimates based on the general damping profile (green), Gaussian damping profile (blue), and exponential damping profile (red). The right panels show the variation of the period of oscillation compared with the theoretical value P_{k}.

so poor during the first cycle or so. The Gaussian estimate therefore does not become poorer than the exponential estimate by the time of $2.5P$ considered in the bottom panel of **Figure 3**, whereas it does in the top panel. Whether the Gaussian or exponential estimate is better therefore depends on not only when the switch occurs but also how much data is considered after that switch. The general damping profile provides the best approximation for all parameters and times, but is also inaccurate when there is significant damping due to the limitations of the TB approximation it is based upon.

The right panels of **Figure 3** show the fractional error in the period of oscillation estimated as P_k by Equation (7). The errors are typically very small since the thin tube approximation ($\omega/k_z = C_k$) is appropriate for our simulations with $L/R = 100$. The error increases with ζ due to the stronger dispersion present in higher contrast loops, and is also found to increase with ϵ (see also **Figures 4**, **6**).

Figure 4 shows the dependence of the kink mode behavior on ϵ. The top panels show results for $\zeta = 2$ at $t = 2.5P$, i.e., the behavior at an early time for a low density contrast ratio. For $\zeta = 2$ the switch for Gaussian to exponential occurs at $t = 3P$ and so the Gaussian and general damping profiles are identical before this time, and are a significantly better approximation than the exponential profile. The bottom panels show results for $\zeta = 7$ at $t = 5P$, i.e., having both a sufficiently high density contrast and a sufficiently large number of cycles for the exponential damping profile to always be a better approximation than the Gaussian profile, though the GDP remains an improvement over both.

Figure 5 shows 2D contours for the amplitude of the kink oscillation at $t = 3P$ (top left panel) and the fractional errors of the corresponding estimates based on the TB approximation. The errors tend to zero in the appropriate limit $\epsilon \to 0$, otherwise each approximation underestimates the amplitude. The Gaussian and GDP estimates are also accurate in the limit $\zeta \to 1$ since they describe the initial stage of resonant absorption, whereas the exponential estimates remain poor in this limit when $\epsilon > 0$.

Figure 6 shows the fractional error in the period of oscillation estimated using the TB approximation (Equation 7). The TB approximation underestimates the period of oscillation. The dependence of the error on ζ and ϵ is similar to that found by Soler et al. (2014) (i.e., being proportional to the strength of the damping due to resonant absorption) but the magnitude is smaller, remaining less than 6%. Soler et al. (2014) report an error of up to 45% in their study which considers ζ up to 20, whereas we restrict our attention to the parameter range most relevant to observations (e.g., $\zeta \leq 3.5$ for the largest values of ϵ in **Figure 2**). However, even accounting for this there remains a discrepancy and Soler et al. (2014) find errors greater than 30% for a comparable parameter range.

Figure 7 shows the difference in fractional error using the exponential damping profile alone compared with the GDP based on **Figure 5**. It indicates the GDP analysis is always an

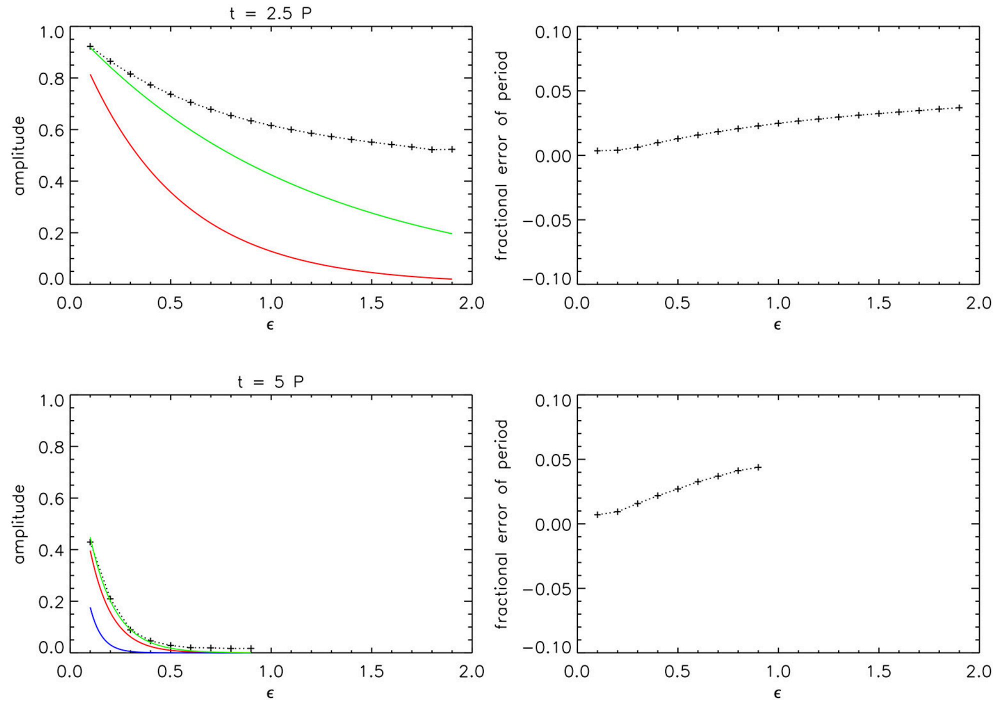

FIGURE 4 | Dependence of the damping of the kink oscillation on the inhomogeneous layer width ϵ. The **top** panels show results for $\zeta = 2$ and the **bottom** panels for $\zeta = 7$. The left panels show the kink oscillation amplitude (plus symbols) taken at a fixed time ($t = 5P$ or $2.5P$) The colored lines show the estimates based on the general damping profile (green), Gaussian damping profile (blue), and exponential damping profile (red). The right panels show the variation of the period of oscillation compared with the theoretical value P_k.

improvement over the exponential profile, and the difference is largest for lower ζ, typically $\sim$ 60% for $\zeta < 2$ and $\sim$ 30% for $\zeta > 2$. The right panel of **Figure 7** shows how the fractional error (averaged over 300 numerical simulations) varies as a function of time for each of the profiles based on the TB approximation. Each of the errors increase in time due to the cumulative effect of overestimating the damping rate, however the GDP remains at all times a significantly better estimate of the kink oscillation amplitude. The GDP (Equation 6) is a simple modification of the exponential damping profile with no additional parameters and so this improved estimate comes at effectively no computational cost. Our LUT method is based on several interpolation routines and so is slower to calculate than the GDP but remains practical.

The larger errors for analysis based on the exponential profile arise because it provides a very poor description for the initial behavior of kink oscillations. Pascoe et al. (2013) demonstrate that the seismological estimate based on the exponential profile is significantly improved by ignoring the first two cycles of the oscillation and only analysing the remaining data. However, this is not a practical solution for detailed analysis of oscillations since it means the initial amplitude cannot be estimated, which is important for nonlinear effects. It would also hinder the potential to detect higher harmonic oscillations which have a shorter period and so typically only exist for the first few cycles of the fundamental mode (e.g., Pascoe et al., 2017a). For example, if the fundamental mode is observable for six cycles then the third harmonic with $P_3 \approx P_1/3$ but the same damping per period would only be detectable during the first two cycles of the fundamental mode.

4. SEISMOLOGICAL APPLICATION

In this section we demonstrate the application of our LUT as a seismological tool to use the observed damping of a kink oscillation to infer information about the transverse density profile of the oscillating loop.

Figure 8 shows the results of a test of our method for a kink oscillation simulated in a loop with $\zeta = 2.15$ and $\epsilon = 0.75$. This data point is not included in version 1.0 of our LUT used in the following analysis. The top panel shows the analyzed oscillation which includes uniformly distributed random noise with a maximum amplitude of 5% of the initial kink oscillation amplitude. The middle and bottom panels show 2D histograms approximating the marginalized posterior probability density function for ζ and ϵ based on 10^5 Markov chain Monte Carlo (MCMC) samples of the GDP and LUT models, respectively (see also Pascoe et al., 2017a, 2018). This data comes from a simulation with an inhomogeneous layer width that is sufficiently large for the TB approximation to produce inaccurate results. The GDP approach overestimates the value of ϵ, and correspondingly underestimates the value of ζ.

The seismological estimates in **Figure 8** demonstrate that it is important to consider the dependence of the damping on ζ

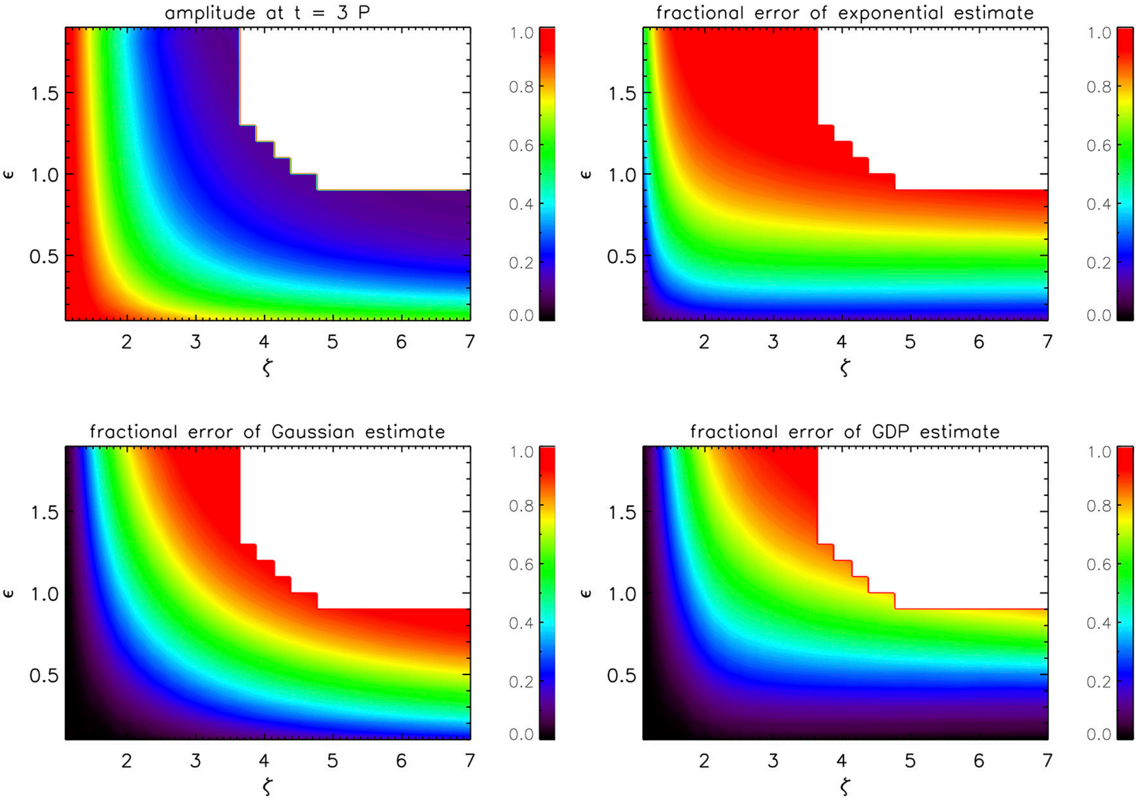

FIGURE 5 | Amplitude of the kink oscillation at $t = 3P$ **(top left)** and the fractional errors of the corresponding estimates based on the TB approximation and an exponential **(top right)**, Gaussian **(bottom left)**, or the general **(bottom right)** damping profiles.

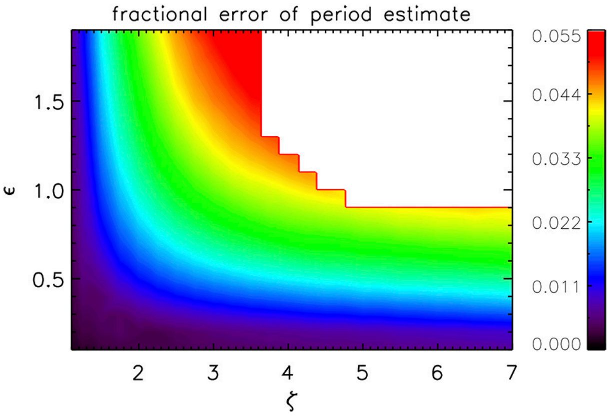

FIGURE 6 | Error in the period of oscillation estimate based on the TB approximation as given by Equation (7).

and ϵ, aside from the quality of the observational data. Due to the asymptotic nature of the inversion curve, the extent to which ζ and ϵ are constrained depends on whether the density contrast is high or low; near the low-ζ asymptote ζ is well-constrained but ϵ is poorly constrained, and vice versa for the high-ζ asymptote. This is demonstrated in **Figure 8** where the GDP inversion underestimates the actual value of $\zeta = 2.15$ and produces very low estimates of ζ. The red bars indicate the 95% credible intervals and show the value of ζ is well-constrained (but excludes the actual value of ζ due to the systematic error from the TB approximation). In comparison, the inversion results using the LUT are less constrained for ζ but the maximum a posteriori probability (MAP) estimate of $\zeta \approx 2.11$ is consistent with the actual value for the synthetic data. The nature of these constraints makes 2D histograms such as those in **Figure 9** the simplest way of representing the available information for the transverse density profile. Quoting confidence intervals alone can be misleading if the asymptotic behavior is not kept in mind. Furthermore, 1D histograms for ζ and ϵ would generally not be well described using a normal distribution (they have been approximated by the exponentially modified Gaussian function by Pascoe et al., 2017a) and so estimates of uncertainties based on assuming this distribution would not be accurate.

Figure 9 shows the results of a test of our method for a loop with a thin boundary layer $\zeta = 3.75$ and $\epsilon = 0.15$ (this data point is again not included in version 1.0 of our LUT). In this limit we see both the GDP and LUT inversions producing good estimates of the actual value of ϵ. The asymptotic behavior means ζ is far less constrained than ϵ, and less constrained for the LUT results since the inferred value of ζ is larger (it is underestimated using the GDP).

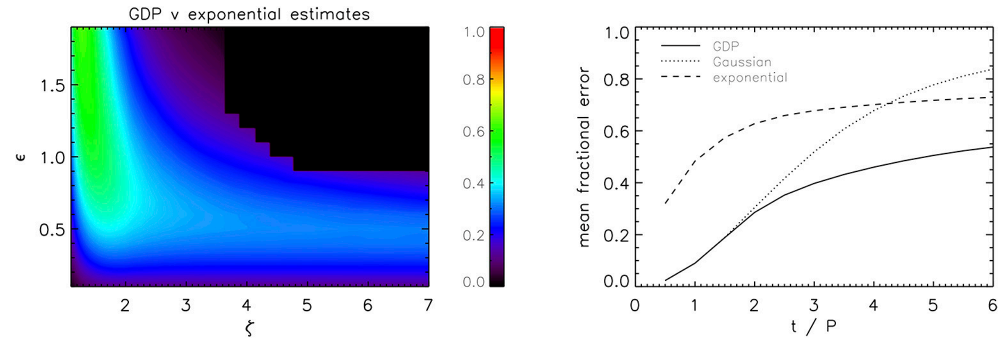

FIGURE 7 | Difference between the fractional error using the exponential damping profile alone compared with the GDP **(left)**, and the mean fractional error as a function of time for each of the three TB profiles **(right)**.

4.1. Comparison With Previous Spatiotemporal Analysis

Pascoe et al. (2018) presented a method for spatiotemporal analysis of coronal loops which used both the transverse EUV intensity profile and the standing kink oscillation to constrain the properties of the coronal loop. In that work the spatial analysis (forward modeling of the transverse EUV profile) provided a value of $\epsilon \approx 0.9$ and so a narrow parametric study for that particular observation was performed to estimate the effect of a thick inhomogeneous layer on the seismological component of their analysis. Here we demonstrate how the results may be reproduced from the much wider parametric study in this paper.

Figure 10 shows the results of applying our method to the oscillation of Leg 1 as previously analyzed. We consider the prior for ϵ with the form of a normal distribution with a mean of 0.9 and standard deviation of 0.1 (e.g., Figure 4 of Pascoe et al., 2018). The seismological analysis of the oscillation then proceeds as in section 4.1 of Pascoe et al. (2018), with results based on 10^6 MCMC samples of a model consisting of a damped sinusoidal oscillation which begins at a start time $t_0 \approx 4$ minutes and having a background trend described by spline interpolation using six reference points across the time series. We consider both the GDP and LUT damping profiles. The top panels in **Figure 10** show the loop position (plus symbols) with the color contour representing the normalized posterior predictive probability density for each damping profile model. The GDP (left panels) results infer a value of $\zeta = 2.1^{+0.4}_{-0.2}$ (based on the MAP value and 95% credible interval) consistent with the previous analysis. The narrow parametric study in section 6.4 of Pascoe et al. (2018) suggested $\zeta \approx 2.8$ as an improved estimate, correcting for the TB approximation used in the GDP. The right panels of **Figure 10** show our analysis using the LUT damping profile, which infers $\zeta = 2.9^{+0.9}_{-0.5}$, consistent with that estimate. The Bayes factor (e.g., Jeffreys, 1961; Kass and Raftery, 1995) for the LUT model compared with the GDP is $K = 1.5$, i.e., too small to distinguish which model is better based on their reproduction of the data alone. This is in contrast to the very strong Bayesian evidence for the GDP compared with an exponential damping profile found in Pascoe et al. (2018). For this data, the shape of the damping profile produced by the LUT is very similar to the shape produced by the GDP (but significantly different to an exponential damping profile), though the inferred values of ζ and ϵ that correspond to that shape differ. Considering that $\epsilon \approx 0.9$ whereas the GDP is based on the TB approximation, the LUT method is more appropriate on the basis of self-consistency. The GDP underestimates the LUT density contrast ratio by approximately 25%, and analysis using an exponential damping profile underestimates ζ by approximately 50%.

The observation considered by Pascoe et al. (2018) was one for which the spatial analysis provided a well-constrained value of ϵ, independent of the seismological analysis. It was therefore possible in that study to consider the correction to the TB approximation in terms of the dependence on ζ alone, requiring only a narrow 1D parametric study for the estimate. The LUT for the 2D parametric study in this paper allows the method in Pascoe et al. (2018) to be extended to a greater number of loops where the spatial information might not be as conclusive on its own but can assist in further constraining the seismologically-inferred parameters.

5. CONCLUSIONS

In this paper we have performed a parametric study for the dependence of the damping of standing kink oscillations by resonant absorption on the density contrast ratio ζ and the width of the inhomogeneous layer ϵ. Previous studies (Van Doorsselaere et al., 2004; Soler et al., 2014) have demonstrated the inaccuracy of the classical analytical description for the damping rate τ_d, which is based on the TB approximation, when applied to loops with large values of ϵ. We have expanded on these studies by developing a description of the damping profile which includes the initial non-exponential regime, and summarized our results into a lookup table which may be used to produce improved estimates of loop parameters.

The method presented in this paper makes analysis simpler in terms of not requiring an additional step to correct for the effect of a wide inhomogeneous layer, as in Pascoe et al. (2018), and automatically propagates the corresponding uncertainties. Being self-consistent also makes the method more suitable than the TB approximation as a starting point to include other

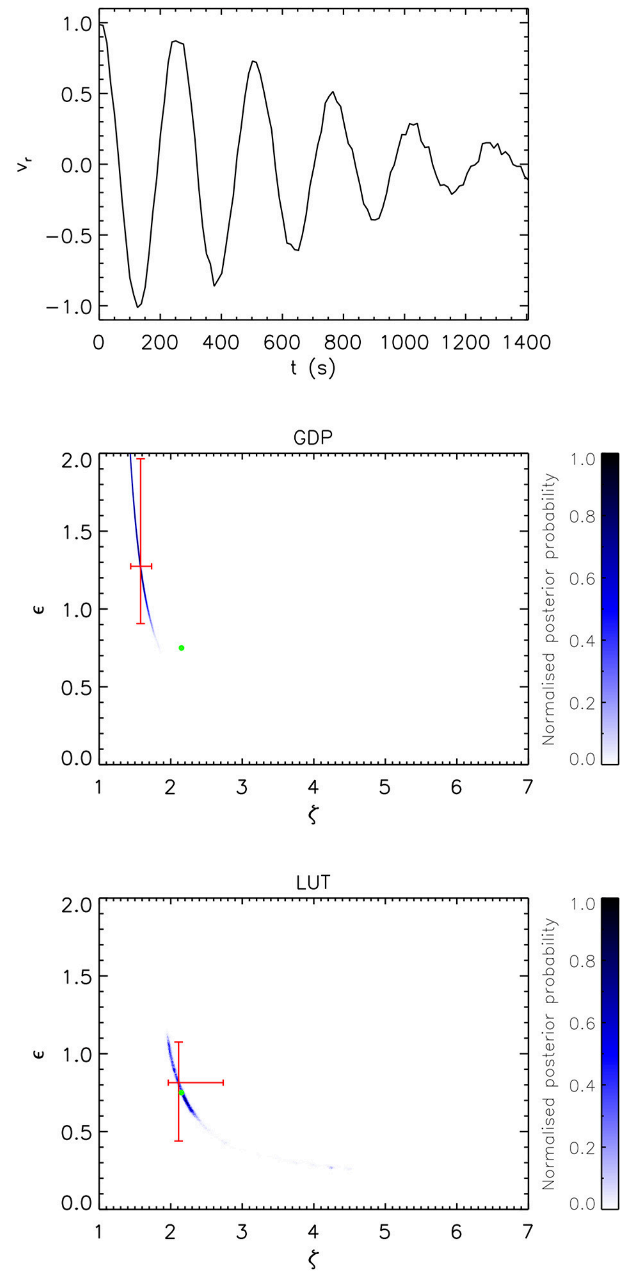

FIGURE 8 | The **top** panel shows a test kink oscillation simulated for $\zeta = 2.15$ and $\epsilon = 0.75$ with noise added. The **middle** and **bottom** panels show the seismologically estimated transverse density structure based on the GDP and LUT methods, respectively. The color contours represent the normalized 2D histograms approximating the marginalized posterior probability density function. The red error bars correspond to the MAP value and 95% credible intervals, and the green circle indicates the actual density profile parameters.

effects which depend on the density profile parameters. On the other hand, this work only accounts for the influence of wide inhomogeneous layers on the kink oscillation damping profile, with other assumptions and approximations needing to be considered.

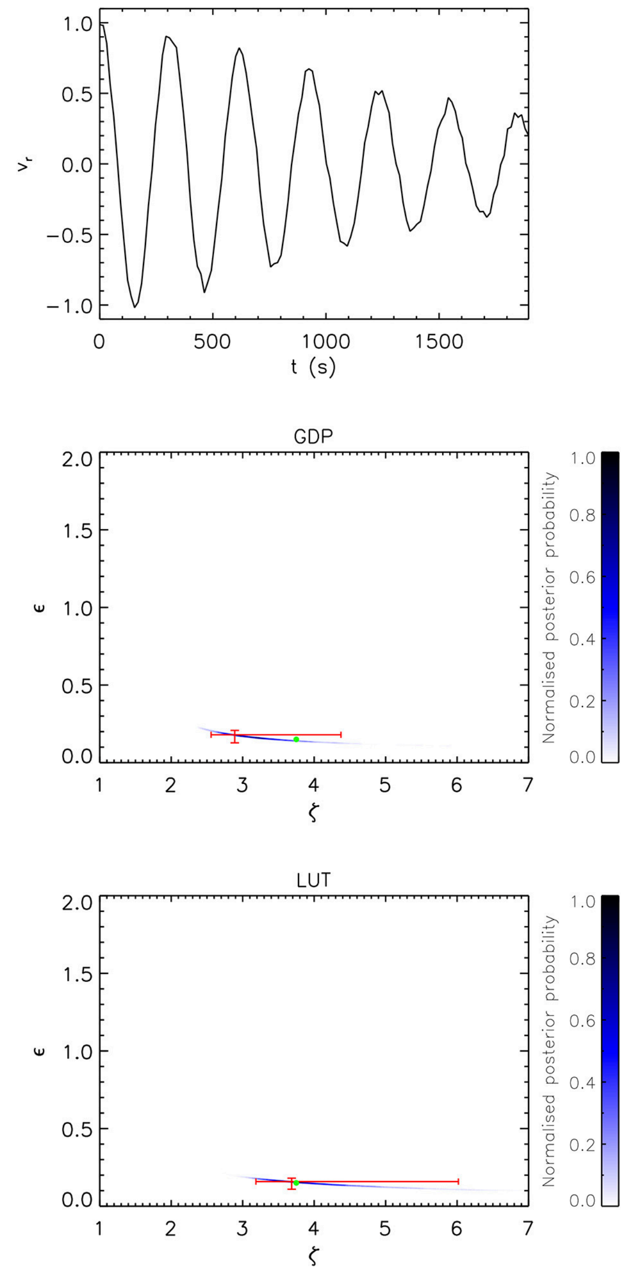

FIGURE 9 | Seismological test as in **Figure 8** for $\zeta = 3.75$ and $\epsilon = 0.2$.

The simulations performed in this paper use a linear profile for the density in the inhomogeneous layer. In terms of the damping rate due to resonant absorption, the key physical parameter is the gradient of the Alfvén speed at the resonance location. Arregui and Goossens (2019) discuss how the choice of density profile (e.g., linear or sinusoidal in the inhomogeneous layer) affects the seismologically-inferred loop parameters, since they have different constants of proportionality (e.g., Goossens et al., 2002; Roberts, 2008; Soler et al., 2014) between the damping time and the loop parameters (ζ, ϵ). Arregui and Goossens (2019) note that seismological applications have so far used the linear profile

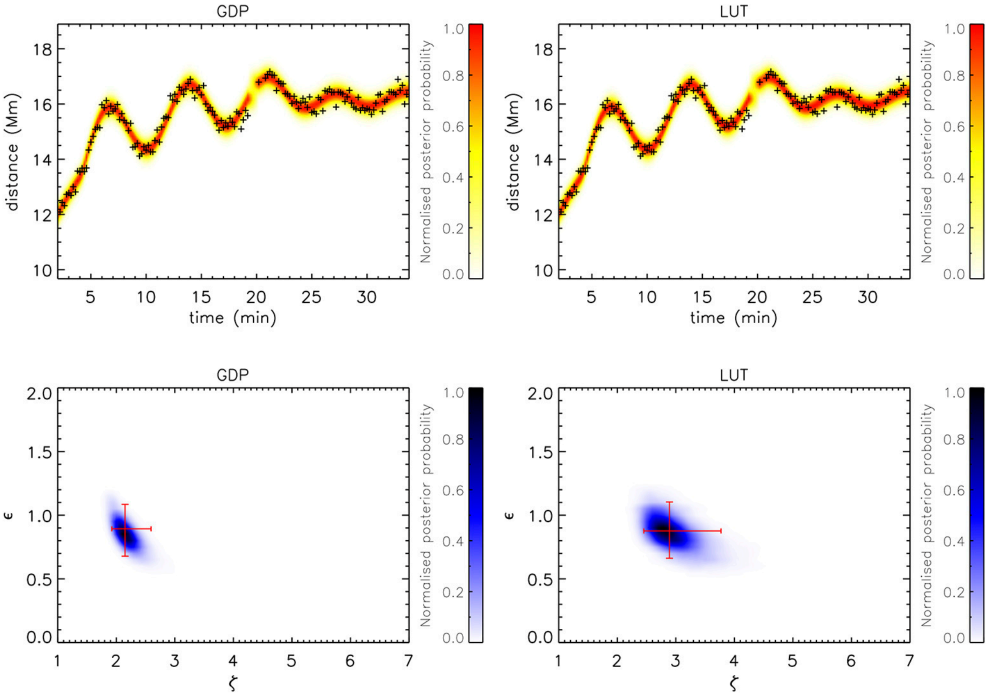

FIGURE 10 | Analysis of the oscillation reported in Pascoe et al. (2018) using the GDP and LUT damping profile. The **top** panels show the position of Leg 1 (plus symbols) with the color contour representing the normalized posterior predictive probability density for each damping model. **Bottom** panels as in **Figure 8**.

and that choosing a different profile would return a different answer. However, presently no such choice exists since the linear profile is the only one for which a full analytical solution is known (Hood et al., 2013; Ruderman and Terradas, 2013). The linear profile is therefore the natural choice of profile for use in this study, to allow a comparison of numerical results with the TB approximations in the limit $\epsilon \rightarrow 0$. Pascoe et al. (2018) estimate that the difference in the seismological results using the linear and sinusoidal density profiles is $\lesssim 10\%$. However, these two profiles are not the only possible choices. If some profile (other than the linear one used) should be shown to be more appropriate for coronal loops then it would be simple (though computationally expensive) to reproduce our parametric study for that profile. If the spatial resolution of loops is sufficiently high then it is possible to test different profiles by forward modeling the EUV profile (e.g., Aschwanden et al., 2007; Goddard et al., 2017; Pascoe et al., 2017b, 2018). Such methods still typically involve further assumptions or approximations (e.g., loops having a cylindrical cross-section and azimuthal symmetry) however the aim of these investigations should not be considered the impossible task of inferring the precise density profile of coronal loops but rather estimating the most appropriate characteristic scales that influence the relevant physical processes. Resonant absorption, phase mixing, and the Kelvin-Helmholtz instability all depend on the transverse loop structure. In this context it is not required that the coronal loop density profile is exactly linear for the analysis based on this profile (or any other simplified model) to provide accurate and useful estimates of parameters such as the size of the transverse inhomogeneity $l = \epsilon R$.

Our LUT is also based on results of numerical simulations for the linear regime and so excludes the effect of the Kelvin-Helmholtz instability (KHI). The current technique is therefore more suitable for loops with wider inhomogeneous layers in which KHI develops at a slower rate. Simulations by Magyar and Van Doorsselaere (2016) suggest KHI is weak for $\epsilon \gtrsim 0.5$ and the weaker development for larger values of ϵ is also evident in simulations by Goddard et al. (2018) and Pagano et al. (2018). In principle the same LUT strategy could be extended to include effects such as KHI by performing a similar parametric study with a third parameter being the amplitude of the oscillation, A_0, with the study in this paper representing the ζ-ϵ plane in the limit $A_0 \rightarrow 0$. However this wider parametric study (ζ, ϵ, A_0) where each data point is based a 3D nonlinear simulation would be orders of magnitude more computationally expensive than our current one. A wider parametric study which describes the evolution of the loop, e.g., the development of fine structure by KHI, would also require additional observable signatures to be modeled and compared with data. In the current study we focus on the shape of the damping profile due to resonant absorption. Additional observational signatures have recently been considered by Antolin et al. (2017) based on forward modeling techniques (Van Doorsselaere et al., 2016) to describe the appearance of loops observed simultaneously in multiple EUV channels.

Our parametric study was also performed for thin loops which satisfy the long wavelength approximation $k_z R \ll 1$. As a first approximation the effect of a large k_z may be considered in terms of reducing the kink mode phase speed from C_{k}, but otherwise not influencing the damping per cycle (Van Doorsselaere et al., 2004). Variations in the loop length in time can account for a time-dependent period of oscillation (e.g., Nisticò et al., 2013; Russell et al., 2015; Pascoe et al., 2017c) but should also remain well-approximated by considering the damping per cycle provided by our LUT as unaffected. The period of oscillation (and ratios of periods for different longitudinal harmonics) can also be affected by longitudinal structuring due to gravity (e.g., Andries et al., 2005). Cooling of coronal loops causes the scale height to vary in time, accompanied by decreases in the period and period ratio (Morton and Erdélyi, 2009) and an amplification of kink oscillation which acts against the damping due to resonant absorption (Ruderman, 2011). Numerical simulations suggest this effect is typically small but could be approximately 10% for larger amplitude oscillations (Magyar et al., 2015). Similarly, the period of oscillation and period ratio can be affected by expansion of the loop at the apex (Verth and Erdélyi, 2008) and a time-dependent expansion can also reduce the damping of kink oscillations (Shukhobodskiy et al., 2018). It may be possible to include effects such as these which modify the period of oscillation relative to P_{k} and introduce additional damping/amplification terms into a more general oscillation model alongside our LUT damping profile for resonant absorption. However, including loop evolution which affects the transverse structuring of the loop, such as KHI, would be more challenging.

AUTHOR CONTRIBUTIONS

DP and TVD contributed conception and design of the study. AH and DP developed the code for the numerical simulations. DP wrote the first draft of the manuscript, and received input from all co-authors.

FUNDING

AH acknowledges funding from the Science and Technology Facilities Council (UK) through the consolidated grant ST/N000609. DP and TVD were supported by the GOA-2015-014 (KU Leuven) and the European Research Council (ERC) under the European Union's Horizon 2020 research and innovation programme (grant agreement No. 724326).

REFERENCES

Andries, J., Arregui, I., and Goossens, M. (2005). Determination of the coronal density stratification from the observation of harmonic coronal loop oscillations. *Astrophys. J. Lett.* 624, L57–L60. doi: 10.1086/430347

Antolin, P., De Moortel, I., Van Doorsselaere, T., and Yokoyama, T. (2017). Observational signatures of transverse magnetohydrodynamic waves and associated dynamic instabilities in coronal flux tubes. *Astrophys. J.* 836:219. doi: 10.3847/1538-4357/aa5eb2

Antolin, P., Okamoto, T. J., De Pontieu, B., Uitenbroek, H., Van Doorsselaere, T., and Yokoyama, T. (2015). Resonant absorption of transverse oscillations and associated heating in a solar prominence. II. Numerical aspects. *Astrophys. J.* 809:72. doi: 10.1088/0004-637X/809/1/72

Arregui, I. (2018). Bayesian coronal seismology. *Adv. Space Res.* 61, 655–672. doi: 10.1016/j.asr.2017.09.031

Arregui, I., and Asensio Ramos, A. (2014). Determination of the cross-field density structuring in coronal waveguides using the damping of transverse waves. *Astron. Astrophys.* 565:A78. doi: 10.1051/0004-6361/201423536

Arregui, I., Asensio Ramos, A., and Pascoe, D. J. (2013). Determination of transverse density structuring from propagating magnetohydrodynamic waves in the solar atmosphere. *Astrophys. J. Lett.* 769:L34. doi: 10.1088/2041-8205/769/2/L34

Arregui, I., and Goossens, M. (2019). No unique solution to the seismological problem of standing kink MHD waves. *Astron. Astrophys.* 622, 1–10. doi: 10.1051/0004-6361/201833813

Arregui, I., Terradas, J., Oliver, R., and Ballester, J. L. (2008). Damping of fast magnetohydrodynamic oscillations in quiescent filament threads. *Astrophys. J. Lett.* 682:L141. doi: 10.1086/591081

Aschwanden, M. J., de Pontieu, B., Schrijver, C. J., and Title, A. M. (2002). Transverse oscillations in coronal loops observed with TRACE II. Measurements of geometric and physical parameters. *Solar Phys.* 206, 99–132. doi: 10.1023/A:1014916701283

Aschwanden, M. J., Fletcher, L., Schrijver, C. J., and Alexander, D. (1999). Coronal loop oscillations observed with the transition region and coronal explorer. *Astrophys. J.* 520, 880–894. doi: 10.1086/307502

Aschwanden, M. J., Nightingale, R. W., and Boerner, P. (2007). A statistical model of the inhomogeneous corona constrained by triple-filter measurements of elementary loop strands with TRACE. *Astrophys. J.* 656, 577–597. doi: 10.1086/510232

Beck, C., Choudhary, D. P., Rezaei, R., and Louis, R. E. (2015). Fast inversion of solar ca ii spectra. *Astrophys. J.* 798:100. doi: 10.1088/0004-637X/798/2/100

Chen, L., and Hasegawa, A. (1974). Plasma heating by spatial resonance of Alfven wave. *Phys. Fluids* 17, 1399–1403. doi: 10.1063/1.1694904

De Moortel, I., and Nakariakov, V. M. (2012). Magnetohydrodynamic waves and coronal seismology: an overview of recent results. *R. Soc. Lond. Philos. Trans. Ser. A* 370, 3193–3216. doi: 10.1098/rsta.2011.0640

De Moortel, I., Pascoe, D. J., Wright, A. N., and Hood, A. W. (2016). Transverse, propagating velocity perturbations in solar coronal loops. *Plasma Phys. Control. Fus.* 58:014001. doi: 10.1088/0741-3335/58/1/014001

Del Zanna, G., Dere, K. P., Young, P. R., Landi, E., and Mason, H. E. (2015). CHIANTI - An atomic database for emission lines. Version 8. *Astron. Astrophys.* 582:A56. doi: 10.1051/0004-6361/201526827

Goddard, C. R., Antolin, P., and Pascoe, D. J. (2018). Evolution of the transverse density structure of oscillating coronal loops inferred by forward modeling of EUV intensity. *Astrophys. J.* 863:167. doi: 10.3847/1538-4357/aad3cc

Goddard, C. R., and Nakariakov, V. M. (2016). Dependence of kink oscillation damping on the amplitude. *Astron. Astrophys.* 590:L5. doi: 10.1051/0004-6361/201628718

Goddard, C. R., Nisticò, G., Nakariakov, V. M., and Zimovets, I. V. (2016). A statistical study of decaying kink oscillations detected using SDO/AIA. *Astron. Astrophys.* 585:A137. doi: 10.1051/0004-6361/201527341

Goddard, C. R., Pascoe, D. J., Anfinogentov, S., and Nakariakov, V. M. (2017). A statistical study of the inferred transverse density profile of coronal loop threads observed with SDO/AIA. *Astron. Astrophys.* 605:A65. doi: 10.1051/0004-6361/201731023

Goossens, M., Andries, J., and Aschwanden, M. J. (2002). Coronal loop oscillations. An interpretation in terms of resonant absorption of quasi-mode kink oscillations. *Astron. Astrophys.* 394, L39–L42. doi: 10.1051/0004-6361:20021378

Goossens, M., Arregui, I., Ballester, J. L., and Wang, T. J. (2008). Analytic approximate seismology of transversely oscillating coronal loops. *Astron. Astrophys.* 484, 851–857. doi: 10.1051/0004-6361:200809728

Goossens, M., Hollweg, J. V., and Sakurai, T. (1992). Resonant behaviour of MHD waves on magnetic flux tubes. III - Effect of equilibrium flow. *Solar Phys.* 138, 233–255. doi: 10.1007/BF00151914

Guo, M., Van Doorsselaere, T., Karampelas, K., Li, B., Antolin, P., and De Moortel, I. (2019). Heating effects from driven transverse and Alfvén waves in coronal loops. *Astrophys. J.* 870. doi: 10.3847/1538-4357/aaf1d0

Heyvaerts, J., and Priest, E. R. (1983). Coronal heating by phase-mixed shear Alfven waves. *Astron. Astrophys.* 117, 220–234.

Hillier, A., Barker, A., Arregui, I., and Latter, H. (2019). On Kelvin-Helmholtz and parametric instabilities driven by coronal waves. *Month. Notices R. Astron. Soc.* 482, 1143–1153. doi: 10.1093/mnras/sty2742

Hollweg, J. V., and Yang, G. (1988). Resonance absorption of compressible magnetohydrodynamic waves at thin 'surfaces'. *JGR Space Phys.* 93, 5423–5436.

Hood, A. W., Ruderman, M., Pascoe, D. J., De Moortel, I., Terradas, J., and Wright, A. N. (2013). Damping of kink waves by mode coupling. I. Analytical treatment. *Astron. Astrophys.* 551:A39. doi: 10.1051/0004-6361/201220617

Jeffreys, H. (1961). *Theory of Probability*. 3rd Edition. Oxford:Clarendon Press.

Karampelas, K., and Van Doorsselaere, T. (2018). Simulations of fully deformed oscillating flux tubes. *Astron. Astrophys.* 610:L9. doi: 10.1051/0004-6361/201731646

Karampelas, K., Van Doorsselaere, T., and Antolin, P. (2017). Heating by transverse waves in simulated coronal loops. *Astron. Astrophys.* 604:A130. doi: 10.1051/0004-6361/201730598

Kass, R. E., and Raftery, A. E. (1995). Bayes factors. *J. Am. Stat. Assoc.* 90, 773–795. doi: 10.1080/01621459.1995.10476572

Lemen, J. R., Title, A. M., Akin, D. J., Boerner, P. F., Chou, C., Drake, J. F., et al. (2012). The Atmospheric Imaging Assembly (AIA) on the Solar Dynamics Observatory (SDO). *Solar Phys.* 275, 17–40. doi: 10.1007/s11207-011-9776-8

Magyar, N., and Van Doorsselaere, T. (2016). Damping of nonlinear standing kink oscillations: a numerical study. *Astron. Astrophys.* 595:A81. doi: 10.1051/0004-6361/201629010

Magyar, N., Van Doorsselaere, T., and Marcu, A. (2015). Numerical simulations of transverse oscillations in radiatively cooling coronal loops. *Astron. Astrophys.* 582:A117. doi: 10.1051/0004-6361/201526287

Markwardt, C. B. (2009). "Non-linear Least-squares Fitting in IDL with MPFIT," in *Astronomical Data Analysis Software and Systems XVIII, Vol. 411*, Astronomical Society of the Pacific Conference Series, eds D. A. Bohlender, D. Durand, and P. Dowler (San Francisco, CA), 251.

Morton, R. J., and Erdélyi, R. (2009). Transverse oscillations of a cooling coronal loop. *Astrophys. J.* 707, 750–760. doi: 10.1088/0004-637X/707/1/750

Nakariakov, V. M., and Ofman, L. (2001). Determination of the coronal magnetic field by coronal loop oscillations. *Astron. Astrophys.* 372, L53–L56. doi: 10.1051/0004-6361:20010607

Nakariakov, V. M., Ofman, L., Deluca, E. E., Roberts, B., and Davila, J. M. (1999). TRACE observation of damped coronal loop oscillations: Implications for coronal heating. *Science* 285, 862–864. doi: 10.1126/science.285.5429.862

Nisticò, G., Nakariakov, V. M., and Verwichte, E. (2013). Decaying and decayless transverse oscillations of a coronal loop. *Astron. Astrophys.* 552:A57. doi: 10.1051/0004-6361/201220676

Okamoto, T. J., Antolin, P., De Pontieu, B., Uitenbroek, H., Van Doorsselaere, T., and Yokoyama, T. (2015). Resonant absorption of transverse oscillations and associated heating in a solar prominence. I. Observational aspects. *Astrophys. J.* 809:71. doi: 10.1088/0004-637X/809/1/71

Pagano, P., Pascoe, D. J., and De Moortel, I. (2018). Contribution of phase-mixing of Alfvén waves to coronal heating in multi-harmonic loop oscillations. *Astron. Astrophys.* 616:A125. doi: 10.1051/0004-6361/201732251

Pascoe, D. J. (2014). Numerical simulations for MHD coronal seismology. *Res. Astron. Astrophys.* 14, 805–830. doi: 10.1088/1674-4527/14/7/004

Pascoe, D. J., Anfinogentov, S., Nisticò, G., Goddard, C. R., and Nakariakov, V. M. (2017a). Coronal loop seismology using damping of standing kink oscillations by mode coupling. II. additional physical effects and Bayesian analysis. *Astron. Astrophys.* 600:A78. doi: 10.1051/0004-6361/201629702

Pascoe, D. J., Anfinogentov, S. A., Goddard, C. R., and Nakariakov, V. M. (2018). Spatiotemporal analysis of coronal loops using seismology of damped kink oscillations and forward modeling of EUV intensity profiles. *Astrophys. J.* 860:31. doi: 10.3847/1538-4357/aac2bc

Pascoe, D. J., Goddard, C. R., Anfinogentov, S., and Nakariakov, V. M. (2017b). Coronal loop density profile estimated by forward modelling of EUV intensity. *Astron. Astrophys.* 600:L7. doi: 10.1051/0004-6361/201730458

Pascoe, D. J., Goddard, C. R., Nisticò, G., Anfinogentov, S., and Nakariakov, V. M. (2016). Coronal loop seismology using damping of standing kink oscillations by mode coupling. *Astron. Astrophys.* 589:A136. doi: 10.1051/0004-6361/201628255

Pascoe, D. J., Hood, A. W., de Moortel, I., and Wright, A. N. (2012). Spatial damping of propagating kink waves due to mode coupling. *Astron. Astrophys.* 539:A37. doi: 10.1051/0004-6361/201117979

Pascoe, D. J., Hood, A. W., De Moortel, I., and Wright, A. N. (2013). Damping of kink waves by mode coupling. II. Parametric study and seismology. *Astron. Astrophys.* 551:A40. doi: 10.1051/0004-6361/201220620

Pascoe, D. J., Russell, A. J. B., Anfinogentov, S. A., Simões, P. J. A., Goddard, C. R., Nakariakov, V. M., et al. (2017c). Seismology of contracting and expanding coronal loops using damping of kink oscillations by mode coupling. *Astron. Astrophys.* 607:A8. doi: 10.1051/0004-6361/201730915

Pascoe, D. J., Wright, A. N., and De Moortel, I. (2010). Coupled Alfvén and Kink Oscillations in Coronal Loops. *Astrophys. J.* 711, 990–996. doi: 10.1088/0004-637X/711/2/990

Pascoe, D. J., Wright, A. N., and De Moortel, I. (2011). Propagating coupled Alfvén and kink oscillations in an arbitrary inhomogeneous corona. *Astrophys. J.* 731:73. doi: 10.1088/0004-637X/731/1/73

Pascoe, D. J., Wright, A. N., De Moortel, I., and Hood, A. W. (2015). Excitation and damping of broadband kink waves in the solar corona. *Astron. Astrophys.* 578:A99. doi: 10.1051/0004-6361/201321328

Roberts, B. (2008). "Progress in coronal seismology," in *IAU Symposium, Vol. 247*, eds R. Erdélyi and C. A. Mendoza-Briceno (Cambridge), 3–19.

Ruderman, M. S. (2011). Resonant damping of kink oscillations of cooling coronal magnetic loops. *Astron. Astrophys.* 534:A78. doi: 10.1051/0004-6361/201117416

Ruderman, M. S., and Roberts, B. (2002). The damping of coronal loop oscillations. *Astrophys. J.* 577, 475–486. doi: 10.1086/342130

Ruderman, M. S., and Terradas, J. (2013). Damping of coronal loop kink oscillations due to mode conversion. *Astron. Astrophys.* 555:A27. doi: 10.1051/0004-6361/201220195

Russell, A. J. B., Simões, P. J. A., and Fletcher, L. (2015). A unified view of coronal loop contraction and oscillation in flares. *Astron. Astrophys.* 581:A8. doi: 10.1051/0004-6361/201525746

Sarkar, S., Pant, V., Srivastava, A. K., and Banerjee, D. (2016). Transverse oscillations in a coronal loop triggered by a jet. *Solar Phys.* 291, 3269–3288. doi: 10.1007/s11207-016-1019-6

Shukhobodskiy, A. A., Ruderman, M. S., and Erdélyi, R. (2018). Resonant damping of kink oscillations of thin cooling and expanding coronal magnetic loops. *Astron. Astrophys.* 619:A173. doi: 10.1051/0004-6361/201833714

Soler, R., Goossens, M., Terradas, J., and Oliver, R. (2014). The behavior of transverse waves in nonuniform solar flux tubes. II. Implications for coronal loop seismology. *Astrophys. J.* 781:111. doi: 10.1088/0004-637X/781/2/111

Stepanov, A. V., Zaitsev, V. V., and Nakariakov, V. M. (2012). *Coronal Seismology: Waves and Oscillations in Stellar Coronae*. Weinheim: Wiley-VCH Verlag GmbH & Co. KGaA.

Terradas, J., Andries, J., Goossens, M., Arregui, I., Oliver, R., and Ballester, J. L. (2008a). Nonlinear instability of kink oscillations due to shear motions. *Astrophys. J. Lett.* 687:L115. doi: 10.1086/593203

Terradas, J., Arregui, I., Oliver, R., Ballester, J. L., Andries, J., and Goossens, M. (2008b). Resonant absorption in complicated plasma configurations: applications to multistranded coronal loop oscillations. *Astrophys. J.* 679, 1611–1620. doi: 10.1086/586733

Terradas, J., Goossens, M., and Verth, G. (2010). Selective spatial damping of propagating kink waves due to resonant absorption. *Astron. Astrophys.* 524:A23. doi: 10.1051/0004-6361/201014845

Van Doorsselaere, T., Andries, J., Poedts, S., and Goossens, M. (2004). Damping of coronal loop oscillations: calculation of resonantly damped kink oscillations of one-dimensional nonuniform loops. *Astrophys. J.* 606, 1223–1232. doi: 10.1086/383191

Van Doorsselaere, T., Antolin, P., and Karampelas, K. (2018). Broadening of the differential emission measure by multi-shelled and turbulent loops. *Astron. Astrophys.* 620:A65. doi: 10.1051/0004-6361/201834086

Van Doorsselaere, T., Antolin, P., Yuan, D., Reznikova, V., and Magyar, N. (2016). Forward modelling of optically thin coronal plasma with the FoMo tool. *Front. Astron. Space Sci.* 3:4. doi: 10.3389/fspas.2016.00004

Van Doorsselaere, T., Nakariakov, V. M., and Verwichte, E. (2007). Coronal loop seismology using multiple transverse loop oscillation harmonics. *Astron. Astrophys.* 473, 959–966. doi: 10.1051/0004-6361:20077783

Verth, G., and Erdélyi, R. (2008). Effect of longitudinal magnetic and density inhomogeneity on transversal coronal loop oscillations. *Astron. Astrophys.* 486, 1015–1022. doi: 10.1051/0004-6361:200809626

White, R. S., and Verwichte, E. (2012). Transverse coronal loop oscillations seen in unprecedented detail by AIA/SDO. *Astron. Astrophys.* 537:A49. doi: 10.1051/0004-6361/201118093

Zimovets, I. V., and Nakariakov, V. M. (2015). Excitation of kink oscillations of coronal loops: statistical study. *Astron. Astrophys.* 577:A4. doi: 10.1051/0004-6361/201424960

Conflict of Interest Statement: The authors declare that the research was conducted in the absence of any commercial or financial relationships that could be construed as a potential conflict of interest.

frontiers
in Astronomy and Space Sciences

REVIEW
published: 08 May 2019
doi: 10.3389/fspas.2019.00033

How Rotating Solar Atmospheric Jets Become Kelvin–Helmholtz Unstable

Ivan Zhelyazkov[1]*, Ramesh Chandra[2] and Reetika Joshi[2]

[1] Faculty of Physics, Sofia University, Sofia, Bulgaria, [2] Department of Physics, Kumaun University, Nainital, India

Recent observations support the propagation of a number of magnetohydrodynamic (MHD) modes which, under some conditions, can become unstable and the developing instability is the Kelvin–Helmholtz instability (KHI). In its non-linear stage the KHI can trigger the occurrence of wave turbulence which is considered as a candidate mechanism for coronal heating. We review the modeling of tornado-like phenomena in the solar chromosphere and corona as moving weakly twisted and spinning cylindrical flux tubes, showing that the KHI rises at the excitation of high-mode MHD waves. The instability occurs within a wavenumber range whose width depends on the MHD mode number m, the plasma density contrast between the rotating jet and its environment, and also on the twists of the internal magnetic field and the jet velocity. We have studied KHI in two twisted spinning solar polar coronal hole jets, in a twisted rotating jet emerging from a filament eruption, and in a rotating macrospicule. The theoretically calculated KHI development times of a few minutes for wavelengths comparable to the half-widths of the jets are in good agreement with the observationally determined growth times only for high order ($10 \leqslant m \leqslant 65$) MHD modes. Therefore, we expect that the observed KHI in these cases is due to unstable high-order MHD modes.

Keywords: magnetic fields, magnetohydrodynamics (MHD), solar jets, MHD waves and instabilities, numerical methods

Edited by:
Tom Van Doorsselaere,
KU Leuven, Belgium

Reviewed by:
Matthew Allcock,
University of Sheffield,
United Kingdom
Manuel Luna,
Instituto de Astrofísica de Canarias,
Spain
Dae Jung Yu,
Kyung Hee University, South Korea

***Correspondence:**
Ivan Zhelyazkov
izh@phys.uni-sofia.bg

Specialty section:
This article was submitted to
Stellar and Solar Physics,
a section of the journal
Frontiers in Astronomy and Space
Sciences

Received: 28 January 2019
Accepted: 18 April 2019
Published: 08 May 2019

Citation:
Zhelyazkov I, Chandra R and Joshi R
(2019) How Rotating Solar
Atmospheric Jets Become
Kelvin–Helmholtz Unstable.
Front. Astron. Space Sci. 6:33.
doi: 10.3389/fspas.2019.00033

1. INTRODUCTION

Solar jets are ubiquitous in the solar atmosphere and recent observations have revealed that they are related to small scale filament eruptions. They are continuously observed by the Extreme-ultraviolet Imaging Spectrometer (EIS) (Culhane et al., 2007) on board *Hinode* (Kosugi et al., 2007) satellite, Atmospheric Imaging Assembly (AIA) (Lemen et al., 2012), on board the *Solar Dynamics Observatory* (*SDO*) (Pesnell et al., 2012), as well as from the *Interface Region Imaging Spectrograph* (*IRIS*) (De Pontieu et al., 2014) alongside the Earth-based solar telescopes. The physical parameters of various kinds of solar jets have been reported in a series of articles (see for instance, Schmieder et al., 2013; Sterling et al., 2015; Panesar et al., 2016a; Chandra et al., 2017; Joshi et al., 2017, and references cited in). It was established that more of the solar jets possess rotational motion. Such tornado-like jets, termed macrospicules, were firstly detected in the transition region by Pike and Mason (1998) using observations by the *Solar and Heliospheric Observatory* (*SOHO*) (Domingo et al. , 1995). Rotational motion in macrospicules was also explored by Kamio et al. (2010), Curdt and Tian (2011), Bennett and Erdélyi (2015), Kiss et al. (2017, 2018). Type II spicules, according to De Pontieu et al. (2012) and Martínez-Sykora et al. (2013), along with the coronal hole EUV jets (Liu et al., 2009; Nisticò et al., 2009, 2010; Shen et al., 2011; Chen et al. , 2012; Hong et al., 2013; Young and Muglach, 2014a,b; Moore et al., 2015), and X-ray jets (Moore et al., 2013), can rotate, too. Rotating EUV jet emerging from a swirling flare (Zhang and Ji, 2014) or formed during a confined filament eruption (Filippov et al., 2015) confirm once again the circumstance that the rotational motion is a common property of many kinds of jets in the solar atmosphere.

The first scenario for the numerical modeling of hot X-ray jets was reported by Heyvaerts et al. (1997) and the basic idea was that a bipolar magnetic structure emerges into a unipolar pre-existing magnetic field and reconnects to form hot and fast jets that are emitted from the interface between the fields into contact. Later on, by examining many X-ray jets in *Hinode*/X-Ray Telescope coronal X-ray movies of the polar coronal holes, Moore et al. (2010) found that there is a dichotomy of polar X-ray jets, namely "standard" and "blowout" jets exist. Fang et al. (2014) studied the formation of rotating coronal jets through numerical simulation of the emergence of a twisted magnetic flux rope into a pre-existing open magnetic field. Another scenario for the nature of solar jets was suggested by Sterling et al. (2015), according to which the X-ray jets are due to flux cancellation and/or "mini-eruptions" rather than emergence. An alternative model for solar polar jets due to an explosive release of energy via reconnection was reported by Pariat et al. (2009). Using three-dimensional MHD simulations, the authors demonstrated that this mechanism does produce massive, high-speed jets. In subsequent two articles (Pariat et al., 2015, 2016), Pariat and co-authors, presented several parametric studies of a three-dimensional numerical MHD model for straight and helical solar jets. On the other side, Panesar et al. (2016b) have shown that the magnetic flux cancellation can trigger the solar quiet-region coronal jets and they claim that the coronal jets are driven by the eruption of a small-scale filament, called a "minifilament." The small-scale chromospheric jets, like microspicules, were first numerically modeled by Murawski et al. (2011). Using the FLASH code, they solved the two-dimensional ideal MHD equations to model a macrospicule, whose physical parameters match those of a solar spicule observed. Another mechanism for the origin of macrospicules was proposed by Kayshap et al. (2013), who numerically modeled the triggering of a macrospicule and a jet.

It is natural to expect, that solar jets, being magnetically structured entities, should support the propagation of different type of MHD waves: fast and slow magnetoacoustic waves and torsional Alfvén waves. All these waves are usually considered as normal MHD modes traveling along the jet. Owing to the presence of a velocity shear near the jet–surrounding plasma interface, every jet can become unstable and the most universal instability which emerges is the Kelvin–Helmholtz (KH) one. The simplest configuration at which one can observe the KHI is the two semi-infinite incompressible magnetized plasmas flowing with different velocities provided that the thin velocity shear at the interface exceeds some critical value (Chandrasekhar, 1961). Recently, Cheremnykh et al. (2018a) theoretically established that shear plasma flows at the boundary of plasma media can generate eight MHD modes, of which only one can be unstable due to the development of the KHI. Ismayilli et al. (2018) investigated a shear instability of the KH type in a plasma with temperature anisotropy under the MHD approximation. The KHI of the magnetoacousic waves propagating in a steady asymmetric slab, and more specifically the effect of varying density ratios was explored by Barbulescu and Erdélyi (2018). A very good review on the KHI in the solar atmosphere, solar wind, and geomagnetosphere in the framework of ideal MHD the reader can find in Mishin and Tomozov, 2016.

In cylindrical geometry, being typical for the solar jets, the KHI exhibits itself as a vortex sheet running on the jet–environment boundary, which like in the flat geometry, is growing in time if the axial velocity of the jet in a frame of reference attached to the surrounding plasma exceeds a threshold value (Ryu et al., 2000). In its non-linear stage, the KHI trigger the wave turbulence which is considered as one of the main heating mechanisms of the solar corona (Cranmer et al, 2015). The development of the KHI in various cylindrical jet–environment configurations has been studied in photospheric jets (Zhelyazkov and Zaqarashvili, 2012), in solar spicules (Zhelyazkov, 2012; Ajabshirizadeh et al., 2015; Ebadi, 2016), in high-temperature and cool solar surges (Zhelyazkov et al., 2015a,b), in magnetic tubes of partially ionized compressible plasma (Soler et al., 2015), in EUV chromospheric jets (Zhelyazkov et al., 2016; Bogdanova et al., 2018), in soft X-ray jets (Vasheghani Farahani et al., 2009; Zhelyazkov et al., 2017), and in the twisted solar wind flows (Zaqarashvili et al., 2014). A review on KHI in the solar atmosphere, including some earlier studies, the reader can find in Zhelyazkov (2015).

The first modeling of the KHI in a rotating cylindrical magnetized plasma jet was done by Bondenson et al. (1987). Later on, Bodo et al. (1989, 1996) carried out a study of the stability of flowing cylindrical jet immersed in constant magnetic field $\boldsymbol{B}_0$. The authors used the standard procedure for exploring the MHD wave propagation in cylindrical flows considering that all the perturbations of the plasma pressure p, fluid velocity $\boldsymbol{v}$, and magnetic field $\boldsymbol{B}$, are $\propto \exp[\mathrm{i}(-\omega t + kz + m\theta)]$. Here, ω is the angular wave frequency, k the propagating wavenumber, and m the azimuthal mode number. Using the basic equations of ideal magnetohydrodynamics, Bodo et al. (1989, 1996) derived a Bessel equation for the pressure perturbation and an expression for the radial component of the fluid velocity perturbation. The found solutions in both media (the jet and its environment) are merged at the perturbed tube boundary through the conditions for continuity of the total (thermal plus magnetic) pressure and the Lagrangian displacement. The latter is defined as the ratio of radial velocity perturbation component and the angular frequency in the corresponding medium. The obtained dispersion relation is used for examining the stability conditions of both axisymmetric, $m = 0$ (Bodo et al., 1989), and non-axisymmetric, $|m| \geqslant 1$ modes (Bodo et al., 1996). In a recent article, Bodo et al. (2016) performed a linear stability analysis of magnetized rotating cylindrical jet flows in the approximation of zero thermal pressure. They focused their analysis on the effect of rotation on the current driven mode and on the unstable modes introduced by rotation. In particular, they found that rotation has a stabilizing effect on the current driven mode only for rotation velocities of the order on the Alfvén speed. The more general case, when both the magnetic field and jet flow velocity are twisted, was studied by Zaqarashvili et al. (2015) and Cheremnykh et al.

(2018b), whose dispersion equations for modes with $m \geqslant 2$, represented in different ways, yield practically identical results.

The main goal of this review article is to suggest a way of using the wave dispersion relation derived in Zaqarashvili et al. (2015) to study the possibility for the rising and development of KHI in rotating twisted solar jets. Among the enormous large number of observational studies of rotating jets with different origin or nature, we chose those which provide the magnitudes of axial and rotational speeds, jet width and height alongside the typical plasma parameters like electron number densities and electron temperature of the spinning structure and its environment. Thus, the targets of our exploration are: (i) the spinning coronal hole jet of 2010 August 21 (Chen et al. , 2012); (ii) the rotating coronal hole jet of 2011 February 8 (Young and Muglach, 2014a), (iii) the twisted rotating jet emerging from a filament eruption on 2013 April 10–11 (Filippov et al., 2015), and (iv) the rotating macrospicule observed by Pike and Mason (1998) on 1997 March 8.

The paper is organized as follows: in the next section, we discuss the geometry of the problem, equilibrium magnetic field configuration and basic physical parameters of the explored jets. Section 3 is devoted to a short, concise, derivation of the wave dispersion relation. Section 4 deals with numerical results for each of the four jets and contain the available observational data. In the last section 5, we summarize the main findings in our research and outlook the further improvement of the used modeling.

2. THE GEOMETRY, MAGNETIC FIELD, AND PHYSICAL PARAMETERS IN A JET MODEL

We model whichever jet as an axisymmetric cylindrical magnetic flux tube with radius a and electron number density n_i (or equivalently, homogeneous plasma density ρ_i) moving with velocity $\boldsymbol{U}$. We consider that the jet environment is a rest plasma with homogeneous density ρ_e immersed in a homogeneous background magnetic field $\boldsymbol{B}_\mathrm{e}$. This field, in cylindrical coordinates (r, ϕ, z), possesses only an axial component, i.e., $\boldsymbol{B}_\mathrm{e} = (0, 0, B_\mathrm{e})$ (Note that the label "i" is abbreviation for *interior*, and the label "e" denotes *exterior*). The magnetic field inside the tube, $\boldsymbol{B}_\mathrm{i}$, and the jet velocity, $\boldsymbol{U}$, we assume, are uniformly twisted and are given by the vectors

$$\boldsymbol{B}_\mathrm{i} = \left(0, B_{\mathrm{i}\phi}(r), B_{\mathrm{i}z}\right) \qquad \text{and} \qquad \boldsymbol{U} = \left(0, U_\phi(r), U_z\right), \tag{1}$$

respectively. We note, that $B_{\mathrm{i}z}$ and U_z, are constant. Concerning the azimuthal magnetic and flow velocity components, we suppose that they are linear functions of the radial position r and evaluated at $r = a$ they correspondingly are equal to $B_{\mathrm{i}\phi}(a) \equiv B_\phi = Aa$ and $U_\phi = \Omega a$, where A and Ω are constants. Here, Ω is the jet angular speed, deduced from the observations. Hence, in equilibrium, the rigidly rotating plasma column, that models the jet, must satisfy the following force-balance equation (see, e.g., Chandrasekhar, 1961; Goossens et al., 1992)

$$\frac{\mathrm{d}}{\mathrm{d}r}\left(p_\mathrm{i} + \frac{B_\mathrm{i}^2}{2\mu}\right) = \frac{\rho_\mathrm{i} U_\phi^2}{r} - \frac{B_{\mathrm{i}\phi}^2}{\mu r}, \tag{2}$$

where μ is the plasma permeability and $p_\mathrm{t} = p_\mathrm{i} + B_\mathrm{i}^2/2\mu$ with $B_\mathrm{i}^2 = B_{\mathrm{i}\phi}^2(r) + B_{\mathrm{i}z}^2$ is the total (thermal plus magnetic) pressure. According to Equation (2), the radial gradient of the total pressure should balance the centrifugal force and the force owing to the magnetic tension. After integrating Equation (2) from 0 to a, taking into account the linear dependence of U_ϕ and $B_{\mathrm{i}\phi}$ on r, we obtain that

$$p_\mathrm{t}(a) = p_\mathrm{t}(0) + \frac{1}{2}\rho_\mathrm{i} U_\phi^2(a) - \frac{B_{\mathrm{i}\phi}^2(a)}{2\mu},$$

where $p_\mathrm{t}(0) = p_1(0) + B_{\mathrm{i}z}^2/2\mu$. Integrating Equation (2) from 0 to any r one can find the radial profile of p_t inside the tube. Such an expression of $p_\mathrm{t}(r)$, obtained, however, from an integration of the momentum equation for the equilibrium variables, have been obtained in Zhelyazkov et al. (2018)—see Equation (2) there. It is clear from a physical point of view that the internal total pressure (evaluated at $r = a$) must be balanced by the total pressure of the surrounding plasma which implies that

$$p_1(0) + \frac{B_{\mathrm{i}z}^2}{2\mu} - \frac{B_{\mathrm{i}\phi}^2(a)}{2\mu} + \frac{1}{2}\rho_\mathrm{i} U_\phi^2(a) = p_\mathrm{e} + \frac{B_\mathrm{e}^2}{2\mu}.$$

This equation can be presented in the form

$$p_1(0) + \frac{1}{2}\rho_\mathrm{i} U_\phi^2(a) + \frac{B_{\mathrm{i}z}^2}{2\mu}\left(1 - \varepsilon_1^2\right) = p_\mathrm{e} + \frac{B_\mathrm{e}^2}{2\mu}, \tag{3}$$

where $p_1(0)$ is the thermal pressure at the magnetic tube axis, and p_e denotes the thermal pressure in the environment. In the pressure balance Equation (3), the number $\varepsilon_1 \equiv B_\phi/B_{\mathrm{i}z} = Aa/B_{\mathrm{i}z}$ represents the magnetic field twist parameter. Similarly, we define $\varepsilon_2 \equiv U_\phi/U_z$ as a characteristics of the jet velocity twist. We would like to underline that the choice of plasma and environment parameters must be such that the total pressure balance Equation (3) is satisfied. In our case, the value of ε_2 is fixed by observationally measured rotational and axial velocities while the magnetic field twist, ε_1, has to be specified when using Equation (3). We have to note that Equation (3) is a corrected version of the pressure balance equation used in Zhelyazkov et al. (2018) and Zhelyazkov and Chandra (2018).

From measurements of n and T for similar coronal hole EUV jets (Nisticò et al., 2009, 2010), we take n inside the jet to be $n_\mathrm{i} = 1.0 \times 10^9$ cm^{-3}, and assume that the electron temperature is $T_\mathrm{i} = 1.6$ MK. The same quantities in the environment are, respectively, $n_\mathrm{e} = 0.9 \times 10^9$ cm^{-3} and $T_\mathrm{e} = 1.0$ MK. Note that the electron number density of the blowout jet observed by Young and Muglach (2014a) is in one order lower. The same applies for its environment. We consider that the background magnetic field for both hole coronal jets is $B_\mathrm{e} = 3$ G. The values of n and T of the rotating jet emerging from a filament eruption, observed by Filippov et al. (2015), were evaluated by us and they are $n_\mathrm{i} = 4.65 \times 10^9$ cm^{-3} and $T_\mathrm{i} = 2.0$ MK, respectively. From the same data set, we have obtained $n_\mathrm{e} = 4.02 \times 10^9$ cm^{-3} and $T_\mathrm{e} = 2.14$ MK. The background magnetic field, B_e, with which the pressure balance Equation (3) is satisfied, is equal to 6 G. For the rotating macrospicule we assume that $n_\mathrm{i} = 1.0 \times 10^{10}$ cm^{-3} and $n_\mathrm{e} = 1.0 \times 10^9$ cm^{-3} to have at least one order denser jet with respect to the surrounding plasma. Our choice for macrospicule temperature is $T_\mathrm{i} = 5.0 \times 10^5$ K, while that of its environment is supposed to be $T_\mathrm{e} = 1.0 \times 10^6$ K. The external magnetic field, B_e, was taken as 5 G. All aforementioned physical parameters of the jets are summarized in **Table 1**. The plasma beta was calculated using $(6/5)c_\mathrm{s}^2/v_\mathrm{A}^2$, where $c_\mathrm{s} = (\gamma k_\mathrm{B} T/m_\mathrm{ion})^{1/2}$ is the sound speed (in which $\gamma = 5/3$, k_B is the Boltzmann's constant, T the electron temperature, and m_ion the ion or proton mass), and $v_\mathrm{A} = B/(\mu n_\mathrm{ion} m_\mathrm{ion})^{1/2}$ is the Alfvén speed, in which expression B is the full magnetic field $=(B_\phi^2 + B_z^2)^{1/2}$, and n_ion is the ion or proton number density.

3. WAVE DISPERSION RELATION

A dispersion relation for the propagation of high-mode ($m \geqslant 2$) MHD waves in a magnetized axially moving and rotating twisted jet was derived by Zaqarashvili et al. (2015) and Cheremnykh et al. (2018b). That equation was obtained, however, under the assumption that both media (the jet and its environment) are incompressible plasmas. As seen from the last column in **Table 1**, plasma beta is greater than 1 in the first, third, and fourth jets which implies that the plasma of each of the aforementioned jets can be considered as a nearly incompressible fluid (Zank and Matthaeus, 1993). It is seen from the same table that the plasma beta of the second jet is less than one as is in each of the jet environments and that is why it is reasonable to treat them as cool media. Thus, the wave dispersion relation, derived, for instance, in Zaqarashvili et al. (2015), has to be modified. In fact, we need two modified versions: one for the incompressible jet–cool environment configuration, and other for the cool jet–cool environment configuration. We are not going to present in details the derivation of the modified dispersion equations on the basis of the governing MHD equations, but will only sketch the essential steps in that procedure. The main philosophy in deriving the wave dispersion equation is to find solutions for the total pressure perturbation, p_tot, and for the radial component, ξ_r of the Lagrangian displacement, $\boldsymbol{\xi}$, and merge them at the tube perturbed boundary through the boundary conditions for their (p_tot and ξ_r) continuity (Chandrasekhar, 1961). In the case of the first configuration, we start with the linearized ideal MHD equations, governing the incompressible dynamics of the perturbations in the spinning jet

$$\frac{\partial}{\partial t}\boldsymbol{v} + (\boldsymbol{U}\cdot\nabla)\boldsymbol{v} + (\boldsymbol{v}\cdot\nabla)\boldsymbol{U} = -\frac{\nabla p_\mathrm{tot}}{\rho_\mathrm{i}} + \frac{(\boldsymbol{B}_\mathrm{i}\cdot\nabla)\,\boldsymbol{b}}{\rho_\mathrm{i}\mu} + \frac{(\boldsymbol{b}\cdot\nabla)\,\boldsymbol{B}_\mathrm{i}}{\rho_\mathrm{i}\mu}, \quad (4)$$

$$\frac{\partial}{\partial t}\boldsymbol{b} - \nabla\times(\boldsymbol{v}\times\boldsymbol{B}_\mathrm{i}) - \nabla\times(\boldsymbol{U}\times\boldsymbol{b}) = 0, \quad (5)$$

$$\nabla\cdot\boldsymbol{v} = 0, \quad (6)$$

$$\nabla\cdot\boldsymbol{b} = 0, \quad (7)$$

where $\boldsymbol{v} = (v_r, v_\phi, v_z)$ and $\boldsymbol{b} = (b_r, b_\phi, b_z)$ are the perturbations of fluid velocity and magnetic field, respectively, and p_tot is the perturbation of the total pressure, $p_\mathrm{t} = p_\mathrm{i} + B_\mathrm{i}^2/2\mu$. The Lagrangian displacement, $\boldsymbol{\xi}$, can be found from the fluid velocity perturbation, $\boldsymbol{v}$, using the relation (Chandrasekhar, 1961)

$$\boldsymbol{v} = \frac{\partial\boldsymbol{\xi}}{\partial t} + (\boldsymbol{U}\cdot\nabla)\,\boldsymbol{\xi} - (\boldsymbol{\xi}\cdot\nabla)\,\boldsymbol{U}. \quad (8)$$

Further on, assuming that all perturbations are $\propto \exp\left[\mathrm{i}\left(-\omega t + m\phi + k_z z\right)\right]$ and considering that the rotation and the magnetic field twists in the jet are uniform, that is,

$$U_\phi(r) = \Omega r \qquad \text{and} \qquad B_{\mathrm{i}\phi}(r) = Ar, \quad (9)$$

where Ω and A are constants, from the above set of Equations (4–8), we obtain the following dispersion equation of the MHD wave with mode number m (for details see Zaqarashvili et al., 2015):

$$\begin{aligned}&\frac{\left(\sigma^2 - \omega_\mathrm{Ai}^2\right)F_m(\kappa_\mathrm{i}a) - 2m\left(\sigma\Omega + A\omega_\mathrm{Ai}/\sqrt{\mu\rho_\mathrm{i}}\right)}{\rho_\mathrm{i}\left(\sigma^2 - \omega_\mathrm{Ai}^2\right)^2 - 4\rho_\mathrm{i}\left(\sigma\Omega + A\omega_\mathrm{Ai}/\sqrt{\mu\rho_\mathrm{i}}\right)^2}\\ &= \frac{P_m(\kappa_\mathrm{e}a)}{\rho_\mathrm{e}\left(\omega^2 - \omega_\mathrm{Ae}^2\right) - \left(\rho_\mathrm{i}\Omega^2 - A^2/\mu\right)P_m(\kappa_\mathrm{e}a)},\end{aligned} \quad (10)$$

where

$$F_m(\kappa_\mathrm{i}a) = \frac{\kappa_\mathrm{i}a I_m'(\kappa_\mathrm{i}a)}{I_m(\kappa_\mathrm{i}a)} \quad \text{and} \quad P_m(\kappa_\mathrm{e}a) = \frac{\kappa_\mathrm{e}a K_m'(\kappa_\mathrm{e}a)}{K_m(\kappa_\mathrm{e}a)}.$$

In above expressions, the prime means differentiation of the Bessel functions with respect to their arguments,

$$\begin{aligned}\kappa_\mathrm{i}^2 &= k_z^2\left[1 - 4\left(\frac{\sigma\Omega + A\omega_\mathrm{Ai}/\sqrt{\mu\rho_\mathrm{i}}}{\sigma^2 - \omega_\mathrm{Ai}^2}\right)^2\right] \quad \text{and}\\ \kappa_\mathrm{e}^2 &= k_z^2\left[1 - (\omega/\omega_\mathrm{Ae})^2\right]\end{aligned}$$

are the squared wave amplitude attenuation coefficients in the jet and its environment, in which

$$\omega_\mathrm{Ai} = \left(\frac{m}{r}B_{\mathrm{i}\phi} + k_z B_{\mathrm{i}z}\right)/\sqrt{\mu\rho_\mathrm{i}} \quad \text{and} \quad \omega_\mathrm{Ae} = k_z B_\mathrm{e}/\sqrt{\mu\rho_\mathrm{e}}$$

are the local Alfvén frequencies in both media, and

$$\sigma = \omega - \frac{m}{r}U_\phi - k_z U_z$$

is the Doppler-shifted angular wave frequency in the jet. We note that in the case of incompressible coronal plasma (Zaqarashvili et al., 2015), $\kappa_\mathrm{e} = k_z$, because at an incompressible environment the argument of the modified Bessel function of second kind, K_m, and its derivative, K_m', is $k_z a$.

The basic MHD equations for an ideal cool plasma are, generally, the same as the set of Equations (4–8) with Equation (6) replaced by the continuity equation

$$\frac{\partial\rho_1}{\partial t} = -\nabla\cdot(\rho_0\boldsymbol{v}_1 + \rho_1\boldsymbol{U}) = 0.$$

TABLE 1 | Jets physical parameters derived from observational data.

Kind of jet	**$B_{\rm e}$ (G)**	**$n_{\rm e}$ ($\times 10^9$ cm^{-3})**	**$n_{\rm i}$ ($\times 10^9$ cm^{-3})**	**$T_{\rm e}$ (MK)**	**$T_{\rm i}$ (MK)**	**$\beta_{\rm e}$**	**$\beta_{\rm i}$**
Standard coronal hole	3.0	0.90	1.00	1.00	1.6	0.348	2.079
Blowout coronal hole	3.0	0.15	0.17	2.00	1.7	0.116	0.115
Filament eruption	6.0	4.02	4.65	2.14	2.0	0.831	17.24
Macrospicule	5.0	0.10	1.00	1.00	0.5	0.139	2.248

Recall that for cold plasmas the total pressure reduces to the magnetic pressure only, that is $p_{\rm t} = B_1^2/2\mu$, the z component of the velocity perturbation is zero, i.e., $\boldsymbol{v}_1 = (v_{1r}, v_{1\phi}, 0)$, while $\boldsymbol{B}_1 = (B_{1r}, B_{1\phi}, B_{1z})$. The above equation, which defines the density perturbation, is not used in the derivation of the wave dispersion relation because we are studying the propagation and stability of Alfvén-wave-like perturbations of the fluid velocity and magnetic field. Following the standard scenario for deriving the MHD wave dispersion relation (Zhelyazkov and Chandra, 2018), we finally arrive at:

$$\frac{\left(\sigma^2-\omega_{\rm Ai}^2\right)F_m(\kappa_{\rm i}^{\rm c}a)-2m\left(\sigma\Omega+A\omega_{\rm Ai}/\sqrt{\mu\rho_{\rm i}}\right)}{\rho_{\rm i}\left(\sigma^2-\omega_{\rm Ai}^2\right)^2-4\rho_{\rm i}\left(\sigma\Omega+A\omega_{\rm Ai}/\sqrt{\mu\rho_{\rm i}}\right)^2} = \frac{P_m(\kappa_{\rm e}^{\rm c}a)}{\rho_{\rm e}\left(\omega^2-\omega_{\rm Ae}^2\right)-\left(\rho_{\rm i}\Omega^2-A^2/\mu\right)P_m(\kappa_{\rm e}^{\rm c}a)}, \qquad (11)$$

where

$$F_m(\kappa_{\rm i}^{\rm c}a) = \frac{\kappa_{\rm i}^{\rm c}aI_m'(\kappa_{\rm i}^{\rm c}a)}{I_m(\kappa_{\rm i}^{\rm c}a)} \quad \text{and} \quad P_m(\kappa_{\rm e}^{\rm c}a) = \frac{\kappa_{\rm e}^{\rm c}aK_m'(\kappa_{\rm e}^{\rm c}a)}{K_m(\kappa_{\rm e}^{\rm c}a)}.$$

Here, the wave attenuation coefficient in the internal medium has the form

$$\kappa_{\rm i}^{\rm c} = k_z\left\{1-4\left(\frac{\sigma\Omega+A\omega_{\rm Ai}/\sqrt{\mu\rho_{\rm i}}}{\sigma^2-\omega_{\rm Ai}^2}\right)^2\right\}^{1/2}\left(1-\frac{\sigma^2}{\omega_{\rm Ai}^2}\right)^{1/2},$$

while that in the environment, with $\Omega = 0$ and $A = 0$, is given by

$$\kappa_{\rm e}^{\rm c} = k_z\left(1-\frac{\omega^2}{\omega_{\rm Ae}^2}\right)^{1/2}.$$

Note that (i) both dispersion relations, (10) and (11), have similar forms—the difference is in the expressions for the wave attenuation coefficient inside the jet, namely $\kappa_{\rm i}^{\rm c} = \kappa_{\rm i}\left[1-\sigma^2/\omega_{\rm Ai}^2\right]^{1/2}$; and (ii) the wave attenuation coefficients in the environments are not surprisingly the same, that is, $\kappa_{\rm e}^{\rm c} = \kappa_{\rm e} \equiv \left[1-\omega^2/\omega_{\rm Ae}^2\right]^{1/2}$.

4. NUMERICAL SOLUTIONS, WAVE DISPERSION, AND GROWTH RATE DIAGRAMS

In studying at which conditions the high ($m \geqslant 2$) MHD modes in a jet–coronal plasma system become unstable, that is, all the perturbations to grow exponentially in time, we have to consider the wave angular frequency, ω, as a complex quantity: $\omega \equiv {\rm Re}(\omega) + {\rm i}\,{\rm Im}(\omega)$ in contrast to the wave mode number, m, and propagating wavenumber, k_z, which are real quantities. The ${\rm Re}(\omega)$ is responsible for the wave dispersion while the ${\rm Im}(\omega)$ yields the wave growth rate. In the numerical task for finding the complex solutions to the wave dispersion relation (10) or (11), it is convenient to normalize all velocities with respect to the Alfvén speed inside the jet, defined as $v_{\rm Ai} = B_{\rm iz}/\sqrt{\mu\rho_{\rm i}}$, and the lengths with respect to a. Thus, we have to search the real and imaginary parts of the non-dimensional wave phase velocity, $v_{\rm ph} = \omega/k_z$, that is, ${\rm Re}(v_{\rm ph}/v_{\rm Ai})$ and ${\rm Im}(v_{\rm ph}/v_{\rm Ai})$ as functions of the normalized wavenumber $k_z a$. The normalization of the other quantities like the local Alfvén and Doppler-shifted frequencies alongside the Alfvén speed in the environment, $v_{\rm Ae} = B_{\rm e}/\sqrt{\mu\rho_{\rm e}}$, requires the usage of both twist parameters, ε_1 and ε_2, and also of the magnetic fields ratio, $b = B_{\rm e}/B_{\rm iz}$. The non-dimensional form of the jet axial velocity, U_z, is given by the Alfvén Mach number $M_{\rm A} = U_z/v_{\rm Ai}$. Another important non-dimensional parameter is the density contrast between the jet and its surrounding medium, $\eta = \rho_{\rm e}/\rho_{\rm i}$. Hence, the input parameters in the numerical task of finding the solutions to the transcendental Equation (10) or (11) (in complex variables) are: m, η, ε_1, ε_2, b, and $M_{\rm A}$. Zaqarashvili et al. (2015) have established that KHI in an untwisted ($A = 0$) rotating flux tube with negligible longitudinal velocity can occur if

$$\frac{a^2\Omega^2}{v_{\rm Ai}^2} > \frac{1+\eta}{1+|m|\eta}\,\frac{(k_z a)^2}{|m|-1}(1+b^2). \qquad (12)$$

This inequality says that each MHD wave with mode number $m \geqslant 2$, propagating in a rotating jet can become unstable. This instability condition can be used also in the cases of slightly twisted spinning jets, provided that the magnetic field twist parameter, ε_1, is a number lying in the range of 0.001–0.005, simply because the numerical solutions, for example, to Equation (10) show that practically there is no difference between the instability ranges at $\varepsilon_1 = 0$, and at 0.001 or 0.005. An important step in our study is the supposition that the deduced from observations jet axial velocity, U_z, is the threshold speed for the KHI occurrence. Then, for fixed values of m, η, $U_\phi = \Omega a$, $v_{\rm Ai}$, and b, the inequality (12) can be rearranged to define the upper limit of the instability range on the $k_z a$-axis

$$(k_z a)_{\rm rhs} < \left\{\left(\frac{U_\phi}{v_{\rm Ai}}\right)^2\frac{1+|m|\eta}{1+\eta}\,\frac{|m|-1}{1+b^2}\right\}^{1/2}. \qquad (13)$$

According to the above inequality, the KHI can occur for nondimensional wavenumbers $k_z a$ less than $(k_z a)_{\rm rhs}$. On the other hand, one can talk for instability if the unstable wavelength, $\lambda_{\rm KH} = 2\pi/k_z$, is shorter than the height of the jet, H, which means that the lower limit of the instability region is given by:

$$(k_z a)_{\rm lhs} > \frac{\pi\,\Delta\ell}{H}, \tag{14}$$

where $\Delta\ell$ is the jet width. Hence, the instability range in the $k_z a$-space is $(k_z a)_{\rm lhs} < k_z a < (k_z a)_{\rm rhs}$. Note that the lower limit, $(k_z a)_{\rm lhs}$, is fixed by the width and height of the jet, while the upper limit, $(k_z a)_{\rm rhs}$, depends on several jet–environment parameters. At fixed U_ϕ, $v_{\rm Ai}$, η, and b, the $(k_z a)_{\rm rhs}$ is determined by the MHD wave mode number, $|m|$. As seen from inequality (13), with increasing the m, that limit shifts to the right, that is, the instability range becomes wider. The numerical solutions to the wave dispersion relation (10) confirm this and for given m one can obtain a series of unstable wavelengths, $\lambda_{\rm KH} = \pi\,\Delta\ell/k_z a$, as the shortest one takes place at $k_z a \approx (k_z a)_{\rm rhs}$. For relatively small mode numbers, when even the shortest unstable wavelengths turn out to be a few tens megameters, that could hardly be associated with the observed KH ones. As observations show, the KHI vortex-like structures running at the boundary of the jet, have the size of the width or radius of the flux tube (see, for instance, **Figure 1** in Zhelyazkov et al., 2018). Therefore, we have to look for such an m, whose instability range would accommodate the expected unstable wavelength presented by its nondimensional wavenumber, $k_z a = \pi\,\Delta\ell/\lambda_{\rm KH}$. An estimation of the required mode number for an $\varepsilon_1 = 0.005$-rotating flux tube can be obtained by presenting the instability criterion (12) in the form

$$\eta|m|^2 + (1-\eta)|m| - 1 - \frac{(k_z a)^2(1+\eta)(1+b^2)}{(U_\phi/v_{\rm Ai})^2} > 0. \tag{15}$$

We will use this inequality for obtaining the optimal m for each of the studied jets by specifying the value of that $k_z a$ (along with the other aforementioned input parameters) which corresponds to the expected unstable wavelength $\lambda_{\rm KH}$.

4.1. Kelvin–Helmholtz Instability in a Standard Polar Coronal Hole Jet

Chen et al. (2012) observationally studied the jet event of 2010 August 21, which occurred in the coronal hole region, close to the north pole of the Sun. **Figure 1** presents the jet's evolution in AIA 304 Å. The jet started around 06:07 UT, reached its maximum height around 06:40 UT. During the evolution of the jet between 06:32 and 06:38 UT, small scale moving blobs appeared on the right boundary. We interpret these blobs, shown by arrows in **Figure 1**, as evidence of KHI. By tracking six identified moving features in the jet, Chen et al. (2012) found that the plasma moved at an approximately constant speed along the jet's axis. Inferred from linear and trigonometric fittings to the axial and transverse heights of the six tracks, the authors have found that the mean values of the axial velocity, U_z, transfer/rotational velocity, U_ϕ, angular speed, Ω, rotation period, T, and rotation radius, a, are 114 $\rm km\,s^{-1}$, 136 $\rm km\,s^{-1}$, $0.81^\circ \rm s^{-1}$ (or 14.1×10^{-3} $\rm rad\,s^{-1}$), 452 s, and 9.8×10^3 km, respectively. The height of the jet is evaluated as $H = 179$ Mm.

It seems reasonable the shortest unstable wavelength, $\lambda_{\rm KH}$, to be equal to 10 Mm (approximately half of the jet width, $\Delta\ell = 19.6$ Mm), which implies that its position on the $k_z a$ one-dimensional space is $k_z a = 6.158$. The input parameters, necessary to find out that MHD wave mode number, whose instability range will contain the nondimensional wavenumber of 6.158, using inequality (15), are accordingly (see **Table 1**) $\eta = 0.9$, $b = 1.834$, $v_{\rm Ai} = 112.75$ $\rm km\,s^{-1}$, and $U_\phi = 136$ $\rm km\,s^{-1}$ (We note, that the values of b and $v_{\rm Ai}$ were obtained with the help of Equation (3) assuming that the magnetic field twist is $\varepsilon_1 = 0.005$). With these entry data, from inequality (15) one obtains that $|m| > 15$ should provide the required instability region or window. The numerical solutions to Equation (10) show that this value of m is overestimated—an $m = 11$ turns out to be perfect for the case. The discrepancy between the predicted and computed value of $|m|$ is not surprising because inequality (15) yields only an indicative value. The input parameters for finding the solutions to the dispersion Equation (10) are as follows: $m = 11$, $\eta = 0.9$, $\varepsilon_1 = 0.005$, $\varepsilon_2 = 1.2$, $b = 1.834$, and $M_{\rm A} = 1.01$ (=114/112.75). The results of computations are graphically presented in **Figure 2**. From that figure, one can obtain the normalized wave phase velocity, $\mathrm{Re}(v_{\rm ph}/v_{\rm Ai})$, and the normalized growth rate, $\mathrm{Im}(v_{\rm ph}/v_{\rm Ai})$, of the unstable $\lambda_{\rm KH} = 10$ Mm wave, both read at the purple cross points. From the same plot, one can find the instability characteristics at another wavelength, precisely $\lambda_{\rm KH} = 12$ Mm, whose position on the $k_z a$-axis is fixed at $k_z a = 5.131$. The values of nondimensional wave phase velocity and growth rate can be read from the green cross points. The KHI wave growth rate, $\gamma_{\rm KH}$, growth time, $\tau_{\rm KH} = 2\pi/\gamma_{\rm KH}$, and wave velocity, $v_{\rm ph}$, in absolute units, estimated from the plots in **Figure 2**, for the two wavelengths, are

$$\gamma_{\rm KH} \cong 23.09 \times 10^{-3}~\rm s^{-1}, \quad \tau_{\rm KH} \cong 4.5~min, \quad v_{\rm ph} \cong 178~km\,s^{-1}, \quad \text{for } \lambda_{\rm KH} = 10~\rm Mm,$$

and

$$\gamma_{\rm KH} \cong 50.65 \times 10^{-3}~\rm s^{-1}, \quad \tau_{\rm KH} \cong 2.1~min, \quad v_{\rm ph} \cong 202~km\,s^{-1}, \quad \text{for } \lambda_{\rm KH} = 12~\rm Mm.$$

Let us recall that the value of the Alfvén speed used in the normalization is $v_{\rm Ai} = 112.75$ $\rm km\,s^{-1}$. We see that the two wave phase velocities are slightly super-Alfvénic and when moving along the $k_z a$-axis to the left, the normalized wave velocity becomes higher. If we fix a $k_z a$-position near the lower limit of the unstable region, $(k_z a)_{\rm lhs} = 0.344$, say, at $k_z a = 0.513$, which means $\lambda_{\rm KH} = 120$ Mm, the KHI characteristics obtained from the numerical solutions to Equation (10) are $\tau_{\rm KH} = 1.4$ min and $v_{\rm ph} = 1\,473$ $\rm km\,s^{-1}$, respectively. As we have discussed in Zhelyazkov et al. (2018), "the KHI growth time could be estimated from the temporal evolution of the blobs in their initial stage and it was found to be about 2–4 min," so the instability developing times of 2.1 and 4.5 min obtained from our plots are in good agreement with the observations.

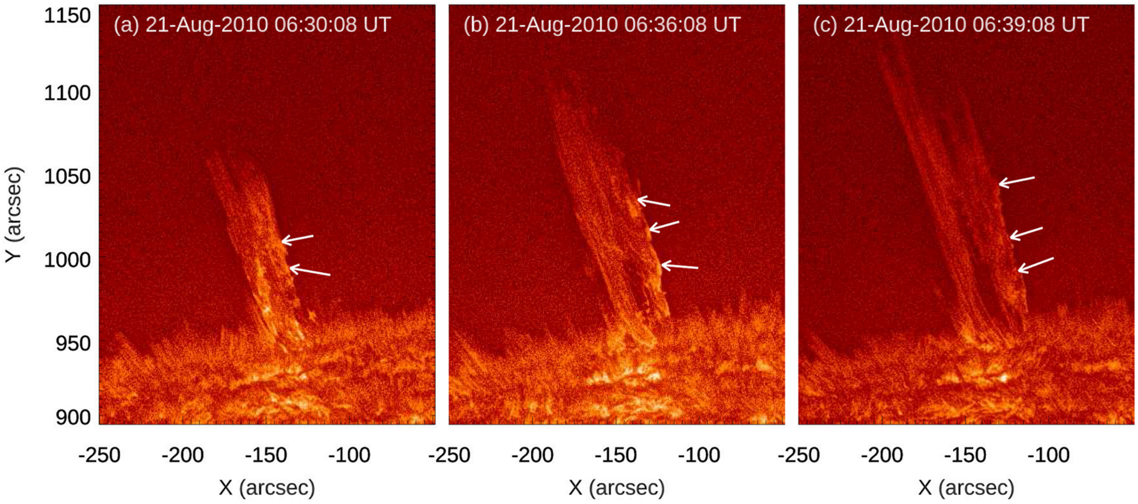

FIGURE 1 | AIA 304 Å images showing the detailed evolution of the jet observed on 2010 August 21. The small moving blobs on the right side boundary of the jet as indicated by white arrows, could be produced by a KHI.

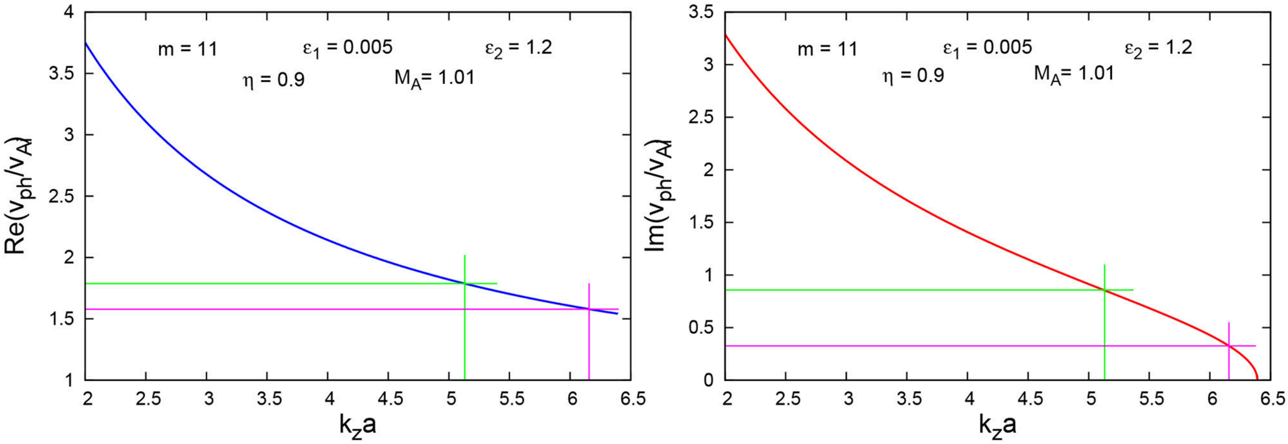

FIGURE 2 | (Left) Dispersion curve of the $m = 11$ MHD mode propagating along a twisted incompressible coronal hole jet at $\eta = 0.9$, $b = 1.834$, $M_\mathrm{A} = 1.01$, $\varepsilon_1 = 0.005$, and $\varepsilon_2 = 1.2$. (Right) Normalized growth rate curve of the $m = 11$ MHD mode computed at the same input parameters as in the left panel. The crosses of purple and green lines yield the normalized values of the wave phase velocity and the wave growth rate at the two unstable wavelengths of 10 and 12 Mm, respectively.

A specific property of the instability $k_z a$-ranges is that for a fixed mode number, m, their widths depend upon ε_1 and with increasing the value of ε_1, the instability window becomes narrower and at some critical ε_1 its width equals zero. In our case that happens with $\varepsilon_1^\mathrm{cr} = 0.653577$ at $(k_z a)_\mathrm{lhs} = 0.344$. In **Figure 3**, curves of dimensionless v_ph and γ_KH have been plotted for several ε_1 values. Note that each larger value of ε_1 implies an increase in $B_{\mathrm{i}\phi}$. But that increase in $B_{\mathrm{i}\phi}$ requires an increase in B_iz too, in order the total pressure balance Equation (3) to be satisfied under the condition that the hydrodynamic pressure term and the environment total pressure are fixed. The increase in B_iz (and in the full magnetic field B_i) implies a decrease both in the magnetic field ratio, b, and in the Alfvén Mach number, M_A. Thus, gradually increasing the magnetic field twist ε_1 from 0.005 to 0.653577, we get a series of dispersion and growth rate curves with progressively diminishing parameters b and M_A. The red growth rate curve in the right panel of **Figure 3** has been obtained for $\varepsilon_1^\mathrm{cr} = 0.653577$ with $M_\mathrm{A} = 0.7652$ and it visually fixes the lower limit of all other instability windows. The azimuthal magnetic field $B_{\mathrm{i}\phi}^\mathrm{cr}$ that stops the KHI, computed at $B_\mathrm{i} = 2.58$ G, is equal to 1.4 G.

4.2. Kelvin–Helmholtz Instability in a Blowout Polar Coronal Hole Jet

Young and Muglach (2014a) observed a small blowout jet at the boundary of the south polar coronal hole on 2011 February 8 at around 21:00 UT. The evolution of jet observed by the AIA is displayed in **Figure 4**. The jet activity was between 20:50 and 21:15 UT. This coronal hole is centered around $x = -400$ arcsec, $y = -400$ arcsec. The jet has very broad and faint

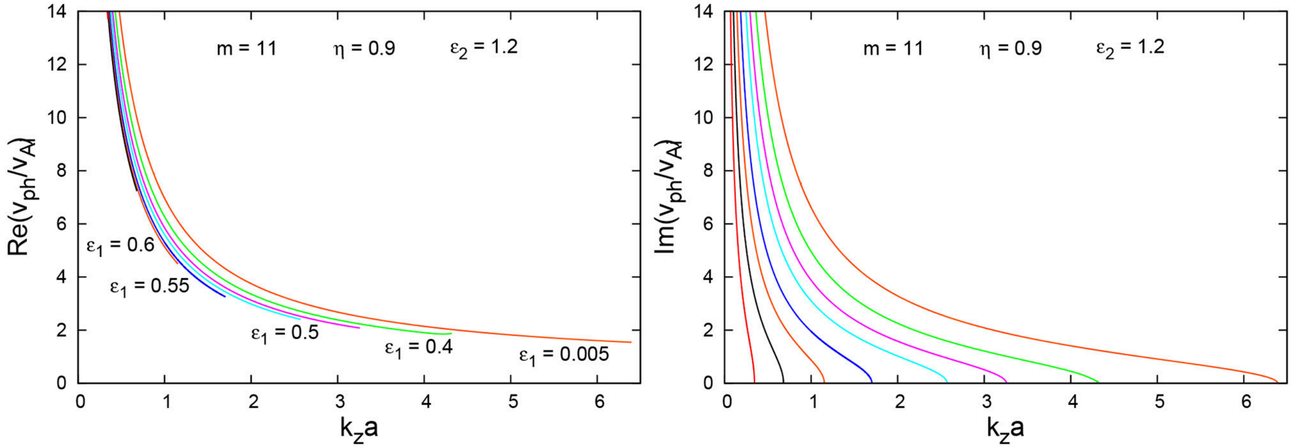

FIGURE 3 | (Left) Dispersion curves of the unstable $m = 11$ MHD mode propagating along a twisted incompressible jet in a coronal hole at $\eta = 0.9$, $\varepsilon_2 = 1.2$, and the following values of ε_1 (from right to left): 0.005, 0.4, 0.5, 0.55, 0.6, 0.625, 0.645, and 0.653577 (red curve in the right plot). Alfvén Mach numbers for these curves are, respectively 1.01, 0.93, 0.88, 0.84, 0.81, 0.79, 0.77, and 0.7653. (Right) Growth rates of the unstable $m = 11$ mode for the same input parameters. The azimuthal magnetic field that corresponds to $\varepsilon_1^{\rm cr} = 0.653577$ (the instability window with zero width) and stops the KHI onset is equal to 1.4 G.

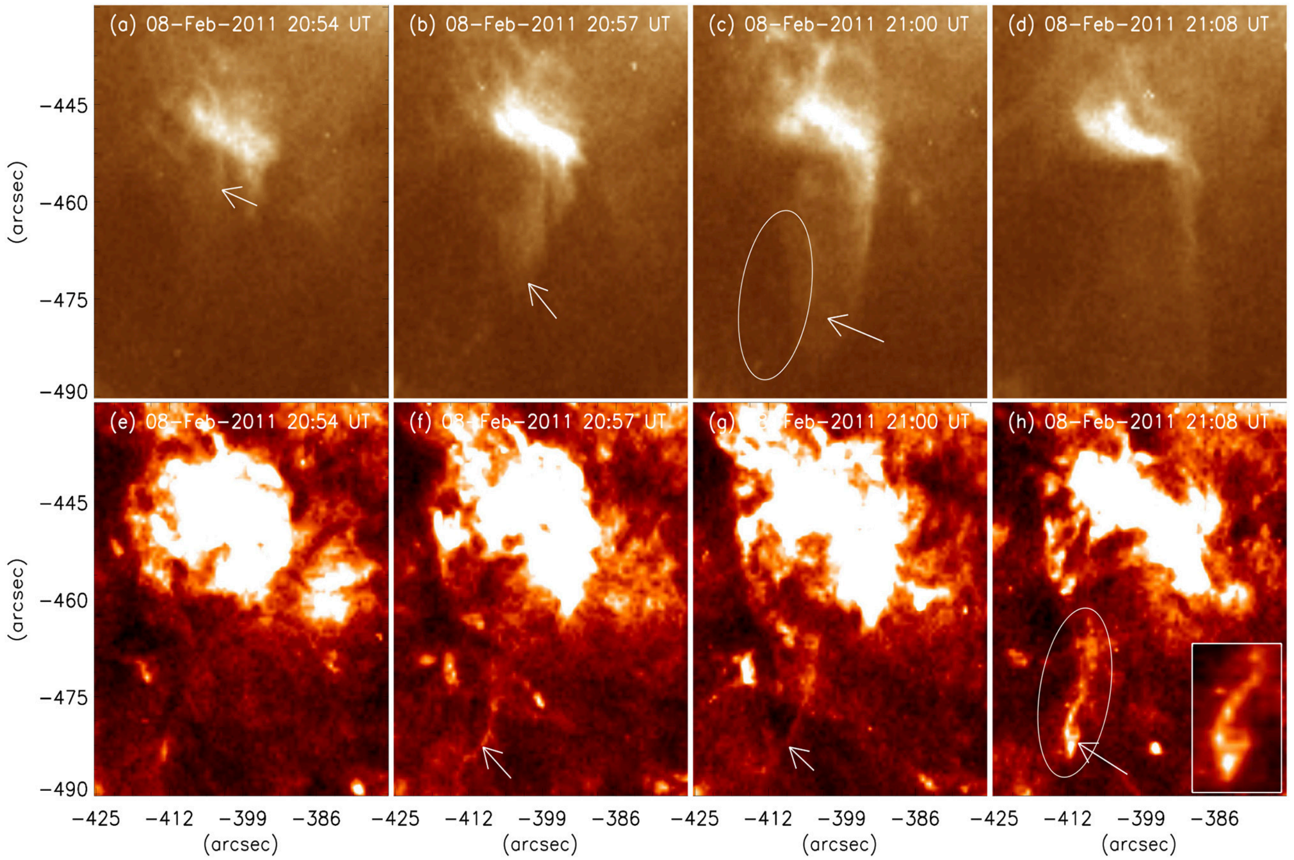

FIGURE 4 | AIA 193 top **(a–d)** and 304 Å bottom **(e–h)** images showing the evolution of the jet observed on 2011 February 8 marked by white arrows could be produced by KHI. For the better visibility of the jet, we have saturated the image at the foot-point. The ellipse in the **(c,h)** represents the east edge of the jets. In 304 Å at ∼21:08 UT we have observed the blob structures at the eastern boundary. The enlarged view of the blobs is shown in the inset in **(h)**.

structure and is ejected in the south direction. We could see the evolution of jet in the AIA 193 Å clearly. However, in AIA 304 Å the whole jet is not visible. Moreover, we observe the eastern boundary of the jet in AIA 304 Å. During its evolution in 304 Å we found the blob structures at the jet boundary. These blobs could be due to the KHI as reported in previous observations (see for example Zhelyazkov et al., 2018). At the jet initiation/base site, we observed the coronal hole bright points. These bright points are the results of coronal low-laying loops reconnection (Madjarska, 2019).

According to Young and Muglach (2014a) estimations, the jet is extended for $H = 30$ Mm with a width of $\Delta\ell = 15$ Mm. The jet duration is 25 min and the bright point is not significantly disrupted by the jet occurrence. The jet n is $n_\mathrm{i} = 1.7 \times 10^8$ cm^{-3}, while that of the surrounding coronal plasma we assume to be $n_\mathrm{e} = 1.5 \times 10^8$ cm^{-3}. The jet temperature is $T_\mathrm{i} = 1.7$ MK and the environment one is $T_\mathrm{e} = 2.0$ MK. The jet axial velocity is $U_z = 250$ km s^{-1} and the rotational one is $U_\phi = 90$ km s^{-1}. Assuming a magnetic field twist $\varepsilon_1 = 0.025$ and $B_\mathrm{e} = 3$ G, from Equation (3), we obtain $\eta = 0.882$, $v_\mathrm{Ai} = 494.7$ km s^{-1} (Alfvén speed in the environment is $v_\mathrm{Ae} = 534.0$ km s^{-1}), and $b = 1.014$. We note, that while in the derivation of Equation (11) we have neglected the thermal pressures, here, in using Equation (3), we kept them. If we anticipate that the shortest unstable wavelength is equal to 7.5 Mm (with $k_z a = 2\pi$), the mode number m whose instability range would accommodate the aforementioned wavelength, according to inequality (15) must be at least $|m| = 71$. The numerics show that the suitable m is $|m| = 65$. Thus, the input parameters for obtaining the numerical solutions to Equation (11) are: $m = 65$, $\eta = 0.882$, $\varepsilon_1 = 0.025$, $\varepsilon_2 = 0.36$

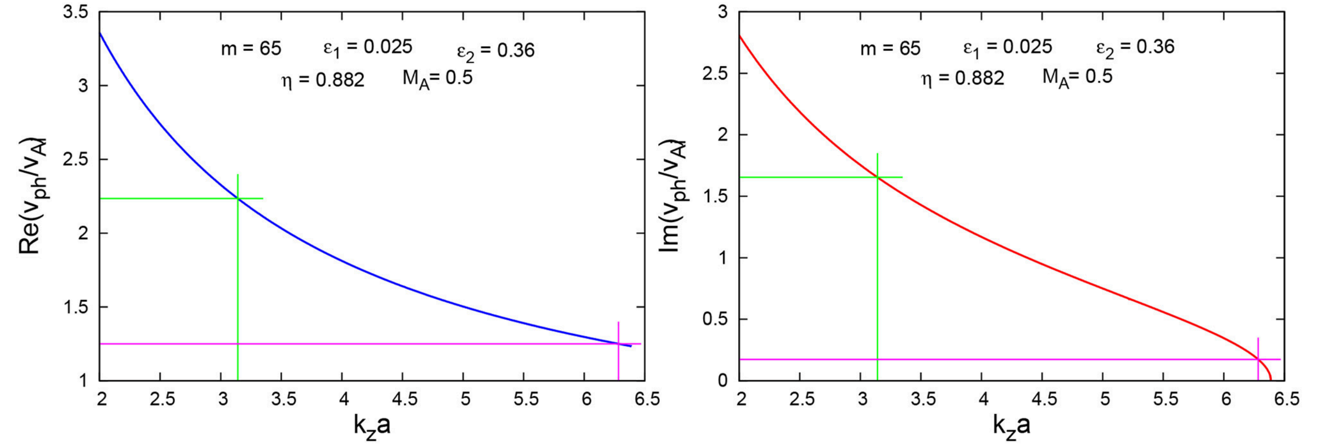

FIGURE 5 | (Left) Dispersion curve of the $m = 65$ MHD mode propagating along a twisted cool coronal hole jet at $\eta = 0.882$, $b = 1.014$, $M_\mathrm{A} = 0.5$, $\varepsilon_1 = 0.025$, and $\varepsilon_2 = 0.36$. (Right) Normalized growth rate curve of the $m = 65$ MHD mode computed at the same input parameters as in the left panel. The crosses of purple and green lines yield the normalized values of the wave phase velocity and the wave growth rate at the two unstable wavelengths of 7.5 and 15 Mm, respectively.

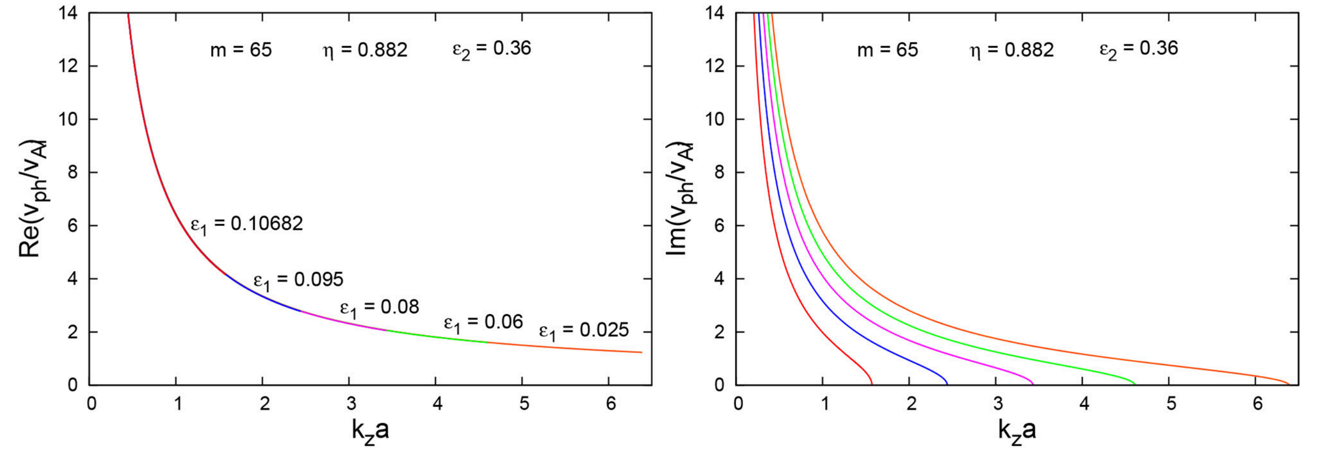

FIGURE 6 | (Left) Dispersion curves of the unstable $m = 65$ MHD mode propagating along a twisted cool jet in a coronal hole at $\eta = 0.882$, $\varepsilon_2 = 0.36$, and the following values of ε_1 (from right to left): 0.025, 0.06, 0.08, 0.095, and 0.10682 (red curve in the right plot). Alfvén Mach numbers for these curves are, respectively 0.505, 0.505, 0.504, 0.503, and 0.5026. (Right) Growth rates of the unstable $m = 65$ mode for the same input parameters. The azimuthal magnetic field that corresponds to $\varepsilon_1^\mathrm{cr} = 0.10682$ (the instability window with zero width) and stops the KHI onset is equal to 0.3 G.

(=90/250), $b = 1.014$, and $M_A = 0.505$ ($\cong$250.0/494.7). The results are illustrated in **Figure 5**. Along with $\lambda_{KH} = 7.5$ Mm (purple lines), we have calculated the KHI characteristics also for $\lambda_{KH} = 15$ Mm (at $k_z a = \pi$) (green lines), and they are

$$\gamma_{KH} = 72.0 \times 10^{-3}\ \text{s}^{-1}, \quad \tau_{KH} \cong 1.5\ \text{min}, \quad v_{ph} \cong 618\ \text{km s}^{-1}, \quad \text{for } \lambda_{KH} = 7.5\ \text{Mm},$$

and

$$\gamma_{KH} \cong 342.75 \times 10^{-3}\ \text{s}^{-1}, \quad \tau_{KH} \cong 0.3\ \text{min}, \quad v_{ph} \cong 1106\ \text{km s}^{-1}, \quad \text{for } \lambda_{KH} = 15\ \text{Mm}.$$

It is seen from the left panel that the unstable $m = 65$ MHD waves are generally super-Alfvénic. Since the instability developing times of the $m = 65$ mode are relatively short, that is, much less than the jet lifetime of 25 min, we can conclude that the KHI in this jet is relatively fast.

With the increase in the parameter ε_1, the instability region, as seen from the right panel of **Figure 6**, becomes narrower and at the lower limit $(k_z a)_{\text{lhs}} = \pi/2$ with $\varepsilon_1^{\text{cr}} = 0.10682$ and $M_A = 0.5026$ its width is equal to zero. In other words, there is no longer instability. Therefore, the critical azimuthal magnetic field that suppresses the KHI is $B_{i\phi}^{\text{cr}} \cong 0.3$ G—obviously a relatively small value.

4.3. Kelvin–Helmholtz Instability in a Jet Emerging From a Filament Eruption

Filippov et al. (2015) observationally studied three jets events originated from the active region NOAA 11715 (located on the

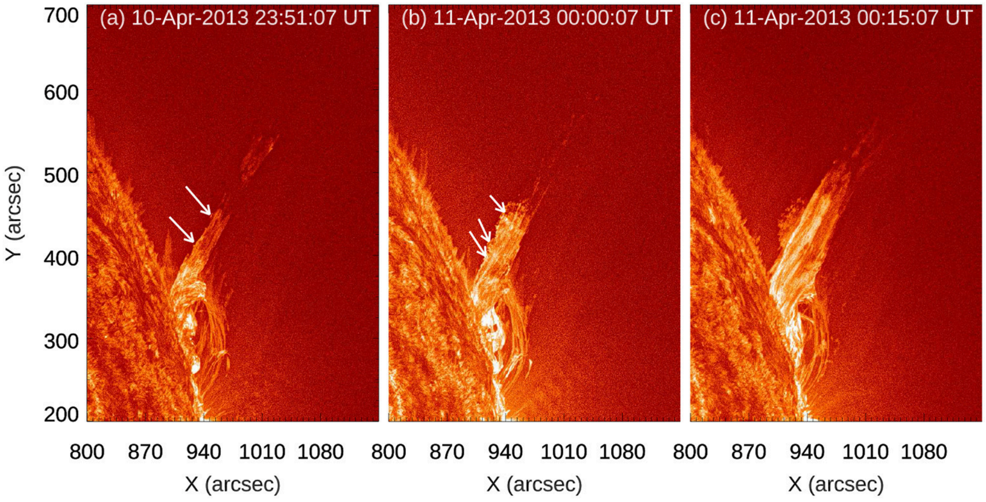

FIGURE 7 | Evolution of the jet associated with a filament eruption observed on 2013 April 10–11 in AIA 304 Å. The structure shown by arrows can be due to the KHI.

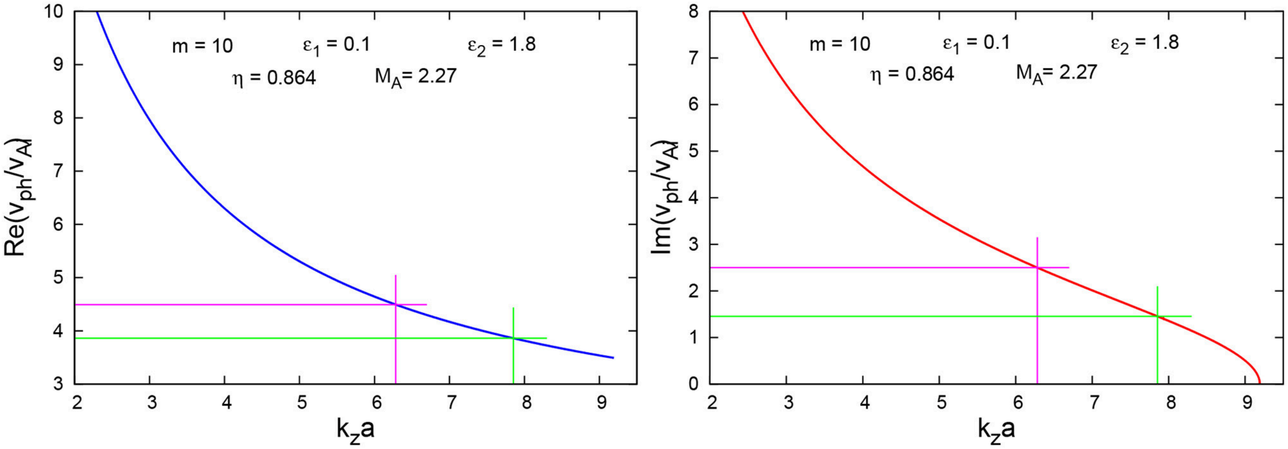

FIGURE 8 | (Left) Dispersion curve of the $m = 10$ MHD mode propagating along a twisted incompressible emerging from a filament eruption jet at $\eta = 0.864$, $b = 4.36$, $M_A = 2.27$, $\varepsilon_1 = 0.1$, and $\varepsilon_2 = 1.8$. (Right) Normalized growth rate curve of the $m = 10$ MHD mode computed at the same input parameters as in the left panel. The crosses of green and purple lines yield the normalized values of the wave phase velocity and the wave growth rate at the two unstable wavelengths of 12 and 15 Mm, respectively.

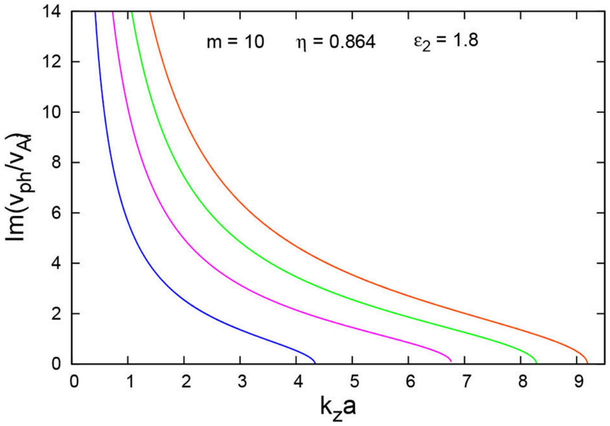

FIGURE 9 | Growth rate curves of the unstable $m = 10$ MHD mode propagating along a twisted incompressible emerging from a filament eruption jet at $\eta = 0.864$, $\varepsilon_2 = 1.8$, and the following values of ε_1 (from right to left): 0.1 (orange), 0.6 (green), 0.8 (purple), and 0.9 (blue).

west limb) on 2013 April 10–11. These authors claim that the jets originated from the emergence of a filament having a null-point (inverted Y) topology. We have considered the second event described in that paper for a detailed study. The jet electron number density, $n_{\rm i}$, and electron temperature, $T_{\rm i}$, both listed in **Table 1**, have been calculated by us using the techniques elaborated by Aschwanden et al. (2013). This technique requires the data from the six 94, 131, 171, 193, 211, and 335 Å AIA/*SDO* EUV channels. In addition to the electron number densities and electron temperatures in the jet and surrounding plasma, we have also estimated the jet width as $\Delta\ell \approx 30$ Mm, its height as $H = 180$ Mm, and have found the jet lifetime to be 30 min. The two important parameters, axial and azimuthal velocities, according to the observations, are $U_z = 100$ and $U_\phi = 180$ km s^{-1}, respectively. The time evolution of the jet in AIA 304 Å is shown in **Figure 7** and we have observed vortex type structures in the eastern side of the jet, which are indicated by arrows. These structures implicitly indicate for occurrence of KHI.

With the typical n and $T_{\rm e}$ (see **Table 1**), rotating velocity $U_\phi = 180$ km s^{-1}, assumed $B_{\rm e} = 6$ G, and $\varepsilon_1 = 0.1$, Equation (3) yields $\eta = 0.864$, $b = 4.36$, and $v_{\rm Ai} = 44.00$ km s^{-1} (for comparison, the Alfvén speed in the environment is $v_{\rm Ae} = 206.3$ km s^{-1}). We note that the choice of ε_1 was made taking into account the fact that the inclination of the treads of the jet in the event on 2013 April 10, detected by *SDO*/AIA, yields a relationship between $B_{{\rm i}\phi}$ and $B_{{\rm i}z}$, which was evaluated as $\varepsilon_1 \approx 0.1$. If we assume that the shortest unstable wavelength is $\lambda_{\rm KH} = 12$ Mm, which is located at $k_z a = 2.5\pi$ on the $k_z a$-axis, from inequality (15) we find that a MHD wave with $|m| = 12$ would provide an instability region, accommodating the non-dimensional $k_z a = 2.5\pi$. It turns out that a suitable mode number is $m = 10$. The wave dispersion and growth rate diagrams are shown in **Figure 8**. In that instability range one can also find the instability characteristics at $k_z a = 2\pi$, which corresponds to $\lambda_{\rm KH} = 15$ Mm. The input parameters for finding the solutions to Equation (10) are: $m = 10$, $\eta = 0.864$, $\varepsilon_1 = 0.1$, $\varepsilon_2 = 1.8$, $b = 4.36$, and $M_{\rm A} = 2.27$ (=100/44) The KHI parameters at the aforementioned wavelengths are as follows:

$$\gamma_{\rm KH} \cong 33.51 \times 10^{-3}\ {\rm s}^{-1},\quad \tau_{\rm KH} \cong 3.1\ {\rm min},\quad v_{\rm ph} \cong 170\ {\rm km\,s}^{-1},\quad {\rm for}\ \lambda_{\rm KH} = 12\ {\rm Mm},$$

and

$$\gamma_{\rm KH} \cong 46.06 \times 10^{-3}\ {\rm s}^{-1},\quad \tau_{\rm KH} \cong 2.3\ {\rm min},\quad v_{\rm ph} \cong 198\ {\rm km\,s}^{-1},\quad {\rm for}\ \lambda_{\rm KH} = 15\ {\rm Mm}.$$

The KHI developing or growth times seem reasonable and the wave phase velocities are super-Alfvénic ones.

It is intriguing to see how the width of the instability range will shorten as the magnetic field twist ε_1 is increased. Our numerical computations indicate that for a noticeable contraction of the instability window one should change the magnitude of ε_1 with relatively large steps. The results of such computations are illustrated in **Figure 9**. It is necessary to underline that at values of ε_1 close to 1, (i) $\beta_{\rm i}$ becomes <1 and the jet has to be treated as a cool medium, which implies a new wave dispersion relation and probably a higher wave mode number, m; (ii) one cannot use $\varepsilon_1 > 1$, because in that case the instability is of another kind, namely kink instability (Lundquist, 1951; Hood and Priest, 1979; Zaqarashvili et al., 2014). At this "pathological" case, one cannot reach the lower limit of the instability range, $(k_z a)_{\rm lhs} = 0.524$, and consequently we are unable to evaluate that azimuthal magnetic field, $B_\phi^{\rm cr}$, which will stop the KHI onset!

4.4. Kelvin–Helmholtz Instability in a Spinning Macrospicule

As we have mentioned in section 1, Pike and Mason (1998) did a statistical study of the dynamics of solar transition region features, like macrospicules. These features were observed on the solar disk and also on the solar limb by using data from the *Coronal Diagnostic Spectrometer* (CDS) onboard *SOHO*. In addition, in their article, Pike and Mason (1998) discussed the unique CDS observations of a macrospicule first reported by Pike and Harrison (1997) along with their own (Pike and Mason) observations from the *Normal Incidence Spectrometer* (NIS). This spectrometer covers the wavelength range from 307 to 379 Å and that from 513 to 633 Å using a microchannel plate and CCD combination detector. The details of macrospicule events observed near the limb are given in Table 1 in Pike and Mason, 1998, while those of macrospicule events observed on the disk are presented in Table 2. The main finding in the study of Pike and Mason (1998) was the rotation in these features based on the red and blue shifted emission on either side of the macrospicule axes. According to the authors, the detected rotation assuredly plays an important role in the dynamics of the transition region. Using the basic observational parameters obtained by Pike and Mason (1998), Zhelyazkov and Chandra (2019) examined the conditions for KHI rising in the macrospicule. Let us discuss that study as follows.

Our (Zhelyazkov and Chandra, 2019) choice for modeling namely the macrospicule observed on 1997 March 8 at 00:02 UT (see Table 2 in Pike and Mason, 1998) was made taking into account the fact that this macrospicule possesses the basic characteristics of the observed over the years tornado-like jets—the axial velocity of the jet was $U_z = 75\ \mathrm{km\,s^{-1}}$, while its rotating speed, we evaluate to be $U_\phi = 40\ \mathrm{km\,s^{-1}}$. For the other characteristics of the macrospicule such as lifetime, maximum width, average flow velocity, and maximum length or height, we used some average values obtained from a huge number of observations and specified in Kiss et al. (2017) as 16.75 ± 4.5 min, 6.1 ± 4 Mm, $73.14 \pm 25.92\ \mathrm{km\,s^{-1}}$, and 28.05 ± 7.67 Mm, respectively. For our study here, we take the macrospicule width to be $\Delta\ell = 6$ Mm, its height $H = 28$ Mm, and lifetime of the order on 15 min. The basic macrospicule physical parameters (see **Table 1**) with $U_\phi = 40\ \mathrm{km\,s^{-1}}$, $\varepsilon_1 = 0.005$, and $B_\mathrm{e} = 5$ G yield (using Equation 3) $\eta = 0.1$, Alfvén speed $v_\mathrm{Ai} = 60.6\ \mathrm{km\,s^{-1}}$ (while in the surrounding plasma we have $v_\mathrm{Ae} \cong 345\ \mathrm{km\,s^{-1}}$), and $b = 1.798$. The excited MHD mode, whose instability window would contain a $\lambda_\mathrm{KH} = 3$ Mm, is $|m| = 52$. Performing the numerical computations with the input parameters: $m = 52$, $\eta = 0.1$, $\varepsilon_1 = 0.005$, $\varepsilon_2 = 0.53$ (=40/75), $b = 1.798$, and $M_\mathrm{A} = 1.24$ (=75/60.6), we get plots very similar to those pictured in **Figure 2**, which (the plots) allow us to find the KHI characteristics for the two wavelengths of 3 and 5 Mm, exactly

$$\gamma_\mathrm{KH} \cong 48.38 \times 10^{-3}\ \mathrm{s^{-1}},\ \ \tau_\mathrm{KH} \cong 2.2\ \mathrm{min},\ \ v_\mathrm{ph} \cong 361\ \mathrm{km\,s^{-1}},\quad \text{for}\ \ \lambda_\mathrm{KH} = 3\ \mathrm{Mm},$$

and

$$\gamma_\mathrm{KH} \cong 184.8 \times 10^{-3}\ \mathrm{s^{-1}},\ \ \tau_\mathrm{KH} \cong 0.57\ \mathrm{min},\ \ v_\mathrm{ph} \cong 556\ \mathrm{km\,s^{-1}},\quad \text{for}\ \ \lambda_\mathrm{KH} = 5\ \mathrm{Mm}.$$

One observes that at both unstable wavelengths the corresponding phase velocities are supper-Alfvénic. Moreover, the two growth times of 2.2 and ∼0.6 min seem reasonable bearing in mind the fact that the macrospicule lifetime is about 15 min, which implies that the KHI at the selected wavelengths is rather fast. The $B_{\mathrm{i}\phi}^{\mathrm{cr}}$ that suppresses the KHI onset, equals 0.57 G and was calculated with $\varepsilon_1^{\mathrm{cr}} = 0.202085$ and $M_\mathrm{A} = 1.2119$. Our study (Zhelyazkov and Chandra, 2019) shows that a decrease in the background magnetic field to $B_\mathrm{e} = 4.8$ G would require the excitation of MHD wave with mode number $m = 48$, at which the KHI characteristics at the wavelengths of 3 and 5 Mm are very close to those obtained with $m = 52$.

5. SUMMARY AND OUTLOOK

In this article, we have studied the emerging of KHI in four different spinning solar jets (standard and blowout coronal hole jets, jet emerging from a filament eruption, and rotating macrospicule) due to the excitation of high-mode ($m \geqslant 2$) MHD waves traveling along the jets. First and foremost, we model each jet as a vertically moving with velocity $\boldsymbol{U}$ cylindrical twisted magnetic flux tube with radius a. There are four basic steps in the modeling as follows:

- *Topology of jet–environment magnetic and velocity fields* For simplicity, we assume that the plasma densities of the jet and its environment, ρ_i and ρ_e, respectively, are homogeneous. Generally they are different and the density contrast is characterized by the ratio $\rho_\mathrm{e}/\rho_\mathrm{i} = \eta$. The twisted internal magnetic and velocity fields are supposed to be uniform, that is, represented in cylindrical coordinates, (r, ϕ, z), by the vectors $\boldsymbol{B}_\mathrm{i} = (0, B_{\mathrm{i}\phi}(r), B_{\mathrm{i}z})$ and $\boldsymbol{U} = (0, U_\phi(r), U_z)$, where their azimuthal components are considered to be linear functions of the radial position r, *viz.* $B_{\mathrm{i}\phi}(r) = Ar$ and $U_\phi(r) = \Omega r$, where A and Ω (the azimuthal jet velocity) are constants. We note that $B_{\mathrm{i}z}$ and U_z are also constants. It is convenient the twists of the magnetic field and the flow velocity of the jet to be characterized by the two numbers $\varepsilon_1 = B_{\mathrm{i}\phi}(a)/B_{\mathrm{i}z} \equiv Aa/B_{\mathrm{i}z}$ and $\varepsilon_2 = U_\phi(a)/U_z \equiv \Omega a/U_z$, respectively. Note that Ωa is the jet rotational speed U_z. The surrounding coronal or chromospheric plasma is assumed to be immobile and embedded in a constant magnetic field $\boldsymbol{B}_\mathrm{e} = (0, 0, B_\mathrm{e})$. In our study, the density contrast, η, varies from 0.1 to 0.9, the magnetic field twist, ε_1, can have a wide range of magnitudes from 0.005 to 0.95 (it has to be less than 1 in order to avoid the rising of the kink instability), while the velocity twist parameter, ε_2, is fixed by the observationally measured rotational and axial speeds.
- *Listing of the basic physical parameters and determination of plasmas betas* In general, at a fixed density contrast, the plasma beta is controlled by the magnetic field (inside or outside the magnetic flux tube) and the electron temperatures of the jet and surrounding plasma. The values of these physical parameters should satisfy the total pressure balance Equation (3) at all levels (equilibrium and perturbational). Our practice is to fix B_e, and using Equation (3) to determine the internal Alfvén speed defined as $v_\mathrm{Ai} = B_{\mathrm{i}z}/\sqrt{\mu\rho_\mathrm{i}}$. It is worth underlying that the usage of Equation (3) requires the specification of ε_1. In our four cases, for finding the KHI characteristics, we took ε_1 to be equal to 0.005, 0.025, or 0.1. The electron temperatures in the jets are from 500,000 K for the macrospicule to 2.0 MK in the jet emerging from a filament eruption. The electron temperatures of surrounding plasmas are 2.14 MK in the active solar region (Filippov et al., 2015), 2.0 MK in the blowout coronal hole jet (Young and Muglach, 2014a), and 1.0 MK in the environments of the standard coronal hole jet (Chen et al. , 2012) and the macrospicule. With background magnetic fields of 3–6 G, rotating velocities of 40–180 $\mathrm{km\,s^{-1}}$, and $\varepsilon_1 = 0.005$, the total pressure balance Equation (3) yields plasma betas of the first, third, and fourth jets greater than 1 and those of the environments and the internal medium of the second jet much <1 (see **Table 1**). With these plasma beta values one can consider the media of the standard coronal hole jet, the rotating jet emerging from a filament eruption, and microspicule as nearly incompressible plasmas, while the internal medium of the blowout coronal hole jet and the surrounding magnetized plasma in the four cases can be treated as a cool medium (Zank and Matthaeus, 1993).
- *Solving of the wave dispersion relation and finding the KHI characteristics* For finding the solutions to the MHD wave dispersion Equations (10) or (11), which are a slight modification of the 'basic' dispersion relation derived in Zaqarashvili et al., 2015, it is necessary to specify the following

input data: the wave mode number, m, the density contrast, η, the two twist parameters ε_1 and ε_2, the magnetic fields ratio, b [obtainable from Equation (3)], and the Alfvén Mach number $M_\mathrm{A} = U_z/v_\mathrm{Ai}$. The roots of the dispersion Equations (10) or (11) are the normalized wave phase velocity and instability growth rate as functions of the non-dimensional wavenumber $k_z a$. From plots which graphically represent the found solutions, one obtains at the anticipated wavelengths (given by their $k_z a$-values on the horizontal $k_z a$-axes) the corresponding $\mathrm{Re}(v_\mathrm{ph}/v_\mathrm{Ai})$ and $\mathrm{Im}(v_\mathrm{ph}/v_\mathrm{Ai})$ values. From them, one can find in absolute units the KHI growth rate, γ_KH, the instability developing or growth time, $\tau_\mathrm{KH} = 2\pi/\gamma_\mathrm{KH}$, and the corresponding wave phase velocity, v_ph. The MHD wave mode numbers at which we were able to calculate the instability characteristics at wavelengths comparable to the radius or width of the jet are between 10 and 65 and the KHI growth times at those wavelengths are of the order on a few minutes, generally in good agreement with the observations. It is curious to note that in searching KHI growth times of the order on few seconds, when studying the dynamics and stability of small-scale rapid redshifted and blueshifted excursions, appearing as high-speed jets in the wings of the Hα line, Kuridze et al. (2016) had to assume the excitation of MHD waves with mode numbers up to 100. A typical property of the instability developing times, owing to the shape of the plotted dispersion curves, is that with increasing the examined wavelength the growth times become shorter—for instance, at $\lambda_\mathrm{KH} = 10$ Mm the KHI developing time in the coronal hole jet (Chen et al. , 2012) is around 4.5 min, while at $\lambda_\mathrm{KH} = 12$ Mm it is equal to $\cong$2.1 min. A change in B_e can influence the MHD mode number m, which would yield an instability region similar or identical to that seen in **Figure 2**. It is necessary to mention that the width of the instability range except by changing the MHD wave mode number, m, can be regulated by increasing or diminishing the parameter ε_1.

- *Finding the critical azimuthal magnetic field which suppresses the emergence of KHI* It was numerically established, that any increase in ε_1 yields to the shortening of the instability range. This observation implies that there should exist some critical ε_1, at which the upper limit of the instability range coincides with the lower one—in that case the width of the instability window is zero, which means that there is no longer any instability. With such an $\varepsilon_1^\mathrm{cr}$, one can calculate the $B_{\mathrm{i}\phi}^\mathrm{cr}$, which stops the KHI appearance. For the rotating blowout coronal hole jet this $B_{\mathrm{i}\phi}^\mathrm{cr}$ is relatively small—it is equal to ≈0.3 G, while for the standard coronal hole jet it is 1.4 G. It is worth noticing that due to the specific parameters of the jet emerging from a filament eruption, we were unable to find a $B_{\mathrm{i}\phi}^\mathrm{cr}$, which would stop the KHI onset because with values of ε_1 close to 1 our dispersion relation becomes inappropriate (the internal medium being nearly incompressible becomes a cool one) and we cannot calculate that ε_1 at which the lower limit, $(k_z a)_\mathrm{lhs} = 0.524$, can be reached (see **Figure 9**).

In this article, we also corrected the total pressure balance equation used in Zhelyazkov et al. (2018) and Zhelyazkov and Chandra (2018), which turns out to be erroneous. The true total balance equation is given by Equation (3). In fact, the corrected pressure balance equation, used here, changes the mode numbers at which the KHI occurs, namely from $m = 12$ to $m = 11$ for the coronal hole jet and from $m = 18$ to $m = 10$ for the rotating jet emerging from a filament eruption. The computed KHI developing or growth times in the aforementioned articles, nonetheless, are not changed noticeably—they are of the same order with these computed in this paper. In addition, there is another improvement issue, scilicet when studying how the increasing ε_1 shortens the instability region, one has to apply Equation (3) for obtaining the appropriate values of $b = B_\mathrm{e}/B_\mathrm{iz}$ and $v_\mathrm{Ai} = B_\mathrm{iz}/\sqrt{\mu\rho_\mathrm{i}}$, and subsequently $M_\mathrm{A} = U_z/v_\mathrm{Ai}$. Thus, one can claim that Equation (3) plays an important role in the numerical studies of the KHI in various solar jets.

Our approach in investigating the KHI in rotating twisted solar jets can be improved in the following directions: (i) to assume some radial profile of the plasma density of the jet, which immediately will require additional study on the occurrence of continuous spectra and resonant wave absorption (Goedbloed and Poedts, 2004), alongside to see to what extent these phenomena will influence the instability growth times; (ii) to investigate the impact of the non-linear azimuthal magnetic and velocity fields radial profiles on the emergence of KHI; and (iii) to derive a MHD wave dispersion relation without any simplifications like considering the jet and its environment as incompressible or cool plasmas—this will show how the compressibility will change the picture. We should also not forget that the non-linearity, as Miura and Pritchett (1982) and Miura (1984) claim, can lead to the saturation of the KHI growth, and to formation of non-linear waves. Nevertheless, even in its relatively simple form, our way of investigating the conditions under which the KHI develops is flexible enough to explore that event in any rotating solar jet in case that the basic physical and geometry parameters of the jet are provided by observations.

AUTHOR CONTRIBUTIONS

IZh wrote the substantial parts of the manuscript. RJ wrote the Introduction section and prepared three figures associated with the observations. RC contributed by writing the parts devoted to observations, as well as in the careful proofreading of the text.

FUNDING

The work of IZh and RC was supported by the Bulgarian Science Fund contract DNTS/INDIA 01/7. RJ was funded by the Department of Science and Technology, New Delhi, India as an INSPIRE fellow. RC was also supported from the SERB-DST project no. SERB/F/7455/2017-17.

ACKNOWLEDGMENTS

We thank Professor Teimuraz V. Zaqarashvili for useful discussions and are deeply grateful to the reviewers for their constructive comments.

REFERENCES

Ajabshirizadeh, A., Ebadi, H., Vekalati, R. E., and Molaverdikhani, K. (2015). The possibility of Kelvin-Helmholtz instability in solar spicules. *Astrophys. Space Sci.* 357:33. doi: 10.1007/s10509-015-2277-8

Aschwanden, M. J., Boerner, P., Schrijver, C. J., and Malanushenko, A. (2013). Automated temperature and emission measure analysis of coronal loops and active regions observed with the atmospheric imaging assembly on the solar dynamics observatory (SDO/AIA). *Sol. Phys.* 283, 5–30. doi: 10.1007/s11207-011-9876-5

Barbulescu, M., and Erdélyi, R. (2018). Magnetoacoustic waves and the Kelvin–Helmholtz instability in a steady asymmetric slab. I: the effects of varying density ratios. *Solar Phys.* 293:86. doi: 10.1007/s11207-018-1305-6

Bennett, S. M., and Erdélyi, R. (2015). On the statistics of macrospicules. *Astrophys. J.* 808:135. doi: 10.1088/0004-637X/808/2/135

Bodo, G., Mamatsashvili, G., Rossi, P., and Mignone, A. (2016). Linear stability analysis of magnetized jets: the rotating case. *Mon. Not. R. Astron. Soc.* 462, 3031–3052. doi: 10.1093/mnras/stw1650

Bodo, G., Rosner, R., Ferrari, A., and Knobloch, E. (1989). On the stability of magnetized rotating jets: the axisymmetric case. *Astrophys. J.* 341, 631–649. doi: 10.1086/167522

Bodo, G., Rosner, R., Ferrari, A., and Knobloch, E. (1996). On the stability of magnetized rotating jets: the nonaxisymmetric modes. *Astrophys. J.* 470, 797–805. doi: 10.1086/177910

Bogdanova, M., Zhelyazkov, I., Joshi, R., and Chandra, R. (2018). Solar jet on 2014 April 16 modeled by Kelvin–Helmholtz instability. *New Astron.* 63, 75–87. doi: 10.1016/j.newast.2018.03.001

Bondenson, A., Iacono, R., and Bhattacharjee, A. (1987). Local magnetohydrodynamic instabilities of cylindrical plasma with sheared equilibrium flows. *Phys. Fluids* 30, 2167–2180. doi: 10.1063/1.866151

Chandra, R., Mandrini, C. H., Schmieder, B., Joshi, B., Cristiani, G. D., Cremades, H., et al. (2017). Blowout jets and impulsive eruptive flares in a bald-patch topology. *Astron. Astrophys.* 598:A41. doi: 10.1051/0004-6361/201628984

Chandrasekhar, S. (1961). *Hydrodynamic and Hydromagnetic Stability*. Oxford: Clarendon Press.

Chen, H.-D., Zhang, J., and Ma, S.-L. (2012). The kinematics of an untwisting solar jet in a polar coronal hole observed by SDO/AIA. *Res. Astron. Astrophys.* 12, 573–583. doi: 10.1088/1674-4527/12/5/009

Cheremnykh, O., Cheremnykh, S., Kozak, L., and Kronberg, E. (2018a). Magnetohydrodynamic waves and the Kelvin-Helmholtz instability at the boundary of plasma mediums. *Phys. Plasmas* 25:102119. doi: 10.1063/1.5048913

Cheremnykh, O., Fedun, V., Ladikov-Roev, Y., and Verth, G. (2018b). On the stability of incompressible MHD modes in magnetic cylinder with twisted magnetic field and flow. *Astrophys. J.* 866:86. doi: 10.3847/1538-4357/aadb9f

Cranmer, S. R., Asgari-Targhi, M., Miralles, M. P., Raymond, J. C., Strachan, L., Tian, H., et al. (2015). The role of turbulence in coronal heating and solar wind expansion. *Philos. Trans. R. Soc. A* 373:20140148. doi: 10.1098/rsta.2014.0148

Culhane, J. L., Harra, L. K., James, A. M., Al-Janabi, K., Bradley, L. J., Chaudry, R. A., et al. (2007). The EUV imaging spectrometer for Hinode. *Sol. Phys.* 243, 19–61. doi: 10.1007/s01007-007-0293-1

Curdt, W., and Tian, H. (2011). Spectroscopic evidence for helicity in explosive events. *Astron. Astrophys.* 532:L9. doi: 10.1051/0004-6361/201117116

De Pontieu, B., Carlsson, M., Rouppe van der Voort, L. H. M., Rutten, R. J., Hansteen, V. H., and Watanabe, H. (2012). Ubiquitous torsional motions in Type II spicules. *Astrophys. J.* 752:L12. doi: 10.1088/2041-8205/752/1/L12

De Pontieu, B., Title, A. M., Lemen, J. R., Kushner, G. D., Akin, D. J., Allard, B., et al. (2014). The interface region imaging spectrograph (IRIS). *Solar Phys.* 289, 2733–2779. doi: 10.1007/s11207-014-0485-y

Domingo, V., Fleck, B., and Poland, A. I. (1995). SOHO: the solar and heliospheric observatory. *Space Sci. Rev.* 72, 81–84. doi: 10.1007/BF00768758

Ebadi, H. (2016). Kelvin-Helmholtz instability in solar spicules. *Indian J. Phys. Res.* 16, 41–45. doi: 10.18869/acadpub.ijpr.16.3.41

Fang, F., Fan, Y., and McIntosh, S. W. (2014). Rotating solar jets in simulations of flux emergence with thermal conduction. *Astrophys. J.* 789:L19. doi: 10.1088/2041-8205/789/1/L19

Filippov, B., Srivastava, A. K., Dwivedi, B. N., Masson, S., Aulanier, G., Joshi, N. C., et al. (2015). Formation of a rotating jet during the filament eruption on 2013 April 10–11. *Mon. Not. R. Astron. Soc.* 451, 1117–1129. doi: 10.1093/mnras/stv1039

Goedbloed, J. P., and Poedts, S. (2004). *Principles of Magnetohydrodynamics: With Applications to Laboratory and Astrophysical Plasmas.* Cambridge: Cambridge University Press.

Goossens, M., Hollweg, J. V., and Sakurai, T. (1992). Resonant behaviour of MHD waves on magnetic flux tubes tiny III. Effect of equilibrium flow. *Solar Phys.* 138, 233–255. doi: 10.1007/BF00151914

Heyvaerts, J., Priest, E. R., and Rust, D. M. (1997). An emerging flux model for the solar flare phenomenon. *Astrophys. J.* 216, 123–137. doi: 10.1086/155453

Hong, J.-C., Jiang, Y.-C., Yang, J.-Y., Zheng, R.-S., Bi, Y., Li, H.-D., et al. (2013). Twist in a polar blowout jet. *Res. Astron. Astrophys.* 13, 253–258. doi: 10.1088/1674-4527/13/3/001

Hood, A. W., and Priest, E. R. (1979). Kink instability of solar coronal loops as the cause of solar flares. *Solar Phys.* 64, 303–321. doi: 10.1007/BF00151441

Ismayilli, R. F., Dzhalilov, N. S., Shergelashvili, B. M., Poedts, S., and Pirguliyev, M. Sh. (2018). MHD Kelvin-Helmholtz instability in the anisotropic solar wind plasma. *Phys. Plasmas* 25: 062903. doi: 10.1063/1.5032161

Joshi, R., Schmieder, B., Chandra, R., Aulanier, G., Zuccarello, F. P., and Uddin, W. (2017). Slippage of jets explained by the magnetic topology of NOAA active region 12035. *Solar Phys.* 292:152. doi: 10.1007/s11207-017-1176-2

Kamio, S., Curdt, W., Teriaca, L., Inhester, B., and Solanki, S. K. (2010). Observations of a rotating macrospicule associated with an X-ray jet. *Astron. Astrophys.* 510: L1. doi: 10.1051/0004-6361/200913269

Kayshap, P., Srivastava, A. K., Murawski, K., and Tripathi, D. (2013). Origin of macrospicule and jet in polar corona by a small-scale kinked flux tube. *Astrophys. J.* 770:L3. doi: 10.1088/2041-8205/770/1/L3

Kiss, T. S., Gyenge, N., and Erdélyi, R. (2017). Systematic variations of macrospicule properties observed by SDO/AIA over half a decade. *Astrophys. J.* 835:47. doi: 10.3847/1538-4357/aa5272

Kiss, T. S., Gyenge, N., and Erdélyi, R. (2018). Quasi-biennial oscillations in the cross-correlation of properties of macrospicules. *Adv. Space Res.* 61, 611–616. doi: 10.1016/j.asr.2017.05.027

Kosugi, T., Matsuzaki, K., Sakao, T., Shimizu, T., Sone, Y., Tachikawa, S., et al. (2007). The *Hinode* (Solar-B) Mission: An Overview. *Solar Phys.* 243, 3–17. doi: 10.1007/s11207-007-9014-6

Kuridze, D., Zaqarashvili, T. V., Henriques, V., Mathioudakis, M., Keenan, F. P., and Hanslmeier, A. (2016). Kelvin–Helmholtz instability in solar chromospheric jets: theory and observation. *Astrophys. J.* 830:133. doi: 10.3847/0004-637X/830/2/133

Lemen, J. R., Title, A. M., Akin, D. J., Boerner, P. F., Chou, C., Drake, J. F., et al. (2012). The Atmospheric Imaging Assembly (AIA) on the Solar Dynamics Observatory (SDO). *Solar Phys.* 275, 17–40. doi: 10.1007/s11207-011-9776-8

Liu, W., Berger, T. E., Title, A. M., and Tarbell, T. D. (2009). An intriguing chromospheric jet observed by Hinode: fine structure kinematics and evidence of unwinding twists. *Astrophys. J.* 707, L37–L41. doi: 10.1088/0004-637X/707/1/L37

Lundquist, S. (1951). On the stability of magneto-hydrostatic fields. *Phys. Rev.* 83, 307–311. doi: 10.1103/PhysRev.83.307

Madjarska, M. S. (2019). Coronal bright points. *Living. Rev. Solar Phys.* 16:2. doi: 10.1007/s41116-019-0018-8

Martínez-Sykora, J., De Pontieu, B., Leenaarts, J., Pereira, T. M. D., Carlsson, M., Hansteen, V., et al. (2013). A detailed comparison between the observed and synthesized properties of a simulated type II spicule. *Astrophys. J.* 771:66. doi: 10.1088/0004-637X/771/1/66

Mishin, V. V., and Tomozov, V. M. (2016). Kelvin-Helmholtz instability in the solar atmosphere, solar wind and geomagnetosphere. *Solar Phys.* 291, 3165–3184. doi: 10.1007/s11207-016-0891-4

Miura, A., and Pritchett, P. L. (1982). Nonlocal stability analysis of the MHD Kelvin-Helmholtz instability in a compressible plasma. *J. Geophys. Res.* 87, 7431–7444. doi: 10.1029/JA087iA09p07431

Miura, A. (1984). Anomalous transport by magnetohydrodynamic Kelvin-Helmholtz instabilities in the solar wind-magnetosphere interaction. *J. Geophys. Res.* 89, 801–818. doi: 10.1029/JA089iA02p00801

Moore, R. L., Cirtain, J. W., Sterling, A. C., and Falconer, D. A. (2010). Dichtonomy of solar coronal jets: standard jets and blowout jets. *Astrophys. J.* 720, 757–770. doi: 10.1088/0004-637X/720/1/757

Moore, R. L., Sterling, A. C., Falconer, D. A., and Robe, D. (2013). The cool component and the dichotomy, lateral expansion, and axial rotation of solar X-ray jets. *Astrophys. J.* 769:134. doi: 10.1088/0004-637X/769/2/134

Moore, R. L., Sterling, A. C., and Falconer, D. A. (2015). Magnetic untwisting in solar jets that go into the outer corona in polar coronal holes. *Astrophys. J.* 806:11. doi: 10.1088/0004-637X/806/1/11

Murawski, K., Srivastava, A. K., and Zaqarashvili, T. V. (2011). Numerical simulations of solar macrospicules. *Astron. Astrophys.* 355:A58. doi: 10.1051/0004-6361/201116735

Nisticò, G., Bothmer, V., Patsourakos, S., and Zimbardo, G. (2009). Characteristics of EUV coronal jets observed with STEREO/SECCHI. *Sol. Phys.* 259:87. doi: 10.1007/s11207-009-9424-8

Nisticò, G., Bothmer, V., Patsourakos, S., and Zimbardo, G. (2010). Observational features of equatorial coronal hole jets. *Ann. Geophys.* 28, 687–696. doi: 10.5194/angeo-28-687-2010

Panesar, N. K., Sterling, A. C., Moore, R. L., and Chakrapani, P. (2016b). Magnetic flux cancelation as the trigger of solar quiet-region coronal jets. *Astrophys. J.* 832:L7. doi: 10.3847/2041-8205/832/1/L7

Panesar, N. K., Sterling, A. C., and Moore, R. L. (2016a). Homologous jet-driven coronal mass ejections from solar active region 12192. *Astrophys. J.* 822:L23. doi: 10.3847/2041-8205/822/2/L23

Pariat, E., Antiochos, S. K., and DeVore, C. R. (2009). A model for solar polar jets. *Astrophys. J.* 691, 61–74. doi: 10.1088/0004-637X/691/1/61

Pariat, E., Dalmasse, K., DeVore, C. R., Antiochos, S. K., and Karpen, J. T. (2015). Model for straight and helical solar jets. I. Parametric studies of the magnetic field geometry. *Astron. Astrophys.* 573:A130. doi: 10.1051/0004-6361/201424209

Pariat, E., Dalmasse, K., DeVore, C. R., Antiochos, S. K., and Karpen, J. T. (2016). Model for straight and helical solar jets. II. Parametric study of the plasma beta. *Astron. Astrophys.* 596:A36. doi: 10.1051/0004-6361/201629109

Pesnell, W. D., Thompson, B. J., and Chamberlin, P. C. (2012). The Solar Dynamics Observatory (SDO). *Solar Phys.* 275, 3–15. doi: 10.1007/s11207-011-9841-3

Pike, C. D., and Harrison, R. A. (1997). Euv observations of a macrospicule: evidence for solar wind acceleration? *Solar Phys.* 175, 457–465. doi: 10.1023/A:1004987505422

Pike, C. D., and Mason, H. E. (1998). Rotating transition region features observed with the SOHO coronal diagnostic spectrometer. *Solar Phys.* 182, 333–348.

Ryu, D., Jones, T. W., and Frank, A. (2000). The magnetohydrodynamic Kelvin-Helmholtz instability: a three-dimensional study of nonliner evolution. *Astrophys. J.* 545, 475–493. doi: 10.1086/317789

Schmieder, B., Guo, Y., Moreno-Insertis, F., Aulanier, G.,Yelles Chaouche, L., Nishizuka, N., et al. (2013). Twisting solar coronal jet launched at the boundary of an active region. *Astron. Astrophys.* 559:A1. doi: 10.1051/0004-6361/201322181

Shen, Y., Liu, Y., Su, J., and Ibrahim, A. (2011). Kinematics and fine structure of an unwinding polar jet observed by the solar dynamic observatory atmospheric imaging assembly. *Astrophys. J.* 735:L43. doi: 10.1088/2041-8205/735/2/L43

Soler, R., Díaz, A. J., Ballester, J. L., and Goossens, M. (2015). Kelvin-Helmholtz instability in partially ionized compressible plasmas. *Astrophys. J.* 749:163. doi: 10.1088/0004-637X/749/2/163

Sterling, A. C., Moore, R. L., Falconer, D. A., and Adams, M. (2015). Small-scale filament eruptions as the driver of X-ray jets in solar coronal holes. *Nature* 523, 437–440. doi: 10.1038/nature14556

Vasheghani Farahani, S., Van Doorsselaere, T., Verwichte, E., and Nakariakov, V. M. (2009). Propagating transverse waves in soft X-ray coronal jets. *Astron. Astrophys.* 498, L29–L32. doi: 10.1051/0004-6361/200911840

Young, P. R., and Muglach, K. (2014a). A coronal hole jet observed with Hinode and the solar dynamics observatory. *Publ. Astron. Soc. Japan* 66:S12. doi: 10.1093/pasj/psu088

Young, P. R., and Muglach, K. (2014b). Solar dynamics observatory and Hinode observations of a blowout jet in a coronal hole. *Sol. Phys.* 289, 3313–3329. doi: 10.1007/s11207-014-0484-z

Zank, G. P., and Matthaeus, W. H. (1993). Nearly incompressible fluids. II: magnetohydrodynamics, turbulence, and waves. *Phys. Fluids* 5, 257–273. doi: 10.1063/1.858780

Zaqarashvili, T. V., Vörös, Z., and Zhelyazkov, R. (2014). Kelvin-Helmholtz instability of twisted magnetic flux tubes in the solar wind *Astron. Astrophys.* 561:A62. doi: 10.1051/0004-6361/201322808

Zaqarashvili, T. V., Zhelyazkov, I., and Ofman, L. (2015). Stability of rotating magnetized jets in the solar atmosphere. I. Kelvin–Helmholtz instability. *Astrophys. J.* 813:123. doi: 10.1088/0004-637X/813/2/123

Zhang, Q. M., and Ji, H. S. (2014). A swirling flare-related EUV jet. *Astron. Astrophys.* 561:A134. doi: 10.1051/0004-6361/201322616

Zhelyazkov, I., Chandra, R., Srivastava, A. K., and Mishonov, T. (2015a). Kelvin–Helmholtz instability of magnetohydrodynamic waves propagating on solar surges. *Astrophys. Space Sci.* 356:231. doi: 10.1007/s10509-014-2215-1

Zhelyazkov, I., Chandra, R., and Srivastava, A. K. (2016). Kelvin–Helmholtz instability in an active region jet observed with Hinode. *Astrophys. Space Sci.* 361:51. doi: 10.1007/s10509-015-2639-2

Zhelyazkov, I., Chandra, R., and Srivastava, A. K. (2017). Modeling Kelvin–Helmholtz instability in soft X-ray solar jets. *Adv. Astron.* 2017:2626495. doi: 10.1155/2017/2626495

Zhelyazkov, I., and Chandra, R. (2018). High mode magnetohydrodynamic waves propagation in a twisted rotating jet emerging from a filament eruption. *Mon. Not. R. Astron. Soc.* 478, 5505–5513. doi: 10.1093/mnras/sty1354

Zhelyazkov, I., and Chandra, R. (2019). Can High-Mode Magnetohydrodynamic Waves propagating in a spinning macrospicule be unstable due to the Kelvin–Helmholtz Instability? *Solar Phys.* 294:20. doi: 10.1007/s11207-019-1408-8

Zhelyazkov, I., Zaqarashvili, T. V., Chandra, R., Srivastava, A. K., and Mishonov, T. (2015b). Kelvin–Helmholtz instability in solar cool surges. *Adv. Space Res.* 56, 2727–2737. doi: 10.1016/j.asr.2015.05.003

Zhelyazkov, I., Zaqarashvili, T. V., Ofman, L., and Chandra, R. (2018). Kelvin–Helmholtz instability in a twisting solar polar coronal hole jet observed by SDO/AIA. *Adv. Space Res.* 61, 628–638. doi: 10.1016/j.asr.2017.06.003

Zhelyazkov, I., and Zaqarashvili, T. V. (2012). Kelvin-Helmholtz instability of kink waves in photospheric twisted flux tubes. *Astron. Astrophys.* 547:A14. doi: 10.1051/0004-6361/201219512

Zhelyazkov, I. (2012). Magnetohydrodynamic waves and their stability status in solar spicules. *Astron. Astrophys.* 537:A124. doi: 10.1051/0004-6361/201117780

Zhelyazkov, I. (2015). On Modeling the Kelvin–Helmholtz instability in solar atmosphere. *J. Astrophys. Astr.* 36, 233–254. doi: 10.1007/s12036-015-9332-2

Conflict of Interest Statement: The authors declare that the research was conducted in the absence of any commercial or financial relationships that could be construed as a potential conflict of interest.

frontiers
in Astronomy and Space Sciences

ORIGINAL RESEARCH
published: 16 May 2019
doi: 10.3389/fspas.2019.00036

High-Frequency Dynamics of Active Region Moss as Observed by IRIS

Nancy Narang[1]*, *Vaibhav Pant*[2], *Dipankar Banerjee*[1] *and Tom Van Doorsselaere*[2]

[1] *Indian Institute of Astrophysics, Bangalore, India,* [2] *Department of Mathematics, Centre for Mathematical Plasma Astrophysics, KU Leuven, Leuven, Belgium*

The high temporal, spatial and spectral resolution of Interface Region Imaging Spectrograph (IRIS) has provided new insights into the understanding of different small-scale processes occurring at the chromospheric and transition region (TR) heights. We study the dynamics of high-frequency oscillations of active region (AR 2376) moss as recorded by simultaneous imaging and spectral data of IRIS. Wavelet transformation, power maps generated from slit-jaw images in the Si IV 1400 Å passband, and sit-and-stare spectroscopic observations of the Si IV 1403 Å spectral line reveal the presence of high-frequency oscillations with ∼1–2 min periods in the bright moss regions. The presence of such low periodicities is further confirmed by intrinsic mode functions (IMFs) as obtained by the empirical mode decomposition (EMD) technique. We find evidence of the presence of slow waves and reconnection-like events, and together they cause the high-frequency oscillations in the bright moss regions.

Keywords: sun, chromopshere, transition region, moss, oscillations, MHD wave

Edited by:
*Mario J. P. F. G. Monteiro,
Universidade do Porto, Portugal*

Reviewed by:
*Krishna Prasad Sayamanthula,
Queen's University Belfast,
United Kingdom
Juan Carlos Martínez Oliveros,
Space Sciences Laboratory, UC
Berkeley, United States*

***Correspondence:**
*Nancy Narang
nancy@iiap.res.in*

Specialty section:
*This article was submitted to
Stellar and Solar Physics,
a section of the journal
Frontiers in Astronomy and Space
Sciences*

Received: *18 January 2019*
Accepted: *24 April 2019*
Published: *16 May 2019*

Citation:
*Narang N, Pant V, Banerjee D and
Van Doorsselaere T (2019)
High-Frequency Dynamics of Active
Region Moss as Observed by IRIS.
Front. Astron. Space Sci. 6:36.
doi: 10.3389/fspas.2019.00036*

1. INTRODUCTION

Understanding the processes responsible for the heating of the upper atmosphere is the central problem in solar physics. Though highly debated (see reviews Klimchuk, 2006; Reale, 2010; Parnell and De Moortel, 2012), two widely accepted mechanisms for converting magnetic energy into thermal energy are impulsive heating by nano-flares (Parker, 1988) and heating by dissipation of waves (Arregui, 2015). The heating processes are generally proposed to occur on small spatial and temporal scales, which were difficult to observe with the typical resolution of the previous instruments. In the very recent past, the advent of instruments with better temporal resolutions, several evidences of high-frequency oscillations of sub-minute periodicities have been reported to be present from the chromosphere (Gupta and Tripathi, 2015; Shetye et al., 2016; Ishikawa et al., 2017; Jafarzadeh et al., 2017) up to the corona (Morton and McLaughlin, 2013, 2014; Testa et al., 2013; Pant et al., 2015; Samanta et al., 2016) at sub-arcsec spatial scales. The small-scale quasi-periodic flows resulting from oscillatory magnetic reconnection as well as the presence of various Magnetohydrodynamic (MHD) waves produce such observed perturbations in imaging and spectroscopic observables. These periodic/quasi-periodic perturbations/oscillations observed at such finer scales in space and time can thus be regarded as the manifestations of the reoccurring dynamic heating processes present at similar spatial (sub-arcsec) and temporal (sub-minute) scales.

Various MHD waves could be present simultaneously along with quasi-periodic flows or their presence could entirely be non-concurrent. The plausible mechanism/s for their origin might also be directly coupled in some cases or completely independent in others. For instances, Gupta and Tripathi (2015) detected short-period variability (30–90 s) within explosive events observed in TR by IRIS (De Pontieu et al., 2014) and related them to repetitive magnetic reconnection events.

On the other hand, Jafarzadeh et al. (2017) observed high-frequency of periods 30–50 s in Ca II H bright-points in the chromosphere using the SUNRISE Filter Imager (SuFI; Gandorfer et al., 2011). They found the evidence of both compressible (sausage mode) and incompressible (kink mode) waves to be present in the magnetic bright-points. Shetye et al. (2016) reported transverse oscillations and intensity variations (∼ 20–60 s) in chromospheric spicular structures using the CRisp Imaging SpectroPolarimeter (CRISP; Scharmer et al., 2008) on the Swedish 1-m Solar Telescope. They argued that high-frequency helical kink motions are responsible for transverse oscillations and compressive sausage modes to result in intensity variations. They further found evidence of mode coupling between compressive sausage and non-compressive kink modes and speculated the presence of other spicules and flows possibly acting as the external drivers for the mode-coupling.

Using the total solar eclipse observations of 11 July 2010 (Singh et al., 2011), Samanta et al. (2016) detected significant oscillations with periods ∼6–20 s in coronal structures. They attributed these high-frequency oscillations as a mixture of different MHD waves and quasi-periodic flows. Using the High-resolution Coronal Imager [Hi-C; Kobayashi et al. (2014)] data, Testa et al. (2013) observed variability on time-scales of 15–30 s to be present in the moss regions as observed in the upper TR, which they found to be mostly located at the foot-points of coronal loops. They regarded such oscillations as the signatures of heating events associated with reconnection occurring in overlying hot coronal loops, i.e., impulsive nano-flares. More recently, from the Chromospheric Lyα SpectroPolarimeter (CLASP; Kano et al., 2012) observations, Ishikawa et al. (2017) also reported short temporal variations in the solar chromosphere and TR emission of an active region with periodicities of ∼10–30 s. They attributed these intensity variations to waves or jets from the lower layers instead of nano-flares. Morton and McLaughlin (2013, 2014) analyzed the same active region moss observations of Hi-C as by Testa et al. (2013) and observed the presence of transverse oscillations with periodicities of 50–70 s. Pant et al. (2015) also studied the same region in Hi-C observations and detected quasi-periodic flows as well as transverse oscillations with short periodicities (30–60 s) in braided structures of the moss. They indicated coupling between the sources of transverse oscillations and quasi-periodic flows, i.e., magnetic reconnection, such that they could be possibly driving each other.

In the present work, we concentrate on the high-frequency (∼1–2 min) dynamics of active region (AR 2376) moss as observed by IRIS. IRIS have provided an unprecedented view of the solar chromosphere and transition region with high temporal, spatial and spectral resolution. The joint imaging and spectroscopic observations of IRIS at high cadence provide us with a unique opportunity to have a detailed analysis of different characteristics and mechanisms involved in the generation of high-frequency oscillations in TR moss regions.

2. DETAILS OF THE OBSERVATION

IRIS observations of active region (AR 2376) moss, observed on 2015-07-05 from 05:16:15 UT to 07:16:23 UT is considered for the present analysis. **Figure 1** shows the observation region on the solar disk, as outlined in the image taken in the 171 Å pass-band of AIA (Atmospheric Imaging Assembly; Lemen et al., 2012) and slit-jaw image (SJI) in 1400 Å at a particular instance observed by the IRIS. The bottom panel shows a typical light-curve at a particular location A (marked in the full FOV above) in the moss region in SJ 1400 Å intensity. The nature of the variation of intensity clearly reveals the presence of small amplitude quasi-periodic variations along with comparatively larger amplitude variations.

Centered at $146'', 207''$, the imaging data (slit-jaw images or SJIs) have a field of view (FOV) of $119'' \times 119''$. The SJIs are taken with a cadence of 13 s and have spatial resolution $\approx 0.33''$. The simultaneous large sit-and stare spectroscopic data has a cadence of 3.3 s with the slit-width of $0.35''$ and pixel size along the solar-Y axis to be $0.1664''$ with slit length of $119''$. Every observation in this data-set has an exposure time of 2 s. The high cadence of these data-sets provides us a unique opportunity to investigate the high-frequency dynamics in this region with high significance level.

We use IRIS SJIs centered at the Si IV 1400 Å passband which samples emission from the transition region (TR). For spectral analysis, we concentrate on the Si IV (1403 Å) line formed at $\log_{10} T \approx 4.9K$ which is one of the prominent TR emission lines observed with the IRIS and is free from other line blends. For density diagnostics, we use the O IV (1401 Å) TR line along with Si IV (1403 Å) (Keenan et al., 2002; Young et al., 2018). The calibrated level 2 data of IRIS is used in the study. Dark current subtraction, flat-field correction, and geometrical correction have been taken into account in the level 2 data. We employ wavelet analysis (Torrence and Compo, 1998) and empirical mode decomposition (EMD; Huang et al., 1998) techniques in order to detect and characterize the high-frequency oscillations in slit-jaw (SJ) intensity (section 3.1) and different spectral properties i.e., total intensity, peak intensity, Doppler velocity, and Doppler width (section 3.2).

3. DATA-ANALYSIS AND RESULTS

3.1. Imaging Analysis From Si IV 1400 Å SJIs

Wavelet analysis is performed at each pixel location of SJ FOV to obtain the period of SJ intensity variability over the observed moss region. As shown in **Figure 1**, a typical light curve corresponding to a single pixel location for the entire duration reveals presence of quasi-periodic small and large amplitude intensity fluctuations. **Figure 2A** shows a representative example (selected at random) of wavelet analysis results corresponding to the pixel location marked as A in SJ FOV (**Figure 1**) for a duration of 20 min. It should be noted that in most of results we show the wavelet and EMD analysis corresponding to 20 min interval only so that the temporal variations in intensity can be studied more carefully, particularly as we are interested in

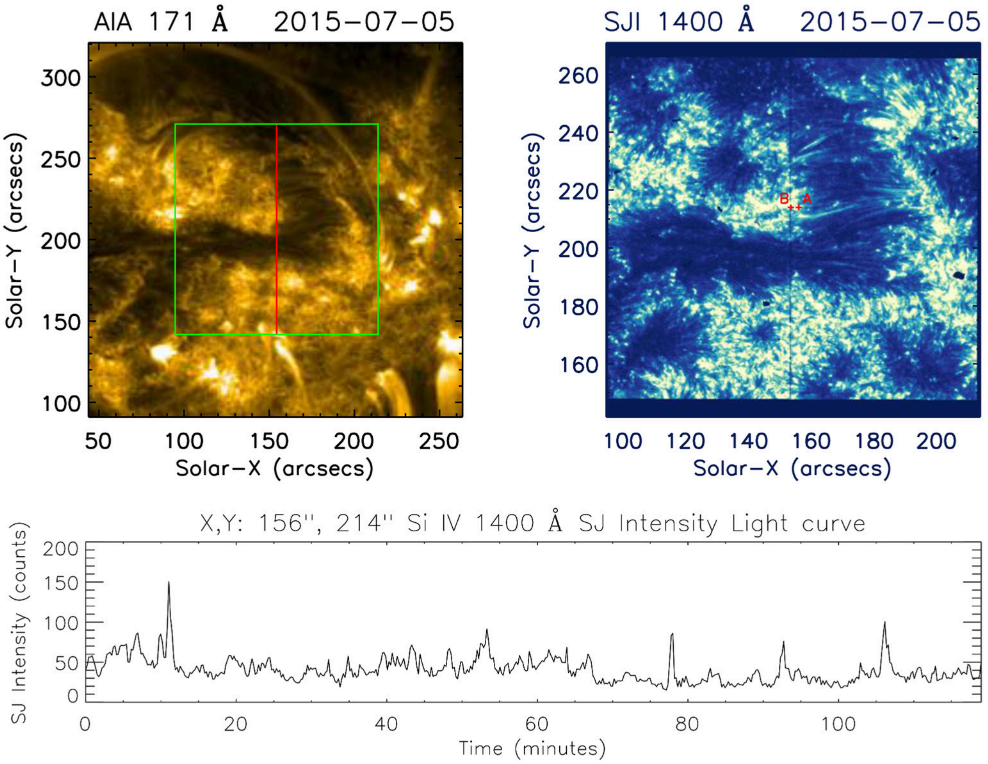

FIGURE 1 | AIA 171 Å image marking the observed region by IRIS and SJI at a particular instance as observed by IRIS in the Si IV 1400 Å passband. The bottom panel shows the SJ intensity light curve at location A marked in SJI FOV for the complete duration of the observation.

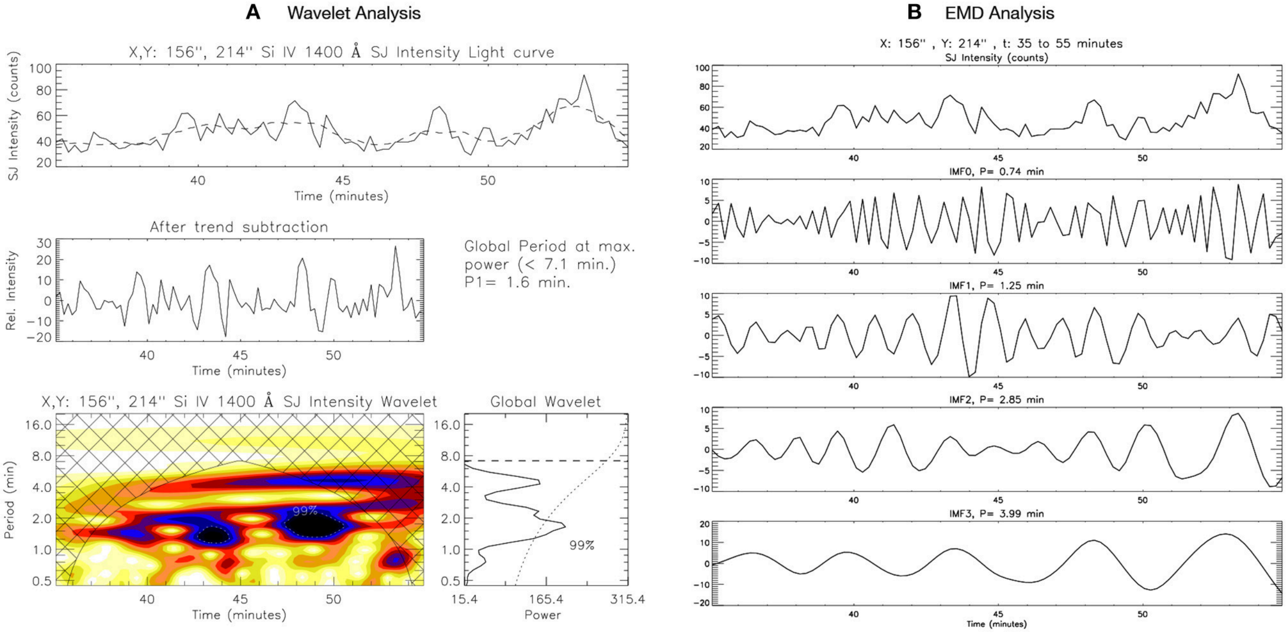

FIGURE 2 | (A) Wavelet analysis, and **(B)** EMD analysis result for the Si IV 1400 Å SJ intensity variation with time from 35 to 55 min of the observation at location A. The details about the different panels are explained in the text (section 3.1).

the shorter periodicities. The top panel in **Figure 2A** shows the variation of SJ intensity with time. The middle-panel shows the background (trend) subtracted intensity which is further used to obtain wavelet power spectrum (lower panels). The background (trend) is obtained by taking the 10-point running average of the intensity variation. The bottom left panel displays a wavelet power spectrum (color inverted) with 99% significance levels and the bottom right panel displays a global wavelet power spectrum (wavelet power spectrum summed over time) with 99% global significance.

The power spectra obtained reveals the presence of short-period variability in the SJ intensity light-curve, with a distinct power peak at a period of 1.6 min. It is important to note that even without considering the background trend, we obtain a power peak at the same period in wavelet spectra but with low significance level. Empirical mode decomposition (EMD) is also employed at a few locations in the SJ FOV. **Figure 2B** shows the different intrinsic mode functions (IMFs) obtained from EMD for the same SJ light-curve as shown in **Figure 2A**. Here only the first four IMFs are shown as the further IMFs contain the larger background trends. The dominant period (P) mentioned in the figure for each IMF is calculated using fast-Fourier transform (FFT). The period of the first four IMFs for the particular example shown in **Figure 2B** are 0.74, 1.25, 2.85, and 3.99 min. The EMD analysis reinforces the detection of the presence of short periodicities (1–2 min) in the moss region as obtained by wavelet analysis. The presence of periodicities < 1 min can also be noted from the **Figure 2**, though these are below the significance level of 99% as shown in wavelet power spectra. Such oscillations have very small amplitudes, are present even for shorter-duration and could be damping fast. Hence, the oscillations with periods < 1 min may carry smaller amount of energy and may not be so important as those with periods > 1 min which may be distributed over larger spatial and temporal extents.

To focus on the distribution of power as calculated from the wavelet method, we obtain the power maps of SJ intensity over the full FOV in 1–2 min and 2–4 min period intervals (**Figure 3**) by considering the entire duration of the observation. The entire duration of the observations is chosen to understand the global dynamics of the active region moss. On comparison of power maps with the SJ images (**Figure 3**) and AIA images (**Figure 1**), it can be observed that the significant power of high-frequency (1–2 min) as well as low-frequency (2–4 min) oscillations is generally present only in bright regions of the moss. **Figure 3** also shows the time-average SJI with the power contours of 1–2 min variability in red and 2–4 min in yellow. The power contours enclose the locations with the value of significant power to be more than 100, in respective period range. The finer and smaller spatial extents of the contours at various locations over the field of view suggest that these oscillations possess high power in the localized regions within the bright moss. Moreover, the comparison of power between short (1–2 min) and long (2–4 min) periodicities, as showcased in **Figure 3**, reveals that the power in 1–2 min variability is, in general, less than that in 2–4 min.

3.2. Spectral Analysis From Si IV 1403 Å Emission Line

To characterize periodicities present in the spectrograph data, we produce power maps of the spectral parameters obtained by fitting a single Gaussian to the Si IV 1403 Å emission spectra using wavelet analysis. The analysis was performed over the entire duration of the observations. At few instances, we interpolate the spectral parameters where a Gaussian fitting could not be performed due to poor signal to noise. The power maps, shown in **Figure 4**, clearly showcase the significant power along the slit, predominantly present in the period range of 0.83–2.36 min corresponding to pixel locations of the bright moss regions (wherever the slit crosses the bright moss). This confirms the presence of short-period oscillations in Si IV 1403 Å spectra along with the Si IV 1400 Å SJ intensity (described in section 3.1) in various locations of the moss region.

Now we shift our focus to shorter time intervals where data gaps due to poor signal-to-noise are absent. This allow us to investigate the correlation between different spectral parameters using wavelet and EMD analysis. Further, taking the intervals of 20 min is sufficient because we are primarily interested in shorter periods like, 1–2 min. **Figure 5A** shows the wavelet maps of total intensity variation for a duration of 20 min at a particular location along the slit (marked as B in the SJ FOV in **Figure 1**). Total intensity signifies the summed intensity over the wavelength range. **Figure 6A** shows the wavelet maps of Doppler velocity at the same location B and same time-interval as shown for total intensity in **Figure 5**. Note that the location B is very close to location A so that a comparison can be made with the periodicities found at location A using SJI. Moreover, the same time-interval is shown in **Figures 2**, **5**, and **6** for better illustration. **Figure 7** shows the variation of peak intensity, Doppler width, total intensity and Doppler velocity of Si IV 1403 Å line at location B along with the spectral line-profile at a particular instance. The observational uncertainties are shown in the left panel over the observed line-profile. These errors are taken into account while fitting the Gaussian profile (*green* solid curve). The fitting errors of the respective spectral parameters are shown in the adjacent light curves in *orange*. It can be clearly observed that the errors in the spectral parameters are much less than the amplitude of oscillations. For instance, the average magnitude of error over the Doppler velocity light curve shown in **Figures 6**, **7** is 0.5 km/s, whereas the amplitude of oscillation of its IMFs (as shown in **Figure 6**) is more than 1 km/s in most of the cases. The oscillations in the spectral parameters are well above the error values in general and thus significant. An animation of the **Figure 7** is available as the supplementary material (**Supplementary Video 1**) in the online version which shows the evolution of the spectral line profile with time.

The background trends for the spectral parameter light curves (in **Figures 5**, **6**) are obtained by considering the 35-point running average of the light-curves. The dominant power peaks are observed to be present 1.5 min for total intensity, 1.7 min for peak intensity, 1.7 min for Doppler velocity, and 1.5 min for Doppler width in the respective power spectra. Here again, the presence of periodicities of < 1 min can be seen in the wavelet.

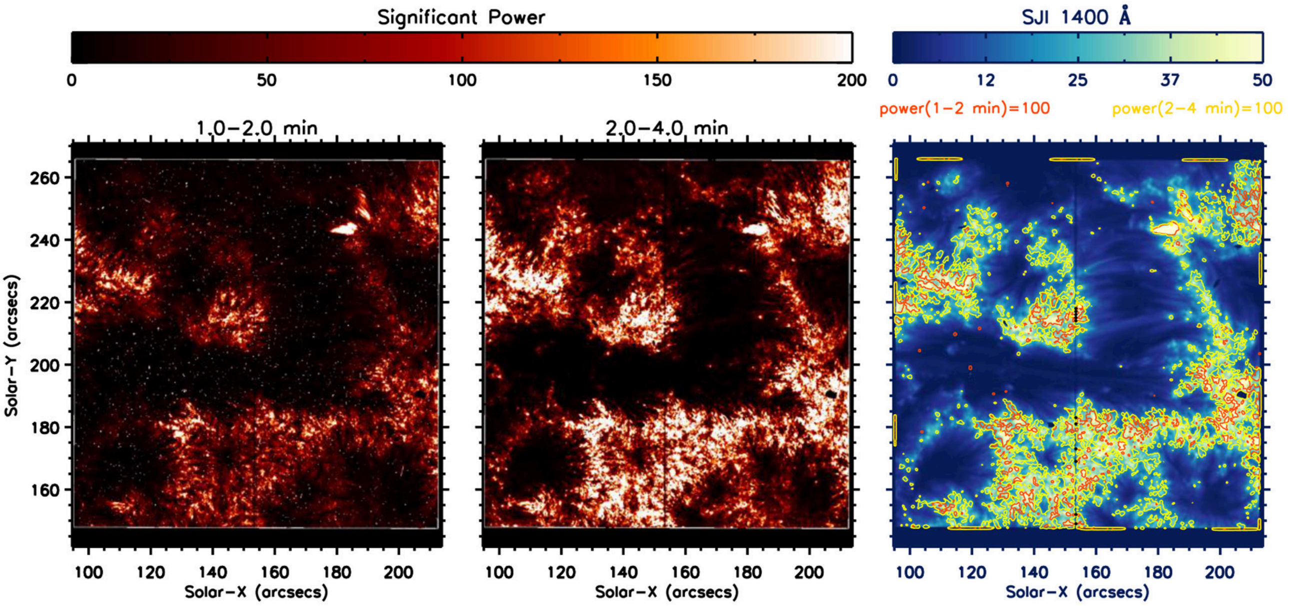

FIGURE 3 | Power maps showing the significant power obtained from the Si IV 1400 Å SJ intensity variation in the period range of 1–2 min and 2–4 min. The rightmost panel shows the average SJ intensity image with contours of significant power in 1–2 min periods in red and 2–4 min in yellow, delineating the bright regions of the moss.

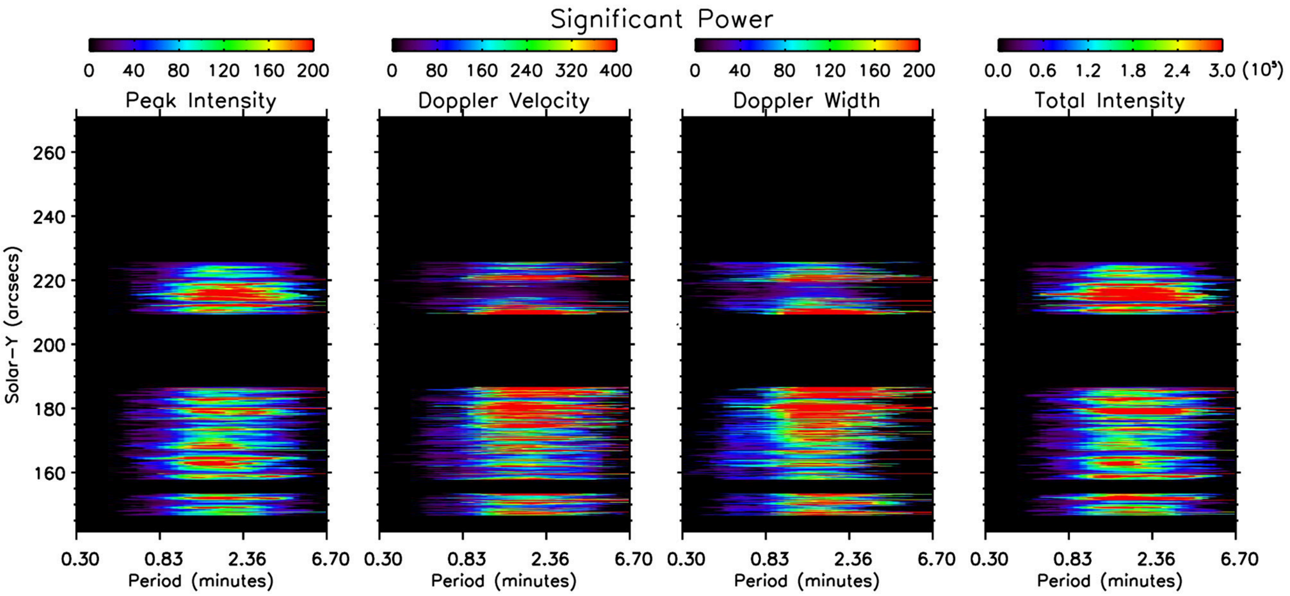

FIGURE 4 | Power maps showing the significant power obtained from the variation of different spectral parameters of Si IV 1403 Å emission line in the period range of 0.3–6.7 min.

It can be clearly observed that such oscillations are present for very short durations and thus of not much significance over the longer durations. Also, such short periodicities could be due to the presence of noise which is picked up by wavelet at higher-frequencies.

The EMD technique is applied over the spectral variations in order to segregate the different periodicities present in their light curves. **Figures 5B**, **6B**, respectively, shows the first four IMFs and their periods (P) of total intensity and Doppler velocity variation for the duration of 20 min at the location B. The first four IMFs (IMF0, IMF1, IMF2, and IMF3) are observed to contain the short-period variabilities (0.2–2 min). The successive IMFs are observed to have periodicities of more than 2 min and hence not discussed in the present analysis. To perform a

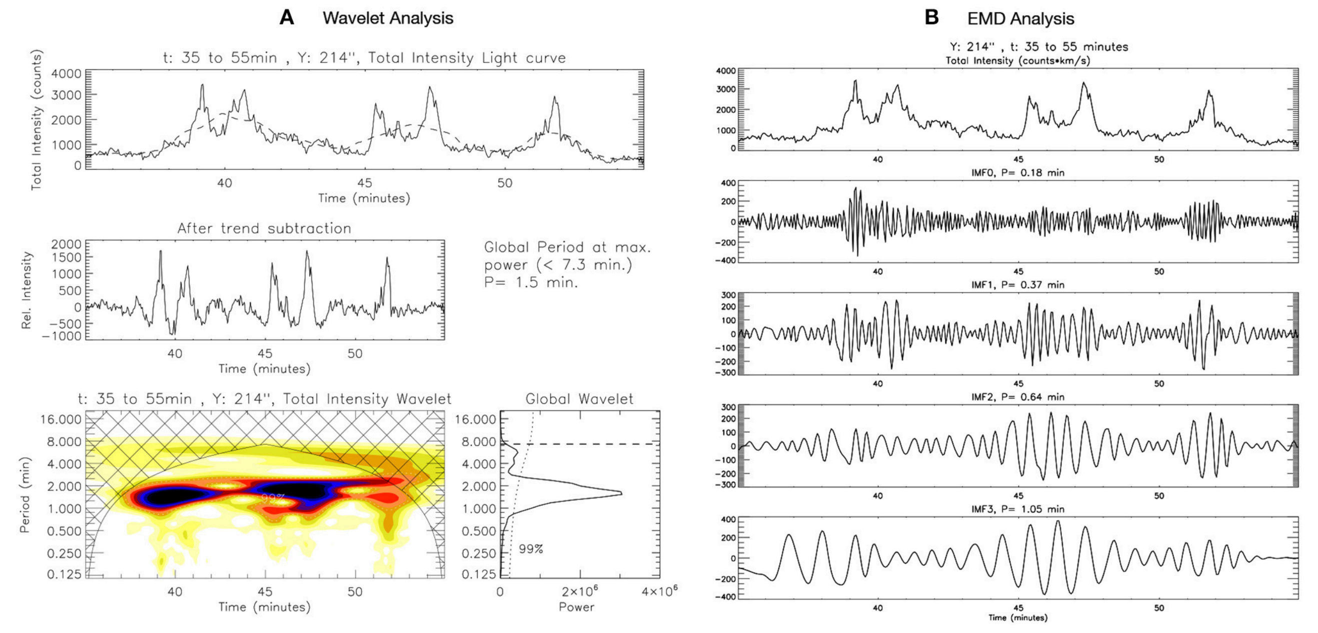

FIGURE 5 | **(A)** Wavelet analysis, and **(B)** EMD analysis result for the Si IV 1403 Å total intensity variation with time from 35 to 55 min of the observation at location B along the slit.

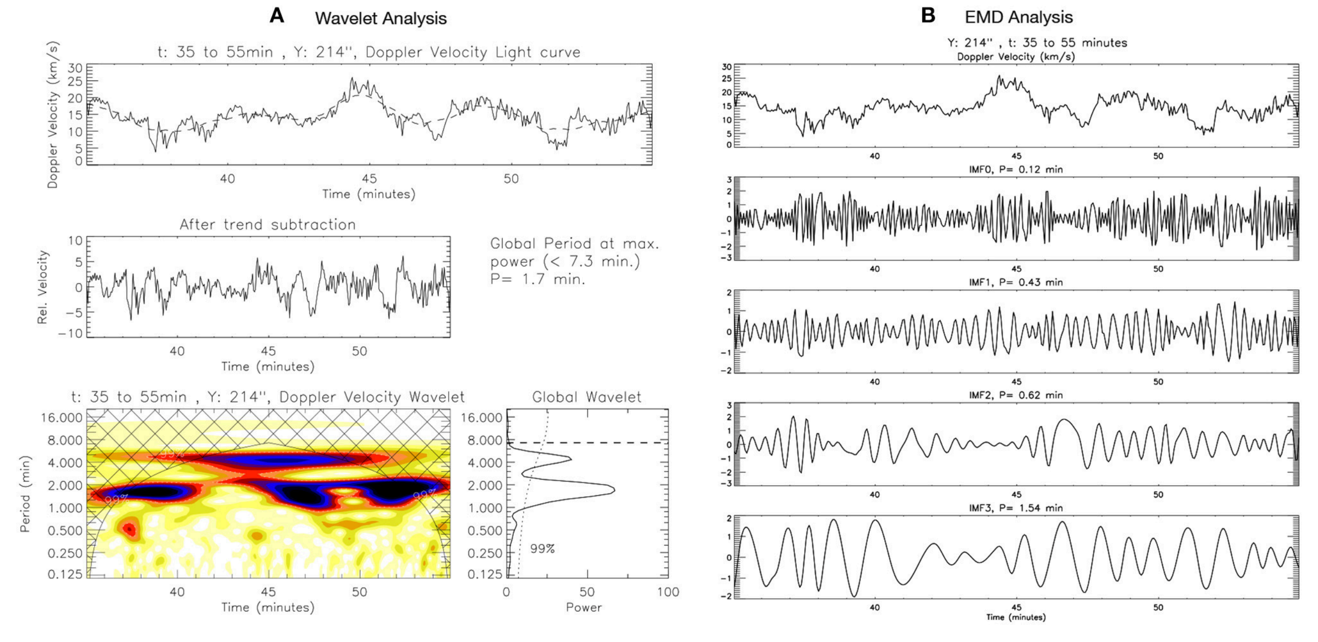

FIGURE 6 | Same as **Figure 5** but for Doppler velocity.

statistical study of correlation and phase-relationship between Doppler velocity and total intensity, we study 40 different light-curves (cases), each of duration 20 min. These cases are selected to be located in the close neighborhood of the power contours of 1–2 min periodicities (red contours in the average SJ image in **Figure 3**). The locations of the selected cases are marked in *black* along the slit in the SJ image in **Figure 3**. Few specific time-intervals are considered at these locations in order to have further study about phase-relationship between Doppler velocity and total intensity.

Figure 8 shows the histograms of the period of oscillations for different IMFs of total intensity and Doppler velocity with the

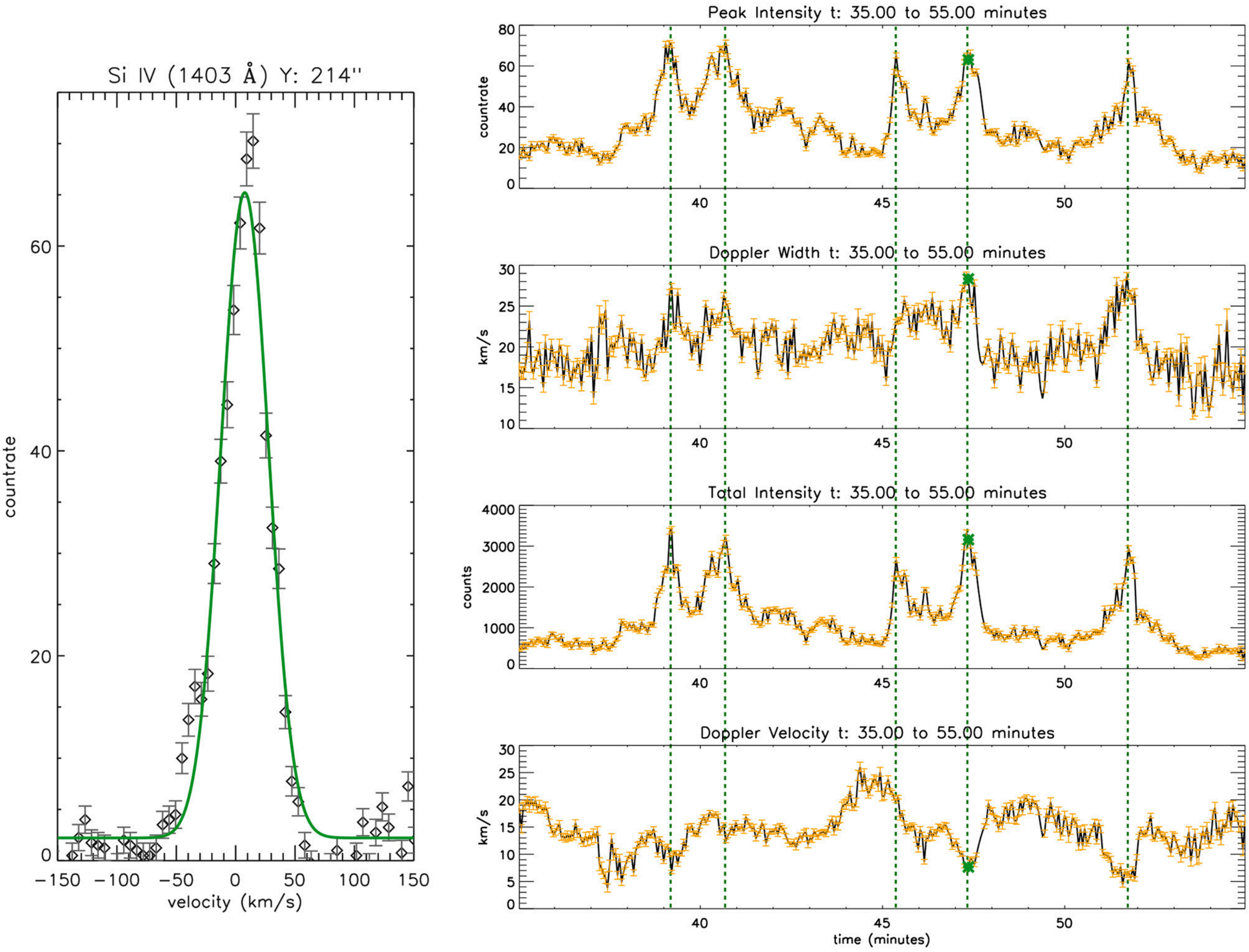

FIGURE 7 | Left panel shows the observed spectral line profile (*black* symbols with the observational errors) of Si IV 1403 Å emission line at location B, with the Gaussian fit (*green* solid curve) for a particular instance. Panels on the right show the light-curves (in *black*) with the fitting errors (in *orange*) of different spectral parameters at B for a duration of 20 min. The *green* solid symbol over the light-curves marks the instant for which the spectral profile is shown in the left panel. The dotted lines shows some instances of the possible reconnection flows. An animation of this figure is available as the supplementary material (**Supplementary Video 1**) in the online version which shows the evolution of the spectral profile with time.

mean periods listed in the figure. As reflected by the value of mean periods, we will further regard the IMF0 to be associated with the periodicity of ∼0.17 min, IMF1 with ∼0.40 min, IMF2 with ∼0.72 min and IMF3 with ∼1.26 min. The power maps in **Figure 4** shows the absence of significant power in the periods below 0.6 min. Henceforth, for the further analysis about phase-relationship, we consider only the third and fourth IMFs, i.e., IMF2 and IMF3. The phase-relation between Doppler velocity and total intensity at the short-periodicities is studied by correlating their respective IMFs for the 40 cases. **Figure 9** shows the histograms of the phase difference between Doppler velocity and total intensity by considering IMF2 and IMF3. The sign convention for the values of phase-shifts considered here is such that the positive values phase-shift signifies the Doppler velocity to be leading with respect to the total intensity. The histogram of IMF2 reveal the presence of preferred phase-shifts at $\sim \pm 3T/8$ ($\sim \pm 3\pi/4$) where $T = 0.72$ min, is the time period of oscillation. The histogram of IMF3 shows the dominant phase-shifts at $\sim -T/2$ ($\sim -\pi$) where $T = 1.26$ min.

The presence of a dominant phase shift of ∼T/2 for periodicities of ∼1.26 min (IMF3) indicates the presence of reconnection events. As shown in **Figure 7**, the increase in the intensity is accompanied by the increase in the Doppler width and decrease in Doppler velocity (blue-shifted flows, De Pontieu et al., 2009; De Pontieu and McIntosh, 2010) at many instances throughout the light-curve. Few of such instances are shown by vertical dotted lines in **Figure 7**. In case of phase-shifts of ∼±T/2 or $\sim\pm\pi$, the reconnection process results in near simultaneous variation in the spectral parameters with the resultant mass flow projected toward the line-of-sight (blue-shifts or negative Doppler velocity). As the TR emission lines are red-shifted in general, the flows toward the line-of-sight (blue-shifted flows)

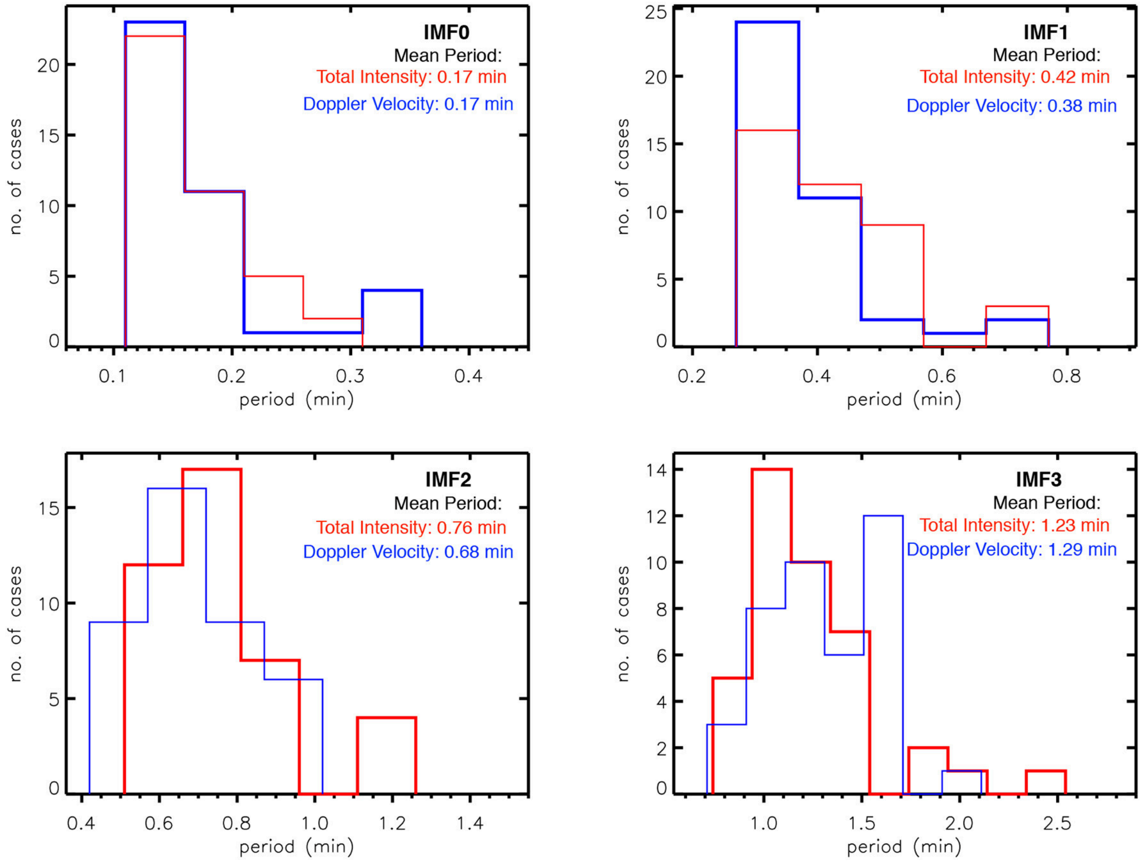

FIGURE 8 | Histograms showing the distribution of periods of the first four IMFs of total intensity in red and Doppler velocity in blue for the 40 selected cases.

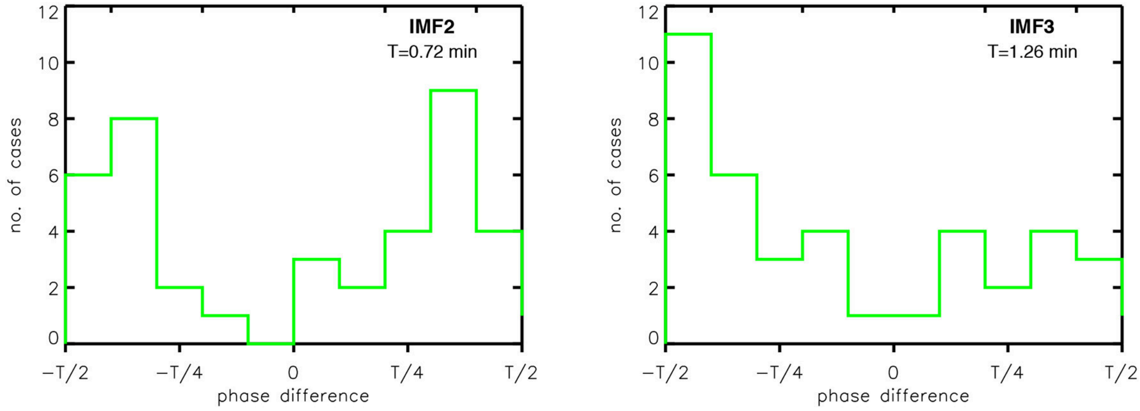

FIGURE 9 | Histograms showing the distribution of phase-difference between total intensity and Doppler velocity for IMF2 and IMF3 for the 40 selected cases.

will appear to decrease the Doppler speeds simultaneously with the increase in the intensity and width (phase-shift of ∼±T/2 or ∼±π). On the other hand, the flows away from the line-of-sight will increase the value of the Doppler speeds with an increase in the line intensity and width (∼ zero phase-shift). It can be observed from **Figure 7** and also indicated by **Figure 9** that the red-shifted flows (cases with zero phase difference) occur less frequently compared to blue-shifted flows (cases with phase shifts of ±T/2). As shown in **Figure 7**, the instances of large amplitude fluctuations, which mostly have phase shift of ∼T/2 between Doppler velocity and total intensity, can be regarded as the clear signatures of quasi-periodic outflows (toward the observer) resulting from the reconnection process. The other instances of small amplitude fluctuations can be due the presence of slow magneto-acoustic waves.

Very recently, Hansteen et al. (2014) and Brooks et al. (2016) have reported the presence of transition region fine loops with the aid of IRIS observations and numerical simulations. Such small scale loops with loop lengths of ∼1 to 2 Mm can harbor slow standing waves with periods of ∼1 min in transition region. It is worth noting at this point that Wang et al. (2003); Taroyan et al. (2007); Taroyan and Bradshaw (2008) reported the presence of standing slow waves exclusively in hot coronal loops. In addition, Pant et al. (2017) reported the existence of standing slow waves in cool coronal loops (∼0.6 MK). In this work, we found evidence of the existence of slow waves in Si IV 1403 Å emission line whose formation temperature is ∼60000 K. In an ideal case, the phase-shift of ∼±T/4 is attributed to the presence of standing slow waves in the solar atmosphere (Wang et al., 2003; Taroyan et al., 2007; Taroyan and Bradshaw, 2008; Moreels and Van Doorsselaere, 2013). Further, it should be noted that the intensity and velocity changes phase in time due to the heating and cooling of the plasma (Taroyan and Bradshaw, 2008) and due to presence of imperfect waveguides and drivers in reality, which deviates from the theoretical considerations (Keys et al., 2018). Thus the phase shift between intensity and velocity oscillations might differ in different regions and different time as showcased in **Figure 10**. **Figure 10** shows the representative examples of the IMFs (IMF2 and IMF3) at location B along the slit. The phase-shift between Doppler velocity and total intensity (ϕ) obtained using the correlation techniques is also mentioned in the respective panels. The comparison between of the respective IMFs of intensity and Doppler velocity fluctuations clearly depicts that the phase-shift between them changes continuously throughout the entire duration. This could be due to the intermittent nature of the flows and waves that might result in departure from the theoretically expected values of the phase-shifts. Hence we conjecture that the statistically dominant phase shift of ∼±3T/8 for periodicities of ∼0.72 min (IMF2) is due to the presence of small-scale flows along with slow standing waves in TR fine loops. This supports both wave and reconnection like scenario to be responsible for the periodicities of 1–2 min in moss regions, which is discussed in details in section 4.

3.3. Density Diagnostics From Si IV 1403 Å and O IV 1401 Å Emission Lines

In order to obtain the information about density variations associated with the presence of waves and/or reconnection flows, in the moss regions, we attempt to estimate density along the slit using Si IV 1403 Å ($\lambda = 1402.77$ Å) and O IV 1401 Å ($\lambda = 1401.16$ Å) spectral lines from the IRIS spectra (as suggested by Young et al., 2018). They introduced an empirical correction factor to normalize Si IV/O IV line intensity ratios. As first mentioned by Dupree (1972), the observed intensities of lines from the lithium and sodium-like iso-electronic sequences are usually stronger than that expected by the emission measures from other sequences formed at the same temperature. Hence, such a correction factor is important to be applied to silicon line intensities. Table 2 of Young et al. (2018) gives the theoretical ratios of different lines after employing the correction factor (see QS DEM method as explained in Young, 2018; Young et al., 2018). We use the Si IV (1402.77)/O IV (1401.16) line ratio from Table 2 of Young et al. (2018) for the estimation of electron density at a temperature of log $T/K = 4.88$ (temperature of maximum ionization of Si IV).

As the O IV 1401 Å line is very weak in IRIS spectra, the spectra is averaged over 7 pixels along the slit. In such averaging, for instance, the data value of the first 7 spatial pixels are replaced by their average value, the next 7 pixels are replaced by their respective average data-value, and so on. Similarly, time-averaging is also performed by considering 4 time steps along the temporal axis. In order to improve S/N, such averaging is performed only over O IV 1401 Å spectra as Si IV 1403 Å spectra contains significantly good signal. **Figures 11A,B** shows the time-sequence maps of peak intensity along the slit for the Si IV 1403 Å and O IV 1401 Å line-profiles. A comparison between the two maps clearly shows that despite averaging the spectra (as explained above), we are able to obtain good S/N only for very few isolated O IV 1401 Å line-profiles in order to perform a reliable Gaussian fit, hence the peak intensity values for the O IV 1401 Å line are shown only for those isolated few pixels.

Figure 11C shows the theoretical Si IV (1403)/O IV (1401) ratio-density curve (Young et al., 2018) in *solid black* and the estimated density values are over-plotted in *magenta*. The density time-sequence map is also showcased in **Figure 11D**. Note that we could estimate the density only at very few instances of some of the locations, as limited by the poor signal in O IV 1401 Å spectra. It can be observed in **Figure 11D** that we cannot find considerable examples of continuous density signal along time for some significant amount of duration over the entire observation. It is completely unreliable to perform any time series analysis over such light-curves. It appears that there are definite changes in the density but to relate those changes with intensity and other line parameters for identification of the wave mode is beyond the quality of the current observations. Thus, we are still unable to obtain any results related to density oscillations with the present data.

4. CONCLUSIONS

In the present article, we study high-frequency dynamics of active region moss by using high spatially and spectrally resolved observations of IRIS, with the fast cadence of 13 s for imaging and 3.3 s for spectral data. The techniques of wavelet and EMD analysis are employed in conjunction to explore the characteristics of the high-frequency oscillations. We have observed the persistent presence of periodicities in the 1–2 min range in the Si IV 1400 Å SJ intensity as well as in different spectral parameters (total intensity, peak intensity, Doppler velocity, and Doppler width) derived from the Si IV 1403 Å emission line. The power maps deduced from the SJ intensity variations show the concentration of power in short-periodicities generally in the bright regions of the moss. This

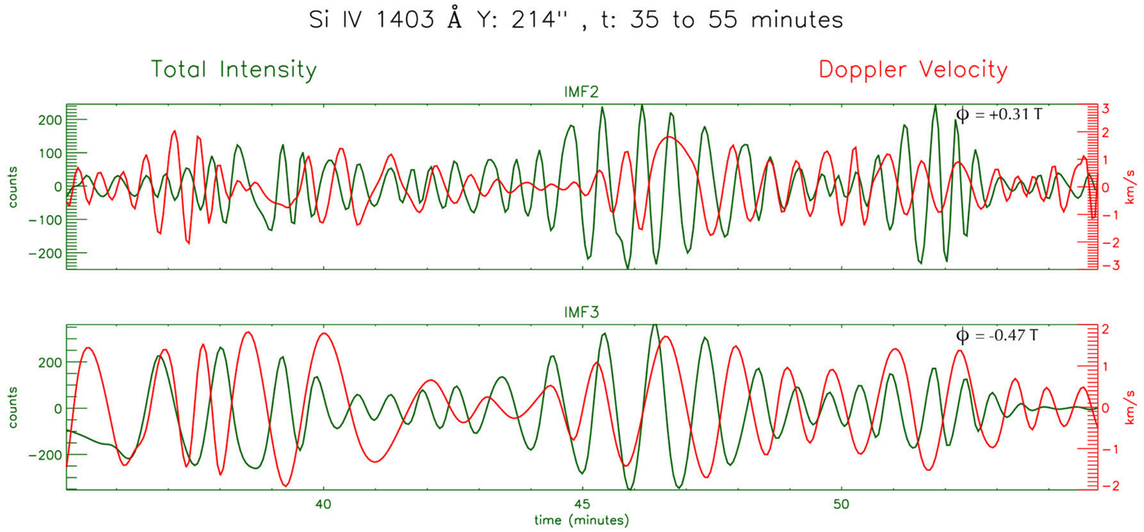

FIGURE 10 | Representative examples of the IMFs at location B along the slit, showing the respective comparisons between Doppler velocity and total intensity oscillations, and depicting that the phase-shift between them changes continuously.

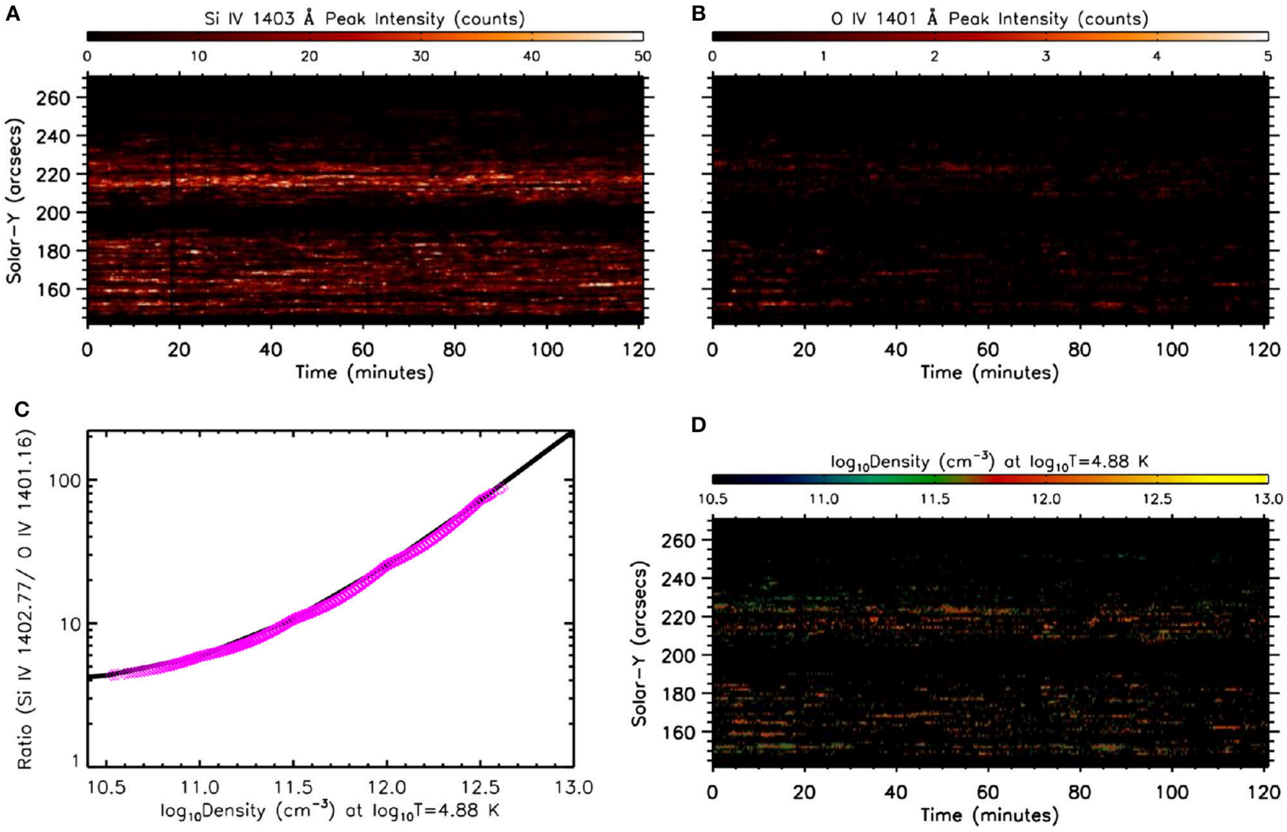

FIGURE 11 | (A,B) Time-sequence maps of peak intensity of the Si IV (1403 Å) and O IV (1401 Å) line. **(C)** Theoretical Si IV (1403)/O IV (1401) ratio density curve in *solid black* and the estimated values of the density in *magenta* corresponding to the observed ratios. **(D)** Time-sequence map of the estimated density.

result is in agreement with the study of Pant et al. (2015), where the authors reported high-frequency quasi-periodic oscillations concentrated over localized regions in the active region moss. However, no attempts were made to understand the nature of variability due to the lack of spectral data. That study was performed using the 193 Å passband of Hi-C which is sensitive to coronal temperatures. In this work, we find similar signatures in TR. Additionally, the power maps of the spectral parameters also reveal the predominance of significant power in the 1–2 min period range.

We study the phase difference between Doppler velocities and total intensity. Our study supports both wave and reconnection like scenario to be responsible for the periodicities of 1–2 min in moss regions. Studying the phase relationships, we can conclude that the periodicity of 1.26 min with dominant phase shifts of $\sim -T/2$ $(\sim -\pi)$ is predominantly due to the outflows resulting from the reconnection process. On the other hand, the periodicity of 0.72 min with dominant phase shifts of $\sim \pm 3\mathrm{T}/8$ $(\sim \pm 3\pi/4)$ can be regarded as the collective signatures of the small-scale flows and slow standing modes existing within the transition region fine loops of lengths 1–2 Mm. Hence qualitatively, we can conjecture that the high-frequency oscillations of ~1 min, observed in the bright moss regions are possibly due to the combination of slow magneto-acoustic waves and reconnection events. As explained in section 3.3, we cannot obtain any reliable results from the density variations, although we are able to estimate the average density of the moss regions but to reliably study the density variation much better quality of data is required. The high-frequency oscillations in the moss regions can be due to compressive waves. The key to distinguish between the different modes conclusively is to study the density variations which is not possible with present data because of low data-counts present in the O IV 1410 Å emission line. Some new instruments, with better sensitivity in the FUV wavelengths, especially in the density sensitive lines, may provide new insight and will enable us to specifically detect the particular wave modes responsible for such oscillations.

AUTHOR CONTRIBUTIONS

VP identified the IRIS data. VP and DB planned the study. NN performed all analysis and wrote the manuscript. VP, DB, and TVD helped in analysing the results. All authors participated in the discussion.

FUNDING

NN is supported by the Senior Research Fellowship scheme of the Council of Scientific and Industrial Research (CSIR) under the Human Resource Development Group (HRDG), India. TVD and VP are supported by the GOA-2015-014 (KU Leuven) and the European Research Council (ERC) under the European Union's Horizon 2020 research and innovation programme (grant agreement No 724326).

ACKNOWLEDGMENTS

Authors acknowledge IRIS team for the publicly available data used in this paper. IRIS is a NASA Small Explorer mission developed and operated by the Lockheed Martin Solar and Astrophysics Laboratory (LMSAL), with mission operations executed at the NASA Ames Research Center and major contributions to downlink communications funded by the Norwegian Space Center (Norway) through a European Space Agency PRODEX contract.

SUPPLEMENTARY MATERIAL

The Supplementary Material for this article can be found online at: https://www.frontiersin.org/articles/10.3389/fspas.2019.00036/full#supplementary-material

REFERENCES

Arregui, I. (2015). Wave heating of the solar atmosphere. *Philos. Trans. R. Soc. Lond. Ser. A* 373:20140261. doi: 10.1098/rsta.2014.0261

Brooks, D. H., Reep, J. W., and Warren, H. P. (2016). Properties and modeling of unresolved fine structure loops observed in the solar transition region by IRIS. *Astrophys. J.* 826:L18. doi: 10.3847/2041-8205/826/2/L18

De Pontieu, B., and McIntosh, S. W. (2010). Quasi-periodic Propagating Signals in the Solar Corona: the Signature of Magnetoacoustic Waves or High-velocity Upflows? *Astrophys. J.* 722, 1013–1029. doi: 10.1088/0004-637X/722/2/1013

De Pontieu, B., McIntosh, S. W., Hansteen, V. H., and Schrijver, C. J. (2009). Observing the roots of solar coronal heating—in the chromosphere. *Astrophys. J.* 701, L1–L6. doi: 10.1088/0004-637X/701/1/L1

De Pontieu, B., Title, A. M., Lemen, J. R., Kushner, G. D., Akin, D. J., Allard, B., et al. (2014). The interface region imaging spectrograph (IRIS). *Solar Phys.* 289, 2733–2779. doi: 10.1007/s11207-014-0485-y

Dupree, A. K. (1972). Analysis of the extreme-ultraviolet quiet solar spectrum. *Astrophys. J.* 178, 527–542. doi: 10.1086/151813

Gandorfer, A., Grauf, B., Barthol, P., Riethmüller, T. L., Solanki, S. K., Chares, B., et al. (2011). The filter imager SuFI and the image stabilization and light distribution system ISLiD of the sunrise balloon-borne observatory: instrument description. *Solar Phys.* 268, 35–55. doi: 10.1007/s11207-010-9636-y

Gupta, G. R., and Tripathi, D. (2015). IRIS and SDO observations of recurrent explosive events. *Astrophys. J.* 809:82. doi: 10.1088/0004-637X/809/1/82

Hansteen, V., De Pontieu, B., Carlsson, M., Lemen, J., Title, A., Boerner, P., et al. (2014). The unresolved fine structure resolved: IRIS observations of the solar transition region. *Science* 346:1255757. doi: 10.1126/science.1255757

Huang, N. E., Shen, Z., Long, S. R., Wu, M. C., Shih, H. H., Zheng, Q., et al. (1998). The empirical mode decomposition and the Hilbert spectrum for nonlinear and non-stationary time series analysis. *Proc. R. Soc. Lond. Ser. A* 454, 903–998. doi: 10.1098/rspa.1998.0193

Ishikawa, S.-N., Kubo, M., Katsukawa, Y., Kano, R., Narukage, N., Ishikawa, R., et al. (2017). CLASP/SJ observations of rapid time variations in the Lyα emission in a solar active region. *Astrophys. J.* 846:127. doi: 10.3847/1538-4357/aa862e

Jafarzadeh, S., Solanki, S. K., Stangalini, M., Steiner, O., Cameron, R. H., and Danilovic, S. (2017). High-frequency oscillations in small magnetic elements observed with sunrise/SuFI. *Astrophys. J. Suppl.* 229:10. doi: 10.3847/1538-4365/229/1/10

Kano, R., Bando, T., Narukage, N., Ishikawa, R., Tsuneta, S., Katsukawa, Y., et al. (2012). "Chromospheric Lyman-alpha spectro-polarimeter (CLASP)," in *Space*

Telescopes and Instrumentation 2012: Ultraviolet to Gamma Ray, Vol. 8443 (Amsterdam), 84434F. doi: 10.1117/12.925991

Keenan, F. P., Ahmed, S., Brage, T., Doyle, J. G., Espey, B. R., Exter, K. M., et al. (2002). The OIV and SIV intercombination lines in the ultraviolet spectra of astrophysical sources. *Mon. Not. Roy. Astron. Soc.* 337, 901–909. doi: 10.1046/j.1365-8711.2002.05988.x

Keys, P. H., Morton, R. J., Jess, D. B., Verth, G., Grant, S. D. T., Mathioudakis, M., et al. (2018). Photospheric observations of surface and body modes in solar magnetic pores. *Astrophys. J.* 857:28. doi: 10.3847/1538-4357/aab432

Klimchuk, J. A. (2006). On solving the coronal heating problem. *Solar Phys.* 234, 41–77. doi: 10.1007/s11207-006-0055-z

Kobayashi, K., Cirtain, J., Winebarger, A. R., Korreck, K., Golub, L., Walsh, R. W., et al. (2014). The high-resolution coronal imager (Hi-C). *Solar Phys.* 289, 4393–4412. doi: 10.1007/s11207-014-0544-4

Lemen, J. R., Title, A. M., Akin, D. J., Boerner, P. F., Chou, C., Drake, J. F., et al. (2012). The atmospheric imaging assembly (AIA) on the solar dynamics observatory (SDO). *Solar Phys.* 275, 17–40. doi: 10.1007/s11207-011-9776-8

Moreels, M. G., and Van Doorsselaere, T. (2013). Phase relations for seismology of photospheric flux tubes. *Astron. Astrophys.* 551:A137. doi: 10.1051/0004-6361/201219568

Morton, R. J., and McLaughlin, J. A. (2013). Hi-C and AIA observations of transverse magnetohydrodynamic waves in active regions. *Astron. Astrophys.* 553:L10. doi: 10.1051/0004-6361/201321465

Morton, R. J., and McLaughlin, J. A. (2014). High-resolution observations of active region moss and its dynamics. *Astrophys. J.* 789:105. doi: 10.1088/0004-637X/789/2/105

Pant, V., Datta, A., and Banerjee, D. (2015). Flows and waves in braided solar coronal magnetic structures. *Astrophys. J. Lett.* 801:L2. doi: 10.1088/2041-8205/801/1/L2

Pant, V., Tiwari, A., Yuan, D., and Banerjee, D. (2017). First imaging observation of standing slow wave in coronal fan loops. *Astrophys. J. Lett.* 847:L5. doi: 10.3847/2041-8213/aa880f

Parker, E. N. (1988). Nanoflares and the Solar X-Ray corona. *Astrophys. J.* 330:474. doi: 10.1086/166485

Parnell, C. E., and De Moortel, I. (2012). A contemporary view of coronal heating. *Philos. Trans. R. Soc. Lond. Ser. A* 370, 3217–3240. doi: 10.1098/rsta.2012.0113

Reale, F. (2010). Coronal loops: observations and modeling of confined plasma. *Living Rev. Solar Phys.* 7:5. doi: 10.12942/lrsp-2010-5

Samanta, T., Singh, J., Sindhuja, G., and Banerjee, D. (2016). Detection of high-frequency oscillations and damping from multi-slit spectroscopic observations of the corona. *Solar Phys.* 291, 155–174. doi: 10.1007/s11207-015-0821-x

Scharmer, G. B., Narayan, G., Hillberg, T., de la Cruz Rodriguez, J., Löfdahl, M. G., Kiselman, D., et al. (2008). CRISP spectropolarimetric imaging of penumbral fine structure. *Astrophys. J.* 689:L69. doi: 10.1086/595744

Shetye, J., Doyle, J. G., Scullion, E., Nelson, C. J., Kuridze, D., Henriques, V., et al. (2016). High-cadence observations of spicular-type events on the Sun. *Astron. Astrophys.* 589:A3. doi: 10.1051/0004-6361/201527505

Singh, J., Hasan, S. S., Gupta, G. R., Nagaraju, K., and Banerjee, D. (2011). Spectroscopic observation of oscillations in the corona during the total solar eclipse of 22 July 2009. *Solar Phys.* 270, 213–233. doi: 10.1007/s11207-011-9732-7

Taroyan, Y., and Bradshaw, S. (2008). Coronal loop oscillations and diagnostics with Hinode/EIS. *Astron. Astrophys.* 481, 247–252. doi: 10.1051/0004-6361:20078610

Taroyan, Y., Erdélyi, R., Wang, T. J., and Bradshaw, S. J. (2007). Forward modeling of hot loop oscillations observed by SUMER and SXT. *Astrophys. J. Lett.* 659, L173–L176. doi: 10.1086/517521

Testa, P., De Pontieu, B., Martínez-Sykora, J., DeLuca, E., Hansteen, V., Cirtain, J., et al. (2013). Observing coronal nanoflares in active region moss. *Astrophys. J. Lett.* 770:L1. doi: 10.1088/2041-8205/770/1/L1

Torrence, C., and Compo, G. P. (1998). A practical guide to wavelet analysis. *Bull. Amer. Meteorol. Soc.* 79, 61–78. doi: 10.1175/1520-0477(1998)079<0061:APGTWA>2.0.CO;2

Wang, T. J., Solanki, S. K., Curdt, W., Innes, D. E., Dammasch, I. E., and Kliem, B. (2003). Hot coronal loop oscillations observed with SUMER: examples and statistics. *Astron. Astrophys.* 406, 1105–1121. doi: 10.1051/0004-6361:20030858

Young, P. R. (2018). Element abundance ratios in the quiet sun transition region. *Astrophys. J.* 855:15. doi: 10.3847/1538-4357/aaab48

Young, P. R., Keenan, F. P., Milligan, R. O., and Peter, H. (2018). A Si IV/O IV electron density diagnostic for the analysis of IRIS solar spectra. *Astrophys. J.* 857:5. doi: 10.3847/1538-4357/aab556

Conflict of Interest Statement: The authors declare that the research was conducted in the absence of any commercial or financial relationships that could be construed as a potential conflict of interest.

The reviewer KS declared a past co-authorship with one of the authors TVD to the handling editor.

frontiers
in Astronomy and Space Sciences

ORIGINAL RESEARCH
published: 21 May 2019
doi: 10.3389/fspas.2019.00038

Amplitudes and Energy Fluxes of Simulated Decayless Kink Oscillations

Konstantinos Karampelas[1]*, Tom Van Doorsselaere[1], David J. Pascoe[1], Mingzhe Guo[1,2] and Patrick Antolin[3]

[1] Department of Mathematics, Centre for Mathematical Plasma Astrophysics, KU Leuven, Leuven, Belgium, [2] Institute of Space Sciences, Shandong University, Weihai, China, [3] School of Mathematics and Statistics, University of St. Andrews, St. Andrews, United Kingdom

Recent observations with the Atmospheric Imaging Assembly (AIA) instrument on the SDO spacecraft have revealed the existence of decayless coronal kink oscillations. These transverse oscillations are not connected to any external phenomena like flares or coronal mass ejections, and show significantly lower amplitudes than the externally excited decaying oscillations. Numerical studies have managed to reproduce such decayless oscillations in the form of footpoint driven standing waves in coronal loops, and to treat them as a possible mechanism for wave heating of the solar corona. Our aim is to investigate the correlation between the observed amplitudes of the oscillations and input the energy flux from different drivers. We perform 3D MHD simulations in single, straight, density-enhanced coronal flux tubes for different drivers, in the presence of gravity. Synthetic images at different spectral lines are constructed with the use of the FoMo code. The development of the Kelvin-Helmholtz instability leads to mixing of plasma between the flux tube and the hot corona. Once the KHI is fully developed, the amplitudes of the decayless oscillations show only a weak correlation with the driver strength. We find that low amplitude decayless kink oscillations may correspond to significant energy fluxes of the order of the radiative losses for the Quiet Sun. A clear correlation between the input energy flux and the observed amplitudes from our synthetic imaging data cannot be established. Stronger drivers lead to higher vales of the line width estimated energy fluxes. Finally, estimations of the energy fluxes by spectroscopic data are affected by the LOS angle, favoring combined analysis of imaging and spectroscopic data for single oscillating loops.

Keywords: solar corona, forward modeling, magnetohydrodynamics, corona loops, decayless oscillations

OPEN ACCESS

Edited by:
Xueshang Feng,
State Key Laboratory of Space Weather, National Space Science Center (CAS), China

Reviewed by:
Alina Catalina Donea,
Monash University, Australia
Sergey Anfinogentov,
Institute of Solar-Terrestrial Physics (RAS), Russia

***Correspondence:**
Konstantinos Karampelas
kostas.karampelas@kuleuven.be

Specialty section:
This article was submitted to Stellar and Solar Physics, a section of the journal Frontiers in Astronomy and Space Sciences

Received: 07 March 2019
Accepted: 30 April 2019
Published: 21 May 2019

Citation:
Karampelas K, Van Doorsselaere T, Pascoe DJ, Guo M and Antolin P (2019) Amplitudes and Energy Fluxes of Simulated Decayless Kink Oscillations. Front. Astron. Space Sci. 6:38. doi: 10.3389/fspas.2019.00038

1. INTRODUCTION

Over the past 20 years, observations of the Sun have shown the existence of waves and oscillations throughout the solar corona (Aschwanden, 2006; De Moortel and Nakariakov, 2012). The discovery of transverse magnetohydrodynamic (MHD) standing (Aschwanden et al., 1999; Nakariakov et al., 1999) waves in coronal loops, and propagating waves in open magnetic field structures (Verwichte et al., 2005) has lead to many observational and numerical studies. The ubiquity of such waves has also been established in prominence threads (Okamoto et al., 2007), coronal loops (McIntosh et al., 2011), as well as greater areas of the corona (Tomczyk et al., 2007; Tomczyk and McIntosh, 2009; Thurgood et al., 2014; Morton et al., 2016), renewing the interest on the effects of these waves in the solar atmosphere.

Analytical studies on the nature of the transverse oscillations in inhomogeneous plasmas (Zajtsev and Stepanov, 1975; Ryutov and Ryutova, 1976; Edwin and Roberts, 1983; Allcock and Erdélyi, 2017) have described the different surface waves expected in a non-uniform plasma. In order to explain the observed damping of such oscillations (Tomczyk and McIntosh, 2009; Terradas et al., 2010; Verth et al., 2010; Pascoe et al., 2016a, 2017; Pascoe et al., 2019), extensive theoretical and numerical work has also been performed. The mechanisms of resonant absorption and mode coupling (Sakurai et al., 1991; Goossens et al., 1992, 2011; Ruderman and Roberts, 2002; Arregui et al., 2005; Pascoe et al., 2012, 2016b, 2018; De Moortel et al., 2016; Yu et al., 2017) are considered the reason behind this spatial and temporal attenuation of the oscillations, by transferring the energy of the global kink mode to local azimuthal Alfvén modes. Through phase mixing (Heyvaerts and Priest, 1983; Soler and Terradas, 2015), the energy is then transferred to ever decreasing smaller scales until it gets dissipated by resistivity and viscosity (Ofman et al., 1994a,b, 1998; Poedts and Boynton, 1996). Observational studies of waves in the solar chromosphere and corona (De Pontieu et al., 2007; Tomczyk and McIntosh, 2009; Morton et al., 2012) suggest the existence of enough energy flux to sustain the radiative losses of $\sim$100 W m^{-2} for the non-active region corona (Withbroe and Noyes, 1977). In De Moortel and Pascoe (2012) it was shown that LOS integration of footpoint driven multistrand coronal loop oscillations leads to an underestimation of the wave energy. In Antolin et al. (2017) it was found for a non-driven oscillating loop that the wave energy ends up underestimated through the localization of the energy by resonant absorption. Recent simulations of coronal loop waves (Pagano and De Moortel, 2017, 2019; Pagano et al., 2018) have not reported sufficient heating to balance the radiative losses.

Alongside the high amplitude, externally initiated, decaying transverse oscillations in coronal loops (Verwichte et al., 2009, 2010; White and Verwichte, 2012; White et al., 2012) a new group of small-amplitude decayless transverse oscillations have been identified in coronal loops (Nisticò et al., 2013; Anfinogentov et al., 2015; Duckenfield et al., 2018), with amplitudes $\sim$0.1–0.4 Mm. These decayless oscillations have been interpreted in different ways over the years. They have been treated as continuously driven kink waves with a footpoint driver (Afanasyev et al., 2019; Guo et al., 2019; Karampelas et al., 2019), as a self-oscillatory process due to the interaction of the loops with quasi-steady flows (Nakariakov et al., 2016), or as a line of sight (LOS) effect from the development of the Kelvin-Helmholtz instability (KHI) (Antolin et al., 2016) in impulsive standing loop oscillations.

The development of the KH instability has been theorized in plasma structures were standing surface waves are observed (Heyvaerts and Priest, 1983; Browning and Priest, 1984; Zaqarashvili et al., 2015; Barbulescu et al., 2019; Hillier et al., 2019), caused by the strong shear velocities generated by the azimuthal Alfvén waves. Recent numerical studies (Terradas et al., 2008, 2018; Antolin et al., 2014; Antolin et al., 2018; Magyar and Van Doorsselaere, 2016; Howson et al., 2017; Karampelas et al., 2017) have confirmed the development of transverse wave induced Kelvin-Helmholtz (TWIKH) rolls for standing kink waves. Additional work has been performed in order to develop methods of identifying the effects of KHI in oscillating loops (Goddard et al., 2018; Van Doorsselaere et al., 2018). Spatially extended TWIKH rolls have been found in the case of continuously driven standing waves, which fully deform the initial monolithic loop cross-section into a fully turbulent one (Karampelas and Van Doorsselaere, 2018; Karampelas et al., 2019). These spatially extended TWIKH rolls in simulations of continuously driven loops have also been reported as sites of mixing of plasma and heating in the solar corona, by effectively spreading the effects of phase mixing across the cross-section of loops (Afanasyev et al., 2019; Karampelas et al., 2017, 2019; Guo et al., 2019).

One of the main challenges in creating an efficient wave heating model is to find a way of providing a high enough energy flux over large periods of time, while still remaining within the constraints imposed by the observational data. The decayless oscillations seem to be ideal candidates for prolonged energy input in such a model, and also pose the constraint of having relatively small oscillation amplitudes. In Guo et al. (2019), the use of a mixed Alfvén and transverse footpoint driver suggested as a way of increasing the total energy input while retaining small amplitudes in the synthetic images. The authors in Afanasyev et al. (2019) suggest the use of broadband drivers as a way to include additional energy for a decreased observational impact, while still maintaining sufficient energy input. In the current work, we study the effects of transverse footpoint drivers of different strengths on the observational signatures of the induced oscillations in synthetic images. The aim is to detect the existence of a correlation between the input energy flux and the oscillation amplitudes and to determine the observed fluxes from synthetic spectroscopic and imaging data, and set possible constraints for future work.

2. MATERIALS AND METHODS

2.1. Basic Setup

For our 3D simulations, we use straight, density-enhanced magnetic flux tubes in a low-β coronal environment, following Karampelas et al. (2019). This setup models gravitationally stratified, active region coronal loops in ideal MHD, in the presence of numerical resistivity. Each loop has a full length (L) of 200 Mm and an initial minor radius (R) of 1 Mm, which is constant with height. The radial density profile of our **cylindrical** flux tubes at the footpoint is

$$\rho(x,y) = \rho_e + (\rho_i - \rho_e)\frac{1}{2}(1 - \tanh((\sqrt{x^2+y^2}/R - 1)\,b)). \quad (1)$$

We denote the basic values of our physical parameters with the index i (e) for internal (external) values, with respect to our tube. The external and internal density at the footpoint are equal to

$\rho_e = 10^9 \mu\, m_p$ cm^{-3} $= 0.836 \times 10^{-12}$ kg m^{-3} ($\mu = 0.5$ and m_p is the proton mass) and $\rho_i = 3 \times \rho_e$. We denote the coordinates in the plane perpendicular to the loop axis by x and y , and by z the coordinate along its axis. $b = 20$ sets the width of the boundary layer to $\ell \sim 0.3R$. For the models studied, we set the temperature to be constant with height and equal to $T_e = 3 \times T_i = 2.7$ MK. Finally, we consider an initial uniform magnetic field parallel to the flux tube axis (along the z-axis) equal to $B_z = 22.8$ G. This gives us a plasma $\beta = 0.018$.

Gravity varies sinusoidally along the flux tube, corresponding to a semi-circular loop with major radius $L\pi^{-1}$, and takes a zero value at the loop apex ($z = 0$) and a maximum absolute value at the footpoints ($z = \pm 100$ Mm). Due to the hydrostatic equilibrium we have stratification of pressure and temperature along the loop. To counteract the initial pressure imbalance at the loop boundary caused by the gravitational stratification, the magnetic field is restructuring inside the flux tube, once we let the system reach a semi-equilibrium state after one period. By the end of the relaxation period, neither of temperature, pressure, nor density deviate significantly from their initial state, as in Karampelas et al. (2019). The radial profiles of density and temperature at several positions along the z-axis are shown in **Figure 1**.

2.2. Boundary Conditions and Driver

Our tubes are driven from the footpoint ($z = 100$ Mm), using a continuous, monoperiodic "dipole-like" driver (Karampelas et al., 2017), inspired by that used by Pascoe et al. (2010). The period of the driver is $P \simeq 2L/c_k$, coinciding with the corresponding fundamental eigenfrequency for our gravitationally stratified flux tube (Edwin and Roberts, 1983; Andries et al., 2005). For a kink speed of $c_k = 1{,}167$ km s^{-1} we obtain a period of $P = 171$ s. The driver at the bottom boundary has a uniform and time varying velocity inside the loop,

$$\{\upsilon_x, \upsilon_y\} = \{\upsilon(t), 0\} = \left\{\upsilon_0 \cos(\frac{2\pi t}{P}), 0\right\}, \tag{2}$$

where υ_0 (in km s^{-1}) is the peak velocity amplitude. Outside the loop, the velocity follows the relation

$$\{\upsilon_x, \upsilon_y\} = \upsilon(t)R^2 \left\{\frac{(x-\alpha(t))^2 - y^2}{((x-\alpha(t))^2 + y^2)^2}, \frac{2(x-\alpha(t))y}{((x-\alpha(t))^2 + y^2)^2}\right\}, \tag{3}$$

where $\alpha(t) = \upsilon_0\,(0.5\,P/\pi)\ \sin(2\pi t/P)$ is a function that recentres the driver, tracking the footpoint. A transition region following the density profile exists between the two areas, in order to avoid any numerical instabilities due to jumps in the velocity.

We study five different models ("D1," "D2," "D4," "D6," and "D8,"), each for a different corresponding value of $\upsilon_0 = 1$, 2, 4, 6, and 8 km s^{-1}.

At the bottom boundary, we also keep the velocity component parallel to the z-axis (v_z) antisymmetric ($z = 100$ Mm) and we extrapolate the values for density and pressure, using the equations for hydrostatic equilibrium. A zero normal gradient condition is used to extrapolate the values of each magnetic field component through the bottom boundary. Studying the fundamental standing kink mode for an oscillating flux tube allows us to take advantage of the inherent symmetries of this mode, as well as the symmetric nature of our driver. In the top boundary at $z = 0$, the location of the loop apex, we kept v_z, B_x, and B_y antisymmetric in the $x-y$ plane at the apex. The rest of the quantities on that boundary are defined as symmetric. Thus, only half the loop is simulated along the loop axis. All side boundaries are set to outflow (Neumann-type, zero-gradient) conditions for all variables.

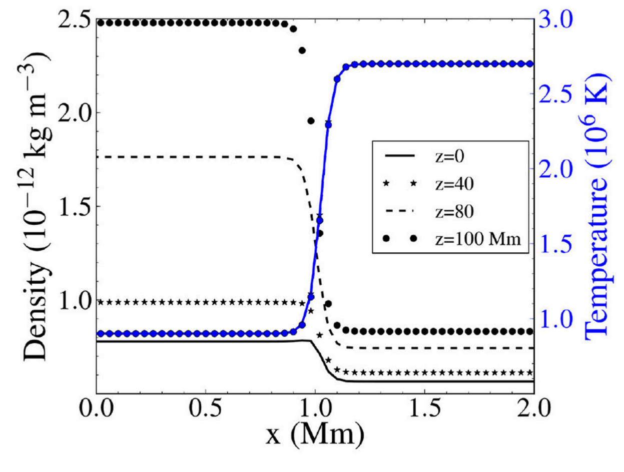

FIGURE 1 | Radial profile of the initial density (with black) and temperature (with blue) for our gravitationally stratified, cylindrical flux tubes at different heights, right before the introduction of the driver. The apex is located at $z = 0$ and the footpoint at $z = 100$ Mm. $x = 0$ is the center of the loop at $t = 0$.

2.3. Numerical Method and Grid

The 3D ideal MHD problem is solved using the PLUTO code (Mignone et al., 2018), with the extended GLM method from Dedner et al. (2002) keeping the solenoidal constraint on the magnetic field. We use the finite volume piecewise parabolic method (PPM) and the characteristic tracing method for the timestep. The domain dimensions are $(x, y, z) = (16, 6, 100)$ Mm for models D1, D2, and D4, and $(x, y, z) = (16, 10, 100)$ Mm for models D6 and D8. The latter was chosen in order to properly resolve the expanded turbulent loop cross-section from the stronger drivers. We have cell dimensions of $40 \times 40 \times 1562.5$ km for all models. The resolution is higher in the $x - y$ plane, to better resolve the small-scale structures that appear in the loop cross section. The density scale height of our setup is 28 Mm, and is close to the value of the loop major radius $L\pi^{-1} \sim 64$ Mm. Alongside the lack of radiation or thermal conduction, this allows for a coarser resolution on the z-axis, that can still sufficiently model the density stratification along the flux tube. In all of our models, we also have the inevitable numerical dissipation effects, which lead to values of effective resistivity and viscosity many orders of magnitude larger than the expected ones in the solar corona.

2.4. Forward Modeling

We use the FoMo code (Van Doorsselaere et al., 2016) to create synthetic images and compare to real observations. We focus on the use of the Fe XII 193 Å emission line, with maximum formation temperature of $\log T = 6.19$, in order to create spectroscopic data of our flux tubes. The 193 Å line tracks the warmer flux tube boundary layer (Antolin et al., 2016, 2017) and is better suited for our studies of driven oscillations with turbulent cross-sections (Karampelas et al., 2019). The same analysis has been performed for the Fe IX 171 Å line. This line has a maximum formation temperature of $\log T = 5.93$, and is more sensitive to the colder plasma from the loop interior. We also use the 'Imaging' functionality of 'fomo-c' from FoMo, in order to create emission images for the corresponding AIA channels.

We create time-distance maps of the loop apex for each model, by placing a slit at LOS angles equal to 0° (perpendicular to the axis of the oscillation, or x axis), 45° and 90° (parallel to the axis of the oscillation). To better compare to the observations of decayless coronal loop oscillations, we degrade the original spatial resolution of the AIA synthetic images to that of SDO/AIA ($0''.6$). Then we resample the data to match the pixel size of the target instrument. A similar process is used for the spectroscopic data, where we try to mimic Hinode/EIS by taking a plate-scale of $1''$ and a Gaussian PSF of $3''$ FWHM (Antolin et al., 2017; Guo et al., 2019), while also adding poisson distributed photon noise. For the spectroscopic data we also reduce the initial spectral resolution from 3 to 36 km s^{-1} for the degraded spectrum. The temporal resolution is kept at $\sim$11 s, which is very close to both that of AIA and EIS instruments.

3. RESULTS

We drive our loops for fifteen cycles. As in Karampelas et al. (2017), the first waves to reach the apex ($z = 0$) are the azimuthal Alfvén waves at the boundary layer of our tube, thanks to their higher propagation speed, followed by the propagating kink waves. Because of the symmetry at the apex, the driver induced waves lead to the initiation of a standing oscillation resembling the fundamental kink mode for gravitationally stratified loops (Andries et al., 2005; Magyar et al., 2015; Karampelas et al., 2019).

Once the standing mode is initiated, we have the gradual development of the KH instability and the expansion of the flux tube cross-section (Karampelas et al., 2017). By performing forward modeling for our setups, we construct time distance maps of our oscillations at the apex, for the different spectral lines. Two examples of these forward modeling time-distance maps are presented in **Figure 2**. There we see the apex displacement over time for the D2 and D4 model in the 171 and 193 Å AIA channels. As expected for loops with turbulent cross-sections (Karampelas et al., 2019), the development of the KH instability and the spatially extended TWIKH rolls lead to extensive mixing of the loop with the surrounding plasma. For our setup of a cold loop embedded in a warmer corona, this leads to a big emission drop in the Fe IX 171 Å line.

By saturating the image of the 171 Å emission line for model D4, we can see that this drop occurs faster for stronger drivers. A smaller drop is also observed in the 193 Å line, for stronger drivers, and is caused by the drop of the average density of the emitting plasma, and its mixing with the surrounding plasma (Karampelas et al., 2017), due to the spatially extended TWIKH rolls. In coronal observations we expect to mostly see the cooling stage of loops (Viall and Klimchuk, 2012). The loops observed performing these decayless observations are expected to be driven for long periods of time, while cooling from higher initial temperatures. Hence, the observed decayless regime should correspond to the later stages of our simulations, where we observe the mixing induced emission drop.

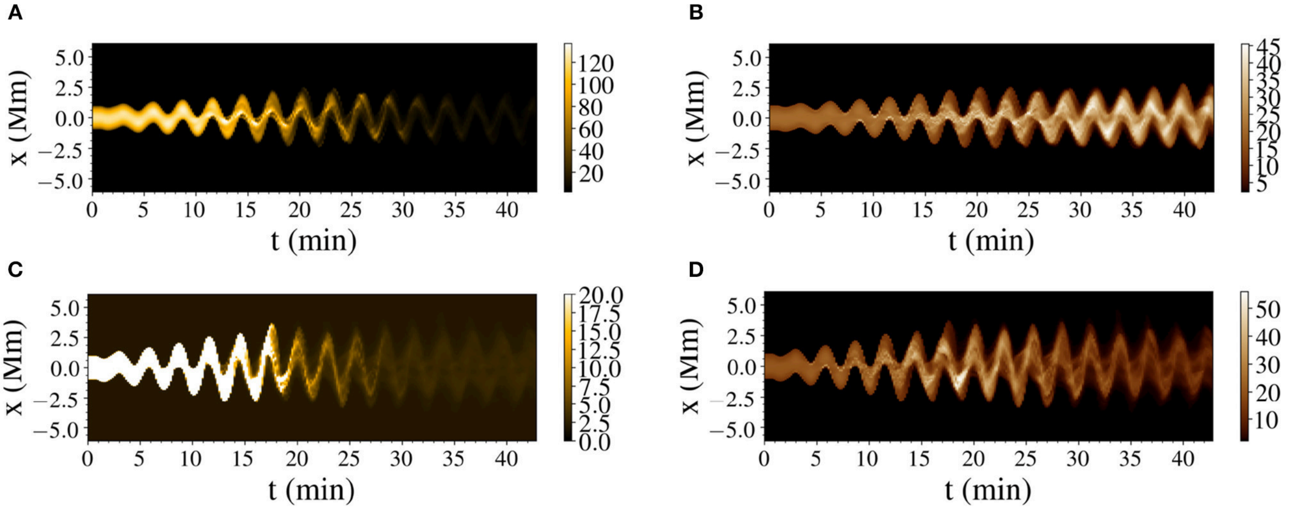

FIGURE 2 | Synthetic time-distance maps for the D2 model in the Fe IX 171 Å **(A)** and Fe XII 193 Å **(B)** and for the D4 model in the Fe IX 171 Å **(C)** and Fe XII 193 Å **(D)** lines at the apex. The time distance maps show the emission (in *ergs* $cm^{-2}s^{-1}sr^{-1}$) for the numerical resolution panels of our model. For the D4 model, the intensity in the 171 Å line is saturated, in order to clearly depict the drop in the emission. The LOS angle is 0°.

In **Figure 3** we present additional synthetic images for the D2 model, both at numerical and instrument resolution. In that figure, we see the 193 Å AIA channel for the emission intensity at 0° LOS angle, as well as the Doppler velocities for the Fe XII 193 Å line at 0 and 90° angles. We observe the development of emission peaks prior to the development of the TWIKH rolls, due to the excitation of higher order harmonics and the deformation of the flux tube from the combined effect of the inertia and fluting modes (Andries et al., 2005; Ruderman et al., 2010; Yuan and Van Doorsselaere, 2016; Antolin et al., 2017; Terradas et al., 2018). Once the KHI develops, we see the emergence of stronger emission peaks in the 193 Å channel, stronger Doppler velocities perpendicular to the direction of the oscillation, and the gradual expansion of the resonant flows across the loop cross-section (Antolin et al., 2015; Karampelas and Van Doorsselaere, 2018). The latter is evident in the bottom panels of **Figure 3**, where we look at the loop from the side. These out of phase movements from the TWIKH rolls are present in all of our models and get more intense and spatially extended the stronger each driver is.

We track the oscillations in the constructed time-distance maps for our models by setting a threshold value off $I_{thr} = I_{min} + 0.1(I_{max} - I_{min})$, where I is the intensity across the loop on each frame, I_{max} is its maximum value and I_{min} is the background intensity. The point with this intensity is defined as the 'edge'of the loop. A spline interpolation for the position is used to inhibit tracking errors, with the number of interpolation points being half the number of frames in the TD map. We present the displacement of the apex for each loop in **Figure 4**, where panels for all the models are shown at a 0° LOS angle. An initial increase of the amplitude is followed by saturation and an eventual drop in the second half of the simulations. This is the stage of the simulations where the decayless regime should correspond to. In the last stages, we see that the D2 and D4 models show similar values of displacement, while the D6 and D8 models show lower amplitudes than the former ones.

We see that similar profiles are obtained for both emission lines used in the present work. The synthetic images in the 171 Å line show higher initial amplitudes than those in the 193 Å line. This is because the loop core has the highest transverse velocities before the development of the KH instability. The loop boundary layer has radially decreasing υ_x velocities, as result of the driver shape that we use at the footpoint, leading to smaller displacements than the loop core, as seen in the two emission lines, each being more sensitive to the corresponding loop region. A similar thing was observed in Antolin et al. (2016). In that work, the loop core showed a higher oscillation amplitude than the loop boundary layer, before the initiation of the KHI. In our models, the constant driving leads to overall

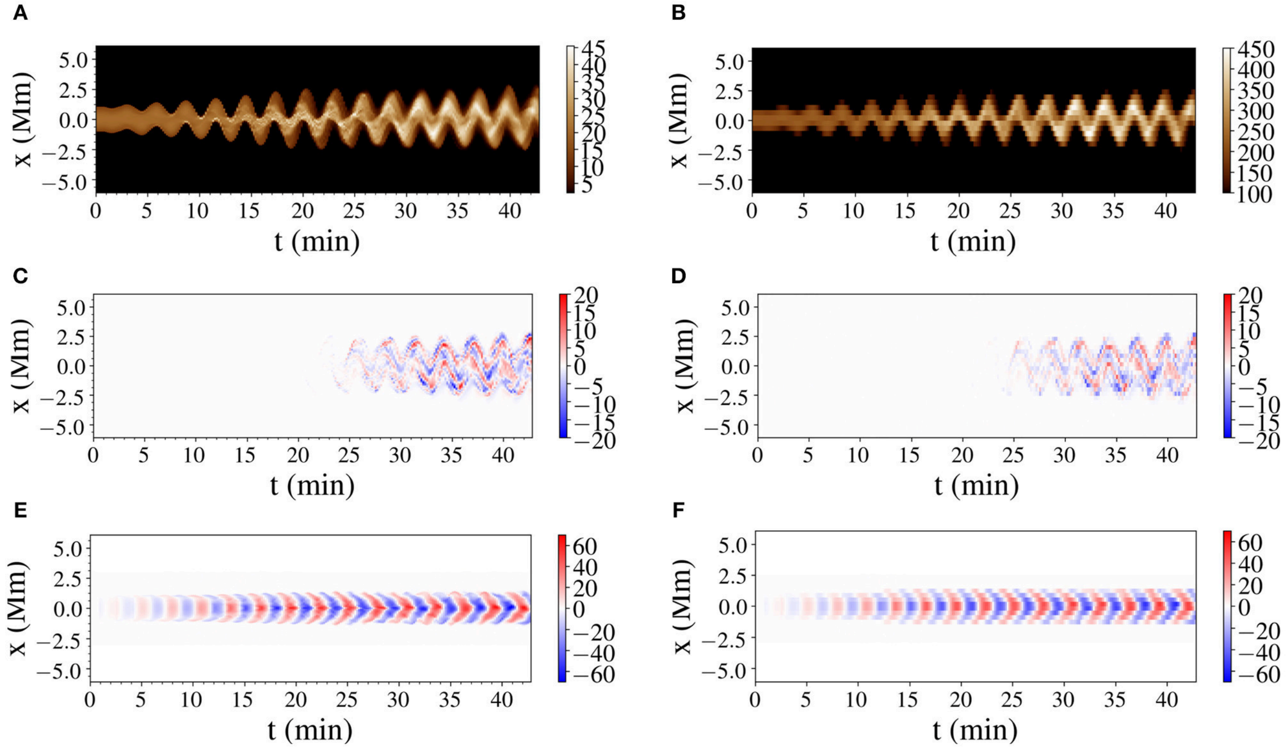

FIGURE 3 | Forward modeling results for the D2 model in the Fe XII 193 Å line at the apex. The left panels show the images for numerical resolution and the right panels the images for the targeted instruments. **(A,B)** Show the emission intensity (in $ergs\ cm^{-2}s^{-1}sr^{-1}$) for numerical and for AIA resolution respectively. **(C,D)** Show the Doppler velocity (in km s^{-1}) at 0°, for numerical and for EIS resolution, respectively. **(E,F)** Doppler velocity (in km s^{-1}) at 90°, for numerical and for EIS resolution, respectively.

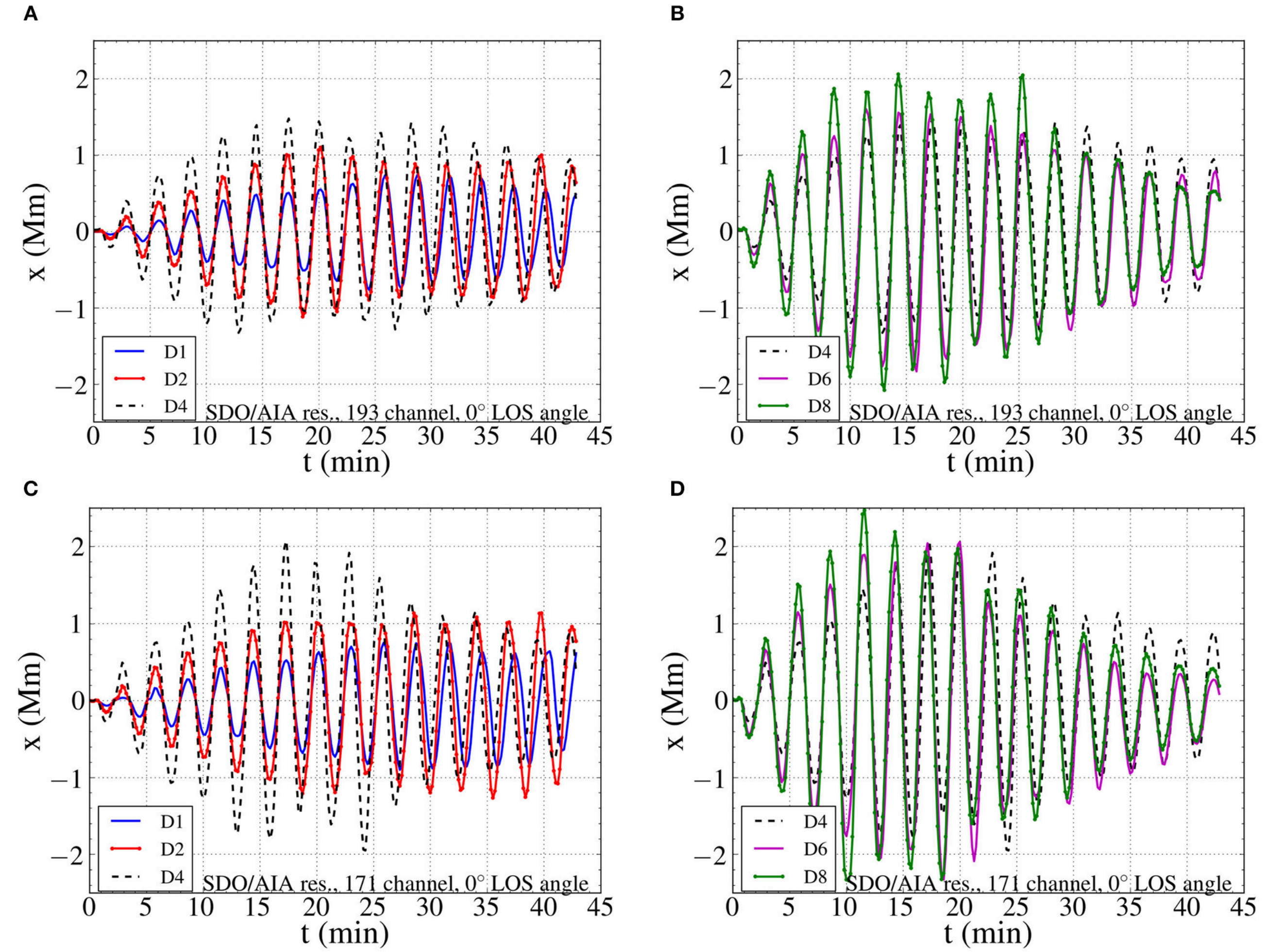

FIGURE 4 | Time distance maps of the oscillation amplitude for the five models. The apex displacements were obtained by tracking the loop edge in synthetic emission images of the Fe XII 193 Å line for **(A,B)** and of the Fe IX 171 Å line for **(C,D)**, at 0°.

stronger displacements, while the deformation of the loop cross-section leads to higher amplitudes in the 193 Å line for the given temperature distribution.

In **Figure 4** we get a small phase difference between the D1 model and all the rest. This small change in the phase between the observed displacement and the driving frequency is a LOS effect and caused by the integration of the emission across TWIKH rolls with varying phases. A similar phase shift was observed for the turbulent layer of oscillating loops performing in Antolin et al. (2016). For the D1 model, the slower development of the KHI leads to a delay in the manifestation of that phase difference. Similar trends have been observed for synthetic images at 45°, with the difference that the obtained displacements are smaller due to the projection of the oscillation plane on the plane of sky (POS).

In order to determine whether the obtained amplitude drop in **Figure 4** is caused purely by the development of strong azimuthal resonant flows and the KH eddies, we plot in **Figure 5** the input energy flux (J m^{-2} s^{-1}) for each driver. The Poynting fluxes are calculated for a surface area of 3 × 3 Mm^2 in the centre of the bottom boundary. This square contains the loop footpoint of each model, and provides 80% of the total energy input from the spatially localized driver. The curves in **Figure 5** represent the time evolution of the average values of the fluxes.

We can see that the efficiency of the drivers change over time, with the strongest changes happening for the stronger drivers. These variations with time are the result of the boundary conditions employed here. The zero normal gradient condition for the magnetic field allowed it to freely evolve with time, instead of fixing its value at the footpoint. This is affecting the Poynting flux from the driver in the bottom boundary, causing the evolution of the energy input, similarly to Guo et al. (2019) and Karampelas et al. (2019). In the scope of this study, we do not focus on creating a realistic model for a driver, but we focus on the effects of the driver strength on the synthetic data. Therefore, tracking the evolution of the driver efficiency is sufficient within the context of the current study. The initial increase in the energy

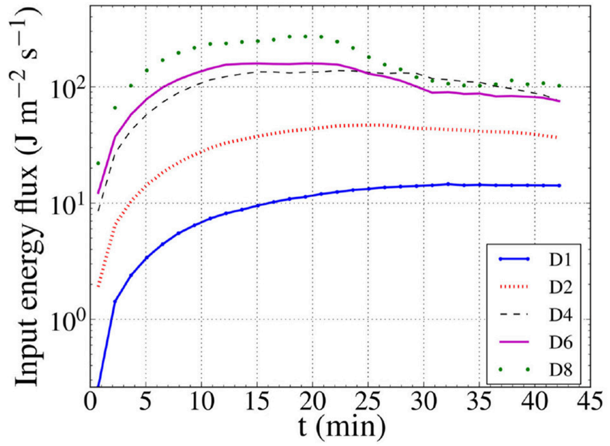

FIGURE 5 | Evolution of the average values of the energy fluxes provided by the driver of each model (in W m^{-2}) over time.

flux is followed by a drop, which is again more pronounced in the models with the stronger drivers. By comparing the curves for the models D2 and D4 with the synthetic images of **Figure 2**, we see place that this drop takes place when the loops become turbulent due to the KHI.

Focusing at the last 6 cycles of the the simulation in **Figure 5**, we see that D4 shows a stronger input than D6, while still remaining weaker than D8. D2 on the other hand remains weaker from all the aforementioned ones, providing almost half or less as much input flux. This is in contrast to the results of **Figure 4**, where the oscillation amplitude of the D2 model was comparable to that of the D4 model, and higher than the respective amplitudes of models D6 and D8. This shows that the previously obtained amplitudes are affected by the development of the out of phase movements of the spatially extended TWIKH rolls. All the drivers provide fluxes within the range of the radiative losses of the non-active region corona (Withbroe and Noyes, 1977), with the exception of D1, which is significantly weaker than the rest.

After calculating the input energy flux and the observed loop displacements, we plot amplitude-flux diagrams in **Figure 6**. For these diagrams, we took the average of the (absolute values) of the maximum displacements and fluxes, for each model, at time intervals 19.95 − 28.5, 28.5 − 34.2, and 34.2 − 42.75 min. The diagrams contain the amplitudes traced from AIA-resolution synthetic images of 171 and 193 AIA channels at both 0 and 45° LOS angle. Taking this and the results from **Figure 4** into account, we explain the differences between the 171 and 193 Å AIA channels as LOS effects of our models. The highest values of the amplitudes are obtained for the highest driver input fluxes. However, a clear correlation is absent for fluxes $\lesssim$110 W m^{-2}. Instead, we see a relatively uniform distribution of amplitudes among the different fluxes in that region. The corresponding amplitudes are below 1 Mm as we look perpendicular to the oscillation direction (0°). At a LOS angle of 45°, the value of these amplitudes is between 0.15 and 0.55 Mm, placing them within the range of the observed decayless oscillations (Nisticò et al., 2013; Anfinogentov et al., 2015).

Finally, we want to calculate the observed kinetic energy flux (W m^{-2}) across the line of sight, for a specific spectral line. Based on the work of Antolin et al. (2017), we calculate the Doppler energy flux as:

$$F_{obs} = \frac{1}{2}\int_{\perp LOS} < \rho_\lambda(l,t) > \upsilon_{Dop,\lambda}(l,t)^2 \frac{c_k}{L_{\perp LOS}} dl_\perp, \tag{4}$$

and the non-thermal energy flux as:

$$F_{obs} = \frac{1}{2}\int_{\perp LOS} < \rho_\lambda(l,t) > \left(\xi_\lambda(l,t)^2 - \xi_{\lambda,th}(l,t)^2\right) \frac{c_k}{L_{\perp LOS}} dl_\perp. \tag{5}$$

With $c_k = 1{,}167$ km s^{-1} we denote the kink speed. $L_{\perp LOS}$ is the length of the domain across the LOS, $\upsilon_{Dop,\lambda}$ the Doppler velocity (in km s^{-1}) for the spectral line, ξ_λ the corresponding Doppler width in km s^{-1}, and the thermal width (in km s^{-1}):

$$\xi_{\lambda,th} = \frac{c}{\lambda_0}\sqrt{\frac{T_\lambda k_B}{\mu m_p}}. \tag{6}$$

With c we denote the speed of light, λ_0 the wavelength at rest for the spectral line, k_B the Boltzmann constant, m_p the proton mass and with μ the atomic weight in proton masses of the emitting element. The emitting temperature T_λ is taken as an approximation from the $\xi_{\lambda,th}$ in the beginning of the simulations, where the velocities along the LOS are practically zero. The quantity $< \rho_\lambda(l,t) >$ is based on the emissivity-weighted average density from Antolin et al. (2017):

$$< \rho_\lambda(l,t) >= \frac{\int_{//LOS} \rho\epsilon(l,t)ds}{\left(\int_{//LOS} \epsilon(l,t)ds\right)|_{max}}, \tag{7}$$

where we instead divide the integral of density times emissivity with the maximum value of the integrated emissivity along the LOS at each frame. The fluxes from all setups are then normalized to the domain dimensions of models D6 and D8 for all setups, to make direct comparisons possible between the different models.

We plot our results for the Fe XII 193 Å spectral line in **Figure 7**, following Hinode/EIS spatial, spectral and temporal resolution. For a LOS angle of 90°, we observe an initial increase in the energy flux estimated by the Doppler velocities, which persisted for the duration of the simulations for models D1 and D2. For the models D4, D6, and D8 we observe a drop in the estimated Doppler energy flux, in the last cycles of the simulations. This drop appears once the turbulent loop cross-section shows very strong out of phase flows, due to the TWIKH rolls. These azimuthal flows do not register in the Doppler velocities at this angle, leading to the aforementioned drop. A similar behavior was observed in Antolin et al. (2017) for a non-driven transverse oscillation. We also see a correlation with the drop of the input energy flux, as observed for the the models D4, D6, and D8. However, a similar correlation is not observed for the D1 and D2 models. This shows that the observed drop in the

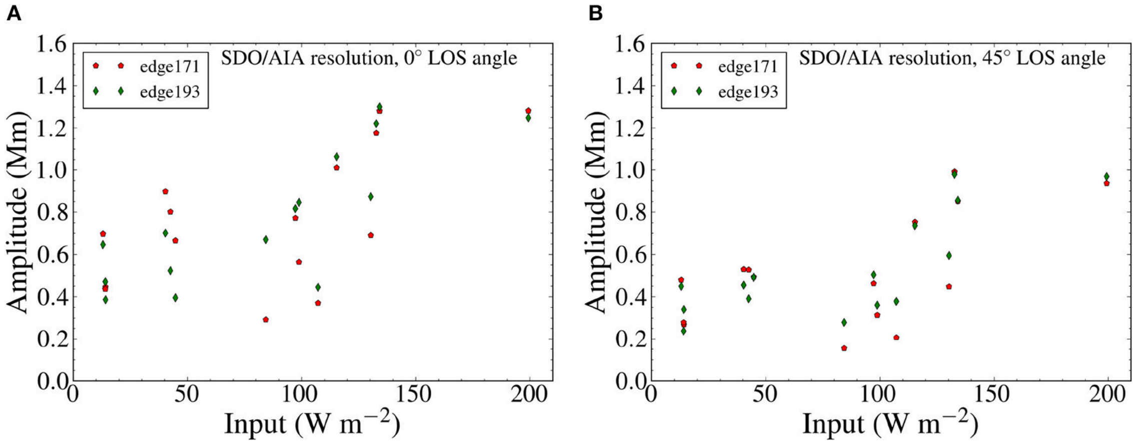

FIGURE 6 | Diagrams of the average oscillation amplitudes as a function of the average energy input for each model. In **(A)** we have a 0° LOS angle and in **(B)** we have a 45° LOS angle. Data from the Fe XII 193 Å line and the Fe IX 171 Å line were used. The loops displacements for the two lines were obtained by tracking their edge in the corresponding synthetic emission images.

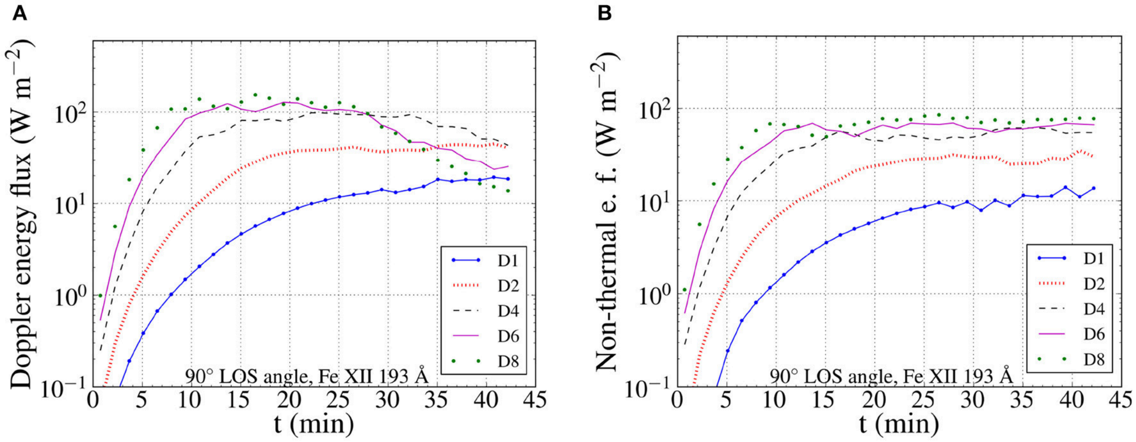

FIGURE 7 | Average values of the Doppler **(A)** and non-thermal **(B)** energy fluxes for a LOS angle of 90°, based on synthetic spectroscopic data from the Fe XII 193 Å line.

Doppler energy flux is the combined result of the input drop and the loop deformation by the TWIKH rolls.

The diagram of the non-thermal energy flux in **Figure 7** shows a saturation once the KHI fully deforms the loop cross-section. This agrees with the results of Antolin et al. (2017), where a similar saturated domain was obtained after the manifestation of the KHI. For the models D4, D6, and D8, this saturation takes place before the drop in the Doppler energy flux. The small increase of the non-thermal energy flux observed in the later parts of the simulation, does not fully compensate for the drop in the Doppler energy flux. This shows that the aforementioned Doppler flux follows closely the input energy flux, in the case of continuously driven oscillating loops. We also observe that the non-thermal energy fluxes are increasing for stronger drivers. This suggests that the observed correlation between line widths and Doppler shifts reported by McIntosh and De Pontieu (2012) can correspond to a continuous input of transverse MHD waves, supporting their hypothesis. However, the use of a single loop for each driver excludes the LOS effects of integrating over many structures, and cannot give a safe statistical result to be compared with the observations (McIntosh and De Pontieu, 2012).

We see a disagreement between the total observed (Doppler + non-thermal) energy flux, for a LOS angle of 90°, and the input in **Figure 5** for models D1 and D2. The former, as seen in **Figure 8** is overestimated with respect to the input energy flux during the later part of the respective simulations. This comes in contrast with the results of Antolin et al. (2017), where the estimated total energy flux was lower than the available energy flux calculated directly from the simulation data. This disagreement is due to the inaccuracies introduced through the method of estimating the density and temperature of the emitting plasma from the synthetic data. The latter appears in the correction for the thermal terms in the non-thermal energy fluxes. Additional uncertainty can be caused by the angle of

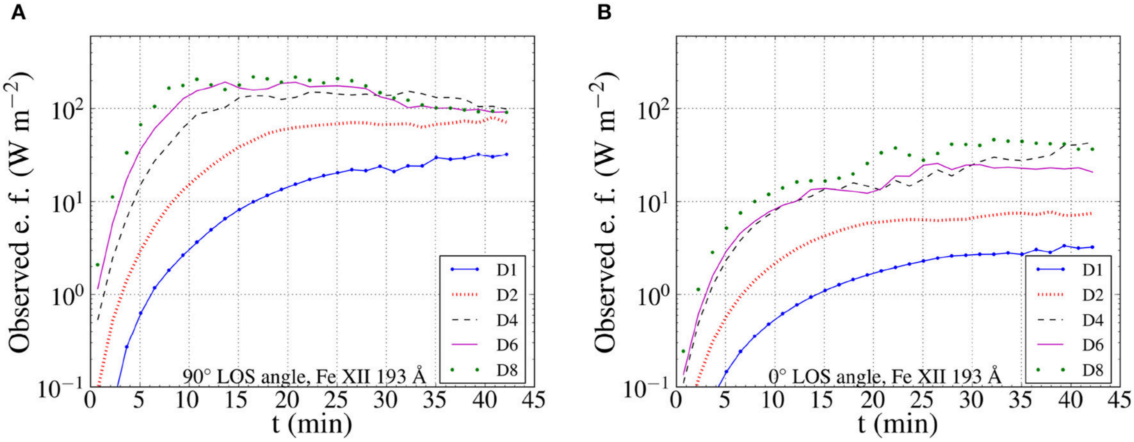

FIGURE 8 | Average values of the total observed (Doppler and non-thermal) energy fluxes, based on synthetic spectroscopic data from the Fe XII 193 Å line. A LOS angle of 90° **(A)** and 0° **(B)** was considered.

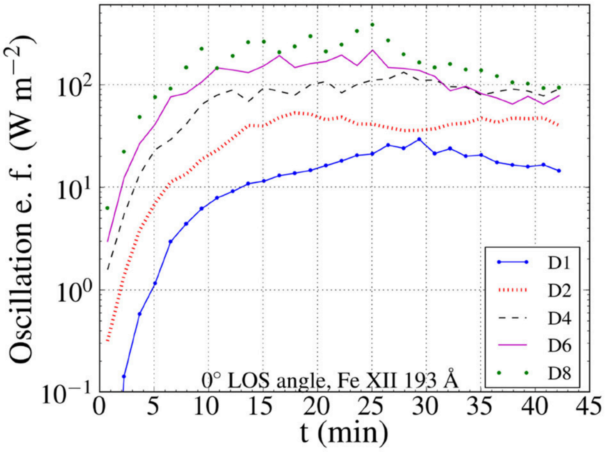

FIGURE 9 | Average values of the total observed (Doppler and non-thermal) energy fluxes with the additional term by tracking the oscillation on the POS. The values are based on the synthetic images for the Fe XII 193 Å line and the 193 AIA channel.

observation. As seen in **Figure 8**, the total observed energy for a LOS angle of 0° follows the development of the TWIKH rolls and leads to an underestimation of the energy flux.

The uncertainty revolving around the LOS angle can be bypassed by a combined approach of multiple observations. Once a small angle of observation is identified by combining the energy diagrams and the spectra, like those in **Figure 4**, we can then approximate the total energy fluxes. We achieve this by adding an additional term to the sum of the Doppler and non-thermal energy fluxes. This additional term is derived from Equation (4), by replacing the Doppler velocities with the the velocity derived from the displacement of the oscillating loop, like in the time-distance maps of **Figure 4**. The results of these calculation are presented in **Figure 9**, and show a better agreement with the input energy than the underestimated fluxes in **Figure 8B**.

4. DISCUSSION

In the present work we aimed to study the effects of different transverse drivers in the dynamics and energetics of decayless oscillations in coronal loops, through the use of synthetic images. We modeled the decayless oscillations as the standing waves from continuously footpoint-driven straight flux tubes, in the presence of gravity. We performed MHD simulations for footpoint drivers of different strengths and performed forward modeling to our data, constructing time-distance maps at the loop apex. We then degraded the spatial and spectral resolution of our signal, targeting different instruments, namely the SDO/AIA and Hinode/EIS. From the created acquired synthetic images for the 193 and the 171 Å lines we studied the oscillation amplitudes in the plane of sky (POS) at the apex, generated by the five different drivers. To do so, we tracked the "edge" of the loop from the emission images, which is defined by threshold value for the intensity, set slightly higher than the background intensity.

In **Figure 2** we observe the drop of the emission in synthetic images for both lines employed here. This drop is the result of the spatially extended TWIKH rolls, expanding the loop cross-section and causing mixing with the surrounding plasma. This drop in the emission is stronger and occurs faster for stronger drivers, as we can see in the example of **Figure 2** for the D2 and D4 models. In observations we mostly expect to observe loops during their cooling stage (Viall and Klimchuk, 2012), starting from unknown higher temperatures of formation. For decayless oscillations, we therefore expect them to be already in a turbulent state, because of the continuous driving. Any change in the strength of the driver could then lead to sudden changes in the observed emission in various lines, depending on the temperature gradient between the loop and the surrounding plasma, as well as the temperature of said coronal plasma.

In **Figure 4** we see that the final values of the amplitudes are comparable between the different drivers. We are mostly interested in the second half of the simulations, during which the KHI has deformed the cross-section of each loop. This is because we expect the loops performing decayless oscillations to be already in a turbulent state. During that phase, we can observe higher oscillation amplitudes from weaker drivers. This becomes obvious by comparing these time distance maps and the input energy flux diagrams of **Figure 5** for the D4 and D8 models. The D4 model showed bigger displacements toward the end of the simulations than D8 model, despite having a less efficient driver at that stage of the simulations. In addition to that, the D2 model showed very similar amplitudes to the D4, D6, and D8 models, despite providing less than half the energy flux of these drivers. This result is a clear indication of the importance of the out of phase flows, developed by the TWIKH rolls, in the characteristics of the observed oscillations.

Following the results of **Figure 7**, we observe a drop in the Doppler energy flux for the models D4, D6, and D8. This drop is primarily related to the respective drop of the input energy flux, and secondarily to the development of the TWIKH rolls, since the drop in the input energy flux of models D1 and D2 does is not followed by a drop in their Doppler flux. This is related to the less deformed loop cross-sections expected for weaker drivers in continuously driven oscillations of coronal loops (Karampelas and Van Doorsselaere, 2018). The connection between the Doppler energy flux and the resonant flows has also been established in Antolin et al. (2017), for a small-amplitude non-driven transverse oscillation of coronal loop.

From the diagram of the non-thermal energy flux over time in **Figure 7**, we observe the saturation of the energy flux, attributed to the turbulent motions present across the loop cross-section. We also observe a positive correlation between the average values of the saturated non-thermal energy fluxes and the driver efficiency from **Figure 5**. This suggests that a continuous input of transverse MHD waves could lead to the observed correlation between line widths and Doppler shifts reported by McIntosh and De Pontieu (2012). However, the small number of measurements (one observation per loop per driver) does not allow us to acquire safe statistical results. Furthermore, our study has excluded the LOS effects of integrating over many structures, which prevents us from making a direct comparison with the observations (McIntosh and De Pontieu, 2012).

By taking into account the results of **Figure 9**, we see that the sum of the non-thermal and Doppler energy flux can lead to different values, depending on the angle of observation and the methods used in the calculations. By adding an additional term, derived by estimating the oscillation velocity from the time-distance maps, we can compensate for the effects of the observation angle when calculating the energy fluxes.

We need to stress here that the observed saturation in the amplitudes is not caused by numerical dissipation, but is instead the combined result of the strong out of phase flows generated by the TWIKH rolls and the effects of plasma mixing in the emission. Scaling tests with setups of higher resolution, as well as past results (Guo et al., 2019; Karampelas et al., 2019) have revealed a similar saturation in the oscillation amplitudes. In Karampelas et al. (2019), we have seen that the input energy from our drivers turns into kinetic energy (strong out of phase flows), magnetic energy and internal energy of the plasma (wave heating). The derived spectra in that study reveal a turbulent profile, represented by the inertial range. This inertial range is connected to the existence of smaller scales and is present as long as the KHI is not suppressed by the very large dissipation parameters. The development of these smaller scales could be observed in the Doppler velocities and non-thermal line-widths from spectroscopic observations. These observations, however, would be dependent upon the angle of observation, the instrumental resolution, as well as the assumptions used for the initial temperature and density profile.

Finally, from **Figure 9** we conclude that we cannot obtain a clear correlation between the driver input and the observed oscillation amplitudes just from the synthetic imaging data. In our setups, the amplitudes between 0.15 and 0.55 Mm were evenly distributed over a wide range of input fluxes, up to 110 W m^{-2}. Small amplitude oscillations can potentially be hiding enough energy to sustain the non-active region corona ($\sim$100 W m^{-2}) (Withbroe and Noyes, 1977). The development of spatially extended TWIKH rolls can mask its observational signatures, by causing out of phase movements of the loop plasma and affecting the emission at various lines. This is relevant when explaining the observed decayless oscillations (Nisticò et al., 2013; Anfinogentov et al., 2015) as the result of continuous footpoint driving of a coronal loop, and stresses the need for combined instrument observations.

To summarize our results, the mixing of plasma caused by the developed KHI affects the emission in synthetic images, leading to a drop once the loop cross-section becomes turbulent. The developed TWIKH rolls show strong out of phase flows, which lead to the saturation of the oscillation amplitudes for each model. For different angles, we obtain oscillation amplitudes near the observed ones, which do not show a clear correlation with the input energy from the driver. These observed amplitudes can potentially carry enough energy to sustain the radiative losses from the Quiet Sun. A better correlation can be obtained between the input energy and the spectroscopic results from the Doppler energy flux and the non-thermal energy fluxes. All of our results, however, are dependent upon the angle of observations and the approximations used, hinting toward the need for combined spectroscopic and imaging observations.

Apart from our suggestion that small-amplitude decayless oscillations contain enough energy flux to support the QS, there are other ways to introduce additional energy within the context of such observed waves. In De Moortel and Pascoe (2012), it was shown that the wave energy is significantly underestimated by integration of multiple loops along the LOS. In that work, the kinetic energy estimated by the LOS Doppler velocities was $\sim 5 - 20\%$ of the energy in the domain. A combination of a kink and Alfvén driver (Guo et al., 2019) can also provide more energy into the system, while retaining a similar profile in AIA synthetic images. Alternatively, the use of a broadband driver could also increase the driver efficiency, for only small deviations from the expected oscillation amplitudes. The detection of such higher harmonics in decayless oscillations by Duckenfield et al. (2018) suggests that the latter method should be studied further in future works.

DATA AVAILABILITY

The datasets generated for this study are available on request to the corresponding author.

AUTHOR CONTRIBUTIONS

KK has performed numerical simulations and forward modeling for the models in this project, and set the basic ideas for the analysis of the results. DP has performed specialized data extraction and analysis of the synthetic images. TVD has set the basic guidelines for this project, consulted during the analysis, and supervised the completion of the project. MG and PA have contributed on the methods of the analysis and have given feedback during the discussion of the results. KK has written the first draft of the current paper, received input from all co-authors, and written the final version of the manuscript.

FUNDING

KK, TVD, and DP and were funded by GOA-2015-014 (KU Leuven). MG is supported by the China Scholarship Council (CSC) and the National Natural Science Foundation of China (41674172). PA acknowledges funding from his STFC Ernest Rutherford Fellowship (No. ST/R004285/1). This project has received funding from the European Research Council (ERC) under the European Union's Horizon 2020 research and innovation programme (grant agreement No 724326).

ACKNOWLEDGMENTS

The computational resources and services used in this work were provided by the VSC (Flemish Supercomputer Center), funded by the Research Foundation Flanders (FWO) and the Flemish Government–department EWI. The results were inspired by discussions at the ISSI-Bern and at ISSI-Beijing meetings.

REFERENCES

Afanasyev, A., Karampelas, K., and Van Doorsselaere, T. (2019). Coronal loop transverse oscillations excited by different driver frequencies. *Astrophys. J.* 876:100. doi: 10.3847/1538-4357/ab1848

Allcock, M., and Erdélyi, R. (2017). Magnetohydrodynamic waves in an asymmetric magnetic slab. *Solar Phys.* 292:35. doi: 10.1007/s11207-017-1054-y

Andries, J., Goossens, M., Hollweg, J. V., Arregui, I., and Van Doorsselaere, T. (2005). Coronal loop oscillations. Calculation of resonantly damped MHD quasi-mode kink oscillations of longitudinally stratified loops. *Astron. Astrophys.* 430, 1109–1118. doi: 10.1051/0004-6361:20041832

Anfinogentov, S. A., Nakariakov, V. M., and Nisticò, G. (2015). Decayless low-amplitude kink oscillations: a common phenomenon in the solar corona? *Astron. Astrophys.* 583:A136. doi: 10.1051/0004-6361/201526195

Antolin, P., De Moortel, I., Van Doorsselaere, T., and Yokoyama, T. (2016). Modeling observed decay-less oscillations as resonantly enhanced Kelvin-Helmholtz vortices from transverse MHD waves and their seismological application. *Astrophys. J. Lett.* 830:L22. doi: 10.3847/2041-8205/830/2/L22

Antolin, P., De Moortel, I., Van Doorsselaere, T., and Yokoyama, T. (2017). Observational signatures of transverse magnetohydrodynamic waves and associated dynamic instabilities in coronal flux tubes. *Astrophys. J.* 836:219. doi: 10.3847/1538-4357/aa5eb2

Antolin, P., Okamoto, T. J., De Pontieu, B., Uitenbroek, H., Van Doorsselaere, T., and Yokoyama, T. (2015). Resonant absorption of transverse oscillations and associated heating in a solar prominence. II. Numerical aspects. *Astrophys. J.* 809:72. doi: 10.1088/0004-637X/809/1/72

Antolin, P., Schmit, D., Pereira, T. M. D., De Pontieu, B., and De Moortel, I. (2018). Transverse wave induced Kelvin-Helmholtz rolls in spicules. *Astrophys. J.* 856:44. doi: 10.3847/1538-4357/aab34f

Antolin, P., Yokoyama, T., and Van Doorsselaere, T. (2014). Fine strand-like structure in the solar corona from magnetohydrodynamic transverse oscillations. *Astrophys. J. Lett.* 787:L22. doi: 10.1088/2041-8205/787/2/L22

Arregui, I., Van Doorsselaere, T., Andries, J., Goossens, M., and Kimpe, D. (2005). Resonantly damped fast MHD kink modes in longitudinally stratified tubes with thick non-uniform transitional layers. *Astron. Astrophys.* 441, 361–370. doi: 10.1051/0004-6361:20053039

Aschwanden, M. J. (2006). Coronal magnetohydrodynamic waves and oscillations: observations and quests. *Philos. Trans. R. Soc. Lond. Ser. A* 364, 417–432. doi: 10.1098/rsta.2005.1707

Aschwanden, M. J., Fletcher, L., Schrijver, C. J., and Alexander, D. (1999). Coronal loop oscillations observed with the transition region and coronal explorer. *Astrophys. J.* 520, 880–894. doi: 10.1086/307502

Barbulescu, M., Ruderman, M. S., Van Doorsselaere, T., and Erdélyi, R. (2019). An analytical model of the Kelvin-Helmholtz instability of transverse coronal loop oscillations. *Astrophys. J.* 870:108. doi: 10.3847/1538-4357/aaf506

Browning, P. K., and Priest, E. R. (1984). Kelvin-Helmholtz instability of a phased-mixed Alfven wave. *Astron. Astrophys.* 131, 283–290.

De Moortel, I., and Nakariakov, V. M. (2012). Magnetohydrodynamic waves and coronal seismology: an overview of recent results. *Philos. Trans. R. Soc. Lond. Ser. A* 370, 3193–3216. doi: 10.1098/rsta.2011.0640

De Moortel, I., and Pascoe, D. J. (2012). The effects of line-of-sight integration on multistrand coronal loop oscillations. *Astrophys. J.* 746:31. doi: 10.1088/0004-637X/746/1/31

De Moortel, I., Pascoe, D. J., Wright, A. N., and Hood, A. W. (2016). Transverse, propagating velocity perturbations in solar coronal loops. *Plasma Phys. Controll. Fusion* 58:014001. doi: 10.1088/0741-3335/58/1/014001

De Pontieu, B., McIntosh, S. W., Carlsson, M., Hansteen, V. H., Tarbell, T. D., Schrijver, C. J., et al. (2007). Chromospheric alfvénic waves strong enough to power the solar wind. *Science* 318:1574. doi: 10.1126/science.1151747

Dedner, A., Kemm, F., Kröner, D., Munz, C.-D., Schnitzer, T., and Wesenberg, M. (2002). Hyperbolic divergence cleaning for the MHD equations. *J. Comput. Phys.* 175, 645–673. doi: 10.1006/jcph.2001.6961

Duckenfield, T., Anfinogentov, S. A., Pascoe, D. J., and Nakariakov, V. M. (2018). Detection of the second harmonic of decay-less kink oscillations in the solar corona. *Astrophys. J. Lett.* 854:L5. doi: 10.3847/2041-8213/aaaaeb

Edwin, P. M., and Roberts, B. (1983). Wave propagation in a magnetic cylinder. *Solar Phys.* 88, 179–191. doi: 10.1007/BF00196186

Goddard, C. R., Antolin, P., and Pascoe, D. J. (2018). Evolution of the transverse density structure of oscillating coronal loops inferred by forward modeling of EUV intensity. *Astrophys. J.* 863:167. doi: 10.3847/1538-4357/aad3cc

Goossens, M., Erdélyi, R., and Ruderman, M. S. (2011). Resonant MHD waves in the solar atmosphere. *Space Sci. Rev.* 158, 289–338. doi: 10.1007/s11214-010-9702-7

Goossens, M., Hollweg, J. V., and Sakurai, T. (1992). Resonant behaviour of MHD waves on magnetic flux tubes. III - Effect of equilibrium flow. *Solar Phys.* 138, 233–255. doi: 10.1007/BF00151914

Guo, M., Van Doorsselaere, T., Karampelas, K., Li, B., Antolin, P., and De Moortel, I. (2019). Heating effects from driven transverse and Alfvén waves in coronal loops. *Astrophys. J.* 870:55. doi: 10.3847/1538-4357/aaf1d0

Heyvaerts, J., and Priest, E. R. (1983). Coronal heating by phase-mixed shear Alfven waves. *Astron. Astrophys.* 117, 220–234.

Hillier, A., Barker, A., Arregui, I., and Latter, H. (2019). On Kelvin-Helmholtz and parametric instabilities driven by coronal waves. *Mon. Not. R. Astron. Soc.* 482, 1143–1153. doi: 10.1093/mnras/sty2742

Howson, T. A., De Moortel, I., and Antolin, P. (2017). Energetics of the Kelvin-Helmholtz instability induced by transverse waves in twisted coronal loops. *Astron. Astrophys.* 607:A77. doi: 10.1051/0004-6361/201731178

Karampelas, K., and Van Doorsselaere, T. (2018). Simulations of fully deformed oscillating flux tubes. *Astron. Astrophys.* 610:L9. doi: 10.1051/0004-6361/201731646

Karampelas, K., Van Doorsselaere, T., and Antolin, P. (2017). Heating by transverse waves in simulated coronal loops. *Astron. Astrophys.* 604:A130. doi: 10.1051/0004-6361/201730598

Karampelas, K., Van Doorsselaere, T., and Guo, M. (2019). Wave heating in gravitationally stratified coronal loops in the presence of resistivity and viscosity. *Astron. Astrophys.* 623:A53. doi: 10.1051/0004-6361/201834309

Magyar, N., and Van Doorsselaere, T. (2016). Damping of nonlinear standing kink oscillations: a numerical study. *Astron. Astrophys.* 595:A81. doi: 10.1051/0004-6361/201629010

Magyar, N., Van Doorsselaere, T., and Marcu, A. (2015). Numerical simulations of transverse oscillations in radiatively cooling coronal loops. *Astron. Astrophys.* 582:A117. doi: 10.1051/0004-6361/201526287

McIntosh, S. W., and De Pontieu, B. (2012). Estimating the ”dark” energy content of the solar corona. *Astrophys. J.* 761:138. doi: 10.1088/0004-637X/761/2/138

McIntosh, S. W., de Pontieu, B., Carlsson, M., Hansteen, V., Boerner, P., and Goossens, M. (2011). Alfvénic waves with sufficient energy to power the quiet solar corona and fast solar wind. *Nature* 475, 477–480. doi: 10.1038/nature10235

Mignone, A., Bodo, G., Vaidya, B., and Mattia, G. (2018). A particle module for the PLUTO code. I. An implementation of the MHD–PIC equations. *Astrophys. J.* 859:13. doi: 10.3847/1538-4357/aabccd

Morton, R. J., Tomczyk, S., and Pinto, R. F. (2016). A global view of velocity fluctuations in the corona below 1.3 R with CoMP. *Astrophys. J.* 828:89. doi: 10.3847/0004-637X/828/2/89

Morton, R. J., Verth, G., Jess, D. B., Kuridze, D., Ruderman, M. S., Mathioudakis, M., et al. (2012). Observations of ubiquitous compressive waves in the Sun's chromosphere. *Nat. Commun.* 3:1315. doi: 10.1038/ncomms2324

Nakariakov, V. M., Anfinogentov, S. A., Nisticò, G., and Lee, D.-H. (2016). Undamped transverse oscillations of coronal loops as a self-oscillatory process. *Astron. Astrophys.* 591:L5. doi: 10.1051/0004-6361/201628850

Nakariakov, V. M., Ofman, L., Deluca, E. E., Roberts, B., and Davila, J. M. (1999). TRACE observation of damped coronal loop oscillations: implications for coronal heating. *Science* 285, 862–864. doi: 10.1126/science.285.5429.862

Nisticò, G., Nakariakov, V. M., and Verwichte, E. (2013). Decaying and decayless transverse oscillations of a coronal loop. *Astron. Astrophys.* 552:A57. doi: 10.1051/0004-6361/201220676

Ofman, L., Davila, J. M., and Steinolfson, R. S. (1994a). “Coronal heating by the resonant absorption of Alfvén waves,” in *IAU Colloq. 144: Solar Coronal Structures*, eds V. Rusin, P. Heinzel, J. C. Vial, 473–477. doi: 10.1017/S0252921100026725

Ofman, L., Davila, J. M., and Steinolfson, R. S. (1994b). Coronal heating by the resonant absorption of Alfven waves: the effect of viscous stress tensor. *Astrophys. J.* 421, 360–371. doi: 10.1086/173654

Ofman, L., Klimchuk, J. A., and Davila, J. M. (1998). A self-consistent model for the resonant heating of coronal loops: the effects of coupling with the chromosphere. *Astrophys. J.* 493, 474–479. doi: 10.1086/305109

Okamoto, T. J., Tsuneta, S., Berger, T. E., Ichimoto, K., Katsukawa, Y., Lites, B. W., et al. (2007). Coronal transverse magnetohydrodynamic waves in a solar prominence. *Science* 318:1577. doi: 10.1126/science.1145447

Pagano, P., and De Moortel, I. (2017). Contribution of mode-coupling and phase-mixing of Alfvén waves to coronal heating. *Astron. Astrophys.* 601:A107. doi: 10.1051/0004-6361/201630059

Pagano, P., and De Moortel, I. (2019). Contribution of observed multi frequency spectrum of Alfvén waves to coronal heating. *arXiv e-prints*. doi: 10.1051/0004-6361/201834158

Pagano, P., Pascoe, D. J., and De Moortel, I. (2018). Contribution of phase-mixing of Alfvén waves to coronal heating in multi-harmonic loop oscillations. *Astron. Astrophys.* 616:A125. doi: 10.1051/0004-6361/201732251

Pascoe, D. J., Anfinogentov, S. A., Goddard, C. R., and Nakariakov, V. M. (2018). Spatiotemporal analysis of coronal loops using seismology of damped Kink oscillations and forward modeling of EUV intensity profiles. *Astrophys. J.* 860:31. doi: 10.3847/1538-4357/aac2bc

Pascoe, D. J., Goddard, C. R., and Nakariakov, V. M. (2016a). Spatially resolved observation of the fundamental and second harmonic standing kink modes using SDO/AIA. *Astron. Astrophys.* 593:A53. doi: 10.1051/0004-6361/201628784

Pascoe, D. J., Goddard, C. R., Nisticò, G., Anfinogentov, S., and Nakariakov, V. M. (2016b). Coronal loop seismology using damping of standing kink oscillations by mode coupling. *Astron. Astrophys.* 589:A136. doi: 10.1051/0004-6361/201628255

Pascoe, D. J., Hood, A. W., de Moortel, I., and Wright, A. N. (2012). Spatial damping of propagating kink waves due to mode coupling. *Astron. Astrophys.* 539:A37. doi: 10.1051/0004-6361/201117979

Pascoe, D. J., Hood, A. W., and Van Doorsselaere, T. (2019). Coronal loop seismology using standing kink oscillations with a lookup table. *Front. Astron. Space Sci.* 6:22. doi: 10.3389/fspas.2019.00022

Pascoe, D. J., Russell, A. J. B., Anfinogentov, S. A., Simões, P. J. A., Goddard, C. R., Nakariakov, V. M., et al. (2017). Seismology of contracting and expanding coronal loops using damping of kink oscillations by mode coupling. *Astron. Astrophys.* 607:A8. doi: 10.1051/0004-6361/201730915

Pascoe, D. J., Wright, A. N., and De Moortel, I. (2010). Coupled Alfvén and Kink oscillations in coronal loops. *Astrophys. J.* 711, 990–996. doi: 10.1088/0004-637X/711/2/990

Poedts, S., and Boynton, G. C. (1996). Nonlinear magnetohydrodynamics of footpoint-driven coronal loops. *Astron. Astrophys.* 306:610.

Ruderman, M., and Roberts, B. (2002). The damping of coronal loop oscillations. *Astrophys. J.* 577:475. doi: 10.1086/342130

Ruderman, M. S., Goossens, M., and Andries, J. (2010). Nonlinear propagating kink waves in thin magnetic tubes. *Phys. Plasmas* 17:082108. doi: 10.1063/1.3464464

Ryutov, D. A., and Ryutova, M. P. (1976). Sound oscillations in a plasma with ”magnetic filaments”. *Sov. J. Exp. Theor. Phys.* 43:491.

Sakurai, T., Goossens, M., and Hollweg, J. V. (1991). Resonant behaviour of MHD waves on magnetic flux tubes. I - Connection formulae at the resonant surfaces. *Solar Phys.* 133, 227–245.

Soler, R., and Terradas, J. (2015). Magnetohydrodynamic kink waves in nonuniform solar flux tubes: phase mixing and energy cascade to small scales. *Astrophys. J.* 803:43. doi: 10.1088/0004-637X/803/1/43

Terradas, J., Andries, J., Goossens, M., Arregui, I., Oliver, R., and Ballester, J. L. (2008). Nonlinear instability of Kink oscillations due to shear motions. *Astrophys. J. Lett.* 687:L115. doi: 10.1086/593203

Terradas, J., Goossens, M., and Verth, G. (2010). Selective spatial damping of propagating kink waves due to resonant absorption. *Astron. Astrophys.* 524:A23. doi: 10.1051/0004-6361/201014845

Terradas, J., Magyar, N., and Van Doorsselaere, T. (2018). Effect of magnetic twist on nonlinear transverse kink oscillations of line-tied magnetic flux tubes. *Astrophys. J.* 853:35. doi: 10.3847/1538-4357/aa9d0f

Thurgood, J. O., Morton, R. J., and McLaughlin, J. A. (2014). First direct measurements of transverse waves in solar polar plumes using SDO/AIA. *Astrophys. J. Lett.* 790:L2. doi: 10.1088/2041-8205/790/1/L2

Tomczyk, S., and McIntosh, S. W. (2009). Time-distance seismology of the solar corona with CoMP. *Astrophys. J.* 697, 1384–1391. doi: 10.1088/0004-637X/697/2/1384

Tomczyk, S., McIntosh, S. W., Keil, S. L., Judge, P. G., Schad, T., Seeley, D. H., et al. (2007). Alfvén waves in the solar corona. *Science* 317:1192. doi: 10.1126/science.1143304

Van Doorsselaere, T., Antolin, P., and Karampelas, K. (2018). Broadening of the differential emission measure by multi-shelled and turbulent loops. *Astron. Astrophys.* 620:A65. doi: 10.1051/0004-6361/201834086

Van Doorsselaere, T., Antolin, P., Yuan, D., Reznikova, V., and Magyar, N. (2016). Forward modeling of EUV and gyrosynchrotron emission from coronal plasmas with fomo. *Front. Astron. Space Sci.* 3:4. doi: 10.3389/fspas.2016.00004

Verth, G., Terradas, J., and Goossens, M. (2010). Observational evidence of resonantly damped propagating kink waves in the solar corona. *Astrophys. J. Lett.* 718, L102–L105. doi: 10.1088/2041-8205/718/2/L102

Verwichte, E., Aschwanden, M. J., Van Doorsselaere, T., Foullon, C., and Nakariakov, V. M. (2009). Seismology of a large solar coronal loop from EUVI/STEREO observations of its transverse oscillation. *Astrophys. J.* 698, 397–404. doi: 10.1088/0004-637X/698/1/397

Verwichte, E., Foullon, C., and Van Doorsselaere, T. (2010). Spatial seismology of a large coronal loop arcade from TRACE and EIT observations of its transverse oscillations. *Astrophys. J.* 717, 458–467. doi: 10.1088/0004-637X/717/1/458

Verwichte, E., Nakariakov, V. M., and Cooper, F. C. (2005). Transverse waves in a post-flare supra-arcade. *Astron. Astrophys.* 430, L65–L68. doi: 10.1051/0004-6361:200400133

Viall, N. M., and Klimchuk, J. A. (2012). Evidence for widespread cooling in an active region observed with the SDO atmospheric imaging assembly. *Astrophys. J.* 753:35. doi: 10.1088/0004-637X/753/1/35

White, R. S., and Verwichte, E. (2012). Transverse coronal loop oscillations seen in unprecedented detail by AIA/SDO. *Astron. Astrophys.* 537:A49. doi: 10.1051/0004-6361/201118093

White, R. S., Verwichte, E., and Foullon, C. (2012). First observation of a transverse vertical oscillation during the formation of a hot post-flare loop. *Astron. Astrophys.* 545:A129. doi: 10.1051/0004-6361/201219856

Withbroe, G. L., and Noyes, R. W. (1977). Mass and energy flow in the solar chromosphere and corona. *Annu. Rev. Astron. Astrophys.* 15, 363–387. doi: 10.1146/annurev.aa.15.090177.002051

Yu, D. J., Van Doorsselaere, T., and Goossens, M. (2017). Resonant absorption of surface sausage and surface kink modes under photospheric conditions. *Astrophys. J.* 850:44. doi: 10.3847/1538-4357/aa9223

Yuan, D., and Van Doorsselaere, T. (2016). Forward modeling of standing kink modes in coronal loops. I. Synthetic views. *Astrophys. J.* 223:23. doi: 10.3847/0067-0049/223/2/23

Zajtsev, V. V., and Stepanov, A. V. (1975). On the origin of pulsations of type IV solar radio emission. Plasma cylinder oscillations (I). *Issledovaniia Geomagnet. Aeron. Fizike Solntsa* 37, 3–10.

Zaqarashvili, T. V., Zhelyazkov, I., and Ofman, L. (2015). Stability of rotating magnetized jets in the solar atmosphere. I. Kelvin-Helmholtz instability. *Astrophys. J.* 813:123. doi: 10.1088/0004-637X/813/2/123

Conflict of Interest Statement: The authors declare that the research was conducted in the absence of any commercial or financial relationships that could be construed as a potential conflict of interest.

frontiers
in Astronomy and Space Sciences

ORIGINAL RESEARCH
published: 22 May 2019
doi: 10.3389/fspas.2019.00039

Linear Waves in Partially Ionized Plasmas in Ionization Non-equilibrium

*Istvan Ballai**

Plasma Dynamics Group, School of Mathematics and Statistics, University of Sheffield, Sheffield, United Kingdom

We aim to investigate the properties of linear Alfvén and slow magnetoacoustic waves in a partially ionized plasma in ionization non-equilibrium. The propagation characteristics of these waves are studied within the framework of a two-fluid plasma in terms of the collisional strength between heavy particles for different degrees of ionization. In the ionization non-equilibrium state the rates of ionization and recombinations are not equal. For analytical progress we assume a background that is ionization equilibrium, the non-equilibrium is driven by perturbations in the system, therefore, non-equilibrium effects are related to the perturbed state of the plasma. Using simple analytical methods, we show that ionization non-equilibrium can provide an additional coupling between ions and neutrals (implicitly a secondary damping mechanism in the collisionless limit) and this process is able to keep the neutrals in the system even in the collisionless limit. Due to the coupling between different species waves become dispersive. The present study improves our understanding of the complexity of dynamical processes partially ionized plasma in the lower solar atmosphere and solar prominences. Our results clearly show that the problem of partial ionization and non-equilibrium ionization introduce new aspects of plasma dynamics with consequences on the evolution waves and their dissipation.

Keywords: partial ionization, plasma, waves and instabilities, solar chromosphere, collision, ionization, recombination

Edited by:
Tom Van Doorsselaere,
KU Leuven, Belgium

Reviewed by:
Jiansen He,
Peking University, China
Piyali Chatterjee,
Indian Institute of Astrophysics, India

****Correspondence:***
Istvan Ballai
i.ballai@sheffield.ac.uk

Specialty section:
This article was submitted to Stellar and Solar Physics, a section of the journal Frontiers in Astronomy and Space Sciences

Received: *18 January 2019*
Accepted: *03 May 2019*
Published: *22 May 2019*

Citation:
Ballai I (2019) Linear Waves in Partially Ionized Plasmas in Ionization Non-equilibrium. Front. Astron. Space Sci. 6:39. doi: 10.3389/fspas.2019.00039

1. INTRODUCTION

One of the most intriguing aspects that have been largely omitted so far in the field of dynamical process in solar plasmas is that the plasma in the lower atmosphere is partially ionized, with plasma made up from charged particles and neutrals that are interacting through collision. Although the exact degree of ionization is not fully known, the ratio of electron density to neutral hydrogen density covers a few orders of magnitude from the photosphere to the top of the chromosphere. The ionization state of the plasma is a very important factor, as the collision between various species will significantly enhance transport processes that control the appearance and evolution of instabilities in the presence of inhomogeneous flows. Depending on the range of frequencies we are interested in, the description of the dynamics in these regions can be described within the framework of single fluid magnetohydrodynamics (MHD) (for frequencies smaller than the ion-neutral frequency), two-fluid MHD (when frequencies of interest are larger than the ion-neutral collisional frequency), or multi-fluid description (in the high-frequency regime when waves' frequency is comparable to the electron-ion collisional frequency).

Research in the dynamical evolution of physical phenomena in the solar atmosphere is based on the assumption of ionization equilibrium and the equilibrium Maxwellian distribution of particles. However, this model is not accurate for rapidly changing phenomena (e.g., high frequency waves, shock waves), for rapid energy releases where high-energy tail of the electron distribution are observed. Non-equilibrium ionization can occur during heating or cooling events, significantly affecting line intensities and subsequently the plasma diagnostics (Bradshaw and Mason, 2003; Bradshaw et al., 2004). Departures from the equilibrium Maxwellian distribution have also been inferred from chromospheric and transition region line emission (Dzifčáková and Kulinová, 2011). In the chromosphere the ionization/recombination relaxation times scales are of the order of $10^3 - 10^5$ s (Carlsson and Stein, 2002), meaning that dynamics occurring below this scales will be affected by non-equilibrium effects. Because the relaxation timescale is much longer than dynamic timescales, H ionization does not have time to reach its equilibrium value and its fluctuations are much smaller than the variation of its statistical equilibrium value appropriate for the instantaneous conditions. The problem of waves and oscillations in two fluid partially ionized plasmas is a relatively new area of solar physics, nevertheless some fundamental properties of such environments are already established (see, e.g., Soler et al., 2010, 2013; Zaqarashvili et al., 2011; Ballester et al., 2018b).

The process of non-equilibrium ionization is very much related to the process of irreversible physics via inelastic collision between particles. In the present paper we will restrict our attention to collision impact ionization and radiative recombination. In addition, we assume that the collision between particles can lead to either ionization of recombination, while the processes of collisions leading to excited states of articles will be neglected. This approximation requires that the collision involving neutrals would imply an energy exchange that is at least equal to the first ionization potential, while excited states (if they appear) will have a lifetime that is much shorter than the dynamical scales involved in our problem.

The paper is structured as follows: in section 2 we introduce the necessary equations with their implications and limitations. Given the complexity of the problem, here we are employing a simplified model. In section 3 we study the propagation characteristics of Alfvén waves and investigate the effect of non-equilibrium ionization on the propagation speed of waves and their damping with respect to the collisional parameter between particles for different ionization degrees of the plasma. Using a simple configuration the wave characteristics of decoupled slow waves are studied in section 4. Finally our results are summarized in section 5.

2. BASIC EQUATIONS AND ASSUMPTIONS

The physical processes of ionization and recombination are far from trivial given the multitude of mechanisms that can result in one or more electrons being removed from a neutral atom and the reversed process of combination between positive ions and an energetic electrons to form neutral atoms. However, for simplicity here we are going to concentrate on collisions, as the main mechanism that can generate ions and neutrals. In order to describe the effects on non-equilibrium ionization and recombination processes let us introduce the quantities Γ_q^r, denoting the interaction rate of process r, affecting fluid q (Leake et al., 2012; Meier and Shumlak, 2012; Maneva et al., 2017). The radiative recombination rate of ions is proportional to the number of ions (with number density n_i) and electrons (with number density n_e) of the system, and it is given by,

$$\Gamma_n^{rec} = n_i n_e R. \tag{1}$$

In the above equation the recombination frequency, R, is given by Cox and Tucker (1969) and Moore and Fung (1972)

$$R = 5.2 \times 10^{-20} \sqrt{X} \left(0.4288 + 0.5 \ln X + 0.4698 X^{-1/3}\right) (\mathrm{m}^3\ \mathrm{s}^{-1}),$$

where $X = A\epsilon_i / T(eV)$ is a quantity that is defined as the ratio between the ionization potential and thermal energy, and the constant A takes the value of 0.6. In can be shown that at temperatures we can find in the lower part of the chromosphere the electrons in hydrogen atoms are predominantly in the ground state (corresponding to $n = 1$ energy level), meaning that ϵ_i is the first ionization potential, therefore $\epsilon_i = 13.6$ eV. Indeed, the relative population at the $n = 2$ energy level compared to the ground level in the hydrogen atom is given by the Boltzmann equation,

$$\frac{N_2}{N_1} = \frac{g_2}{g_1} e^{-(E_2 - E_1)/k_B T},$$

where $g_n = 2n^2$ is the statistical weight of each energy level, $E_1 = \epsilon_i$ and $E_2 = 3.4$ eV are the energies of electrons on the two levels. In a H plasma at $T = 10^4$ K we can obtain that $N_2/N_1 = 2.5 \times 10^{-5}$, while at $T = 4 \times 10^3$ K, this ratio is of the order of 10^{-13}. We should point out here that the radiative recombination should be treated with care. Under normal circumstances the recombination takes place as a result of the collision between a positive ion (proton in a H plasma) and an electron that has an energy, at least, equal to ϵ_i. As a result of this interaction a photon is emitted that can further ionize the neutral H atoms. With a significant amount of neutral H, the emitted photon will have a higher probability of being absorbed by a neutral atom in the neighborhood of emission, with a creation of an ion. Therefore, recombination to the ground state has virtually no effect on the ionization state of the plasma. However, in our analysis we are going to consider that the photon emitted during recombination escapes, this corresponds to the response of optically thin plasma to ionizing radiation.

Since we are dealing with spatial scales that are larger than the Debye radius in a H plasma, the plasma can be considered to be quasi-neutral, therefore, $n_e = n_i$. In addition, for simplicity we are going to deal with a uni-thermal plasma, where $T_e = T_i = T_n = T$.

The impact ionization reaction takes place as a result of the collisional interaction between neutrals (with number density n_n)

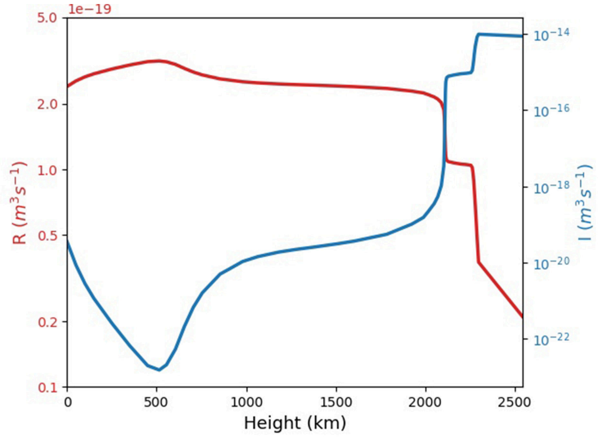

FIGURE 1 | The variation of the real and imaginary part of the dimensionless frequency for slow magnetoacoustic waves with respect to the dimensionless collisional frequency, a_1, for two different values of the ionization degree of the plasma (color coded). Solid lines represent solutions obtained in the ionization non-equilibrium and dashed lines denote the slow waves in ionization equilibrium.

and electrons with energies larger than the ionization potential. As a result, the ionization rate of neutrals is given by,

$$\Gamma_i^{ion} = n_n n_e I = n_n n_i I, \tag{2}$$

where I is the ionization rate and is given empirically by Cox and Tucker (1969) and Moore and Fung (1972)

$$I = 2.34 \times 10^{-14}\sqrt{X}e^X \quad (\mathrm{m}^3\ \mathrm{s}^{-1}).$$

In order to determine the variation of the ionization/recombination rates in the solar atmosphere we use the VAL III C model (Vernazza et al., 1981) to plot the height dependence of these two quantities on logarithmic scale (see **Figure 1**). It is obvious that the variation with height of these rates follows closely the variation of the characteristic values typical for the atmospheric model employed here. Accordingly, the height-dependance of the recombination rate (R) resembles the height-dependance of the number density, while the ionization rate (I) shows similarity with the variation of the temperature, meaning that these physical quantities are the ones that determine the shape of variation with height. Both rates show an extreme value at the height of about 500 km (bottom of chromosphere, the point corresponding to the temperature minimum in the VALIII C model). The ionization rate overcomes the recombination rate at a height of 2 Mm, a height that corresponds to a temperature of approximately 7660 K.

The other effect we are going to consider is the collision between particles. Assuming a uni-thermal plasma, electrons will have their velocity (thermal velocity) $\sqrt{m_i/m_e}$ times larger than the thermal velocity of ions (and neutrals), where m_e and m_i are the masses of electrons and ions, respectively. During collisions between electrons and neutrals, electrons suffer a large change in momentum, but small change in their energy (given approximately by $\sqrt{m_e/m_i}$). In contrast, ion-neutral collisions are less frequent than electron-neutral collisions, however, the momentum exchange between these particles can influence the most propagation of waves, therefore, we are going to consider this effect as the dominant collisional mechanism. Collision between ions and neutrals will also ensure that neutrals (that are not influenced by the presence of magnetic field) are kept in the system.

In order to assess the importance of all physical effects included in our model, let us define the characteristic times involved connected to ionization, recombination, and collision as

$$\tau_i = \frac{1}{n_n I}, \quad \tau_r = \frac{1}{n_i R}, \quad \tau_c = \frac{1}{\nu_{in}},$$

where ν_{in} is the collisional frequency between ions and neutrals defined as,

$$\nu_{in} = 4n_n\sigma_{in}\left(\frac{k_B T}{\pi m_i}\right)^{1/2},$$

with $\sigma_{in} = 1.16 \times 10^{-18}$ m^2 being the ion-neutral collisional cross section (Vranjes and Krstic, 2013), and k_B is the Boltzmann constant. Obviously, the waves we are interested in must have periods that are larger than any of these times. It is clear that the smallest time scale is the collisional time scale (basically τ_c gives the time between two consecutive collisions) and for most of lower solar atmosphere this characteristic time is several orders of magnitude smaller than ionization and recombination time. For temporal scales that are near or shorter than the ion-neutral collisional time the plasma dynamics has to be described within the framework of two-fluid magnetohydrodynamics, where charged particles (here denoted by index i) and neutrals (denoted by an index n) can have separate behavior, depending on the relative strength of collision.

Before embarking on finding the characteristics of waves in non-equilibrium plasmas we need to discuss one more limitation of the problem we are going to consider. In the presence of non-equilibrium ionization and recombination, the linearized mass conservation equations for the two species are written as,

$$\frac{\partial\rho_i}{\partial t} + \rho_{0i}\nabla\cdot\mathbf{v}_i = m_i\left(\Gamma_i^{ion} + \Gamma_i^{rec}\right), \tag{3}$$

$$\frac{\partial\rho_n}{\partial t} + \rho_{0n}\nabla\cdot\mathbf{v}_n = m_n\left(\Gamma_n^{ion} + \Gamma_n^{rec}\right), \tag{4}$$

where $\rho_{0i,0n} and \rho_{i,n}$ are the background and perturbation values of the densities for ions and neutrals, respectively and $\mathbf{v}_i$ and $\mathbf{v}_n$ are the velocity perturbations for the two species. In the above equations $\Gamma_i^{ion} = -\Gamma_n^{ion}$ and $\Gamma_i^{rec} = -\Gamma_n^{rec}$. A direct consequence of the above two equation is that the processes of ionization and recombination are not balanced, particles are created and annihilated during the temporal length of the dynamics we are interested in. In addition, these two equations also imply that under normal circumstances (and in a static equilibrium) the equilibrium density of ions and neutrals should be time dependent quantities, i.e., the background state of the plasma is changing in time. In the absence of this temporal change the ionization and recombination rates must be equal and the system will be in equilibrium. Unfortunately, the description of a physical process when the background is a time-dependent is one of the most complex tasks, as it requires cumbersome mathematics.

We have three possibilities to deal with this problem. The first possibility is to leave the background as time dependent, and determine the evolution of perturbations. This task could be easily accomplished by numerical investigations. The second possibility to deal with the temporal variation of the background that makes the problem mathematically tractable would be to impose the condition that the ionization and recombination rates are much longer than the variation rate of the equilibrium density, that could be occurring over the scales presented by Carlsson and Stein (2002). In addition, temporal variation of perturbations (for instance their frequency) are of the same order as the ionization and recombination rates, so

$$\frac{1}{\rho_{0i}}\frac{d\rho_{0i}}{dt}, \frac{1}{\rho_{0n}}\frac{d\rho_{0n}}{dt} \ll \omega, n_nI, n_iR.$$

Finally, as a third possibility is to deal with this problem by assuming that non-equilibrium effects appear only in the perturbed state (and this is the possibility employed in the present paper). Similar to the assumption by, e.g., Brandenburg and Zweibel (1995), we can fix the rate of ionization and the recombination rate is chosen in such a way that in the unperturbed stage the right-hand sides of Equations (3, 4) are identically zero. The problem with this approach is that only one of the rates can be realistic, the chosen value of the other rate is artificially imposed. Assuming a VAL IIIC atmospheric model this assumption agrees with realistic values in the photosphere, i.e., in a weakly ionized region of the solar atmosphere. In our study we will employ the later assumption and choose,

$$R = \frac{n_{0n}}{n_{0i}}I.$$

With this assumption the characteristic times for ionization and recombination defined earlier become equal. This assumption also means that the empirical formula for R given earlier becomes redundant, as its value will be always given in terms of I, as above

The dynamics of the coupled two fluids is given by a set of linearized equations that describe the conservation of mass (given earlier by Equations 3–4), together with a conservation of momentum, induction equation and energy equation (see, e.g., Zaqarashvili et al., 2011; Khomenko et al., 2014; Maneva et al., 2017; Martinez-Gomez et al. , 2017),

$$\rho_{0i}\frac{\partial \mathbf{v}_i}{\partial t} + \nabla p_i - \frac{1}{\mu_0}(\nabla \times \mathbf{b}) \times \mathbf{B}_0 = m_i\mathbf{v}_n\Gamma_i^{ion} - m_i\mathbf{v}_i\Gamma_n^{rec} + m_{in}n_i\nu_{in}(\mathbf{v}_n - \mathbf{v}_i) =$$

$$= \rho_{0i}\left(\frac{\nu_{in}}{2} + n_{0n}I\right)(\mathbf{v}_n - \mathbf{v}_i) \tag{5}$$

$$\rho_{0n}\frac{\partial \mathbf{v}_n}{\partial t} + \nabla p_n = m_i\mathbf{v}_i\Gamma_n^{rec} - m_i\mathbf{v}_n\Gamma_i^{ion} - m_{in}n_i\nu_{in}(\mathbf{v}_n - \mathbf{v}_i) =$$

$$= -\rho_{0i}\left(\frac{\nu_{in}}{2} + n_{0n}I\right)(\mathbf{v}_n - \mathbf{v}_i) \tag{6}$$

$$\frac{\partial \mathbf{b}}{\partial t} = \nabla \times (\mathbf{v}_i \times \mathbf{B}_0), \tag{7}$$

$$\frac{\partial p_i}{\partial t} = -c_{Si}^2\rho_{0i}\nabla\cdot\mathbf{v}_i + c_{Si}^2 m_i\left(\Gamma_i^{ion} + \Gamma_i^{rec}\right) \tag{8}$$

$$\frac{\partial p_n}{\partial t} = -c_{Sn}^2\rho_{0n}\nabla\cdot\mathbf{v}_n + c_{Sn}^2 m_n\left(\Gamma_n^{ion} + \Gamma_n^{rec}\right) \tag{9}$$

$$\nabla\cdot\mathbf{b} = 0, \tag{10}$$

where $\mathbf{B}_0$ is the background magnetic field, $\mathbf{v}_i = (v_{ix}, v_{iy}, v_{iz})$ and $\mathbf{v}_n = (v_{nx}, v_{ny}, v_{nz})$ are the components of the velocity perturbation of ions and neutrals, p_i and p_n are the pressure perturbations of the ion and neutral fluids, $\mathbf{b} = (b_x, b_y, b_z)$ is the magnetic field perturbation, and $m_{in} = m_im_n/(m_i + m_n) \approx m_i/2$ is the reduced mass. Frictions between charged and neutral (close-range interaction) particles is ensured via collisional processes. The above equations must be supplemented by the equation of state for ions and neutrals $p_{i,n} = n_{i,n}k_BT_{i,n}$

As explained earlier, the ionization non-equilibrium is present only in the perturbed state, the perturbations we are considering to take place will drive the system out of ionization equilibrium. Equations (5, 6) are the linearized momentum equations of the ion-electron fluid and neutrals, respectively. The terms on their right-hand side express the transfer of momentum between ions and neutrals through the diffusion of one species into the other. As a result of collisions, particles can loose energy and momentum.The same equations reveal an interesting aspect of non-equilibrium plasma. When the background is in equilibrium, in the limit of vanishing collisions ($\nu_{in} = 0$) the only dynamics that can be described is related to ions and the momentum equation reduces to the standard equation used in MHD. Of course, such a limit cannot exist as in that case there is nothing that can keep neutrals in the system and the two-fluid description is meaningless. However, in the ionization non-equilibrium the two-fluid description can be applied even in the vanishing collision limit, as the creation and annihilation of ions generates a force per unit volume that acts to keep neutrals in the system.

The above system of equations will be used to study the properties of magnetic and slow magnetoacoustic waves propagating in non-equilibrium plasma and compare these with the values we obtain in the ionization equilibrium.

3. ALFVÉN WAVES

The simplest wave to study are Alfvén waves, for which the only restoring force is the Lorentz force and the driving force of Alfvén waves is the magnetic tension. We assume a homogeneous equilibrium magnetic field, B_0, pointing in the z-direction. Alfvén waves will propagate plasma along the magnetic field and they will be polarized in the y-direction. Given the properties of Alfvén waves, the pressure terms in Equations (5–6) are neglected and, therefore, Equations (8, 9) are not needed. As a result, the dynamics of Alfvén waves is described by the system of Equations

$$\rho_{0i}\frac{\partial v_{iy}}{\partial t}=\frac{B_0}{\mu}\frac{\partial b_y}{\partial z}+\rho_{0i}\tilde{\nu}_{in}(v_{ny}-v_{iy}), \tag{11}$$

$$\rho_{0n}\frac{\partial v_{ny}}{\partial t}=-\rho_{0i}\tilde{\nu}_{in}(v_{ny}-v_{iy}), \tag{12}$$

$$\frac{\partial b_y}{\partial t}=B_0\frac{\partial v_{iy}}{\partial z}, \tag{13}$$

where

$$\tilde{\nu}_{in}=\frac{\nu_{in}}{2}+n_{0n}I,$$

is the modified ion-neutral collisional frequency by the ionization non-equilibrium effects. Obviously, if $I=0$, then we recover the case of Alfvén waves in ionization equilibrium, a case discussed earlier by Zaqarashvili et al. (2011).

Let us Fourier-analyse the system of Equations (11–13) considering that all perturbations are proportional to $\exp[i(kz-\omega t)]$, where k is the real wavenumber along the z-axis. The neutral fluid exerts a drag force against the motion of ions around the magnetic field and, therefore, Alfvén waves will decay. As a result, the frequency of waves, ω, will be a complex quantity, with negative imaginary part of it describing the damping of waves. After simple calculations the dispersion relation of Alfvén waves is obtained to be

$$\omega^3+i\omega^2\tilde{\nu}_{in}(1+\chi)-k^2v_A^2\omega-ik^2v_A^2\chi\tilde{\nu}_{in}=0, \tag{14}$$

where $\chi=n_{0i}/n_{0n}\approx\rho_{0i}/\rho_{0n}$. In the absence of any partially ionized effects (e.g., $\tilde{\nu}_{in}=0$) the dispersion relation would reduce to the standard dispersion relation for Alfvén waves $\omega=\pm kv_A$. The third order polynomial (14) describes the propagation of two Alfvén waves (propagating in opposite direction) and a third mode that is non-oscillatory (i.e., its frequency has a zero real part).

Let us introduce the dimensionless quantities,

$$\Omega=\frac{\omega}{kv_A},\quad a=\frac{\nu_{in}}{kv_A},\quad \xi_n=\frac{\rho_{0n}}{\rho_0},\quad \tilde{I}=\frac{n_0I}{kv_A}, \tag{15}$$

where $n_0=n_{0i}+n_{0n}$ is the total number density of the plasma and ρ_0 is the total mass density. After some simple calculations the dispersion relation can be written in dimensionless form as,

$$\Omega^3+i\Omega^2N(1+\chi)-\Omega-i\chi N=0, \tag{16}$$

where $N=a/2+\xi_n\tilde{I}$. Luckily some analytical progress can be made by assuming that Alfvén waves will have a small damping. Accordingly, the dimensionless frequency of waves can be written as $\Omega=\Omega_r+i\Omega_i$ (with both Ω_r, Ω_i real quantities) and we write $|\Omega_i|\ll|\Omega_r|$. Focussing only on the forward propagating modes, the real and imaginary part of the frequencies can be easily obtained as,

$$\Omega_r=\left(1-\frac{\xi_n(a+2\xi_n\tilde{I})^2}{4\xi_n^2+(a+\xi_n\tilde{I})^2}\right)^{1/2}, \tag{17}$$

and

$$\Omega_i=-\xi_n^2\frac{a+2\xi_n\tilde{I}}{4\xi_n^2+(a+\xi_n\tilde{I})^2}. \tag{18}$$

It is obvious that the imaginary part of the frequency is negative, meaning that waves will damp, regardless what is the strength of collisions between particles or degree of ionization. The corresponding values for ionization equilibrium can be found once the quantity $\tilde{I}$ is set to zero. In ionization equilibrium the imaginary part of the frequency tends to zero when the collisional frequency, a, is set to zero, i.e., Alfvén waves in collisionless plasma do not damp. In this case the governing equations describe the dynamics of ions alone, while the dynamics of neutrals becomes undetermined. Since ions and neutrals do not interact through collisions, the possibility of having neutrals in such systems becomes a problem (technically speaking the plasma can be considered collisionless when the mean free path between collisions is much larger than the lengths over which the plasma quantities vary). In the limit of strong collisions ($a\gg1$) the imaginary part of the frequency becomes smaller and at $a\to\infty$ the mixture of ions and neutrals behaves like a single fluid with no damping; this limit corresponding to the MHD limit. Before further discussion we need to clarify that the term “collisionless" used above refers to the case when the collisional frequency between ions and neutrals becomes zero. However, this does not exclude the possibility of having collisions between ions and electrons and neutrals and electrons, i.e., the collisions that affect the ionization state of the plasma.

In contrast, in the ionization non-equilibrium, when we set the collisional frequency to zero we arrive to a critical damping rate,

$$\Omega_i^{cr}=-\frac{\xi_n\tilde{I}}{2+2\tilde{I}^2}, \tag{19}$$

meaning that Alfvén waves will damp even in the absence of collisions between ions and neutrals and the ionization/recombination processes will ensure that the mixture of ions and neutrals stay coupled. The damping whose rate is given by Equation (19) constitute a new damping mechanism that roots itself in the additional drag force generated by different drift velocities of ions and neutrals during the process of ionization and recombination. For the sake of completeness, we should mention that Landau damping is also a mechanism that appears in collisionless plasmas, and this damping is not associated with an increase in entropy, and therefore is a thermodynamically reversible process. It remains to be seen whether the damping mechanism described in the present study has the same properties as Landau damping. The damping we discuss here can be due to the fact that with the number of ions changing in time, more and more ions become attached to

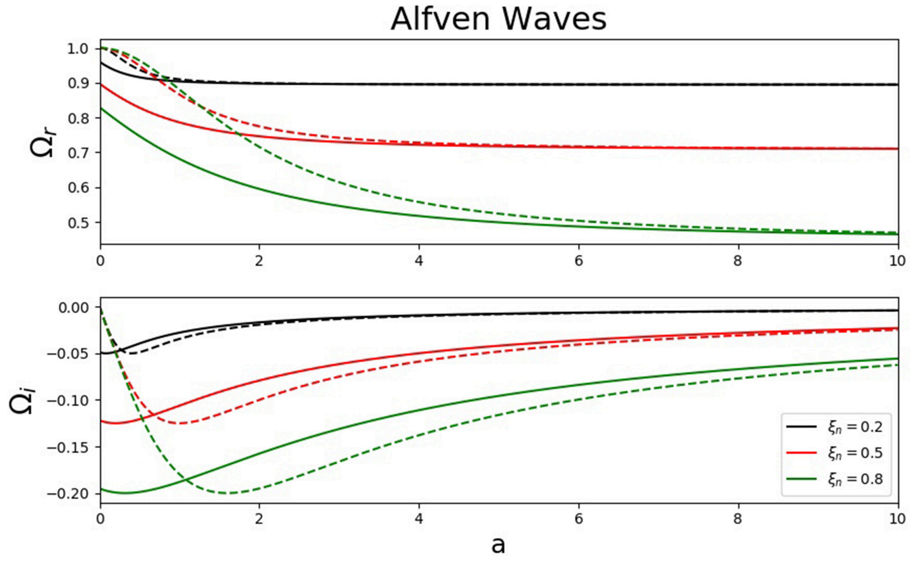

FIGURE 2 | The variation of the recombination rate (*R*, shown in red line) and the ionization rate (*I*, blue line) with height (on logarithmic scale) in the lower solar atmosphere based on a VALIII C solar atmosphere model (Vernazza et al., 1981).

magnetic field lines, increasing their inertia, eventually causing the attenuation of Alfvén waves.

Let us investigate the variation of the real and imaginary parts of the dimensionless frequency of forward propagating Alfvén waves in terms of the dimensionless collisional frequency, *a* for three different values of the relative neutral density ($\xi_n = 0.2, 0.5, 0.8$). Clearly $\xi_n = 0$ describes a fully ionized plasma, while the limit $\xi_n = 1$ corresponds to a completely neutral fluid. The upper panel of **Figure 2** shows the variation of the real part of the dimensionless frequency (solid lines) for the three values of ξ_n and the corresponding dispersion curves corresponding to the ionization equilibrium (shown by dashed lines). Here the dimensionless quantity Ω can be understood as the propagation speed of Alfvén waves in units of Alfvén speed, v_A.

First of all it is clear that for very large collisional frequency the propagation speed of Alfvén waves and damping rate in the two regimes become identical and in a strongly collisional plasma the propagation speed of Alfvén waves and their damping rate are not influenced by collisions between ions and neutrals. Secondly, Alfvén waves in ionization non-equilibrium will propagate with a lower speed and the difference in propagation speed increases with the number of neutrals in the system. Furthermore, the more ionized the plasma is, the faster these Alfvén waves will propagate. Similarly, as long as the collisional frequency is larger than $(\sqrt{\tilde{I}^2+4}-\tilde{I})\xi_n$, Alfvén waves in ionization equilibrium will have a larger damping rate (smaller damping time) than those waves that propagate in a plasma in ionization non-equilibrium, however, these differences are not significant. For collisional frequency smaller than this threshold value, Alfvén waves damp much quicker in a non-equilibrium plasma. As pointed our earlier, the damping rate of Alfvén waves in equilibrium plasma tends to zero in the collisionless plasma. In contrast, in a non-equilibrium collisionless plasma, Alfvén waves damp with a rate given by Ω_i^{cr}. In conclusion, in a strongly collisional plasma the propagation and attenuation of Alfvén waves is independent whether the plasma is in ionization equilibrium or not. Here the collisional time is at least one order of magnitude larger than the characteristic time for ionization and any non-uniformity that could potentially influence the characteristics of waves is smoothed out by collisions.

Finally we need to mention that Alfvén waves in the present configuration become dispersive, and dispersion is proportional to $\tilde{\nu}_{in}^2$. **Figure 2** also shows that for a given collisional parameter, *a*, waves with shorter wavelength will propagate slower and the larger the amount of neutrals in the system, the more dispersive Alfvén waves are.

4. SLOW MAGNETOACOUSTIC MODES

To be able to decouple magnetoacoustic modes, we assume that slow magnetoacoustic waves propagate along the background magnetic field and the dominant dynamics occurs in the *z* direction. Since the species of the plasma have the same temperature, we can write

$$c_{Si}^2 = \frac{\gamma(p_i+p_e)}{\rho_{i0}} = \frac{\gamma k_B(T_i+T_e)}{m_i} = \frac{2\gamma k_B T_n}{m_n} = \frac{2\gamma p_n}{\rho_{0n}} = 2c_{Sn}^2.$$

Since slow waves propagate along the background magnetic field we assume that all perturbations are proportional to $e^{i(kz-\omega t)}$. This particular choice for the form of perturbations and background magnetic field can reduce the slow waves to acoustic modes. The dynamics of linear slow waves propagating along the magnetic field in a partially ionized plasma in the presence of non-equilibrium ionization is described by the system of Equations (3–10) where perturbations are considered to be proportional to the exponential factor introduced above. Accordingly the set of equations used are,

$$\rho_i = k\frac{in_{0i}I\rho_{0n}v_{nz} + \rho_{0i}(\omega + in_{0i}I)v_{iz}}{\omega(\omega + in_{0i}I)}, \tag{20}$$

$$\rho_n = k\frac{\rho_{0n}(\omega + in_{0n}I)v_{nz} + in_{0n}\rho_{0i}Iv_{iz}}{\omega(\omega + in_{0i}I)}, \tag{21}$$

$$(\omega + i\tilde{\nu}_{in})v_{iz} - \frac{kc_{Si}^2}{\rho_{0i}}\rho_i - i\tilde{\nu}_{in}v_{nz} = 0, \tag{22}$$

$$(\omega + i\tilde{\nu}_{in})v_{nz} - \frac{kc_{Sn}^2}{\rho_{0n}}\rho_i - i\tilde{\nu}_{in}v_{iz} = 0. \tag{23}$$

These four equations can be reduced a set of coupled equations for the z-components of ion and neutral velocities. The compatibility condition of this system gives us the dispersion relation,

$$\omega^4 + i\omega^3 A - \omega^2 B - ik^2\omega C + D = 0, \tag{24}$$

where the coefficients A, B, C, and D depend on the parameters of the problem. This fourth-order polynomial in ω describes the propagation of two families of waves: one associated to ions, and the other one to neutrals. Due to collisions and non-equilibrium effects, the two kinds of modes are coupled. Again, let us introduce similar dimensionless quantities as in the case of Alfvén waves, but now we use the quantity kc_{Sn} to write variables and constants in dimensionless form. As a result, the dispersion relation reduces to,

$$\Omega^4 + i\Omega^3 A_1 - \Omega^2 B_1 - i\Omega C_1 + D_1 = 0, \tag{25}$$

where the constant coefficients are given by,

$$A_1 = 2\tilde{I}_1 + \frac{a_1}{2\xi_n}, \quad B_1 = 3 + \tilde{I}_1^2 + \frac{a_1\tilde{I}_1}{2\xi_n} +$$

$$C_1 = (2-\xi_n)\left[\frac{a_1}{2} + \tilde{I}_1(1+\xi_n)\right], \; D_1 = 2 + \frac{a_1\tilde{I}_1}{2\xi_n}(2-\xi_n) + \tilde{I}_1^2(2-\xi_n)$$

where the parameters a_1 and $\tilde{I}_1$ are defined in the same way as parameters a and $\tilde{I}$ given by Equation (15), but the quantity that is used to write them in dimensionless form is kc_{Sn}. In the absence of collisions and ionization non-equilibrium the two pairs of sound waves are propagating with the sound speed of ions and neutrals, with the wave associated to ions propagating faster.

Figure 3 shows the variation of the dimensionless frequency of slow waves (or the phase speed of slow waves in units of the neutral sound speed) with respect to the dimensionless collisional parameter, a_1, for two distinct values of the ionization factor, ξ_n (0.2 and 0.8, respectively). Due to the collision between particles and non-equilibrium effects, the quantity Ω is complex, where the imaginary part describes the temporal modification of the amplitude of waves. The upper panel of **Figure 3** shows the real part of Ω, while the lower panel shows the imaginary part of this quantity. Similar to the plot obtained for Alfvén waves, the solid lines denote the dispersion curves for slow waves in ionization non-equilibrium, while dashed line correspond to the case when the plasma is in ionization equilibrium.

It is clear that for the whole spectrum of parameters, the imaginary part of the frequency will be negative, meaning that slow waves will damp; this result is in agreement with the conclusions of previous studies by, e.g., Braginskii (1965) and Zaqarashvili et al. (2011). The two sets of waves shown in **Figure 3** have different behavior in terms of collisional frequency. Let us concentrate first on the dispersion curves obtained for the real part of the frequency. Depending on the amount of neutrals in the system, the ion-acoustic waves can have an enhanced propagation speed in the limit of weakly collisional plasma. For $\xi_n = 0.2$ (black curves) the slow wave that corresponds to an ionization equilibrium travels slightly faster, however very quickly the propagation speed of these slow waves in the two regimes is equal. When the amount of neutrals is increased (red lines) we can see that the wave corresponding to the non-equilibrium state propagates faster but at the value of $a_1 \approx 2.5$ the two speeds become identical. At this point the collisions between ions and neutrals become so frequent that their effect can overcome any modification due to the additional change in the ionization degree of the plasma.

On the other hand the slow waves associated to neutrals display a completely different behavior. In a plasma with $\xi_n = 0.2$ these slow waves have a smaller phase speed, and the speed in a non-equilibrium plasma is slightly larger than the corresponding value obtained in an equilibrium state. Once the amount of neutrals is increased (the curves corresponding to $\xi_n = 0.8$) the slow waves in an equilibrium plasma is larger, and this relation is maintained again, until the dimensionless collisional frequency, a, reaches the value of $a_1 \approx 2.5$, after which, for a given value of a_1, the neutral slow waves in equilibrium plasma propagates faster. It is also clear that at $a_1 \approx 2.5$ the propagation speed of ion-slow waves and neutral-slow wave is equal. Similar to the results obtained by Zaqarashvili et al. (2011), the neutral-slow waves can exist up to a certain level of collisional rate and the value of collision where these waves cease to exist increases with the amount of neutrals in the system. At this point the collision between neutrals and ions is so frequent that the mixture of charged and neutral particles starts behaving like a single fluid. Increasing the frequency of collisions between ions and neutrals cause a slow down of neutral-slow waves.

Now let us concentrate on the imaginary part of the frequency. It is clear that regardless what is the ionization degree of the plasma, the damping rate of ion-acoustic modes is very small, practically these waves can propagate with no attenuation for any value of collision. In contrast, the neutral-slow waves have a very different behavior. These waves show a very strong damping (with damping times of the order of the period of waves, or larger). For both ionization degrees chosen here, the damping time of neutral-slow waves is decreasing with the increase in the collisional frequency. Comparing the results we obtained in the two regimes, it is clear that the neutral-slow waves in an

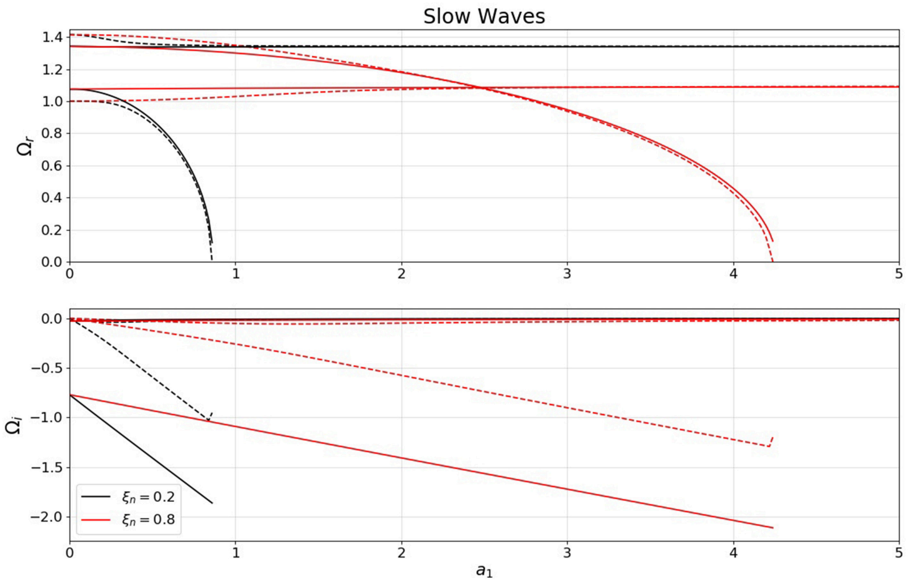

FIGURE 3 | The variation of the real **(Upper)** and imaginary part **(Lower)** of the dimensionless frequency, Ω, for Alfvén waves with respect to the dimensionless collisional frequency, *a* for three different values of the ionization degree of the plasma (color coded). Solid lines represent solutions obtained in the ionization non-equilibrium while dashed line denote the Alfvén waves in ionization equilibrium.

ionization equilibrium plasma have no damping in the absence of collision (as we would expect), however, in the presence of non-equilibrium these waves decay due to ionization/recombination processes and—in the absence of collisions—the damping time of these waves is independent on the amount of neutrals in the system. Once the collisional rate in increased, the mode that corresponds to smaller amount of neutrals will have a shorter damping time.

Similar to Alfvén waves, slow magnetoacoustic modes will also be dispersive, however the ion-acoustic modes will be practically non-dispersive (similar to the slow waves in the MHD description), while neutral-acoustic modes are strongly dispersive, again waves with larger wavelength traveling faster. **Figure 3** also shows that in the case of neutral-acoustic modes there will be always a critical wavenumber above which these modes do not propagate.

It is very likely that the problem of propagation and decay of these waves will display a different behavior once the full polarization in the *xz* plane is considered. In that case slow waves will have a magnetic component and it remains to be seen how these waves will behave for different value of plasma-beta. However, this consideration requires numerical investigation.

5. CONCLUSIONS

Given the nature of partially ionized plasma in the lower solar plasma and prominences requires a different approach. For particular high frequencies range a two-fluid description is needed and neutrals can considerably influence the properties of waves. This framework was used to study the characteristics of Alfvén and slow waves propagation along a unidirectional homogeneous magnetic field. The novelty of our research resides in consideration of the effects of ionization non-equilibrium, i.e., the case when the rates at which neutrals are ionized through impact ionization and ions recombine with energetic electrons through radiative recombination are not equal. Our results show that this effect is more important when the collisional frequency is comparable with the frequency of waves. Any information about the existence of two fluids and the drag forces exerted by neutrals upon ions is lost in the case of strong collisions. Here the plasma behaves like a single fluid and the dynamics can be confidently described within the framework is MHD. We ought to mention that the non-equilibrium applies only to the perturbed state of the plasma; in the background state the plasma remains in ionization equilibrium. This assumption was needed to be able to make analytical progress.

Using a simple configuration we studied separately Alfvén and slow magnetoacoustic modes. The collision between heavy particles and non-equilibrium effects renders the frequency of waves to be complex, where the imaginary part of it describes damping. One of the main results of our investigation is that in a plasma that is in ionization non-equilibrium waves can damp even in the collisionless limit. In this case waves will damp due to the drag forces by neutrals that appear due to the ionization non-equilibrium. Given that waves are damped even in the collisionless limit makes us to think about the physical explanation of this effect to be similar as the theory of Landau damping. However, this statement needs to be investigated properly in the future. The processes of ionization and recombination will increase the degree of entropy in the system that could cause the additional damping.

Finally we should mention our results should treated with precaution when making far reaching conclusions valid for the whole photosphere and/or chromosphere. For simplicity the present study assumed collisional ionization and radiative recombination as the dominant mechanisms that determine the non-equilibrium, however, in reality this can change from region to region in the solar atmosphere. It is very likely that in the dense photosphere photoinduction and three-body recombination are more important effects. In addition, most of the partially ionized plasma is optically thick, in which case a similar treatment as presented by Ballester et al. (2018a) is needed. Moreover, the relatively low temperature plasma in these regions means that the gravitational scale-height is short, therefore, in the case of waves traveling over long distances in the solar lower atmosphere, the gravitational stratification could influence the propagation of waves and work against the damping of waves. It remains to be seen how a realistic variation of ionization and recombination rate together with stratification will affect the characteristics of waves.

AUTHOR CONTRIBUTIONS

IB is the sole author of this paper and it contains original research.

ACKNOWLEDGMENTS

IB acknowledges the financial support by STFC UK.

REFERENCES

Ballester, J. L., Alexeev, I., Collados, M., Downes, T., Pfaff, R. F., Gilbert, H., et al. (2018b). Partially ionized plasmas in astrophysics. *Space Sci. Rev.* 241, 58–206. doi: 10.1007/s11214-018-0485-6

Ballester, J. L., Carbonell, M., Soler, R., Terradas, J. (2018a). The temporal behaviour of MHD waves in partially ionised prominence-like plasma: effect of heating and cooling. *Astron. Astrophys.* 609, 6–22. doi: 10.1051/0004-6361/201731567

Bradshaw, S. J., Del Zanna, G., and Mason, H. E. (2004). On the consequences of a non-equilibrium ionisation balance for compact flare emission and dynamics. *Astron. Astrophys.* 425, 287–299. doi: 10.1051/0004-6361:20040521

Bradshaw, S. J., and Mason, H. E. (2003). The radiative response of solar loop plasma subject to transient heating. *Astron. Astrophys.* 407, 1127–1138. doi: 10.1051/0004-6361:20030986

Braginskii, S. I. (1965). Transport Processes in a Plasma. *Rev. Plasma Phys.* 1, 205–283.

Brandenburg, A., and Zweibel, E. G. (1995). Effects of pressure and resistivity on the ambipolar diffusion singularity: too little, too late. *Astrophys. J.* 448, 734–635. doi: 10.1086/176001

Carlsson, M., and Stein, R. F. (2002). Dynamic hydrogen ionization. *Astrophys. J.* 572, 626–635. doi: 10.1086/340293

Cox, D. P., and Tucker, W. H. (1969). Ionization equilibrium and radiative cooling of a low-density plasma. *Astrophys. J.* 157:1157. doi: 10.1086/150144

Dzifčáková, E., and Kulinová, A. (2011). Diagnostics of the κ-distribution using Si III lines in the solar transition region. *Astron. Astrophys.* 531, 122–131. doi: 10.1051/0004-6361/201016287

Khomenko, E., Collados, M., Diaz, A., and Vitas, N. (2014). Fluid description of multi-component solar partially ionised plasma. *Phys. Plasmas* 21:092901. doi: 10.1063/1.4894106

Leake, J. E., Lukin, V. S., Linton, M. G., and Meier, E. T. (2012). Multi-fluid simulations of chromospheric magnetic reconnection in a weakly ionized reacting plasma. *Astrophys. J.* 760, 109–120. doi: 10.1088/0004-637X/760/2/109

Maneva, Y. G., Alvarez Laguna, A., Lani, A., Poedts, S. (2017). Multi-fluid modeling of magnetosonic wave propagation in the solar chromosphere: effects of impact ionization and radiative recombination. *Astrophys. J.* 836, 197–211. doi: 10.3847/1538-4357/aa5b83

Martinez-Gomez, D., Soler, R., and Terradas, J. (2017). Multi fluid approach to high-frequency waves in plasmas. II small amplitude regime in partially ionised medium. *Astrophys. J.* 837, 80–97. doi: 10.3847/1538-4357/aa5eab

Meier, E. T., and Shumlak, U. (2012). A general nonlinear fluid model for reacting plasma-neutral mixtures. *Phys. Plasmas* 19: 072508. doi: 10.1063/1.4736975

Moore, R. L., and Fung, P. C. W. (1972). Structure of the chromosphere-corona transition region. *Sol. Phys.* 23, 78–102. doi: 10.1007/BF00153893

Soler, R., Carbonell, M., Ballester, J. L., and Terradas, J. (2013). Alfvén waves in partially ionised to-fluid plasmas. *Astrophys. J.* 767, 171–184. doi: 10.1088/0004-637X/767/2/171

Soler, R., Oliver, R., and Ballester, J. L. (2010). Time damping on non-adiabatic MHD waves in partially ionised prominence plasmas: the effect of He. *Astron. Astrophys.* 512, 28–32. doi: 10.1051/0004-6361/200913478

Vernazza, J. E., Avrett, E. H., Loeser, R. (1981). Structure of the solar chromosphere. III - Models of the EUV brightness components of the quiet-sun. *Astrophys. J. Suppl. S.* 45, 635–725. doi: 10.1086/190731.

Vranjes, J., and Krstic, P. S. (2013). Collisions, magnetization, and transport coefficients in the lower solar atmosphere. *Astron. Astrophys.* 554, 22–32. doi: 10.1051/0004-6361/201220738

Zaqarashvili, T. V., Khodachenko, M. L., and Rucker, H. O. (2011). Magnetohydrodynamic waves in solar partially ionized plasmas: two-fluid approach. *Astron. Astrophys.* 529, 82–90. doi: 10.1051/0004-6361/201016326

Conflict of Interest Statement: The author declares that the research was conducted in the absence of any commercial or financial relationships that could be construed as a potential conflict of interest.

frontiers
in Physics

ORIGINAL RESEARCH
published: 04 June 2019
doi: 10.3389/fphy.2019.00085

Influence of Resonant Absorption on the Generation of the Kelvin-Helmholtz Instability

Patrick Antolin[1]* and *Tom Van Doorsselaere*[2]

[1] School of Mathematics and Statistics, University of St. Andrews, St. Andrews, United Kingdom, [2] Department of Mathematics, Centre for mathematical Plasma Astrophysics, KU Leuven, Leuven, Belgium

The inhomogeneous solar corona is continuously disturbed by transverse MHD waves. In the inhomogeneous environment of coronal flux tubes, these waves are subject to resonant absorption, a physical mechanism of mode conversion in which the wave energy is transferred to the transition boundary layers at the edge between these flux tubes and the ambient corona. Recently, transverse MHD waves have also been shown to trigger the Kelvin-Helmholtz instability (KHI) due to the velocity shear flows across the boundary layer. Also, continuous driving of kink modes in loops has been shown to lead to fully turbulent loops. It has been speculated that resonant absorption fuels the instability by amplifying the shear flows. In this work, we show that this is indeed the case by performing simulations of impulsively triggered transverse MHD waves in loops with and without an initially present boundary layer, and with and without enhanced viscosity that prevents the onset of KHI. In the absence of the boundary layer, the first unstable modes have high azimuthal wavenumber. A boundary layer is generated relatively late due to the mixing process of KHI vortices, which allows the late onset of resonant absorption. As the resonance grows, lower azimuthal wavenumbers become unstable, in what appears as an inverse energy cascade. Regardless of the thickness of the initial boundary layer, the velocity shear from the resonance also triggers higher order azimuthal unstable modes radially inwards inside the loop and a self-inducing process of KHI vortices occurs gradually deeper at a steady rate until basically all the loop is covered by small-scale vortices. We can therefore make the generalization that all loops with transverse MHD waves become fully turbulent and that resonant absorption plays a key role in energizing and spreading the transverse wave-induced KHI rolls all over the loop.

Keywords: magnetohydrodynamics (MHD), sun: activity, sun: corona, sun: oscillations, resonant absorption, instabilities

Edited by:
Luis Eduardo Antunes Vieira,
Instituto Nacional de Pesquisas
Espaciais (INPE), Brazil

Reviewed by:
Abhishek Kumar Srivastava,
Indian Institute of Technology (BHU),
India
Tongjiang Wang,
The Catholic University of America,
United States
Michael S. Ruderman,
University of Sheffield,
United Kingdom
Tardelli Ronan Coelho Stekel,
Federal Institute of São Paulo, Brazil

***Correspondence:**
Patrick Antolin
patrick.antolin@st-andrews.ac.uk

Specialty section:
This article was submitted to
Stellar and Solar Physics,
a section of the journal
Frontiers in Physics

Received: *05 March 2019*
Accepted: *17 May 2019*
Published: *04 June 2019*

Citation:
Antolin P and Van Doorsselaere T
(2019) Influence of Resonant
Absorption on the Generation of the
Kelvin-Helmholtz Instability.
Front. Phys. 7:85.
doi: 10.3389/fphy.2019.00085

1. INTRODUCTION

The solar corona is continuously disturbed by perturbations at photospheric and chromospheric levels, either locally by means of e.g., convective motions or reconnection, or globally, by means of the internal oscillations of the Sun leaking radially outwards (and particularly p-modes). These continuous perturbations generate stress in the magnetic field and energy release processes lead to upflow of material that fills the coronal magnetic field with plasma, thereby generating coronal loops.

The particulars of coronal loop generation and destruction is, however, still a matter of debate. Observations mostly show the cooling stage of coronal loops [1], in which loops appear and disappear in specific bandpasses a time that can be either large or small [2], depending on the radiative cooling time and also on the unresolved substructure of loops [3–5]. Loops are thought to be composed of elementary substructures called strands. These strands may be elementary in the magnetic sense, being associated with tiny concentrations of magnetic field in the photosphere (of a few 100 km in width, e.g., [6]), or may be elementary in the sense of their independent thermodynamic evolution due to the fact that transport coefficients in the corona, and thus most plasma processes, are field aligned. On the other hand, the heating stage of the strands forming a loop is still unresolved, and are thought to occur in very short time and on very small spatial scales. Estimations of loop widths in the corona are thus based on the observed widths during the process of cooling, assuming that neighboring field lines composing the loop evolve more or less similarly. Even though there is a debate on how many strands actually compose a coronal loop on average [7], there seems to be consensus over the observed width of coronal loops (or the envelope of the strand bundle). Indeed, observations in coronal lines indicate an average coronal loop width of roughly 2 Mm [4, 8, 9], confirmed also at higher resolution by the characteristic width of coherent catastrophic cooling of loops [10, 11].

Besides the substructure of loops, other very relevant questions in coronal loop dynamics are how large are their boundary layers and what actually defines them [12–14]. The relevance lies particularly in the field of MHD waves. Kink waves (a particular class of transverse MHD waves characterized by the transverse displacement of the entire waveguide, [15, 16]) have been shown to permeate the corona and may be a candidate to heat the corona [17–20]. An observational characteristic of these waves is their fast damping and the leading theory explaining the damping is resonant absorption [21–26], also known as mode coupling in the case of propagating modes, contrary to standing modes [27–31]. During this process the plasma motions involved in the kink mode vary, and pass from initially being coherent lateral displacements of the loop's axis (thus affecting the whole loop) to azimuthal displacements highly localized in the regions within the loop where the resonance occurs. This happens where the kink speed matches the local Alfvén speed (or, in the case of driven propagating modes, where the kink frequency matches the local Alfvén frequency). These locations are usually assumed to be primarily at the edges of loops, although non-uniform loop distributions with resonance locations within the loop evolve similarly due to the collective nature of the kink mode [32, 33].

The formation process of coronal loops is very likely 3D, involving the local magnetic field topology and the conversion of the magnetic free energy into kinetic and thermal energies. This means that the initial energy deposition can have a characteristic area across the field over which magnetic field lines are affected roughly equally. This is the case for instance either through magnetic reconnection (case in which the field lines reconnect along separatrices) or through waves (case in which the diffusion process is linked to the 3D nature of the wave). This argument therefore poses a big question on how is the boundary layer of a coronal loop characterized. If the heating process is very spatially localized (which may be more the case of magnetic reconnection) it may suggest that the subsequent upflow into the loop from chromospheric evaporation is equally highly localized and therefore that the boundary layer separating the loop with the external medium is very thin [12]. If, however, the heating process has a smooth spatial distribution (for instance in the case of a wave produced by convective motions, which are usually coherent over some area) the width of the loop should be broader from the beginning.

The thinner the boundary layer, the more concentrated the azimuthal motions from resonant absorption will be [34] and therefore the larger the velocity shear produced with the surroundings. This velocity shear is additional to the velocity shear that is naturally produced by the (global) lateral displacement from the kink mode [35]. This velocity shear from the global motion happens between the internal motion of the loop and the (dipole-like) motion of the external plasma (produced by the displacement of the loop). On the other hand, it has been speculated that the resonance increases the shear with the external (dipole-like) motion due to the increase in amplitude in the azimuthal motions around the loop edge that the resonance entails [36]. Additionally, the resonance also produces an internal velocity shear between the inner shells of the loop due to phase mixing [37]. For these reasons it has been assumed that resonant absorption enhances the generation of dynamic instabilities due to shear flows [38]. In this paper, we study the effects of these additional shearing layers from the resonance and assess their influence on the generation of dynamic instabilities, and in particular the Kelvin-Helmholtz instability.

Transverse wave-induced Kelvin-Helmholtz rolls (also known as TWIKH rolls) are expected to exist from a large amount of recent numerical simulations in coronal conditions [36, 39–41], and also in prominences [38] and spicules [42]. Although TWIKH rolls have still not been observed directly due to the lack of instrumental resolution [43], there are a number of indirect observational characteristics that seem to match current spectroscopic and imaging observations, such as the generation of strand-like structure [36], the observed 3D motion of prominence strands combined with heating [38, 44], the differential emission measure broadening of loops [45] or the corrugated Doppler shift transitions across spicules [42]. Karampelas and Van Doorsselaere [46] have shown that the continuous driving of kink waves in loops leads to fully turbulent loops due to the TWIKH rolls. The potential existence of TWIKH rolls is particularly interesting for coronal heating since it provides a means to the waves to dissipate their energy [47]. Indeed, the generated turbulent-like regime of vortices and current sheets in the TWIKH rolls leads to additional wave dissipation [38, 41].

TWIKH rolls differ from the more generally known velocity shear-induced KHI vortices [48–51] in that the velocity shear is not laminar, constant and field-aligned, but oscillatory and at an angle to the magnetic field (perpendicular in the case of non-twisted flux tubes). The non-zero angle of the wave vector with the magnetic field implies a lower magnetic tension opposing the development of the instability. [52, 53] have analytically shown that this constitutes a major difference leading to flux tubes being always K-H unstable to such flow, regardless of the amount of twist. This finding supports previous numerical results of TWIKH rolls produced by very low amplitude kink modes [36].

The article is organized as follows. We introduce the numerical model in section 2, together with the initial conditions, MHD equations and details of the code. In section 3 we present the results, which we discuss in section 4 and conclude the paper.

2. NUMERICAL MODEL

2.1. Initial Conditions

The numerical model consists of a straight, cylindrical flux tube (with circular cross-section) in pressure equilibrium with the background, representing a coronal loop. Our experiments (and the results we obtain) are largely independent of the conditions within the flux tube and the corresponding contrast with the ambient corona. This is because the specifics of the KHI are relatively insensitive to the density and magnetic field contrast, compared to the velocity shear, boundary layer thickness and loop radius to length ratio. For instance, uniform temperature or uniform magnetic field (hence, a cool or hot loop) would lead to the same results [43]. The presence of magnetic twist in the loop delays the onset of the KHI [51, 54, 55] but does not suppress it [52].

As observed in some loops [25], here we choose loops that are all hotter and denser than the background by a factor of 3, i.e., $T_i/T_e = 3$ and $\rho_i/\rho_e = 3$. Correspondingly, the loop-aligned magnetic field is slightly lower than the background field to keep pressure balance. We set the external temperature and total number density to $T_e = 10^6$ K and $n_e = 10^9$ cm^{-3}, respectively. The external and internal magnetic fields are $B_e = 18.63$ G and $B_i = 17.87$ G, respectively. The plasma β parameter outside and inside the flux tube is equal to 0.01 and 0.098, respectively.

We consider different cases of loops with and without boundary layer. This layer connects the internal and external plasma and is described as follows:

$$\rho(x,y) = \rho_e + (\rho_i - \rho_e)\zeta(x,y), \tag{1}$$

where

$$\zeta(x,y) = \frac{1}{2}\left(1 - \tanh\left(b\left(r(x,y) - \frac{1}{2}\right)\right)\right). \tag{2}$$

Here, (x,y) denotes the plane perpendicular to the loop axis (along z). The $r(x,y) = \sqrt{(x^2 + y^2)}/w$ term denotes the normalized distance from the loop center and $w = 2$ Mm denotes the loop width (diameter). We take the case of a loop with $b = 0.01$, which essentially describes a step function between internal and external plasma (and therefore no boundary layer), and a second case with $b = 16$, leading to a boundary layer width of $0.4\,R$, with $R = 1$ Mm, the radius of the loop.

At $t = 0$ a transverse perturbation in x aimed at triggering mainly the fundamental kink mode is set by imposing a velocity perturbation along the loop that has the same spatial distribution of the density. That is, we have $v_x = v_0\sin(z\pi/L)\zeta(x,y)$, where z denotes the distance along the loop, $L = 200$ Mm, and $v_0 = 16.6$ km s^{-1}. Given that the internal Alfvén speed is $v_{A,i} = 1006$ km s^{-1}, the initial amplitude A relative to internal Alfvén speed corresponds to $A/v_{A,i} = 0.0165$, and can therefore be considered nonlinear, since, as defined by Ruderman and Goossens [56], the non-linearity parameter $\nu \approx \frac{AL}{R} = 3.3$ *is larger than 1*. This velocity is chosen to mimic usually observed kink mode amplitudes (most of the energy of the initial perturbation leaks out, and the average velocity in the first quarter oscillation is equal to ≈ 9 km s^{-1}). Following the perturbation, the loop oscillates with a standing kink mode with a period of $P \approx 315$ s, approximately equal to the expected period, given that the kink speed is $c_k = 1256$ km s^{-1}. It is worth mentioning that this numerical model corresponds to the impulsively excited loop model used in Van Doorsselaere et al. [45].

The choice of no boundary layer initially for one of our flux tube cases has a 2-fold motivation. As explained in the introduction, it is not unreasonable to think that when a loop first forms, presumably by an impulsive heating event somewhere along the loop, if the heating is very localized in space it may trigger very localized chromospheric evaporation, thereby producing a sharp boundary layer. The second reason behind this choice has to do with the late onset of resonant absorption, a time delay that allows to investigate more properly the role it has on the KHI.

2.2. MHD Equations and Numerical Scheme

We solve the following set of resistive MHD equations without gravity:

$$\frac{\partial\rho}{\partial t} + \nabla\cdot(\rho\vec{v}) = 0, \tag{3}$$

$$\frac{\partial}{\partial t}(\rho\vec{v}) + \nabla\cdot\left[\rho\vec{v}\vec{v} + \left(p + \frac{\vec{B}^2}{8\pi}\right)\vec{I} - \frac{\vec{B}\vec{B}}{4\pi}\right] = 0, \tag{4}$$

$$\frac{\partial\vec{B}}{\partial t} + \nabla\times(\frac{\eta}{\mu}\vec{j} - \vec{v}\times\vec{B}) = 0, \tag{5}$$

$$\frac{\partial}{\partial t}\left(\frac{p}{\gamma-1} + \frac{1}{2}\rho\vec{v}^2 + \frac{\vec{B}^2}{8\pi}\right) + \nabla\cdot\left[\left(\frac{\gamma p}{\gamma-1} + \frac{1}{2}\rho\vec{v}^2\right)\vec{v} + \left(\frac{\eta}{c}\vec{j} - \frac{1}{4\pi}\vec{v}\times\vec{B}\right)\times\vec{B}\right] = 0, \tag{6}$$

$$p = \frac{2k_b}{m_p}\rho T, \tag{7}$$

where $\rho, T, p, \vec{v}, \vec{B}$ and $\vec{j}$ denote the usual quantities of mass density, temperature, pressure, velocity, magnetic field and current density, respectively. We take a fully ionized hydrogen plasma, so that $\rho = \frac{1}{2}m_p n$, with m_p the proton mass and n the total number density (hence, we assume that the electron number density is half the value of n). The quantity $\vec{I}$ denotes the identity tensor. Also, k_b denotes Boltzmann's constant, c is the speed of light, μ is the magnetic permeability and η is the resistivity. We adopt an anomalous resistivity model following Sato and Hayashi

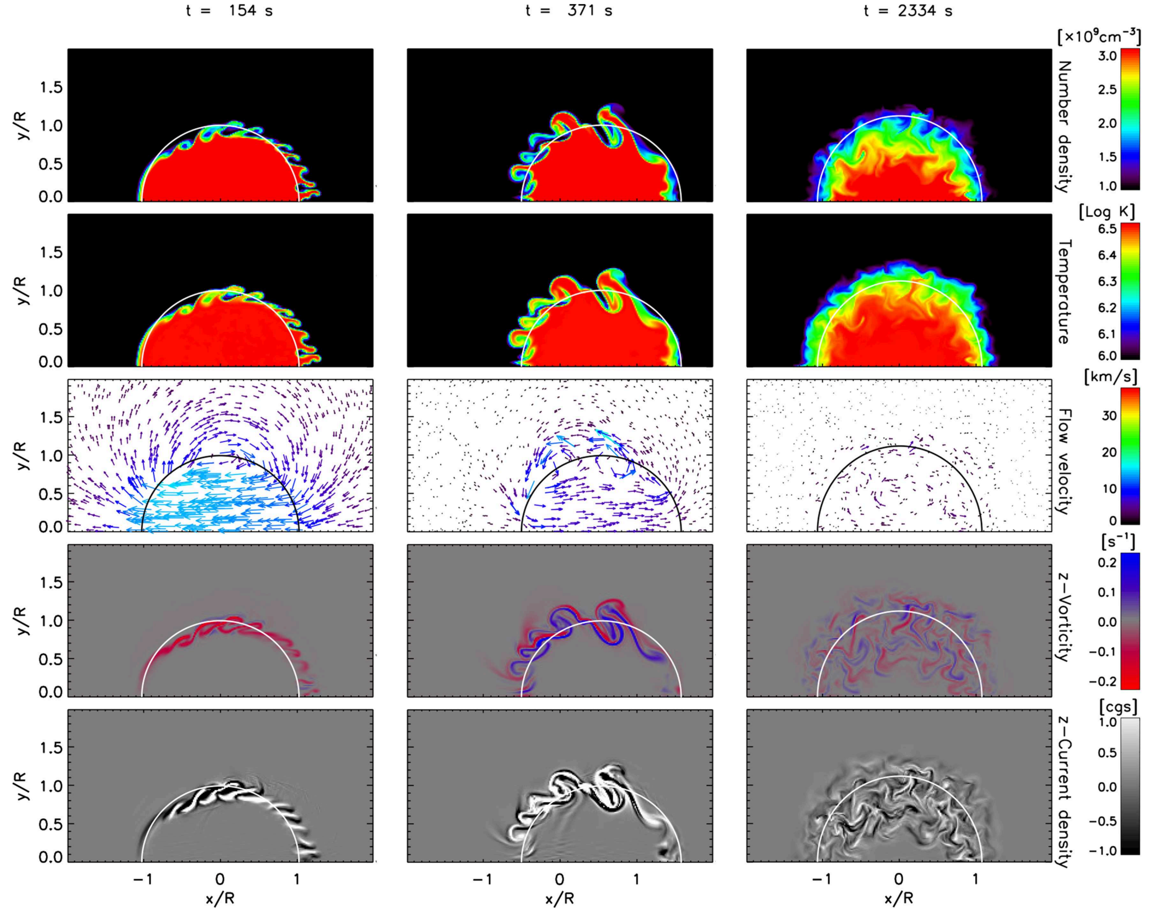

FIGURE 1 | TWIKH vortices throughout, for a loop without initial boundary layer and no viscosity. From top to bottom rows we have the cross-section at the apex of the loop of, respectively, the total number density (in units of 10^9 cm^{-3}), the temperature ($\log T$), the flow velocity (in km s^{-1}), the $z-$vorticity component (in s^{-1}) and the $z-$current density component (in cgs units). The 3 columns, from left to right, show 3 instances in time, respectively at $t = 154$ $s \approx P/2$, $t = 371$ $s \approx 1.2$ P, and $t = 2,334$ $s \approx 7.4$ P, where $P = 315$ s is the period of the kink mode. The half ellipse in white (or black in the flow velocity panels) corresponds to the ellipses calculated in section 3.2. See also the accompanying movie in the **Supplementary Material**.

[57], Ugai [58], and Miyagoshi and Yokoyama [59], given by:

$$\eta = \begin{cases} 0, & \text{for } v_d < v_c, \\ \eta_0 (v_d/v_c - 1)^2, & \text{for } v_d \geq v_c, \end{cases} \tag{8}$$

where η_0 is the resistivity parameter, $v_d \equiv j/(en)$ is the ion-electron drift velocity (with e the elementary electric charge and $j = \sqrt{(j_x^2 + j_y^2 + j_z^2)}$ the total current density), v_c is the threshold above which anomalous resistivity sets in. We set $\eta_0 = 3.3 \times 10^{14}$ cm^{-2} s^{-1}, which is much higher than the Spitzer resistivity in the solar corona (10^4 cm^{-2} s^{-1}) and decreases the magnetic Reynolds number down to 10-100, that is, 3 orders of magnitude smaller than in cases without resistivity. This ensures fast dissipation of the strong currents. The average value of v_d in our simulation is 2.5×10^{-4} km s^{-1}. We therefore choose $v_c = 0.15$ km s^{-1}, which ensures that the anomalous resistivity only comes into play when strong currents are produced. This treatment ensures a spatial localization of the anomalous resistivity and helps deal more realistically with current sheets (see [60] for the effect of this parameter on magnetic reconnection in current sheets). In particular, the use of anomalous resistivity in our model ensures that strong currents generated, for instance, by the sharp spatial gradients, do not produce spurious results in the solution of the MHD equations. We note however that in the present simulations we do not obtain such strong currents and the threshold velocity drift v_c is almost never reached.

Our model also includes an explicit, constant and artificial viscosity [61], and by controlling its magnitude we can model conditions close to ideal (and more realistic, by setting it to very small values), or highly viscous (unrealistic) conditions that prevent dynamic instabilities to set in. We choose to include the case of a flux tube with boundary layer and with enhanced viscosity in order to artificially prevent the onset of the KHI. All other simulated models have very low viscosity and close to ideal.

The numerical simulations are performed with the CIP-MOCCT code [62], which uses the cubic-interpolated pseudoparticle/propagation scheme (CIP, [63]) to solve the

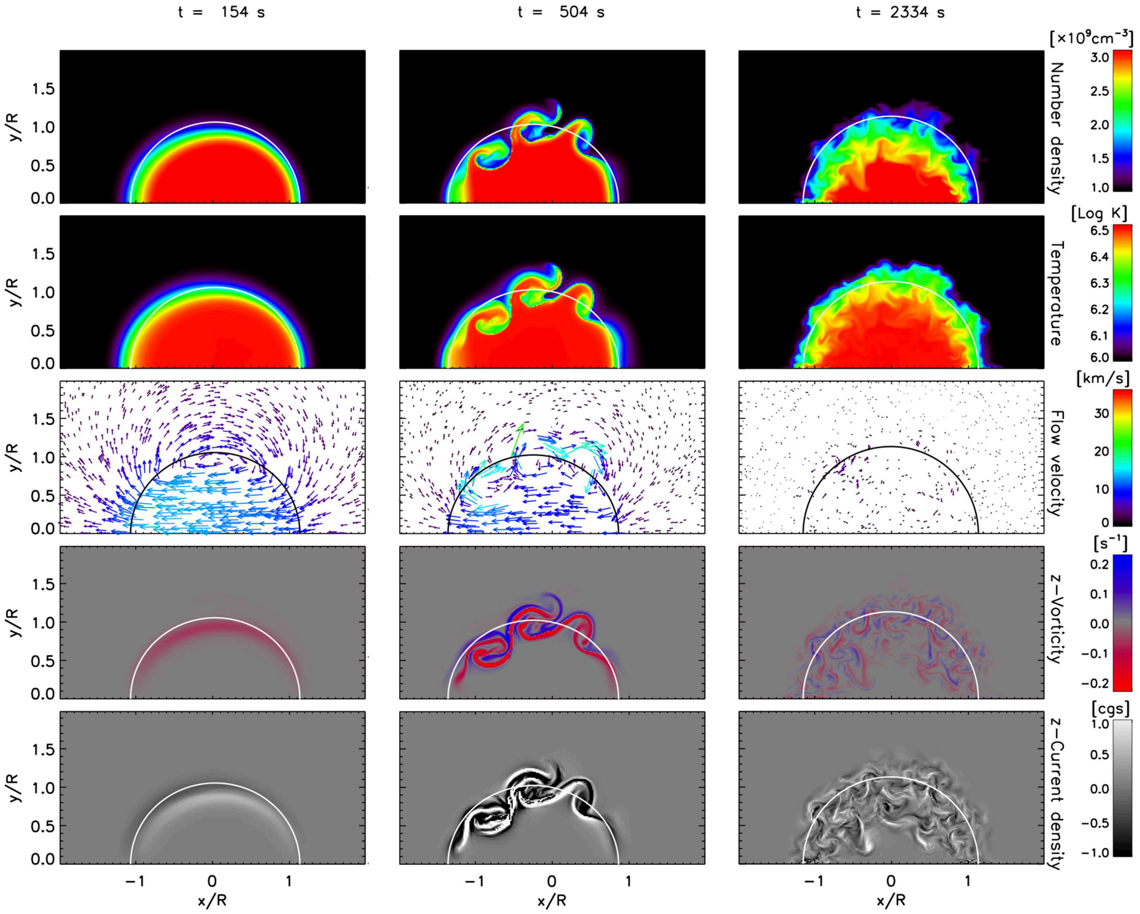

FIGURE 2 | TWIKH vortices throughout for a loop with initial boundary layer and no viscosity. The same variables as in **Figure 1** are shown, setting the same minima and maxima for better visualization. The same times are shown, except for the middle panel, for which we select a later time of $t = 504$ s $\approx 1.6\,P$, corresponding to the first formation of KHI vortices. See also the accompanying movie in the **Supplementary Material**.

mass conservation, momentum and energy equations, while the method of characteristics-constrained transport (MOCCT, [64, 65]) is used to solve the induction equation. The CIP-MOCCT code has been shown to maintain sharp contact surfaces [66, 67], thereby reducing the effect of diffusivity on the sharp spatial gradients in our model and those obtained by the dynamic instabilities.

The numerical box has a size of $(512, 256, 50)$ in (x, y, z) and we model only a quarter of a loop profiting of the kink mode's symmetries, in order to have a high spatial resolution while keeping the simulation at feasible levels. The box has a non-uniform grid along x and y, where these axes describe the plane perpendicular to the loop, x is along the direction of oscillation, and only half the loop is modeled in y. The box has a uniform grid along z, which is parallel to the loop axis and only half the length of the loop is modeled. We use symmetric boundary conditions in all boundary planes except for the x boundary planes, where periodic boundary conditions are imposed. In this way the full loop hosting a fundamental kink mode is modeled. The smallest grid cell in the (x, y) plane has a size of 15.6 km and is kept constant in the region where the loop oscillates. The x and y grids cell sizes are allowed to increase above distances of $\approx 4\,R$ (where R is the radius) and the maximum distance from the center is 16 R along both axes. The grid cell along z is uniform and has a size of $2,000$ km. From a parameter study, we estimate that the effective (combined explicit and numerical) Reynolds and Lundquist numbers in the code are of the order of $10^4 - 10^5$ [38]. The simulation with enhanced viscosity has a Lundquist number of the order of $10 - 100$.

3. RESULTS

3.1. TWIKH Rolls Throughout the Loop

We show in **Figures 1–3** different instances of the evolution for various quantities for the 3 loop cases we have considered (no boundary layer and no viscosity, with boundary layer and no viscosity, and with boundary layer and with viscosity). Among these quantities we show the z-component of the vorticity, $\omega_z = \partial v_y/\partial x - \partial v_x/\partial y$, and the z-component of the current density, $j_z = 1/\mu(\partial B_y/\partial x - \partial B_x/\partial y)$. These quantities are particularly useful to track the development of resonant absorption and KHI vortices and current sheets generated by dynamic instabilities.

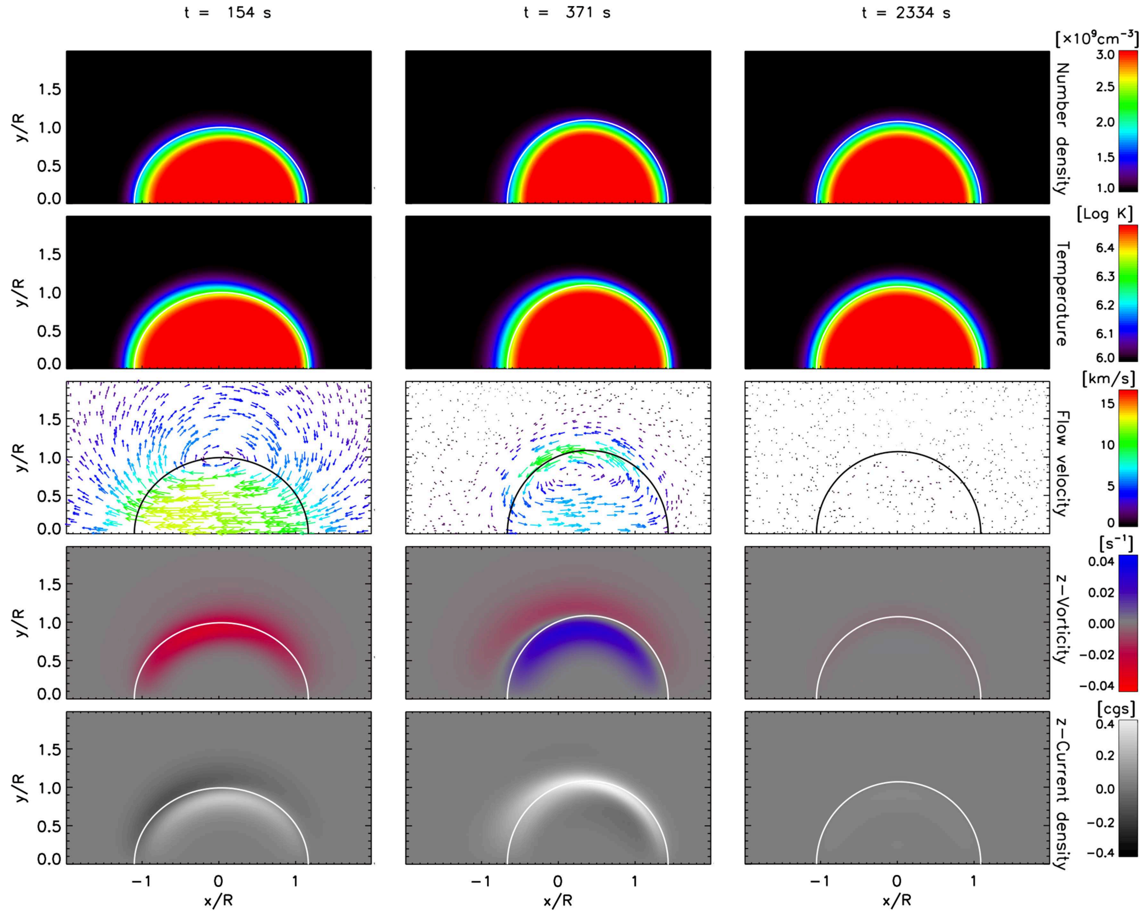

FIGURE 3 | No TWIKH vortices for a loop with initial boundary layer and with enhanced viscosity. The same variables as in **Figure 1** are shown. Note that the minima and maxima (notably for the velocities, vorticity and the current density) are smaller than for **Figures 1**, **2** due to the enhanced viscosity. The same times as in **Figure 1** are shown. See also the accompanying movie in the **Supplementary Material**.

Due to the sharp contact discontinuity around the loop for the case without boundary layer and no viscosity, as soon as the perturbation starts, TWIKH rolls form around the side edges. This is expected since a flux tube (straight or twisted) is always unstable to the KHI [52], the sharp contact discontinuity and no viscosity ensures that the scale length where the velocity shear first exists is small enough to trigger these high azimuthal modes, and high azimuthal mode numbers have the highest growth rate. Additionally to these vortices at the side of the loop, we can see vortices at the wake. These vortices correspond to Rayleigh-Taylor (RT) vortices (and also lead to rolls in 3D, extending all along the loop), characterized by the finger-like structures (also produced for strong perturbations in dense, spicule-like structures with thicker boundary layers, [42]). As seen in **Figure 2**, these initial small-scale vortices (both, RT and KHI types) are absent for the case with initial boundary layer and no viscosity, since the scale length where the velocity shear first exists is larger than the size of these unstable modes.

After a period of oscillation (second column in **Figures 1**, **2**) we note the appearance of larger vortices for the cases without viscosity. The boundary layer thickness is increased due to the vortices. After several periods (third column in **Figures 1**, **2**) the global mode oscillation has largely damped (true for all cases), the boundary layer thickness has significantly increased to a radius or so without any significant difference between the models without viscosity and the vortices have expanded radially outwards and inwards. At a late stage only small-scale vortices remain, seen mainly in the vorticity and current density maps. On the other hand, the case with viscosity shows no dynamic instabilities and its boundary layer thickness remains largely unchanged between the initial and final stages (**Figure 3**).

In **Figure 4** we show the evolution of the displacement of the loop axis at the apex and along the direction of oscillation. Since the models have slightly different maximum velocities and, correspondingly, different maximum displacements (all within 0.5 R and 0.6 R), to better visualize the damping we normalize the displacement by the respective maximum values. The displacement of the flux tube can be calculated in multiple ways. One way is to calculate the center of mass of the middle slice $y = 0$ at the apex for each time step. Another way is

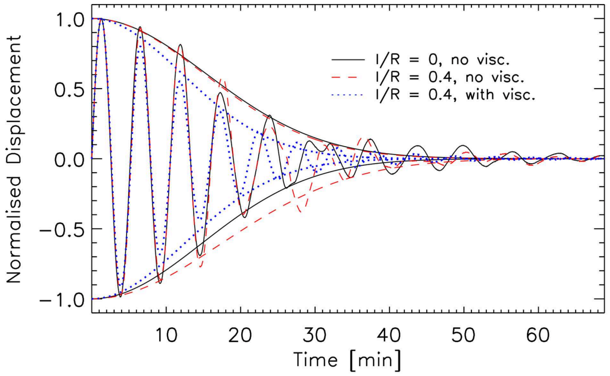

FIGURE 4 | Displacement of the loop axis (at apex) with time. For each time step we define the center of the loop as the center of mass. The result over time is plotted for the loop with no initial boundary and no viscosity (black solid curve), with initial boundary layer and no viscosity (red dashed curve) and with initial boundary layer and viscosity (blue dotted curve). We also overlay the fits to the maxima and minima of each profile performed with a damped Gaussian function (see text for details).

to fit a Gaussian of the density profile along the direction of oscillation at each time step. We choose the former method to calculate the damping, since this method suffers less influence from the vortices at the boundaries. In the rest of the paper, and in particular for section 3.2 we are more interested in the displacement of the boundary of the flux tube rather than the displacement of the loop's core, and hence we choose the second method for those cases.

In **Figure 4** we can see that the effect on the damping time of not having an initial boundary layer and no viscosity is to extend it. This is expected since resonant absorption is delayed due to the initial absence of the boundary layer, which is created soon after by the KHI and RT vortices. As demonstrated by Pascoe et al. [68], Pascoe et al. [69], and Hood et al. [70], the damping of a fundamental kink mode due to resonant absorption is first governed by a Gaussian envelope and later on by an exponential envelope, and the switching time depends on the boundary layer thickness and the density contrast. To better quantify the damping time we therefore choose to fit the maxima of each profile with damped Gaussians of the form $v(t)\exp(-t^2/L_g^2)$ (and we therefore define the damping time only by the Gaussian envelope time). Doing so we obtain damping times of 1,303 s (= 4.13 P), 1,280 s (= 4.06 P), and 1,030 s (= 3.27 P), respectively, for the cases of no initial boundary layer and no viscosity, initial boundary layer and no viscosity, and initial boundary layer and viscosity. The absence of an initial boundary layer means that the switch occurs slightly later and therefore less damping is obtained, as can indeed be seen. Also, by comparing the cases with and without viscosity, we can see that the presence of viscosity strongly reduces the damping time. In addition, at long times the cases with dynamic instabilities and no viscosity never damp completely. We discuss probable causes for this effect in section 4.

To compare with observations we can fit the envelopes of the oscillating profiles with an exponential rather than a Gaussian, and we find values between 2.2 and 2.6 P for all models. Accordingly, there is not much difference between the models since a boundary transition layer is rapidly formed due to the KHI. Comparing with linear damping (≈ 3.2 P, [21, 71]) we can see that the damping from our models with KHI with nonlinear amplitudes lead to stronger damping compared to the linear case, as has been found already by Magyar and Van Doorsselaere [40], who suggested this mechanism to explain the observed dependence of kink oscillation damping on the amplitude [72].

To see the extent of the KHI vortices we plot in **Figure 5** the time-distance maps of density and z-vorticity cuts parallel to the y axis, moving with the flux tube and always crossing its center (where the center is defined with the Gaussian fit method as explained above). This method is better than tracking the center of mass since it takes more properly into account the radial extent of the KHI and RT vortices (relative to the Gaussian fit, the center of mass is displaced much less). **Figure 5**, and particularly the z-vorticity maps for the cases without viscosity show that the radial layers where the TWIKH rolls are generated move more rapidly inward than outward at a fast rate in the $1-2$ periods (to $t = 7-10$ min), from $y = 0.6\ R$ to $y = 1.3\ R$. Note that during this time interval the boundary layer thickness for the case without initial boundary layer increases steadily, while the increase is more abrupt for the case with initial boundary layer. This is due to the absence of small-scale KHI vortices initially for the latter model. The vortices then largely stop extending outward while they keep extending inward more gradually and at a steady rate until the end of the simulation ($t = 69$ min, corresponding to 13 periods), when the vortices have extended from $y = 0.2\ R$ to $y = 1.4\ R$. The inward extension of vortices for the case with initial boundary layer seems to be slightly slower. On the other hand, the model with viscosity has a much lower vorticity that is concentrated around the resonant layer, and is diffused away relatively rapidly. An important consequence of this result is that impulsively excited kink waves generate turbulent loops, and thus that probably all loops in the solar corona are in a turbulent state.

The density panels of **Figure 5** for the cases without viscosity show that the first set of vortices at the boundary edge increase in size, producing deep entrances of the external material toward the loop center. The following sets of vortices that continuously develop are only internal and small-scale vortices, seen mainly in the vorticity maps since they do not produce large density changes. We can see that the changes in both the density and vorticity are slightly larger in the case of no initial boundary layer. The herringbone pattern seen in the vorticity panel reflects an apparent super slow wave propagation of the kind discussed by Kaneko et al. [73], produced by the phase mixing of the continuously produced KHI vortices.

3.2. Effect From Resonant Absorption

As investigated in, e.g., [43], the KHI smoothens the boundary layer. Hence, the influence of the KHI on resonant absorption is to increase the layer where the resonance (and phase mixing) occurs. In our simulation with no initial boundary layer we have only the KHI at first and only at later times (even if shortly after) the combined effect from KHI and resonant absorption. On the other hand, the simulation with enhanced viscosity has no

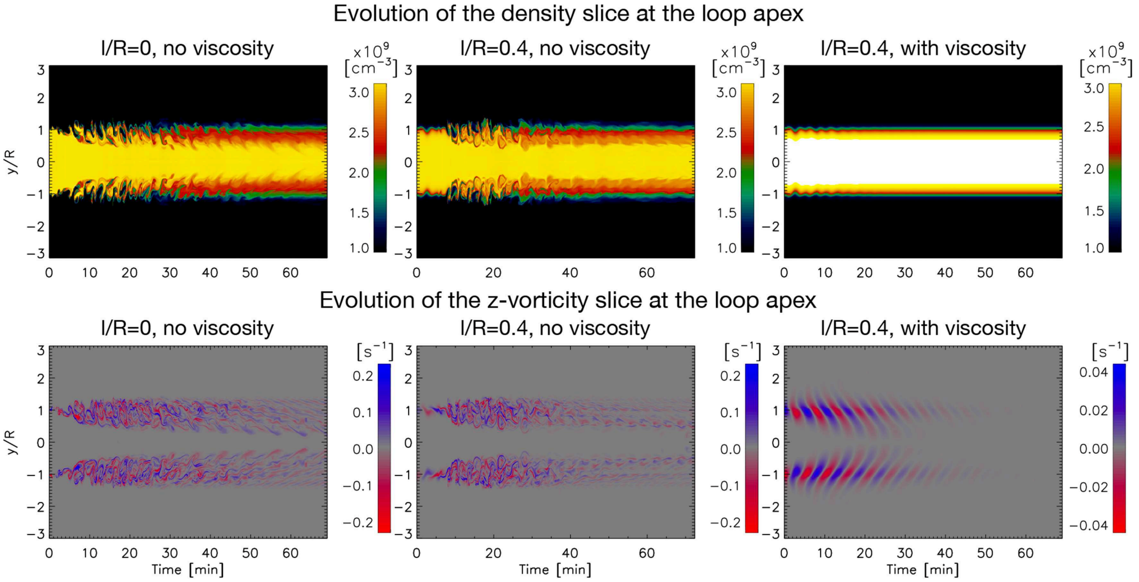

FIGURE 5 | Outward and inward expansion of the vortices. For each loop model we take a parallel cut to the *y* axis across the loop passing through its center at each time step (see text for details on the procedure) and plot the resulting time-distance maps of the density (top panels) and $z-$vorticity (bottom panels) cuts. From left to right the columns correspond, respectively, to the model with no initial boundary layer and no viscosity, the model with initial boundary layer and no viscosity, and the model with initial boundary layer and viscosity. Note that the time range in the simulation with initial boundary layer and viscosity is slightly more extended in order to better visualize the inner vortices reaching the core of the loop. Note also that the extrema for the $z-$vorticity are much smaller for the enhanced viscosity case.

KHI and only resonant absorption. Hence, by comparing these 3 models we can investigate the effect of the resonance on the KHI.

To investigate more carefully the development of resonant absorption we calculate the azimuthal velocity v_ϕ for each loop model, taking the center of the loop obtained through Gaussian fitting of the density profile explained previously. For each radial distance from the loop's center, we then calculate the azimuthal velocity amplitude by averaging the absolute value over ellipses around the center. We choose ellipses instead of circles since the loop cross-section deforms considerably due to high order radial modes and the KH and RT vortices [43, 55]. Since the ellipses are modified over time, we define the radial distance as the distance from the loop's center along the cut parallel to the *y* axis. For each time step, we find the semi-major and semi-minor axes of an ellipse along *x* and the axis parallel to *y* passing through the loop's center by locating (through interpolation) the position where the density is equal to 2 $n_e(t = 0)$, that is, the intermediate value between the internal and external density values at the beginning of the simulation. Therefore, we define this density point as the middle of the loop boundary layer. We also apply a temporal smoothing to the obtained variation of the ellipse axes over time, in order to get rid of the high frequency perturbations from the vortices. The temporal smoothening for the ellipse' s semi-axis parallel to the *y* axis has a very long boxcar width of 950 s in order to catch the long term variations only and not those from the high-frequency ones from the vortices. For a given time step we then take different self-similar ellipses with respect to the ellipse that fits the loop edge by changing the radial distance and keeping the same ratio between the axes. In **Figures 1–3** (and the accompanying movies in the **Supplementary Material**) we overlay for each panel the ellipse fitting the loop edge obtained with this technique.

In **Figure 6** we show for each loop model the time-distance diagram of the azimuthal velocity amplitude averaged along each self-similar ellipse located at different radial distances from the loop's center. The fringe pattern indicating high azimuthal velocity power has double the frequency of the kink mode, as expected. Note that the fringes within a short radius distance decrease in amplitude. This damping also reflects the damping seen in **Figure 4**. At the same time the amplitude of the region located within the contour where the kink speed is roughly equal to the local Alfvén speed increases. This is characteristic of resonant absorption. Note that for the model without initial boundary layer the amplitude within this contour reaches a maximum at $t \approx 15$ min (roughly 3 periods) and extends to $\approx$ 26 min. For the model with initial boundary layer and no viscosity the maximum amplitude in the resonant layer is found at $\approx$ 7 min and extends to $\approx$ 23 min. On the other hand, the model with enhanced viscosity shows a maximum amplitude in the resonant layer at $\approx$ 7 min and extends to only $\approx$ 16 min due to the enhanced viscosity. Note that for the models with KHI the region of resonance is shifted inward toward the loop's center in time. We have checked that the kink speed is roughly constant throughout the simulation. Hence, this shift is due to the variation of the boundary layer due to the KHI. The regions outside of the contour show also significant amplitudes that grow with a similar rate as resonant absorption. At $t > 30$ min in both models most of the power within the resonant region has disappeared, while the regions of highest power have now shifted inwards (with a smaller power region outward). This shows

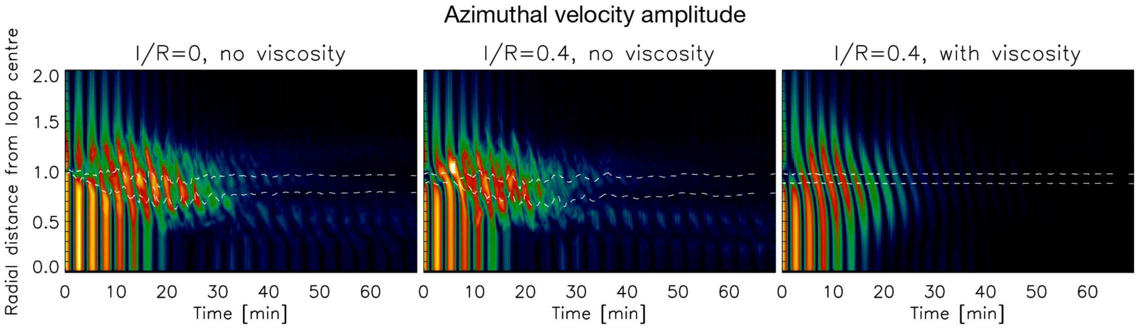

FIGURE 6 | Azimuthal velocity amplitude from the loop's center. For each loop model, the azimuthal velocity amplitude (in absolute value) is calculated along moving ellipses around the loop's center that evolve through time. The ellipses are self-similar and their semi-major to semi-minor axis ratio matches the ellipse fitting the edge of the loop at each time step. Hence, for each ellipse at a given radial distance from the loop's center, we obtain an average value of the azimuthal velocity amplitude (in absolute value). The upper and lower dashed contours correspond, respectively, to the regions where the local Alfvén speed is 10% higher and 10% lower than the kink speed (see text for further details). From left to right the columns correspond, respectively, to the model with no initial boundary layer and no viscosity, the model with initial boundary layer and no viscosity, and the model with initial boundary layer and viscosity. Note that the color table has not been normalized to the same maximum between all loop models.

that the energy from the resonant flows have transferred to the TWIKH rolls within the loop, themselves being triggered by the velocity shear produced by the resonance.

Hence we can see that the effect of the resonance on the KHI is to trigger the instability within the loop. The resonance acts as a localized energy reservoir by incrementing the azimuthal velocity shear in the loop's boundary layer.

3.3. High Azimuthal Wave Modes

We investigate now more closely the contribution from high azimuthal wavenumbers on the KHI dynamics. For this we follow the procedure of Terradas et al. [55] and calculate the Discrete Fourier Transform on the radial (v_{rR}) and azimuthal velocities ($v_{\phi R}$), and also on the density (ρ_R) at a distance R from the loop center. These quantities are computed over the ellipses described in the previous section. The mapping of these quantities along the circumference of the ellipses is uniform with respect to the angle ϕ. Using the same notation as in Terradas et al. [55] we calculate:

$$G(p) = \frac{1}{N}\sum_{k=0}^{N-1} g(k)e^{-i\frac{2\pi}{N}pk}, \tag{9}$$

where $g(k)$ denotes either $v_{\phi R}, v_{rR}$ or ρ_R, N is the total number of modes ($p = 0, 1, ...N - 1$). We show for all models the contribution for the first 5 azimuthal modes to each quantity in **Figure 7**. It is worth to mention that due to the parity of $v_{\phi R}, v_{rR}$ and ρ_R they are, respectively, purely imaginary, real and real functions, and that the dominant terms are shown in **Figure 7** and the following figures.

The $p = 1$ mode has the dominant contribution overall for all models and for all quantities, except for $\rho_R(t < 10$ min). For the models developing KHI, the $p = 2$ mode has a significant power, similar or even higher to the $p = 1$ mode in some instances for the azimuthal velocity (and for the density at the beginning of the simulation). The higher order modes ($p > 2$) also have significant power. For the model without initial boundary layer, these higher order modes have the dominant power at the beginning of the simulation for the azimuthal velocity and density, compared to the model with initial boundary layer and no viscosity. For the latter, the higher order modes become dominant after $1 - 2$ periods. And at the end of the simulations with KHI all modes for the azimuthal velocity have similar power.

As explained in Terradas et al. [55] in the absence of KHI the excitation of the $p = 2$ is produced mostly by the nonlinear effect of the inertia from the loop's motion (a squashing effect, described analytically in Ruderman and Goossens [56]), its frequency is double that of the kink mode, and the amplitude of the $p = 2$ mode is smaller than that of the $p = 1$ mode by the square of the amplitude. These properties can be seen in **Figure 7** for the model with initial boundary layer and viscosity. The higher azimuthal wavenumbers increase their power only once the KHI has set in, as can be seen when comparing the 3 models. The higher order modes correspond to the small KHI and RT vortices that populate the edge of the loop, which are the fastest growing unstable modes in the model without initial boundary layer. In the case with an initial boundary layer the length scale over which velocity shear exists is larger, and therefore the first unstable modes have larger wavelength, and it is only in the nonlinear stage of the instability that higher order modes develop.

In the cases with KHI, all the high order modes have much higher power than that predicted by linear theory. The ellipses we construct are co-moving with the loop's edge and therefore we largely reduce the power coming from the deformation of the loop due to its inertia and also the nonlinear influence from the radial modes (hence, the power of $p = 1$ and $p = 2$). The large power still present in these modes and the higher order ones is due to the fact that the edge of the flux tube does not correspond to the spatial extent of the KHI vortices (as can be seen in **Figures 1**, **2** and the accompanying movies in the **Supplementary Material**). Hence, the vortices cross the ellipse boundary each time they form. This is particularly the case at the

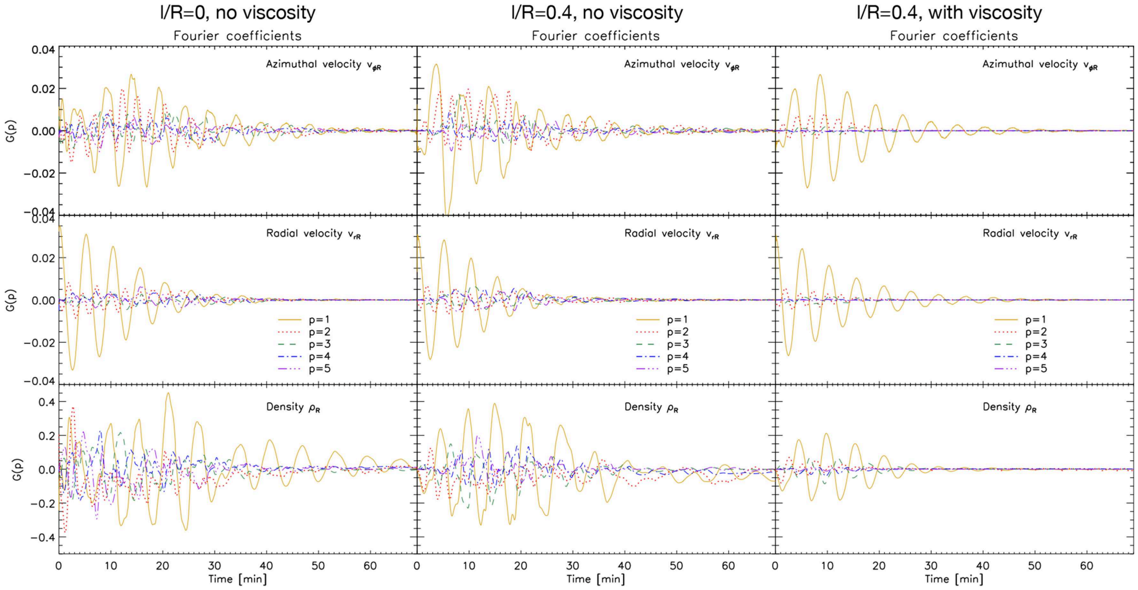

FIGURE 7 | Fourier coefficients for the azimuthal and radial velocities and the density. We show the contribution of the azimuthal modes to each quantity along an ellipse fitting the edge of the loop by calculating the Discrete Fourier Transform (Equation 9). We only show the first 5 modes (see legend for line style).

beginning of the simulation (when the deformation of the flux tube is large). Hence, the significant power at the beginning of the simulation without initial boundary layer comes mostly from the KHI. The observed increase of the power of all modes over the first 15 min (matching the time at maximum azimuthal velocity amplitude) is due to an influence from resonant absorption. The overall effect over the first 15 min is to have an apparent inverse energy cascade, where the lower order modes have increasing power in time (a trend that is particularly clear in the $v_{\phi R}$ and ρ_R panels in **Figure 7**). Indeed, this is not observed in the case with initial boundary layer and no viscosity, for which once the higher order modes set in, all modes show an amplitude that remains roughly constant until $t \approx 20$ min.

To investigate the generation of high azimuthal wavenumbers across each loop's cross section we now calculate the Discrete Fourier Transform on the azimuthal velocity along various of the self-similar ellipses located at different radii from the loop's center, described in the previous section. We thus take $v_{\phi r}$ for $r = 0.3\ R, 0.4\ R, 0.5\ R, 0.6\ R, 0.8\ R, 1\ R, 1.2\ R$ and $1.4\ R$ and show in **Figures 8–10** (respectively for the loop without initial boundary layer and no viscosity, with initial boundary layer and no viscosity and with initial boundary layer and with viscosity) the corresponding contribution of the first 5 modes to the total signal.

Away from the region where most of the KHI occurs we mostly have the dipole (azimuthal) field generated by the kink mode ($R_1 = 1.4\ R$ panel in **Figure 8**), and its damping is similar to the damping observed in the same layer in the model without KHI. Note however, that higher order modes have nonetheless higher power even at this distance from the loop's center, reflecting a rapid but small influence of the KHI even at this distance. As we approach the KHI region in the models without viscosity, an increase of power in all modes can be seen, as noted previously ($R_2 = 1.2\ R, R_3 = 1\ R, R_4 = 0.8\ R$ panels in **Figures 8**, **9**). As we pass from $r = R$ to $r = 0.8\ R$ we can see for the model without initial boundary layer that the time of maximum power of all modes has been shifted to later times, from $t = 15$ min to $t = 20 - 25$ min. For the model with initial boundary layer, significant power in the high order modes at $r = 0.8\ R$ can be observed until $t \approx 20$ min. This time shift (and time interval) matches the time of maximum resonance (or significant resonance), which is seen in **Figure 6**, and the spatial shift of the resonance from R to $0.8\ R$ in the same time interval. Therefore, this further supports that the resonance is acting as catalyst of the KHI in both models without viscosity, irrespective of the presence of an initial boundary layer.

As we move further radially inward in the case without KHI, no significant difference in power for $v_{\phi R_i}$ is observed. On the other hand, for the cases with KHI we note a temporal shift to later times of the power increase in the high azimuthal wave modes. This suggests that the KHI self-induces itself, layer after layer deeper into the loop, starting from the resonant layer at the edge of the flux tube, which acts as an energy reservoir for the velocity shear. Moreover, even after the energy from the resonance has largely disappeared the inner vortices continue to trigger deeper KHI vortices. Thus, we can predict that both entire loops become eventually turbulent.

As mentioned in section 3 the model without initial boundary layer shows a slightly faster inward propagation of the KHI vortices. This can be explained by the fact that by allowing the boundary layer to develop naturally due to the KHI, the velocity shear that is produced by resonant absorption is slightly higher than in the model with initial boundary layer, thereby increasing the effectiveness for KHI.

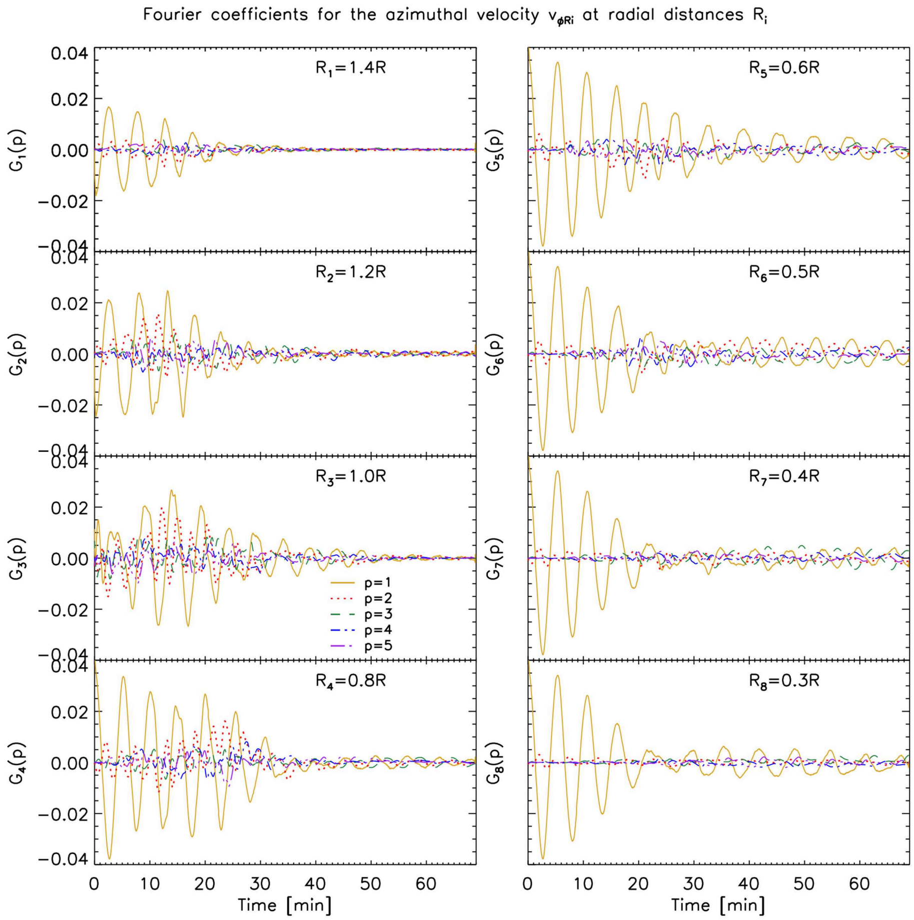

FIGURE 8 | Fourier coefficients for the azimuthal velocity $v_{\phi R_i}$ at radial distances R_i for the case without initial boundary layer and no viscosity. We show the contribution of the azimuthal modes to the azimuthal velocity along self-similar ellipses whose semi-minor axis has various lengths R_i (as indicated in the panels). The semi-major to semi-minor axis ratio of all ellipses matches the ellipse fitting the edge of the loop at each time step (see text for further details). We show the first 5 azimuthal wave modes (see the legend for the corresponding line style).

4. DISCUSSION AND CONCLUSIONS

In this paper we have taken three different loop models: a coronal loop without an initial boundary layer, a coronal loop with initial boundary layer, and a coronal loop with initial boundary layer and unrealistically high viscosity. We have simulated a perturbation leading to a fundamental kink mode, matching the usually observed amplitudes of transverse MHD waves. Although the case without an initial boundary layer is a rather extreme case of coronal loop formation and may be unrealistic, we do this mainly to investigate the effect that resonant absorption has on the development of the KHI. Also, a possible physical justification for sharp boundary layers is the case of a highly spatially confined energy deposition, for instance through magnetic reconnection, that would result in a spatially confined chromospheric evaporation and therefore sharp boundary layer for a loop.

By taking a sharp boundary layer we manage to delay the onset of resonant absorption in that loop compared to the case with initial boundary layer. As soon as the loop starts oscillating the small length scale over which the velocity shear takes place at the edges of the flux tube triggers the TWIKH rolls. At the wake of the flux tube RT rolls are also generated. High azimuthal wave modes are generated first, as expected since they are the fastest growing modes [52]. Lower and more energetic wave modes grow after 1 − 2 periods, not only from the KHI but also due to the squashing of the loop produced by the inertia [55, 56]. These low order modes are the first ones that grow in the case of an initial boundary layer. Higher order modes follow as well in the nonlinear stage of the KHI. Hence, this initial process can be seen as an apparent inverse energy cascade, produced mainly by the initially sharp boundary layer in that loop model. Due to KHI, the layer thickens quickly, and with it resonant absorption starts to take place. As the resonance reaches a maximum amplitude so does the power of high azimuthal wave modes. The time interval and spatial extent of significant resonance power matches the time interval and spatial extent of significant power in the high order azimuthal modes. The resonance triggers, in particular, TWIKH rolls radially inwards inside the loops and a self-inducing process of TWIKH rolls

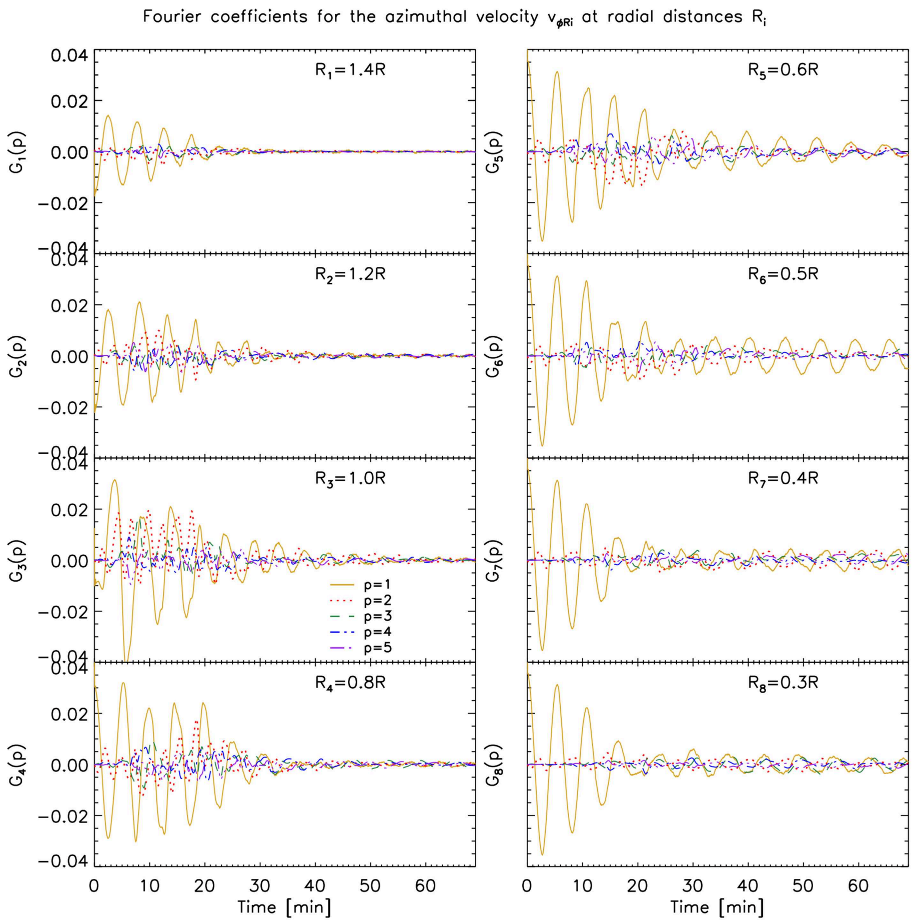

FIGURE 9 | Fourier coefficients for the azimuthal velocity $v_{\phi R_i}$ at radial distances R_i for the case with initial boundary layer and no viscosity. See **Figure 8** for more details.

occurs gradually deeper at a steady rate (producing a super slow apparent wave propagation of the kind discussed by Kaneko et al. [73]) until they end up covering basically the entire loops.

In this paper, we have proven that also impulsively excited loops, regardless of their initial boundary layer thickness eventually render the loop's cross-section to a turbulent state, as was previously proven for continuously driven loops [46]. This has as important implication that probably all observed loops (which undergo transverse oscillations at some point in their life, [20]) are in a turbulent state.

This investigation shows that resonant absorption is key to energize TWIKH rolls and spread them all over the loop. In our cases of only one perturbation only high azimuthal wave modes reach the loop center, and therefore the energy transfer to the inner layers is small in the absence of continuous driving. K-H rolls have also been analytically and numerically predicted from the shear flow of other transverse waves, such as torsional Alfvén waves [37, 47, 51, 74]. Our results suggest that in the absence of continuous driving the absence of resonant absorption in these cases may lead to important differences. Namely, the absence of velocity shear at the resonance layer would fail to induce inner KHI vortices eventually making the entire loop turbulent in the self-induction process we have found.

In the case of the loop with an initially present boundary layer, resonant absorption starts occurring immediately after the impulsive excitation, which produces a slightly stronger damping than in a case with no initial boundary layer and hence a relatively faster switch from a Gaussian damping profile to an exponential damping profile [68–70]. From **Figure 4** we can see that some differences indeed arise between cases with or without initial boundary layer. But more importantly, there are strong deviations from both the Gaussian and exponential damping during the evolution, due to the KHI. Since the switch between the Gaussian and exponential damping profiles is mostly defined by the density ratio and the boundary layer thickness, It is usually considered that the envelope can be used for seismology. This is of course not valid in our models, since this switch is controlled by the width of the boundary layer that varies extremely over time due to KHI.

Based on the comparison between the models with and without boundary layers leading to TWIKH rolls, we predict that loops with larger boundary transitions would lead to somewhat longer times (but on the same order) for the loops to become fully turbulent. This is because thicker boundary layers imply lower velocity shear and hence a delay on the onset of the KHI. On the other hand, a loop with a thicker boundary

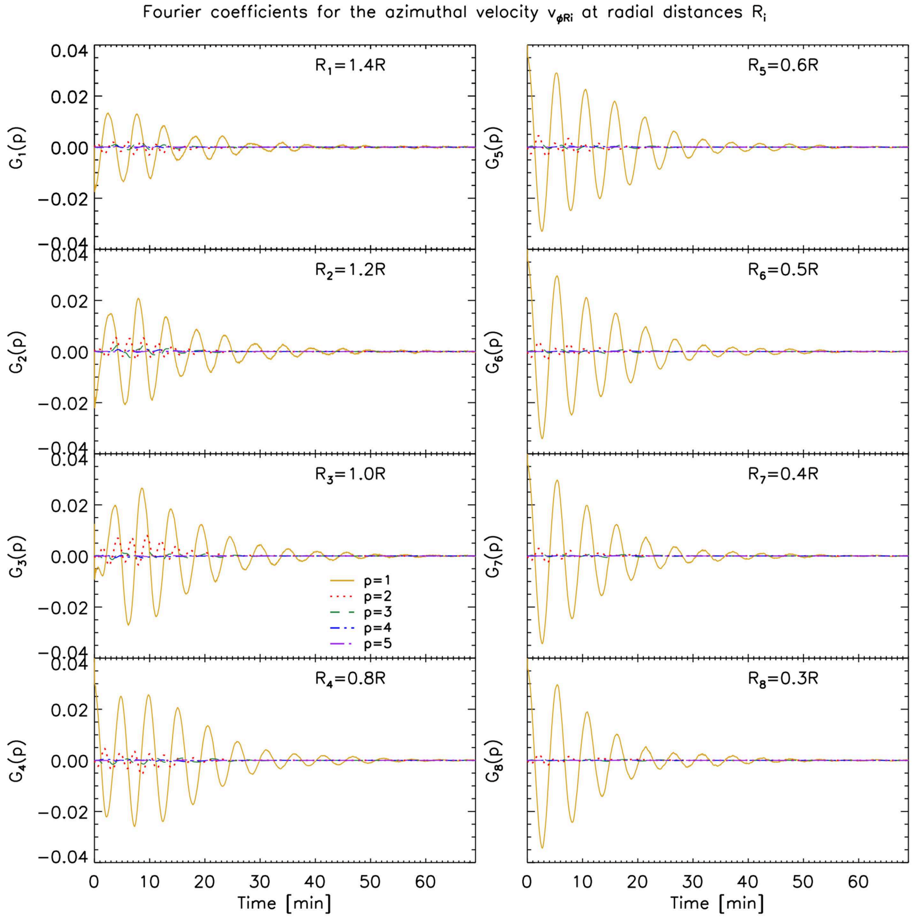

FIGURE 10 | Fourier coefficients for the azimuthal velocity $v_{\phi R_i}$ at radial distances R_i for the case with initial boundary layer and with viscosity. See **Figure 8** for more details.

transition implies a more energetic resonant flow, and therefore a larger energy reservoir for the self-inducing process of KHI inwards. Hence, the vortices reaching the loop core may be larger (more energetic).

Another interesting feature seen in **Figure 4** and in **Figures 8–10** is that the global kink mode ($p = 1$) does not seem to damp completely for $t > 30$ min within the flux tube (for $r < 0.5\ R$). This result was also noticed by Magyar and Van Doorsselaere [40], and they suggested an explanation based on KHI energy being transferred to the core of the loop. Indeed, our experiments confirm this hypothesis. It is also possible to have a feedback mechanism from the TWIKH rolls on the loop, due to an overall vorticity imbalance (and therefore momentum imbalance) within the loop due to the TWIKH rolls, as is observed in the phenomenon of vortex shedding [75, 76]. The slight change in period and beat at $t \approx 25 - 30$ min for the inner shells and for the center of mass oscillation (**Figure 4**), compared to the model without KHI, supports this theory. If true, this could be another possible mechanism to generate the observed decayless transverse oscillations [20, 77, 78].

Given that loops eventually become fully turbulent following a kink oscillation, a relevant question is the timescale on which this happens. This is particularly relevant in the context of coronal heating, since the small scales produced by dynamic instabilities can be a means for wave dissipation. Our models show that the loops become fully turbulent after $13 - 14$ periods ($69 - 72$ min), which is a very long timescale for coronal heating and therefore the wave dissipation rate over the entire loop may be too small to account for coronal heating. In the cases of continuous driving at the natural frequency of the loop, as in the numerical experiments by Karampelas and Van Doorsselaere [46], the situation improves, since the amplitudes obtained at the apex are on average stronger and the loops become fully turbulent after ≈ 7.5 periods (2000 s in their model), which may still be considered long for coronal heating.

DATA AVAILABILITY

The datasets generated for this study are available on request to the corresponding author.

AUTHOR CONTRIBUTIONS

PA conducted the simulations and analysis, TVD has provided feedback on the analysis of the results.

FUNDING

PA acknowledges funding from his STFC Ernest Rutherford Fellowship (No. ST/R004285/1). TVD was funded by GOA-2015-014 (KU Leuven). This project has received funding from the European Research Council (ERC) under the European Union's Horizon 2020 research and innovation programme (grant agreement No. 724326).

ACKNOWLEDGMENTS

Numerical computations were carried out on Cray XC50 at the Center for Computational Astrophysics, NAOJ.

SUPPLEMENTARY MATERIAL

The Supplementary Material for this article can be found online at: https://www.frontiersin.org/articles/10.3389/fphy.2019.00085/full#supplementary-material

Video 1 | TWIKH vortices throughout, for a loop without initial boundary layer and no viscosity. From top to bottom rows we have the cross-section at the apex of the loop of, respectively, the total number density (in units of 10^9 cm^{-3}), the temperature ($\log T$), the flow velocity (in km s^{-1}), the $z-$vorticity component (in s^{-1}) and the $z-$current density component (in cgs units). The half ellipse in white (or black in the flow velocity panels) corresponds to the ellipses calculated in section 3.2. This animation corresponds to **Figure 1**.

Video 2 | TWIKH vortices throughout for a loop with initial boundary layer and no viscosity. The same variables as in **Video 1** (or **Figure 1**) are shown, setting the same minima and maxima for better visualisation. This animation corresponds to **Figure 2**.

Video 3 | No TWIKH vortices for a loop with initial boundary layer and with enhanced viscosity. The same variables as in **Video 1** (or **Figure 1**) are shown. Note that the minima and maxima (notably for the velocities, vorticity, and the current density) are smaller than for **Videos 1**, **2** (**Figures 1**, **2**) due to the enhanced viscosity. This animation corresponds to **Figure 3**.

REFERENCES

1. Viall NM, Klimchuk JA. Evidence for widespread cooling in an active region observed with the SDO atmospheric imaging assembly. *Astrophys J.* (2012) **753**:35. doi: 10.1088/0004-637X/753/1/35
2. Viall NM, Klimchuk JA. Modeling the line-of-sight integrated emission in the corona: implications for coronal heating. *Astrophys J.* (2013) **771**:115. doi: 10.1088/0004-637X/771/2/115
3. Magyar N, Van Doorsselaere T. The instability and non-existence of multi-stranded loops when driven by transverse waves. *Astrophys J.* (2016) **823**:82. doi: 10.3847/0004-637X/823/2/82
4. Brooks DH, Warren HP, Ugarte-Urra I, Winebarger AR. High spatial resolution observations of loops in the solar corona. *Astrophys J Lett.* (2013) **772**:L19. doi: 10.1088/2041-8205/772/2/L19
5. Brooks DH, Reep JW, Warren HP. Properties and modeling of unresolved fine structure loops observed in the solar transition region by IRIS. *Astrophys J Lett.* (2016) **826**:L18. doi: 10.3847/2041-8205/826/2/L18
6. Solanki SK. Smallscale solar magnetic fields-an overview. *Space Sci Rev*. (1993) **63**:1–2. doi: 10.1007/BF00749277
7. Reale F. Coronal loops: observations and modeling of confined plasma. *Living Rev Solar Phys*. (2010) **7**:5. doi: 10.12942/lrsp-2010-5
8. Watko JA, Klimchuk JA. Width Variations along Coronal Loops Observed by TRACE. *solar Phys.* (2000) **193**:77–92. doi: 10.1007/978-94-010-0860-0_5
9. Peter H, Bingert S, Klimchuk JA, de Forest C, Cirtain JW, Golub L, et al. Structure of solar coronal loops: from miniature to large-scale. *Astron Astrophys.* (2013) **556**:A104. doi: 10.1051/0004-6361/201321826
10. Antolin P, Rouppe van der Voort L. Observing the fine structure of loops through high-resolution spectroscopic observations of coronal rain with the CRISP instrument at the swedish solar telescope. *Astrophys J.* (2012) **745**:152. doi: 10.1088/0004-637X/745/2/152
11. Antolin P, Vissers G, Pereira TMD, Rouppe van der Voort L, Scullion E. The multithermal and multi-stranded nature of coronal rain. *Astrophys J.* (2015) **806**:81. doi: 10.1088/0004-637X/806/1/81
12. Cargill PJ, De Moortel I, Kiddie G. Coronal density structure and its role in wave damping in loops. *Astrophys J.* (2016) **823**:31. doi: 10.3847/0004-637X/823/1/31
13. Pascoe DJ, Goddard CR, Nisticò G, Anfinogentov S, Nakariakov VM. Coronal loop seismology using damping of standing kink oscillations by mode coupling. *Astron Astrophys.* (2016) **589**:A136. doi: 10.1051/0004-6361/201628255
14. Pascoe DJ, Anfinogentov S, Nisticò G, Goddard CR, Nakariakov VM. Coronal loop seismology using damping of standing kink oscillations by mode coupling. II. additional physical effects and Bayesian analysis. *Astron Astrophys.* (2017) **600**:A78. doi: 10.1051/0004-6361/201629702
15. Aschwanden MJ, Fletcher L, Schrijver CJ, Alexander D. Coronal loop oscillations observed with the transition region and coronal explorer. *Astrophys J.* (1999) **520**:880–94. doi: 10.1086/307502
16. Nakariakov VM, Ofman L, Deluca EE, Roberts B, Davila JM. TRACE observation of damped coronal loop oscillations: implications for coronal heating. *Science.* (1999) **285**:862–4. doi: 10.1126/science.285.5429.862
17. De Moortel I, Nakariakov VM. Magnetohydrodynamic waves and coronal seismology: an overview of recent results. *R Soc Lond Philos Trans A*. (2012) **370**:3193–216. doi: 10.1098/rsta.2011.0640
18. Tomczyk S, McIntosh SW, Keil SL, Judge PG, Schad T, Seeley DH, et al. Alfvén waves in the solar corona. *Science.* (2007) **317**:1192. doi: 10.1126/science.1143304
19. Arregui I, Oliver R, Ballester JL. Prominence oscillations. *Living Rev Solar Phys*. (2012) **9**:2. doi: 10.12942/lrsp-2012-2
20. Anfinogentov SA, Nakariakov VM, Nisticò G. Decayless low-amplitude kink oscillations: a common phenomenon in the solar corona? *Astron Astrophys.* (2015) **583**:A136. doi: 10.1051/0004-6361/201526195
21. Goossens M, Andries J, Aschwanden MJ. Coronal loop oscillations. An interpretation in terms of resonant absorption of quasi-mode kink oscillations. *Astron Astrophys.* (2002) **394**:L39–42. doi: 10.1051/0004-6361:20021378
22. Goossens M, Andries J, Arregui I. Damping of magnetohydrodynamic waves by resonant absorption in the solar atmosphere. *R Soc Lond Philos Trans A*. (2006) **364**:433–46. doi: 10.1098/rsta.2005.1708
23. Van Doorsselaere T, Andries J, Poedts S, Goossens M. Damping of coronal loop oscillations: calculation of resonantly damped kink oscillations of one-dimensional nonuniform loops. *Astrophys J.* (2004) **606**:1223–32. doi: 10.1086/383191
24. Goossens M, Erdélyi R, Ruderman MS. Resonant MHD Waves in the Solar Atmosphere. *Space Sci Rev*. (2011) **158**:289–338. doi: 10.1007/s11214-010-9702-7
25. Verwichte E, Van Doorsselaere T, White RS, Antolin P. Statistical seismology of transverse waves in the solar corona. *Astron Astrophys.* (2013) **552**:A138. doi: 10.1051/0004-6361/201220456
26. Goddard CR, Nisticò G, Nakariakov VM, Zimovets IV. A statistical study of decaying kink oscillations detected using SDO/AIA. *Astron Astrophys.* (2016) **585**:A137. doi: 10.1051/0004-6361/201527341
27. Allan W, Wright AN. Magnetotail waveguide: fast and Alfvén waves in the plasma sheet boundary layer and lobe. *J. Geophys. Res*. (2000) **105**:317–28. doi: 10.1029/1999JA900425

28. Pascoe DJ, Wright AN, De Moortel I. Coupled Alfvén and kink oscillations in coronal loops. *Astrophys J.* (2010) **711**:990–6. doi: 10.1088/0004-637X/711/2/990
29. De Moortel I, Pascoe DJ, Wright AN, Hood AW. Transverse, propagating velocity perturbations in solar coronal loops. *Plasma Phys Control Fusion*. (2016) **58**:014001. doi: 10.1088/0741-3335/58/1/014001
30. Terradas J, Goossens M, Verth G. Selective spatial damping of propagating kink waves due to resonant absorption. *Astron Astrophys.* (2010) **524**:A23. doi: 10.1051/0004-6361/201014845
31. Verth G, Terradas J, Goossens M. Observational evidence of resonantly damped propagating kink waves in the solar corona. *Astrophys J Lett.* (2010) **718**:L102–5. doi: 10.1088/2041-8205/718/2/L102
32. Terradas J, Arregui I, Oliver R, Ballester JL, Andries J, Goossens M. Resonant absorption in complicated plasma configurations: applications to multistranded coronal loop oscillations. *Astrophys J.* (2008) **679**:1611–20. doi: 10.1086/586733
33. Pascoe DJ, Wright AN, De Moortel I. Propagating coupled Alfvén and kink oscillations in an arbitrary inhomogeneous corona. *Astrophys J.* (2011) **731**:73. doi: 10.1088/0004-637X/731/1/73
34. Goossens M, Ruderman MS, Hollweg JV. Dissipative MHD solutions for resonant Alfven waves in 1-dimensional magnetic flux tubes. *Solar Phys.* (1995) **157**:75–102. doi: 10.1007/BF00680610
35. Goossens M, Soler R, Terradas J, Van Doorsselaere T, Verth G. The transverse and rotational motions of magnetohydrodynamic kink waves in the solar atmosphere. *Astrophys J.* (2014) **788**:9. doi: 10.1088/0004-637X/788/1/9
36. Antolin P, Yokoyama T, Van Doorsselaere T. Fine strand-like structure in the solar corona from magnetohydrodynamic transverse oscillations. *Astrophys J Lett.* (2014) **787**:L22. doi: 10.1088/2041-8205/787/2/L22
37. Browning PK, Priest ER. Kelvin-Helmholtz instability of a phased-mixed Alfven wave. *Astron Astrophys.* (1984) **131**:283–90.
38. Antolin P, Okamoto TJ, De Pontieu B, Uitenbroek H, Van Doorsselaere T, Yokoyama T. Resonant absorption of transverse oscillations and associated heating in a solar prominence. II. numerical aspects. *Astrophys J.* (2015) **809**:72. doi: 10.1088/0004-637X/809/1/72
39. Terradas J, Andries J, Goossens M, Arregui I, Oliver R, Ballester JL. Nonlinear instability of kink oscillations due to shear motions. *Astrophys J Lett.* (2008) **687**:L115–8. doi: 10.1086/593203
40. Magyar N, Van Doorsselaere T. Damping of nonlinear standing kink oscillations: a numerical study. *Astron Astrophys.* (2016) **595**:A81. doi: 10.1051/0004-6361/201629010
41. Karampelas K, Van Doorsselaere T, Antolin P. Heating by transverse waves in simulated coronal loops. *Astron Astrophys.* (2017) **604**:A130. doi: 10.1051/0004-6361/201730598
42. Antolin P, Schmit D, Pereira TMD, De Pontieu B, De Moortel I. Transverse wave induced kelvin-helmholtz rolls in spicules. *Astrophys J.* (2018) **856**:44. doi: 10.3847/1538-4357/aab34f
43. Antolin P, De Moortel I, Van Doorsselaere T, Yokoyama T. Observational signatures of transverse magnetohydrodynamic waves and associated dynamic instabilities in coronal flux tubes. *Astrophys J.* (2017) **836**:219. doi: 10.3847/1538-4357/aa5eb2
44. Okamoto TJ, Antolin P, De Pontieu B, Uitenbroek H, Van Doorsselaere T, Yokoyama T. Resonant absorption of transverse oscillations and associated heating in a solar prominence. I. observational aspects. *Astrophys J.* (2015) **809**:71. doi: 10.1088/0004-637X/809/1/71
45. Van Doorsselaere T, Antolin P, Karampelas K. Broadening of the differential emission measure by multi-shelled and turbulent loops. *Astron Astrophys.* (2018) **620**:A65. doi: 10.1051/0004-6361/201834086
46. Karampelas K, Van Doorsselaere T. Simulations of fully deformed oscillating flux tubes. *Astron Astrophys.* (2018) **610**:L9. doi: 10.1051/0004-6361/201731646
47. Guo M, Van Doorsselaere T, Karampelas K, Li B, Antolin P, De Moortel I. Heating effects from driven transverse and Alfvén waves in coronal loops. *Astrophys J.* (2019) **870**:55. doi: 10.3847/1538-4357/aaf1d0
48. Ofman L, Thompson BJ. SDO/AIA observation of kelvin-helmholtz instability in the solar corona. *Astrophys J Lett.* (2011) **734**:L11. doi: 10.1088/2041-8205/734/1/L11
49. Zhelyazkov I, Zaqarashvili TV, Chandra R, Srivastava AK, Mishonov T. Kelvin-Helmholtz instability in solar cool surges. *Adv Space Res*. (2015) **56**:2727–37. doi: 10.1016/j.asr.2015.05.003
50. Li X, Zhang J, Yang S, Hou Y, Erdélyi R. Observing kelvin–helmholtz instability in solar blowout jet. *Sci Rep*. (2018) **8**:8136. doi: 10.1038/s41598-018-26581-4
51. Zaqarashvili TV, Zhelyazkov I, Ofman L. Stability of rotating magnetized jets in the solar atmosphere. I. kelvin-Helmholtz instability. *Astrophys J.* (2015) **813**:123. doi: 10.1088/0004-637X/813/2/123
52. Barbulescu M, Ruderman MS, Van Doorsselaere T, Erdélyi R. An analytical model of the Kelvin-Helmholtz instability of transverse coronal loop oscillations. *Astrophys J.* (2019) **870**:108. doi: 10.3847/1538-4357/aaf506
53. Hillier A, Barker A, Arregui I, Latter H. On Kelvin-Helmholtz and parametric instabilities driven by coronal waves. *Month Notices R Astron Soc.* (2019) **482**:1143–53. doi: 10.1093/mnras/sty2742
54. Howson TA, De Moortel I, Antolin P. Energetics of the Kelvin-Helmholtz instability induced by transverse waves in twisted coronal loops. *Astron Astrophys.* (2017) **607**:A77. doi: 10.1051/0004-6361/201731178
55. Terradas J, Magyar N, Van Doorsselaere T. Effect of magnetic twist on nonlinear transverse kink oscillations of line-tied magnetic flux Tubes. *Astrophys J.* (2018) **853**:35. doi: 10.3847/1538-4357/aa9d0f
56. Ruderman MS, Goossens M. Nonlinear kink oscillations of coronal magnetic loops. *Solar Phys*. (2014) **289**:1999–2020. doi: 10.1007/s11207-013-0446-x
57. Sato T, Hayashi T. Externally driven magnetic reconnection and a powerful magnetic energy converter. *Phys Fluids*. (1979) **22**:1189–202. doi: 10.1063/1.862721
58. Ugai M. Computer studies on development of the fast reconnection mechanism for different resistivity models. *Phys Fluids B* (1992) **4**:2953–63. doi: 10.1063/1.860458
59. Miyagoshi T, Yokoyama T. Magnetohydrodynamic simulation of solar coronal chromospheric evaporation jets caused by magnetic reconnection associated with magnetic flux emergence. *Astrophys J.* (2004) **614**:1042–53. doi: 10.1086/423731
60. Yokoyama T, Shibata K. What is the condition for fast magnetic reconnection? *Astrophys J Lett.* (1994) **436**:L197–200. doi: 10.1086/187666
61. Lapidus A. A detached shock calculation by second-order finite differences. *J Comput Phys*. (1967) **2**:154–77. doi: 10.1016/0021-9991(67)90032-0
62. Kudoh T, Matsumoto R, Shibata K. Numerical MHD simulation of astrophysical problems by using CIP-MOCCT method. *Comput Fluid Dyn J*. (1999) **8**:56–68.
63. Yabe T, Aoki T. A universal solver for hyperbolic equations by cubic-polynomial interpolation I. One-dimensional solver. *Comput Phys Commun*. (1991) **66**:219–32. doi: 10.1016/0010-4655(91)90071-R
64. Evans CR, Hawley JF. Simulation of magnetohydrodynamic flows - A constrained transport method. *Astrophys J.* (1988) **332**:659–77. doi: 10.1086/166684
65. Stone JM, Norman ML. ZEUS-2D: a radiation magnetohydrodynamics code for astrophysical flows in two space dimensions. I - The hydrodynamic algorithms and tests. *Astrophys J Suppl.* (1992) **80**:753–90. doi: 10.1086/191680
66. Yabe T, Xiao F. Description of complex and sharp interface during Shock wave interaction with liquid drop. *J Phys Soc Jpn*. (1993) **62**:2537. doi: 10.1143/JPSJ.62.2537
67. Kudoh T, Matsumoto R, Shibata K. Magnetically driven jets from accretion disks. III. 2.5-dimensional nonsteady simulations for thick disk case. *Astrophys J.* (1998) **508**:186–99. doi: 10.1086/306377
68. Pascoe DJ, Hood AW, de Moortel I, Wright AN. Spatial damping of propagating kink waves due to mode coupling. *Astron Astrophys.* (2012) **539**:A37. doi: 10.1051/0004-6361/201117979
69. Pascoe DJ, Hood AW, De Moortel I, Wright AN. Damping of kink waves by mode coupling. II. Parametric study and seismology. *Astron Astrophys.* (2013) **551**:A40. doi: 10.1051/0004-6361/201220620
70. Hood AW, Ruderman M, Pascoe DJ, De Moortel I, Terradas J, Wright AN. Damping of kink waves by mode coupling. I. Analytical treatment. *Astron Astrophys.* (2013) **551**:A39. doi: 10.1051/0004-6361/201220617
71. Ruderman MS, Roberts B. The damping of coronal loop oscillations. *Astrophys J.* (2002) **577**:475–86. doi: 10.1086/342130

72. Goddard CR, Nakariakov VM. Dependence of kink oscillation damping on the amplitude. *Astron Astrophys.* (2016) **590**:L5. doi: 10.1051/0004-6361/201628718
73. Kaneko T, Goossens M, Soler R, Terradas J, Van Doorsselaere T, Yokoyama T, et al. Apparent cross-field superslow propagation of magnetohydrodynamic waves in solar plasmas. *Astrophys J*. (2015) **812**:121. doi: 10.1088/0004-637X/812/2/121
74. Srivastava AK, Shetye J, Murawski K, Doyle JG, Stangalini M, Scullion E, et al. High-frequency torsional Alfvén waves as an energy source for coronal heating. *Sci Rep*. (2017) **7**:43147. doi: 10.1038/srep43147
75. Gruszecki M, Nakariakov VM, van Doorsselaere T, Arber TD. Phenomenon of Alfvénic vortex shedding. *Phys Rev Lett*. (2010) **105**:055004. doi: 10.1103/PhysRevLett.105.055004
76. Emonet T, Moreno-Insertis F, Rast MP. The zigzag path of buoyant magnetic tubes and the generation of vorticity along their periphery. *Astrophys J*. (2001) **549**:1212–20. doi: 10.1086/319469
77. Anfinogentov S, Nisticò G, Nakariakov VM. Decay-less kink oscillations in coronal loops. *Astron Astrophys.* (2013) **560**:A107. doi: 10.1051/0004-6361/201322094
78. Nisticò G, Nakariakov VM, Verwichte E. Decaying and decayless transverse oscillations of a coronal loop. *Astron Astrophys.* (2013) **552**:A57. doi: 10.1051/0004-6361/201220676

Conflict of Interest Statement: The authors declare that the research was conducted in the absence of any commercial or financial relationships that could be construed as a potential conflict of interest.

The reviewer MR declared a past co-authorship with one of the authors (TVD) to the handling editor.

frontiers
in Astronomy and Space Sciences

ORIGINAL RESEARCH
published: 27 June 2019
doi: 10.3389/fspas.2019.00045

The Effect of Cooling on Driven Kink Oscillations of Coronal Loops

Chris J. Nelson[1,2]*, **Alexander A. Shukhobodskiy**[2,3], **Robertus Erdélyi**[2,4] **and Mihalis Mathioudakis**[1]

[1] Astrophysics Research Centre, School of Mathematics and Physics, Queen's University, Belfast, United Kingdom, [2] Solar Physics and Space Plasma Research Centre, School of Mathematics and Statistics, University of Sheffield, Sheffield, United Kingdom, [3] School of Computing, Creative Technologies & Engineering, Leeds Beckett University, Leeds, United Kingdom, [4] Department of Astronomy, Eötvös Loránd University, Budapest, Hungary

Ever since their detection two decades ago, standing kink oscillations in coronal loops have been extensively studied both observationally and theoretically. Almost all driven coronal loop oscillations (e.g., by flares) are observed to damp through time often with Gaussian or exponential profiles. Intriguingly, however, it has been shown theoretically that the amplitudes of some oscillations could be modified from Gaussian or exponential profiles if cooling is present in the coronal loop systems. Indeed, in some cases the oscillation amplitude can even increase through time. In this article, we analyse a flare-driven coronal loop oscillation observed by the Solar Dynamics Observatory's *Atmospheric Imaging Assembly* (SDO/AIA) in order to investigate whether models of cooling can explain the amplitude profile of the oscillation and whether hints of cooling can be found in the intensity evolution of several SDO/AIA filters. During the oscillation of this loop system, the kink mode amplitude appears to differ from a typical Gaussian or exponential profile with some hints being present that the amplitude increases. The application of cooling coronal loop modeling allowed us to estimate the density ratio between the loop and the background plasma, with a ratio of between 2.05 and 2.35 being returned. Overall, our results indicate that consideration of the thermal evolution of coronal loop systems can allow us to better describe oscillations in these structures and return more accurate estimates of the physical properties of the loops (e.g., density, scale height, magnetic field strength).

Keywords: solar corona, coronal loop oscillations, magnetohydrodynamics, kink oscillations, cooling

Edited by:
Patrick Antolin,
University of St. Andrews,
United Kingdom

Reviewed by:
Petra Kohutova,
University of Oslo, Norway
Vaibhav Pant,
KU Leuven, Belgium
Ramon Oliver,
University of the Balearic Islands,
Spain

***Correspondence:**
Chris J. Nelson
c.j.nelson@sheffield.ac.uk

Specialty section:
This article was submitted to
Stellar and Solar Physics,
a section of the journal
Frontiers in Astronomy and Space
Sciences

Received: 18 January 2019
Accepted: 27 May 2019
Published: 27 June 2019

Citation:
Nelson CJ, Shukhobodskiy AA,
Erdélyi R and Mathioudakis M (2019)
The Effect of Cooling on Driven Kink
Oscillations of Coronal Loops.
Front. Astron. Space Sci. 6:45.
doi: 10.3389/fspas.2019.00045

1. INTRODUCTION

Standing kink oscillations were first observed in coronal loops by Aschwanden et al. (1999) and Nakariakov et al. (1999) using high-resolution imaging data collected by the *Transition Region And Coronal Explorer* (TRACE; Handy et al., 1999). Those authors found that a flare in the local Active Region (AR) caused the magnetic field guide of the coronal loop to shake from side-to-side in a manner analogous to oscillations of a guitar string. One of the most interesting aspects of kink oscillations in coronal loops was their rapid damping profiles, with many examples of flare-driven coronal loop oscillations damping to sub-resolution spatial scales within two or three periods. Such damping has been explained through a number of physical mechanisms, such as resonant absorption (e.g., Goossens et al., 2002; Ruderman and Roberts, 2002), phase mixing, and foot-point damping.

Over the past decade, data from the Solar Dynamics Observatory's *Atmospheric Imaging Assembly* (SDO/AIA; Lemen et al., 2012) has been used to perform statistical analyses of coronal loop oscillations (e.g., Zimovets and Nakariakov, 2015; Goddard et al., 2016). Specifically, Goddard et al. (2016) analyzed the damping profiles of 58 coronal loops finding that the amplitudes through time of the majority of oscillations could be modeled by exponential or quasi-exponential (close to but not exactly exponential) profiles. More recently, Pascoe et al. (2016) suggested that Gaussian profiles may model damping profiles of coronal loops as well, if not better, than exponential profiles in a large number of cases. It was, however, pointed out by Goddard et al. (2016) that some events were non-exponential (and also likely non-Gaussian) meaning, for some coronal loop oscillations, additional physics must be employed to explain the amplitude profiles. Interestingly, it has been shown analytically that it is possible that some driven coronal loops could oscillate and damp in a manner not adequately modeled by Gaussian nor exponential profiles through time.

As the majority of modeling of coronal loop oscillations is conducted using static background parameters (e.g., temperature, density), one opportunity to consider additional physics theoretically is to incorporate some form of time-dependence (see for example, Dymova and Ruderman, 2005; Al-Ghafri and Erdélyi, 2013; Erdélyi et al., 2014). Morton and Erdélyi (2009) considered the damping of coronal loops due to cooling through time and found, that for typical oscillatory periods, cooling could play a key role in explaining observed damping profiles (this was shown further in Morton and Erdélyi, 2010). The idea that amplification of coronal loop oscillations could occur due to cooling within coronal loops that contained flow was first suggested by Ruderman (2011b). This work was expanded upon in Ruderman (2011a) with the inclusion of a resonant layer, where it was found that cooling could cancel out the damping due to resonant absorption in some cases. The effects of loop expansion were considered for cooling coronal loops when no resonant layer was observed by Ruderman et al. (2017). Again it was found that amplification of the coronal loop oscillations could occur.

A more complete analysis comprising of loop expansion, resonant absorption, and cooling was recently conducted by Shukhobodskiy and Ruderman (2018) and Shukhobodskiy et al. (2018) for time independent and time dependent densities, respectively. Those authors found that in some cases, the combined effects of expansion and cooling could dominate over resonant absorption leading to a slowing down of the damping of the oscillations or even, in some cases, a brief amplification in kink mode coronal loop oscillations. Such amplification would only be short-lived and would be followed by the continued decay of the oscillation to sub-resolution levels. Additionally, assuming that both the external and internal densities were longitudinally stratified, the authors showed that the ratio of the frequency of a fundamental mode on the decrement of the kink oscillation is independent on the particular form of the density profile. A similar result was obtained previously by Dymova and Ruderman (2006) for kink oscillations in non-expanding magnetic flux tubes. It is possible, therefore, that accounting for cooling when modeling coronal loop oscillations may provide better fits for coronal loop oscillations, especially when increases in amplitude are evident. Additionally, important seismological information could be obtained from the system (such as the density ratio between the loop and the background) if one were to consider cooling which could help improve future numerical modeling.

The development of modeling of time-dependent coronal loop temperatures has a strong foundation in observations. Numerous authors have discussed the temperature evolution of coronal loop arcades, with cooling often being inferred through the observed progression of loops from hot to cold channels through time (see for example, Winebarger and Warren, 2005; López Fuentes et al., 2007; Aschwanden and Terradas, 2008). It is well-known that coronal loops can cool quickly, over the course of two or three oscillatory periods (e.g., Aschwanden and Terradas, 2008), through processes such as the thermal instability, which can often lead to the occurrence of coronal rain (see Antolin et al., 2015 and references within). Such cooling means the application of theories which are not magnetohydrostatic, such as those recently developed by Shukhobodskiy et al. (2018), are important for further understanding and modeling coronal loop oscillations more generally. It should be noted that Morton and Erdélyi (2010) did conduct an application of theoretical work to observed kink oscillations, however, those authors did not include effects which could lead to amplification in their model.

In this article, we apply the theoretical models developed by Shukhobodskiy et al. (2018) to the amplitude profile of a kink oscillation in a coronal loop within AR 11598. We aim to showcase the seismological potential of cooling models through the inference of the density ratio between the loop and the background plasma. Our work is setup as follows: In the Observations section we describe the data studied here and the data analysis methods; In the Results section we present our results including the application of the theoretical modeling and any evidence for cooling in the AR; In the Discussion and Conclusions we draw our conclusions and provide some suggestions about future work.

2. OBSERVATIONS

2.1. Data and Feature Selection

The data studied in this article were sampled by the SDO/AIA instrument on the 20th October 2012 between 17:50 UT and 18:50 UT. The $300'' \times 300''$ field-of-view (FOV) analyzed here was focused on AR 11598 and was initially centered on co-ordinates of $x_c = -959''$, $y_c = -85''$. Four channels (namely the 304 Å, 171 Å, 193 Å, and 131 Å) were downloaded for analysis, using the *ssw_cutout_service.pro* routine, meaning we are able to make inferences about the thermal evolution of the loop system. The loop system is only weakly detectable in the 131 Å images and, as such, these data are not studied in detail in the remainder of this article. These data do, however, indicate that the coronal loop existed at non-flaring temperatures. Data in the UV sampled by the SDO/AIA instrument have a typical cadence of 12 s and a pixel scale of $0.6''$. As the oscillations analyzed here were driven by a flare in the same AR as the coronal loops, some frames

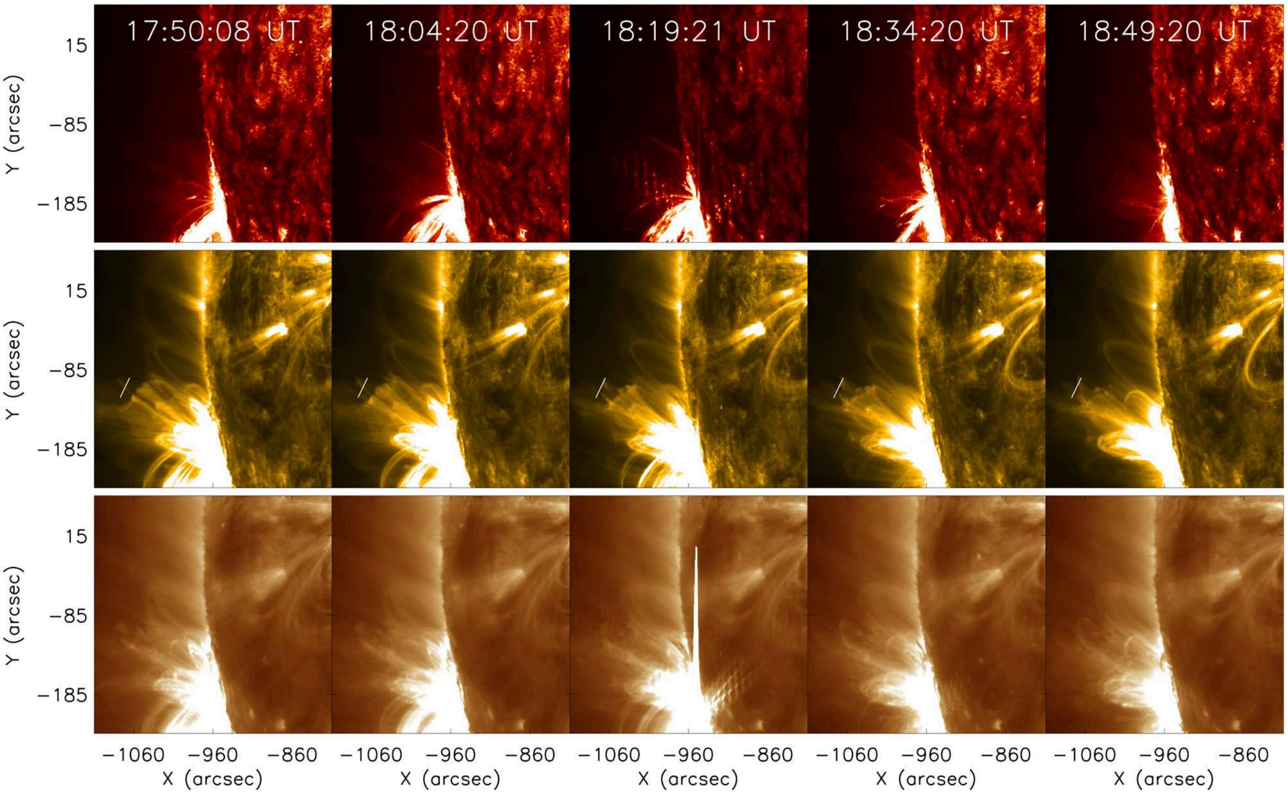

FIGURE 1 | The evolution of the coronal loop system during the hour around the oscillations analyzed here. Plotted are the SDO/AIA 304 Å **(top)**, 171 Å **(middle)**, and 193 Å **(bottom)** channels. The white slit over-laid on the middle row indicates the location of the slit analyzed in this article.

were returned with a lower exposure time meaning the loop was difficult to detect due to the lower signal to noise ratio. For these frames, synthetic filling data was created with the intensity of each pixel being taken as the average intensity for that pixel in the frame before and the frame after. This should have no influence on our results as the loop analyzed here oscillates with periodicities well above the cadence of that data. This coronal loop oscillation was previously discussed by Goddard et al. (2016) (Event 40, Loop 2) and its damping was classified as being best described by a combination of exponential and non-exponential fitting. This event was further analyzed by Pascoe et al. (2016, 2017) who suggested that the presence of multiple harmonics could explain the complicated amplitude profiles observed within this event. This interpretation was supported by the research of Pagano et al. (2018).

The general evolution of the loop system analyzed here is plotted in **Figure 1** for the 304 Å (top row), 171 Å (middle row), and 193 Å (bottom row) channels. At 17:50 UT, the coronal loop system can be detected in both the 171 Å and 193 Å channels, with the white line over-laid on the 171 Å images indicating the location of the slit studied here. The location of the flare in the AR, which occurred at approximately 18:08 UT, is pin-pointed by the typical disturbance patterns on the 193 Å image in the third column. In the southern part of the FOV (around 100″ south of the oscillation analyzed here), a large coronal loop arcade can be observed in all panels up until 18:19 UT. Over the subsequent 30 min (between 18:20 UT and 18:50 UT), however, the loop system completely fades from view in the coronal channels and large amounts of coronal rain are detected in the 304 Å data, draining material from the loops. The loop system completely fades from view by 18:49 UT.

2.2. Tracking the Loop Displacement and Model Fitting

In **Figure 2**, we plot a zoomed in FOV of the oscillation analyzed here for five time-steps (top row). The white line over-laid on these images indicates the location of the slit analyzed in this article. The co-ordinates of this slit are the same as for Loop 40, Event 2 included in the table of Goddard et al. (2016). This event was studied subsequently by Pascoe et al. (2016, 2017); Pagano et al. (2018). Following the construction of the time-space diagram from 171 Å images (plotted in the bottom panel of **Figure 2**), we applied a Canny edge-detection algorithm to obtain approximations for the coronal loop boundaries. The output for this edge detection routine is over-laid on the time-space diagram in **Figure 3** (blue lines). In order to model the oscillation of the loop axis, we assumed that the displacement is guided by midpoints between the boundaries of the upper loop as shown by the red dots in **Figure 3**. If we assume that the loop is cylindrical and radially symmetric, then the errors

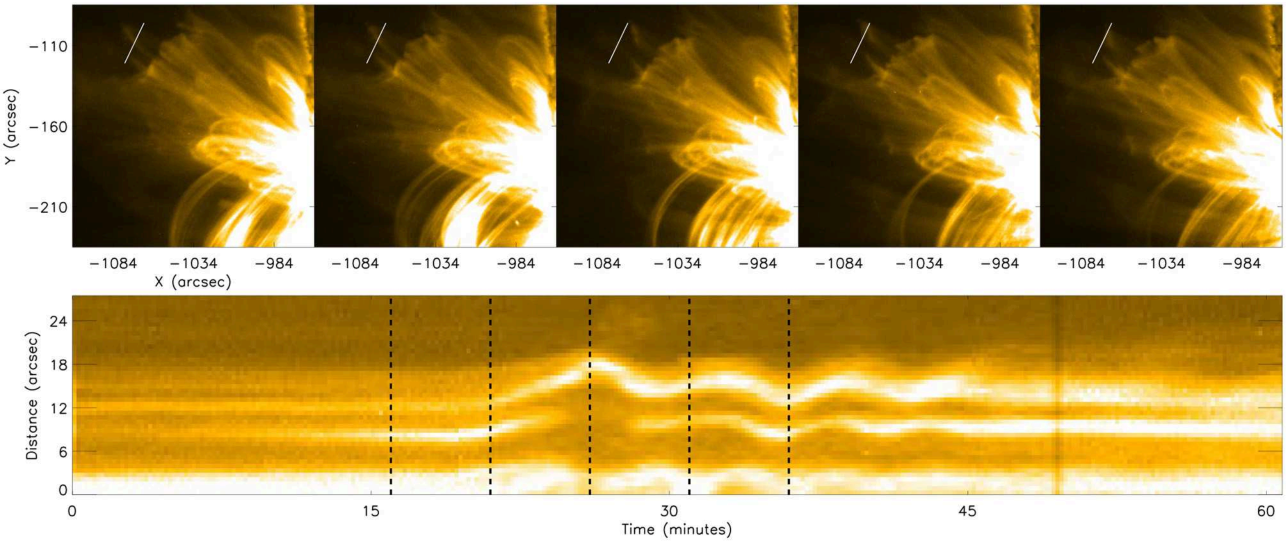

FIGURE 2 | (Top) The coronal loop system analyzed here plotted using 171 Å data at five times during the oscillation. The white lines indicate the slit studied in this article, which corresponds to Loop 40, Event 2 from Goddard et al. (2016). **(Bottom)** Time-space diagram constructed from the slit over-laid on the 171 Å data. The dashed vertical lines indicates the time steps plotted in the top row (from left to right). The bright chord starting and finishing at 12″ is the oscillation studied in this article.

associated by this fitting can be assumed to be less than 1 pixel. Understanding whether such assumptions are justified would require much higher resolution data and so should be studied in the future. As the loop axis returned through time is qualitatively similar to that plotted in Figure 1 of Pascoe et al. (2016) for the same event, in the following we assume that this oscillation profile is accurate and, therefore, neglect any further potential errors in our fitting. Ignoring any further errors introduced through the loop fitting is justified in this case, as our study aims to show, in principle, that including the effects of cooling could have important implications for coronal loop modeling. A larger statistical study conducted using a variety of fitting methods in the future will be required to fully understand the prevalence and importance of coronal loop cooling on kink-mode oscillations.

The oscillation extracted from this time-space diagram is plotted with red dots in **Figure 4**. The approximate background trend of the loop was modeled by a polynomial of the 8th degree on all obtained data points (i.e., from frame 0 to 300) and is over-laid for the region of interest (between frames 130 and 230) as the green line in **Figure 4**. The 8th order polynomial was selected as it best tracked the background of the amplitude profile throughout the entire time-series (including the parts where no oscillation was detected). It should be noted that a number of background trends with different orders were tested with each returning similar seismological results. This is because the ratio of the internal and external densities, which we can calculate from this model, is dependent only on where, in this case, the increment to the amplitude is (which did not change for any background trend), not how large it is. This will be discussed in further detail later in the article.

The numerical fitting of the red points is done by considering the summation of four equations of Gaussian form:

$$f(amp) = \sum_{i=1}^{4} A_i \exp[-(-\mu_i + t)^2/(2\sigma_i^2)]/(\sqrt{2\pi}/\sigma_i^2), \qquad (1)$$

where A_i, μ_i, and σ_i are variables to be fitted for each peak, t is time (in frames), and $f(amp)$ is the final fitted function. The benefit of such fits over a typical sinusoidal fit is that no periodicity is assumed a priori. This fitting was completed using the Wolfram Mathematica 11.3 procedure *Non-linearModelFit* (which guarantees continuity of the summed functions) and is plotted as the blue line over-laid on **Figure 4**. It is clear that this blue line accurately models the detected oscillation, however, it does slightly under-estimate the returned amplitude between frames 170 and 200. Therefore, we stress that the increase in amplitude detected during this oscillation (discussed subsequently) will be under-estimated by our model.

3. RESULTS

3.1. Theoretical Modeling and Observed Amplitude Profiles

In this section, we fit the observed oscillatory profile plotted in **Figure 4** using the theoretical model proposed by Shukhobodskiy et al. (2018). The model proposed by those authors consisted of a straight magnetic flux tube with varying cross section along its length. The tube was modeled with three layers: the core which contained an arbitrary flow and oscillated as a solid body; a transitional layer (or annulus) with monotonically

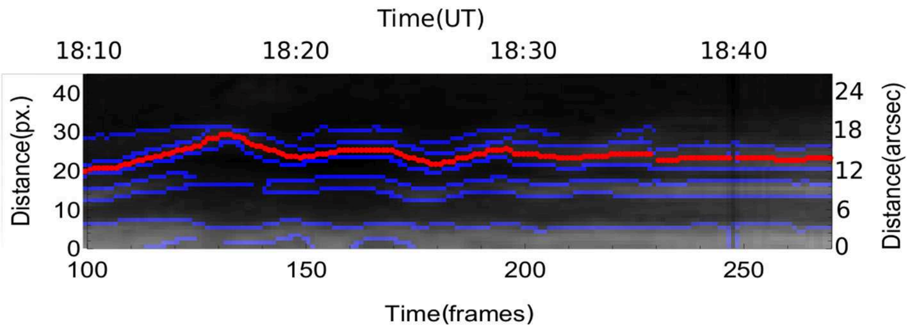

FIGURE 3 | Zoomed time-space diagram from **Figure 2** with the Canny edge-detection output (blue lines) and the returned oscillation profile (red line) over-laid. The returned oscillation is qualitatively similar to the oscillation returned by Pascoe et al. (2016) for the same event.

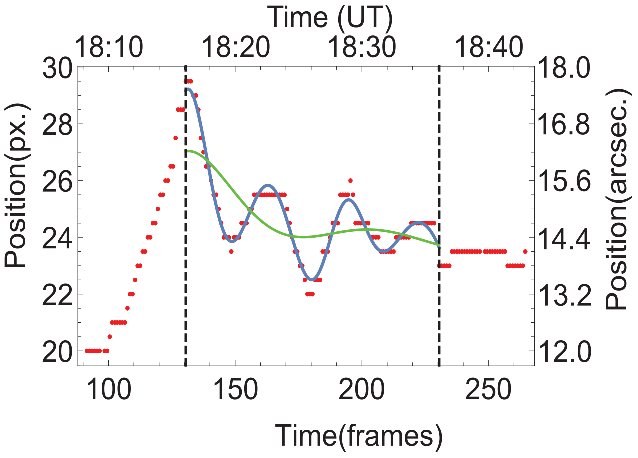

FIGURE 4 | The position-time dependence of the coronal loop. Red dots correspond to data points collected from the 171 Å time-space diagram plotted in **Figure 3**. The green line corresponds to the fitted 8th-order background trend and the blue line is the Gaussian fit of the observed data points computed of the form (Equation 1). The two vertical dashed lines indicate the boundaries of the area over which numerical fitting took place. The Gaussian fit under-estimates the oscillation amplitude between frames 170 and 200 meaning the amplitude at this time will be under-estimated.

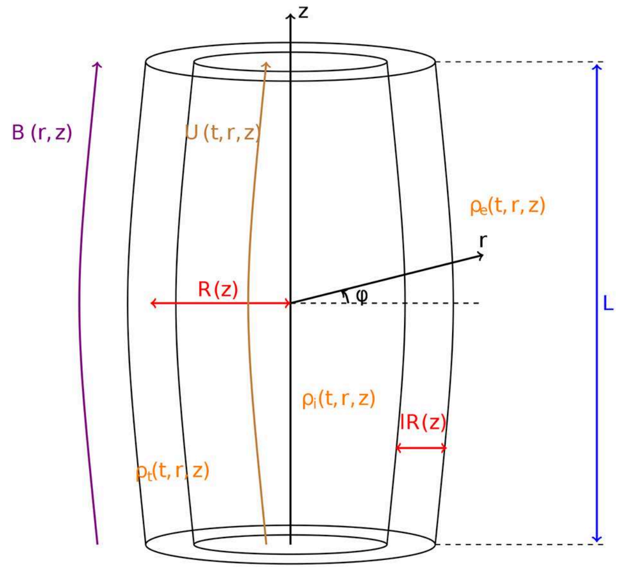

FIGURE 5 | Equilibrium configuration of theoretical model. The black lines with labels r, ϕ, and z correspond to the cylindrical polar coordinates system. $B(r, z)$ is the background magnetic field, $U(t, r, z)$ is the background flow parallel to the magnetic field, $R(z)$ is the radius of the tube, l is a constant determining the thickness of the transitional layer, $\rho_i(t, r, z)$ is the density in the internal region, $\rho_e(t, r, z)$ is the density in external region, $\rho_t(t, r, z)$ is the monotonically decaying density in the transitional layer from $\rho_i(t, r, z)$ to $\rho_e(t, r, z)$, L is the length of tube for the standing waves and the characteristic value of the wavelength for propagating waves.

decaying density from the core to the external layer; and the surrounding background plasma. See **Figure 5** for a detailed schematic of this model. Ruderman et al. (2017) obtained the governing equation for such a model under the assumptions of a thin tube with thin boundaries, by considering jumps of displacement and pressure across the transitional layer. However, this equation was not closed as jump conditions were not defined in terms of the displacement. Later, Shukhobodskiy and Ruderman (2018) and Shukhobodskiy et al. (2018), closed that system for the time independent and time dependent densities, respectively.

In the model applied here, we consider a loop of half-circular shape, where the curvature affects only the density distribution. The temperature is modeled to be exponentially decaying in time (similar to the profiles studied in, for example, Aschwanden and Terradas, 2008; Morton and Erdélyi, 2010; Ruderman, 2011a; Ruderman et al., 2017) and is approximated by:

$$T(t) = T_0 \exp(-t/t_{cool}), \tag{2}$$

where T_0 is the constant external temperature and t_{cool} is the cooling time (assumed to be the total lifetime of the oscillation here). Additionally, we describe the variation of the loop cross-section with height, z, in a manner similar to that discussed by Ruderman et al. (2008, 2017) and Shukhobodskiy et al. (2018).

This takes the form:

$$R(z) = R_f \lambda \sqrt{\frac{\cosh(L/2L_c) - 1}{\cosh(L/2L_c) - \lambda^2 + (\lambda^2 - 1)\cosh(z/L_c)}}, \qquad (3)$$

where R_f is the radius of the magnetic flux tube at the foot-points, $\lambda = R(0)/R_f$ is the expansion factor and L_c is an arbitrary constant. Please note that L_c should be selected such that the expansion factor can be consistent with observations of coronal loops ($1 < \lambda < 1.5$). We also assume, similarly to Ruderman and Roberts (2002) and Goossens et al. (2002), that the density in the transitional layer has a linear profile modeled by:

$$\rho_t(r, z) = \frac{\rho_i + \rho_e}{2} + (\rho_i - \rho_e)\frac{R - r}{lR}, \qquad (4)$$

where l is a constant determining the width of the transition layer and ρ_i and ρ_e are the internal and external densities, respectively.

Using these equations, Shukhobodskiy et al. (2018) showed that the dimensionless amplitude, A where $A(0) = 1$, of the kink mode may be approximated by:

$$\frac{d(\varpi \Pi_+ A^2)}{dt} = -\alpha \varpi^2 |\Pi_-| A^2, \qquad (5)$$

where:

$$\Pi_\pm = \int_0^1 X^2 \lambda^4 \left[\zeta \exp\left(-\kappa e^\tau \cos\frac{\pi z}{2}\right) \pm \exp\left(-\kappa \cos\frac{\pi z}{2}\right)\right] dZ, \qquad (6)$$

$$\alpha = \frac{\pi l C_f t_{cool}}{4L}, \qquad (7)$$

and:

$$\zeta = \frac{\rho_i}{\rho_e},\ Z = \frac{2z}{L},\ \tau = \frac{t}{t_{cool}},\ \varpi = \frac{\omega L}{C_f},$$

$$\kappa = \frac{L}{\pi H_0},\ C_f^2 = \frac{2\zeta B_f^2}{\mu_0 \rho_f (1 + \zeta)}. \qquad (8)$$

Here, μ_0 is the magnetic permeability of the free space, ω is the oscillation frequency, H_0 is the external scale height, and ρ_f and B_f are the density of plasma and magnetic field strength at the foot-points inside the loop. Additionally, X is determined by the following boundary value problem:

$$\frac{\partial^2 X}{\partial Z^2} + \frac{\varpi^2 \lambda^4 X}{4(\zeta + 1)}\left[\zeta \exp\left(-\kappa e^\tau \cos\frac{\pi Z}{2}\right) + \exp\left(-\kappa \cos\frac{\pi Z}{2}\right)\right] = 0, \qquad (9)$$

where X is the function of Z defined by the boundary values:

$$X = 0 \quad \text{at} \quad Z = -1, \qquad X = 0 \quad \text{at} \quad Z = 1. \qquad (10)$$

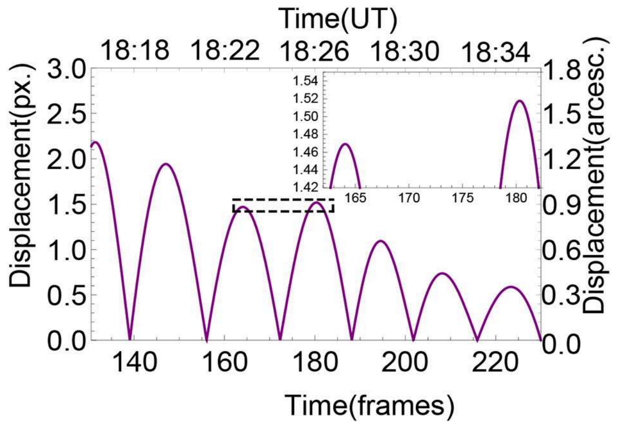

FIGURE 6 | The absolute value of the displacement of the Gaussian fitted position profile (blue line from **Figure 4**) from the background 8*th* order polynomial trend (green line from **Figure 4**) through time. The cut-out in the top right corner provides a magnified view of the region on the graph bounded by the black dashed box. This cut-out clearly shows the deviation of the damping profile from a typical Gaussian or exponential fit during this time due to a slight increase in the measured amplitude (compared to the background trend). Similar results are found for other background polynomial trends.

In order to obtain results comparable with observed amplitude profiles, we set $A_t = A(0)A_{Ob}(0)$, where $A_{Ob}(0)$ is the measured initial amplitude of the observed oscillation, A_t is the factor by which the dimensionless amplitude is scaled, and set $L/L_c = 6$ (similar to the values used by Ruderman et al., 2008, 2017; Shukhobodskiy et al., 2018). This allows us to obtain results for loop expansion factors in the range of 1–1.5, consistent with values discussed in the literature for coronal loops (see for example, Klimchuk, 2000; Watko and Klimchuk, 2000). In **Figure 6**, we plot the absolute displacement of the observed oscillation through time by subtracting the fitted displacement (blue line in **Figure 4**) from the background trend (green line in **Figure 4**). We define the initial amplitude of the oscillation, $A_{Ob}(0)$, by the first peak in **Figure 6**. The observed amplitude profile is then constructed by calculating all values of the peaks in **Figure 6** and using the *Interpolation* procedure in Wolfram Mathematica 11.3.

The most interesting region of **Figure 6** (denoted by the dashed black box over-laid between frames 160 and 185) is plotted in the zoomed cut-out in the top right corner of the panel. It is immediately clear that peak four is slightly larger than peak three indicating an amplitude increase potentially occurs through time. Such an increase would be in agreement with the theoretical model of Shukhobodskiy et al. (2018) which suggests that cooling in the loop system can lead to wave amplification. We note that cooling does not strictly lead to an amplification of the oscillation, it only modifies the damping profile from Gaussian or exponential. Therefore, although the amplitude increase plotted here is sub-resolution, the fact that the oscillation is not damping in a manner consistent with a Gaussian or exponential profile is enough to suggest some sort of cooling may be occurring. It should also be noted that larger amplitude increases (greater than 1 pixel) were found for lower order polynomials, however, we only focus on the 8th order fitting here as that is sufficient as a proof of concept. The increase in the amplitude can be

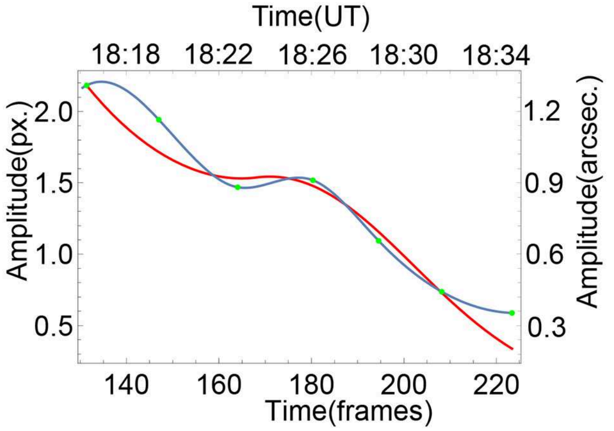

FIGURE 7 | The dependence of the amplitude of the coronal loop oscillation on time. Green points correspond to maxima of the peaks plotted in **Figure 6**, the blue line is the fitted observed amplitude-time profile, and the red line represents the theoretical amplitude-time profile with $\zeta = 2.2$, $\lambda = 1.05$, $\kappa = 2.4$, and $\alpha = 1.4$.

clearly seen in **Figure 7**, where the blue line plots a fit between the measured peak amplitudes (green circles) through time. The red line over-laid on **Figure 7** indicates the line of best fit calculated by solving the system of Equations (2–10) numerically. A maximum χ^2 value was found by looping over all variables, hence this is numerically expensive. It was assumed that the cooling starts at the first peak and ends in the last peak of **Figure 6** (i.e., that t_{cool} is equal to the lifetime of the oscillation).

The software used to obtain these theoretical solution is Wolfram Mathematica 11.3. The numerical procedure for obtaining the theoretical results may be summarized as follows: To obtain the solution to the boundary value problem, Equations (9) and (10), we used the *NDEigensystem* procedure; Equation (6) was then integrated numerically using the *NIntegrate* procedure subject to the *GlobalAdaptive* method (which uses various numerical integration methods and chooses the most accurate and fastest version for the particular problem). Finally we obtained the amplitude of the oscillation by using the *NDSolve* procedure.

The application of this model revealed several interesting effects with regards seismology of the loop system. Firstly, it was found that ζ (the density ratio at the foot-points of the loop at $t = 0$) and κ (the scale height) determine the position of the turning points of the amplitude profile (i.e., where the gradient of the amplitude profile is zero). However, the effect of κ on the position of the turning point reduces as the value of κ itself increases. As a result, we can neglect this effect for sufficiently long loops with $\kappa > 1.6$. Therefore, by minimizing the difference between the turning points of the theoretical and observed amplitude profiles we can determine an approximate value of ζ for this system without knowing any other background parameters. For the example studied here, fitting a density ratio of between 2.05 and 2.35 provides sufficiently good approximations for the position of the local amplitude increase. As this work aims to provide a proof-of-concept of the application of cooling theory to coronal loop oscillations and as the density ratio is only dependent on where the amplitude deviates from a Gaussian or exponential decay, we neglect any errors in the measured amplitude (green dots) here; however, the effects of any errors on our seismological should be analyzed using a larger statistical sample in the future. The differences in nature between the red and blue curves are due to the spline fitting used here. Secondly, the values of κ, α, and λ determine the speed of the amplitude decay. Unfortunately, for the example studied here, various sets of these parameters return similar shapes and amplitude profiles meaning we are unable to provide accurate seismological estimates at this stage. A larger statistical sample of cooling events and further numerical work will be required to attempt to estimate such values in the future.

3.2. Evidence for Cooling in the AR

Evidence of cooling in the coronal loop system can be inferred through analysis of the intensities within SDO/AIA imaging channels. For the loop studied here, no evidence of coronal rain formation was found in the 304 Å filter indicating that catastrophic cooling likely did not take place within this loop. The loop intensity within the 171 Å and 193 Å filters did appear to decrease slightly (potentially below any level of significance) during the oscillation, however, whether this was due to cooling, some line-of-sight effects (e.g., the supposition of multiple loops within one pixel), or purely noise is unknown. The flare within the local AR lead to large swathes of saturation and fringing patterns on the 193 Å data meaning we were unable to study the temporal evolution of the loop in detail in this wavelength during the period of interest for cooling for this event. Future work should aim to analyse a larger statistical sample of coronal loop oscillations with non-Gaussian and non-exponential damping profiles in order to detect whether direct signatures of cooling can be found within the loops themselves.

Significant cooling can be inferred elsewhere in this AR during the course of this oscillation, however. Large amounts of coronal rain can be observed in the 304 Å channel in the loop system approximately 100″ south of the loop analyzed here potentially indicating the occurrence of the thermal instability during the flare. The after-effects of this rain are evident in the top row of **Figure 1** (at approximately $x_c = -200''$, $y_c = -990''$). Initially (at 17:50 UT), the loop is bright in the 304 Å channel. As the rain forms, the loop system completely fades from view (by 18:50 UT). The coronal rain in the chromospheric 304 Å channel is accompanied by a reduction in the intensity of the loop system in the coronal 171 Å and 193 Å channels further supporting the hypothesis that cooling occurred. The application of the theories tested here on loops which are catastrophically cooling would be an interesting project for the future.

4. DISCUSSION AND CONCLUSIONS

In this article, we have studied a flare-driven kink oscillation in a coronal loop observed in AR 11598 by the SDO/AIA instrument (**Figure 1**). This oscillation corresponded to Loop

40, Event 2 from Goddard et al. (2016). The specific slit analyzed here is indicated by the white line over-laid on the top row of **Figure 2**, with the returned time-space diagram being plotted in the bottom panel of **Figure 2**. In **Figure 3** the time-space diagram is plotted with the output from a Canny edge-detection algorithm over-laid in blue. The mid-points between the edge-detection outputs (red dots) were assumed to track the displacement of the center of the loop as it oscillated. The returned oscillation was qualitatively similar to that returned by Pascoe et al. (2016) for the same event indicating that our fitting method was sound. This oscillation was then fitted with a summation of four Gaussian functions (corresponding to the four peaks in the oscillation) of the form Equation 1 and an 8-th order background trend removed (the blue and green lines in **Figure 4**, respectively). Again, it should be emphasized that numerous background trends were tested in order to assure that we were not introducing important effects in our subsequent analysis.

Once the oscillation and the background had been fitted, we removed the background trend from the oscillation and plotted the absolute values of the kink mode (see **Figure 6**) through time. The cut-out over-laid on **Figure 6** clearly highlights a deviation in oscillatory amplitude from a typical Gaussian or exponential damping between frames 160 and 185 (18:22 UT – 18:27 UT). Indeed, there are even hints that an amplitude increase could be present, however, this is small. It should be noted that some background trends returned profiles with amplitude increases of over 1 pixel. Such an amplitude increase would obviously not be expected from a typical Gaussian or exponential decay (as has been considered previously by, for example, Goddard et al., 2016; Pascoe et al., 2016). However, models proposed by Shukhobodskiy and Ruderman (2018) and Shukhobodskiy et al. (2018) which consider cooling within the system can account for amplitude increases. Therefore, in addition to the multiple harmonics scenario suggested by Pascoe et al. (2017), future work should consider cooling when trying to understand complex amplitude profiles in coronal loop oscillations.

Although there were some hints that the loop faded slightly in the coronal 171 Å and 193 Å channels over the course of the hour-long dataset analyzed here, it is unclear whether this is an effect of cooling, due to line-of-sight effects, or purely noise. Little other evidence for cooling could be obtained through analysis of SDO/AIA time-series. Additionally, no evidence of coronal rain was observed in the 304 Å channel. More obvious cooling could be observed within the local AR, however, in a loop system located approximately 100″ south of the loop analyzed here. This loop contains large amounts of coronal rain in the 304 Å channel potentially hinting at the occurrence of the thermal instability, or catastrophic cooling. The effects of such catastrophic cooling on coronal loop oscillations would be an interesting topic for future study.

The key seismological result obtained here is that the location in time at which the amplitude begins to increase (an effect of the cooling on the oscillation) is dictated solely by the ratio between the internal and external densities for sufficiently large coronal loops. Therefore, fitting the model such that the difference between the observed turning point and the theoretical fitting point is minimized (as is shown in **Figure 7**) allows us to calculate an estimate of the density ratio, ζ, an important parameter for modeling. For this loop, inversions of the theoretical model provide a good fit to the observed amplitude profiles when ζ is in the range 2.05–2.35 (i.e., the loop foot-point is initially more than twice as dense as its surroundings).

In order to follow on from this work, we aim to complete two further studies. Firstly, we will conduct a statistical analysis of oscillations within potentially cooling coronal loops in the solar corona. This will provide important constraints on density ratios of loops for future modeling. Secondly, through further numerical work, it should prove possible to conduct further seismology in order to return values such as the scale height of the loop and the annulus thickness. These values will, again, provide further constraints for future modeling. Overall, the theoretical work of Shukhobodskiy et al. (2018) has proved adept at modeling the oscillations of the loop analyzed here and should be considered by authors in the future when analysing coronal loop oscillations.

AUTHOR CONTRIBUTIONS

CN drafted the manuscript and lead the observational analysis with help from AS. AS drafted section Theoretical Modeling and Observed Amplitude Profiles and completed the theoretical work. AS and CN completed the model fitting. All authors contributed to the interpretation of the results and helped draft the manuscript.

FUNDING

The authors acknowledge the Science and Technology Facilities Council (STFC) for financial support (Grant numbers: ST/M000826/1 and ST/P000304/1).

ACKNOWLEDGMENTS

SDO data are courtesy of NASA/SDO and the AIA and HMI science teams.

REFERENCES

Al-Ghafri, K. S., and Erdélyi, R. (2013). Effect of variable background on an oscillating hot coronal loop. *Solar Phys.* 283, 413–428. doi: 10.1007/s11207-013-0225-8

Antolin, P., Vissers, G., Pereira, T. M. D., Rouppe van der Voort, L., and Scullion, E. (2015). The multithermal and multi-stranded nature of coronal rain. *Astrophys. J.* 806:81. doi: 10.1088/0004-637X/806/1/81

Aschwanden, M. J., Fletcher, L., Schrijver, C. J., and Alexander, D. (1999). Coronal loop oscillations observed with the transition region and coronal explorer. *Astrophys. J.* 520, 880–894. doi: 10.1086/307502

Aschwanden, M. J., and Terradas, J. (2008). The effect of radiative cooling on coronal loop oscillations. *Astrophys. J. Lett.* 686:L127. doi: 10.1086/592963

Dymova, M. V., and Ruderman, M. S. (2005). Non-axisymmetric oscillations of thin prominence fibrils. *Solar Phys.* 229, 79–94. doi: 10.1007/s11207-005-5002-x

Dymova, M. V., and Ruderman, M. S. (2006). Resonantly damped oscillations of longitudinally stratified coronal loops. *Astron. Astrophys.* 457, 1059–1070. doi: 10.1051/0004-6361:20065051

Erdélyi, R., Hague, A., and Nelson, C. J. (2014). Effects of stratification and flows on P_1/P_2 ratios and anti-node shifts within closed loop structures. *Solar Phys.* 289, 167–182. doi: 10.1007/s11207-013-0344-2

Goddard, C. R., Nisticò, G., Nakariakov, V. M., and Zimovets, I. V. (2016). A statistical study of decaying kink oscillations detected using SDO/AIA. *Astron. Astrophys.* 585:A137. doi: 10.1051/0004-6361/201527341

Goossens, M., Andries, J., and Aschwanden, M. J. (2002). Coronal loop oscillations. An interpretation in terms of resonant absorption of quasi-mode kink oscillations. *Astron. Astrophys.* 394, L39–L42. doi: 10.1051/0004-6361:20021378

Handy, B. N., Acton, L. W., Kankelborg, C. C., Wolfson, C. J., Akin, D. J., Bruner, M. E., et al. (1999). The transition region and coronal explorer. *Solar Phys.* 187, 229–260. doi: 10.1023/A:1005166902804

Klimchuk, J. A. (2000). Cross-sectional properties of coronal loops. *Solar Phys.* 193, 53–75. doi: 10.1007/978-94-010-0860-0_4

Lemen, J. R., Title, A. M., Akin, D. J., Boerner, P. F., Chou, C., Drake, J. F., et al. (2012). The Atmospheric Imaging Assembly (AIA) on the Solar Dynamics Observatory (SDO). *Solar Phys.* 275, 17–40. doi: 10.1007/s11207-011-9776-8

López Fuentes, M. C., Klimchuk, J. A., and Mandrini, C. H. (2007). The temporal evolution of coronal loops observed by GOES SXI. *Astrophys. J.* 657, 1127–1136. doi: 10.1086/510662

Morton, R. J., and Erdélyi, R. (2009). Transverse oscillations of a cooling coronal loop. *Astrophys. J.* 707, 750–760. doi: 10.1088/0004-637X/707/1/750

Morton, R. J., and Erdélyi, R. (2010). Application of the theory of damping of kink oscillations by radiative cooling of coronal loop plasma. *Astron. Astrophys.* 519:A43. doi: 10.1051/0004-6361/201014504

Nakariakov, V. M., Ofman, L., Deluca, E. E., Roberts, B., and Davila, J. M. (1999). TRACE observation of damped coronal loop oscillations: implications for coronal heating. *Science* 285, 862–864. doi: 10.1126/science.285.5429.862

Pagano, P., Pascoe, D. J., and De Moortel, I. (2018). Contribution of phase-mixing of Alfvén waves to coronal heating in multi-harmonic loop oscillations. *Astron. Astrophys.* 616:A125. doi: 10.1051/0004-6361/201732251

Pascoe, D. J., Goddard, C. R., Nisticò, G., Anfinogentov, S., and Nakariakov, V. M. (2016). Damping profile of standing kink oscillations observed by SDO/AIA. *Astron. Astrophys.* 585:L6. doi: 10.1051/0004-6361/201527835

Pascoe, D. J., Russell, A. J. B., Anfinogentov, S. A., Simões, P. J. A., Goddard, C. R., Nakariakov, V. M., et al. (2017). Seismology of contracting and expanding coronal loops using damping of kink oscillations by mode coupling. *Astron. Astrophys.* 607:A8. doi: 10.1051/0004-6361/201730915

Ruderman, M. S. (2011a). Resonant damping of kink oscillations of cooling coronal magnetic loops. *Astron. Astrophys.* 534:A78. doi: 10.1051/0004-6361/201117416

Ruderman, M. S. (2011b). Transverse oscillations of coronal loops with slowly changing density. *Solar Phys.* 271, 41–54. doi: 10.1007/s11207-011-9772-z

Ruderman, M. S., and Roberts, B. (2002). The damping of coronal loop oscillations. *Astrophys. J.* 577, 475–486. doi: 10.1086/342130

Ruderman, M. S., Shukhobodskiy, A. A., and Erdélyi, R. (2017). Kink oscillations of cooling coronal loops with variable cross-section. *Astron. Astrophys.* 602:A50. doi: 10.1051/0004-6361/201630162

Ruderman, M. S., Verth, G., and Erdélyi, R. (2008). Transverse oscillations of longitudinally stratified coronal loops with variable cross section. *Astrophys. J.* 686, 694–700. doi: 10.1086/591444

Shukhobodskiy, A. A., and Ruderman, M. S. (2018). Resonant damping of kink oscillations of thin expanding magnetic tubes. *Astron. Astrophys.* 615:A156. doi: 10.1051/0004-6361/201732396

Shukhobodskiy, A. A., Ruderman, M. S., and Erdélyi, R. (2018). Resonant damping of kink oscillations of thin cooling and expanding coronal magnetic loops. *Astron. Astrophys.* 619:A173. doi: 10.1051/0004-6361/201833714

Watko, J. A., and Klimchuk, J. A. (2000). Width Variations along Coronal Loops Observed by TRACE. *Solar Phys.* 193, 77–92. doi: 10.1007/978-94-010-0860-0_5

Winebarger, A. R., and Warren, H. P. (2005). Cooling active region loops observed with SXT and TRACE. *Astrophys. J.* 626, 543–550. doi: 10.1086/429817

Zimovets, I. V., and Nakariakov, V. M. (2015). Excitation of kink oscillations of coronal loops: statistical study. *Astron. Astrophys.* 577:A4. doi: 10.1051/0004-6361/201424960

Conflict of Interest Statement: The authors declare that the research was conducted in the absence of any commercial or financial relationships that could be construed as a potential conflict of interest.

The reviewer RO declared a past co-authorship with one of the authors CN to the handling editor.

frontiers
in Astronomy and Space Sciences

ORIGINAL RESEARCH
published: 12 July 2019
doi: 10.3389/fspas.2019.00048

Magnetohydrodynamic Waves in Multi-Layered Asymmetric Waveguides: Solar Magneto-Seismology Theory and Application

Matthew Allcock[1], *Daria Shukhobodskaia*[1], *Noémi Kinga Zsámberger*[1,2,3] and *Robert Erdélyi*[1,4]*

[1] *Solar Physics and Space Plasma Research Centre, School of Mathematics and Statistics, University of Sheffield, Sheffield, United Kingdom,* [2] *Institute of Physics, University of Debrecen, Debrecen, Hungary,* [3] *Doctoral School of Physics, University of Debrecen, Debrecen, Hungary,* [4] *Department of Astronomy, Eötvös L. University, Budapest, Hungary*

OPEN ACCESS

Edited by:
Tom Van Doorsselaere,
KU Leuven, Belgium

Reviewed by:
Abhishek Kumar Srivastava,
Indian Institute of Technology (BHU), India
Youra Taroyan,
Aberystwyth University, United Kingdom
Inigo Arregui,
Instituto de Astrofísica de Canarias, Spain

***Correspondence:**
Robert Erdélyi
robertus@sheffield.ac.uk

Specialty section:
This article was submitted to Stellar and Solar Physics, a section of the journal Frontiers in Astronomy and Space Sciences

Received: *25 February 2019*
Accepted: *24 June 2019*
Published: *12 July 2019*

Citation:
Allcock M, Shukhobodskaia D, Zsámberger NK and Erdélyi R (2019) Magnetohydrodynamic Waves in Multi-Layered Asymmetric Waveguides: Solar Magneto-Seismology Theory and Application. Front. Astron. Space Sci. 6:48. doi: 10.3389/fspas.2019.00048

Diagnosing the solar atmospheric plasma is one of the major challenges in solar physics. Magnetohydrodynamic (MHD) waves, by means of applying the powerful concept of solar magneto-seismology (SMS), provide a tool to obtain diagnostic insight into the magnetized solar plasma in MHD waveguides. This paper provides a road-map of simple but applicable models of solar atmospheric waveguides in the framework of Cartesian geometry. We focus on exploiting the diagnostic potential of waveguide asymmetry and consider the effects of steady flow. In particular, the dispersion relation describing linear MHD wave propagation along a multi-layered MHD waveguide is derived. Aiming at lower solar atmospheric applications of SMS, the special case of a single magnetic slab embedded in an asymmetric magnetized plasma environment is revisited. As a proof of concept, the Amplitude Ratio Method is used to make a seismological estimate of the local Alfvén speed in several chromospheric fibrils that exhibit asymmetric oscillations. Absolute ratios of boundary oscillations between 1.29 and 3.42 are detected and, despite the significant errors expected, the local Alfvén speed estimates agree with previously derived estimates from magnetic field extrapolations. Finally, the effects of asymmetric shear flows present in these slab MHD waveguides are considered as a suitable model of Kelvin-Helmholtz instability initiation that is applicable, for example, to coronal mass ejection flanks.

Keywords: solar atmosphere, plasma, waves, magnetohydrodynamics (MHD), magnetic fields, magneto-seismology, fibrils, magnetic bright points

1. INTRODUCTION

Over the past few decades, vast improvements in solar telescope technology, with the likes of both space-borne instrumentation, e.g., Solar and Heliospheric Observatory (SoHO), Solar Dynamics Observatory (SDO), and Interface Region Imaging Spectograph (IRIS), and ground-based solar observing facilities, e.g., Dunn Solar Telescope (DST) and Swedish Solar Telescope (SST), have enabled us to resolve the fine sub-structure within many of the larger magnetic features that bejewel the solar atmosphere. Considering the development of the next generation of observational mega-projects, such as the rather imminent commencement of the Daniel K. Inouye Solar

Telescope (DKIST) and, within a decade, that of European Solar Telescope (EST), this trend looks set to continue, which motivates solar physicists to fill the gaps in theoretical understanding.

Magnetohydrodynamic (MHD) waves are a key in our understanding of the physical processes in the hot solar plasma. MHD waves are not only a mechanism to transfer non-thermal energy between distant locations in the solar plasma, that is then dissipated by physical processes that are yet to be fully understood, like resonant absorption (Goossens et al., 2011), phase mixing (Heyvaerts and Priest, 1983), non-linear shock damping (Ballai and Ruderman, 2011), rather, they are also excellent tools to be exploited for plasma diagnostics by solar magneto-seismology (SMS) (see the reviews by Andries et al., 2009; Ruderman and Erdélyi, 2009; Mathioudakis et al., 2013). SMS employs the measured properties of MHD waves, e.g., amplitude, frequency, and phase speed, and, using a suitable inversion, yields information about the waveguide properties that are often very hard to measure (e.g., magnetic field, gravity, magnetic scale heights, or density).

There are two geometric building-blocks that are popular to model solar atmospheric waveguides: the cylindrical flux tube and the magnetic slab waveguides. The present work focuses on the latter, which can be used in the first approximation to model a wide variety of solar atmospheric structures, including prominences, magnetic bright points, light bridges and their corresponding light walls, coronal hole boundary layers, the flank structure of coronal mass ejections, as well as several magnetospheric regions. First studied as an interface between two semi-infinite plasmas (Roberts, 1981b), the currently frequently used and popular format of the theory of MHD wave propagation in Cartesian geometry has been developed to describe magnetic slabs embedded in symmetric (Roberts, 1981a; Edwin and Roberts, 1982) and asymmetric environments (Allcock and Erdélyi, 2017; Zsámberger et al., 2018), and multi-layered plasmas (Ruderman, 1992; Shukhobodskaia and Erdélyi, 2018). Collective standing modes of a multi-layered Cartesian waveguide modeling multi-fibril prominence oscillations (Díaz et al., 2005; Díaz and Roberts, 2006) and coronal loop oscillations (Luna et al., 2006) have been studied. MHD wave theory in Cartesian waveguides has been explored in terms of SMS by Roberts et al. (1984), and more recently by Allcock and Erdélyi (2018).

Aside from providing a description and nomenclature of solar atmospheric wave physics, the theoretical studies have driven progress in SMS. The asymmetric environment of solar waveguides has been theoretically proposed as a proxy for local inhomogeneity, e.g., in the magnetic field, density, and temperature. This inhomogeneity, through the Amplitude Ratio and the Minimum Perturbation Shift Methods, can be exploited for SMS (Allcock and Erdélyi, 2018). With the sub-structure resolution that these techniques require being reached by some of the currently available instrument suits for solar atmospheric waveguide structures, we are now able to apply these techniques.

The aims of this paper are two-fold. First, we bring together the linear theory of MHD wave propagation in Cartesian waveguides modeled by magnetic steady slab equilibria, focusing on the effects of asymmetry surrounding the slab and steady states representing plasma flows. Secondly, we exploit the SMS diagnostic power of waveguide asymmetry by making the first inversion of the local Alfvén speed in chromospheric fibrils using the Amplitude Ratio Method, an SMS technique that has developed out of asymmetric waveguide theory.

The structure of the paper is as follows. Section 2 introduces a general model of a multi-layered MHD waveguide, for which the dispersion relation for linear magneto-acoustic waves is derived. Special cases of this model are discussed in section 3, including a magnetic slab in an asymmetric non-magnetic environment (section 3.1) and magnetic environment (section 3.2). Section 4 applies these models to the low solar atmosphere, first, to estimate the local Alfvén speed in chromospheric fibrils using solar magneto-seismology (section 4.1), then to present mode identification in high-plasma-beta regions (section 4.2). Section 5 analyses the effects of steady flows on linear MHD perturbations and instabilities of a multi-layered solar plasma.

2. GENERAL MULTI-LAYERED WAVEGUIDE MODEL

Let us first consider a model of a plasma structured by an arbitrary number of interfaces with different homogeneous magnetic fields, temperatures, and densities, illustrated by **Figure 1** in Cartesian geometry. Such a model could be useful for studying linear MHD wave propagation in observed solar atmospheric structures closer to the photosphere, such as magnetic bright points, sunspot light bridges, or light walls.

In what follows, we consider an infinite compressible inviscid structured static plasma with magnetic field $B(x)\,\hat{\mathbf{z}}$, where

$$B(x) = \begin{cases} B_0, & \text{for } x < x_0, \\ B_1, & \text{for } x_0 \le x < x_1, \\ \dots \\ B_n, & \text{for } x_{n-1} \le x < x_n, \\ B_{n+1}, & \text{for } x \ge x_n. \end{cases}$$

We ignore the effects of gravity. We denote the equilibrium kinetic plasma pressure, the density, and temperature by p_j, ρ_j, and T_j, respectively, with subscript **j** that varies from 0 to $n+1$. In total, there are $n+2$ regions, all of which, in general, are magnetized.

We assume that the perturbations within the magnetic slab are governed by the ideal MHD equations,

$$\begin{aligned} \rho\frac{D\mathbf{v}}{Dt} &= -\nabla p - \frac{1}{\mu_0}\mathbf{B}\times(\nabla\times\mathbf{B}), \\ \frac{\partial\rho}{\partial t} &+ \nabla\cdot(\rho\mathbf{v}) = 0, \\ \frac{D}{Dt}\left(\frac{p}{\rho^\gamma}\right) &= 0, \\ \frac{\partial\mathbf{B}}{\partial t} &= \nabla\times(\mathbf{v}\times\mathbf{B}), \end{aligned} \tag{2.1}$$

where μ_0 is the magnetic permeability of free space, γ is the adiabatic index, variables $\mathbf{v} = (v_x, v_y, v_z)$, $\mathbf{B}$, p, and ρ are velocity, magnetic field, kinetic pressure, and density, at time t. The Alfvén

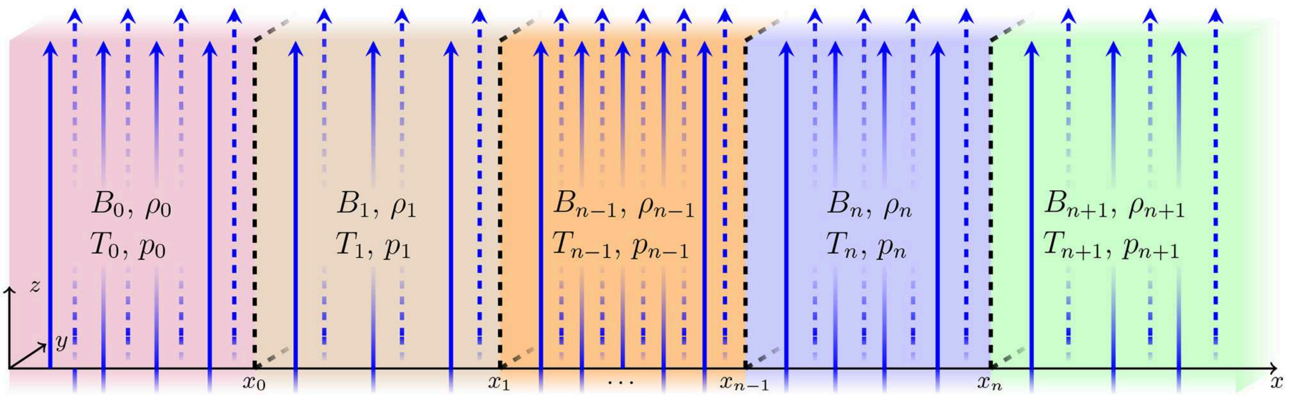

FIGURE 1 | The equilibrium configuration of a layered magnetized plasma. The blue arrows represent the vertical magnetic field, $B(x)\hat{\mathbf{z}}$. The kinetic pressure, $\mathrm{p_j}$, density, ρ_j, and temperature, $\mathrm{T_j}$ are equilibrium parameters. The subscript j corresponds to the relevant slab and varies from 0 to $n+1$.

and sound speeds in the jth region are $v_{Aj} = B_j/\sqrt{\mu\rho_j}$ and $c_j = \sqrt{\gamma p_j/\rho_j}$, respectively. For the system to remain in equilibrium, pressure balance across each interface is required, i.e.,

$$p_0 + \frac{B_0^2}{2\mu} = p_1 + \frac{B_1^2}{2\mu} = \ldots = p_n + \frac{B_n^2}{2\mu}. \tag{2.2}$$

Equation (2.2) yields the following relation between characteristic speeds and density ratios for any two regions:

$$\frac{\rho_i}{\rho_j} = \frac{c_j^2 + \frac{1}{2}\gamma v_{Aj}^2}{c_i^2 + \frac{1}{2}\gamma v_{Ai}^2}$$

We linearize the governing equations by setting, for each variable $f, f = \mathrm{f_j} + f'$, where $\mathrm{f_j}$ is the background variable in region j and f' is the comparatively much smaller perturbation variable, then neglecting terms of quadratic or higher order in perturbation variables. For brevity, we drop the $'$ hereafter. We seek plane wave solutions to the linearized governing equations of the form

$$v_x(\mathbf{x}, t) = \widehat{v}_x(x)e^{i(kz-\omega t)},\ v_y(\mathbf{x}, t) = 0,\ v_z(\mathbf{x}, t) = \widehat{v}_z(x)e^{i(kz-\omega t)}, \tag{2.3}$$

representing wave propagation in the $\widehat{\mathbf{z}}$−direction, where ω is the angular frequency and $\mathbf{k}$ is the wavenumber in the $\widehat{\mathbf{z}}$-direction. Substituting solutions (2.3) into the system of Equation (2.1), and combining the obtained equations, we derive an ordinary differential equation for $\widehat{v}_x$ representing transverse motions inside the magnetic slab,

$$\frac{d^2\widehat{v}_x}{dx^2} - m_j^2\widehat{v}_x = 0, \tag{2.4}$$

where

$$m_j^2 = \frac{(k^2v_{Aj}^2 - \omega^2)(k^2c_j^2 - \omega^2)}{(c_j^2 + v_{Aj}^2)(k^2c_{Tj}^2 - \omega^2)}, \quad c_{Tj}^2 = \frac{c_j^2v_{Aj}^2}{c_j^2 + v_{Aj}^2}. \tag{2.5}$$

Note that $k = (0, 0, k)$, the system is homogeneous in the y-direction, and this derivation deals with magnetoacoustic modes and not Alfvén modes, since $v_y = 0$. Now, we assume that the perturbations vanish at infinity, so that $\widehat{v}_x \to 0$ as $x \to \pm\infty$. We note that m_j^2 may take positive or negative values for j from 1 to n. Since the wave amplitudes decay exponentially at infinity, we obtain a general solution of Equation (2.4) given by

$$\widehat{v}_x(x) = \begin{cases} \mathrm{P}_0(\cosh m_0x + \sinh m_0x), & \text{for } x < x_0, \\ \mathrm{P}_1\cosh m_1x + \mathrm{Q}_1\sinh m_1x, & \text{for } x_0 < x < x_1, \\ \ldots & \\ \mathrm{P}_n\cosh m_nx + \mathrm{Q}_n\sinh m_nx, & \text{for } x_{n-1} < x < x_n, \\ \mathrm{P}_{n+1}(\cosh m_{n+1}x - \sinh m_{n+1}x), & \text{for } x > x_n, \end{cases} \tag{2.6}$$

where $\mathrm{P_i}$ and $\mathrm{Q_j}$ are constants with $i = 0, 1, \ldots n+1$ and $j = 1, 2, \ldots n$.

The total (kinetic plus magnetic) pressure perturbation, $P_T(\mathbf{x}, t)$, satisfies the equation

$$\frac{\partial P_T}{\partial t} = \rho_j v_{Aj}^2\frac{\partial v_z}{\partial z} - \rho_j(c_j^2 + v_{Aj}^2)\nabla\cdot\mathbf{v}. \tag{2.7}$$

Considering $P_T(\mathbf{x}, t)$ in a Fourier form, $P_T(\mathbf{x}, t) = \widehat{p}(x)e^{i(kz-\omega t)}$, and using Equations (2.1) and (2.7), we obtain

$$\widehat{p}(x) = \widehat{\mathbf{v}}_\mathbf{x}(\mathrm{x})\begin{cases} \Lambda_0/m_0, & \text{for } x < x_0, \\ \Lambda_1/m_1, & \text{for } x_0 < x < x_1, \\ \ldots & \\ \Lambda_n/m_n, & \text{for } x_{n-1} < x < x_n, \\ \Lambda_{n+1}/m_{n+1}, & \text{for } x > x_n, \end{cases} \tag{2.8}$$

with

$$\Lambda_j = -\frac{i\rho_j(k^2v_{\mathrm{Aj}}^2 - \omega^2)}{m_j\omega}, \quad \text{for} \quad j = 0, 1, \ldots n+1. \tag{2.9}$$

Let us now establish appropriate boundary conditions. For physical solutions, the velocity, $v_x(\mathbf{x}, t)$, and total pressure,

$P_T(\mathbf{x}, t)$, have to be continuous across the boundaries $x = x_j$ for $j = 0 \ldots n$. Equations (2.6) and (2.8) give us $2(n+1)$ coupled homogeneous algebraic equations:

$$\begin{aligned}
\mathrm{P}_0(\cosh m_0x_0 + \sinh m_0x_0) &= \mathrm{P}_1 \cosh m_1x_0 + \mathrm{Q}_1 \sinh m_1x_0,\\
\Lambda_0\mathrm{P}_0(\cosh m_0x_0 + \sinh m_0x_0) &= \Lambda_1(\mathrm{P}_1 \sinh m_1x_0 + \mathrm{Q}_1 \cosh m_1x_0),\\
\mathrm{P}_1 \cosh m_1x_1 + \mathrm{Q}_1 \sinh m_1x_1 &= \mathrm{P}_2 \cosh m_2x_1 + \mathrm{Q}_2 \sinh m_2x_1,\\
\Lambda_1(\mathrm{P}_1 \sinh m_1x_1 + \mathrm{Q}_1 \cosh m_1x_1) &= \Lambda_2(\mathrm{P}_2 \sinh m_2x_1\\
&\quad + \mathrm{Q}_2 \cosh m_2x_1), \ldots\\
\mathrm{P}_{n-1} \cosh m_{n-1}x_{n-1} &+ \mathrm{Q}_{n-1} \sinh m_{n-1}x_{n-1}\\
&= \mathrm{P}_n \cosh m_nx_{n-1}\\
&\quad + \mathrm{Q}_n \sinh m_nx_{n-1},\\
\Lambda_{n-1}(\mathrm{P}_{n-1} \sinh m_{n-1}x_{n-1} &+ \mathrm{Q}_{n-1} \cosh m_{n-1}x_{n-1})\\
&= \Lambda_n(\mathrm{P}_n \sinh m_nx_{n-1}\\
&\quad + \mathrm{Q}_n \cosh m_nx_{n-1}),\\
\mathrm{P}_n \cosh m_nx_n &+ \mathrm{Q}_n \sinh m_nx_n = \mathrm{P}_{n+1}\\
&\quad (\cosh m_{n+1}x_n - \sinh m_{n+1}x_n),\\
\Lambda_n(\mathrm{P}_n \sinh m_nx_n &+ \mathrm{Q}_n \cosh m_nx_n) = \Lambda_{n+1}\mathrm{P}_{n+1}\\
&\quad (\sinh m_{n+1}x_n - \cosh m_{n+1}x_n),
\end{aligned} \tag{2.10}$$

where P_i and Q_j are constant with respect to x. Then, we define $\mathrm{Q}_0 = \mathrm{P}_0$ and $\mathrm{Q}_{n+1} = -\mathrm{P}_{n+1}$ and rewrite the above boundary conditions into the following compact form

$$\begin{aligned}
\mathrm{P}_j \cosh m_jx_j + \mathrm{Q}_j \sinh m_jx_j &= \mathrm{P}_{j+1} \cosh m_{j+1}x_j\\
&\quad + \mathrm{Q}_{j+1} \sinh m_{j+1}x_j,\\
\Lambda_j(\mathrm{P}_j \sinh m_jx_j + \mathrm{Q}_j \cosh m_jx_j) &= \Lambda_{j+1}(\mathrm{P}_{j+1} \sinh m_{j+1}x_j\\
&\quad + \mathrm{Q}_{j+1} \cosh m_{j+1}x_j),
\end{aligned} \tag{2.11}$$

for $j = 0, 1, \ldots n$. One of the advantages of the above form is its simplistic format which enables it to be used in numerical studies for sufficiently large values of n.

We now rearrange the obtained boundary conditions into the following compact matrix form:

$$\mathbf{M}\left(\mathrm{P}_0,\ \mathrm{P}_1,\ \mathrm{Q}_1,\ \ldots\ \mathrm{P}_n,\ \mathrm{Q}_n,\ \mathrm{P}_{n+1}\right)^T = \mathbf{0}, \tag{2.12}$$

where $\mathbf{M}$ is a $[2n+2] \times [2n+2]$ matrix. The precise form of the matrix is given in **Appendix A** by Equations (A1)–(A5).

In order to have a non-trivial solution of the system, the determinant of the matrix $\mathbf{M}$ must be equal to zero:

$$\det \mathbf{M} = 0. \tag{2.13}$$

Equation (2.13), the general dispersion relation, prescribes the nature of linear MHD waves that can propagate along a static multi-layered waveguide, visualized by **Figure 1**. The solutions to this equation, given by the angular frequency, ω, as a function of the wavenumber, k, correspond to the eigenfrequencies of the system.

3. MAGNETIC SLAB IN AN ASYMMETRIC ENVIRONMENT

In order to make analytical progress, we now analyze two special cases of this model in Cartesian geometry, namely, a slab in an asymmetric non-magnetic (section 3.1) and magnetic (section 3.2) homogeneous background plasma. These special cases bring the waveguide model closer to reality as there are several phenomena in the solar atmosphere that can be well modeled by isolated magnetic slabs, including prominences (Arregui et al., 2012), elongated magnetic bright points (Berger and Title, 1996), and light walls (Yang et al., 2015), to name a few.

3.1. Slab in an Asymmetric Non-magnetic Environment

By letting $n = 1$ and letting the left and right regions be magnetic field free, i.e., $B_0 = B_2 = 0$, we reduce the general multi-waveguide structure to a single magnetic slab waveguide in a non-magnetic environment (**Figure 2**). This waveguide model was studied by Allcock and Erdélyi (2017) and is summarized in this section.

Under this configuration, the parameters m_j and Λ_j reduce to

$$m_0^2 = k^2 - \frac{\omega^2}{c_0^2}, \quad m_1^2 = \frac{(k^2v_{\mathrm{A}}^2 - \omega^2)(k^2c_1^2 - \omega^2)}{(c_1^2 + v_{\mathrm{A1}}^2)(k^2c_{\mathrm{T1}}^2 - \omega^2)}, \quad m_2^2 = k^2 - \frac{\omega^2}{c_2^2}, \tag{3.1}$$

and

$$\Lambda_0 = \frac{i\rho_0\omega}{m_0}, \quad \Lambda_1 = -\frac{i\rho_1(k^2v_{\mathrm{A1}}^2 - \omega^2)}{m_1\omega}, \quad \Lambda_2 = \frac{i\rho_2\omega}{m_2}, \tag{3.2}$$

respectively. By letting $x_0 = -x_1$, the matrix form of the dispersion relation, Equation (2.13), reduces to

$$\det\begin{pmatrix} C_0 - S_0 & -C_1 & S_1 & 0\\ \Lambda_0(C_0 - S_0) & \Lambda_1S_1 & -\Lambda_1C_1 & 0\\ 0 & C_1 & S_1 & S_2 - C_2\\ 0 & \Lambda_1S_1 & \Lambda_1C_1 & -\Lambda_2(S_2 - C_2) \end{pmatrix} = 0, \tag{3.3}$$

where $C_i = \cosh m_ix_1$ and $S_i = \sinh m_ix_1$, for $i = 0, 1, 2$. This can be written in non-matrix form as

$$\Lambda_1^2 + \Lambda_0\Lambda_2 + \Lambda_1(\Lambda_0 + \Lambda_2)\coth 2m_1x_1 = 0. \tag{3.4}$$

Using the original notation, the dispersion relation is

$$\omega^4m_1^2 + \frac{\rho_1}{\rho_0}m_0\frac{\rho_1}{\rho_2}m_2(k^2v_{\mathrm{A1}}^2 - \omega^2)^2 - m_1\omega^2(k^2v_{\mathrm{A1}}^2 - \omega^2) \left(\frac{\rho_1}{\rho_0}m_0 + \frac{\rho_1}{\rho_2}m_2\right)\coth 2m_1x_1 = 0. \tag{3.5}$$

This agrees with the dispersion relation derived by Allcock and Erdélyi (2017), with a different subscript labeling.

This has implications for mode identification. Most notably, **Table 1** highlights that merely observing cross-sectional oscillation is insufficient for the identification of sausage modes, and merely observing axial oscillation is insufficient for the

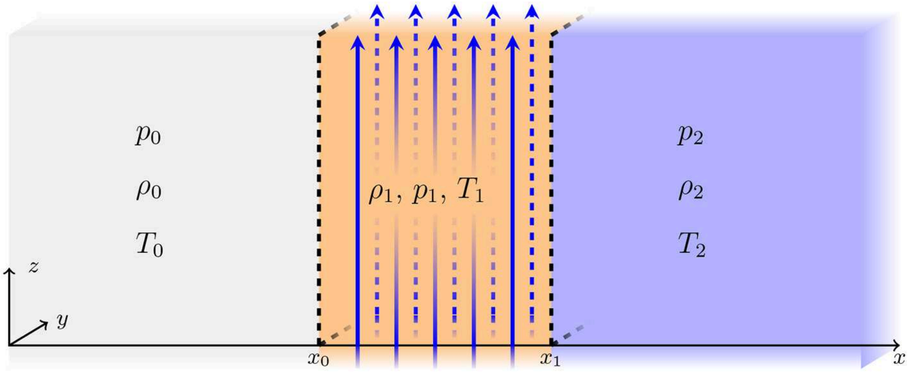

FIGURE 2 | The equilibrium configuration for a magnetic slab in an asymmetric non-magnetic environment.

identification of kink modes. It is a combination of these features and the phase relationship of the boundary oscillations that allows us to accurately identify these modes.

The eigenmodes can be further categorized as surface and body modes, depending on whether the solution to the governing equations is evanescent or spatially oscillatory, respectively, within the slab. The main physical implication of this is that the amplitude, or wave power in observations, peaks at the boundaries of the waveguide for surface modes, and at one or more anti-nodes within the waveguide for body modes. Compared to body modes, surface modes are significantly more sensitive to the background plasma and hence the background asymmetry (Allcock and Erdélyi, 2017).

3.2. Slab in an Asymmetric Magnetic Environment

Generalizing the stationary slab embedded in an asymmetric plasma leads us to the model of the magnetic slab embedded in an asymmetric magnetic environment. By letting $n = 1$, but keeping the magnetic fields in the external regions (unlike in section 3.1), we reduce the general multi-waveguide structure to a single magnetic slab waveguide in an asymmetric homogeneous non-magnetic environment (see **Figure 3**, and also Zsámberger et al., 2018).

In this case, the parameters related to the wavenumbers and the total pressure in all three domains are expressed as

$$m_j^2 = \frac{\left(k^2 v_{Aj}^2 - \omega^2\right)\left(k^2 c_j^2 - \omega^2\right)}{\left(v_{Aj}^2 + c_j^2\right)\left(k^2 c_{Tj}^2 - \omega^2\right)},$$

$$\Lambda_j = -\frac{i\rho_j}{\omega}\frac{k^2 v_{Aj}^2 - \omega^2}{m_j}, \qquad \text{for } j = 0, 1, 2. \tag{3.6}$$

By letting $x_0 = -x_1$, we obtain the following dispersion relation

$$m_1^2\left(k^2 v_{A0}^2 - \omega^2\right)\left(k^2 v_{A2}^2 - \omega^2\right) + \frac{\rho_1}{\rho_0} m_0 \frac{\rho_1}{\rho_2} m_2 \left(k^2 v_{A1}^2 - \omega^2\right)^2 + \rho_1 m_1 \left(k^2 v_{A1}^2 - \omega^2\right)\left[\frac{m_2}{\rho_2}\left(k^2 v_{A0}^2 - \omega^2\right) + \frac{m_0}{\rho_0}\left(k^2 v_{A2}^2 - \omega^2\right)\right] \coth 2m_1 x_1 = 0. \tag{3.7}$$

TABLE 1 | The defining characteristics of each category of eigenmode.

Mode	Boundary oscillation phase relationship	Cross-sectional oscillation?	Axial oscillation?
Sausage	In anti-phase	Yes	No
Kink	In phase	No	Yes
Quasi-sausage	In anti-phase	Yes	Yes
Quasi-kink	In phase	Yes	Yes

For the full derivation of the dispersion relation using the shifted coordinate system (defined by $x_0 = -x_1$, as in section 3.1), see Allcock and Erdélyi (2017) for the externally field-free, and Zsámberger et al. (2018) for the externally magnetic asymmetric slab system. Note also that if we remove the external magnetic fields, Equation (3.7) reduces to the dispersion relation for the externally field-free one-slab system (Equation 3.5).

In general, the solutions of the exact dispersion relation for both the externally field-free and magnetic asymmetric slab systems are the mixed-nature quasi-sausage and quasi-kink modes. **Figure 4** shows a few characteristic examples of how the introduction of asymmetry influences the distribution of the transverse velocity perturbation of these eigenmodes under circumstances corresponding to lower solar atmospheric environments.

4. APPLICATION TO THE LOWER SOLAR ATMOSPHERE

In this section, we discuss two of the different diagnostic approaches and methods that are possible to pursue with asymmetric slab models. First, we demonstrate the power of the so-called amplitude ratio method with a specific application to surface waves, by briefly outlining the solar magneto-seismology theory of asymmetric MHD waveguides (section 4.1.1), and then applying this theory we estimate the Alfvén speed in several chromospheric fibrils (sections 4.1.2–4.1.7). Then, to illustrate how body waves can be used for diagnostic purposes, we discuss the analytical solutions of the asymmetric slab environment when

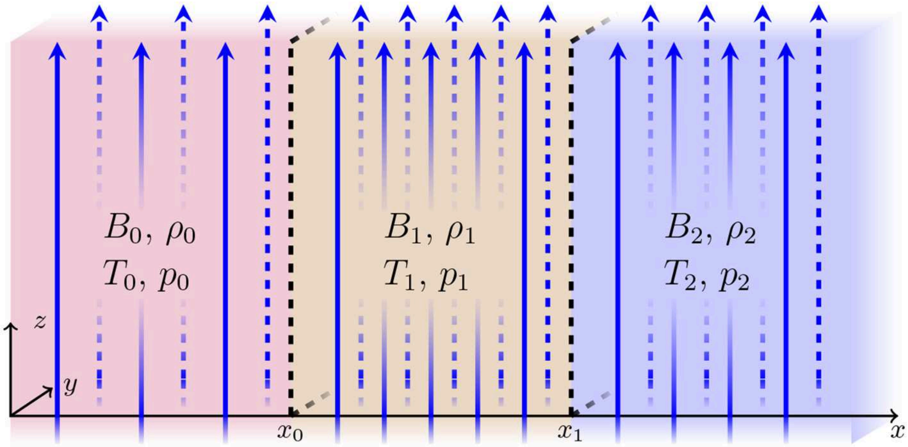

FIGURE 3 | Equilibrium configuration for the magnetic slab in an asymmetric magnetic environment.

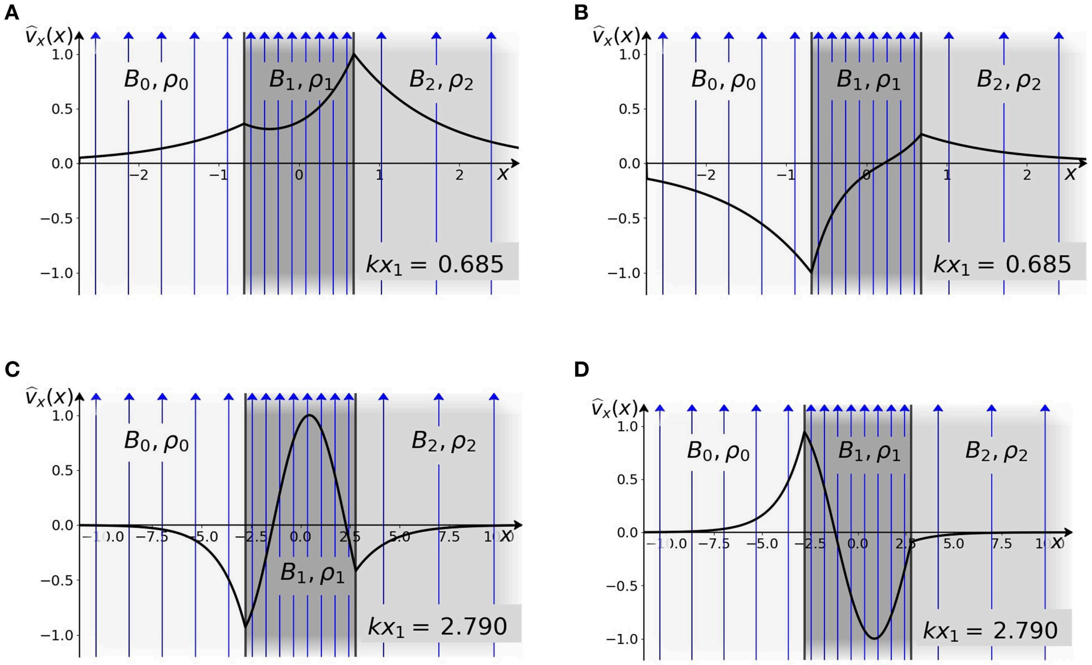

FIGURE 4 | Distribution of the transverse velocity perturbation amplitude ($\hat{v}_x$) in a strongly magnetized slab and its rarefied asymmetric environment, plotted with solid black curves, as a function of the transverse spatial coordinate, x. Lighter gray shading represents lower background densities, while the blue arrows show the equilibrium magnetic fields, and darker gray shading corresponds to higher background densities. In **(A)**, a slow quasi-kink surface mode, in **(B)**, a slow quasi-sausage surface mode, in **(C)**, a fast quasi-kink body mode of order one, and in **(D)**, a fast quasi-sausage body mode of order one is presented. **(A,B)** correspond to a thin slab ($kx_1 = 0.685$), while **(C,D)** represent a wide slab ($kx_1 = 2.790$). These solutions to the dispersion relation (Equation 3.7) were obtained numerically, for a slab system characterized by $v_{A1} = 0.7c_1$, $v_{A0} = 0.2c_1$, $v_{A2} = 0.1c_1$, $c_0 = 2.23c_1$, $c_2 = 1.87c_1$, $\rho_0/\rho_1 = 0.28$, and $\rho_2/\rho_1 = 0.4$.

the kinetic pressure dominates the magnetic pressure, as occurs in the low solar atmosphere (section 4.2).

4.1. Solar Magneto-Seismology With Asymmetric Waveguides

At present, some properties of the solar atmosphere, such as the strength of the magnetic field in the chromosphere and the corona, are very hard to measure directly from emitted or absorbed radiation. To get an estimate of such parameters, we must rely on observables which depend on the unknown parameter by proxy. The asymmetry of solar MHD waveguides is a proxy for the internal magnetic field. In this section, we summarize the Amplitude Ratio Method for solar magneto-seismology of asymmetric waveguides, first derived by Allcock and Erdélyi (2018), and use it to make the first demonstration of an inversion of the local Alfvén speed in the solar atmosphere using asymmetric MHD waves.

4.1.1. Amplitude Ratio Method

MHD waves perturb waveguides in the solar atmosphere in a non-uniform manner. Moreover, the wave power is distributed transversely across the waveguide in a way unique to the mode of oscillation and the background parameters. In particular, asymmetry in the background parameters is mirrored by asymmetry in the transverse distribution of wave power, that is, in the eigenfunction (e.g., **Figure 4**). One way to quantify this asymmetry is to take the ratio of the signed amplitudes, R_{A}, at each interface of the waveguide, i.e.,

$$R_{\mathrm{A}} = \frac{\hat{\xi}_x(x_1)}{\hat{\xi}_x(-x_1)}, \tag{4.1}$$

where $\hat{\xi}_x$ is the transverse displacement and is evaluated at each boundary, $\pm x_1$. Through derivation of the eigenfunctions for each mode (see Allcock and Erdélyi, 2018, for more details), we can express this in terms of the wave parameters and equilibrium parameters,

$$R_{\mathrm{A}} = -\frac{\rho_0 m_2}{\rho_2 m_0}\left[\frac{(k^2 v_{\mathrm{A}1}^2 - \omega^2) m_0 \frac{\rho_1}{\rho_0} - \omega^2 m_1 \frac{1}{\tanh m_1 x_1}}{(k^2 v_{\mathrm{A}1}^2 - \omega^2) m_2 \frac{\rho_1}{\rho_2} - \omega^2 m_1 \frac{1}{\tanh m_1 x_1}}\right], \tag{4.2}$$

for quasi-sausage modes, and

$$R_{\mathrm{A}} = \frac{\rho_0 m_2}{\rho_2 m_0}\left[\frac{(k^2 v_{\mathrm{A}1}^2 - \omega^2) m_0 \frac{\rho_1}{\rho_0} - \omega^2 m_1 \tanh m_1 x_1}{(k^2 v_{\mathrm{A}1}^2 - \omega^2) m_2 \frac{\rho_1}{\rho_2} - \omega^2 m_1 \tanh m_1 x_1}\right], \tag{4.3}$$

for quasi-kink modes. For quasi-sausage modes, the amplitude ratio is negative due to the anti-phase boundary oscillations, and for quasi-kink modes, the amplitude ratio is positive due to the in-phase boundary oscillations. By taking all the other parameters as measured inputs, the internal Alfvén speed, v_{A1}, can be estimated by numerically inverting this equation. In the following application of this SMS technique, we use the Amplitude Ratio Method, as described above, to estimate the Alfvén speed in several chromospheric fibrils.

4.1.2. Alfvén Speed Inversion of Chromospheric Fibrils

The Alfvén speed in the chromospheric quiet Sun is highly inhomogeneous, due to the many magnetic structures that make up the magnetic canopy, and undergoes a steep gradient from 15 $\mathrm{km\,s^{-1}}$ in photospheric flux tubes to $1,000\ \mathrm{km\,s^{-1}}$ in the corona (van Ballegooijen et al., 2011). Techniques including photospheric magnetic field extrapolation and magneto-seismology make up an arsenal of methods for characterizing the chromospheric magnetic field, yet the Alfvén speed in specific chromospheric structures remains hard to determine (Wiegelmann et al., 2014). Here, we apply the Amplitude Ratio Method to diagnose the Alfvén speed in several chromospheric fibrils as a demonstration of a new magneto-seismology technique to add to the picture.

The data were taken from observations close to the disk center with a narrow-band 0.25 Å Hα core (6562.8 Å) filter on the 29th September 2010 using the Rapid Oscillations in the Solar Atmosphere (ROSA) imager on the Dunn Solar Telescope (Jess et al., 2010). The data show a dynamic sea of dark dense fibrils that map, at least partially, the inter-network magnetic field overlying the bright and less dense plasma that permeates the quiet Sun (Leenaarts et al., 2012). The implementation of the Amplitude Ratio Method involves resolving sub-fibril structure, for which the ROSA instrument's high spatial (150 km) and temporal resolution (7.68 s) were necessary and just barely sufficient, with 10-20 pixels across each fibril.

More information about the observations is detailed by Morton et al. (2012), who originally used the same data for the analysis of ubiquitous MHD waves in the chromosphere. They interpreted the observed fibril oscillations as concurrent sausage and kink modes of circular cross-sectional magnetic flux-tubes. In the present analysis, we propose an alternative interpretation that the oscillations are MHD oscillations in asymmetric waveguides. Evidence in favor of the present interpretation comes from the observation that the oscillations in the transverse axial displacement, the cross-sectional width, and the integrated intensity across the fibrils are both in phase and demonstrate a similar phase speed (see Morton et al., 2012). However, we wish to make it clear that this interpretation is taken mainly to *demonstrate* a new SMS technique which depends on the existence of waveguide asymmetry. The evidence for or against either interpretation (concurrent modes in symmetric waveguides or individual modes in asymmetric waveguides) is too weak to be strongly conclusive.

In the absence of MHD wave theory in asymmetric cylindrical waveguides, we model each fibril as an isolated magnetic slab whose boundaries are parallel discontinuities between the uniform internal plasma and the asymmetric external plasma (e.g., **Figure 2**). Only sufficiently isolated fibrils that maintain their structure for at least a full period were analyzed.

4.1.3. Boundary Tracking

A primary slit is placed perpendicularly across each fibril and time-distance data produced from an average of the intensities across the primary slit and two parallel neighboring slits, placed at a distance of 1 pixel either side (**Figure 5A**). This averaging technique over several slits is used to increase the signal-to-noise ratio.

To find the boundaries of the fibrils so that the boundary oscillation amplitudes can be determined, we fit a Gaussian function to each time frame of the time-distance data (**Figure 5B**). The boundaries are taken to be the positions along the slit at which the fitted Gaussian reaches half-maximum. Due to the limited number of data-points across each fibril, the high signal-to-noise ratio, and to improve the fitting stability, for time frames when the Gaussian fitting failed, the fitting domain was reduced to 10 pixels either side of the boundaries on the previous time step.

Fibrils for which the stabilized Gaussian fitting failed on a significant proportion of time steps were omitted from the analysis. The boundaries were cross-checked and the small

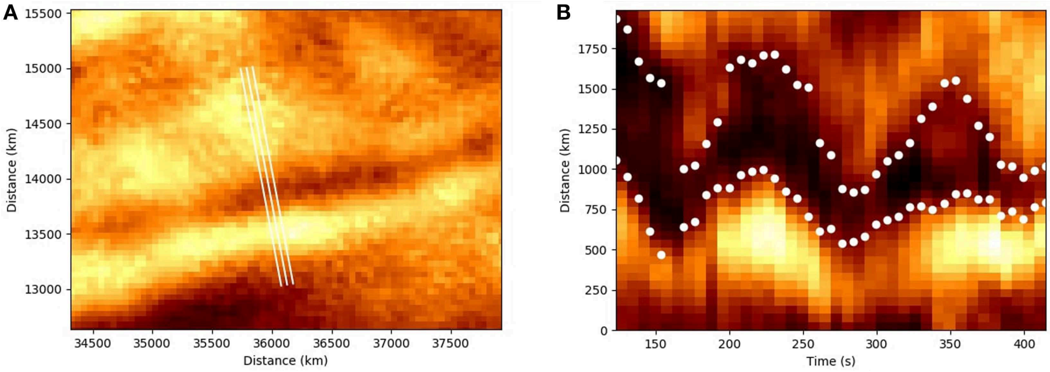

FIGURE 5 | (A) A typical example of a ROSA Hα fibril taken at $t = 399.36$ s from the start of the observational window. The middle slit is placed perpendicular to the fibril. The mean of the intensities along the middle slit and two parallel slits at a pixel each side at each time step is plotted in **(B)**. The white dots correspond to the boundaries of the fibril, calculated as the position of half-maximum of the fitted Gaussian. Axis values are in units from the bottom left of the observational domain.

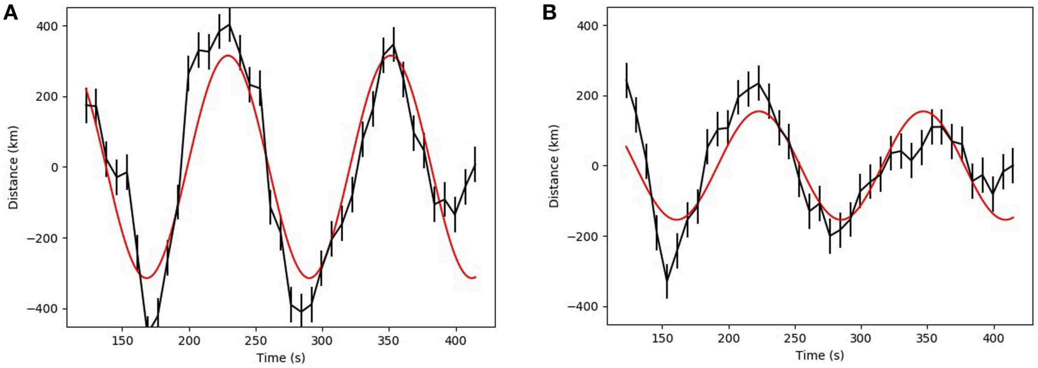

FIGURE 6 | (A) Top and **(B)** bottom boundary positions along the averaged slits given in **Figure 5A** (black line), detrended with a cubic polynomial. The error bounds on each point are the pixel size and therefore correspond to the error in the observations rather than the error in the trend fitting so represent a lower bound on the total error. The boundaries are fitted with a sinusoid (red line).

number of isolated anomalous points were smoothed over using a linear interpolation between the preceding and following time frames. The width of each fibril was taken as the mean distance between the boundaries throughout the time window for which the stabilized Gaussian fitting was successful.

4.1.4. Frequency and Amplitude Measurement

For each fibril, both sets of boundary data were then detrended with a cubic polynomial fit by least-squares regression. The detrended boundaries were then fit with a sinusoidal curve (**Figure 6**) due to there being too few data points to make wavelet analysis useful. The frequency of each wave is taken to be the average of the frequencies of both boundary sinusoids. The amplitude ratio is the signed ratio of the amplitudes of the boundary sinusoids.

4.1.5. Phase Speed Measurement

For each fibril, we plotted the cross-sectional width variation through time at five parallel slits, each five pixels apart and perpendicular the fibril. The widths at each time-step were calculated as the position of the half-maximum of the fitted Gaussian function along each slit. The intensity along each of the five slits used for the phase speed measurement is the mean of the intensities across three parallel slits spaced a pixel apart, as described in section 4.1.3. The width variation was smoothed with a 3-point box-car function and the temporal lag in the smoothed width variation was fitted with a straight line (see **Figure 7**). The gradient of this line is the estimated phase speed.

The measured phase speeds assume that the fibril waveguides are parallel to the plane-of-sky (PoS). In reality, the waveguides are inclined at some angle θ to the PoS. Therefore, the true phase speed will be a factor of $\sec(\theta)$ greater than the measured phase speed. Unfortunately, using the given data it is impossible to infer the angle θ. The best we can do is use the fact that the fibrils tend to track the magnetic field of the magnetic canopy, which is dominated by a horizontal magnetic field, to motivate the assumption that θ is small. Under this assumption, we can take $\sec(\theta) \approx 1$, to leading order, from which it follows that the true phase speed is approximately equal to the measured phase speed in the observational plane.

Additionally, it might appear that we have assumed that the oscillations are approximately polarized in the PoS because the

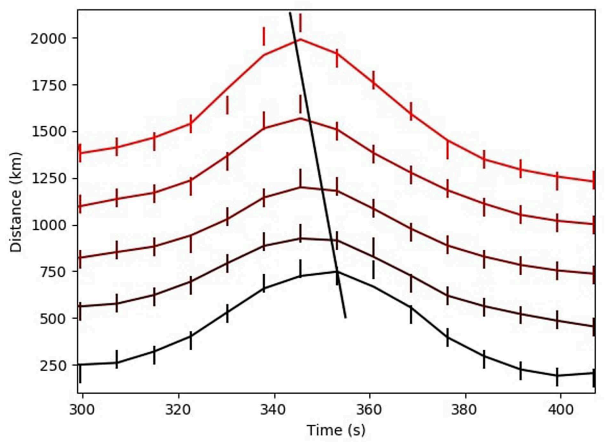

FIGURE 7 | Five parallel slits, spaced by five pixels, are placed perpendicular to each fibril. The widths, calculated from the fitted Gaussian along each slit, are plotted and displaced in the y-direction by five pixels = 250 km, the distance between each slit. The peaks and troughs of the width oscillations are fitted by a straight line, the gradient of which is approximately the phase speed.

amplitudes are measured in the observational plane. However, the amplitudes only enter the inversion calculation as a ratio, therefore eliminating any projection effects anyway.

4.1.6. Inversion Procedure

Using the results from section 4.1.2, we employed a numerical inversion procedure to estimate the Alfvén speed within the fibrils (more information can be found in Allcock and Erdélyi, 2018). First, for each fibril oscillation, the mode of oscillation (quasi-sausage or quasi-kink) was determined by assessment of the phase-shift between the oscillations on each boundary. After prescribing all the parameters apart from the internal Alfvén speed, v_{A1}, in Equations (4.2) or (4.3) (depending on the mode identified), the secant method was used to find the Alfvén speed estimation.

For each inversion, we specified an internal sound speed of $c_0 = 10$ km s^{-1} and density ratios of $\rho_1/\rho_0 = 0.1$ and $\rho_2/\rho_0 = 0.2$, and vice versa depending on which side had the largest amplitude. In the absence of any density-sensitive proxies from the data, they were chosen to match the order of magnitude difference between the densities external and internal to the fibrils as expected from previous fibril observations (Leenaarts et al., 2012; Morton et al., 2012).

To reduce the chance of finding the wrong root when the inverse problem is multi-valued, a hundred initial values for v_A evenly spaced between 1 and 200 km s^{-1} were tried and only fibrils for which the inversion produced the same value for almost all of the initial values were included in the results.

4.1.7. Results

We made a successful inversion of five chromospheric fibrils and recorded the parameters in **Table 2**. Two of the fibrils were identified as oscillating in the quasi-kink mode and three in the quasi-sausage mode. All of the identified MHD modes are expected to be fast modes due to their phase speeds exceeding the expected sound speed. Fibril 1 exhibited a change in direction of propagation before breaking up. The other fibril oscillations propagated in one direction for the duration of the time for which Gaussian fitting was successful. The inverted Alfvén speeds agree with expected values for chromospheric fibrils (Morton et al., 2012). Although, we acknowledge the high degree of uncertainty in present and previous chromospheric Alfvén speed estimates.

The error in the inversions due to the input parameters comes mainly from the density ratios. In Allcock and Erdélyi (2018), we determined that the relative errors in the density ratios are reduced by a factor of two when propagated into the errors in the inverted Alfvén speed. However, this was calculated by using an analytical inversion procedure, which involved taking a further approximation of the model. In the present work, we have used a numerical inversion procedure to avoid having to make such an approximation. To determine how the density errors propagate through the numerical inversion implemented here, we ran the inversion for a range of density parameters. We found that the relative error in each density ratio is approximately halved after propagating through the numerical inversion. As an example, for fibril 1, an input density ratio of $\rho_2/\rho_0 = 0.4$ rather than 0.2, i.e., a 100% difference, leads to an Alfvén speed estimate of 44.8 km s^{-1}, approximately 50% greater than the 30.5 km s^{-1} estimated using $\rho_2/\rho_0 = 0.2$.

4.2. High-Beta Asymmetric Slab Eigenmodes

The dispersion relations of each slab configuration provide us with a wide variety of normal solutions. Since a completely general analytical description of all these waves does not seem possible, it is a worthwhile endeavor to further study the various solutions and uncover certain fundamental analytical relationships between the relevant parameters, next to, of course, applying the above-mentioned numerical inversion schemes.

One possible avenue is to examine how the ratios of plasma and magnetic pressures in all the domains influence the existence and properties of the different types of normal modes. This ratio is described by the plasma-β parameter, defined as $\beta_j = p_j/p_{j,m}$ for a domain j, where p_j is the plasma pressure and $p_{j,m}$ is the magnetic pressure in the given domain.

As the solar atmosphere shows a range of complex and fine magnetic structures, we have chosen the externally magnetic asymmetric slab model to provide an example of the theoretical side of the investigation. Furthermore, since we have primarily focused on lower solar atmospheric applications, we will limit this section to the discussion of high-β asymmetric slab systems.

For the case when Λ_2 is of the same order as Λ_0, it is possible to derive an approximate decoupled dispersion relation, which is given by

$$(k^2 v_{A1}^2 - \omega^2)\left[\frac{\rho_1}{\rho_0}\frac{m_0}{(k^2 v_{A0}^2 - \omega^2)} + \frac{\rho_1}{\rho_2}\frac{m_2}{(k^2 v_{A2}^2 - \omega^2)}\right] + 2m_1\begin{pmatrix}\tanh\\ \coth\end{pmatrix}\{m_1 x_1\} = 0. \qquad (4.4)$$

Unlike the full dispersion relation (Equation 3.7), this relation, applicable to the special case of weak asymmetry, decouples

TABLE 2 | A table of measured parameters, identified mode, and estimated local Alfvén speed of five chromospheric fibrils.

Fibril	Width km	Frequency s^{-1}	Phase speed km s^{-1}	Amplitude ratio	Asymmetric eigenmode	Estimated alfvén speed km s^{-1}
1	463	0.0285	63 (and −63)	1.29	Quasi-kink	30.5
2	997	0.0328	63	−0.407	Quasi-sausage	91.7
3	1120	0.0800	63	−3.42	Quasi-sausage	75.5
4	530	0.0198	31	−3.13	Quasi-sausage	49.4
5	551	0.0511	129	2.04	Quasi-kink	63.1

into a separate equation for quasi-sausage (tanh version) and quasi-kink (coth version) eigenmodes, which is analogous to the decoupling of the symmetric case detailed in Edwin and Roberts (1982). In the infinite-β limit, magnetic forces are negligible compared to the pressure gradient force, i.e., $c_j/v_{Aj} \gg 1$, for $j = 0, 1, 2$. In this scenario, only essentially purely acoustic body waves occur. If we take into account that the total pressure must balance across the boundaries, and that the pressure in this case is purely the kinetic pressure, the dispersion relation (Equation 4.4) can be reduced to

$$\begin{pmatrix}\tan\\ -\cot\end{pmatrix}\{n_{1z}x_1\} = \frac{1}{2}\left(\frac{m_{0z}}{n_{1z}}\frac{c_0^2}{c_1^2} + \frac{m_{2z}}{n_{1z}}\frac{c_2^2}{c_1^2}\right), \tag{4.5}$$

where

$$m_{jz} = \left(\frac{k^2c_j^2 - \omega^2}{c_j^2}\right)^{1/2}, \qquad \text{for } j = 0, 1, 2, \tag{4.6}$$

and $n_{1z}^2 = -m_{1z}^2$ is a modified wavenumber coefficient introduced in the description of body waves (see e.g., Edwin and Roberts, 1982). For trapped body waves to exist, the conditions n_{1z}, m_{0z} and $m_{2z} > 0$ must be fulfilled. This necessitates that the angular frequency of the waves should satisfy $k^2c_1^2 < \omega^2 < \min(k^2c_0^2, k^2c_2^2)$. The band of fast body waves therefore exists in the phase speed interval between the internal sound speed and the lower of the two external ones. Due to the periodicity of the tangent and cotangent functions, an infinite number of harmonics exist in the direction of structuring. Introducing the notation $c_m = \min(c_0, c_2)$, the waves are expected to behave as $\omega^2 = k^2c_m^2[\rho_m/\rho_1]\left[1 + \nu/(kx_1)^2\right]$. By using the general method of describing body waves irrespective of plasma-β value (see e.g., Roberts, 1981a; Allcock and Erdélyi, 2017), the coefficients ν_j can be determined. This leads to the following expression for the quasi-sausage mode solutions:

$$\omega^2 = k^2c_m^2\frac{\rho_m}{\rho_1}\left[1 + \frac{\pi^2\left(j - \frac{1}{2}\right)^2}{k^2x_1^2}\right]. \tag{4.7}$$

The approximation for quasi-kink modes becomes

$$\omega^2 = k^2c_m^2\frac{\rho_m}{\rho_1}\left[1 + \frac{\pi^2 j^2}{k^2x_1^2}\right]. \tag{4.8}$$

A basic diagnostic purpose may be fulfilled by making these approximations. Namely, Equations (4.7) and (4.8) showcase a simple connection between the lower external sound speed, and the ratio of the same side's external density to the internal one for any given value of the wavenumber and angular frequency of a given order body mode. Thus, knowledge of one of these parameters can provide an estimate of the other.

In accordance with our analytical expectations, seeking numerical solutions in a few interesting high-β configurations reveals that, while a few types of eigenmodes will not occur in high-β slab systems, we can still hope to detect several types of waves in lower solar atmospheric conditions. For example, **Figure 8A** illustrates the results of the numerical examination in a typical high-β equilibrium configuration. There is a band of fast body modes confined between the sound speeds and a band of slow body modes between the internal Alfvén and cusp speeds. Here, slow surface waves are present as well, which would not occur in the low-β limit (corresponding more closely to higher atmospheric conditions).

Since the magnetic pressure is negligible compared to the plasma pressure in the high-β limit, the possible eigenmodes would not change qualitatively if the relative magnitudes of the external and internal Alfvén speeds were interchanged. On the contrary, if the internal sound speed were greater than the external ones ($c_1 > c_0, c_2$), no fast waves (neither body, nor surface) could be expected in the system, only slow surface and body waves.

Additionally, **Figure 8B** illustrates an exciting characteristic not just of high-β systems, but of asymmetric slab systems in general. In this diagnostic diagram, we find slow body modes ($c_{T1} < v_{ph} < v_{A1}$) and slow surface modes ($v_{A1} < v_{ph} < c_1$) in the region of lower phase speeds. Interestingly, the slow surface quasi-kink mode starts out in the band of fast body modes for thin slabs (small kx_1), while the slow surface quasi-sausage mode begins as a slow body mode. Both of them change character as they progress toward wider slabs (kx_1 increases). Additionally, the region of trapped fast body modes is split into three narrower bands ($c_1 < v_{ph} < c_{T0}$, $v_{A0} < v_{ph} < c_{T2}$, and $v_{A2} < v_{ph} < c_0$). This is due to the fact that the asymmetry introduces new cut-off frequencies for the dispersion curves, potentially excluding significant phase speed intervals from the regime of trapped oscillations.

5. ASYMMETRIC NON-STATIONARY WAVEGUIDES

So far, we have considered one-slab and multi-slab systems filled with static plasma. However, the study of waveguides

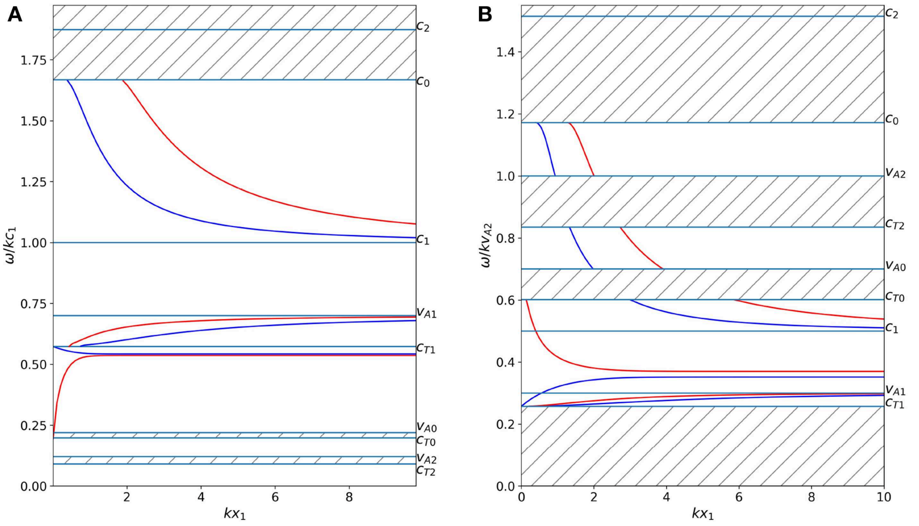

FIGURE 8 | Solutions to the dispersion relation for high-β cases. **(A)** Slow and fast mode body waves, as well as slow surface waves are present when $v_{A1} = 0.7c_1$, $v_{A0} = 0.2c_1$, $v_{A2} = 0.1c_1$, $c_0 = 1.6683c_1$, $c_2 = 1.8742c_1$, $\rho_0/\rho_1 = 0.5$, $\rho_2/\rho_1 = 0.4$. **(B)** Three bands of fast body modes, one band of slow body modes, and a pair of slow surface modes exist when $v_{A1} = 0.2v_{A2}$, $v_{A0} = 0.7v_{A2}$, $c_1 = 0.5v_{A2}$, $c_0 = 1.1v_{A2}$, $c_2 = 1.8v_{A2}$, $\rho_0/\rho_1 = 0.2008$, $\rho_2/\rho_1 = 0.1163$. In each panel, only a couple of examples in each band of body modes are displayed. Blue (red) curves illustrate quasi-sausage (quasi-kink) modes. No trapped oscillations exist in the hatched regions.

incorporating steady flows has also been an important aspect of solar atmospheric research (see e.g., Nakariakov and Roberts, 1995; Terra-Homem et al., 2003). The inclusion of flows in our models modifies the phase speeds and cut-off speeds of the observable modes, and it opens up the possibility for the Kelvin-Helmholtz instability (KHI) to appear in the system. In order to showcase some of these meaningful physical additions to the behavior of perturbations in our MHD waveguides, in this section we will analyse MHD wave propagation in a few non-stationary slab systems that characterize solar waveguides with bulk flows present.

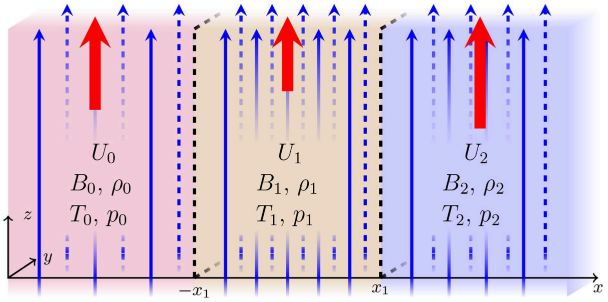

FIGURE 9 | The equilibrium configuration for a steady and magnetized slab embedded in a steady, magnetized, and asymmeric semi-infinite plasma. The notation is the same as in the previous figures, with the addition of the thick red arrows representing the vertical plasma flow, $U(x)\hat{z}$.

5.1. General Non-stationary Slab

The complex and dynamic solar atmosphere is observed to contain plasma flows and instances of Kelvin-Helmholtz Instability (KHI) throughout (e.g., Ryutova et al., 2010; Ofman and Thompson, 2011; Zhelyazkov, 2015). In the light of these detections, we can further extend the applicability of our slab models if we lift the restriction of static plasma, and allow for the presence of background bulk flow motions in one or several domains in the equilibrium.

Let us therefore consider a new one-slab model that incorporates asymmetric plasma with magnetic fields and steady flows. The slab is bounded by two interfaces at $\pm x_1$. Both the slab and the semi-infinite domains that enclose it are filled with uniform, compressible, inviscid plasma of different density, ρ, pressure, p, and temperature, T. Each part of the system is permeated by vertical magnetic fields, $\hat{\mathbf{B}} = B\hat{\mathbf{z}}$, of different strength, and is subject to steady flows in the vertical direction, $\hat{\mathbf{U}} = U\hat{\mathbf{z}}$, of different speeds:

$$F(x) = \begin{cases} F_0 & x < -x_1, \\ F_1 & -x_1 < x < x_1, \\ F_2 & x_1 < x, \end{cases} \tag{5.1}$$

where F_j denotes any of the five physical scalar parameters listed above, namely $F_j =$ constant , for $j = 0, 1, 2$ (**Figure 9**).

We assume, as before, that perturbations within the system are governed by the ideal MHD equations (Equations 2.1). This time, we linearize these in the presence of U_j equilibrium steady flows, and then we perform Fourier-analysis, seeking plane wave solutions that propagate along the slab. Thus, a governing equation is obtained for each domain, which is formally similar to the case of the stationary slab systems:

$$\hat{v}_x'' - M_j^2 \hat{v}_x = 0, \tag{5.2}$$

where

$$M_j^2 = \frac{\left(k^2 v_{Aj}^2 - \Omega_j^2\right)\left(k^2 c_j^2 - \Omega_j^2\right)}{\left(v_{Aj}^2 + c_j^2\right)\left(k^2 c_{Tj}^2 - \Omega_j^2\right)}, \qquad \textit{for } j = 0, 1, 2. \tag{5.3}$$

Due to the presence of a steady background flow, however, instead of the angular frequency, ω, it is the Doppler-shifted frequency, defined as

$$\Omega_j = \omega - kU_j, \qquad \textit{for } j = 0, 1, 2, \tag{5.4}$$

that appears in all the coefficients.

Physically realistic trapped wave solutions still have to be evanescent far away from the slab (as $x \to \pm\infty$), and uphold the continuity of the total pressure perturbation and the Lagrangian displacement across the slab boundaries. In order to find a non-trivial solution for the system of equations formulated by these boundary conditions, we have to solve

$$\det \begin{pmatrix} \frac{C_0 - S_0}{\Omega_0} & \frac{-C_1}{\Omega_1} & \frac{S_1}{\Omega_1} & 0 \\ 0 & \frac{C_1}{\Omega_1} & \frac{S_1}{\Omega_1} & -\frac{C_2 - S_2}{\Omega_2} \\ \Lambda_0(C_0 - S_0) & \Lambda_1 S_1 & -\Lambda_1 C_1 & 0 \\ 0 & \Lambda_1 S_1 & \Lambda_1 C_1 & -\Lambda_2(S_2 - C_2) \end{pmatrix} = 0, \tag{5.5}$$

where

$$\Lambda_j = -\frac{i\rho_j}{\Omega_j M_j}(k^2 v_{Aj}^2 - \Omega_j^2), \quad C_j = \cosh M_j x_1, \quad S_j = \sinh M_j x_1. \tag{5.6}$$

Written in terms of the characteristic speeds, the dispersion relation, Equation (5.5), of the general steady asymmetric slab system, takes the following form:

$$\frac{M_1^2}{\rho_1^2(k^2 v_{A1}^2 - \Omega_1^2)^2} + \frac{M_0 M_2}{\rho_0 \rho_2 (k^2 v_{A0}^2 - \Omega_0^2)(k^2 v_{A2}^2 - \Omega_2^2)} + \frac{M_1}{(k^2 v_{A1}^2 - \Omega_1^2)} \left(\frac{M_0}{\rho_0^2 (k^2 v_{A0}^2 - \Omega_0^2)} + \frac{M_2}{\rho_2^2 (k^2 v_{A2}^2 - \Omega_2^2)} \right) \coth 2M_1 x_1 = 0. \tag{5.7}$$

This relation is formally analogous to Equation (3.7) governing the static asymmetric slab system in a magnetic environment. Here, however, flows are present in all the domains, therefore, the Doppler-shifted frequencies take the place of the "ordinary" angular frequency in every expression.

Furthermore, just like in the case of the static asymmetric slab system, an approximate, decoupled dispersion relation can be obtained if conditions are different, but closely similar on the two sides of the slab:

$$(k^2 v_{A1}^2 - \Omega_1^2) \left[\frac{\rho_1}{\rho_0} \frac{M_0}{(k^2 v_{A0}^2 - \Omega_0^2)} + \frac{\rho_1}{\rho_2} \frac{M_2}{(k^2 v_{A2}^2 - \Omega_2^2)} \right] + 2M_1 \begin{pmatrix} \tanh \\ \coth \end{pmatrix} \{M_1 x_1\} = 0. \tag{5.8}$$

For any unspecified measure of asymmetry, though, we have to note that (similarly to the stationary case) the dispersion relation of the asymmetric slab system does not decouple into separate equations for traditional (i.e., symmetric) sausage and kink modes, but instead, remains as one expression describing both quasi-sausage and quasi-kink modes. We can therefore say that in the most general description of a uniform, asymmetric one-slab system, the eigenmodes will reflect the differences between the external parameters on either side of the slab and possess mixed characteristics of the traditional (symmetric) sausage and kink mode oscillations.

5.2. Steady Slab in an Asymmetric Non-magnetic Environment

A special case of the general steady one-slab model has been studied by Barbulescu and Erdélyi (2018), whose results are summarized and adapted to our notation in the following subsection. They analyzed the propagation of magnetoacoustic waves and the threshold for the KHI in a magnetic slab under the effect of a steady flow, which was enclosed in an asymmetric, non-magnetic environment filled with stationary plasma (**Figure 10**). They derived the full dispersion relation of this configuration, which, in our notation, becomes

$$M_1^2 \omega^4 + \frac{\rho_1}{\rho_0} m_0 \frac{\rho_1}{\rho_2} m_2 \left(k^2 v_{A1}^2 - \Omega_1^2\right)^2 - M_1 \omega^2 \left(k^2 v_{A1}^2 - \Omega_1^2\right) \left(\frac{\rho_1}{\rho_0} m_0 + \frac{\rho_1}{\rho_2} m_2 \right) \coth 2M_1 x_1 = 0, \tag{5.9}$$

where

$$m_j^2 = \frac{\left(k^2 v_{Aj}^2 - \omega^2\right)\left(k^2 c_j^2 - \omega^2\right)}{\left(v_{Aj}^2 + c_j^2\right)\left(k^2 c_{Tj}^2 - \omega^2\right)}, \quad \text{for } j = 0, 2,$$

$$M_1^2 = \frac{\left(k^2 v_{A1}^2 - \Omega_1^2\right)\left(k^2 c_1^2 - \Omega_1^2\right)}{\left(v_{A1}^2 + c_1^2\right)\left(k^2 c_{T1}^2 - \Omega_1^2\right)}, \quad \Omega_1 = \omega - kU_1. \tag{5.10}$$

Equation (5.9) can be obtained as a special case of Equation (5.7) by setting the external magnetic fields and flows to $B_0 = B_2 = U_0 = U_2 = 0$.

In the presence of internal or external flows, it is worthwhile to extend the investigation of eigenmodes to negative phase speeds as well, since the symmetry between forward- and backward-propagating modes that characterizes stationary slabs, becomes broken in the presence of a steady state. Barbulescu and Erdélyi (2018) demonstrated that a strong enough internal flow is able to shift backward propagating modes into forward propagating ones. The presence of external asymmetry does not influence this phenomenon; instead, it manifests through the introduction of new, additional cut-off frequencies for trapped oscillations. Furthermore, any deviation from symmetry of the parameters in the external plasma regions leads to a greater range of slab widths (kx_1) for which the system is KH unstable.

An exciting application of this model can be found, e.g., in the form of KHI detected at the flank of a coronal mass ejection (CME). Based on observations of Foullon et al. (2011),

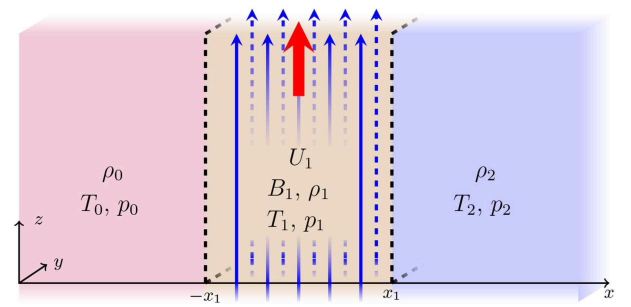

FIGURE 10 | The equilibrium configuration for a steady and magnetized slab in an asymmetric non-magnetic environment.

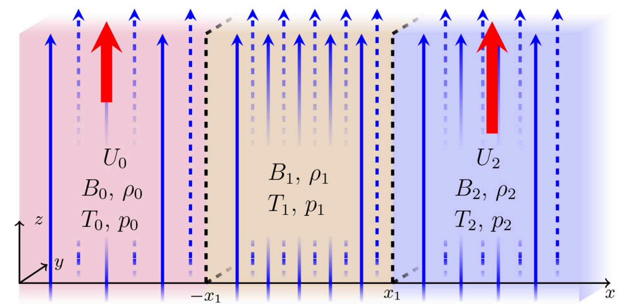

FIGURE 11 | The equilibrium configuration for a slab with two external flows.

made using the Atmospheric Imaging Assembly on board the Solar Dynamics Observatory on November 3, 2010, Barbulescu and Erdélyi (2018) modeled the structure made up of the CME core, the CME flank, and the lower-density solar corona as a non-stationary slab enclosed between two static regions. They interpreted the observations as a slow kink mode and, by finding numerical solutions to the dispersion relation that agreed with the observed values, provided an estimate for the density of the CME ejecta.

The authors noted, however, that a limitation on the validity of this result stems from the inability of the model to explain why the KHI was not observed between the CME core and flank regions. A further approximation they made was that they considered the CME core to be static, since on the timescale of the KHI, the flow in that region is much slower than on the flank (Barbulescu and Erdélyi, 2018). Considering these simplifications, it might be advantageous to use a more complex model that includes external magnetic fields everywhere, as well as flows in the external domains, such that will be described in the following section.

5.3. Steady Slab in an Asymmetric Magnetic Environment With Bulk Flows

An interesting generalization of the steady slab problem, which offers some analytical simplification and reduces the number of parameters needed for a possible inversion from observational data, but still keeps the broad applicability of the model, is a configuration in which different magnetic fields permeate all parts of the asymmetric slab system, while only the internal plasma is stationary (**Figure 11**). For such a model, the dispersion relation (Equation 5.7) reduces to

$$\frac{m_1^2}{(k^2 v_{A1}^2-\omega^2)^2}+\frac{\rho_1}{\rho_0}\frac{\rho_1}{\rho_2}\frac{M_0 M_2}{(k^2 v_{A0}^2-\Omega_0^2)(k^2 v_{A2}^2-\Omega_2^2)} + \frac{m_1}{(k^2 v_{A1}^2-\omega^2)}\left(\frac{\rho_1}{\rho_0}\frac{M_0}{(k^2 v_{A0}^2-\Omega_0^2)}+\frac{\rho_1}{\rho_2}\frac{M_2}{(k^2 v_{A2}^2-\Omega_2^2)}\right) \coth 2m_1 x_1 = 0, \tag{5.11}$$

with

$$m_1^2=\frac{(k^2 v_{A1}^2-\omega^2)(k^2 c_1^2-\omega^2)}{(v_{A1}^2+c_1^2)(k^2 c_{T1}^2-\omega^2)},$$
$$M_j^2=\frac{\left(k^2 v_{Aj}^2-\Omega_j^2\right)\left(k^2 c_j^2-\Omega_j^2\right)}{\left(v_{Aj}^2+c_j^2\right)\left(k^2 c_{Tj}^2-\Omega_j^2\right)}, \quad \text{for } j=0,2. \tag{5.12}$$

The decoupled dispersion relation also takes a simpler form:

$$(k^2 v_{A1}^2-\omega^2)\left[\frac{\rho_1}{\rho_0}\frac{M_0}{(k^2 v_{A0}^2-\Omega_0^2)}+\frac{\rho_1}{\rho_2}\frac{M_2}{(k^2 v_{A2}^2-\Omega^2)}\right] + 2m_1\begin{pmatrix}\tanh\\ \coth\end{pmatrix}\{m_1 x_1\}=0. \tag{5.13}$$

Of particular interest is once again the case when the system is filled with high-β plasma in each region, which is representative of the conditions in the lower atmospheric layers of our Sun. In order to better demonstrate the effect that the bulk flows have on the permitted modes, we can convert the previous two-flow system into a configuration containing one internal and one external flow by changing the frame of reference. Now $U_{2,\text{new}}=0$, $U_{1,\text{new}}=-U_{2,\text{old}}$, and $U_{0,\text{new}}=U_{0,\text{old}}-U_{2,\text{old}}$. In the analytically tractable approximation of infinite-β, to describe fast body modes, Equation (5.13) in the new frame of reference simply becomes

$$\frac{1}{2}\left(\frac{c_0}{c_1}\frac{M_0}{N_1}\frac{\Omega_1^2}{\Omega_0^2}+\frac{c_2}{c_1}\frac{m_2}{N_1}\frac{\Omega_1^2}{\omega^2}\right)=\begin{pmatrix}\tan\\ -\cot\end{pmatrix}\{N_1 x_1\}, \tag{5.14}$$

where $N_1^2=-M_1^2$. The analytical description of the expected backward- and forward-propagating fast body waves, in this case, becomes

$$\omega=k\left(U_{1,\text{new}}\pm c_1\left[1+\frac{\left\{j-\frac{1}{2}\right\}^2\pi^2}{\left\{kx_1\right\}^2}\right]^{1/2}\right), \quad \text{for } j=1,2,3..., \tag{5.15}$$

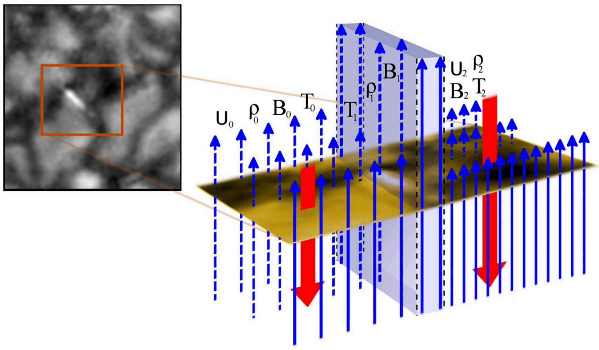

FIGURE 12 | An elongated magnetic bright point visualized as a non-stationary slab. The sketch is based on Figure 12 of Liu et al. (2018), showing TiO 7058 Å observations taken by the New Vacuum Solar Telescope, and a further development on the model featured in Zsámberger et al. (2018). Blue arrows represent the magnetic field lines, and red arrows represent flowing plasma.

for quasi-sausage modes, and

$$\omega = k\left(U_{1,\mathrm{new}} \pm c_1\left[1+\frac{j^2\pi^2}{\{kx_1\}^2}\right]^{1/2}\right), \quad \text{for } j = 1, 2, 3..., \tag{5.16}$$

for quasi-kink modes. The equilibrium bulk flow directly affects the phase speed of the guided waves, as it can be seen. Further numerical evaluations reveal that both the internal and external flow speeds can significantly change the angular frequency of the supported modes and influence the magnitudes of cut-off frequencies.

Although it is possible to convert such a configuration into an analytically more advantageous one, due to the initial asymmetry between the steady and static regions, new, unique variations arise in this configuration, which cannot be made symmetric or fully externally stationary simply by a change in the frame of reference, like it was possible in the case of a symmetric plasma environment described by Nakariakov and Roberts (1995).

A prime candidate for applying the high-beta two-flow slab model can be found in magnetic bright points in the solar photosphere. These small concentrations of intense magnetic field are wedged into the dark inter-granular lanes. Often, MBPs display an elongated shape (Liu et al., 2018), which makes it possible to treat them as asymmetric magnetic slabs (for the details and limitations of this approach, see Zsámberger et al., 2018). Let us now consider an isolated MBP enclosed in-between two segments of an inter-granular lane, which will serve as the asymmetric environment, as illustrated by **Figure 12**. Since the sound speed in the photosphere is around 7 km/s (Hurlburt et al., 2002), we will assume $c_0 = 7$ km s^{-1} and $c_2 = 8$ km s^{-1} to demonstrate our point. Following Keys et al. (2013), we set the internal sound speed to $c_1 = 12$ km s^{-1}, and choose the internal Alfvén speed as $v_{A1} = 10$ km s^{-1}. Taking into consideration that the magnetic field is significantly weaker outside a bright point, we assume external Alfvén speeds of $v_{A0} = 2.05$ km s^{-1} and $v_{A2} = 3$ km s^{-1}. We note that the actual values chosen are estimates and serve to demonstrate how asymmetry is relevant to wave propagation or to the formation of the KHI threshold. To apply our model, we consider the equilibrium bulk flow speed inside the slab to be negligible ($U_1 = 0$ km s^{-1}), and set the other two to values that we could realistically expect in the downflows of intergranular lanes (see Briand and Solanki 1998; Socas-Navarro et al. 2004; Danilovic et al. 2010): $U_0 = -2$ km s^{-1}, $U_1 = -8$ km s^{-1} (where the negative signs correspond to downflows, while positive values would quantify upflows). The resulting wave solutions to the dispersion relation can be seen in **Figure 13**.

For this particular parameter set, only slow mode solutions exist. While in the static case, the characteristic speeds delineate the cut-off frequencies, in a steady slab, these have to be modified by the flow speeds, which makes the propagation of not only slow surface modes (as in the static case for the same set of characteristic speeds and densities), but also that of slow body modes ($-c_0 + U_0 < v_{ph} < -c_{T1}$) possible. In the presence of such high flow speeds, the symmetry between backward- and forward-propagating modes is strongly broken, as **Figure 13** illustrates. This diagnostic diagram contains the real parts of the solutions colored blue, and the imaginary parts (of the surface modes) colored red, in order to let us discern stable and unstable modes. Namely, only the latter possess a non-zero imaginary component, which corresponds to an amplitude growth factor (Barbulescu and Erdélyi, 2018). In the case of the model MBP that we use here to demonstrate the permitted solutions of the dispersion relation, the surface mode solutions (having phase speeds in the range $-c_{T1} < v_{ph} < c_{T0} + U_0$) are subject to KHI easily (see the dashed part of the blue curve in **Figure 13**) if the slab is thin. In a wide slab, on the other hand, the wave perturbations can be stable (continuous blue curves), but they do not exist as trapped oscillations for every value of the dimensionless slab width (kx_1): in the hatched regions, only leaky modes are found. The solutions would not become unstable for any value of kx_1 if the slab was symmetric and the flow speeds did not exceed the internal Alfvén speed. Due to the introduction of the asymmetry, however, the KHI-threshold is lowered, and the instability can set in in this model MBP even though both of the external flow speeds are sub-Alfvénic.

A further application of the asymmetric slab configuration containing two (or even three) different flows can be found in the alternating spine-intraspine pattern of the fibrillar structure in the penumbrae of sunspots, which is closely connected to the Evershed-flow (Tsiropoula, 2000; Borrero and Ichimoto, 2011). Besides the solar atmosphere, the triad of the Earth's magnetopause, magnetosheath, and bow shock region can also be locally considered as a slab-like structure that incorporates varying flows and magnetic fields (Turkakin et al., 2013). Since the asymmetry in the system enables the KHI to develop for a wide range of parameters (Barbulescu and Erdélyi, 2018), this model can also offer a possible explanation of the observed instability in both of these locations.

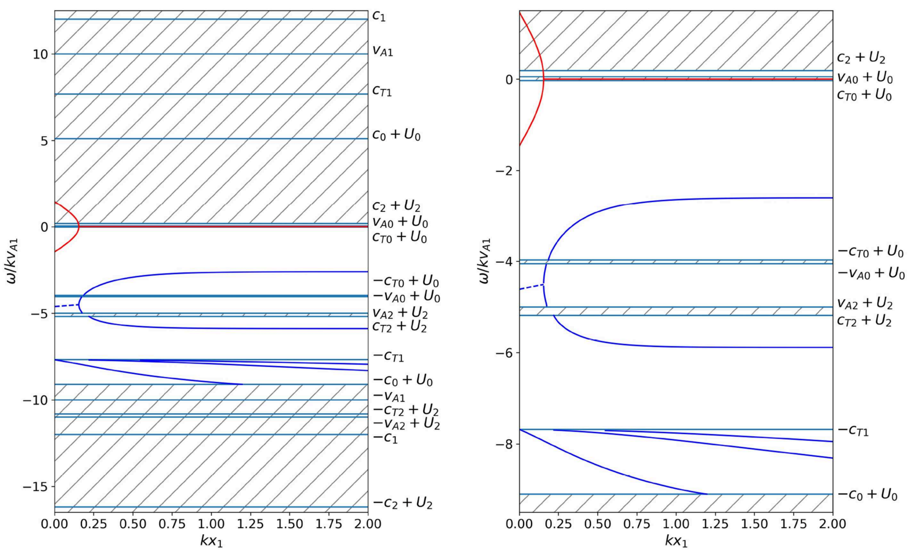

FIGURE 13 | Solutions to the dispersion relation for a high-β MBP. The diagram on the left displays the full range of characteristic speeds, while for the one on the right, the narrower band of interest is enlarged. While in the static case, the characteristic speeds delineate the cut-off frequencies, in a steady slab, these have to be modified by the flow speeds.

6. CONCLUSIONS

The propagation of linear MHD waves in a multi-layered magnetized plasma structure is studied in the Cartesian slab geometry approximation. Each magnetic slab is uniform and non-stratified (i.e., neither density nor magnetic stratification is considered). A general dispersion relation is derived for a mathematical model of this plasma structured by an arbitrary number of interfaces and two special cases of a plasma slab embedded in an asymmetric non-magnetic and magnetic environment are considered. Unlike the symmetric case, the obtained dispersion relation does not decouple into two dispersion relations of independent wave mode solutions. This coupling manifests as mixed properties of the eigenmodes, which are referred to as quasi-kink and quasi-sausage wave solutions to the governing linear magneto-acoustic equations. These newly obtained eigenmodes are generalizations of the traditionally known sausage and kink modes of symmetric linear MHD waveguides (**Table 1**).

The asymmetry of waveguides, which is highly likely in many solar structures due to the structural inhomogeneity of the various observed MHD waveguides in the solar atmosphere, is a proxy for background parameters of the waveguide. Motivated by this idea, the Amplitude Ratio Method from Allcock and Erdélyi (2018) is employed, as a proof of concept, to estimate the local Alfvén speed in five chromospheric fibrils using Hα data from the ROSA imager. We find that many of the observed fibrils displayed asymmetric oscillatory behavior, which we interpret here as quasi-kink and quasi-sausage eigenmodes, depending on the phase relationship between the boundary oscillations. The estimates of the local Alfvén speed, obtained after inverting the observed information, agree with highly uncertain expected values from photospheric extrapolations.

Incorporating asymmetric external magnetic fields into the slab model provides a further useful middle-ground between the breadth of applications and analytical tractability. From coronal hole boundaries, through prominences, to MBPs of the photosphere, a variety of solar atmospheric fine structures can be more closely described as a magnetized asymmetric slab system. Next to numerical root-finding methods, making certain well-known approximations, such as investigating the limit of a thin or a wide slab, low or high values of the plasma-β, allows us to concisely describe the various quasi-sausage, quasi-kink, surface, or body modes that we expect, and to identify some of their fundamental characteristics.

A further step in generalizing the newly developed asymmetric slab models is to move away from stationary plasmas, and incorporate equilibrium bulk flows (i.e., steady states) in one or more regions. This generalization has the consequence that the angular frequencies are replaced by their Doppler-shifted counterparts in the dispersion relations, and the cut-off frequencies for the different eigenmodes are influenced by the magnitudes of the flows. An externally stationary asymmetric slab system serves as a reasonable approximation of CME flank regions. Including multiple external bulk flows widens the scope of applicability to e.g., MBPs residing between sections of different inter-granular flows, fibrils in the dynamic sunspot penumbra, and the magnetosheath region of Earth's magnetosphere. Therefore, for all these features, such a slab configuration can offer a reasonable initial model that explains the observed KHI.

The one- or multi-slab approach to asymmetric waveguides has wide applicability in different layers of the solar atmosphere.

MHD waves have been observed in many structures of our Sun, and to correctly interpret some of them, the asymmetry of their environments should be taken into account.

A variety of waves have been observed in sunspot structures, for example, in the penumbra, which itself shows a filamentary structure. Neighboring filaments may be modeled by different plasma and magnetic parameters, and they have been observed to support upward propagating slow-mode magneto-acoustic waves in the form of running penumbral waves (Bloomfield et al., 2007; Freij et al., 2014; Löhner-Böttcher and Bello González, 2015). The multi-slab model may be a good approximation for high-frequency waves. Another sunspot element where asymmetry of the plasma environment could heavily influence wave propagation is the light bridge and corresponding light wall reaching up into higher layers of the atmosphere, which are trapped between two, sometimes vastly different umbral cores. Oscillations recently detected in light walls have been interpreted as signatures of propagating magneto-acoustic (shock) waves (Yang et al., 2015; Zhang et al., 2017).

Small, bright magnetic flux concentrations are located in the intergranular lanes wedged in-between two granular cells, whose plasma and magnetic properties can potentially be highly different. This asymmetry then naturally affects the characteristics of any waves present in the above-mentioned MBPs. These small-scale magnetic elements, which might take on the appearance of a nearly circular flux tube or a strongly elongated slab-like structure, have been put forward as the photospheric anchor points of chromospheric waveguides that show sausage-mode oscillations (Morton et al., 2012). The existence of a wealth of magneto-acoustic oscillations within MBPs themselves has also been concluded from high-cadence observations performed at different altitudes (Jess et al., 2012). Chromospheric manifestations of bright points have been confirmed to sway around their photospheric counterparts, signaling the presence of kink type oscillations (Xiong et al., 2017).

In section 4, we have already addressed that chromospheric fibrils exist in a complex, asymmetric environment, and whether they are considered as flux tubes or as magnetic slabs, the asymmetry can lead to the appearance of different-looking modes, for which previously the only explanation was the simultaneous presence of sausage and kink type waves (Morton et al., 2012; Mooroogen et al., 2017). Higher up in the solar atmosphere, MHD waves are also found in prominences (Arregui et al., 2018), which themselves lie between different layers of the vertically stratified corona. Another coronal example of applicability could be the studies of MHD wave propagation at the boundary of coronal holes (see e.g., Banerjee et al., 2000; Banerjee, 2012).

Additionally, Alfvén waves are also known to propagate in the solar atmosphere. However, Alfvén waves are local waves as opposed to the sausage and kink waves that have a global character. Alfvén waves propagate along constant magnetic surfaces. If there is a suitable driver, each magnetic surface supports its own Alfvén wave, which will be characterized by the properties of the individual flux sheets and will not be strongly affected by the rest of the plasma environment. Because of this, Alfvén waves are not very promising disturbances for the application of our magneto-seismological technique described in this paper.

As detailed above, recent high-resolution state-of-the-art ground-based or space-borne observations clearly show that there is strong structuring (inhomogeneity) and dynamics in the observed solar (and magnetospheric) MHD waveguides. Solar MHD wave theory is boosted by the development of solar magneto-seismology; see the avalanche of Space Sci. Reviews since 2010. SMS is an excellent tool to obtain sub-resolution information about MHD waveguides present in the Sun. Here we make a step forward by applying this tool to structured MHD waveguides by demonstrating, as a proof-of-concept in a limited number of test cases, how this newly developed tool can be used for the much wanted solar plasma diagnostics. This latter result has an additional importance, given that the field of solar physics is at the brink of its greatest historic development: the imminent commencing of our 4 m aperture ground-based DKIST telescope.

DATA AVAILABILITY

The datasets for this manuscript are not publicly available because Data can be requested freely directly from the corresponding author. Requests to access the datasets should be directed to robertus@sheffield.ac.uk.

AUTHOR CONTRIBUTIONS

The research concept was formulated and the project led by RE. MA derived the results of the asymmetric slab in a non-magnetic environment, including the associated solar magneto-seismology theory, and application to observations. DS derived the results of the general multi-layered waveguide. NZ derived the results of the asymmetric slab in a magnetic environment and the generalizations to flowing plasma, and prepared the sample parametric solutions presented.

ACKNOWLEDGMENTS

MA acknowledges support from the University Prize Scholarship awarded by the University of Sheffield. DS acknowledges support from the University of Sheffield. NZ is grateful for the support of the University of Debrecen and the University of Sheffield. RE is grateful to Science and Technology Facilities Council (STFC_grant_nr_ST/M000826/1) UK for the support received. Observations were obtained at the National Solar Observatory, operated by the Association of Universities for Research in Astronomy, Inc. (AURA), under agreement with the National Science Foundation. We would like to thank the technical staff at the DST for their help and support during the observations. Further thanks are required for M. Mathioudakis Francis Keenan (Queen's University Belfast, UK) for ROSA support in 2010 when the observing proposal was awarded and data taken. For the relevant ROSA data discussed in the paper please contact RE, while access to the overall ROSA archive is available via weblink[1].

---

[1] https://star.pst.qub.ac.uk/wiki/doku.php/public/research_areas/solar_physics/rosa_reconstructed_archive

All authors acknowledge the valuable input from M. Barbulescu regarding waves and instabilities in steady plasma and thank him for making available the PyTES software package (https://github.com/BarbulescuMihai/PyTES). The authors are also grateful to F. Allian for use of and assistance with his code for processing the ROSA Hα data.

REFERENCES

Allcock, M., and Erdélyi, R. (2017). Magnetohydrodynamic waves in an asymmetric magnetic slab. *Solar Phys.* 292:35. doi: 10.1007/s11207-017-1054-y

Allcock, M., and Erdélyi, R. (2018). Solar magnetoseismology with magnetoacoustic surface waves in asymmetric magnetic slab waveguides. *Astrophys. J.* 855:90. doi: 10.3847/1538-4357/aaad0c

Andries, J., van Doorsselaere, T., Roberts, B., Verth, G., Verwichte, E., and Erdélyi, R. (2009). Coronal seismology by means of Kink oscillation overtones. *Space Sci. Rev.* 149, 3–29. doi: 10.1007/s11214-009-9561-2

Arregui, I., Oliver, R., and Ballester, J. L. (2012). Prominence oscillations. *Living Rev. Solar Phys.* 9:2. doi: 10.12942/lrsp-2012-2

Arregui, I., Oliver, R., and Ballester, J. L. (2018). Prominence oscillations. *Living Rev. Sol. Phys.* 15:3. doi: 10.1007/s41116-018-0012-6

Ballai, I., and Ruderman, M. S. (2011). Nonlinear effects in resonant layers in solar and space plasmas. *Space Sci. Rev.* 158, 421–450. doi: 10.1007/s11214-010-9717-0

Banerjee, D. (2012). "Diagnosing chromosphere- Corona connection by waves in open structures," in *39th COSPAR Scientific Assembly, Vol. 39* (Mysore), 96.

Banerjee, D., Teriaca, L., Doyle, J. G., and Lemaire, P. (2000). Polar Plumes and Inter-plume regions as observed by SUMER on SOHO. *Solar Phys.* 194, 43–58. doi: 10.1023/A:1005253413687

Barbulescu, M., and Erdélyi, R. (2018). Magnetoacoustic waves and the Kelvin-Helmholtz instability in a steady asymmetric slab. I: the effects of varying density ratios. *Solar Phys.* 293:86. doi: 10.1007/s11207-018-1305-6

Berger, T. E., and Title, A. M. (1996). On the dynamics of small-scale solar magnetic elements. *Astrophys. J.* 463:365. doi: 10.1086/177250

Bloomfield, D. S., Lagg, A., and Solanki, S. K. (2007). The nature of running penumbral waves revealed. *Astrophys. J.* 671, 1005–1012. doi: 10.1086/523266

Borrero, J. M., and Ichimoto, K. (2011). Magnetic structure of sunspots. *Living Rev. Sol. Phys.* 8:4. doi: 10.12942/lrsp-2011-4

Briand, C., and Solanki, S. K. (1998). Velocity fields below the magnetic canopy of solar flux tubes: evidence for high-speed downflows? *Astron. Astrophys.* 330, 1160–1168.

Danilovic, S., Schüssler, M., and Solanki, S. K. (2010). Magnetic field intensification: comparison of 3D MHD simulations with Hinode/SP results. *Astron. Astrophys.* 509:A76. doi: 10.1051/0004-6361/200912283

Díaz, A. J., Oliver, R., and Ballester, J. L. (2005). Fast magnetohydrodynamic oscillations in a multifibril Cartesian prominence model. *Astron. Astrophys.* 440, 1167–1175. doi: 10.1051/0004-6361:20052759

Díaz, A. J., and Roberts, B. (2006). Fast magnetohydrodynamic oscillations in a fibril prominence model. *Solar Phys.* 236, 111–126. doi: 10.1007/s11207-006-0137-y

Edwin, P. M., and Roberts, B. (1982). Wave propagation in a magnetically structured atmosphere. III - The slab in a magnetic environment. *Solar Phys.* 76, 239–259. doi: 10.1007/BF00170986

Foullon, C., Verwichte, E., Nakariakov, V. M., Nykyri, K., and Farrugia, C. J. (2011). Magnetic Kelvin-Helmholtz instability at the sun. *Astrophys. J. Lett.* 729:L8. doi: 10.1088/2041-8205/729/1/L8

Freij, N., Scullion, E. M., Nelson, C. J., Mumford, S., Wedemeyer, S., and Erdélyi, R. (2014). The detection of upwardly propagating waves channeling energy from the chromosphere to the low corona. *Astrophys. J.* 791:61. doi: 10.1088/0004-637X/791/1/61

Goossens, M., Erdélyi, R., and Ruderman, M. S. (2011). Resonant MHD waves in the solar atmosphere. *Space Sci. Rev.* 158, 289–338. doi: 10.1007/s11214-010-9702-7

Heyvaerts, J., and Priest, E. R. (1983). Coronal heating by phase-mixed shear Alfven waves. *Astron. Astrophys.* 117, 220–234.

Hurlburt, N. E., Alexander, D., and Rucklidge, A. M. (2002). Complete models of axisymmetric sunspots: magnetoconvection with coronal heating. *Astrophys. J.* 577, 993–1005. doi: 10.1086/342154

Jess, D. B., Mathioudakis, M., Christian, D. J., Keenan, F. P., Ryans, R. S. I., and Crockett, P. J. (2010). ROSA: A high-cadence, synchronized multi-camera solar imaging system. *Solar Phys.* 261, 363–373. doi: 10.1007/s11207-009-9500-0

Jess, D. B., Shelyag, S., Mathioudakis, M., Keys, P. H., Christian, D. J., and Keenan, F. P. (2012). Propagating wave phenomena detected in observations and simulations of the lower solar atmosphere. *Astrophys. J.* 746:183. doi: 10.1088/0004-637X/746/2/183

Keys, P. H., Mathioudakis, M., Jess, D. B., Shelyag, S., Christian, D. J., and Keenan, F. P. (2013). Tracking magnetic bright point motions through the solar atmosphere. *Mon. Not. Roy. Astron. Soc.* 428, 3220–3226. doi: 10.1093/mnras/sts268

Leenaarts, J., Carlsson, M., and Rouppe van der Voort, L. (2012). The formation of the Hα line in the solar chromosphere. *Astrophys. J.* 749:136. doi: 10.1088/0004-637X/749/2/136

Liu, Y., Xiang, Y., Erdélyi, R., Liu, Z., Li, D., Ning, Z., et al. (2018). Studies of isolated and non-isolated photospheric bright points in an active region observed by the new vacuum solar telescope. *Astrophys. J.* 856:17. doi: 10.3847/1538-4357/aab150

Löhner-Böttcher, J., and Bello González, N. (2015). Signatures of running penumbral waves in sunspot photospheres. *Astron. Astrophys.* 580:A53. doi: 10.1051/0004-6361/201526230

Luna, M., Terradas, J., Oliver, R., and Ballester, J. L. (2006). Fast magnetohydrodynamic waves in a two-slab coronal structure: collective behaviour. *Astron. Astrophys.* 457, 1071–1079. doi: 10.1051/0004-6361:20065227

Mathioudakis, M., Jess, D. B., and Erdélyi, R. (2013). Alfvén waves in the solar atmosphere. From theory to observations. *Space Sci. Rev.* 175, 1–27. doi: 10.1007/s11214-012-9944-7

Mooroogen, K., Morton, R. J., and Henriques, V. (2017). Dynamics of internetwork chromospheric fibrils: basic properties and magnetohydrodynamic kink waves. *Astron. Astrophys.* 607:A46. doi: 10.1051/0004-6361/201730926

Morton, R. J., Verth, G., Jess, D. B., Kuridze, D., Ruderman, M. S., Mathioudakis, M., et al. (2012). Observations of ubiquitous compressive waves in the Sun's chromosphere. *Nat. Commun.* 3:1315. doi: 10.1038/ncomms2324

Nakariakov, V. M., and Roberts, B. (1995). Magnetosonic waves in structured atmospheres with steady flows, I. *Solar Phys.* 159, 213–228. doi: 10.1007/BF00686530

Ofman, L., and Thompson, B. J. (2011). SDO/AIA observation of Kelvin-Helmholtz instability in the solar corona. *Astrophys. J. Lett.* 734:L11. doi: 10.1088/2041-8205/734/1/L11

Roberts, B. (1981a). Wave propagation in a magnetically structured atmosphere - II - waves in a magnetic slab. *Solar Phys.* 69, 39–56. doi: 10.1007/BF00151254

Roberts, B. (1981b). Wave propagation in a magnetically structured atmosphere. I - surface waves at a magnetic interface. *Solar Phys.* 69, 27–38. doi: 10.1007/BF00151253

Roberts, B., Edwin, P. M., and Benz, A. O. (1984). On coronal oscillations. *Astrophys. J.* 279, 857–865. doi: 10.1086/161956

Ruderman, M. S. (1992). Soliton propagation on multiple-interface magnetic structures. *J. Geophys. Res.* 97:16. doi: 10.1029/91JA02672

Ruderman, M. S., and Erdélyi, R. (2009). Transverse oscillations of coronal loops. *Space Sci. Rev.* 149, 199–228. doi: 10.1007/s11214-009-9535-4

Ryutova, M., Berger, T., Frank, Z., Tarbell, T., and Title, A. (2010). Observation of plasma instabilities in quiescent prominences. *Solar Phys.* 267, 75–94. doi: 10.1007/s11207-010-9638-9

Shukhobodskaia, D., and Erdélyi, R. (2018). Propagation of surface magnetohydrodynamic waves in asymmetric multilayered plasma. *Astrophys. J.* 868:128. doi: 10.3847/1538-4357/aae83c

Socas-Navarro, H., Martínez Pillet, V., and Lites, B. W. (2004). Magnetic properties of the solar internetwork. *Astrophys. J.* 611, 1139–1148. doi: 10.1086/422379

Terra-Homem, M., Erdélyi, R., and Ballai, I. (2003). Linear and non-linear MHD wave propagation in steady-state magnetic cylinders. *Solar Phys.* 217, 199–223. doi: 10.1023/B:SOLA.0000006901.22169.59

Tsiropoula, G. (2000). Physical parameters and flows along chromospheric penumbral fibrils. *Astron. Astrophys.* 357, 735–742. Available online at: https://ui.adsabs.harvard.edu/abs/2000A&A...357..735T

Turkakin, H., Rankin, R., and Mann, I. R. (2013). Primary and secondary compressible kelvin-helmholtz surface wave instabilities on the earth's magnetopause. *J. Geophys. Res.* 118, 4161–4175. doi: 10.1002/jgra.50394

van Ballegooijen, A. A., Asgari-Targhi, M., Cranmer, S. R., and DeLuca, E. E. (2011). Heating of the solar chromosphere and corona by Alfvén wave turbulence. *Astrophys. J.* 736:3. doi: 10.1088/0004-637X/736/1/3

Wiegelmann, T., Thalmann, J. K., and Solanki, S. K. (2014). The magnetic field in the solar atmosphere. *Astron. Astrophys. Rev.* 22:78. doi: 10.1007/s00159-014-0078-7

Xiong, J., Yang, Y., Jin, C., Ji, K., Feng, S., Wang, F., et al. (2017). The characteristics of thin magnetic flux tubes in the lower solar atmosphere observed by hinode/SOT in the G band and in Ca II H bright points. *Astrophys. J.* 851:42. doi: 10.3847/1538-4357/aa9a44

Yang, S., Zhang, J., Jiang, F., and Xiang, Y. (2015). Oscillating light wall above a sunspot light bridge. *Astrophys. J. Lett.* 804:L27. doi: 10.1088/2041-8205/804/2/L27

Zhang, J., Tian, H., He, J., and Wang, L. (2017). Surge-like oscillations above sunspot light bridges driven by magnetoacoustic shocks. *Astrophys. J.* 838:2. doi: 10.3847/1538-4357/aa63e8

Zhelyazkov, I. (2015). On modeling the Kelvin-Helmholtz instability in solar atmosphere. *J. Astrophys. Astron.* 36, 233–254. doi: 10.1007/s12036-015-9332-2

Zsámberger, N. K., Allcock, M., and Erdélyi, R. (2018). Magneto-acoustic waves in a magnetic slab embedded in an asymmetric magnetic environment: the effects of asymmetry. *Astrophys. J.* 853:136. doi: 10.3847/1538-4357/aa9ffe

Conflict of Interest Statement: The authors declare that the research was conducted in the absence of any commercial or financial relationships that could be construed as a potential conflict of interest.

The handling editor declared a past co-authorship with one of the authors RE.

A. APPENDIX

A.1. Boundary Conditions in Matrix Form

We rewrite the boundary conditions (2.10) in the compact matrix form (2.12) with $[2n+2]\times[2n+2]$ matrix $\mathbf{M}$. The precise form of the matrix with the first row corresponding to the continuity of the velocity at $x = x_0$, is

$$\begin{aligned}\mathbf{M}[1,1] &= \cosh m_0x_0 + \sinh m_0x_0, \quad \mathbf{M}[1,2] = -\cosh m_1x_0,\\ \mathbf{M}[1,3] &= -\sinh m_1x_0.\end{aligned} \tag{A1}$$

The second row represents the continuity of the total pressure at $x = x_0$:

$$\begin{aligned}\mathbf{M}[2,1] &= \Lambda_0(\cosh m_0x_0 + \sinh m_0x_0), \quad \mathbf{M}[2,2] = -\Lambda_1\sinh m_1x_0,\\ \mathbf{M}[2,3] &= -\Lambda_1\cosh m_1x_0.\end{aligned} \tag{A2}$$

The last but one row corresponds to the continuity of the velocity at $x = x_n$:

$$\begin{aligned}&\mathbf{M}[2n+1,2n] = \cosh m_nx_n, \quad \mathbf{M}[2n+1,2n+1] = \sinh m_nx_n,\\ &\qquad \mathbf{M}[2n+1,2n+2] = \sinh m_{n+1}x_n - \cosh m_{n+1}x_n.\end{aligned} \tag{A3}$$

Finally, the last row represents the continuity of the total pressure at $x = x_n$ and is

$$\begin{aligned}\mathbf{M}[2n+2,2n] &= \Lambda_n\sinh m_nx_n, \quad \mathbf{M}[2n+2,2n+1] = \Lambda_n\cosh m_nx_n,\\ \mathbf{M}[2n+2,2n+2] &= \Lambda_{n+1}(\cosh m_{n+1}x_n - \sinh m_{n+1}x_n).\end{aligned} \tag{A4}$$

For $1 \le j \le n-1$, general boundary condition takes the form

$$\begin{aligned}\mathbf{M}[2j+1,2j] &= \cosh m_jx_j,\\ \mathbf{M}[2j+1,2j+1] &= \sinh m_jx_j,\\ \mathbf{M}[2j+1,2j+2] &= -\cosh m_{j+1}x_j,\\ \mathbf{M}[2j+1,2j+3] &= -\sinh m_{j+1}x_j,\\ \mathbf{M}[2j+2,2j] &= \Lambda_j\sinh m_jx_j,\\ \mathbf{M}[2j+2,2j+1] &= \Lambda_j\cosh m_jx_j,\\ \mathbf{M}[2j+2,2j+2] &= -\Lambda_{j+1}\sinh m_{j+1}x_j,\\ \mathbf{M}[2j+2,2j+3] &= -\Lambda_{j+1}\cosh m_{j+1}x_j.\end{aligned} \tag{A5}$$

For the rest of the values i and j, $\mathbf{M}[i,j] = 0$.

Introducing the notation

$$\mathrm{C}_j^{(i)} = \cosh m_ix_j, \qquad \mathrm{S}_j^{(i)} = \sinh m_ix_j, \tag{A6}$$

and using Equations (A1)–(A5), the matrix in explicit form can be written as:

$$\begin{pmatrix} C_0^{(0)}+S_0^{(0)} & -C_0^{(1)} & -S_0^{(1)} & 0 & \cdots & \cdots\cdots & \cdots & 0 & 0 & 0 & 0\\ \Lambda_0(C_0^{(0)}+S_0^{(0)}) & -\Lambda_1S_0^{(1)} & -\Lambda_1C_0^{(1)} & 0 & \cdots & \cdots\cdots & \cdots & 0 & 0 & 0 & 0\\ 0 & C_1^{(1)} & S_1^{(1)} & -C_1^{(2)} & -S_1^{(2)} & 0\ \cdots & \cdots & 0 & 0 & 0 & 0\\ 0 & \Lambda_1S_1^{(1)} & \Lambda_1C_1^{(1)} & -\Lambda_2S_1^{(2)} & -\Lambda_2C_1^{(2)} & 0 & & \vdots & \vdots & \vdots & \vdots\\ \vdots & \vdots & \vdots & \vdots & & \ddots & & \vdots & \vdots & \vdots & \vdots\\ 0 & 0 & 0 & 0 & \cdots & \cdots\cdots & C_{n-1}^{(n-1)} & S_{n-1}^{(n-1)} & -C_{n-1}^{(n)} & -S_{n-1}^{(n)} & 0\\ 0 & 0 & 0 & 0 & \cdots & \cdots\cdots & \Lambda_{n-1}S_{n-1}^{(n-1)} & \Lambda_{n-1}C_{n-1}^{(n-1)} & -\Lambda_nS_{n-1}^{(n)} & -\Lambda_nC_{n-1}^{(n)} & 0\\ 0 & 0 & 0 & 0 & \cdots & \cdots\cdots & \cdots & 0 & C_n^{(n)} & S_n^{(n)} & S_n^{(n+1)}\\ 0 & 0 & 0 & 0 & \cdots & \cdots\cdots & \cdots & 0 & \Lambda_nS_n^{(n)} & \Lambda_nC_n^{(n)} & \Lambda_{n+1}(C_n^{(n+1)}-S_n^{(n+1)}) \end{pmatrix} \tag{A7}$$

frontiers
in Astronomy and Space Sciences

ORIGINAL RESEARCH
published: 13 August 2019
doi: 10.3389/fspas.2019.00057

The Temperature-Dependent Damping of Propagating Slow Magnetoacoustic Waves

S. Krishna Prasad[1]*, **David B. Jess**[1,2] and **Tom Van Doorsselaere**[3]

[1] Astrophysics Research Centre, School of Mathematics and Physics, Queen's University Belfast, Belfast, United Kingdom, [2] Department of Physics and Astronomy, California State University Northridge, Northridge, CA, United States, [3] Centre for Mathematical Plasma Astrophysics, KU Leuven, Leuven, Belgium

The rapid damping of slow magnetoacoustic waves in the solar corona has been extensively studied in previous years. Most studies suggest that thermal conduction is a dominant contributor to this damping, albeit with a few exceptions. Employing extreme-ultraviolet (EUV) imaging data from SDO/AIA, we measure the damping lengths of propagating slow magnetoacoustic waves observed in several fan-like loop structures using two independent methods. The dependence of the damping length on temperature has been studied for the first time. The results do not indicate any apparent decrease in damping length with temperature, which is in contrast to the existing viewpoint. Comparing with the corresponding theoretical values calculated from damping due to thermal conduction, it is inferred that thermal conduction is suppressed in hotter loops. An alternative interpretation that suggests thermal conduction is not the dominant damping mechanism, even for short period waves in warm active region loops, is also presented.

Keywords: magnetohydrodynamics (MHD), methods: observational, sun: atmosphere, sun: corona, sun: oscillations

Edited by:
Alina Catalina Donea,
Monash University, Australia

Reviewed by:
Keiji Hayashi,
Northwest Research Associates, United States
Rui Liu,
University of Science and Technology of China, China
Sergey Anfinogentov,
Institute of Solar-Terrestrial Physics (RAS), Russia

***Correspondence:**
S. Krishna Prasad
krishna.prasad@qub.ac.uk

Specialty section:
This article was submitted to Stellar and Solar Physics, a section of the journal Frontiers in Astronomy and Space Sciences

Received: *27 February 2019*
Accepted: *29 July 2019*
Published: *13 August 2019*

Citation:
Krishna Prasad S, Jess DB and Van Doorsselaere T (2019) The Temperature-Dependent Damping of Propagating Slow Magnetoacoustic Waves. Front. Astron. Space Sci. 6:57. doi: 10.3389/fspas.2019.00057

1. INTRODUCTION

Propagating waves along fan-like active region loops have been a common observational feature since their initial discovery in the solar corona (Ofman et al., 1997; Deforest and Gurman, 1998; Berghmans and Clette, 1999; De Moortel et al., 2000). Recent multi-wavelength observations have established the origin of these waves in the photosphere (Jess et al., 2012; Krishna Prasad et al., 2015), from where they could be channeled by magnetic fields into the corona (De Pontieu et al., 2005; Erdélyi, 2006; Khomenko et al., 2008). It is believed that these waves are a manifestation of propagating slow magnetoacoustic oscillations that are generated via mode conversion (Spruit, 1991; Cally et al., 1994) in the lower atmospheric layers. Their physical properties found in a variety of coronal structures have been extensively studied both from theoretical and observational vantage points (De Moortel, 2009; Wang, 2011; Krishna Prasad et al., 2012b; Banerjee and Krishna Prasad, 2016). In the solar corona, the slow magnetoacoustic waves undergo rapid damping and are consequently visible only over a small fraction of the loop length. A number of physical mechanisms such as thermal conduction, compressive viscosity, optically thin radiation, gravitational stratification, divergence of the magnetic field, etc., are known to affect the amplitude of slow magnetoacoustic waves. Thermal conduction, however, has been put forward as the dominant contributor for their damping (De Moortel and Hood, 2003, 2004). It must be noted that slow magnetoacoustic waves also exhibit frequency-dependent damping, with stronger dissipation at higher frequencies (Krishna Prasad et al., 2014, 2017) which, as well, is shown to be consistent with generalized damping via thermal conduction (Mandal et al., 2016).

Marsh et al. (2011) studied slow magnetoacoustic waves propagating within a coronal loop using stereoscopic images from STEREO/EUVI (Wuelser et al., 2004) and simultaneous spectroscopic data from Hinode/EIS (Culhane et al., 2007). It was found that thermal conduction was insufficient to explain the observed damping, and instead magnetic field divergence appeared to be the dominant factor. Marsh et al. (2011) explained that the discrepancy was due to the relatively longer oscillation periods (∼10 min) and colder temperatures (∼0.84 MK) observed within the loop. Following a method developed by Van Doorsselaere et al. (2011), Wang et al. (2015) estimated the polytropic index from the temperature and density perturbations corresponding to a standing slow magnetoacoustic wave observed in a hot flare loop. Based upon the value of the polytropic index ($\gamma = 1.64 \pm 0.08$) they obtained, Wang et al. (2015) inferred that thermal conduction is suppressed and that the observed damping could be explained by a slightly enhanced compressive viscosity term, which was later validated through magnetohydrodynamic (MHD) simulations (Wang et al., 2018). Krishna Prasad et al. (2018) investigated propagating slow magnetoacoustic waves in a number of active region fan-like loops and found a temperature dependency of the polytropic indices, whereby hotter loops corresponded to larger polytropic index values. However, the authors concluded that the polytropic index could be, in fact, affected by a range of physical processes, including an unknown heating mechanism, radiative losses, plasma flows, turbulence, etc., suggesting that a direct association between the polytropic index and thermal conduction cannot be unequivocally deduced. Indeed, Zavershinskii et al. (2019, private communication) found that an imbalance in the embedded plasma heating and cooling processes can actually cause temperature-dependent variations in the polytropic index. Here, we study the damping of short period (∼3 min) oscillations in quiescent active region fan-like loop structures, which was previously suggested to be the result of thermal conduction. The temperature dependency of the damping length is also investigated to find whether there are signatures of thermal conduction being suppressed in hotter loops. Details on the observational data used, the analysis methods employed, and the results obtained are presented in the subsequent sections, followed by a discussion of the obtained results and their implications for future studies of the solar corona.

2. OBSERVATIONS

Extreme-ultraviolet (EUV) imaging observations of solar coronal fan loops taken by the Atmospheric imaging assembly (AIA; Lemen et al., 2012) on-board the Solar Dynamics Observatory (SDO; Pesnell et al., 2012) are utilized for the present study. AIA captures the entire Sun in 10 different wavelength channels, from which 6 are mainly dedicated to coronal observations. Using online data browsing tools, such as Helioviewer[1], we selected 30 different active regions (ARs) with fan-like loop structures, where propagating oscillation signatures are clearly observed. The observations of these ARs span from 2011 to 2016, although a majority of them were taken between 2012 and 2014 (i.e., during the last solar maximum). For each active region, a 1-h-long image sequence, comprising of a small subfield ($\approx 180'' \times 180''$) surrounding the desired loop structures, is extracted for all 6 dedicated SDO/AIA coronal channels (94 Å, 131 Å, 171 Å, 193 Å, 211 Å, and 335 Å). The spatial sampling and the cadence of the data are $0.6''$ per pixel and 12 s, respectively. All of the data were processed using the `aia_prep` routine, which is available within the Solar SoftWare (SSW) environment, to perform the roll angle and plate scale corrections required for subsequent scientific analysis. To achieve accurate alignment between the data from multiple channels, and to successfully implement some of the above processing steps, we employed the robust pipeline developed by Rob Rutten[2]. This dataset was previously used in the study by Krishna Prasad et al. (2018), where complete observational details, including the locations, start times, active region numbers, etc., of the individual image sequences are listed.

3. ANALYSIS AND RESULTS

The fan-like loop structures within a sample active region (NOAA AR 12553) from the selected dataset are displayed in **Figure 1a**. Compressive oscillations, with a periodicity of ≈180 s, are found propagating outwards along these loop structures. In order to identify the oscillations and understand their propagation behavior, a time-distance map (De Moortel et al., 2000) is constructed from one of the loop segments bounded by the two solid blue lines marked in **Figure 1a**. The specific details of the method employed here are described in Krishna Prasad et al. (2012a), but in general, the intensities corresponding to the pixels across a selected loop segment are averaged to build a one-dimensional intensity profile along the loop, with similar profiles from successive images stacked together to generate a time-distance map. The final map obtained is shown in **Figure 1b**, with the x-axis displaying time in minutes and the y-axis displaying distance along the loop in megameters (Mm). Slanted ridges of alternating brightness, visible in this map, reveal the propagating waves along the selected loop. Previous studies of such oscillations, especially those propagating along similar fan-like loop structures that are usually rooted in sunspots, confirm their nature as propagating slow magnetoacoustic waves (e.g., Kiddie et al., 2012; Krishna Prasad et al., 2012b). To enhance the visibility of the ridges, the time series at each spatial position was filtered to allow only a narrow band of frequencies around the dominant oscillation period to remain. The filtered time-distance map is displayed in **Figure 1c**. It is clear that the amplitude of the oscillations is not constant, but instead varies with time and, in particular, decreases with distance along the loop from the corresponding foot point. The temporal modulation of the oscillation amplitude has been linked to the characteristics of

---

[1] https://helioviewer.org/

[2] http://www.staff.science.uu.nl/~rutte101/rridl/sdolib/

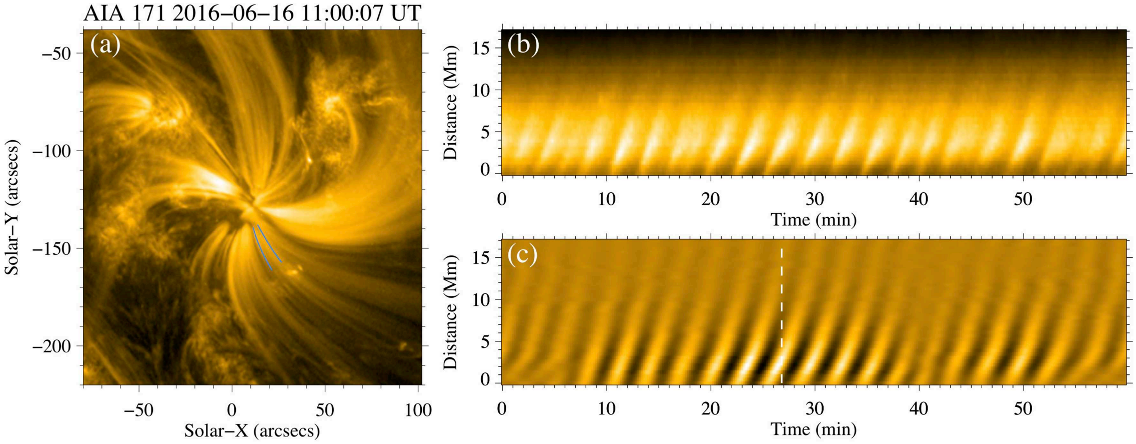

FIGURE 1 | (a) A snapshot of the fan-like loop structures from NOAA AR 12553 captured in the SDO/AIA 171 Å channel. The blue solid lines mark the boundaries of a chosen loop segment. **(b)** Time-distance map depicting the evolution of the loop segment shown in **(a)**. The alternating slanted bands of brightness apparent in this map indicate the presence of propagating compressive oscillations due to slow magnetoacoustic waves. **(c)** Same as **(b)**, but processed to enhance the visibility of the brightness ridges by filtering the time series at each spatial position to allow only a narrow band of frequencies around the dominant oscillation period. The white dashed line marks the temporal location chosen to study the spatial damping characteristics shown in **Figure 2**.

the wave driver, with closely-spaced frequencies causing a beat-like phenomenon (e.g., Krishna Prasad et al., 2015), whereas the spatial damping is mainly due to physical wave dissipation and some geometrical factors. As discussed in section 1, thermal conduction is believed to play a key role in the observed spatial damping.

We identify a total of 35 loop structures from the 30 active regions, where signatures of propagating slow magnetoacoustic waves are prominent. The prominence of oscillations is determined through a visual inspection of time-distance maps constructed from multiple loop structures within each active region. It may be noted that these loop structures are the same as those studied by Krishna Prasad et al. (2018), where the periodicity of the oscillations observed, the temperature and density of the plasma within the loop structures, the polytropic index, among other parameters, are discussed. The temperature, in particular, was derived from the peak location in the corresponding differential emission measure (DEM) curve, which was extracted by employing a regularized inversion method (Hannah and Kontar, 2012) on the near-simultaneously observed intensities across all 6 SDO/AIA coronal channels. However, the main focus in the present study is on the damping characteristics of the oscillations. In order to study the damping properties of slow magnetoacoustic waves across the different loop structures selected, we estimate a characteristic damping length employing two independent methods, namely, a phase tracking method and an amplitude tracking method, as described in the following sections.

3.1. Phase Tracking Method

A temporal location (marked by a white-dashed line in **Figure 1c**), where the oscillation amplitude is relatively strong, is initially chosen to investigate the spatial variation of the oscillation phase. Note that the selection of this location is purely based on the strength of the oscillations as may be seen from **Figure 1c**. Same criterion is applied to all the other loop structures studied. The filtered intensities from three consecutive frames (i.e., ±12 s) around the selected temporal location are averaged to improve the signal-to-noise, then normalized by the corresponding background to construct a representative spatial intensity profile such as that shown in **Figure 2A**. The background is constructed from the intensities obtained by smoothing the original observed values to remove any oscillations with periodicities below 10 min. The spatial profile clearly demonstrates a rapid decrease in the oscillation amplitude with distance along the loop. The vertical bars indicate respective uncertainties in the imaging intensities that are estimated from noise contributions in the SDO/AIA 171 Å channel (following the methodology of Yuan and Nakariakov, 2012), which includes noise from various sources besides the dominant photon and readout components (Jess et al., 2019). An exponentially decaying sine wave function of the form,

$$I(x) = A_0\, e^{\left(\frac{-x}{L_d}\right)} \sin\left(\frac{2\pi x}{\lambda} + \phi\right) + B_0 + B_1 x\,, \tag{1}$$

is fitted to the spatial profile. Here, I is the normalized pixel intensity, x is the distance along the loop, B_0 and B_1 are appropriate constants, and A_0, L_d, λ, and ϕ are the amplitude, damping length, wavelength and phase of the oscillation, respectively. Applying the Levenberg-Marquardt least-squares minimization technique (Markwardt, 2009), the best fitment to the data is shown as a black solid curve in **Figure 2A**. The damping length of the oscillation, as estimated from the fitted curve, is 3.7±0.4 Mm. The orange diamond symbols in **Figure 2B** display the damping lengths obtained from all 35 selected loop structures, plotted as a function of the corresponding localized temperature on a log-log scale. The vertical bars denote the respective uncertainties on damping length derived from the fit whereas the horizontal bars highlight the associated uncertainties on temperature propagated from the respective errors given by the regularized inversion method (Hannah and Kontar, 2012). Since the temperature is determined from a double-Gaussian fit to the individual DEMs (Krishna Prasad et al., 2018), the uncertainty on peak location is estimated by scaling the corresponding error on the nearest point by a factor of $1/\sqrt{N}$, where, N is the number of data points involved in the fit. Subsequently, to get a representative temperature value for each loop, a weighted mean across all spatio-temporal locations near the foot point is considered. The associated uncertainty is then estimated from the weighted standard deviation of values across the same locations. It may be noted that the uncertainties on loop temperature reported by Krishna Prasad et al. (2018) are fairly small compared to those shown here (**Figure 2B**) which is because the authors did not incorporate the temperature errors given by the DEM inversion method but simply quoted the errors obtained from the Gaussian fit alone. The actual temperature values might also marginally differ because of the weighted averages employed here. Another important aspect to note here is that in about 5 cases, the damping lengths are measured from pairs of loops from the same active region some of which exhibit distinct values. The differences in values obtained in such cases reflect the different physical conditions of the loop structures despite belonging to the same active region.

3.2. Amplitude Tracking Method

Since the phase tracking method involves manually choosing a specific temporal location from each of the time-distance maps, it is possible that such human intervention naturally biases the obtained results. Also, it is not trivial to apply this technique to all temporal locations since the signal-to-noise at a large number of locations is low due to aspects of amplitude modulation. To circumvent this problem and verify the reliability of our results, we estimate the damping lengths using the alternative technique of amplitude tracking. In this method, the amplitude of the oscillation, A, at each spatial position is directly measured in relation to the standard deviation, σ, of the respective filtered time series using $A = \sqrt{2}\sigma$. This formula assumes that the observed oscillations can be represented by a pure sinusoidal signal. The time-averaged intensities from the original time series (i.e., collapsing the time domain in **Figure 1b**) are used as the background for normalization to obtain relative amplitudes as a function of distance along the loop. Since the amplitude at each spatial position is derived from the full time series, the median error on respective pixel intensities is used to estimate the corresponding uncertainty. The diamond symbols in **Figure 3A** show the spatial dependence of amplitude values thus obtained for the fan-like loop structure highlighted in **Figure 1a**. The vertical bars represent the associated uncertainties. These data were then fit with a decaying exponential model satisfying the functional form,

$$A(x) = A_0 \, e^{\left(\frac{-x}{L_d}\right)} + C \, , \tag{2}$$

where x is the distance along the loop, A_0 and C are appropriate constants, and L_d is the damping length.

The initial few locations where the wave amplitude is found to increase are ignored in order to isolate the purely decaying phase of the oscillation for fitment. The black solid line in **Figure 3A** represents the best exponential fit obtained. The corresponding damping length is 4.8 ± 1.5 Mm, which is on the same order as that obtained using the phase tracking method outlined in section 3.1. Following the same procedure, the damping lengths for the oscillations observed in all 35 selected loop structures have been estimated. For a handful of loop structures, it is found that the model does not converge properly, producing damping lengths either far greater than the loop length itself ($>$ 1000 Mm) or far less than one pixel ($<$ 0.1 Mm). Upon inspection of the time-distance maps corresponding to these individual cases, we found that there are unusual brightenings, perhaps in the form of transient events manifesting in the loop background, at certain spatio-temporal locations, which naturally contaminate the amplitude extraction process and thereby prevent a robust fitment of the data. While this could be avoided by manually restricting the time series for each particular case, the main strength of this method was in the alleviation of human intervention. As such, we chose to ignore specific loop structures where the model fitting did not converge to commonly expected values. The orange diamond symbols in **Figure 3B** represent the damping lengths obtained from the remaining 31 cases, plotted as a function of the loop temperature on a log-log scale. The vertical bars highlight the corresponding uncertainties on damping length whereas the horizontal bars denote the respective uncertainties on temperature. The loop temperature and the associated uncertainties are estimated in the same way as that described in section 3.1.

3.3. Theoretical Calculations

Theoretical and numerical calculations in the past have suggested that thermal conduction is the dominant physical mechanism responsible for the damping of slow magnetoacoustic waves in the solar corona (De Moortel and Hood, 2003; Klimchuk et al., 2004). Considering one-dimensional linear wave theory for slow magnetoacoustic waves with thermal conduction as the damping mechanism (e.g., De Moortel and Hood, 2003; Krishna Prasad et al., 2012b), the dispersion relation between the wave number, k, and the angular frequency, ω, can be shown to be,

$$d c_\mathrm{s}^4 k^4 + i\omega c_\mathrm{s}^2 k^2 - \gamma d \omega^2 c_\mathrm{s}^2 k^2 - i\omega^3 = 0 \, . \tag{3}$$

Here, c_s is the sound speed, $d = \frac{(\gamma-1)\kappa_\parallel T_0}{\gamma c_\mathrm{s}^2 p_0}$ is the thermal conduction parameter, $\kappa_\parallel = \kappa_0 T_0^{5/2}$ is the parallel thermal conduction, and $p_0 = 2 n_0 k_B T_0$ is the gas pressure, where κ_0 is the thermal conduction coefficient, T_0 is the equilibrium temperature, and n_0 is the number density. For propagating waves, the frequency, ω, is constant and in the limit of weak thermal conduction (i.e., when $d\omega \ll 1$), the solutions for wave number, k, may be found as $k = \frac{\omega}{c_\mathrm{s}} - i\frac{1}{L_\mathrm{d}}$, where $L_\mathrm{d} = \frac{2c_\mathrm{s}}{d\omega^2(\gamma-1)}$ is the damping length. The interested reader is referred to Mandal et al. (2016) for a detailed derivation.

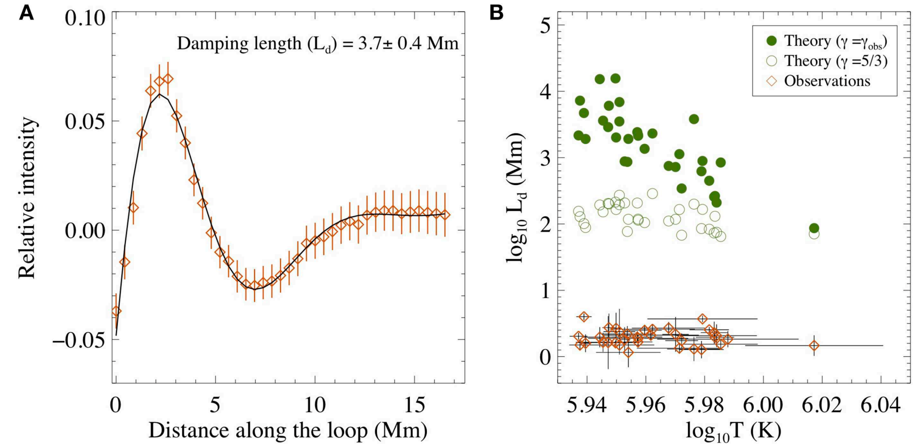

FIGURE 2 | (A) Spatial variation of the relative intensity at the temporal location marked by the white dashed line in **Figure 1c**. The vertical bars denote the respective uncertainties. The solid curve represents the best fit to the data for an exponentially decaying sine wave model following Equation (1). The obtained damping length value from the fitted curve is listed in the upper-right corner of the plot. **(B)** Damping lengths extracted from all of the selected loop structures, plotted as a function of the localized temperature on a log-log scale. The orange diamonds represent the values obtained following the phase tracking method shown in **(A)**, whereas the green circles represent the theoretical values estimated from damping due to thermal conduction. The open and filled circles, respectively, highlight the values computed from a constant γ (= 5/3) and those computed using γ values extracted from observations (Krishna Prasad et al., 2018). The vertical and horizontal bars on the observed values denote the corresponding propagated uncertainties.

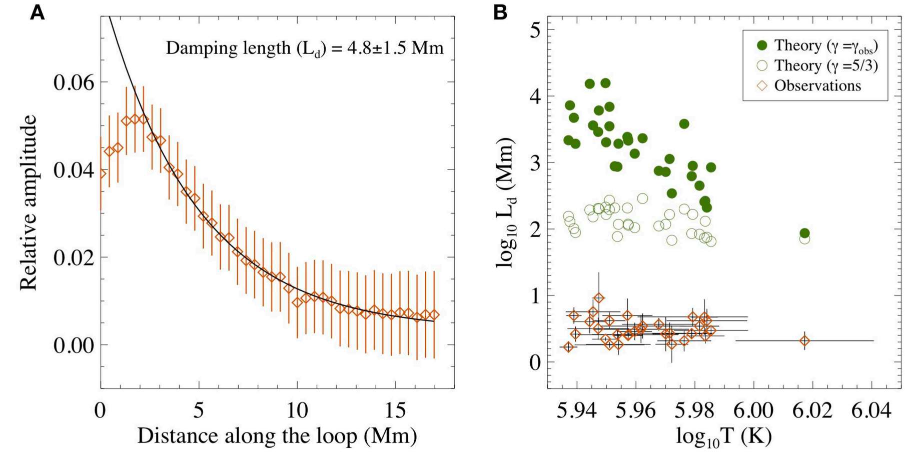

FIGURE 3 | (A) Relative amplitudes of the oscillations as a function of distance along the loop segment marked by the solid blue lines in **Figure 1a**. The vertical bars denote the respective uncertainties. The black solid line represents an exponential fit to the decaying phase of the data following Equation (2). The obtained damping length value from the fitted curve is listed in the plot. **(B)** Damping lengths extracted from all the selected loop structures plotted as a function of the local temperature on a log-log scale. The orange diamonds represent the observational values following the amplitude tracking method shown in **(A)**, whereas the green circles represent the theoretical values estimated from the damping due to thermal conduction. The open and filled circles, respectively, highlight the values computed from a constant γ (= 5/3) and those computed using γ values extracted from observations (Krishna Prasad et al., 2018). The vertical and horizontal bars on the observed values denote the corresponding uncertainties.

As described in section 3, Krishna Prasad et al. (2018) studied the same set of loop structures that are presented here. They applied a regularized inversion method (Hannah and Kontar, 2012) on observed intensities in 6 coronal channels of SDO/AIA to compute corresponding DEM. Subsequently, by employing a double-Gaussian fit to the DEM curve, the temperature and the density of the plasma are calculated from the peak location and the area under the curve, respectively. The density is estimated by assuming the apparent width of the loop as equivalent to the emission depth along the line of sight effectively ignoring any background/foreground emission although a contribution to the latter from hot plasma is carefully discarded from the double-Gaussian fit. Using the theoretical relation between the relative oscillation amplitudes in temperature and density associated with a slow wave, the polytropic index of the plasma is determined after eliminating the corresponding phase shifts. The periodicity of the oscillations is also calculated through a simple Fourier analysis on the intensity fluctuations. Utilizing the respective values of these parameters computed by Krishna Prasad et al. (2018) for each loop, we estimate the expected damping lengths from the above theory.

The filled green circle symbols shown in **Figures 2B**, **3B** represent the theoretically computed values. It may be noted that the respective $d\omega$ values were found to reside in the interval $0.01 - 0.16$, so the assumption of weak thermal conduction (i.e., $d\omega \ll 1$) is inherently valid across our range of coronal datasets. The classical Spitzer values for thermal conduction, following $\kappa_{\parallel} = 7.8 \times 10^{-7} T_0^{5/2}$ ergs cm^{-1} s^{-1} K^{-1}, are employed in our calculations. As can be seen from the figures, the damping lengths are expected to be considerably shorter for hotter loops. Since it is very common to assume the polytropic index, γ, is equal to 5/3 in the solar corona, we additionally compute damping lengths arising from a constant (5/3) value for γ. The open green circles shown in **Figures 2B**, **3B** represent these values which suggest a similar but much shallower dependence on temperature. Moreover, the damping lengths in this case are shorter by up to an order of magnitude or more which clearly divulges the effect of polytropic index on the damping length. It is worth noting here that the scatter in the theoretically computed damping lengths is mainly due to the different physical conditions of the loop structures studied.

4. DISCUSSION AND CONCLUDING REMARKS

The spatial damping characteristics of propagating slow magnetoacoustic waves, observed in 35 fan-like loop structures selected from 30 different active regions, have been studied. The damping length, in particular, is measured using two independent methods: a phase tracking method and an amplitude tracking method. Employing the temperature information acquired from DEM analysis, the temperature dependence of the damping length has been investigated for the first time (**Figures 2B**, **3B**). These results do not indicate any apparent decrease in damping length with temperature as would be expected by the stronger thermal conduction in that case. It may be noted that the results from previous studies (e.g., Krishna Prasad et al., 2012b), who based their conclusions on the measurement of damping lengths for a single loop structure observed in multiple temperature channels, are inconsistent with the current findings. However, those studies are purely qualitative and the results are often based on just two temperature channels. Furthermore, the sensitivities of the measured damping lengths from the intensity perturbations to the filter/instrument used (e.g., Klimchuk et al., 2004) are also not taken into consideration in previous studies. In the present case, we employ damping length measurements from multiple loop structures observed in the same filter (SDO/AIA 171 Å). Hence, we naturally consider the current results more reliable due to the conservation of instrument characteristics across all independent measurements.

Utilizing the temperatures, densities, polytropic indices, and oscillation periods that have previously been derived for the same set of loop structures (Krishna Prasad et al., 2018), we calculated the theoretical damping lengths expected from the dissipation due to thermal conduction. In contrast to the observations, the theoretical calculations show a steep decrease in the damping length with temperature. Damping lengths were also computed assuming a fixed value, 5/3, for the polytropic index, in line with the previous studies. These values display a similar but shallower dependence. The discrepancy between the observational and theoretical dependences perhaps indicates that thermal conduction is suppressed in hotter loop structures. In fact, the increase in the polytropic indices of these loops with temperature, as reported by Krishna Prasad et al. (2018), also implies the suppression of thermal conduction in hotter loops (e.g., in accordance with Wang et al., 2015), although a direct conclusion could not be drawn from these results alone since the polytropic index of the coronal plasma is dependent on several other physical processes besides thermal conduction. The current results, on the other hand, appear to show direct evidence for the suppression of thermal conduction with increasing temperature.

Alternatively, one could argue that thermal conduction is perhaps not the dominant damping mechanism for slow magnetoacoustic waves, as previously reported by Marsh et al. (2011) and Wang et al. (2015). Indeed, as can be seen from **Figures 2B**, **3B**, the theoretical damping lengths are $2 - 3$ orders of magnitude higher than those obtained from the observations. One may also note that a simple visual inspection of oscillation amplitudes, in **Figures 1b,c** for example, reveals significant damping within 10 Mm scales whereas the expected damping lengths due to thermal conduction are at least 100 Mm or more which clearly demonstrates the extent of mismatch between the observations and the theory. The differences in the temperature dependence would further add to this discrepancy. We note, however, that the incongruity between the theory and observations is less if we consider the calculations for $\gamma = 5/3$. Also, the distances measured along the observed loop structures are projected onto the image plane, meaning the obtained damping lengths are only lower limits. Nevertheless, the difference between the theoretical and the observed scales is too large to ignore, and would not likely be accounted for even if a fractional contribution from the other damping mechanisms (e.g., compressive viscosity and optically thin radiation) is included.

Lastly, we would like to bring out some of the major caveats of our results. The temperature range of the loops investigated is limited especially considering the large uncertainties on temperature. While the magnitude of change in the expected damping lengths over the same temperature range and the extent of mismatch between the observed and theoretical values still make our results valid, it is imperative to state that a larger temperature range would make the results more reliable. Additionally, it should be noted that different DEM inversion methods can result in different peak temperatures although the difference can be marginal depending on the temperature range investigated. Also, it can be argued whether the peak emission in a DEM sufficiently represents the plasma within the loop. Keeping these limitations in mind, we believe further investigations, both theoretical and observational, are necessary to understand the damping of slow magnetoacoustic waves in the solar corona. In particular, the impetus is on increasing the temperature range studied to include hotter loop structures to examine whether these traits are consistent across the full spectrum of coronal magnetism.

DATA AVAILABILITY

The data analyzed in this study was obtained by the Atmospheric Imaging Assembly onboard NASA's Solar Dynamics Observatory. The data are not restricted, and requests to access these datasets should be directed to the Joint Science Operations Center (http://jsoc.stanford.edu/ajax/lookdata.html).

AUTHOR CONTRIBUTIONS

SK and DJ planned and designed the study. SK processed the data, performed the analysis and wrote the first draft of the manuscript. TV assisted in theoretical calculations. DJ and TV contributed to the interpretation of the results. All authors took part in the manuscript revision, read and approved the submitted version.

FUNDING

The authors gratefully acknowledge the financial support from the following research grants: STFC—ST/K004220/1, ST/L002744/1, ST/R000891/1, Randox Laboratories Ltd.—059RDEN-1, European Research Council (ERC)—724326, and KU Leuven—GOA-2015-014.

ACKNOWLEDGMENTS

The authors thank all the referees for their valuable comments/suggestions. SK would like to thank the UK Science and Technology Facilities Council (STFC) for support. DJ gratefully acknowledges STFC for the award of an Ernest Rutherford Fellowship, in addition to Invest NI and Randox Laboratories Ltd. for the award of a Research & Development Grant (059RDEN-1). This project has received funding from the European Research Council (ERC) under the European Union's Horizon 2020 research and innovation programme and KU Leuven. The SDO/AIA imaging data employed in this work are courtesy of NASA/SDO and the AIA science team. We acknowledge the use of pipeline developed by Rob Rutten to extract, process, and co-align AIA cutout data.

REFERENCES

Banerjee, D., and Krishna Prasad, S. (2016). "MHD waves in coronal holes," in *Low-Frequency Waves in Space Plasmas*, eds A. Keiling, D.-H. Lee, and V. Nakariakov, 419–430. doi: 10.1002/9781119055006.ch24

Berghmans, D., and Clette, F. (1999). Active region EUV transient brightenings - First Results by EIT of SOHO JOP80. *Solar Phys.* 186, 207–229.

Cally, P. S., Bogdan, T. J., and Zweibel, E. G. (1994). Umbral oscillations in sunspots: absorption of p-modes and active region heating by mode conversion. *Astrophys. J.* 437, 505–521. doi: 10.1086/175014

Culhane, J. L., Harra, L. K., James, A. M., Al-Janabi, K., Bradley, L. J., Chaudry, R. A., et al. (2007). The EUV imaging spectrometer for Hinode. *Solar Phys.* 243, 19–61. doi: 10.1007/s01007-007-0293-1

De Moortel, I. (2009). Longitudinal Waves in Coronal Loops. *Space Sci. Rev.* 149, 65–81. doi: 10.1007/s11214-009-9526-5

De Moortel, I. and Hood, A. W. (2003). The damping of slow MHD waves in solar coronal magnetic fields. *Astron. Astrophys.* 408, 755–765. doi: 10.1051/0004-6361:20030984

De Moortel, I. and Hood, A. W. (2004). The damping of slow MHD waves in solar coronal magnetic fields. II. The effect of gravitational stratification and field line divergence. *Astron. Astrophys.* 415, 705–715. doi: 10.1051/0004-6361:20034233

De Moortel, I., Ireland, J., and Walsh, R. W. (2000). Observation of oscillations in coronal loops. *Astron. Astrophys.* 355, L23–L26. Available online at: https://ui.adsabs.harvard.edu/abs/2000A%26A...355L..23D/abstract

De Pontieu, B., Erdélyi, R., and De Moortel, I. (2005). How to channel photospheric oscillations into the corona. *Astrophys. J. Lett.* 624, L61–L64. doi: 10.1086/430345

Deforest, C. E., and Gurman, J. B. (1998). Observation of quasi-periodic compressive waves in solar polar plumes. *Astrophys. J. Lett.* 501:L217. doi: 10.1086/311460

Erdélyi, R. (2006). "Magnetic seismology of the lower solar atmosphere," in *Proceedings of SOHO 18/GONG 2006/HELAS I, Beyond the Spherical Sun*, Vol. 624 (Noordwijk: ESA Special Publication), 15.1

Hannah, I. G., and Kontar, E. P. (2012). Differential emission measures from the regularized inversion of Hinode and SDO data. *Astron. Astrophys.* 539:A146. doi: 10.1051/0004-6361/201117576

Jess, D. B., De Moortel, I., Mathioudakis, M., Christian, D. J., Reardon, K. P., Keys, P. H., et al. (2012). The source of 3 minute magnetoacoustic oscillations in coronal fans. *Astrophys. J.* 757:160. doi: 10.1088/0004-637X/757/2/160

Jess, D. B., Dillon, C. J., Kirk, M. S., Reale, F., Mathioudakis, M., Grant, S. D. T., et al. (2019). Statistical signatures of nanoflare activity. I. Monte Carlo simulations and parameter-space exploration. *Astrophys. J.* 871:133. doi: 10.3847/1538-4357/aaf8ae

Khomenko, E., Centeno, R., Collados, M., and Trujillo Bueno, J. (2008). Channeling 5 minute photospheric oscillations into the solar outer atmosphere through small-scale vertical magnetic flux tubes. *Astrophys. J. Lett.* 676:L85. doi: 10.1086/587057

Kiddie, G., De Moortel, I., Del Zanna, G., McIntosh, S. W., and Whittaker, I. (2012). Propagating disturbances in coronal loops: a detailed analysis of propagation speeds. *Solar Phys.* 279, 427–452. doi: 10.1007/s11207-012-0042-5

Klimchuk, J. A., Tanner, S. E. M., and De Moortel, I. (2004). Coronal seismology and the propagation of acoustic waves along coronal loops. *Astrophys. J.* 616, 1232–1241. doi: 10.1086/425122

Krishna Prasad, S., Banerjee, D., and Singh, J. (2012a). Oscillations in active region fan loops: observations from EIS/ hinode and AIA/SDO. *Solar Phys.* 281, 67–85. doi: 10.1007/s11207-012-0098-2

Krishna Prasad, S., Banerjee, D., and Van Doorsselaere, T. (2014). Frequency-dependent damping in propagating slow magneto-acoustic waves. *Astrophys. J.* 789:118. doi: 10.1088/0004-637X/789/2/118

Krishna Prasad, S., Banerjee, D., Van Doorsselaere, T., and Singh, J. (2012b). Omnipresent long-period intensity oscillations in open coronal structures. *Astron. Astrophys.* 546:A50. doi: 10.1051/0004-6361/201219885

Krishna Prasad, S., Jess, D. B., and Khomenko, E. (2015). On the source of propagating slow magnetoacoustic waves in sunspots. *Astrophys. J. Lett.* 812:L15. doi: 10.1088/2041-8205/812/1/L15

Krishna Prasad, S., Jess, D. B., Van Doorsselaere, T., Verth, G., Morton, R. J., Fedun, V., et al. (2017). The frequency-dependent Damping of Slow Magnetoacoustic Waves in a Sunspot Umbral Atmosphere. *Astrophys. J.* 847:5. doi: 10.3847/1538-4357/aa86b5

Krishna Prasad, S., Raes, J. O., Van Doorsselaere, T., Magyar, N., and Jess, D. B. (2018). The polytropic index of solar coronal plasma in sunspot fan loops and its temperature dependence. *Astrophys. J.* 868:149. doi: 10.3847/1538-4357/aae9f5

Lemen, J. R., Title, A. M., Akin, D. J., Boerner, P. F., Chou, C., Drake, J. F., et al. (2012). The atmospheric imaging assembly (AIA) on the solar dynamics observatory (SDO). *Solar Phys.* 275, 17–40. doi: 10.1007/s11207-011-9776-8

Mandal, S., Magyar, N., Yuan, D., Van Doorsselaere, T., and Banerjee, D. (2016). Forward modeling of propagating slow waves in coronal loops and their frequency-dependent damping. *Astrophys. J.* 820:13. doi: 10.3847/0004-637X/820/1/13

Markwardt, C. B. (2009). "Non-linear least-squares fitting in IDL with MPFIT," in *Astronomical Data Analysis Software and Systems XVIII, Astronomical Society of the Pacific Conference Series*, Vol. 411, eds D. A. Bohlender, D. Durand, and P. Dowler (Quebec City, QC), 251.

Marsh, M. S., De Moortel, I., and Walsh, R. W. (2011). Observed damping of the slow magnetoacoustic mode. *Astrophys. J.* 734:81. doi: 10.1088/0004-637X/734/2/81

Ofman, L., Romoli, M., Poletto, G., Noci, G., and Kohl, J. L. (1997). Ultraviolet coronagraph spectrometer observations of density fluctuations in the solar wind. *Astrophys. J. Lett.* 491:L111. doi: 10.1086/311067

Pesnell, W. D., Thompson, B. J., and Chamberlin, P. C. (2012). The solar dynamics observatory (SDO). *Solar Phys.* 275, 3–15. doi: 10.1007/s11207-011-9841-3

Spruit, H. C. (1991). "Absorption of p-mode waves by magnetic fields. in *Challenges to Theories of the Structure of Moderate-Mass Stars*, *Lecture Notes in Physics*, Vol. 388, eds D. Gough and J. Toomre (Berlin: Springer Verlag), 121–134.

Van Doorsselaere, T., Wardle, N., Del Zanna, G., Jansari, K., Verwichte, E., and Nakariakov, V. M. (2011). The first measurement of the adiabatic index in the solar corona using time-dependent spectroscopy of hinode/EIS observations. *Astrophys. J. Lett.* 727:L32. doi: 10.1088/2041-8205/727/2/L32

Wang, T. (2011). Standing slow-mode waves in hot coronal loops: observations, modeling, and coronal seismology. *Space Sci. Rev.* 158, 397–419. doi: 10.1007/s11214-010-9716-1

Wang, T., Ofman, L., Sun, X., Provornikova, E., and Davila, J. M. (2015). Evidence of thermal conduction suppression in a solar flaring loop by coronal seismology of slow-mode waves. *Astrophys. J. Lett.* 811:L13. doi: 10.1088/2041-8205/811/1/L13

Wang, T., Ofman, L., Sun, X., Solanki, S. K., and Davila, J. M. (2018). Effect of transport coefficients on excitation of flare-induced standing slow-mode waves in coronal loops. *Astrophys. J.* 860:107. doi: 10.3847/1538-4357/aac38a

Wuelser, J.-P., Lemen, J. R., Tarbell, T. D., Wolfson, C. J., Cannon, J. C., Carpenter, B. A., et al. (2004). "EUVI: the STEREO-SECCHI extreme ultraviolet imager," in *Proceedings of the SPIE Telescopes and Instrumentation for Solar Astrophysics*, Vol. 5171, eds S. Fineschi and M. A. Gummin, 111–122. doi: 10.1117/12.506877

Yuan, D., and Nakariakov, V. M. (2012). Measuring the apparent phase speed of propagating EUV disturbances. *Astron. Astrophys.* 543:A9. doi: 10.1051/0004-6361/201218848

Zavershinskii, D. I., Kolotkov, D. Y., Nakariakov, V. M., Molevich, N. E., and Ryaschikov, D. S. (2019). Formation of quasi-periodic slow magnetoacoustic wave trains by the heating/cooling misbalance. *arXiv:1907.08168*.

Conflict of Interest Statement: The authors declare that the research was conducted in the absence of any commercial or financial relationships that could be construed as a potential conflict of interest.

Advantages of publishing in Frontiers

OPEN ACCESS
Articles are free to read for greatest visibility and readership

FAST PUBLICATION
Around 90 days from submission to decision

HIGH QUALITY PEER-REVIEW
Rigorous, collaborative, and constructive peer-review

TRANSPARENT PEER-REVIEW
Editors and reviewers acknowledged by name on published articles

Frontiers
Avenue du Tribunal-Fédéral 34
1005 Lausanne | Switzerland

Visit us: www.frontiersin.org
Contact us: info@frontiersin.org | +41 21 510 17 00

REPRODUCIBILITY OF RESEARCH
Support open data and methods to enhance research reproducibility

DIGITAL PUBLISHING
Articles designed for optimal readership across devices

FOLLOW US
@frontiersin

IMPACT METRICS
Advanced article metrics track visibility across digital media

EXTENSIVE PROMOTION
Marketing and promotion of impactful research

LOOP RESEARCH NETWORK
Our network increases your article's readership